University of Rome
"Tor Vergata"

Faculty of Engineering

Wireless Technologies for Future Multi-Gigabit Communications Beyond 60 GHz

Design Issues and Performance Analysis for Terrestrial and Satellite Applications

Thesis submitted for the Degree of

Doctor of Philosophy in

"Telecommunications and Microelectronic Engineering"

Candidate

Eng. Cosimo Stallo

Tutor

Prof. Marina Ruggieri

Coordinator

Prof. Giuseppe Bianchi

XXII PHD CYCLE

Academic Year 2009-2010

Acknowledgements

Throughout my all life I have found there are several constants, which I feel should be acknowledged first and foremost because without them, I would not have been able to write this thesis. The most significant go to my family, to which I will be forever grateful. My parents have been my backbone from the very start and still continue to provide me love and support every day. I truly believe it is impossible to have better parents than I have. Mother, there are no words to describe how much I love you and appreciate the guidance you have given me over the years. Father, if I am half the man you are one day, I will have led a very successful life. I certainly need to thank my brother, Giuseppe, who means the world to me, as he has been a nuisance, a model, and a "comedian" at the same time, but most importantly he has been my best friend. To my aunt Anna, who has a heart of gold, I could not imagine being where I am at today if it were not for you as well.

In particular, I need to thank my girlfriend, Marianna, who has provided me with the encouragement necessary for me to succeed, as well as having the patience to deal with the amount of time that comes with success. With all of your love and support, I consider myself the luckiest man in the world. It has truly been an honor to have you by my side and I hope to continue our relationship for many years to come.

Last but definitely not least, my professional thanks start to Professor Marina Ruggieri, who has given me this research opportunity and offered her guidance along the way. She taught me the fundamentals of research as well as valuable life lessons that will never be forgotten. I have learned a great deal from her and I am very appreciative of the commitment she has not only shown me, but to every student who walks through her door despite her busy schedule.

I would also like to express my gratitude to my colleagues, Dr. Ernestina Cianca, Dr. Mauro De Sanctis, Dr. Tommaso Rossi, Dr. Marco Lucente, and Dr. Sandeep Mukherjee, who have taken the time to help me throughout these three years. Ernestina Cianca deserves as much credit as anyone for her help in creating the design presented in this thesis and her support in being a real mentor to me.

These people I have mentioned have done more work for me than I have done for this degree. Therefore, I will not see my name on the diploma, but a list of names who contributed much more than myself. I consider it to be as much theirs as it is mine.

Abstract

Demand for very high-speed wireless communications is proportionally growing with respect to the increasing data rates reachable by optical fibers. In fact, the emerging research trend in computer networks is to cut more and more cables and to provide mobile and nomadic users with a data rate at least comparable with that one of wired Ethernet. GbE standard is now widespread and 10 GbE standard has been available since 2002.

While established and well-known fiber-optic data-transfer devices can provide multigigabit per second data rates, infrastructure costs and deployment time can be too expensive for some applications. Wireless links can be used to bridge the gaps in the fiber network and they can be deployed very rapidly, without the need for costly and complex trenching actions. Multigigabit wireless applications will include fiber segment replacement in future 3G and 4G backhauls, in distributed antenna systems, in enterprise connectivity, and in consumer-level applications, such as HDTV. Future home and building environments are a domain where, in the coming decade, large quantitative and qualitative changes can be expected in services and applications, that ultimately will benefit from wireless multigigabit/s communication. Therefore, the need for such high data rates arises both in short-range scenarios and in medium-long range scenarios.

Where a very huge bandwidth for multigigabit wireless communications can be made available as free spectrum without interference issues? The unique possibility is to look at EHF. Recently, there has been a lot of interest in the development of 60 GHz systems for the indoor [I] and outdoor [II] applications, because this bandwidth has been allocated in many countries as free spectrum. However, because of higher propagation loss due to oxygen absorption at this band, it is not suitable for very long links.Further, the FCC has made available 13 GHz of spectrum in the 70-95 GHz (away from the oxygen absorption band, in order to facilitate longer range communication) for semi-unlicensed use for directional point-to-point “last mile” links. However, above 60 GHz, both for long and short range, there is a lack of discussion on modulation, equalization, and algorithm design at physical layer. This work mainly aims at investigating the possibility to use innovative and advanced radio interfaces, as one based on IR UWB transmission technique, to realise multigigabit/s communications beyond 60 GHz [IV], [V]. In particular, this work shows how an IR UWB communication system is sensitive to typical H/W not

idealities beyond 60 GHz (Phase Noise, Timing Jitter, LNA and HPA distortions) and compares its performance with the ones of a more classical continuous wave communications system based on FSK modulation.

The exploitation of such higher frequencies represents the most suitable solution to develop a cooperative global information infrastructure in order to guarantee the so-called "Gigabit Connectivity" through aerospace links making such a radio segment a potential "backbone on the air" for global wireless connectivity. Therefore, the use of "beyond Q/V bands" will be the necessary condition to develop a multipurpose network, as integration of terrestrial and space systems, in order to support forthcoming high-data-rate services demands. W band (75-110 GHz, respectively 4 -2.7 mm) could represent the answer to these needs due to the high bandwidth availability, short wavelength, reduced interference, small antenna size, allowing to propose many innovative services that need high-volume transfers. Currently, however, the performance behaviour of any solution for data transportation over W band frequencies across the Troposphere is still unknown, since no scientific and/or telecommunication mission has been realised, either on an experimental basis or in an operating mode. Therefore, missions in W band have to be studied in order to perform a first empirical evaluation of the Troposphere effects on the radio channel. Consequently, the last part of this work has been focused on the analysis and performance evaluation of future missions for the exploitation of W band too for satellite communications aiming at designing a full line of P/Ls operating in such a frequency range [VI], [VII]. The design and performance analysis of missions to perform a first empirical evaluation of the Troposphere effects on the W band radio channel represent the preliminary useful step for realising a "System of Systems" which is able to meet the high-quality data transmission requirements for a large number of end-users and data-oriented services.

REFERENCES

I. S. K. Yong and C. C. Chong, “An Overview of Multigigabit Wireless Through Millimeter Wave Technology: Potentials and Technical Challenges,” EURASIP Journal Wireless Communications, ID 78907, 2007.

II. K. Ohata, K. Maruhashi, M. Ito, S. Kishimoto, K. Ikuina, T. Hashiguchi, K. Ikeda, and N. Takahashi, “1.25 Gbps Wireless Gigabit Ethernet Link at 60 GHz-band,” in Proceedings of IEEE RFIC Symposium, Jun. 2003, pp. 509–512, Paper TU4D-6.

III. V. Dyadyuk, J. D. Bunton, J. Pathikulangara, R. Kendall, O. Sevimli, L. Stokes, and D. A. Abbott, “A Multigigabit Millimeter-Wave Communication System with Improved Spectral Efficiency” , IEEE Transactions on Microwave Theory and Techniques, Vol. 55, No. 12, December 2007.

IV. C. Sacchi, T. Rossi, M. Menepace, F. Granelli, "Utilization of UWB Transmission Techniques for Broadband Satellite Connections operating in W-band", IEEE GLOBECOMM Workshop of Exploitation of Higher Frequency Bands in Broadband Aerospace Communications, New Orleans, Nov., 30, 2008.

V. C. Stallo, E. Cianca, M. De Sanctis, T. Rossi, D. Valente, S. Mukherjee, M. Ruggieri, “UWB for multi-gigabit communications in EHF-band”, Proceedings of the Networking and Electronic Commerce Research Conference (NAEC 2009), October 8-11, 2009, in Riva Del Garda, Italy, pp. 294-303.

VI. C. Sacchi, G. Gera, C. S. Regazzoni, “W-band physical layer design issues in the context of the DAVID-DCE experiment”, International Journal of Satellite Communications, Vol. 22, Issue 2, 2004.

VII. M. Lucente, T. Rossi, T., C. Stallo, E. Cianca, ”WAVE phase A2, Final Report”, University of Rome “Tor Vergata”, 2008.

Table of Contents

Index of Figures

INDEX OF TABLES

ABBREVIATIONS AND ACRONYMS

ACM	Adaptive and Coding Modulation
AD	Applicable Document
ADC	Analog to Digital Converter
ADS	Advanced Design Systems
AFSPC	Air Force Space Command
AGC	Automatic Gain Control
ALC	Automatic Level Control
AO	Any Option
AOCS	Attitude and Orbit Control Subsystem
ARU	Automatic Restart Unit
ASI	Italian Space Agency
ASK	Amplitude Shift Keying
AWGN	Additive White Gaussian Noise
BDUA	Broadband Distributed User Access
BER	Bit Error Rate
BFN	Beam Forming Network
BI-L	Bi-level
BiCMOS	Bipolar Complementary Metal Oxide Semiconductor
BMSS	Broadband Multimedia Satellite Systems
BPE	Beam Pointing Error
BPF	Band Pass Filter
BPSK	Binary Phase Shift Keying
BSS	Broadcasting Satellite Services
BTN	Baia Terra Nova
CAMP	Channel Amplifier
C/N	Carrier to Noise Ratio
COAX	Coaxial Cable
COTS	Commercial Off The Shelf

CMOS	Complementary Metal Oxide Semiconductor
CEM	Constant Envelope Modulation
CPM	Continuos Phase Modulation
CPS	Content Provider Station
CW	Continuous Wave
DAVID	DAta and Video Interactive Distribution
DCE	Data Collection Experiment
DDS	Direct Digital Synthesis
DRS	Data Relay Satellites
DSP	Digital Signal Processing
DSSS	Direct Sequence Spread Spectrum
DTR	Digital Tracking Receiver
DVB-RCS	Digital Video Broadcasting Return Channel Satellite
DVBS-2	Digital Video Broadcasting Satellite Second Generation
EHF	Extremely High Frequency
EIRP	Effective Isotropic Radiated Power
EOC	Edge Of Coverage
EOL	End of Life
EPC	Electronic Power Conditioner
EQM	Engineering Qualification Model
ERO	European Communication Office
ESA	European Space Agency
ETSI	European Telecommunications Standardization Institute
FCC	Federal Communication Commission
FD	Frequency Doubler
FDMA	Frequency Division Multiple
FEC	Forward Error Correction
FHSS	Frequency Hopping Spread Spectrum
FFT	Fast Fourier Transform
FOM	Figure Of Merit
FSK	Frequency Shift Keying

FSS	Fixed Satellite Services
G/T	Gain over System Noise Temperature Ratio
GaAs	Gallium Arsenide
GEO	Geostationary Earth Orbit
GESN	Global Extremely High Frequency Satellite Network
GbE	Gigabit Ethernet
GII	Global Information Infrastructure
GS	Ground Segment
GW	Gateway
HAP	High Altitude Platform
HBT	Heterojunction Bipolar Transistor
HDMI	High-Definition Multimedia Interface
HDTV	High Definition Television Transmission
HEMT	High Electron Mobility Transistor
HEO	Highly Elliptical Orbit
HPA	High Power Amplifier
HPBW	Half Power Beam Width
HSC	Hughes Space and Communications Company
H/W	Hardware
JAXA	Japan Aerospace Exploration Agency
IFFT	Inverse Fast Fourier Transform
IFMT	Interference and Fading Mitigation Technique
IIN	Integrated Interplanetary Network
IKNOW	In-orbit Key test and validatioN Of W-band
IKPL	IKnow PayLoad
IKSAT	Iknow SATellite
IMUX	Input Multiplexer
InP	Indium Phosphide
IPFD	Input Power Flux Density
IC	Integrated Circuit
IIN	Integrated Inter-Planetary Network

IPL	Inter-Planetary Link
I/Q	In-Phase/Quadrature-Phase
IR	Impulse Radio
ISI	Inter Symbol Interference
ISL	Inter-Satellite Link
ISM	Industrial, Scientific and Medical
IT	Information Technology
ITS	Intelligent Transportation Systems
ITU	International Telecommunication Union
LDPC	Low-Density Parity-Check
LEO	Low Earth Orbit
LNA	Low Noise Amplifier
LO	Local Oscillator
LOS	Line of Sight
LPF	Low Pass Filter
MAX	Maximum Available Gain
MEMS	Micro Electro-Mechanical Systems
MEO	Medium Earth Orbit
MER	Modulation Error Ratio
MIMO	Multiple Input Multiple Output
MMIC	Monolithic Microwave Integrated Circuit
MPA	Medium Power Amplifier
MT	Mobile Terminal
NA	Not Applicable
NASDA	National Space Development Agency
NCA	National Command Authority
NDR	Negative Differential Resistance
NF	Noise Figure
NGSO	Non Geostationary Orbit
NLOS	Not Line of Sight

NMOS	N-channel Metal Oxide Semiconductor
OBC	On-Board Computer
OBDH	On-Board Data Handling
OBP	On Board Processing
OFB	Over Full Bandwidth
OFDM	Orthogonal Frequency-Division Multiplexing
OFTR	Over Full Temperature Range
OMT	Ortho Mode Transducer
OMUX	Output Multiplexer
P/L	Payload
PA	Power Amplifier
PAPR	Peak to Average Power Ratio
Pe	Probability of Error
PER	Packet Error Rate
PERLA-W	Propagation Experiment for a Radio Link Analysis at W band
PFM	Proto Flight Model
PG	Pulse Generator
PLC	PayLoad Controller
PIMTs	Propagation Impairments Mitigation Techniques
PLDRO	Phase Locked Dielectric Resonator Oscillator
PN	Pseudo Noise
PPM	Pulse Position Modulation
PRF	Pulse Repetition Frequency
PSK	Phase Shift Keying
PSU	Power Supply Unit
QFD	Quality Function Deployment
QoS	Quality of Service
QZSS	Quasi-Zenith Satellite System
RD	Reference Document
RF	Radio Frequency

RMS	Root Mean Square
RSE	Resource Sharing Experiment
SC	Single Carrier
SCM	Single Carrier Modulation
SDE	Source-Drain Extension
SDR	Sequence Determined Redundancy
S/H	Sample/Hold
SHA	Sample/Hold Amplifier
SHF	Super High Frequency
SiGe	Silicon Germanium
SIT	Satellite Interactive Terminal
SIW	Substrate Integrated Waveguide
SNR	Signal to Noise Ratio
SSPA	Solid State Power Amplifier
TBC	To be Confirmed
TBD	To Be Defined
TDMA	Time Division Multiplexing Access
TH	Time Hopping
THz	TeraHertz
TI	Time Interleaved
TLC	Telecommunications
TLM	Telemetry
TT&C	Telemetry, Tracking and Command
TWTA	Travelling Wave Tube Amplifier
U.S.	United States
UB	Useful Bandwidth
UHF	Ultra High Frequency
UWB	Ultra Wide Band
VBS	V-Band Supplement
VSA	Vector Signal Analyzer
VSWR	Voltage Standing Wave Ratio

WAVE	W-band Analysis and VErification
w.r.t	With Respect To
WG	Waveguide
Wi-Fi	Wireless Fidelity
WiMAX	Worldwide Interoperability for Microwave Access
WLAN	Wireless Local Area Network
WPAN	Wireless Personal Area Network
XPD	Cross-Polar Discrimination
3G	Third Generation
4G	Fourth Generation
4QAM	Four Quadrature Amplitude Modulation

1 INTRODUCTION AND SCIENTIFIC MOTIVATIONS

Advances in wireless technology such as 3G and later portable phones, IEEE 802.11/a/b/g (WiFi), and IEEE 802.11.16 (WiMAX) and exclusive subscriber growth for those applications have been triggering a big scarcity of available radio frequency resources in the microwave band. The increasing demand for wireless connectivity and crowding of unlicensed spectra has pushed the regulatory agencies to be ever more aggressive in providing new ways to use spectra.

In the past, the approach for spectrum allocation was based on specific band assignments designed for a particular service, as illustrated by the FCC's frequency allocation chart. Currently, this spectrum chart contains overlapping allocations in most frequency bands and seems to indicate a high degree of spectrum scarcity. On the other hand, a new demand for increased capacity to handle much larger data, as uncompressed high definition video, has been rising steadily. The unique possibility to satisfy this request is to look at EHF bands. The millimeter wave band from 60-95 GHz offers large swathes of unlicensed and semi-unlicensed spectrum, which may well form the basis for the next revolution in wireless communication, in which wireless catches up with wires.

Recently, wireless systems above 1Gb/s have been demonstrated using the millimeter-wave 60 GHz unlicensed band [1-1], [1-2]. However, those systems are targeting indoor short-range use because atmospheric attenuation due to oxygen is large. Meanwhile, in the frequency band ranging from 70 GHz to 100 GHz, the atmospheric attenuation is relatively small, and therefore, that frequency band-the so called "second radio window", is more suitable for medium-range point-to-point communications. The recently allocated 71–76 GHz and 81–86 GHz bands provide an opportunity for LOS links with longer range and higher data rates, ideally suited for fiber replacement and backhaul applications.

Current commercial point-to-point wireless links [1-3], [1-4], [1-5], [1-6], [1-7] in the millimeter-wave spectrum are limited to speeds up to 1.25 Gbit/s and use simple modulation techniques like ASK or BPSK with spectral efficiency below 1 bit/s/Hz. As an alternative, a 120 GHz band photonic wireless link with 10 Gbit/s data rate has been reported achieving error-free transmission of 10 GbE signals over a distance of 200 m [1-

8]. In this case, the millimeter-wave signal was optically modulated by intensity modulation and demodulated by envelope detection. The signal occupied 17 GHz bandwidth with a 0.6 bit/s/Hz spectral efficiency.

Another research group [1-9] has reported 5.2 Gbit/s combined data rate over a 60 m outdoor path using 4QAM over three separate RF bands (2–7 GHz) with 1.6 bit/s/Hz spectral efficiency, and it has suggested that 10.4 Gbit/s could be achieved if combined with polarization based frequency reuse.

A concept demonstrator with 6 Gbit/s aggregate data rate in the 81-86 GHz band and 2.4 bit/s/Hz spectral efficiency has been built and tested indoors and on a 250 m outdoor range [1-10]. In [1-10], a novel frequency-domain multichannel multiplexing approach is used, which allows to increase the spectral efficiency. This 6 Gbps link is the fastest wireless transmission published thus far in this frequency range.

Higher frequency bands, up to 350 GHz are also currently under investigation for short-range applications. Frequencies around 350 GHz are especially interesting as they lie in a low absorption atmospheric window with 47 GHz of available unregulated bandwidth. In [1-11], performance investigation of signal coverage and data rates in future multigigabit/s communications systems at THz frequencies, in real application scenario, have shown that good signal coverage is possible not only in direct LOS scenario but also with single and double bounce ones. NLOS scenarios also guarantee a high degree of robustness against shadowing. However, in order to operate with data rates of multigigabit/s in such conditions, omni-directional dielectric mirrors should be used as passive repeaters.

In all these works, both for long and short range, there is a lack of discussion on modulation, equalization, and algorithm design at physical layer.

Moreover, RF H/W with ideal characteristics is very difficult to design for frequencies above 60 GHz. At the circuitry level, while EHF provide the benefit of very small radio equipments, there are intrinsic difficulties in the development of technologies for the effective management of the communication signals without any type of distortion or impairment. Phase noise of the oscillators, nonlinear response of the PAs, I/Q phase & amplitude imbalance at frequencies above 60 GHz make the design of the RF architecture a challenging topic which cannot be disjoint anymore from the choice of the transmission techniques. Therefore, an optimized joint design of the RF and baseband parts, taking into account specific properties and not idealities of the technology and very high channel impairments at frequency bands beyond 60 GHz and for such high data rates, is needed. The first part of my Ph. D work mainly aims at investigating the use of IR based

communication systems, in particular the IR UWB transmission technique, to realise multigigabit/s communication beyond 60 GHz.

The purpose of my study is to demonstrate that the IR UWB technology could provide different alternatives RF architectures more suitable for transmission beyond 60 GHz, both in terms of performance and robustness to the impairments of such high frequency bands and in terms of lower cost design.

In order to fulfil this objective, this work shows how an IR UWB communication system is sensitive to typical hardware not idealities beyond 60 GHz and compares its performance with the ones of a more classical continuous wave communications system with FSK modulation.

The design of novel radio architectures for EHF multigigabit/s communications could be considered as a preliminary useful step toward the exploitation of "beyond Q/V bands" frequencies to support forthcoming high-data-rate services demands, aiming at developing a multipurpose network-of-the-future that will integrate terrestrial and space systems.

In fact, in the last few years the research in Telecommunications Systems has been oriented toward the development of a GII aiming at spreading information and offering users a broadband access to a wide range of services. The success and spread of communication systems represent a "milestone" in the way to conceive them and related services. We have passed from a "system-centric" vision, according to which users had to adapt their requests to the features of the used network, to a "user-centric" approach, according which user is the main actor of the system, and to whose requirements the system services have to be adapted.

In this scenario, the exploitation of such high frequencies represents the most suitable solution to develop a cooperative GII in order to guarantee the so-called "Gigabit Connectivity" through aerospace links making such a radio segment a potential "backbone on the air" for global wireless connectivity.

However, in this framework, one of the most important issues for the exploitation of frequency bands beyond 60 GHz (in particular of the W band) is the knowledge of the terrestrial propagation channel and satellite one [1-12].

Today, the performance behaviour of any solution for data transportation over W band frequencies across the Troposphere is still unknown, since still no scientific and/or telecommunication mission has been realised, either on an experimental basis or in an operating mode. This frequency band shows very interesting features for research

purposes, being never used for telecommunication applications but being extensively used (in particular the 90-95 GHz range) in radio-astronomy and radar applications.

Therefore, future missions to the purpose of utilising such a frequency band shall aim at performing a first empirical evaluation of the troposphere effects on the W-band radio channel and, at the same time, at determining the future methodologies to accomplish systematic measurements and gain much more information on such effects.

This attractive and challenging topic has represented the other key point of my Ph.D activities. They have been focused on design of future mission architectures for the exploitation of W band for satellite telecommunications purposes together with some preliminary P/L analysis [1-13].

In this framework a preliminary useful step toward the W band exploitation in satellite telecommunications is represented by the analysis and the validation of a terrestrial link operating at those frequencies. Some experiments could give important feedback from the technology point of view and also for the channel characterisation: a terrestrial air link at W band can be considered representative of more challenging satellite to ground link operating at same frequencies [1-14]. Specifically, a terrestrial link reproduces many of the dynamic atmospheric conditions experienced by a satellite link, allowing to evaluate how atmosphere affects signal propagation and to identify and test possible countermeasures such as PIMTs. Consequently, tests conducted on this terrestrial link would allow to quantify how to improve the performance of the communication systems operating at W band. This would constitute an expertise acquired on the field to be potentially extended to the future satellite links establishment.

On the basis of previously introduced scenario, a 96 GHz the feasibility study of a terrestrial point-to-point link with the capability to carry out transmission/reception experiments over a distance of around 7.5 Km between University of “Tor Vergata” and “Villa Mondragone” (Frascati) has been performed [1-15].

Finally, the last part of my thesis has been focused on the definition, design and performance evaluation of a Small LEO Satellite P/L mission, called IKNOW [1-16]. The IKNOW mission definition has been driven by the need to develop the receiving/transmitting chain using MMIC devices, in order to fit cost, power and weight constraints, typically limited for a spacecraft.

In this study, technological critical items have been highlighted, focusing on the present state of the art and presenting some architectural choices.

1.1 OVERVIEW OF THE DOCUMENT

This document is organised in three main parts.

In Chapter 2 the open issues related to transceiver design at the target frequencies are identified and discussed, through an in-depth analysis and overview of the technical literature available.
As the current state-of-the-art mostly refers to 60 GHz transmissions, this section provides preliminary insights to identify the most critical transceiver design issues in the EHF context of interest. The candidate transmission scheme beyond 60 GHz should be robust against RF circuit impairments (phase noise of oscillators, I/Q imbalances, and LNA and HPA nonlinearities), in addition to AWGN and fading too.
Chapter 3 investigates the possibility to use IR-UWB technique for multigigabit/s transmission at frequency bands above 60 GHz.
In this section, several IR-UWB architectures in the W band transmission scenario are proposed outlining advantages and disadvantages of each configuration.
In particular, proper models of phase noise of oscillators, LNA and HPA nonlinearities are used to compare a PPM TH IR UWB architecture operating at frequencies beyond 60 GHz and more traditional SC schemes, as one based on FSK modulation, both in terms of perfomance degradation and complexity of the RF and baseband subsystems design. Simulation results demonstrate that the IR-UWB technology is able to provide different RF architecture alternatives more suitable than traditional schemes for transmission beyond 60 GHz, both in terms of performance and robustness to the EHF impairments and lower cost design.

Chapter 4 shows the feasibility study, together with orographic analysis, system architecture design and performance evaluation, of a 96 GHz terrestrial point-to-point link over a distance of around 7.5 Km between University of “Tor Vergata” and “Villa Mondragone” (Frascati).
Chapter 5 firstly reports a background on the state of art of EHF broadband satellite systems. Then, the main EHF satellite propagation issues are described. The design techniques recommended for predicting propagation effects are presented; rain, atmospheric gases, clouds and scintillation attenuation phenomena are deeply analysed and some simulation results on the use of those models for W band link are provided.

Chapter 6 shows a development strategy of missions for the future exploitation of W band for satellite communications, principally focusing on the feasibility study of a W band Small P/L satellite, together with main systems and P/L architectures.

Chapter 7 reports the conclusions derived from this Ph. D work.

REFERENCES

[1-1] K. Maruhashi, S. Kishimoto, M, Ito , K. Ohata, Y. Hamada, T. Morimoto, and H. Shimawaki, "Wireless Uncompressed-HDTV Signal Transmission System Utilizing Compact 60-GHz-Band Transmitter and Receiver', IEEE MTT-S International Microwave Symposium, 2005, pp. 1867-1868.

[1-2] S. Kato, "R&D on Millimeter Wave (60 GHz) Systems and IEEE Standrdization Updates", Proceedings of IEEE International Conference on Ultra-Wideband 2007, pp. 514-517.

[1-3] Loea 2500 Link Specifications. [Online]. Available: http://www.loeacom.com/Loea2500_L1061-S-Aug06.pdf.

[1-4] GigaLink Series Technical Specifications. [Online]. Available: http://www.proxim.com/downloads/products/gigalink/DS_0407_Gigalink_US.pdf.

[1-5] FlexWave MMW Link Specifications. [Online]. Available: http://www.bridgewave.com/downloads/DS_GEO_AR80_FE80U.pdf.

[1-6] BridgeWave GE80, AR80 and FE80U Wireless Link Specifications. [Online]. Available: http://www.bridgewave.com/downloads/DS_GEO_AR80_FE80U.pdf.

[1-7] FiberAir Gigamax-60 Link Product Description. [Online]. Available: http://www.ceragon.com/site/Products.asp?ID=20.

[1-8] A. Hirata, T. Kosugi, H. Takahashi, R. Yamaguchi, F. Nakajima, T. Furuta, H. Ito, H. Sugahara, Y. Sato, and T. Nagatsuma, "120-GHz-band millimeter-wave photonic wireless link for 10 Gbit/s data transmission", IEEE Transactions Microwave Theory Technology, vol. 54, no. 5, pp. 1037-1044, May 2006.

[1-9] T. Quinlan, S. E. M. Dudley, and S. D. Walker, "Towards a 10 GHz bandwidth antenna array operating within the 2 GHz to 11 GHz frequency window," in IEEE Loughborough Antennas Propagation Conference, Apr. 2005, pp. 108–111.

[1-10] V. Dyadyuk, J. D. Bunton, J. Pathikulangara, R. Kendall, O. Sevimli, L. Stokes, and D. A. Abbott, "A Multigigabit Millimeter-Wave Communication System with Improved Spectral Efficiency" , IEEE Transactions on Microwave Theory and Techniques, Vol. 55, No. 12, December 2007.

[1-11] R. Piesiewicz, M. Jacob, M. Koch, J.Schoebel and T. Kurner, "Performance Analysis of Future Multigigabit Wireless Communication Systems at THz Frequencies With Highly Directive Antennas in Realistic Indoor Environments," IEEE Journal of Selected Topics in Quantum Electronic, Vol. 14, No. 2, March/April 2008.

[1-12] A. Jebril, M. Lucente, E. Re, T. Rossi, M. Ruggieri, C.Sacchi, V. Dainelli, "Perspective of W band for Space Communications", IEEE Aerospace Conference 2007, BigSky, Montana, USA.

[1-13] M. Lucente, E. Re, T. Rossi, E. Cianca, C. Stallo, M. Ruggieri, A. Jebril, C. Dionisio, G. Codispoti, L. Zuliani, "IKNOW Mission: Payload Design for In Orbit Test of W Band Technology", IEEE Aerospace Conference 2008, Big Sky, Montana, 1-8 March.

[1-14] C. Dainelli, M. Ferri, A. De Fazio, L. Ricci, M. Ruggieri, "W Band Communication Link, Design and on Ground Experimentation", IEEE Aerospace Conference 2005, Big Sky, Montana, 5-12 March.

[1-15] M. Lucente, T. Rossi, C. Stallo, D. Valente, M. Ruggieri, V. Dainelli, L. Ricci, "Preliminary Design of a Propagation Experiment for a RadioLink Analysis at W Band", Globecom 2008 – IEEE Workshop/EHF -AEROCOMM, "Exploitation of Higher Frequency Bands in Broadband Aerospace Communications", November 30 – December 4, 2008, New Orleans, LA, USA, ISBN: 978-1-4244-3061-1.

[1-16] M. Lucente, T. Rossi, C. Stallo, M. Ruggieri, A. Iera, A. Molinaro, S. Pulitanò, 2008, "IKNOW: a Small LEO Satellite for W Band Experimentation", 26th International Communications Satellite Systems Conference (ICSSC), June, 10-12, 2008, San Diego, CA.

2 STATE OF THE ART OF MULTI-GIGABIT MILLIMETER WAVE COMMUNICATION

Millimeter wave communication has the potential of sparking the next revolution in wireless communication in particular, and telecommunications, in general. While cellular and WLANs at lower frequencies (1-5 GHz) constantly struggle with the scarcity of spectrum, the millimeter wave band has huge swathes of spectrum available at no cost.

EHF bands offer the great opportunity for delivering data transmission at speed in excess of 10 Gbit/s and so promising to be a popular alternative in locations where it is particularly challenging to lay fiber-optic cables for trunk-line data network systems.

Mountainous regions and areas with rivers, roads or rail tracks all exacerbate the difficulties that are associated with build-out of buried fiber-optic networks. In this scenario, wireless multigigabit/s links represent the best solution to bridge the gaps in the fiber network since they can be deployed very rapidly, without the need for costly and complex trenching actions.

In U.S. there is 7 GHz of unlicensed spectrum in the 60 GHz "oxygen absorption" band that is well suited to short-range indoor and outdoor links. Further, the FCC has made available 13 GHz of spectrum in the 70-95 GHz for semi-unlicensed use to realise longer range communication, since this frequency range is subjected to a relatively low level of attenuation by atmospheric gases.

Effective exploitation of this spectrum may well enable wireless to finally "catch up" with wires, leading to systems such as "Wireless USB", "Gigabit Wireless Ethernet", and "Wireless Fiber". Figure 2-1 shows a typical Gigabit WPAN configuration for home environment.

Moreover, low-cost implementations for RF front-ends, thanks to the rapid scaling of silicon processes, are on the horizon, obtaining thus the economies of scale necessary for proliferation of millimeter wave systems in commercial applications. Traditionally 60 GHz RF technology has been the domain of expensive chip technologies based on III-V compound materials such as GaAs and InP. These technologies were mainly intended for military applications for which the cost is not very relevant.

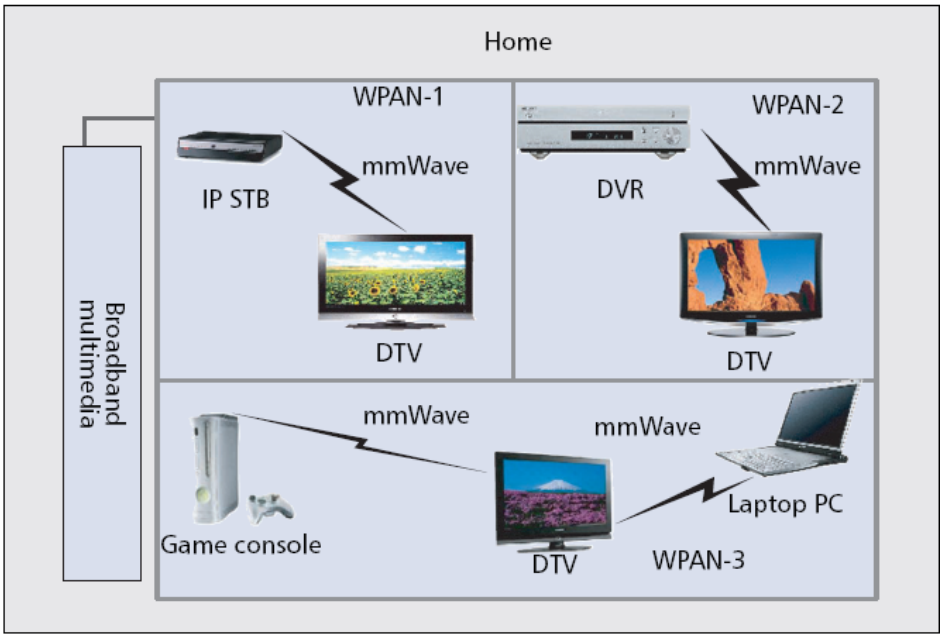

Figure 2-1: Configuration of Gigabit WPANs in a typical home environment

Currently, considerable RF performances are achieved with low-cost process technologies based on silicon. With SiGe technology [2-1], the maximum frequency of operation, (f_{max}), amounts to hundreds of GHz, and it has the best physical properties for providing sufficient RF performance [2-2], [2-3]. The RF performance of a baseline CMOS is worse but increases more rapidly due to the enormous world-wide effort to scale to lower gate-lengths, which implies a higher fmax. The speed of analog CMOS circuits increases by roughly one order of magnitude every ten years. PAs implemented in today's 90 nm RF-CMOS technology can produce an output power level of about 6 dBm with sufficient linearity, whereas LNAs with a noise figure of 4.5 dB are realistic [2-4]. The CMOS chip industry already invests massively in 65 nm technology, with 35 nm as the next step, promising increasing performance in the future. This makes CMOS the lowest cost option and with its rapid performance improvement due to continuous scaling, CMOS is becoming the future technology of choice to address the low-cost millimeter-wave market. The time is ripe, therefore, to develop and validate system concepts that address some of the fundamental challenges associated with high-speed, millimeter wave communication.

First, millimeter wave links are fundamentally a LOS technology, being highly vulnerable to blockage. This is because diffraction around obstacles is severely curtailed (relative to that at lower carrier frequencies) because of the smaller wavelengths: as a rule of thumb, an obstacle that is a few wavelengths across effectively blocks the wave.

Second, according to the Friis formula for free space propagation, the propagation loss scales as λ^2, where λ is the carrier wavelength, so that, for given transmit and receive antenna directivities, millimeter wave links incur much higher losses than existing cellular and WLAN links. However, it is easier to synthesize highly directive antennas at smaller wavelengths, and for a given antenna size, the directivity scales as $\frac{1}{\lambda^2}$. Thus, if we fix the area of the antennas used at each end, the overall propagation loss scales as $\frac{1}{\lambda^2}$, so that we actually win by using lower wavelengths. Of course, this approach has significant associated challenges, including the issue of how to direct the transmit and receive antennas at each other (electronic beamsteering becomes crucial for enabling flexible and robust deployments), and how to design network protocols that work with highly directional beams.

Third, at speeds of multi-Gigabit/s, the modern paradigm of digital communication transceiver design, which is heavily centered on DSP becomes difficult to realise. This is because high-speed, high-precision ADC are too costly and power-hungry. The solution in the short term is to come up with creative hybrid analog/digital baseband designs. However, an all-digital, DSP-centric approach is attractive in the longer term, because it enables us to ride Moore's law to obtain the economies of scale associated with low-cost IC implementations.

Finally, based on the spectral chunks available, and the feasible bandwidths for RF and baseband processing, channel bandwidths for millimeter wave systems are expected to be of the order of 1-5 GHz. Attaining optical speeds of 40 Gigabits/s over such a channel is a challenging task. The use of very large constellations is prohibited not only for complexities of processing them, but also for their excessive power requirements. One approach is to employ power-efficient signaling, but to increase spectral efficiency by employing spatial multiplexing. However, unlike lower frequency systems, where spatial multiplexing originates from rich scattering, we must obtain it in the LOS regime.

From these considerations, it is clear that there is plenty of room for innovative system design in the context of emerging, ultra high-speed millimeter wave communication networks.

Goal of this section is to analyse the global scenario for the future generation of multigigabit/s EHF systems; a state of the art analysis has been carried out in order to identify the proposed and the operative 60 GHz and beyond communication systems.

2.1 STATE OF THE ART OF 60 GHZ COMMUNICATION SYSTEMS

The growth of wireless communications is spurred by the consumer desire for un-tethered access to information and entertainment.

While contemporary unlicensed systems support light and moderate levels of wireless data traffic, as seen in Bluetooth and WLANs, current technology is unable to provide data rates comparable to wired standards like Gigabit Ethernet and HDMI. Fortunately, multiple GHz of internationally available, unlicensed spectrum surrounding the 60 GHz (60G) carrier frequency shows the ability to support high-throughput unlicensed wireless communications.

In 2001, the FCC allocated the 57-64 GHz band for general unlicensed use in the United States. In Europe, the 59-63 GHz band is mainly assigned to WPAN applications, while the 63-64 GHz frequency range is reserved for ITS. However, frequency regulations for 57-66 GHz band is not finalized yet [2-5], [2-6].

The MWFSG in Korea allocated the 57-64 GHz spectrum to indoor WPANs with a maximum transmit power of 10 dBm, while in Japan, the band is defined at [59-66] GHz with similar power limits.

Figure 2-2 shows the allocation of the unlicensed 60 GHz band for Europe, Australia, Japan, Korea, Canada and United States.

While the availability of this free spectrum makes it very attractive for wireless applications, 60 GHz implementations must overcome many challenges.

The wireless channel at this frequency range shows from 20 to 40 dB increased free space path loss and suffers from 15 up to 30 dB/km atmospheric absorption depending on the atmospheric conditions.

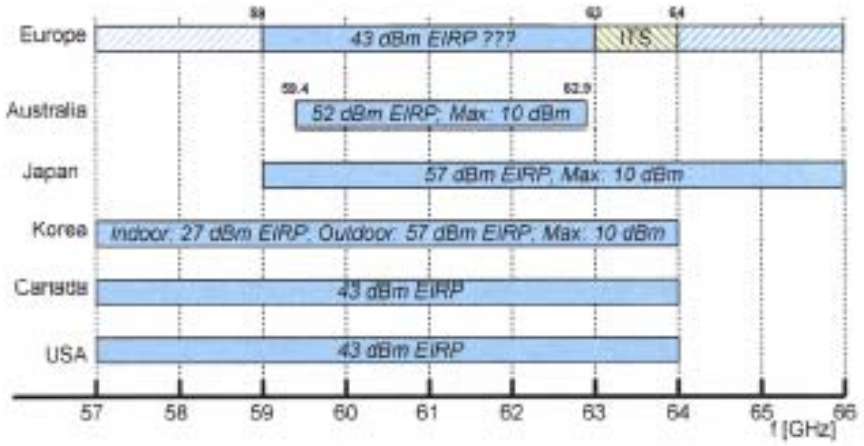

Figure 2-2: Spectrum Allocation in the unlicensed 57-66 GHz spectrum

Multipath effects, except for indoor reflections, are vastly reduced at 60 GHz making NLOS communication very difficult.

Furthermore, millimeter-wave transceivers show new design challenges such as increased phase noise, limited amplifier gain, and the need for transmission line modeling of circuit components. Consequently, the design of 60 GHz systems is not straightforward.

There is a lack of a detailed discussion on equalization, modulation and algorithm design at the physical layer, both for long and short range.

The goal of this paragraph is to show an exhaustive review of design tradeoffs for algorithms in the 60 GHz physical layer including modulation, equalization, and space-time processing. This review, in the following sections of the paragraph, is enhanced by considering the characteristics of the effective wireless channel (including antennas), limitations in circuit design, main developed 60GHz air interfaces with their principal advantages and drawbacks, and performance requirements to support current and next generation 60GHz wireless communication applications.

2.1.1 60 GHz Wireless Channel Characterisation

Wireless channel characteristics have to be well investigated to determine the appropriate system design at 60 GHz. Large-scale effects suggest range limitations for LOS communication.

Material propagation of 60 GHz radiation characterises the performance indoors. The extent of multipath determines the complexity of receiver structures for equalization as well as the ability to communicate in NLOS scenarios.

Multipath can be considered in several contexts. In the context of transmit and receive antennas, the severity of multipath depends both on antenna directivity and polarization. How the multipath changes with time determines the time coherence of the channel while the spatial richness of the multipath suggests whether spatial processing techniques are worthwhile. In this section, the properties of the 60 GHz channel and its implications are summarised.

2.1.1.1 LARGE SCALE AND OUTDOOR CHANNEL EFFECTS

Path loss is a measure of average radio wave energy decay as a function of distance, frequency, and other location specific parameters. Simple calculations using the Friis free-space path loss formula show a 20–40 dB power penalty for 60 GHz versus unlicensed communication at operating frequencies below 6 GHz. Loss due to atmospheric absorption can account for an additional 7–15.5 dB/km power loss in the received signal at 57–64bGHz carrier frequencies [2-7]. Although water vapor does not contribute greatly to signal attenuation at normal concentrations, rain droplets that form when the atmosphere becomes saturated can further attenuate the signal. For example, given a rainfall rate of 50 mm/hour, different models predict between 8–18 dB/km additional atmospheric attenuation [2-7]. Precipitation also decreases cross-polarization discrimination (XPD), reducing the benefits of the extra dimension afforded by antenna polarization [2-8].

In principle, the use of antennas with more pattern directivity can compensate the 60 GHz channel losses while maintaining small antenna dimensions.

When such antennas are used, however, antenna obstruction (e.g., by a human body) and mispointing may easily cause a substantial drop of received power, which may nullify the gain provided by the antennas.

This effect is typical for millimeter waves because the diffraction of them (i.e., the ability to bend around edges of obstacles) is weak.

Therefore, the erosive effects on signal due to 60 GHz channel impairments suggest that systems operating at such a frequency band will have to compensate for lower received

signal energy, and that outdoor systems may be infeasible for communication over distances beyond a few kilometers.

2.1.1.2 MATERIAL ATTENUATION

The attenuation shown by 60 GHz electromagnetic fields through indoor materials is summarised and compared to 2.5 GHz in Table 2-1. Although not always drastic or necessarily consistent (see glass attenuation), there is a basic trend of higher material attenuation observed at 60 GHz. This effect, combined with the increased path loss contains signals to a single room for 60 GHz indoor wireless propagation [2-9]. This allows for increased security and decreased interference from adjacent networks while at the same time complicating multi-room coverage.

Material	Loss at 60 GHz	Loss at 2.5 GHz
Glass	11.3 (dBm/cm)	20.0 (dB/cm)
Mesh Glass	31.9 (dB/cm)	24.1 (dB/cm)
Drywall	2.4 (dB/cm)	2.1 (dB/cm)
Whiteboard	5.0 (dB/cm)	0.3 (dB/cm)

Table 2-1: Office Material attenuation at 60 GHz and 2.5 GHz

2.1.1.3 MULTIPATH CONTRIBUTIONS

Multiple paths in the 60 GHz propagation channel create multipath interference. The delay and attenuation associated with each multipath component corresponds to path length differences due to surface reflections, scattering by small objects, and propagation through different mediums. The scattering effect is drastically reduced since scattering occurs when objects are similar in dimension to the operating wavelength. Transmission through most objects is also reduced as a consequence of the limited ability to penetrate solid substances [2-9]. Although these traditional sources of multipath are diminished, reflection effects are amplified. Reflection occurs on objects larger than the dimensions of operating wavelength

implying that objects traditionally acting as scattering objects now become reflectors at 60G. The RMS delay spread, T_{RMS}, quantifies the temporal spreading effect (in seconds) of the wireless channel.

Table 2-2 shows the approximated measurements from [2-10] for indoor scenarios. As a rule of thumb, a system experiencing an RMS delay spread of T_{RMS}, will suffer $\left|f_s T_{RMS} - 1\right|$ symbols of ISI in the wireless channel given f_s as the data symbol frequency. Since 60 GHz systems will likely operate on very large bandwidth channels (on the order of GHz) even traditionally small RMS delays spreads, as in Table 2-2, provide appreciable ISI. Hence, as it will be discussed in the next section, 60 GHz wireless communication systems indoors or in vehicles must employ antenna techniques and/or complex receiver equalization to eliminate the severe ISI.

Dimensions (m^3)	Wall Material	$T_{RMS,90\%}$ (ns)	$T_{RMS,10\%}$ (ns)
24.5 x 11.2 x 4.5	wood	40	45
30 x 21 x 6	rock wool	30	35
43 x 41 x 7	concrete	40	60
33.5 x 32.2 x 3.1	concrete	40	70
44.7 x 2.4 x 3.1	metal	60	80
44.7 x 2.4 x 3.1	metal	60	80
9.9 x 8.7 x 4.0	metal	40	45
12.9 x 8.9 x 4.0	wood	15	25
11.3 x 7.3 x 3.1	concrete	25	30

Table 2-2: Approximate T_{RMS} for indoor scenarios. $T_{RMS} < T_{RMS,90\%}$ for x% of the time

2.1.1.4 INFLUENCE OF ANTENNA PARAMETERS ON MULTIPATH

The choice of transmit and receive antennas influences the multipath that is observed at receiver side.

Directive antennas can be employed in order to reduce multipath contributions by limiting the elevation and azimuth angular range from which the radiation is emitted and captured.

In [2-11] authors demonstrated that the use of an antenna with 3 dB beamwidth of 5º instead of omnidirectional one allows to reduce T_{RMS} from 18 ns to 1 ns. The polarization

of antennas can also influence propagation. In [2-12] it was observed that circularly polarized signals reduce RMS delay spread values by a factor of 2 over linearly polarized signals. Consequently, many 60 GHz systems use highly directional antennas with circular polarization to limit the digital equalization of ISI resulting from excessive multipath.
This forces the transmitter and receiver to somehow "point" to each other in order to communicate, resulting in undesired additions to medium access control (MAC) and physical layer functionality.

2.1.1.5 SPATIAL CHARACTERISTIC OF MULTIPATH

The spatial characteristic of multipath is often measured using angular spread, which is defined with respect to a mean angle of arrival or departure. An angular spread of value 1 indicates an observed channel that varies heavily with azimuth angle at the receiver while 0 indicates a channel that does not vary with azimuth angle. In [2-13] the authors characterised spatial properties of angular spread. It was discovered that the angular spread typically measures from 0.3 to 0.8 in indoor environments, suggesting that space-time processing techniques are viable. Outdoor scenarios, however, have a reduced angular spread of 0.1 to 0.5.
Reflections contribute to the majority of received multipath and the material of the reflective element (i.e., wall) is very critical in determining the angular spread. These angular spread statistics suggest that, while space-time processing techniques may not be helpful in outdoor channels, the spatially rich nature of indoor channels allows 60 GHz systems to take advantage of recent advances in array processing and MIMO one.

2.1.1.6 TIME VARIATION IN THE CHANNEL

The Doppler Frequency is proportional to the transmitted signal frequency and it represents the maximum frequency difference between received signals and transmitted ones due to the mobility of the transmitter, receiver, or objects in the channel.
Hence, increasing the carrier frequency in wireless systems induces proportionally magnified Doppler effects. It follows that the Doppler Effect for 60 GHz systems is approximately ten times that of a 6 GHz one under the same mobility conditions. Since there is also a proportional relationship between the Doppler Effect and the time varying

nature of the wireless channel, channel information must be estimated ten times more frequently. Then, the transmitter, on the basis of this information, adapts the modulation scheme or transmission mode for increased reliability and throughput, while the receiver exploits this information in channel equalization. As a result, 60G systems can expect increased overhead to obtain the channel estimation at transmitter side through feedback, or at receiver one using training/pilot symbols. This can be particularly troubling for outdoor and inter-vehicle communications that must operate under high mobility.

2.2 60 GHZ SYSTEMS DESIGN ISSUES

Traditionally, 60 GHz RF technology has been the domain of III/V compound materials, such as GaAs and InP, then resulting in expensive multichip implementations [2-14]. Those tecnologies, in fact, do not allow combining in a low-cost single chip solution analog, digital and RF subsystems and are normally much more expensive in terms of die cost than silicon based technologies. Moreover, those circuits need many low impedance connections between individual chips, leading to higher power dissipation.

Therefore, for the commercial market that will access the unlicensed 60 GHz spectrum, such technologies are ill suited due to limited digital integration, high relative cost, and low power efficiency.

Recent scaling improvements in silicon based technologies, such as standard CMOS and more interestingly SiGe BiCMOS (a standard CMOS process that also includes HBT with a constantly graded doped Germanium Base), have shown that they are able to provide more viable options than III-V materials (in particular GaAs and InP) [2-15], [2-16], [2-17], [2-18], [2-19].

Higher integration and more efficient manufacturing process offered by the CMOS technology should allow to realise RF, analog and digital subsystems together with antenna section in a single low-cost multi-functional chip.

Low static power consumption, high noise immunity are other advantages offered by the CMOS technology.

However, the RF performance of a baseline CMOS is worse but increases more rapidly due to enormous world-wide effort to scale to lower gate-lenghts, which implies a higher $f_{\max}$.

The speed of analog CMOS circuits increases by roughly one order of magnitude every ten years.

Recent works have demonstrated millimeter-wave building blocks using deep sub-micron CMOS technologies such as LNAs, mixers [2-20] and oscillators [2-21].

Currently, PAs implemented in 90 nm RF-CMOS technology can produce an output power level of about 6 dBm with sufficient linearity [2-22], whereas LNAs with a noise figure of 4.5 dB are realistic [2-22].

A 60 GHz receiver front-end chip fabricated in 90 nm CMOS process has been reported in [2-23]. The CMOS chip industry already invests massively in 65 nm [2-24], [2-25], [2-26], and 45 nm [2-27], [2-28] technologies, with 35 nm as the next step, promising increasing performance in the future.

Implementing transceivers operating near frequency limits of a given technology requires a careful optimization at all levels: device, circuit, and system architecture.

At the transistor level, a clear understanding of the fundamental limitations of CMOS transistors is necessary to design and lay out an optimal device for operation at millimeter wave frequencies.

For baseband and digital circuits, the dominant parasicts limiting the performance of CMOS transistors are the capacitors, driving the process engineer to optimize the technology for the highest operating frequency.

While reducing parasitic capacitors helps high-frequency performance, at millimeter wave frequencies resistive losses due to transistor and layout parasitics play an increasingly important role since they dissipate power that cannot be restored. This limitation is best captured by the maximum frequency of oscillation ($f_{\max}$) figure of merit, that is the maximum frequency at which the device remains active.

The value of $f_{\max}$ is not only determined by sizing and bias conditions, but it is also highly dependent on these resistive parasitics. Theoretically, $f_{\max}$ is independent of the number of fingers of a multi-finger transistor, as long as the device dimensions are much smaller than a wavelength. Although interconnect wiring to connect the gates of multiple devices will add parasitic capacitance, this capacitance is generally high-Q and does not greatly impact $f_{\max}$. Therefore, it is sufficient to be concerned only with the optimal layout for a single finger of a multi-finger transistor.

As mentioned, $f_{\max}$ is limited by resistive losses, the most significant being the gate resistance (R_G), series source/drain resistances (R_S, R_D), non-quasi-static channel resistance (r_{nqs}), and resistive substrate network (R_{sb}, R_{db}, and R_{bb}). The simplified physical model for one finger of an NMOS device is shown in Figure 2-3.

R_S, R_D are dominated by the intrinsic spreading resistance in the SDE region near the channel. The not-quasi-static channel resistance models the effective increase in gate resistance due to the finite channel charging time, and it can be shown to be inversely proportional to g_m. R_G accounts for the distributed RC nature of the polysilicon gate, and can be approximated using a single lumped resistor. Additionally, series inductors must be added to all terminals (L_G, L_S, L_D) to properly model the delay effects associated with interconnect wiring.

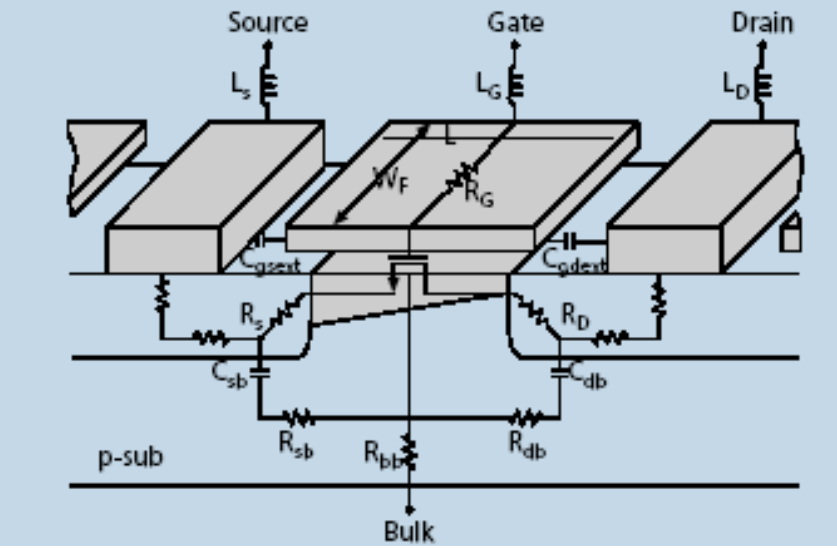

Figure 2-3: Simplified physical model for one finger of an NMOS device

If the gate resistance was negligible, scaling the finger width would not significantly influence $f_{\max}$. Unfortunately, for CMOS devices with polysilicon gates, the gate resistance is often quite large and can not be negletected. However, by using narrow finger widths, the effect of the gate resistance can be reduced if compared to the other parasitic effects [2-29].

Another advantage of using narrow fingers is represented by the fact that the substrate contacts can be placed very close to the device to minimize substrate losses. Therefore,

with optimal layout, f_{max} is not limited by gate resistance, but mainly determined by the series source/drain resistances and substrate resistive network.

One of the most important differences between silicon and compound semiconductor technologies is represented by the lossy nature of the substrate. The silicon substrate of a modern CMOS process has a resistivity of around 10 $\Omega \cdot$cm, whereas a III-V semi-insulating substrate shows a resistivity of around 10^7 - 10^9 $\Omega \cdot$cm so it can effectively be treated as an ideal dielectric. The lossy substrate represents a real issue for both active and passive devices. For transistors, signals which couple to the substrate through the source and drain junction capacitors incur significant losses at millimeter frequencies. For passive components, as inductors, capacitors, and transmission lines, the close proximity of the lossy substrate to the metal conductors reduces the attainable quality-factor (Q) of the passives.

Another important characteristic of a CMOS process is the metallization stack. The gate material for a silicon MOSFET is silicided polysilicon, which has a much higher sheet resistance (~10 Ω/cm) than that of the metal used for the gates of GaAs FETs. Modern CMOS technologies have also migrated towards all-copper interconnects. While copper presents the advantage of a higher conductance than aluminum or gold, the fabrication steps require a uniform density of all metal layers. Thus, floating dummy fill metal must be added to empty areas to increase the local density. Conversely, large areas of metal (e.g., for ground planes) are forced to have slots in order to reduce the density. The slots result in additional conductor loss, while the floating dummy metal can create unwanted and unpredictable coupling if exclusion areas are not defined.

The performance margins of CMOS transistors at 60 GHz are exceedingly small. Thus, accurate device models capable of predicting the wideband performance of the transistors are a top priority. Conventional RF CMOS transistor models are based on a compact model, such as BSIM3, with external parasitics to model substrate and gate resistance [2-30], [2-31]. These models have been verified and used effectively up to low GHz frequencies.

At higher frequencies, signal delay becomes well-rendered, and with the introduction of inductors in series with the terminals, the effects of the delay can be included.

Moreover, the accurate values for the parasitics are so tightly coupled with the layout (input and output connections, locations of ground and substrate contacts, number of

fingers, etc.), that a general purpose scalable model for arbitrary layouts will inevitably introduce modeling errors.
The traditional microwave approach to transistor modeling is based on measured S-parameters data for fixed device layouts. S-parameter models are very accurate as they implicitly account for all parasitics and any distributed effects, and they are adeguate for the design of many small-signal circuits.
Therefore, combinating these two methodologies is mandatory to develop new design rules for CMOS at higher frequencies accounting for travelling wave delay since the operating wavelength is on the order of circuit dimensions.

Finally, another issue to be faced is represented by the fact that CMOS power amplifiers currently are unable to provide the desidered output power. Three techniques are generally used: a power combining circuit, an external power amplifier, or an antenna array to spatially distribute the signal.

The CMOS technology, despite the many unsolved issues illustrated above, represents the most suitable solution to design a single, low-cost and multi-functional chip for 60 GHz and beyond applications.
In the following paragraphs, some considerations about 60 GHz key RF building blocks design challenges are firstly illustrated.
Finally, the state of art on transceiver architectures and modulation schemes for applications at 60 GHz is reported.

2.2.1 KEY RF BUILDING BLOCKS

This section discusses crucial radio design options for each of the critical millimeter wave subsystems included in a typical 60 GHz transceiver.
Moreover, some potential solutions, taking also into account the technical constrains imposed by the use of silicon-based 60 GHz RF technology, are shown.

2.2.1.1 Mixers

Mixers are of the critical importance in transceivers, since they greatly influence the overall design and system performance. One of the most important figures of merit to be

considered in the design of a mixer is represented by the linearity. This parameter is significant since the mixer, if used in a down-conversion stage, is the first block in the receiver to handle large power, being located immediately after LNA. The dynamic range of mixers mainly depends on the compression point at 1 dB. A higher 1 dB compression point will also result in a higher IM3 intercept. Therefore, this last parameter is an alternative way to evaluate the mixer's signal handling capability.

High linearity can be achieved with passive mixer configurations. However, their obvious drawback is the associated high conversion loss since the mixer's zero power consumption cannot boost the strength of the frequency converted signal. Therefore, minimising the signal loss is crucial since sufficiently high power may be needed to drive the subsequent receiver stages. In fact, as reported above, it is a challenge to obtain high gain at 60 GHz in the previous LNA section. It is thus necessary to provide minimum conversion loss in the subsequent down-conversion mixer stage.

The challenging design of high-gain CMOS LNAs together with millimeter wave CMOS modelling difficulties limit the use of complex mixer topologies.

Another drawback offered by the design of advanced CMOS processes is represented by the high cost of chip area. This translates to a need to reduce the design area for achieving a specific function under certain performance requirements. The use of slow-wave transmission lines instead of conventional microstrip line allows to reduce chip area [2-32].

The Gilbert cell mixer configuration is ubiquitous in low GHz CMOS designs [2-33], but in addition to its complexity, a different LO would be required. Therefore, simpler architectures are preferred. Low-loss diodes are not available in a standard digital CMOS process, so other alternatives such as single-transistor mixer [2-34] or dual-gate mixers [2-35] topologies have been investigated.

A single-gate mixer is a trans-conductance mixer, as the time-varying $g_m(t)$ of the common-source stage is the main source of frequency conversion. The LO signal, applied at the gate of the transistor together with the RF signal, varies the g_m around the dc bias point, and therefore modulates the RF gain of the common-source stage, which consequently provides frequency conversion. The realisation of a single-gate mixer is quite complex since they require a hybrid or elaborate power combining circuit to combine the LO and RF signals. Typically the hybrids are bulky, and their insertion-loss adds directly to mixer's noise figure. Fortunately, due to the high frequency operation at 60 GHz, the hybrid can be easily integrated on-chip.

The pseudo-dual gate mixer is a cascade topology. The gate of the trans-conductor is driven by an RF signal where its $g_m(t)$ is modulated by the LO signal applied to the gate of the cascode. This mixer is compact and provides a degree of isolation between the RF and LO. Since the cascode transistor is degenerated by the common-source transistor, capacitance at the source terminal of the cascode may give rise to negative resistance seen by the LO. Thus, stability of this topology must be carefully analyzed and simulated.

Table 2-3 exhibits state of art of performance for some 60 GHz down-conversion mixer configurations in terms of Conversion Gain (dB), LO Power (dBm), Input 1 dB Compression Point (dBm), Power Consumption (mW) and Die Size (mm³).

Reference	Process	Topology	RF (GHz)	IF (GHz)	Conversion Gain (dB)	LO Power (dBm)	Input P_{1dB} (dBm)	P_{diss} (mW)	Die Size(mm³)
[2-34]	0.13µm CMOS	Single-gate Mixer	60	2	-2	0	-3.5	2.4	1.6 x 1.7
[2-36]	0.13µm CMOS	Current-Mode Single-Ended Mixer	60	2	1	0	2	3	1.4 x 1
[2-32]	90 nm CMOS	Dual Gate + Buffer	60	4	-1.2	1.5	0.2	29.4	0.61 x 0.8
[2-37]	p-HEMT	Cascode	60	1	6.3	2.6	-	8	1.6 x 1.6
[2-38]	0.25 SiGe	Single-Balanced Mixer	60	5	2.5	-3	-5	15.5	0.48
[2-35]	0.13µm CMOS	Dual-Gate Mixer	60	5	-2.7	-0	-8	16.8	1.0 x 0.9

Table 2-3: 60 GHz Down-Conversion Mixers Performance Comparison

2.2.1.2 Local Oscillators

VCO are crucial building blocks in wired and wireless communication systems. Typically, the oscillation frequency of the VCO is limited by the losses of passive components and the high-frequency capabilities of the active devices. Due to recent advances in fabrication technology, transistors with a cut-off frequency (f_T) and a maximum oscillation frequency ($f_{\max}$) beyond 100 GHz are available in a standard CMOS process.

However, the losses of the on-chip passives including inductors and capacitors cannot be effectively reduced by the on-going device scaling. To compensate for the losses, the rule

of thumb in conventional VCO designs is to maintain the desirable output frequency within 2/3 or even ½ of the transistor's f_{max}. Therefore, deep-submicron technologies are mandatory in the realisation of CMOS VCOs at millimeter-wave frequencies [2-39], [2-40], [2-41], [2-42], [2-43], [2-44], [2-45] leading to a higher implementation cost.

In order to overcome the limitations imposed on the high-frequency VCOs, various design strategies have been proposed [2-46], [2-47], [2-48], [2-49], [2-50], [2-51], [2-52], [2-53], [2-54], [2-55], [2-56].

Among these techniques, one effective approach for extended oscillation frequency in a given process technology is to utilise a push-push circuit topology [2-57], [2-58], [2-59], [2-60]. The principle of a push-push oscillator is illustrated on Figure 2-4. It consists of two symmetrical and individual sub-oscillators, each one operating at 180º out of phase, and working at half the output frequency.

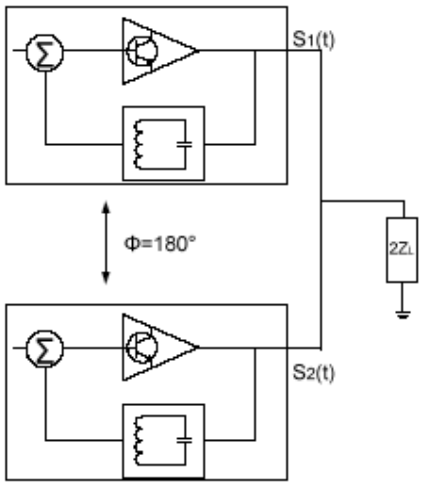

Figure 2-4: Principle of a Push-Push Oscillator

The signals generated by the two sub-oscillators are expressed by the following equations:

$$s_1 = \sum_0^\infty a_n \sin(\omega_n t + \varphi_n) \tag{2-1}$$

$$s_1 = \sum_0^\infty a_n \sin(\omega_n t + \varphi_n + (n+1)\pi) \tag{2-2}$$

$$s = s_1 + s_2 = \sum_{k=0}^\infty 2a_{2k+1} \sin(\omega_{2k+1} t + \varphi_{2k+1}) \tag{2-3}$$

Due to their symmetry, the two oscillators get almost the same spectral components with the same amplitude a_n but they differ in phase by $n\pi$. The output signal is generated by

the sum of the two sub-oscillators. As a result of the sub-oscillators phase differences regarding the fundamental frequency and the odd harmonics, the power distributed to the load is delivered only by the even harmonics while frequency contributions of odd harmonics cancel out.

Since the oscillator core operates at half the output frequency, a push-push VCO presents lower phase noise under lower power consumption. It also a way to deal with low quality factors of passive components at such high frequencies. Regardless of this advantage, this structure has lower capability to deliver high output power as it works on its second harmonics.

To facilitate differential circuit operations for the push-push VCOs, an extraction technique has been proposed recently [2-61].

However, at the presence of device mismatch and process variations, the output imbalance and insufficient fundamental rejection may become serious design issues. In [2-62], authors proposed an admittance-transforming method for LC-tank in the design of fundamental VCOs operating at millimeter wave frequencies. In the design of the CMOS VCOs, a cross-coupled pair, as shown in Figure 2-4, is widely used to compensate for the losses in the resonators. For circuit operations at millimeter wave frequencies, the required trans-conductance and device sizes are typically large for the cross-coupled pairs due to the increasing losses of on-chip inductors and varactors.

However, the capacitive loadings contributed by the MOS transistors impose stringent limitations on the VCO performance especially for the oscillation frequency and the tuning range.

The admittance-transforming technique allows to enhance the equivalent negative conductance of the cross-coupled pair through the on-chip transmission lines without increasing the transistor size. As a result, a VCO circuit with an oscillation frequency close to the maximum frequency of transistors is obtained.

Another approach, commonly used in millimeter-wave systems, is to use a lower-frequency LO in conjunction with a frequency multiplier. Using a lower-frequency LO also eliminates the need for a frequency divider operating at the carrier, which would dissipate a huge amount of power. Table 2-4 exhibits state of art of performance for some oscillators operating around 60 GHz in terms of LO Power (dBm), Output Point (dBm), Frequency Range, Power Consumption (mW) and FOM.

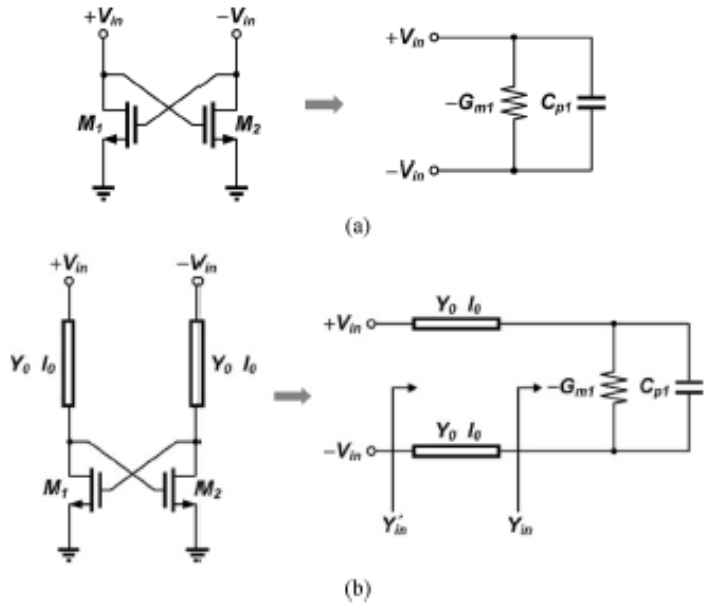

Figure 2-5: (a) Conventional Cross-Coupled Pair and (b) the Admittance-Transforming Topology proposed in [2-62]

Reference	Process	LO (GHz)	Phase Noise (dBc/Hz)	Pout (dBm)	Frequency Range	Power Consumption	FOM
[2-63]	90 nm SOI CMOS/ f_{max} = 160 GHz	56	-90 (@1MHz)	-7	14%	21 mW	171
[2-64]	0.12µm CMOS	51	-85 (@1MHz)	-	1.4%	9.25 mW	169
[2-65]	0.25 µm CMOS	63	-85 (@1MHz)	-	1.6%	119 mW	159
[2-66]	0.18 µm SiGe HBT	59	-103 (@10MHz)	4	13%	240 mW	178
[2-58]	0.13 µm SiGe:C BiCMOS	68	-110 (@10MHz)	-14	7.5%	36 mW	170
[2-58]	0.13 µm SiGe:C BiCMOS	68	-110 (@10MHz)	-14	7.5%	36 mW	170
[2-67]	0.25 µm SiGe BiCMOS	61.1	-92 (@10MHz)	-16	8%	150 mW	171

Table 2-4: Performance Comparison of Oscillators developed for 60 GHz applications

Another approach, commonly used in millimeter-wave systems, is to use a lower-frequency LO in conjunction with a frequency multiplier. Using a lower-frequency LO also

eliminates the need for a frequency divider operating at the carrier, which would dissipate a huge amount of power. Table 2-4 exhibits state of art of performance for some oscillators operating around 60 GHz in terms of LO Power (dBm), Output Point (dBm), Frequency Range, Power Consumption (mW) and FOM.

2.2.1.3 PAs

CMOS scaling allows to improve noise performance and gain at millimeter-wave frequencies but it exacerbates the difficulty of generating sufficient output power at the transmitter. It is well known that transistors need to increase in size to provide enough power to drive radiating devices such as transmit antennas. Increasing transistor size, however, also reduces the gain such that the performance of the PA is compromised. Multi-stage PAs are then essential to obtain adequate gain at 60 GHz and beyond. Novel circuit topologies for power combining (e.g., distributed active transformer [2-68]) may be required to generate sufficient output power with low supply voltages. Another approach consists of using a spatial power combining scheme, as shown in Figure 2-6, to improve the requirements on single PAs. Compared to corporate power combining structures, which become excessively lossy and bulky as the number of devices increases, the combining efficiency of spatial power combiners is approximately independent of the number of individual PAs [2-69]. The reduced output power from each amplifier eases matching network design, a traditional source of loss in an integrated PA. If needed, coarse power control is simply obtained by turning off parallel stages.

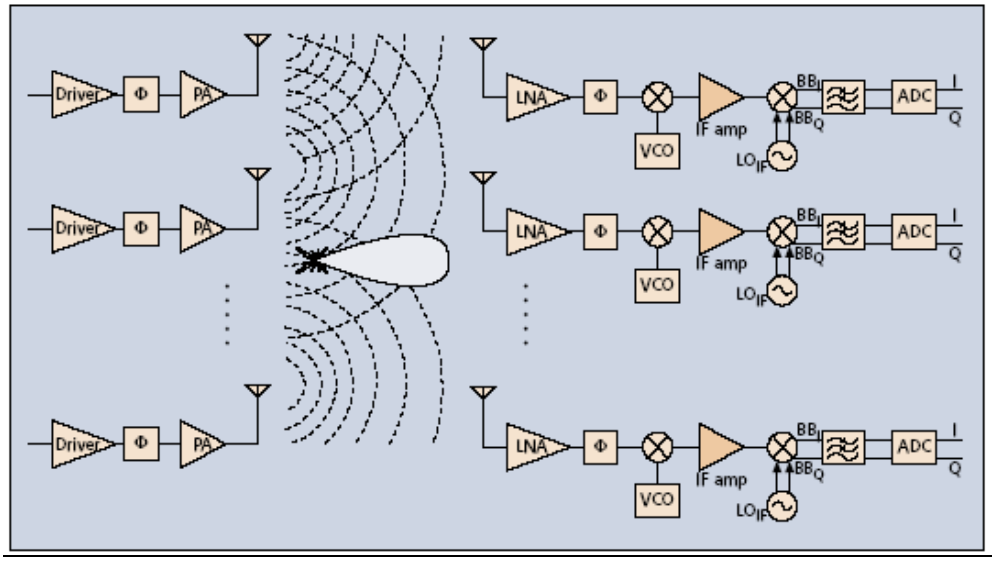

Figure 2-6: Multiple-Antenna Transceiver Architecture based on Beam Steering

2.2.1.4 LNAs

It is well known as the frequency operation for transistors in an amplifier increases, the available effective gain per transistor decreases. Although the severity of this trend depends on the technology implemented, it can be universally stated that the design of 60 GHz PAs and LNAs is a gain-limited challenge.

At the same time, high power gain from LNA, according to the classic Friis formula, is crucial in order to suppress the noise contribution of mixer and other receiver stages.

To obtain a high power gain (e.g., 15-20 dB) at 60 GHz bands, a multi-stage design is essential due to low MAG from active devices (e.g., 8 dB per transistor in a 90 nm bulk CMOS technology) and high insertion loss of passive components (e.g., about 1dB/mm loss for a typical coplanar waveguide implementation [2-70].

The method of inductive degeneration, common in low GHz design, is avoided to maximize gain. CPW transmission lines are used extensively to realise small active inductive reactances in matching networks and for all interconnect wiring.

The design of proper ac coupling and bypass capacitors is nontrivial at those frequencies due to self-resonance. If a by-pass capacitor is oversized or designed incorrectly, it may self-resonate below 60 GHz and produce unwanted oscillations. Finger MIM capacitors have been often used instead of parallel-plate MIM capacitors for compatibility with a generic CMOS process [2-71].

2.2.2 STATE OF THE ART OF 60 GHZ TRANSCEIVER ARCHITECTURES

Standard wireless receivers typically are based on heterodyne or homodyne architectures.

Heterodyne receivers, after a coarse filtering operation, translate the modulated signal to an intermediate frequency where a higher precision channel-select filter (to remove out-of band components) is easier to design. The translation from a higher frequency to a lower frequency is accomplished by mixing the signal with a local oscillator and then by low pass filtering stage to remove imaged components.

The homodyne receiver removes the intermediate frequency conversion and converts the received modulated signal directly to baseband. Direct conversion receivers are popular due to integration ability in CMOS technology.

Heterodyne and homodyne receiver architectures, when applied to 60 GHz systems, experience aggravated phase noise effects. Oscillator signals, like those used for mixing at the transmitter and receiver chains, are commonly derived from a reference oscillator.

A multiplier circuit scales this reference to the desired oscillator signal frequency. Reference oscillator phase noise amounts to variability of the oscillator's signal frequency with time. The phase noise effect is random and there currently exists no way to correct the problem in traditional receivers, aside from frequency stabilization, which is large unsuccessful [2-72].

Some oscillator configurations, as the one based on push-push approach, have been proposed, but they show lower capability of delivering high output power.

Another approach for minimising phase noise effects is to include better reference oscillators, but this significantly increases the analog design cost.

Assuming the same reference oscillator, 60 GHz signals suffer from phase noise that is ten times greater when compared to unlicensed wireless systems below 6 GHz.

This effect leads to degraded signal quality and has proven to be a major limiting factor for the production of low-cost 60 GHz radios [2-73].

Modulation for 60 GHz digital wireless communication must consider all of the facets of 60 GHz wireless systems including the channel characteristics, antenna configurations, circuit limitations, and the nature of the data traffic. Unfortunately, there is not and cannot be a clear choice for the best modulation scheme at 60 GHz.

OFDM, constant envelope modulation, and linear single carrier scheme are potentially applicable since all offer advantages to the 60 GHz wireless system, but in different situations.

Like most designs, the modulation choice results from a consideration of design tradeoffs as summarized in Table 2-5.

Modulation Scheme	Advantages	Disadvantages
CEM/CPM	Maximum Power Efficiency	Poor Spectral Efficiency; High Complexity Receiver Designs
OFDM	High Spectral Efficiency; Simple Transmitter and Receiver Designs; Flexible Frequency Allocation	Sensitive to Phase Noise; Poor Power Efficiency; Added Complexity due to Coding and IFFT
Linear SC	Simple Transmitter and Receiver; Performance vs. Efficiency Compromise	Non-ideal Spectral Efficiency; Non-ideal Power Efficiency

Table 2-5: Modulation Strategy Summary

Therefore, in order to use the huge available bandwidth in this frequency range, two main approaches can be identified:

1. sending the information over the whole bandwidth, by using extremely spectrally inefficient modulations (BPSK, FSK, binary ASK, but also IR-UWB) but at a very high rate;
2. splitting the information over several narrower bandwidths using some kinds of frequency-domain multiplexing (those bandwidth slices could be separated by a guard interval as in FDMA or, more efficiently, some kind of OFDM can be used). In each narrow band, more spectrally efficient modulation schemes can be employed.

Several 60 GHz transceiver architectures have been proposed in literature. This section is devoted to show the state of art of these configurations, considering the main advantages and drawbacks offered by each architecture.
This section will be also focused on the study of emerging technologies and the analysis of their impact on the progression of the 60 GHz wireless design.

2.2.2.1 60 GHz Transceiver Architectures Based on OFDM Approach

As illustrated above, the choice of modulation scheme and values of the associated parameters is crucial since it determines important figures of merit, such as spectral efficiency, power efficiency, required level of transmit power, required coding overhead, and system complexity.
The OFDM is one of the more used digital modulation schemes in broadband wireless systems because of its many inherent advantages, such as its high spectral efficiency, considerable robustness against multipath and good equalization properties.
By representing the information bearing elements in the frequency domain (with an IFFT at the transmitter and a cyclic prefix with FFT operation at the receiver), the OFDM system is able to send information over approximately flat frequency components of a frequency selective channel.
For severely frequency selective channels (as with the large bandwidth channels for high data rate applications at 60 GHz), the total complexity of OFM to eliminate ISI is less than half that of single carrier time-domain equalization [2-74].

OFDM also offers high spectral efficiency when adapting the power and signal constellation over each frequency flat component of the frequency selective channel.
Finally, by selectively activating or annulling subcarriers, OFDM is easily adapted to different bandwidths, making its application very desirable.
OFDM, however, suffers from many drawbacks that complicate its application at 60 GHz and then beyond this band.
The time domain transmitted signal is observed to have large "peaks" when compared to average power values over the OFDM symbol (i.e., large PAPR). To maintain linearity, ordinary transmitters must limit output power levels leading to less efficiency in terms of power consumption (resulting in shorter battery life) and power transmitted (resulting in shorter range). To enable operation at a higher average power, more complex and expensive PAs are employed, increasing H/W costs in OFDM systems.
Moreover, OFDM systems are severely susceptible to frequency offsets culminating in higher design costs for synchronization. Consequently, phase noise will trouble OFDM implementations to a higher degree. Finally, although OFDM enables simple equalization, it will require significant error control coding to protect against frequency selective fades.
While OFDM is attractive for its equalization properties and spectral efficiency, the design of OFDM transceivers operating at 60 GHz is very difficult due to phase noise effects and PA limitations. Therefore, I/Q imbalance, phase noise and PA non linearity effects deeply influence BER performance for a OFDM system if used at 60 GHz [2-75], [2-76], [2-77], [2-78], [2-79], [2-80]. Additionally, OFDM does not allow for simple coding/decoding methods for reducing complexity in large bandwidth frequency selective channels at 60 GHz.

2.2.2.2 60 GHz Transceiver Architectures Based on CEM Approach

CEM transmits a signal with the information-bearing element contained entirely within its phase. CE modulation is ideal in terms of power efficiency since its constant magnitude baseband signal does not suffer from nonlinear distortion. CEM signals can operate in the nonlinear saturation region of PA at the transmitter. One specific and popular CEM implementation is CPM where the phase is a continuous function of time, creating a bandwidth efficient signal. CEM and CPM systems show some drawbacks.
From a capacity perspective, CEM and CPM systems have a lower achievable throughput, especially for high SNR [2-81].

In terms of implementation, optimal non-differential receiver and equalization structure for CPM systems can be highly complex since CPM signals are differentially coded at the transmitter. Frequency domain equalization for CPM signals is successful in reducing receiver complexity. However, even using this technique, as the constellation size grows, equalization quickly becomes complex [2-82]. CEM systems that operate with differential or symbol-by-symbol detectors are less complex, but will be highly sensitive to phase noise effects and multipath. Consequently, although CEM eases amplifier design at 60 GHz by its linearity independence, the susceptibility of higher-order CEM receivers to phase noise, the suboptimal spectral efficiency of CEM signals, and the complexity of CPM receivers suggest that only low-order CEM (such as PSK) or CPM techniques (such as MSK) will find any application at 60 GHz band.

2.2.2.3 60 GHz Transceiver Architectures Based on LINEAR SCM Approach

SC systems implemented with linear modulation (e.g. QAM and PAM constellations) offer a good compromise for many of the qualities discussed in previous paragraphs. SC systems, while not necessarily constant envelope, show better PAPR values than OFDM. With ISI equalization, linear SC receivers do not have to account for memory, lowering its complexity with respect to CPM. Various equalization algorithms can be implemented, although the complexity of time-domain equalization will exceed that of OFDM for severely frequency selective channels (like the 60 GHz indoor channel). In this case, the frequency domain equalization can be employed for SC systems in order to decrease complexity and to achieve performance comparable to OFDM. Finally, the linear SC systems are more robust to phase noise than CEM constellations of the same order, since they usually send information using the amplitude and phase of the symbol. The choice of linear modulated SC systems offers a good compromise for power efficiency, spectral efficiency, and receiver complexity while at the same time showing phase noise tolerance that is desirable for 60 GHz systems. However, OFDM or CEM may be preferred over linear SCM if maximal spectral or power efficiency is required, respectively.

2.2.2.4 60 GHz Transceiver Architectures Based on IR UWB Approach

UWB radio is an emerging technology that has attracted a great deal of interest from academia, industry, and global standardization bodies [2-83], [2-84], [2-85], 2-86], [2-87], [2-88], [2-89], [2-90].

The UWB technique has been used since around the 1960s for radar and military applications. On February 14, 2002, the FCC issued the First Report and Order (R&O) [2-91] which allowed unlicensed UWB operation and commercial deployment of UWB devices. There are three classes of devices defined in the R&O document:

i. imaging systems (e.g., ground penetrating radar systems, wall imaging systems, through-wall imaging systems, surveillance systems, and medical systems);
ii. vehicular radar systems;
iii. communication and measurement systems.

The FCC allocated a block of unlicensed radio spectrum from 3.1 – 10.6 GHz for the above applications where each category was allocated a specific spectral mask as described in [2-91]. A measurement metric appropriate for UWB signals is the fractional bandwidth, B_f, defined as [2-92]:

$$\mathrm{B}_f = \frac{2\cdot\left(f_{\mathrm{H}} - f_L\right)}{f_H + f_L} \tag{2-4}$$

where f_H and f_L represents the higher and lower -3 dB bandwidth, respectively.

Defense Advanced Research Project Agency defined UWB signals as signals with B_f greater than 25% [2-92]. This is much wider than any existing communications system. On the other hand, narrowband signals are defined as signals with B_f less than 1%, while wideband signals are between 1-25% [2-93].

Note that FCC only specified a spectral mask, and the bandwidth limitations of a UWB device, but not the type of signal and modulation scheme. According to FCC rules, a signal is defined as UWB if *its absolute bandwidth*, *B*, is at least 500 MHz or B_f is greater than 20% [2-91]. According to (2-4), f_H and f_L are now defined as the higher and lower -10 dB bandwidth, respectively. In general, the spectral mask associated with the FCC UWB regulation was designed to protect other spectrum users from undesiderable levels of interference caused by UWB transmissions. For wireless communications, the FCC regulated power levels are very low (i.e., -41.3 dBm/MHz), which allows UWB technology to overlay with available services such as GPS and the IEEE 802.11 WLAN. Additionally, the FCC prohibits UWB communications in toys, aircrafts or satellites.

On the basis of these considerations, the UWB technology represents a novel way of designing communication systems in comparison to current wireless communication systems. They are, in fact, predominantly narrowband: their carrier frequency is

significantly larger than the channel bandwidth, such as for example cellular telephony. The narrowband systems primarily rely on increasing the capacity, since they operate on spectrum constrained environment. On the contrary, the UWB systems mainly count on bandwidth. Broadband wireless requires the redefinition of circuit design techniques and the development of novel transceiver architectures as compared to narrowband systems. Additionally, given that narrowband front -end filters cannot be used, in-band interference and co-existence with other systems become a major consideration [2-94].

Since the 1990's, interest in commercial applications has increased due to several advantages offered by the UWB communication systems with respect to conventional narrowband ones, such as [2-95],[2-96]:

i. high data rate transmission. Current UWB systems can support more than 500 Mbps data transmission within 10 meters, which enables new services and applications;
ii. low complexity and low cost. These benefits arise from the essentially baseband nature of the signal transmission. Unlike conventional radio systems, the transmitter in an UWB IR architecture produces a very short time domain pulse, which is able to propagate without the need for an additional RF mixing stage. The latter takes a baseband signal and 'injects' a carrier frequency or translates the signal to a frequency which has desirable propagation characteristics. The very wideband nature of the UWB signal means it spans frequencies commonly used as carrier frequencies. The signal will propagate well without the need for additional up-conversion and amplification. The reverse process of down-conversion is also not required in the UWB receiver. Again, this means the omission of a local oscillator in the receiver, and the removal of associated complex delay and phase tracking loops.
iii. single chip architecture. UWB systems can be implemented nearly all-digitally with small-size, low cost and low power on a single chip architecture (e.g., CMOS) since the RF carrier can be eliminated. Such architecture is essential for handheld devices such as a MT;
iv. low power spectral density. UWB systems have low power spectral density that allows them to coexist with other services such as cellular systems, WLANs, GPS, etc. [2-97], [2-98];

v. security. Since UWB systems operate below the noise floor, they are inherently covert and extremely difficult for unintended users to detect [2-99], [2-100];

vi. fading robustness. UWB systems are immune to multipath fading and capable of resolving multipath environments. Resolvable paths can be combined to reduce the fading margin and enhance system performance [2-101], [2-102];

vii. high precision ranging. UWB systems have good time-domain resolutions and can promise sub-centimeter resolution capability for location and tracking applications. The very narrow time domain pulses mean that UWB technology is potentially able to offer timing precision much better than GPS and other radio systems [2-103], [2-104];

viii. low loss penetration. UWB systems can penetrate obstacles and thus operate under both LOS and non-LOS conditions [2-105], [2-106];

ix. scalability. UWB systems are very flexible because their common architecture is software re-definable so that it can dynamically trade-off high-data throughput for range [2-107], [2-108].

There are two main techniques for generating UWB signals are:

1. IR-UWB: in this case the signal is generated by short, very low duty cycle, baseband electrical impulses. Figure 2-7 shows a classical IR-UWB transceiver for center frequencies around 1-10 GHz: as no carrier is used to up-convert the signals, such systems are often called carrier free baseband or impulse radio communication systems.
2. CW-UWB. This method for generating UWB signals uses more traditional spreading techniques that are based on either the single carrier (DSSS or FHSS) or multi carrier technique (OFDM) or combination of both. Such systems involve traditional heterodyning architectures and can be treated as either single band or multiband (MB-UWB) designs. Such techniques present better spectral control properties than carrier free UWB due to the difficulty of controlling the exact shape of the impulse and consequently the shape of the frequency response. UWB systems for commercial purposes, such as 802.15a are carrier based UWB.

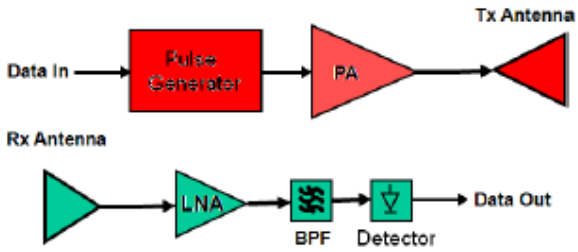

Figure 2-7: Classical IR-UWB Transceiver Scheme

However, the possibility offered by IR-UWB systems to avoid oscillators and mixers, that constitute the up and down conversion stages of carrier-based systems, has a twofold advantage in the specific case of use at EHF bands:

1. reduction of the complexity, cost and size of the transceiver since, as it has been shown above, implementing these components at higher frequencies is not trivial and it can be obtained with easily integrated technology;
2. the additional jitter related to the high phase noise of oscillators operating at these frequencies could also be avoided.

In [2-109] the authors proposed a 60 GHz transceiver based on IR-UWB architecture as shown in Figure 2-8.

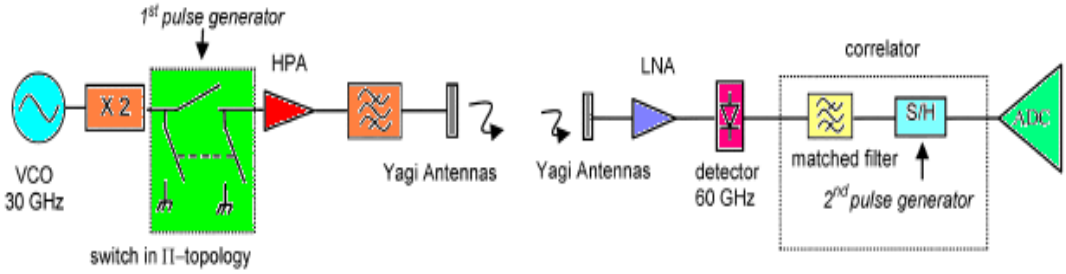

Figure 2-8: 60 GHz IR-UWB Transceiver proposed in [2-109]

In this configuration, the transmitter includes a simple free running MMIC VCO or VCDRO at 30 GHz and a frequency doubler. The output signal at 60 GHz is digitally modulated by the PPM pulses generated by the pulse former. This modulation is realized with a switch topology (on/off state). The receiver mainly consists of a detector/correlator. After low noise amplification and detection of the received signal, matched filtering and fast S/H operations are achieved. A second PG is used to control the sampler.

This system configuration is very simple, since the need for up/down carrier and frequency recovery loops in the system can be eliminated, compared to a conventional vectorial modulation scheme. Moreover, this simple RF structure makes it possible to reach a low-cost and low-power transceiver.

However, the major limit of this architecture is the limited switch ON/OFF ratio.

In [2-110] wavelets are generated with optimum fast start-up oscillator in the 4-5 GHz band for telecommunication. In [2-111], very short pulses occupying very high bandwidth are generated for radar applications using an optimum 24 GHz band-pass filter. The major drawback of this technique is the output waveform that contains tails due to the band-pass roll-off filter characteristics.

In [2-112], the authors proposed a transceiver architecture based on upon the fast start-up pulsed oscillator at 30 GHz trigged by a pulse generation exhibiting very fast transition times. In Figure 2-9, the scheme of a 60 GHz PPM TH UWB-IR transceiver architecture with pulsed-injected locked oscillator is shown.

The transmitter consists of a 30-GHz NDR oscillator triggered by a PG. This oscillator, based on 0.14 μm p-HEMT technology, is injection locked on the n^{th} harmonic component of the PRF and exhibits infinite switch ON/OFF ration.

The gate-source biasing voltage of the HEMT is achieved by the output voltage of the PG. When the PG output is at its low state the channel of the HEMT is pinched off so that the oscillation can only start when the output of the PG is at its high state. Because of its very fast transition times, the oscillator can lock on one of the numerous n^{th} harmonics created by the PG. The PPM-modulated pulses control the output of the 30 GHz source envelope. This PPM-modulated RF signal is then injected through FD and a MPA in order to obtain a pulsed-stable 60 GHz modulated signal.

For the receiver, after low-noise amplification, the envelope is retrieved using an RF detector. The signal is then demodulated using a matched filter and a SHA. The very simple demodulation scheme does not need any template generator such as in conventional PPM demodulators. The synchronization is described in [2-113]. This total baseband process (demodulation and synchronization) is fully analog and does not need any ADC.

However, despite the low power design, the DC consumption for this transceiver architecture is too high considering its application in autonomous objects or sensor networks. Moreover, this configuration does not present a low-integration solution.

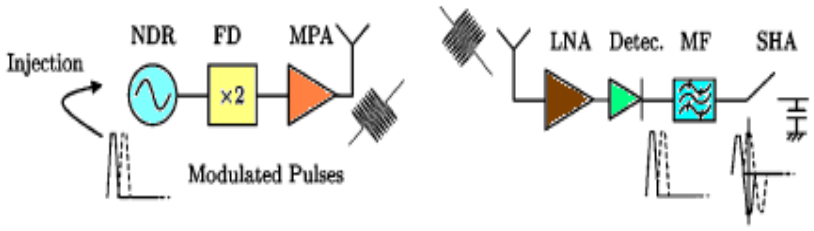

Figure 2-9: 60 GHz PPM TH IR-UWB Transceiver proposed in [2-112]

In [2-114], the authors reported a PPM TH IR UWB transceiver architecture using 0.13 µm SiGe BiCMOS technology in order to realize a integrated solution in a 60 GHz single chip. This solution, shown in Figure 2-10, is based on the architecture already demonstrated in [2-112], [2-113]. In this configuration, after the up-conversion of sub-nanosecond pulses (pulse width around 350 ps in order to reach 3 GHz bandwidth capacity) using a switch (implemented through a three HBT common-emitter stage amplifier), the signal is amplified and filtered by a Gaussian filter. The latter transforms the rectangular pulses into Gaussian ones in order to respect the pattern recommended by ERO in the [59-62] GHz band for use in WLAN communication. The transmitter output power is 9 dBm and the global DC-power consumption is below 150 mW.

To realise the receiver, either a detector or a mixer can be used. If a mixer is employed, an oscillator with high frequency stability at 60 GHz has to be designed. This is not required when a topology with a detector is chosen.

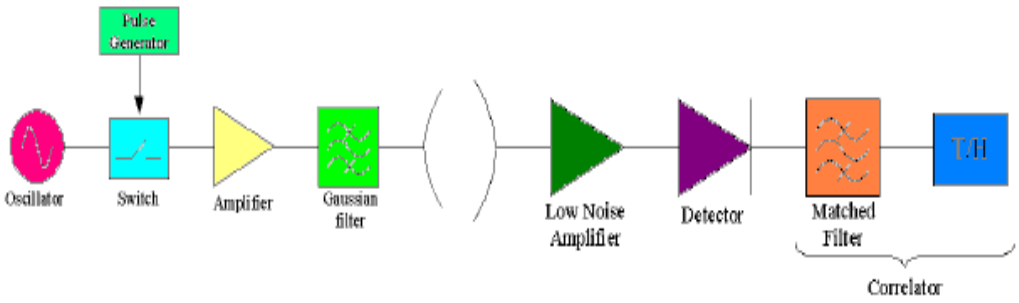

Figure 2-10: 60 GHz PPM TH IR-UWB Transceiver based on 0.13 µm SiGe BiCMOS technology as proposed in [2-114]

However, the transceiver architecture configurations reported above show as even an IR-UWB system operating at 60 GHz cannot be considered a carrier-free system: some kind of up and down conversion is needed in order to realize the transposition of a baseband signal at higher frequencies.

2.2.2.5 EMERGING TECHNOLOGIES FOR 60 GHZ SYSTEMS DEVELOPMENT

The future of 60 GHz systems will be shaped by emerging technologies to enable advanced techniques in the wireless transceiver. In this paragraph, two examples of innovative technologies are reported since they will have a large impact on the progression of 60G wireless design.

As previously discussed, high-gain antennas may be implemented to overcome fading margins in the link budget. As a result of the inherent "pointing" problems associated with these high gain antennas, many designers have proposed steerable beam antennas [2-115].

Such antenna configurations discover the best direction to point through a searching algorithm and then either mechanically alter the configuration of the antenna (as in MEMS systems), or use several antenna elements to construct a phased array with optimized radiation patterns. While such configurations have been demonstrated, it is yet to be observed in a practical commercial transceiver with a small form-factor required for WPAN and WLAN devices. If such technologies become practical, it will help enable 60 GHz systems that do not rely on LOS links.

2.3 REFERENCES

[2-1] S. K. Yong and C-C. Chong, "An Overview of Multi-Gigabit Wireless Through Millimeter Wave Technology: Potentials and Technical Challenges," EURASIP Journal Wireless Communications and Networking, vol. 2007, 2007.

[2-2] U. R. Pfeiffer et al., "A Chip-Scale Packaging Technology for 60-GHz Wireless Chipsets," IEEE Transaction on Microwave Theory and Techniques, vol. 54, no. 8, Aug. 2006, pp. 3387–97.

[2-3] S. Sarkar and J. Laskar, "A Single-Chip 25pJ/bit Multi-Gigabit 60 GHz Receiver Module," Proceedings on IEEE/MTT-S IMS '07, June 3–8, 2007, Honolulu, HI, 2007, pp. 475–78.

[2-4] T. Yao et al.,"60-GHz PA and LNA in 90-nm RF-CMOS," IEEE RFIC Symposium, June 2006, 4 pages.

[2-5] CEPT Reccomandation TR 22-03, "Provisional Reccomended Use of the Frequency Range 54.25-66 GHz by Terrestrial Fixed and Mobile Systems", Athens 1990.

[2-6] "Compatibility studies between Multiple Gigabit Wireless Systems in frequency range {57-66} GHz and other services and systems (except in 63-64 GHz)", ECC Report 114, September 2007.

[2-7] F. Giannetti, M. Luise, and R. Reggiannini, "Mobile and Personal Communications in 60 GHz band: A Survey", Wireless Personal Communications, vol. 10, pp. 207-243, 1999.

[2-8] D. Rogers, "Propagation Considerations for Satellite Broadcasting at Frequencies above 10 GHz", IEEE Journal on Selected Area Communications, vol. 3, no. 1, pp. 100-110, 1985.

[2-9] C. Anderson and T. Rappaport, "In-building wideband partition loss measurements at 2.5 GHz and 60 GHz," IEEE Transaction on Wireless Communications, vol. 3, no. 3, pp. 922-928, 2004.

[2-10] P. Smulders and A. Wagemans, "Wideband indoor radio propagation measurements at 58 GHz", Electronics Letters, vol. 28, no. 13, pp. 1270-1272, 1992.

[2-11] T. Manabe, Y. Miura, and T. Ihara, “Effects of antenna directivity and polarization on indoor multipath propagation characteristics at 60 GHz,” IEEE Journal on Selected Areas Communications, vol. 14, no. 3, pp. 441–448, 1996.

[2-12] T. Manabe, K. Sato, H. Masuzawa, K. Taira, T. Ihara, Y. Kasashima, and K. Yamaki, “Polarization dependence of multipath propagation and high-speed transmission characteristics of indoor millimeter-wave channel at 60 GHz,” IEEE Transaction on Vehicular Technology, vol. 44, no. 2, pp. 268–274, 1995.

[2-13] H. Xu, V. Kukshya, and T. Rappaport, “Spatial and Temporal Characteristics of 60-GHz Indoor Channels”, IEEE Journal on Selected Areas Communications, vol. 20, no. 3, pp. 620-630, 2002.

[2-14] J. A. Howarth, N. Weste, J. Harrison, L. M. Davis and A. Parker, “Towards a 60 GHz Gigabit system-on-chip”, Wireless World Research Forum.

[2-15] B. Razavi, "A 60-GHz CMOS Direct Conversion Receiver Front End," IEEE Journal on Solid-State Circuits, vol. 41, pp. 17-22, Jan. 2006.

[2-16] S. Reynolds et al., “60 GHz Transceiver Circuits in SiGe Bipolar Technology”, IEEE International Solid-State Circuits Conference Dig. Tech. Papers, Feb. 2004, pp. 442-43.

[2-17] W. Winkler, J. Borngräber, H. Gustat, F. Korndörfer, “60 GHz Transceiver Circuits in SiGe: C BiCMOS Technology”, Proceedings of the 30th European Solid-State Circuits Conference, 20-24, September, 2004, Leuven, Belgium, pp. 83-86.

[2-18] U. R. Pfeiffer et al., “A Chip-Scale Packaging Technology for 60-GHz Wireless Chipsets”, IEEE Transaction on Microwave Theory and Techniques, vol. 54, no. 8, Aug. 2006, pp. 387-97.

[2-19] S. Sarkar and J. Laskar, “A Single-Chip 25 pj/bit Multi-Gigabit 60 GHz Receiver Module”, proc. IEEE/MTT-s IMS’07, June, 3-8, Honolulu, HI, 2007, pp. 475-78.

[2-20] H. Doan et al., "A 60-GHz Down-converting CMOS Single-Gate Mixer," RFIC Dig. Tech. Papers, pp. 163-166, 2005.

[2-21] T. Mitomo, R. Fujimoto, N. Ono, R. Tachibana, H. Hoshino, Y. Yoshihara, Y. Tsutsumi, and I. Seto, “A 60-GHz CMOS Receiver Front-End With Frequency Synthesizer”, IEEE Journal on Solid State Circuits, Vol. 43, No.4, Apr. 2008.

[2-22] T. Yao et al., “60 GHz PA and LNA in 90-nm RF-CMOS,”, IEEE RFIC Symposium, June 2006, 4 pages.

[2-23] C. Marcu, et al., "90 nm CMOS Low Power 60 GHz Transceiver with Integrated Baseband Circuitry", IEEE International Journal of Solid-State Circuits, Vol. 44, Issue 12, Dec. 2009, pp. 3434-3447.

[2-24] A. Tomkins, et al., "A Zero-IF 60 GHz 65 nm CMOS Transceiver With Direct BPSK Modulation Demonstrating up to 6 Gb/s Data Rates Over a 2 m Wireless Link", IEEE Custom Integrated Circuits Conference (CICC), 2008, pp. 2085-2099.

[2-25] Y. Chiu et al., "A 65nm low-power CMOS transceiver for 802.11n portable application", Radio Frequency Integrated Circuits (RFIC) Symposium, 2008, Volume 17, Issue 17, June 2008, pp. 97-100.

[2-26] C. Mounet, A. Siligaris, A. Michel, M. Capodiferro, "Employing 65 nm CMOS SOI for 60 GHz WPAN applications", 2008 International Conference on Microwaves, Communications, Antennas and Electronic Systems (COMCAS), Vol. 13, Issue 14, May 2008, pp. 1 – 10.

[2-27] A. Tomkins, et al., "Circuit performance characterization of digital 45-nm CMOS technology for applications around 110 GHz", 2008 IEEE Symposium on VLSI Circuits, Vol. 18, Issue 20, June 2008, pp. 162-163.

[2-28] D. Ponton et al., "Design of ultra-wideband low-noise amplifiers in 45-nm CMOS technology: comparison between planar bulk and SOI FinFET devices", Special issue on ISCAS2008, Volume 56, Issue 5, May 2009, pp. 920-932.

[2-29] C. Doan, S. Emami, D. Sobel, and R. Brodersen, "Design Considerations for 60 GHz CMOS Radios", IEEE Communications Magazine, vol. 42, no. 12, pp. 132-140, 2004.

[2-30] C. Enz, "An MOS Transistor Model for RF IC Design Valid in all Regions of Operation", IEEE Transaction on Microwave Theory Techniques, vol. 50, January 2002, pp. 342-59.

[2-31] S. Emami et al., "Large-signal Millimeter-wave CMOS modeling with BSIM3", IEEE RFIC Symposium Dig., June 2004, pp. 163-166.

[2-32] C-H. Lai Ivan, K. Yuki, and F. Minoru, "60-GHz CMOS Down-Conversion Mixer with Slow-Wave Matching Transmission Lines," IEEE ASSCC, pp. 195-198, November 2006.

[2-33] C. S. Lin, P. S. Wu, H. Y. Chang and H. Wang, "A 9–50-GHz Gilbert cell down-conversion mixer in 0.13-μm CMOS technology," IEEE Microw. Wireless Compon. Lett., vol. 16, no. 5, pp. 293 – 295, May 2006.

[2-34] S. Emami, C. H. Doan, A. M. Niknejad, and R. W. Brodersen, "A 60-GHz down-converting CMOS single-gate mixer," in IEEE RFIC Symposium. Dig., pp. 163–166, Jun. 2005.

[2-35] H. Kuo, C. Yang, J. Yeh, H. Chuang and T. Huang, "Design of a 60-GHz Down-Converting Dual-Gate Mixer in 130 nm CMOS Technology", Proceedings of 39th European Microwave Conference, 2009, pp. 405-408, September, 29 - October, 1, Rome, Italy.

[2-36] F. R. Shahroury, and C-Y. Wu, "The Design of Low LO-Power 60-GHz CMOS Quadrature-Balanced Self-Switching Current-Mode Mixer," in IEEE MWCL, pp. 692–694, October 2008.

[2-37] J. Kim, M. Jeon, D. Kim, J. Jeong, and Y. Kwon, "High-performance V-band cascode HEMT mixer and downconverter module," IEEE MTT, pp. 805-810, March 2003.

[2-38] V. Subramanian, V. Do, W. Keusgen, and G. Boeck., "60 GHz SiGe HBT downconversion mixer," IEEE EMICC, pp. 76-79, Oct. 2007.

[2-39] L. M. Franca-Neto, R. E. Bishop, and B. A. Bloechel, "64 GHz and 100 GHz VCOs in 90 nm CMOS using optimum pumping method," in IEEE ISSCC Dig., Feb. 2004, pp. 444–538.

[2-40] Z.-M. Tsai, C.-S. Lin, C. F. Huang, J. G. J. Chern, and H.Wang, "A fundamental 90-GHz CMOS VCO using new ring-coupled quad," IEEE Microwave Wireless Components Letters, vol. 17, pp. 226–228, Mar. 2007.

[2-41] K. Ishibashi, M. Motoyoshi, N.Kobayashi, and M. Fujishima, "76 GHz CMOS voltage-controlled oscillator with 7% frequency tuning range," in Symposium VLSI Circuits Dig., Jun. 2007, pp. 176–177.

[2-42] B. Heydari, M. Bohsali, E. Adabi, and A. M. Niknejad, "Millimeter wave devices and circuits block up to 104 GHz in 90 nm CMOS," IEEE Journal Solid-States Circuits, vol. 42, no. 12, pp. 2893–2903, Dec. 2007.

[2-43] E. Laskin, M. Khanpour, R. Aroca, K. W. Tang, P. Garcia, and S. P. Voinigescu, "A 95 GHz receiver with fundamental-frequency VCO and static frequency divider in 65 nm digital CMOS," in IEEE ISSCC Dig., Feb. 2008, pp. 180–605.

[2-44] H. M. Cheema, R. Mahmoudi, M. A. T. Sanduleanu, and A. van Roermund, "A 44.5 GHz differentially tuned VCO in 65 nm bulk CMOS with 8% tuning range," in IEEE Radio Frequency Integrated Circuits Symposium Dig., Jun. 2008, pp. 649–652.

[2-45] J. Lee, M. Liu, and H. Wang, "A 75-GHz phase-locked loop in 90-nm CMOS technology," IEEE Journal Solid-State Circuits, vol. 43, no. 6, pp. 1414–1426, Jun. 2008.

[2-46] H. Wu and A. Hajimiri, "Silicon-based distributed voltage-controlled oscillators," IEEE Journal Solid-State Circuits, vol. 36, no. 3, pp. 493–502, March 2001.

[2-47] H. Shigematsu, T. Hirose, F. Brewer, and M. Rodwell, "Millimeter wave CMOS circuit design," IEEE Transaction Microwave Theory Technique, vol. 53, no. 2, pp. 472–477, February 2005.

[2-48] W. F. Andress and D. Ham, "Standing wave oscillators utilizing wave adaptive tapered transmission lines," IEEE Journal Solid-State Circuits, vol. 40, no. 3, pp. 638–651, March 2005.

[2-49] C. Cao and K. K. O, "Millimeter-wave voltage-controlled oscillators in 0.13-μm CMOS technology," IEEE Journal Solid-State Circuits, vol. 41, no. 6, pp. 1297–1304, June 2006.

[2-50] H.-H. Hsieh, Y.-C. Hsu, and L.-H. Lu, "A 15/30-GHz dual-band multiphase voltage-controlled oscillator in 0.18 μm CMOS," IEEE Transaction Microwave Theory Technique, vol. 55, no. 3, pp. 474–483, March 2007.

[2-51] H.-H. Hsieh, Y.-H. Chen, and L.-H. Lu, "A millimeter wave CMOS LC-tank VCO with an admittance-transforming technique," IEEE Transaction Microwave Theory Technique, vol. 55, no. 9, pp. 1854–1861, September 2007.

[2-52] Y.-H. Cho, M.-D. Tsai, H.-Y. Chang, C.-C. Chang, and H. Wang, "A low phase noise 52-GHz push-push VCO in 0.18 μm bulk CMOS technologies," in IEEE Radio Frequency Integrated Circuits Symposium Dig., Jun. 2005, pp. 131–134.

[2-53] P.-C. Huang, R.-C. Liu, H.-Y. Chang, C.-S. Lin, M.-F. Lei, H. Wang, C.-Y. Su, and C.-. L. Chang, "A 131 GHz push-push VCO in 90-nm CMOS technology," in IEEE Radio Frequency Integrated Circuits Symposium Dig., June 2005, pp. 613–616.

[2-54] C. Cao, E. Seok, and K. K. O, "192 GHz push-push VCO in 0.13 μm CMOS," IEEE Electronic Letters, vol. 42, no. 4, pp. 208–210, February 2006.

[2-55] P.-C. Huang, M.-D. Tsai, G. D. Vendelin, H. Wang, C.-H. Chen, and C.-S. Chang, "A low-power 114-GHz push-push CMOS VCO using LC source degeneration," IEEE Journal Solid-State Circuits, vol. 42, no. 6, pp. 1230–1239, June 2007.

[2-56] C. Cao, Y. Ding, and K. K. O, "A 50 GHz phase-locked loop in 0.13 μm CMOS," IEEE Journal Solid-State Circuits, vol. 42, no. 8, pp. 1649–1656, Aug. 2007.

[2-57] R. Wanner, R. Lachner, G. R. Olbrich, “Low phase noise SiGe push-push oscillators for cm- and mm-wave applications,” IEEE Microwave Conference Proceedings, Vol. 2, Issue, 4-7, December 2005.

[2-58] C. Ameziane, D. Belot, R. Plana, T. Taris, Y. Deval, and J.-B. Begueret, “A 64GHz Push-Push Oscillator in 0.13 μm”, Proceedings of the 39th Microwave Conference, September, 29 – October, 1, Rome, Italy, 2009.

[2-59] F.- H. Huang, Y. – J. Chan, “V-Band CMOS Injection-Locked Oscillator Using Fundamental Harmonic Injection”, IEEE Microwave and Wireless Components Letters, Vol. 17, Issue 12, pp. 882-884, December 2007.

[2-60] P.-C. Huang, M.-D. Tsai, G. D. Vendelin, H. Wang, C.-H. Chen and C.- S. Chang, “A Low-Power 114-GHz Push-Push CMOS VCO Using LC Source Degeneration”, IEEE Journal Solid-State Circuits, vol. 42, no. 6, pp. 1230-1239, June 2007.

[2-61] H. Shin and H. Kim, “Extraction technique of differential second harmonic output in CMOS LC VCO,” IEEE Microwave Wireless Components Letters, vol. 17, pp. 379–381, May 2007.

[2-62] H.-H. Hsieh, and L.-H. Lu, “A V-Band CMOS VCO With an Admittance-Transforming Cross-Coupled Pair”, IEEE Journal of Solid-State Circuits, vol. 44, no. 6, June 2009.

[2-63] F. Ellinger, T. Morf, G. Buren et al., “60 GHz VCO with wideband tuning range fabricated on VLSI SOI CMOS Technology”, IEEE MTT-S International Conference, vol. 3, pp. 1329 – 1332, June 2004.

[2-64] M. Tiebout, et al., “A 1 V 51 GHz fully-integrated VCO in 0.12 μm CMOS”, IEEE ISSCC Technoloy Dig., vol. 1, pp. 300-301, February 2002.

[2-65] R.-C. Liu, et al., "63-GHz VCO using a standard 0.25μm CMOS process," ISSCC Digest, pp. 446-447, Feb 2004.

[2-66] C. Lee, T. Yao, A. Mangan, K. Yau, M. A. Copeland, S.P. Voinigescu, “SiGe BiCMOS 65-GHz BPSK transmitter and 30 to 122 GHz LC-varactor VCOs with up to 21% tuning range”, SCICSS pp. 179-182, 2004.

[2-67] M. G. M. Notten and H. Veenstra, “60 GHz Qudrature Signal Generation with a Single Phase VCO and Polyphase Filter in a 0.25 μm SiGe BiCMOS Technology”, IEEE Bipolar/BiCMOS Circuits and Technology Meeting (BCTM) 2008, vol.13, Issue 15, pp. 178 –181, October 2008.

[2-68] I. Aoki, et al., "Fully integrated CMOS Power Amplifier Design Using the Distributed Active-Transformer Architecture", IEEE Journal of Solid-State Circuits, vol. 37, March 2001, pp. 371-383.

[2-69] R. A. York, "Some Considerations for Optimal Efficiency and Low Noise in Large Power Combiners," IEEE Transaction Microwave Theory Technique, vol. 49, August 2001, pp. 1477–82.

[2-70] Y. Jin, M. Sanduleanu, and J. Long, "A wideband millimeter wave power amplifier with 20 dB linear power gain and +8 dBm maximum saturated output power," IEEE Journal Solid-State Circuits, vol. 43, no. 7, pp. 1553–1562, July 2008.

[2-71] C. Doan, et al., "Design Considerations for 60 GHz CMOS Radios", IEEE Communications Magazine, pp. 132-140, December 2004.

[2-72] Y. Shoji, K. Hamaguchi, and H. Ogawa, "Millimeter-wave remote self-heterodyne system for extremely stable and low-cost broad-band signal transmission", IEEE Transaction Microwave Theory and Techniques, vol. 50, no. 6, pp. 1458-1468, 2002.

[2-73] D. Cabric, M. S. W. Chen, D. A. Sobel, S. Wang, J. Yang, and R. W. Brodersen, "Novel Radio Architectures for UWB, 60 GHz, and cognitive wireless systems." EURASIP Journal on Wireless Communications and Networking, vol. 2006, 2006.

[2-74] P. Smulders, "Exploiting the 60 GHz band for local wireless multimedia access: Prospects and Future Directions", IEEE Communications Magazine, vol. 40, no. 1, pp. 140-147, 2002.

[2-75] T. Pollet, M. V. Bladel, and M. Moeneclaey, "BER Sensitivity of OFDM Systems to Carrier Frequency Offset and Wiener Phase Noise," IEEE Transaction Communications, vol. COM-43, 1995, pp. 191–93.

[2-76] C-L. Liu, "Impacts of I/Q Imbalance on QPSK-OFDMQAM Detection," IEEE Transaction Consumer Electronics, vol. 44, no. 3, Aug. 1998, pp. 984–89.

[2-77] J. Tubbax et al., "OFDM Versus Single Carrier: A Realistic Multi-Antenna Comparison," EURASIP Journal Applied Signal Processing, vol. 2004: 9, 2004, pp. 1275–87.

[2-78] D. Cabric et al., "Novel Radio Architectures for UWB, 60-GHz, and Cognitive Wireless Systems," EURASIP Journal Wireless Communications and Networking, vol. 2006, 2006.

[2-79] X. Jiang, Z. Wang, and M. F. Chang, "A 2 Gs/s 6b ADC in 0.18um CMOS," Proceedings IEEE ISSCC '03, San Francisco, CA, Feb. 2003, pp. 322–23.

[2-80] C. Rapp, “Effects of HPA-Nonlinearity on a 4-DPSK/OFDMSignal for a Digital Sound Broadcasting System,” Proceedings ECSC-2, Oct. 1991, Liege, Belgium, pp. 179–84.

[2-81] K. Yu, and A. Goldsmith, “Linear models and capacity bounds for continuous phase modulation”, Proceedings of IEEE International Conference on Communications, vol. 2, 2002, pp. 722-726.

[2-82] J. Tan and G. Stuber, “Frequency-domain equalization for continuous phase modulation”, IEEE Transaction on Wireless Communications, vol. 4, no. 5, pp. 2479-2490, 2005.

[2-83] M. Z. Win and R. A. Scholtz, “Impulse Radio: How it works”, IEEE Communications Letters, vol. 2, no. 2, pp. 36-38, February 1998.

[2-84] R. A. Scholtz et. al., “Ultra-wide Bandwith Time-Hopping Spread-Spectrum Impulse Radio for Wireless Multiple-Access Communications,” IEEE Transaction on Communications, vol. 48, no. 4 , pp. 679-691, April 2000.

[2-85] Intel White Paper, “Ultra-Wide Band (UWB) Technology: Enabling High-Speed Wireless Personal Area Networks”, 2004. [Online]. Available: http://www.intel.com/technology/comms/uwb.

[2-86] MultiBand OFDM Alliance Special Interest Group (MBOA-SIG) White Paper, “Ultrawideband: High Speed, Short-Range Technology with far-reaching effects”, September 1, 2004. [Online]. Available: http://www.alereon.com/technology/white-papers.

[2-87] Freescale Semiconductor, Inc. White Paper, “USB without wires: Understanding different approaches using ultra-wideband technology”, February 2006. [Online]. Available: www.freescale.com/uwb.

[2-88] Standard ECMA-368: High Rate Ultra Wideband PHY and MAC Standard 3rd Edition, Std. December 2008. [Online]. Available: http://www.ecma-international.org/publications/standards/Ecma-368. htm.

[2-89] IEEE 802.15 WPAN High Rate Alternative PHY Task Group 3a (TG3a), Std. [Online]. Available: http://www.ieee802.org/15/pub/TG3a/html.

[2-90] IEEE 802.15 WPAN Low Rate Alternative PHY Task Group 4a (TG4a), Std. [Online]. Available: http://www.ieee802.org/15/pub/TG4a/html.

[2-91] Federal Communications Commission, “Revision of part 15 of the Commission’s Rules regarding Ultra-Wideband Transmission Schemes, first report and order (ET Docket 98-153),”. Adopted February 2002, Released April 22, 2002.

[2-92] OSD/DARPA Ultra-Wideband Radar Review Panel, "Assessment of Ultra-Wideband (UWB) Technology", Battelle Tactical Technology Center, July 13, 1990, Contract No. DAAH01-88-C-0131, ARPA Order 6049.

[2-93] J. D. Taylor, "Introduction to Ultra-Wideband Radar Systems". Boca Raton, FL: CRC Press, 1995.

[2-94] R.Gharpurey and P.Kinget, "Ultra-Wideband Circuits, Transceivers and Systems", Springer, 2008.

[2-95] I. Oppermann, M. Hämäläilen and J. Iinatti, "UWB Theory and Applications", J. Wiley and Sons. Ltd., 2004

[2-96] M.Ghavami, L. B. Michael and R. Kohno, "Ultra Wideband Signals and Systems in Communication Engineering", J. Wiley and Sons. Ltd., 2004.

[2-97] M. Hämäläilen, V. Hovinen, R. Tesi, J. H. Iinatti, and M. Latva-aho, "On the UWB system coexistence with GSM900, UMTS/WDCMA, and GPS", IEEE Journal on Selected Areas Communications, vol. 20, no. 9, pp. 1712-1721, December 2002.

[2-98] R. Giuliano, and F. Mazzenga. "On the coexistence of power-controlled ultrawide-band systems with UMTS, GPS, DCS1800, and fixed wireless systems", IEEE Transaction on Vehicular Technology, vol. 54, no. 5, pp. 1623-1631, September 2005.

[2-99] M. Z. Win and R. A. Scholtz, "On the robustness of ultra-wide bandwidth signals in dense multipath environments", IEEE Communications Letters, vol. 2, no. 2, pp. 51-53, February 1998.

[2-100] D. R. McKinstry and R. M. Buehrer, "Issues in the performance and covertness of UWB communication systems", in Proceedings of 45th Midwest Symposium on Circuits and System, vol. 3, Tulsa, OK, August 2002, pp. 601-604.

[2-101] R. A. Scholtz et. al., "On the robustness of ultra-wide bandwidth signals in dense multipath environments", IEEE Communications Letters, vol. 2, no. 2, pp. 51-53, February 1998.

[2-102]W. Suwansantisuk, et. al., "On the performance of wide-bandwidth signal acquisition in dense multipath channel", in IEEE Conference on Ultra Wideband Systems and Technologies, Baltimore, MD, May 2002, pp. 105-109.

[2-103] S. Gezici, et. al., "Localization via ultra-wideband radios: a look at positioning aspects for future sensor networks", IEEE Signal Processing Magazine, vol. 22, pp. 70-84, July 2005.

[2-104] D. Dardari, C.-C. Chong, and M. Z. Win, "Analysis of threshold-based TOA estimator in UWB channels", in Proceedings of European Signal Processing Conference (EUSIPCO), Florence, Italy, September 2006.

[2-105] A. F. Molish, et. al. "Ultra-wideband Propagation channels-theory, measurement and modeling", IEEE Transaction on Vehicular Technology, vol. 54, no. 5, pp. 1528-1545, September 2005.

[2-106] C. C. Zhong et. al, "Statistical Characterization of the UWB propagation channel in indoor residential environment", vol. 5, no. 5, pp. 503-512, August 2005.

[2-107] C. C. Zhong et. al, "On the performance of non-coherent and differential-coherent UWB –DCC system", in Proceedings of IEEE Wireless Communications and Networking Conference, Las Vegas, NE, April 2006.

[2-108] C. C. Zhong et. al, "UWB-DSCK communication systems for low rate WPAN applications", in Proceedings of IEEE International Symposium on Personal, Indoor and Mobile Radio Communications, Berlin, Germany, September, 2005.

[2-109] N. Deparis, et. al., "Transposition of a Baseband UWB Signal at 60 GHz for High Data Rate Indoor WLAN", IEEE Microwave and Wireless Components Letters, Vol. 15, no. 10, , pp. 609-611, October 2005.

[2-110] D. Barras, et. al., "Low-power ultrawideband wavelets generator with fast start-up oscillator", IEEE Transaction on Microwave Theory and Techniques, vol. 54, no. 5, pp. 2138-2145, May 2006.

[2-111] Y. Kawano, et. al, "RF Chipset for Impulse UWB Radar using 0.13 μm InP-HEMT Technology", IEEE Transaction on Microwave Theory and Techniques, vol. 54, no. 12, pp. 4489-4497, December 2006.

[2-112] N. Deparis, et. al., "60 GHz UWB-IR Transceiver With Pulsed-Injected Locked Oscillator", in Proceedings of the 37th European Microwave Conference, pp. 1038-1041, Munich, October 2007.

[2-113] N. Deparis, A. Bo, C. Loyez, et. al., "Receiver and Synchronization for UWB impulse radio signals," in Dig. IEEE International Microwave Symposium, June 2006, pp. 1414–1417.

[2-114] M. Devulder, et. al., "60 GHz UWB Transmitter for Use in WLAN Communication", IEEE International Conference on UWB 2007, (ICUWB 2007), pp. 432 – 435, September, 24-26, 2007.

[2-115] K. Chang et. al., "Novel low-cost beam-steering techniques", IEEE Transaction on Antennas Propagation, vol. 50, no. 5, pp. 618-627, 2002.

3 On The Use of IR-UWB Technology for Multi-Gigabit Wireless Communications Beyond 60 GHz

The recent rapid growth in technology and the successful commercial deployment of wireless communications are significantly affecting our daily lives. The transition from analog to digital cellular communications, the rise of third- and fourth-generation radio systems, and the replacement of wired connections with Wi-Fi and Bluetooth are enabling consumers to access a wide range of information from anywhere and at any time. As the consumer demand for higher capacity, faster service, and more secure wireless connections increases, new enhanced technologies have to find their place in the overcrowded and scarce RF spectrum. This is because every radio technology allocates a specific part of the spectrum; for example, the signals for TVs, radios, cell phones, and so on are sent on different frequencies to avoid interference to each other. As a result, the constraints on the availability of the RF spectrum become more and more strict with the introduction of new radio services. In order to perform communications without interference issues, the only possibility is to look at the EHF band and hence exploit the huge bandwidth, available at those frequencies range, with no constraints. Therefore, many researchers have turned their attention to the possibility of using millimeter wave bands for wireless communications. As largely described in the last chapter, the availability of free bandwidth of 7 GHz around the 60 GHz can be exploited to perform indoor communications. However, the attenuation due to oxygen absorption makes communication at this frequency range unsuitable for long range. Moreover, the recently allocated 71–76 GHz and 81–86 GHz bands provide an opportunity for LOS links with longer range and higher data rates. However, the exploitation of frequencies beyond 60 GHz (in particular included in W band) for outdoor wireless communications, both terrestrial and satellite, presents some uncertainity and risks. The most critical issues are related to non-idealities of components operating at those frequencies (phase noise of oscillators and mixers, non-linear amplifier distortions, timing uncertainities, etc.) and the lack of knowledge in the signal propagation modalities for frequencies higher than 50 GHz. In order to exploit such a frequency range for broadband

wireless communications, the design of a transceiver robust to these non-idealities and also able to deliver very high data rates (of the order of multi-gigabit/s) requires a novel design approach with respect to the one followed so far in transmissions below 60 GHz. Therefore, an optimised joint design of the RF and baseband parts, taking into account the not idealities of the technology and the beyond 60 GHz channel and for such high data rates, is mandatory.

3.1 SCIENTIFIC MOTIVATIONS AND WORK AIMS

The objective of this work is to investigate the feasibility and provide guidelines for the design of wireless communication systems operating in the frequency ranges above 60 GHz, and able to achieve data rates on the order of multigigabit/s. As the request for high quality multimedia, voice and data services rises, the communication technology is experiencing the need for multigigabit/s speeds. Novel solutions for spectrum use (such as cognitive radios), advances in MIMO, cooperative paradigms are nowadays being investigated to approach the goal of gigabit/s communications (see, for instance, the IMT-Advanced concept under development). However, in the long run, there is no alternative but to turn towards higher carrier frequencies to support ultra-broadband information carrying signals. In fact, Shannon's theory imposes a precise upper bound to achievable spectral efficiency over generic band limited channels. In some cases, such limits are almost approaching. For instance, IEEE 802.11n can reach up to 320 Mb/s in very short range and under optimal condition, with a spectral efficiency of 15 b/s/Hz. However, it is not reasonable to push for higher spectral efficiency over overcrowded bandwidth portions like ISM ones. This is the reason why "the great escape" towards higher and higher frequency carriers has begun since some years. Recently, 60 GHz band has been considered for terrestrial UWB applications and some experimental trials are carried on to test the feasibility of the exploitation of W-band for terrestrial and satellite communications. In few words, the exploration of still unknown EHF domain or millimeter wave domain is now a subject of relevant research interest. Nevertheless, this field is still highly explorative. Different propagation conditions than at lower frequency bands (for instance, strong atmospheric attenuation and weak diffraction), lack of components with good (i.e. near to ideal) characteristics (for instance, limited non linearities, small phase noise), limitations on the pass-band of digital devices (A/D converters), can limit the

efficient use of these high frequency bands to achieve multigigabit/s communications, when traditional design approaches are considered. The difficulty in using those high frequency bands turns out in a spectral efficiency that decreases with the increase of the carrier frequency. Therefore, a re-thinking of the transceiver design could change this trend. Recently, a lot of work has been spent in the design of short-range 60 GHz wireless communication systems. Nevertheless, there is a lack of discussions and investigations on the most suitable modulation, equalization, and algorithm design at the physical layer. Therefore, the main objective of this work is to provide guidelines for the design of the RF and baseband sections of transmission links providing multigigabit/s communications at such high frequency bands. To this end, some novel approaches will be investigated and compared. Point-to-point wireless links with a coverage range of around 1-10 km, ideally suited for fiber replacement in applications such as enterprise connectivity, can be identified as the ideal applicative scenario within which the present work is set. Moreover, in this phase in which research on this topic is still at its very initial step, this section wants mainly to show the feasibility of such high-speed data transfer in those frequency bands, regardless of the specific scenario and application.

Two main research objectives have been identified and this section tries to describe the possible way to follow in order to satisfy them.

- *Objective #1,* that consists of providing an answer to the question: "*What is the best way to use the huge bandwidth available at those high frequency bands?*"

Two main different approaches can be adopted:

1) we could send the information over the whole bandwidth, by using extremely spectrally inefficient modulations (BPSK, FSK, binary ASK, but also UWB) but at a very high rate (let us say, a 20 GHz bandwidth for 10 Gigabit/sec);

2) or we could split the information over several narrower bandwidths using some kind of frequency-domain multiplexing techniques (those bandwidth slices could be separated by a guard interval as in FDMA or, more efficiently, some kind of OFDM can be used). In each narrow band, more spectrally efficient modulation schemes must be used.

On the other hand, UWB transmissions, in particular IR-UWB used at those high frequency bands, could show interesting advantages in terms of simplicity of the RF and baseband designs. Some of the questions this work aims to give an answer are:

i. What is the best way to generate an UWB signals centered at those frequency bands?
ii. Would it be possible to avoid classical up-conversion with oscillators?

One of the major Ph.D activities has been focused on the investigation of the use of the IR-UWB technique in order to perform multigigabit/s transmission at frequency bands beyond 60GHz. The work has been pointed towards the definition of innovative RF architectures in order to design transceivers able to realise multi-gigabit wireless communications using "beyond 60 GHz" frequencies. In particular, some RF architectures based on IR-UWB technology for communications beyond 60 GHz will be analysed, both in terms of robustness to the EHF impairments and lower cost design. The non-ideal characteristics of the components, which are experienced in reality and which lead to so called Dirty RF effects, are taken into consideration. The models are either based on measurement data of real components or on simulation methods that are extended to the UWB case. The influence of each non-linear effect on the performance of a PPM TH IR UWB transceiver operating at W band frequencies will be analysed in terms of BER curves. Then, a comparison of the BER performance degradation in presence of main non-idealities will be carried out between an IR UWB architecture and a single carrier FSK scheme (with same data rate). Finally, different choices on the RF components will be discussed.

- *Objective #2: Channel characterisation*

One key issue about which this study aims to give a contribution is the outdoor channel characterization at W band. It is still an open issue. The experimental channel characterisation of this part of the EHF range (up to 110GHz) represents an important step towards the proper use of those frequency bands for wireless communications. The analysis and validation of a terrestrial link operating at those frequencies, with the capability to carry out transmission/reception experiments, could give important feedback from the technology point of view and also for the channel characterisation. The procedure of W band channel characterisation is foreseen to be challenging and, at the best of my knowledge, there are not reported experiments at the frequency bands of interest. In particular, the University of Rome "Tor Vergata" is developing a W-band link between two locations that are 7.4 km away in LOS, using available components provided by the company RHI. The W-band link has been designed to perform channel measurements (attenuation) and BER evaluation considering simple low order modulations (FSK and QPSK). In this frame, the following chapter will firstly report a preliminary orographic analysis of the terrestrial link on 7.4 Km between the Electronic Department of University of Rome "Tor Vergata" and Villa Mondragone. Then, a detailed insight into transmitter and receiver schemes will be reported taking into account constraints related to the

characteristic of the available H/W in RHI Italy. Finally, an accurate link budget for dimensioning the system in terms of maximum link capability will be reported.

To summarise, the expected results by this work consist of:

1) guidelines for the design of the RF and baseband of transmission links providing multigigabit/s communications at such high frequency bands;
2) a more clear understanding of the limits and the feasibility of those high data rates at such high frequency bands considering the state of art of technology.

3.2 COMMUNICATIONS AT EHF BAND

Where a huge bandwidth for UWB communications can be made available without interference issues? The unique possibility is to look at the EHF band.

The EHF spectrum allocation for fixed and mobile terrestrial radio communications services [3-1] is summarized in Table 3-1. The use of the EHF spectrum on an unlicensed basis requires a careful determination of the emission limits, but it represents an interesting topic for the application in directive LOS building-to-building connections or indoor short range networks (as already shown due to the use of 60 GHz band), where even low transmission power could allow to carry out multi-gigabit/s communications.

In Europe, 60 GHz regulations are considered by the Electronic Communications Committee (ECC) of the European Conference of Postal and Telecommunications Administrations (CEPT) for WPAN applications [3-2]. Furthermore, the European Radiocommunication Committee (ERC) considered the use of 57–59 GHz band for fixed services without requiring frequency planning [3-3]. Later, the ECC recommended the use of point-to-point fixed services in the 64–66 GHz band [3-4]. ECC also recommended the use of the 57-64 GHz frequency band for point-to-point fixed wireless systems [3-5]. Under these proposal, 9 GHz of unlicensed spectrum is allocated for 60 GHz operation between 57 GHz and 66 GHz [3-6]. The actual band is used for many purposes. In fact, there are two types of licence-free applications in the European regulations. One of them is the RTTT (Road Transport and Traffic Telematics) between 63 –64 GHz. The other licence-free application is the use of Multiple-Gigabit WAS/RLAN Short Range Devices with very restricted output power. However, at higher output power, the European

regulations recommend licences or light licensing methods (ECC/REC/(05)02, ECC/REC/(09)01) or they don't deal with the method of licensing (ERC/REC 12-09).

Frequency (GHz)	Region 1	Region 2	Region 3
30.0 - 31.0	-	-	-
31.0 - 31.3	fixed, mobile	fixed, mobile	fixed, mobile
31.3 - 31.5	-	-	-
31.5 - 31.8	fixed, mobile	-	fixed, mobile
31.8 - 33.4	fixed	fixed	fixed
33.4 - 36.0	-	-	-
36.0 - 43.5	fixed, mobile	fixed, mobile	fixed, mobile
43.5 - 47.0	mobile	mobile	mobile
47.0 - 47.2	-	-	-
47.2 - 50.2	fixed, mobile	fixed, mobile	fixed, mobile
50.2 - 50.4	-	-	-
50.4 - 52.6	fixed, mobile	fixed, mobile	fixed, mobile
52.6 - 55.78	-	-	-
55.78 - 66.0	fixed, mobile	fixed, mobile	fixed, mobile
66.0 - 71.0	mobile	mobile	mobile
71.0 - 76.0	fixed, mobile	fixed, mobile	fixed, mobile
76.0 - 81.0	-	-	-
81.0 - 86.0	fixed, mobile	fixed, mobile	fixed, mobile
86.0 - 92.0	-	-	-
92.0 - 94.0	fixed, mobile	fixed, mobile	fixed, mobile
94.0 - 94.1	-	-	-
94.1 - 100.0	fixed, mobile	fixed, mobile	fixed, mobile
100.0 - 102.0	-	-	-
102.0 - 109.5	fixed, mobile	fixed, mobile	fixed, mobile
109.5 - 111.8	-	-	-
111.8 - 114.25	fixed, mobile	fixed, mobile	fixed, mobile
114.25-122.25	-	-	-
122.25-123.0	fixed, mobile	fixed, mobile	fixed, mobile
123.0 - 130.0	-	-	-
130.0 - 134.0	fixed, mobile	fixed, mobile	fixed, mobile
134.0 - 141.0	-	-	-
141.0 - 148.5	fixed, mobile	fixed, mobile	fixed, mobile
148.5 - 151.5	-	-	-
151.5 - 164.0	fixed, mobile	fixed, mobile	fixed, mobile
164.0 - 167.0	-	-	-
167.0 - 174.8	fixed, mobile	fixed, mobile	fixed, mobile
174.8 - 191.8	-	-	-
191.8 - 200.0	fixed, mobile	fixed, mobile	fixed, mobile
200.0 - 209.0	-	-	-
209.0 - 226.0	fixed, mobile	fixed, mobile	fixed, mobile
226.0 - 231.5	-	-	-
231.5 - 235.0	fixed, mobile	fixed, mobile	fixed, mobile
235.0 - 238.0	-	-	-
238.0 - 241.0	fixed, mobile	fixed, mobile	fixed, mobile
241.0 - 252.0	-	-	-
252.0 - 275.0	fixed, mobile	fixed, mobile	fixed, mobile
275.0 – 3000	not allocated	not allocated	not allocated

Table 3-1: Frequency slots in EHF band allocated for fixed and mobile terrestrial communications in ITU Regions

In U.S., the FCC allocated 7 GHz in the 54–66 GHz band for unlicensed use [3-7]. FCC specified the total maximum transmit power of 500 mW for an emission bandwidth greater than 100 MHz. If license free 60 GHz regulatory constraint on the emission is too

restricting for the application requirements, EHF licensed frequency bands can be still used effectively. In fact, the cost per unit of bandwidth for spectrum license generally decreases by increasing the center frequency. The 71-76 and 81-86 GHz bands, widely known as "E-band", are permitted worldwide for ultra high capacity point-to-point communications. In Europe, the channel arrangements for the 71-76 GHz and 81-86 GHz bands are defined in [3-8]. These two bands are divided into 250 MHz channels, but the aggregation of the channels within each band is permitted. In 2005, the FCC introduced a non-exclusive, internet-based, "light license" process for the allocations of the bands: 71-76 GHz, 81-86 GHz, 91-94 GHz and 94.1-95 GHz. This novel system allows a rapid license application and approval at a cost much lower than traditional licenses. This process, also available in UK, has encouraged the adoption of competitive high data rate services in the U.S., with over 100 links registered in 2006, its first full year of operation. Recently, the slot 94.1-95 GHz has been extended both fixed and mobile services and unified in a common slot from 94.1 GHz to 100 GHz (see Table 3-1). Even more bandwidth can be made available if frequency bands higher than 100 GHz are considered. In Table 3-1, it is shown that beyond 252 GHz there is a lot of available bandwidth for fixed and mobile terrestrial communications services considering both allocated and not allocated frequencies. However, the radio spectrum stretches up to 3 THz only (RR 1.5). In this spectrum, the range 1–3 THz inside the atmosphere is almost completely opaque so there is no practical possibility for terrestrial radio use.

A transmission scheme with high spectral efficiency and significant link reliability requires a high SNR or signal power at the receiver, which results in a trade-off between spectral efficiency and transmission range. Furthermore, the transmission range depends on the degree of link losses. Link losses increase with frequency bands thus requiring LOS links with directional antennas so that most of the transmitted power is concentrated to the aperture of the receive antenna.

The propagation channel at EHF band shows increase of every term of the propagation losses:

- free space losses. The free space path loss increases with the square of the frequency, but by using directive antennas at both transmitting and receiving ends, the increase of the loss is much more than compensated;
- atmospheric absorption: at 60 GHz the oxygen absorption dominate with specific attenuation of 15 dB/km and it exceeds the specific attenuation of the 20 dB/km at 180 GHz;

- rain attenuation: the specific attenuation due to rain is a function of frequency and rain rate. In heavy rain conditions, the specific attenuation due to rain exceeds 40 dB/km in EHF band.

Diversity techniques based on space, frequency, time and polarization separation are effective means to counteract atmospheric absorption and rain attenuation. However, in these conditions, diversity techniques require a too high level of separation, and hence, point-to-point LOS communication links are infeasible for distances higher than few km. However, high propagation losses allow more efficient frequency reuse and decrease interference effects. Multipath propagation at EHF band is reduced in outdoor conditions, but is increased in indoor environments. NLOS propagation is thus very difficult in outdoor, since scattering effects, which are the main causes of multipath propagation in outdoor, are negligible at higher frequencies. It is due to the fact that the wavelength is smaller than the dimension of the objects. On the other hand, reflections are amplified at high frequencies and, hence, multipath propagation is very easy in single room indoor environments where signals do not have to penetrate walls. In fact, material attenuation generally increases with the frequency and, hence, multi room coverage is difficult at EHF band.

At the circuitry level, while EHF provide the benefit of very small radio equipments, there are intrinsic difficulties in the development of technologies for the effective management of the communication signals without any type of distortion or impairment: phase noise of the LOs, nonlinear response of the PAs, I/Q imbalance.

These non linear effects make the design of the RF architecture operating at “beyond 60 GHz” a challenging topic which cannot be disjoint anymore from the choice of the transmission techniques as novel architectures have to be designed.

In this scenario, the use of a solution based on Carrier-less UWB approach represents a very attractive and challenging topic.

3.3 IR-UWB FOR MULTI-GIGABIT COMMUNICATIONS BEYOND 60 GHZ

To use the huge available bandwidth in the frequency range of EHF, two main approaches can be adopted:

1) sending the information over the whole bandwidth, by using extremely spectrally inefficient modulations (BPSK, FSK, ASK, but also UWB) but at a very high rate (for example, a 20 GHz bandwidth for 10 Gigabit/s).

2) splitting the information over several narrower bandwidths using some kinds of frequency-domain multiplexing techniques (these bandwidth slices could be separated by a guard interval as in FDMA or, more efficiently, some kind of OFDM can be used). In each narrow band, more spectrally efficient modulation schemes have to be employed.

In the case of using UWB technology, two methods for generating UWB signals can be mainly identified:

i. IR-UWB. In this case, the signal is generated by short, very low duty cycle, baseband electrical impulses. As no carrier is used to up-convert the signals, such systems are often called carrier free baseband or impulse radio communication systems.

ii. CW-UWB. This method of generating UWB signals involves more traditional spreading techniques that are based on either the single carrier (DSSS or FHSS) or multi carrier technique (OFDM) or combination of both. Such systems are implemented using traditional heterodyning architectures and can be treated as either single band or multiband (MB-UWB) designs. Such techniques present better spectral control properties compared with the first approach.

The analysis in this work has been oriented on the investigation of the use of IR-UWB technology to realise multi-gigabit communications beyond 60 GHz.

In comparison with conventional spread-spectrum techniques, IR-UWB communications offer the same advantage of expanded bandwidth, but the method to achieve this large bandwidth represents the main difference between the two approaches. In conventional spread-spectrum systems, the signals are continuous-wave sinusoids that are modulated with a fixed carrier frequency and a duty cycle equals to 100%, while IR-UWB systems are typically implemented in a carrier-less way. Conventional RF wideband architectures have an up-conversion stage to allocate the signal in the assigned frequency domain from the base-band. Conversely, UWB systems can directly modulate a very narrow impulse that occupies several GHz of bandwidth, therefore the transmitted signal is not a simple base-band signal. The implementation of a transceiver with those characteristics is relative simple: the carrier-less transmission means no need for a carrier recovery stage.

On the basis of these considerations, two main approaches can be identified in order to design an IR-UWB transceiver operating at W band:

1. a conventional approach, as shown in Figure 3-1. This method is based on the generation of narrowband pulses (like standard ns UWB pulses used to perform unlicensed communications in the frequencies range between 3.1 to 10.6 GHz) followed by an up-conversion stage to W band;

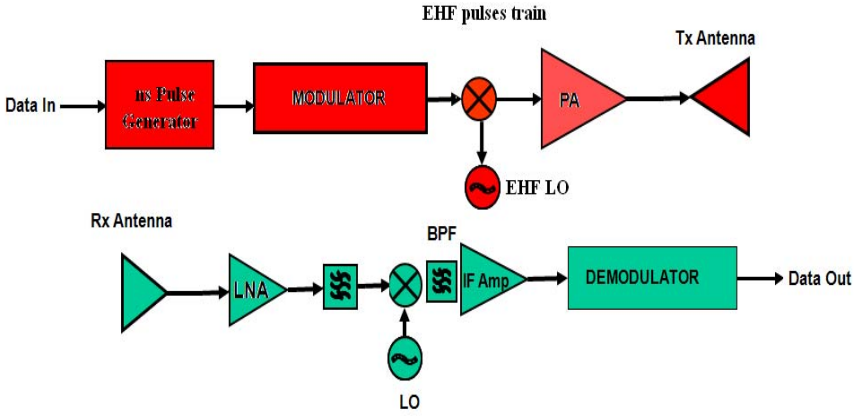

Figure 3-1: EHF IR-UWB Transceiver Classical Approach

2. an alternative approach as reported in Figure 3-2. This method "foresees" the generation of ps pulses having bandwidths of the order of hundreds of GHz followed by a bandpass filtering stage, able to select the correct W band frequencies [3-9], [3-10].

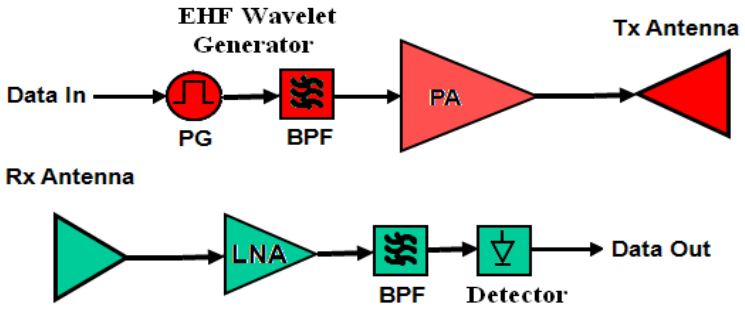

Figure 3-2: EHF IR-UWB Transceiver Alternative Approach

The first architecture foresees the insertion of LOs, mixers and bandpass filtering stages in the UWB transmission chain (and on the other hand also in the receiving chain). According to this approach, the circuit design is complex as it involves oscillators and mixers which are tricky to design in W-band increasing thus the overall costs.

On the other hand, the pulse is not affected by shape distortions. Moreover, this architecture offers the inherent advantage that the power of the upconverted pulses is sufficiently high so that the design specification of the HPA is less stringent.

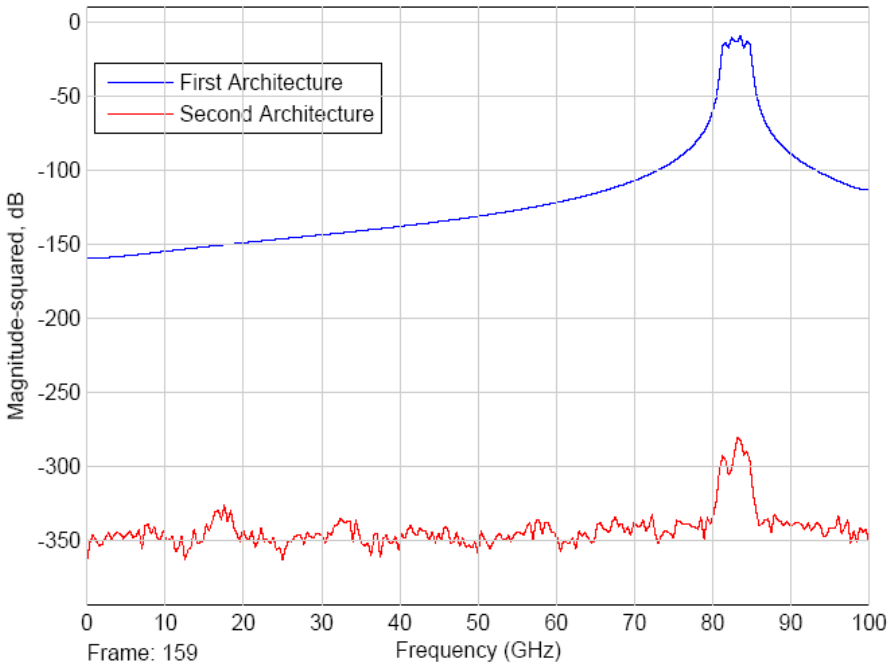

Figure 3-3: Spectrum comparison of W-band UWB pulses generated using two different architectures

The second architecture is based on the design of an ultra-short pulse generator: it does not represent a technological critical aspect, even if the complexity is certainly increased with respect to the standard IR-UWB scheme. However, this alternative approach offers the advantage that there is no need of complex design of mixers and LOs, as required by the conventional architecture, so its design is relatively simpler.

On the other hand, this second approach introduces distortions on the generated pulse, due to the complexity of filtering operation directly at W band. It is worthy to underline that this architecture needs a strict control on ultra-short pulse generator in order to "center" the maximum of the pulse spectrum in the desired W-band frequencies. Therefore, the design of the HPA is very critical since a lot of pulse power is wasted in band-pass filtering stage.

The spectrum of the W-band UWB generated pulses using the two different methods is shown in Figure 3-3 [3-11]. The blue solid line is the spectrum of an up-converted ns pulse, having a bandwidth of 4 GHz, from 81 to 85 GHz, while the red solid line represents

the spectrum of the W-band pulse generated through a narrow-band filtering of an ultra-short pulse. It can be noticed an additional drawback of the second approach: the need for high Tx front-end amplification, being the greatest part of power lost during the pass-band filtering operation. On the basis of these considerations, my work has been oriented on the analysis of the conventional W Band IR-UWB architecture carefully modeling each subsystem and its main parameters and non-linearities.

3.3.1 0.825 NS PULSE GENERATOR DESIGN

This paragraph is devoted to the design and simulation of a 0.825 ns pulse generator using the commercial AlGaAs/InGaAs pHEMT FPD6836 device. It is fabricated by Filtronic Compound Semiconductor Ltd and it is characterised by a 0.25μm x 360μm Schottky barrier gate. Therefore, the obtained waveform will be used to simulate the more realistic pulse generator behaviour in the final W Band IR-UWB transceiver model to evaluate the BER performance, as it will be shown in the following paragraphs.

There are several methods to implement a pulse generator [3-12], [3-13], [3-14], [3-15], [3-16], [3-17], [3-18], [3-19], [3-20]. In [3-12], [3-13] an avalanche transistor is used to generate a monocycle pulse, as shown in Figure 3-4. The pulse generation is based on operating the transistor in avalanche mode, which requires a high voltage.

The bias circuit of the pulse generator provides a fixed bias voltage across the capacitor C7. This voltage level is about 100-130 V, which is near the transistor's (TR3) avalanche breakdown voltage. This voltage is also provided across charging capacitor C8, which dumps a large charge through transistor TR3 when the avalanche breakdown voltage is required. This is achieved by the pulse position modulated message signal, which is fed to the base of the avalanche transistor. As the avalanche breakdown takes place, the emitter voltage of TR3 rises dramatically for a short time ($\approx$ 10 ns), and then falls to negative equivalent voltage due to the inductance connected between the emitter and ground. After charging capacitor C8 has dumped its charge, it takes a few tens of μs to attain the level required for a new avalanche breakdown. This pulse generation method is feasible for applications with high voltage levels and monocycles with relatively large length, such as RADAR.

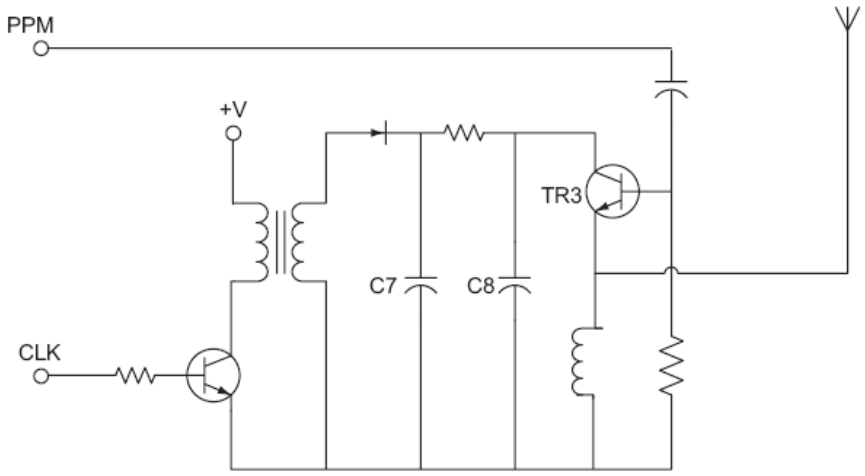

Figure 3-4: Transmitter Driver including the Pulse Generator [Morgan et. al.]

A recent pulse generation method [3-14], [3-15] is based on Step Recovery Diode (SRD), Schottky Diode and charging and discharging circuitry, as reported in Figure 3-5. The SRD provides an impulse, which is high-pass filtered in a RC-circuit. The result is a Gaussian-like pulse, which is fed to a pair of tranmission lines. The generated pulse is divided in two and propagates in both branches after the capacitor C. The first half of the pulse propagates directly to the load resistor, and the other half of the pulse propages to the short. The transmission lines are designed to have a such length that the propagation delay of the second half of the pulse (the one propating to the short) is equal to the length of the pulse. The pulse will be inverted when the pulse reflects from the short circuit in the end of the transmission line. The resulting pulse seen across the load is the superposition of the two branches. The pulse width is controlled by the SRD. Another embodiment of this development has been introduced [3-16]. The basic idea is the same as in [3-14], except that there is an additional MESFET as an amplifying unit.

Another method of generating a monocycle is based on the use of a multiplier that combine two pulses with a time delay. In particular, one of the pulses is multiplied by 1 and the other pulse by -1, as reported in [3-17]. By changing the multiplier's control signals, the phase of the produced monocycle may be changed 180 degrees, and the multiplier acts as a binary pulse amplitude modulator. In the case of PPM, the modulator structure in McCorkle's work is not required, so the circuit may be simplified. Such a circuit is reported in [3-18]. This pulse generator subtracts two differential pulses with a time delay corresponding to the lentgh of the pulses from each other, thus producing a differential

monocycle. This is done by an analogue subtraction circuit which is much simpler than any multiplier. The top level schematic of the pulse generator is shown in Figure 3-6.

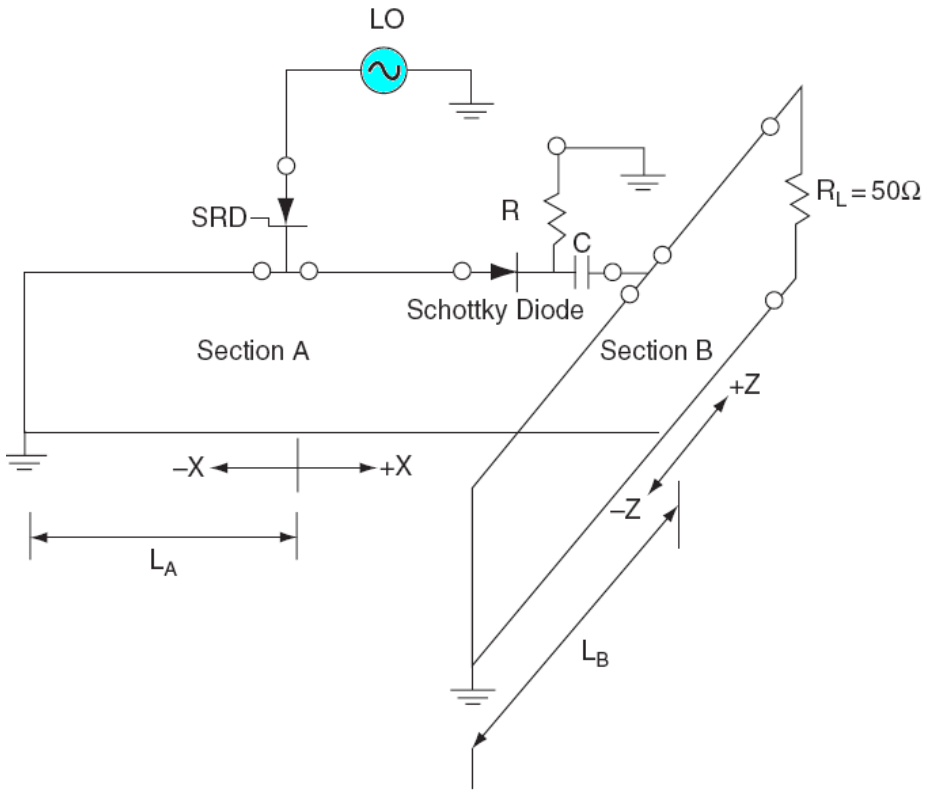

Figure 3-5: Monocycle Generator [Lee et. al.]

Another method of generating pulses is based on the use of logic gates. The delay between the two pulses can be realised by a simple delay element consisting two inverters and a PMOS varactor, which provides the opportunity to tune the length of the delay. Figure 3-7 and Figure 3-8 show two methods of generating short pulses, [3-19], [3-20].

The first one uses an XOR gate and the second method is based on an AND gate. The XOR gate operates so that whenever both input signals are at different logical levels, the output is is at high level, i.e. logical '1', and when both input signals have the same logical levels the output is at low level, i.e., logical '0'. The length of the high-level output can be adjusted by the phase difference between the inputs. This is also provided by a simple delay element.

The AND-gate operates so that whenever both the inputs are at a high level, the output is at high level. An inverter is connected to one of the inputs of the AND gate, and a clock signal is connected to both the inverter and the AND gate. The output of the AND gate is now at low level at all times, but the output still reacts to the rising edge of the clock. This

is because the inverter has a delay during which its output is still at zero, while the clock has already risen. This effect is called glitch, or a hazard, which results in a short pulse with length corresponding to one of the inverter's delay.

The delay can be adjusted by connecting a varactor from the output of the inverter to ground. If the delay is very short, the resulting pulse might not have time to rise all the way up to the logical '1', but is still useful for generating a short pulse. Exploiting this circuit, the PRF decreases to half that when using the XOR-circuit, since the short pulse will occur only on the rising edge of the clock. The XOR reacts to both the rising and falling edge of the clock. A NAND-gate may also be used.

The operation is the same as in case of an AND gate, the difference being that the pulse will occur on the falling edge of the clock and the pulse is from high to low level. The NAND-gate is faster than the AND-gate and is therefore used in the implementation of the transceiver.

The shape of the pulse is defined by the RC time constant of the used gate in all of the three circuits. Figure 3-9 shows the pulse generator schematic based on NAND gate using HEMT technology.

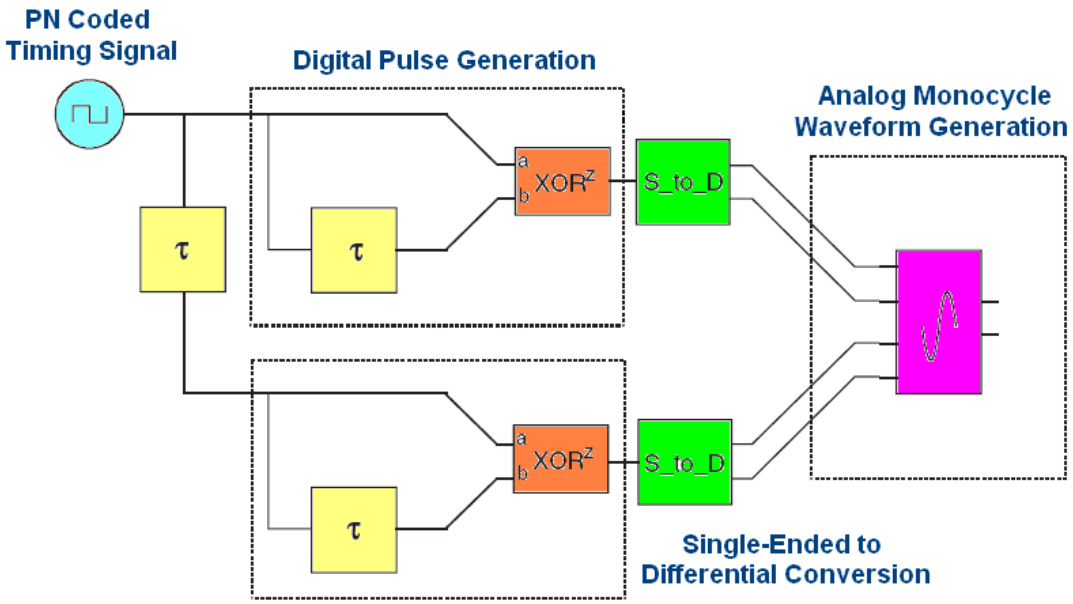

Figure 3-6: Top Level Schematic of Pulse Generator proposed in [3-18]

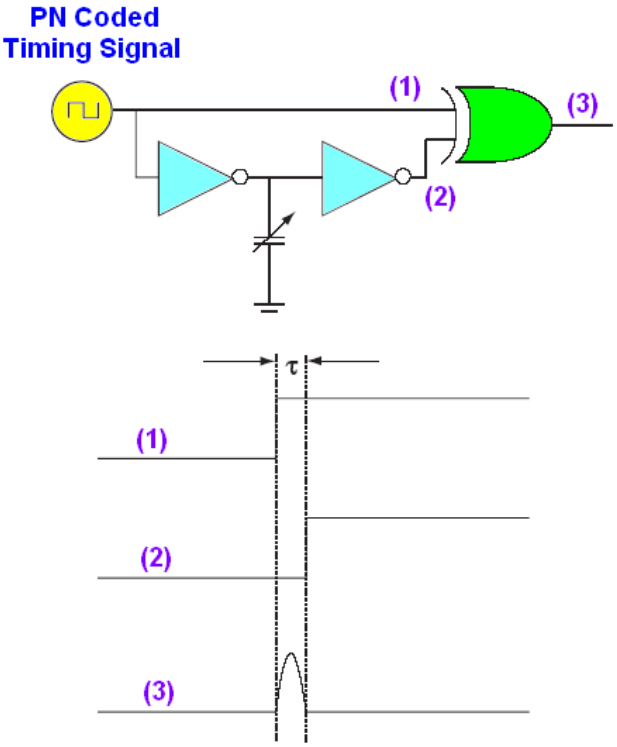

Figure 3-7: Digital Pulse Generation by an XOR-gate

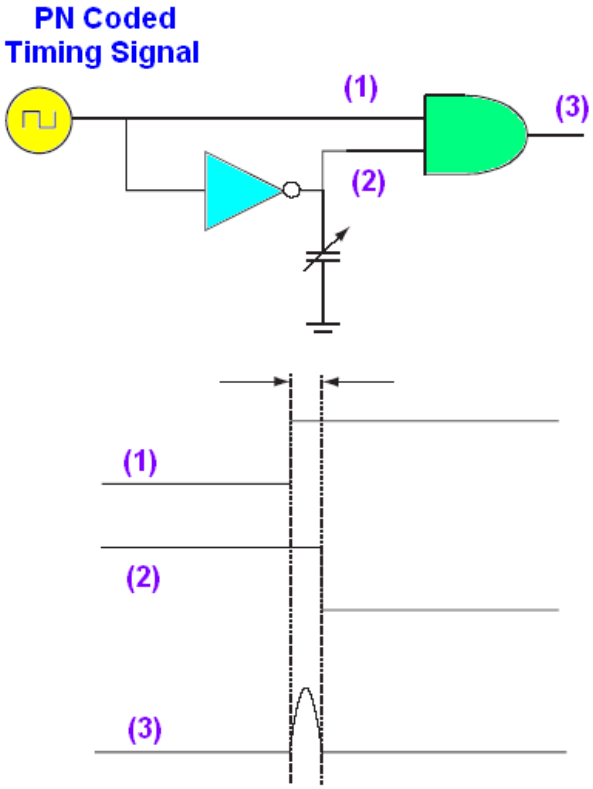

Figure 3-8: Digital Pulse Generation by an AND-gate

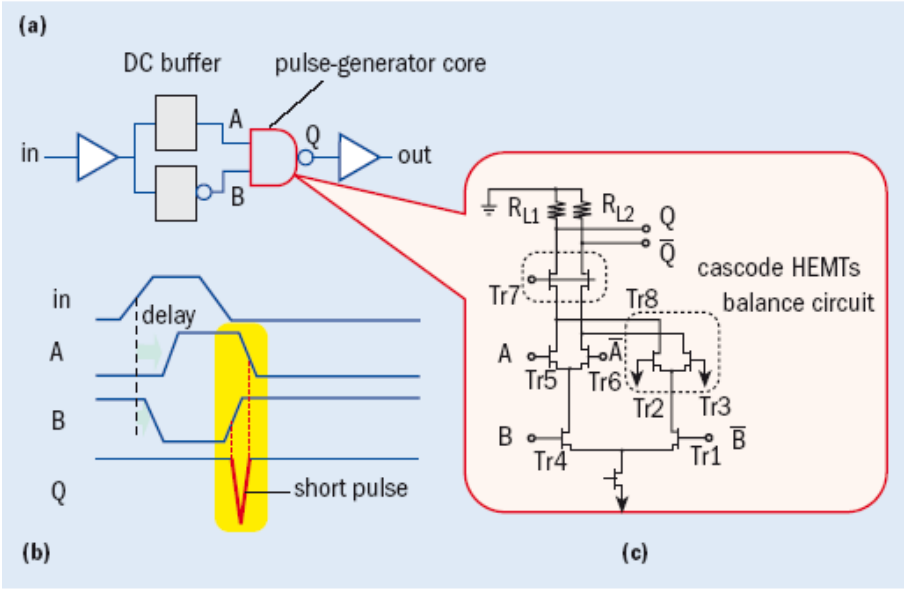

Figure 3-9: Pulse generator based on NAND gate using HEMT technology

They generate the baseband pulse whose width is nearly equal to the overlap time between inputs, which are delayed and inverted one another.

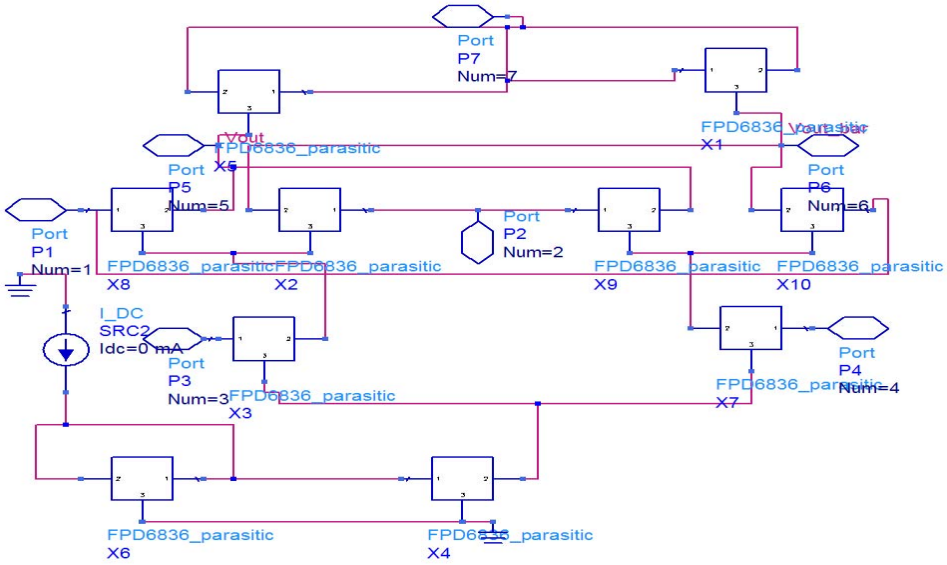

Figure 3-10: Pulse generator based on XOR gate using FPD6836 pHEMT technology

Figure 3-10 shows the pulse generator schematic based on XOR gate using FPD6836 pHEMT technology. The TOM3 model has been used for the FPD6836 discrete p-HEMT device in order to simulate the pulse generator using the ADS software. This model provides a good fit to the measured data and allows to accurately model the device over a

wide range of operating conditions. Figure 3-11 reports the FPD6836 p-HEMT schematic considering the external parasitics due to the package. Delaying and inverting one another the two XOR gate inputs, a sub-ns pulse has been generated using commercial devices.

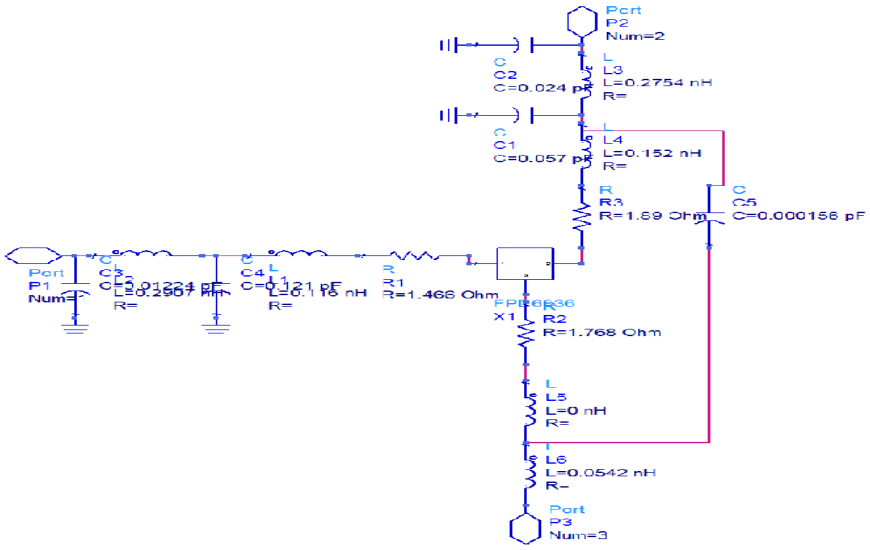

Figure 3-11: FPD6836 p-HEMT with external parasitics

Figure 3-12 shows the time chart of the p-HEMT pulse generator. The Full Width Half Maximum (FWHM) was as small as 0.825 ns and the amplitude of the pulse was 0.3 V, as shown in Figure 3-13.

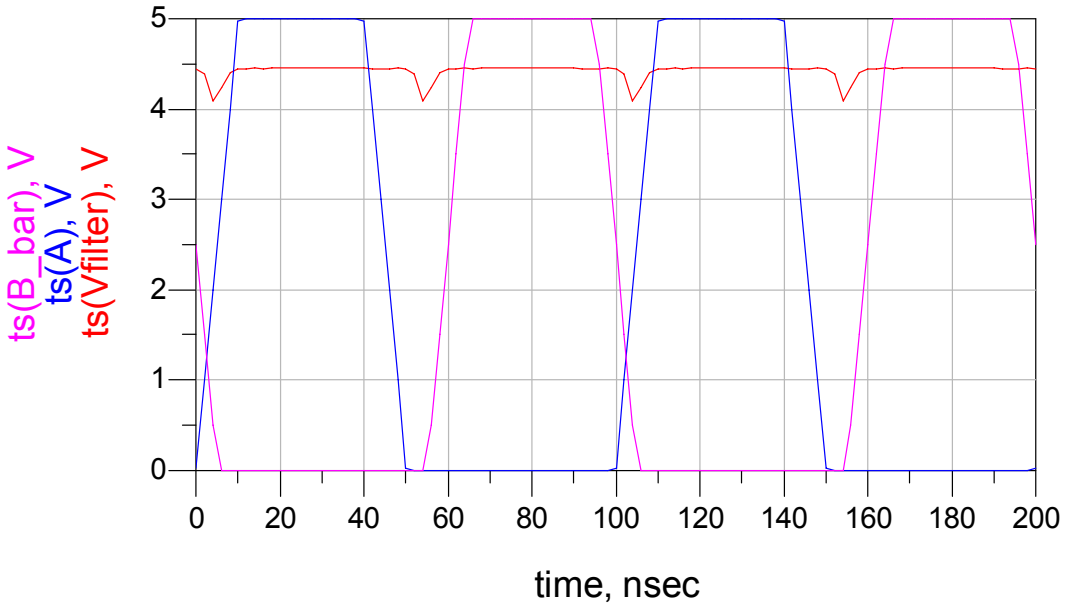

Figure 3-12: Time chart of the FPD6836 p-HEMT pulse generator

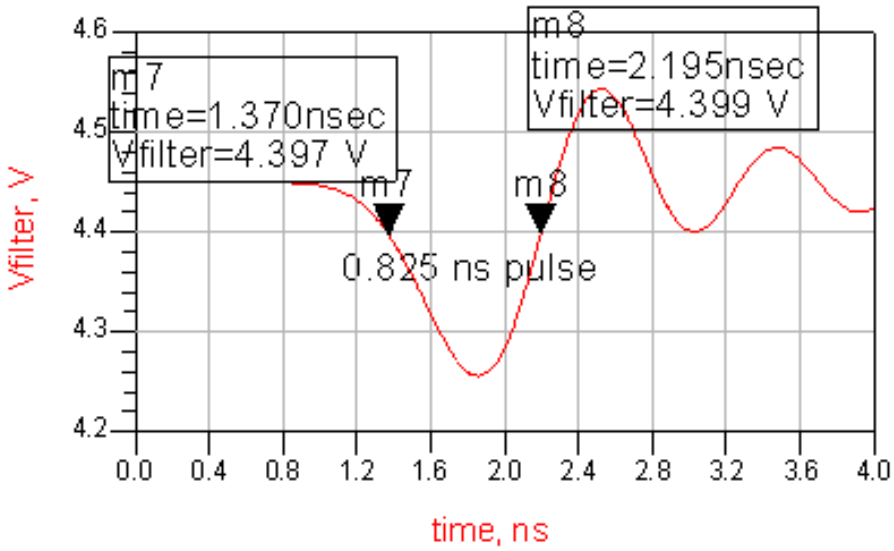

Figure 3-13: Simulated pulse waveform generated from the FPD6836 p-HEMT XOR

3.3.2 EHF MCL BAND-PASS FILTER DESIGN

According to the approach above described, if the pulse generator has sufficient performance to produce ps pulses (using not commercial devices, but technology as 0.13 µm InP HEMT as reported in [3-10]), a broadband radio system operating in the millimeter wave band can be easily realised. A band-pass filtering stage is then required to get the UWB pass-band signal operating at W band frequencies. In order to prevent the pulse shape from the distortion, the BPF has to show a flat insertion loss and a small delay group variation in the selected frequencies. A BPF filter using a Multi-stage Microstrip Coupled Line (MCL) configuration has been designed and its performance simulated through the ADS software. The number of MCL stages has been calculated and the line width, W, line length, L, and line spacing, S, has been optimized for each MCL stage. The BPF has been designed for frequencies range from 73 to 83 GHz in a five stage cascade on a GaAs substrate. Figure 3-14 shows the MCL BPF filter schematic, while Figure 3-15 and Figure 3-16 report the simulated Scattering parameters. The simulated insertion losses are at maximum 2.5 dB in 73-83 GHz frequencies range. Hence, this configuration is a good compromise between insertion loss and flatness and easy design to fabricate a Wavelet Generator for W Band IR-UWB transmitters.

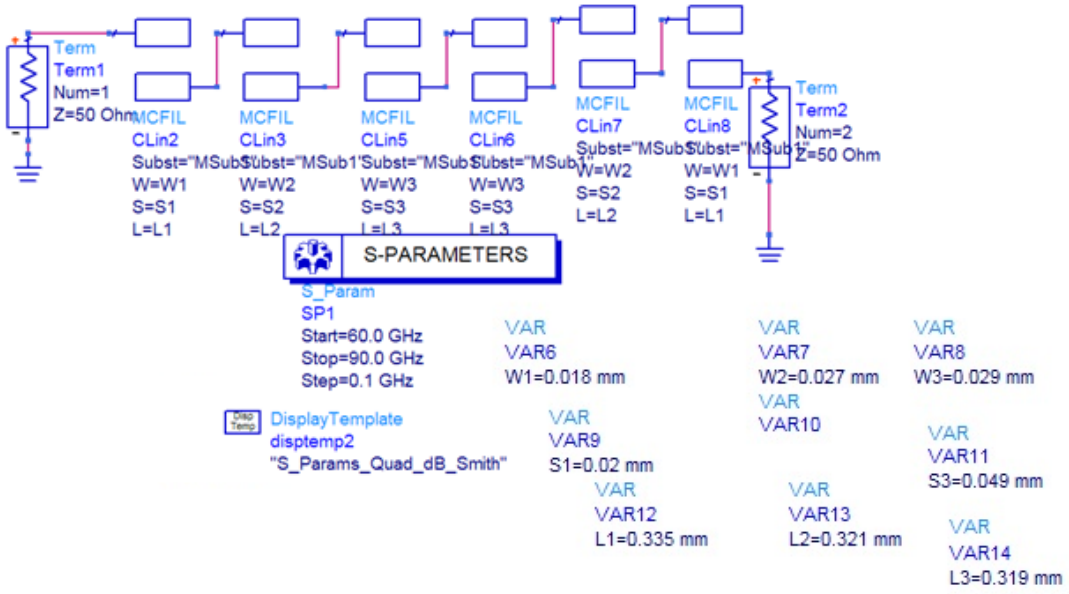

Figure 3-14: Schematic of the [73-83] GHz MCL BPF filter

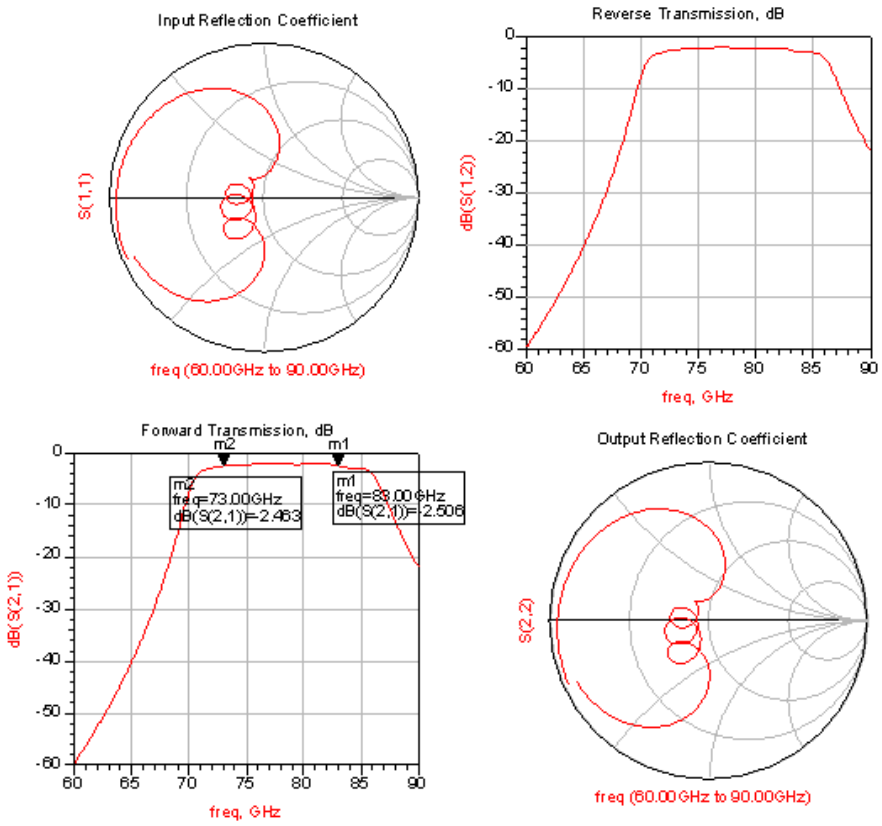

Figure 3-15: Simulated S-Parameters for the [73-83] GHz MCL BPF

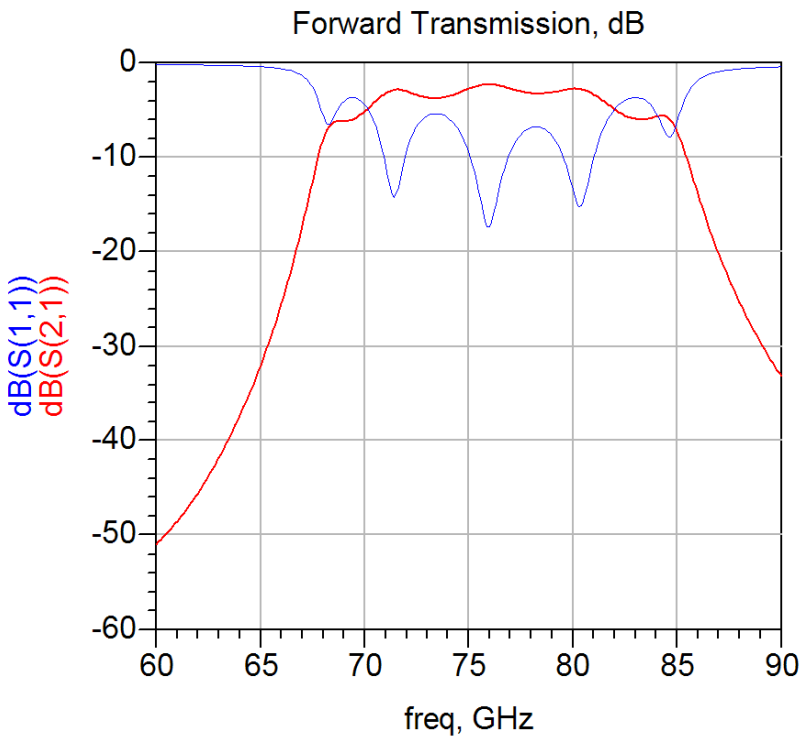

Figure 3-16: Simulated S21 Parameter for the [73-83] GHz MCL BPF

3.3.3 85 GHz IR-UWB Transceiver based on the first Architecture

This section evaluates the performance of PPM TH-IR UWB technique in presence of H/W distortions at W band.

RF H/W with ideal characteristics is very difficult to design for the frequency bands beyond 60 GHz. Problems such as a HPA non–linearity, oscillator phase noise, synchronization errors, LNA and mixer non idealities are more prominent for these circuits than for ones designed for low frequencies. Therefore, these effects should be taken into account in the overall communications channel. The non-ideal characteristics of the components, which are experienced in reality and which lead to so called Dirty RF effects are taken into consideration. The models are either based on measurement data of real components or on simulation methods that are extended to the UWB case. In scheme reported in Figure 3-17, the UWB baseband transmitter generates very short Gaussian pulses having duration lower than 1 ns. One transmitted symbol is spread over N_s monocycles to achieve processing gain that may be used to combat noise and RF distortions.

To eliminate catastrophic collisions in multiple accessing, an additional time shift, unique to each user, is added to each pulse in the pulse train.

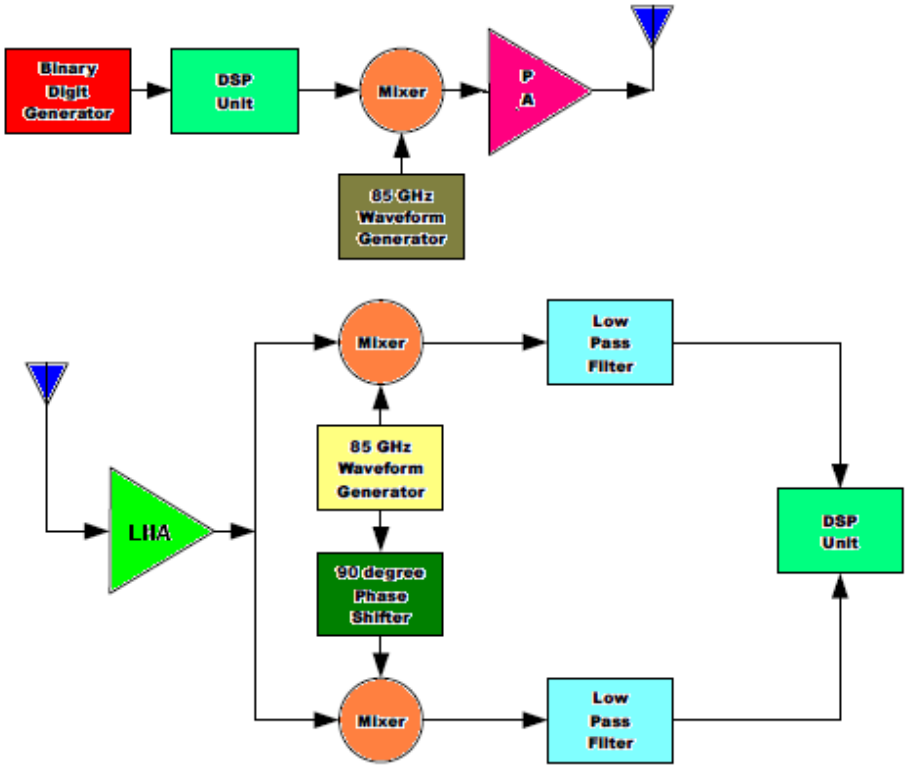

Figure 3-17: Schematic of an UWB W band Transceiver Architecture based on Up-Conversion of ns Gaussian Pulses

Finally, an additional time shift is introduced for each pulse through the PPM technique: when the data symbol is 0, no additional time shift is modulated on the monocycle, but a time shift of is added to the pulse waveform when the symbol is 1.

Therefore, the PPM TH-IR UWB signal for *kth* user is given by [3-21]:

$$s^{k}(t)=\sum_{j=-\infty}^{+\infty}\mathrm{A}_{d[j/N_s]}^{k}p\left(t-j\mathrm{T}_f-c_j^{(k)}T_c-\delta_{[j/N_s]}^{(k)}\right) \tag{3-1}$$

where $\mathrm{A}^{(k)}$ is the signal amplitude, $p(t)$ represents the second derivative of Gaussian pulse, with pulse width T_p, T_f is the frame duration (a frame is divided into N_{th} time slots with duration T_c). The pulse shift pattern $c_j^{(k)}$, $0 \le c_j^{(k)} \le N_{th}$ ($N_{th}T_c = T_f$) is the time hopping sequence for the *kth* user and it is pseudorandom with period T_c. $\delta^{(k)}$ is the additional time

shift introduced by PPM, as described above. The baseband signal is then up-converted using an 85 GHz oscillator, amplified by the HPA and then transmitted.

The UWB receiver shown in Figure 3-17 uses a direct conversion scheme, thereby eliminating the need of image rejection filter and complicated phase synchronization circuits. In receiver, the received signal is first amplified by a LNA, and then it is down-converted to baseband by two 85 GHz oscillators operating in phase and quadrature. I and Q components are low pass filtered and fed to the DSP section. Here they are combined, demodulated and decoded.

The following paragraphs deal with the description of the model used for some components of the transceiver as oscillators [3-22], [3-23], [3-24], [3-25], [3-26], [3-27], [3-28], [3-29] and oscillators [3-30], [3-31], [3-32], [3-33], [3-34] which have a non-linear behaviour introducing additional harmonics and noise in the final system.

In the current work, the direct conversion configuration has been preferred to superheterodyne one in order to implement the receiver section.

In the superheterodyne receiver configuration, the signal is first downconverted into a lower (but non-zero) frequency called the Intermediate Frequency (IF) and then demodulated. In the Direct Conversion receiver configuration, the RF signal is directly down-converted to baseband without using any IF [3-35].

The advantage of the first technology is that there is no need of any phase synchronization between the oscillators at the transmitter and receiver, but this technique suffers from the difficulty that the down-converted signal to IF has still a larger bandwidth as compared to the original baseband signal. Hence, the conversion of the signal to digital will need ADCs with a very high sampling rate as per Nyquist sampling theorem. This issue is very challenging in the present case since the bandwidth of the baseband signal is inherently very high.

In the direct conversion technique, a very good (if not perfect) synchronization is required between the two local oscillators which is complex to achieve at frequencies beyond 60 GHz. Two diffferent solutions to this problem could be adopted:

- using I and Q demodulation stage in the receiver using two local oscillators operating at the same frequency but at 90° phase difference. Then, combining two outputs allows to achieve a final output that becomes independent of the phase difference between the transmitter and receiver oscillators;
- applying, firstly, the superheterodyning technique to down-convert the original

signal at beyond 60 GHz to a lower RF signal (like in Ku band), and then the direct conversion operation to take the signal back to baseband. The main advantage of this approach is represented by the fact that to achieve phase synchronization in Ku-band is much easier than in higher frequencies.

In this work, the direct conversion method has been used, assuming perfect synchronization between the transmitter and receiver oscillators. However, this assumption can be waived using one of the two techniques mentioned above.

3.3.4 TH PPM IR-UWB INTERFACE

The binary PPM-TH-UWB interface has been developed as it follows.

Given the binary sequence to be transmitted:

$$b = (..., b_0, b_1, ... b_k, b_{k+1}, ...) \tag{3-2}$$

generated at a rate of R_b (bit/s), where $R_b = \frac{1}{T_b}$. The first block in the UWB interface, as shown in Figure 3-18, repeats each bit N_s times and generates a binary sequence:

$$\begin{gathered}(\ldots, \underbrace{b_0, b_0, \ldots, b_0}_{N_s}, b_1, b_1, \ldots, b_1, \ldots, b_k, b_k, \ldots, b_k, b_{k+1}, b_{k+1}, \ldots, b_{k+1}, \ldots) = \\ (\ldots, a_0, a_1, \ldots, a_j, a_{j+1}, \ldots) = \mathbf{a}\end{gathered} \tag{3-3}$$

at a rate of R_{cb} bit/s, where $R_{cb} = \frac{N_s}{T_b} = \frac{1}{T_f}$. T_f is frame time, or average pulse repetition period. This block introduces redundancy and it is a $(N_s,1)$ block coder indicated as a code repetition coder.

A second block called a Transmission Coder applies an integer-value code:

$$c = (..., c_0, c_1, ... c_j, c_{j+1}, ...) \tag{3-4}$$

to the binary sequence $a = (..., a_0, a_1, ... a_j, a_{j+1}, ...)$ and generates a new sequence *d*. The generic element of the sequence *d* is expressed as follows:

$$d_j = c_j T_c + a_j \delta \tag{3-5}$$

where T_c and δ are, respectively, the Chip Time and the PPM shift. They are constant terms that satisfy the condition:

$$c_j T_c + \delta < T_f \text{ for all } c_j \tag{3-6}$$

Note that *d* is a real-valued sequence as opposed to *a*, which is binary, and to *c*, that is integer-valued. We assume that *c* is a pseudorandom code and its generic element c_j an integer verifying $0 \le c_j \le N_h - 1$. The code *c* might be periodic and its period is indicated by N_p. The coded real-valued sequence *d* enters a third block, the PPM modulator, which generates a sequence of unit pulses (Dirac pulses, δ(t), at a rate of R_p pulses/s), where:

$$R_p = \frac{N_s}{T_b} = \frac{1}{T_f} \tag{3-7}$$

These pulses are located at times $jT_f + d_j$. Pulses occur at times $jT_f + c_j T_c + a_j \delta$. Note that the shift introduced by the PPM modulator, $a_j \delta$, is usually much smaller than one added by TH code,. $jc_j T_c$.

The last block represents the pulse shaper filter with impulse response $p(t)$. The impulse response, $p(t)$, has to be such that the signal at the output of the pulse shaper filter is a sequence of strictly non-overlapping pulses. The signal, $s(t)$, for the generic *kth* user, at the output of cascade of these blocks, in accordance with (3-1), can be expressed as follows:

$$s^k(t) = \sum_{j=-\infty}^{+\infty} A^k p\left(t - jT_f - c_j^{(k)} T_c - \delta^k\right) \tag{3-8}$$

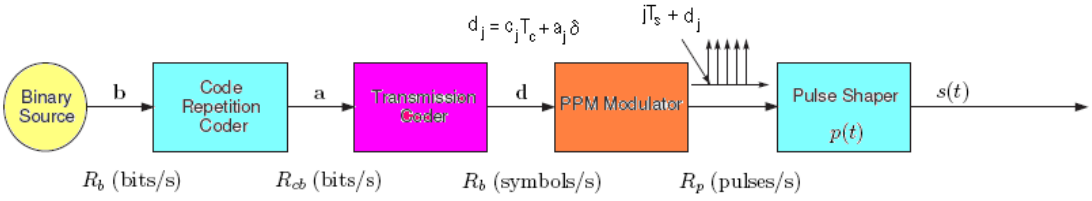

Figure 3-18: PPM TH IR UWB Baseband Interface

3.3.5 CORRELATOR AND OPTIMUM DETECTOR SUBSYSTEMS

In order to analyse only the influence of RF effects on BER communications and assuming that this application is oriented to LOS multi-gigabit last mile links, we do not consider the multipath effects.

The useful signal at the receiver, $r_u(t)$, is corrupted by additive noise $n(t)$, typically thermal noise, which is assumed to be a realisation of a stochastic Gaussian process with bilateral Power Spectral Density (PSD), $N_0/2$.

The received signal is expressed by:

$$r(t) = r_u(t) + n(t) \tag{3-9}$$

where $r_u(t)$ is an attenuated and delayed version of the transmitted signal, $s(t)$, that is:

$$r_u(t) = \alpha \cdot s(t-\tau) \tag{3-10}$$

Both channel gain, α, and channel delay, τ, in (3-9) depend on the distance of propagation D between transmitter and receiver. For α, one can assume:

$$\alpha = \frac{c_0}{\sqrt{D^\gamma}} \tag{3-11}$$

where:

- γ is the exponent of the power attenuation law, that is, the path loss;
- c_0 is a constant that can be tuned to obtain a reference gain α_0 at the reference distance $D_0 = 1$ m.

The γ value is equal to 2 for propagation over the free space; it is higher than 2 for typically Non-Line of Sight (NLOS) propagation.

With reference to c_0, it is important to note that for having:

$$A_{dB} = 10\log_{10}\left(\frac{E_{TX}}{E_{RX}}\right) \tag{3-12}$$

at $D_0 = 1$ m, it follows:

$$c_0 = 10^{-\frac{A_{dB}}{20}} \tag{3-13}$$

Regarding the delay, τ:

$$\tau = \frac{D}{c} \tag{3-14}$$

where c is the speed of light in vacuum ($c \approx 3 \cdot 10^8$ m/s).

We assume a perfect synchronization between transmitter and receiver, that is, the value of τ is known at the receiver side. This hypothesis will be maintained throughout this paragraph. Synchronization issues will be discussed later.

As it is well-known, the optimum receiver for the AWGN channel is composed of two systems: the correlator and the detector. The role of the correlator is to convert the received

signal of (3-9) into a set of decision variables $\{Z\}$. The role of the detector is to decide which signal waveform was transmitted based on the observation of $\{Z\}$. Assume that the transmitter sends information in a digital form using *M* different waveform $s_m(t)$, whit *m* = 0, . . . , *M* −*1*. Within an interval of duration *T,* called the symbol interval, one of $s_m(t)$ waveforms is transmitted.

The $s_m(t)$ waveforms belong to an ensemble that can be generated by N or-thonormal basis functions $\{\psi_k(t)\}$, with *k = 0, . . . ,* $N-1$. One can thus write:

$$s_m(t) = \sum_{k=0}^{N-1} s_{mk} \Psi_k(t) \tag{3-15}$$

with $t \in [0, T]$ and where:

$$s_{mk} = \int_0^T s_m(t) \Psi_k(t) dt \tag{3-16}$$

The energy E_m of $s_m(t)$ over time *T* is:

$$E_m = \int_0^T (s_m(t))^2 dt = \int_0^T \left(\sum_{k=0}^{N-1} s_{mk} \Psi_k(t) \right)^2 dt = \sum_{k=0}^{N-1} s_{mk}^2 \quad \forall m = 0,...,M-1 \tag{3-17}$$

By introducing (3-15) into (3-9) and (3-10), the received signal in [*0, T*] corresponding to a generic transmitted $s_m(t)$ is rewritten as:

$$r(t) = \sum_{k=0}^{N-1} \alpha s_{mk} \Psi_k(t-\tau) + n(t) \tag{3-18}$$

The correlator receiver for $r(t)$ in (3-18) is composed of a bank of *N* cross-correlators, which output *N* decision variables Z_k are given by:

$$Z_k = \int_\tau^{T+\tau} r(t) \Psi_k(t-\tau) dt = \alpha s_{mk} + n_k \quad \forall k = 0,...,N-1 \tag{3-19}$$

with:

$$n_k = \int_\tau^{T+\tau} n(t) \Psi_k(t-\tau) dt \tag{3-20}$$

Figure 3-19 shows the reference scheme for the correlator described by (3-19). The detector estimates which waveform is transmitted, based on the set $\{Z\} = \{Z_0,...Z_{N-1}\}$. It can be shown that the noise components n_k of (3-20) are uncorrelated Gaussian variables with zero mean and a variance, $\sigma_n^2 = N_0 / 2$.

The optimum detector for the signal expressed by (3-16) applies the Maximum Likelihood (ML) criterion. It selects, among the *M* possible transmitted waveforms, the one which maximizes the conditional probability $p\left(Z|s_m(t)\right)$. This is equivalent to say that the selected $s_m(t)$ is characterized by a set of coefficients $s_m = \{s_{m0},...s_{m(N-1)}\}$, which is closest to the set $\{Z\} = \{Z_0,...Z_{N-1}\}$. Applying ML criterion allows to minimise the following function:

$$e\left(r(t),s_m\right) = \sum_{k=0}^{N-1}\left(Z_k - s_{mk}\right)^2 = \sum_{k=0}^{N-1} Z_k^2 + \sum_{k=0}^{N-1} s_{mk}^2 - 2\sum_{k=0}^{N-1} s_{mk} Z_k = \\ = \sum_{k=0}^{N-1} Z_k^2 - 2\left(\sum_{k=0}^{N-1} s_{mk}^2 - \frac{1}{2}\sum_{k=0}^{N-1} s_{mk} Z_k\right) \tag{3-21}$$

(3-21) indicates that the waveform that minimizes $p\left(Z|s_m(t)\right)$ is the one that maximises the correlation function:

$$C\left(r(t),s_m\right) = \sum_{k=0}^{N-1} s_{mk} Z_k - \frac{1}{2}\sum_{k=0}^{N-1} s_{mk}^2 = \sum_{k=0}^{N-1} s_{mk} Z_k - \frac{E_m}{2} = \int_{\tau}^{T+\tau} r(t) s_m(t-\tau)dt - \frac{E_m}{2} \tag{3-22}$$

The optimum detector, therefore, selects the $s_m(t)$, which maximises $C\left(r(t),s_m\right)$. (3-22) also suggests that the optimum receiver operates as follows:

- the received waveform, $r_u(t)$, is cross-correlated with the M possible transmitted waveforms, $s_m(t)$;
- $\frac{E_m}{2}$ is subtracted from each correlation output;
- the maximum over the *M* resulting values is selected.

A reference scheme for this receiver is shown in Figure 3-20.

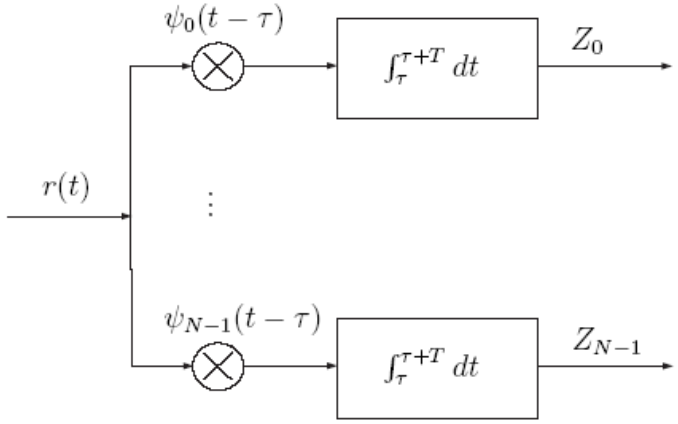

Figure 3-19: Signal Correlator Block Diagram

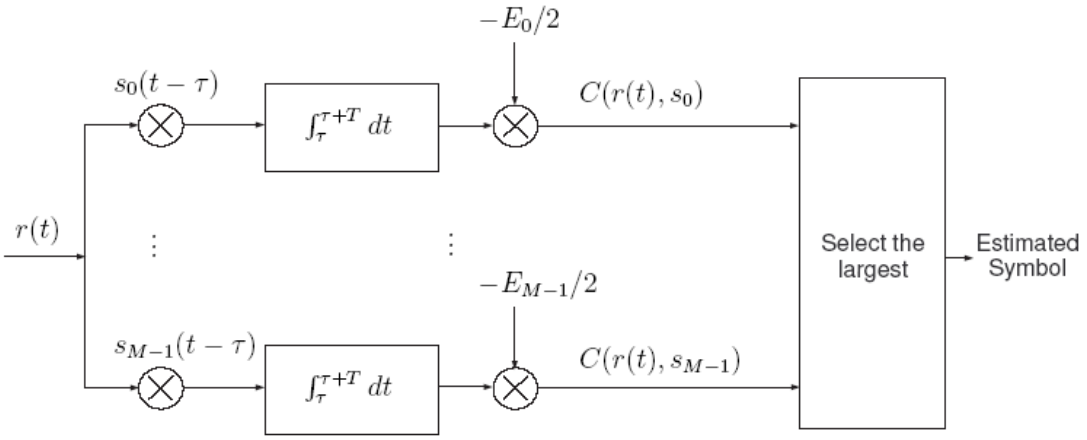

Figure 3-20: Optimum Receiver Scheme (based on ML criterion)

In binary orthogonal PPM, *M = 2*, and the two possible transmitted signals, considering the transmission of the single pulse, are:

$$s_m(t) = \begin{cases} \sqrt{E_{TX}}\, p_0(t) & for \quad b = 0 \\ \sqrt{E_{TX}}\, p_1(t) = \sqrt{E_{TX}}\, p_0(t-\delta) & for \quad b = 1 \end{cases} \tag{3-23}$$

where:

- $p_0(t)$ is the energy-normarlised waveform of the pulse;
- E_{TX} is the transmitted energy per pulse;
- δ is the time shift introduced by PPM.

If ε is larger than pulse duration, T_p, the set of orthonormal functions can be formed by $p_0(t)$ and $p_1(t)$, that is:

$$s_m(t) = s_{m0}\, p_0(t) + s_{m1}\, p_1(t) \;\; m=0,1 \tag{3-24}$$

where:

$$\begin{cases} s_{00} = \sqrt{E_{TX}} \\ s_{01} = 0 \\ s_{10} = 0 \\ s_{11} = \sqrt{E_{TX}} \end{cases} \tag{3-25}$$

The optimum receiver scheme for this format signal consists of a bank of two correlators, as shown in Figure 3-21.

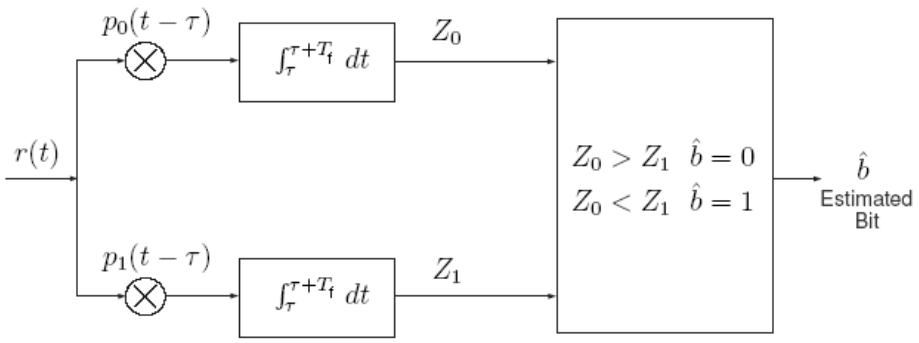

Figure 3-21: Optimum Receiver Scheme (based on ML criterion) considering orthogonal 2PPM signal format

The decision variables at the output of correlators are expressed as follows:

$$Z_0 = \alpha s_{m0} + n_0 \tag{3-26}$$

$$Z_1 = \alpha s_{m1} + n_1 \tag{3-27}$$

where n_0 and n_1 are two indipendent and equally distributed Gaussian random variables with zero mean and variance $\frac{N_0}{2}$. In the presence of TH coding, the correlator scheme of Figure 3-21 may be modified into Figure 3-22, where the c_j term is the generic *j-th* coefficient of the TH code assigned to the user under examination.

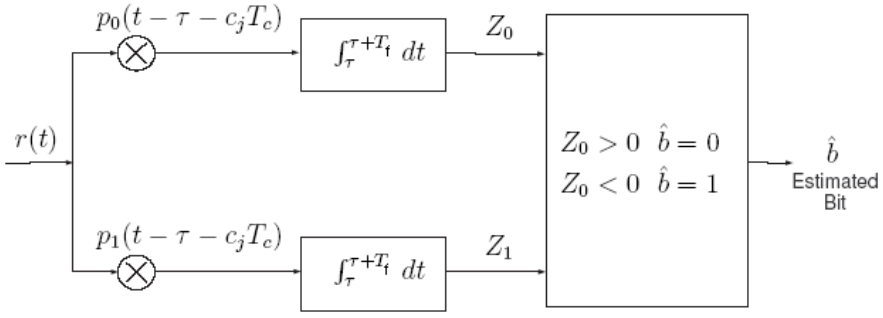

Figure 3-22: Optimum Receiver Scheme (based on ML criterion) considering orthogonal 2PPM Signal Format

Note that the scheme in Figure 3-22 can be simplified into an equivalent scheme that uses only one correlator, as shown in Figure 3-23.

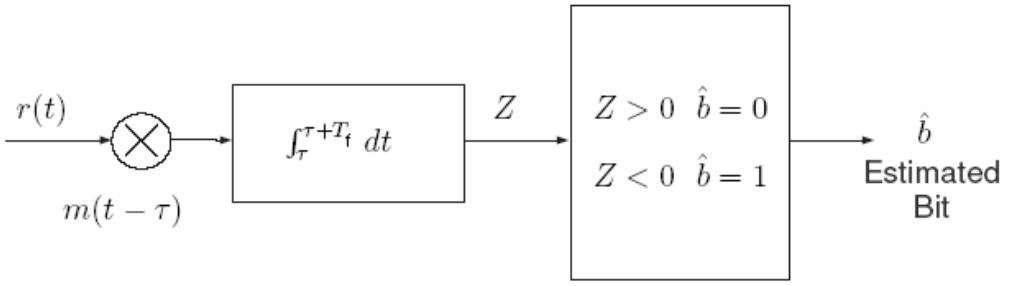

Figure 3-23: 2 PPM-TH Optimum Receiver Scheme (based on ML criterion) using one Correlator

In the one-correlator scheme in Figure 3-23, the incoming signal is multiplied by $m(t)$, indicated as the correlation mask, where:

$$m(t) = p_0(t - \tau - c_j T_c) - p_0(t - \tau - c_j T_c - \delta) \tag{3-28}$$

The output of the correlator is:

$$Z_0 = \alpha s_m + n_0 - n_1 \tag{3-29}$$

where:

$$s_m(t) = \begin{cases} s_0 = \sqrt{E_{TX}} & for \quad b = 0 \\ s_1 = -\sqrt{E_{TX}} & for \quad b = 1 \end{cases} \tag{3-30}$$

For independent and equally probabe transmitted bits, the average Error Probability, P_e for an optimum receiver is given by:

$$\begin{aligned} P_e &= \frac{1}{2}\Pr ob(Z > 0 | b = 1) + \frac{1}{2}\Pr ob(Z < 0 | b = 0) = \Pr ob(Z < 0 | b = 0) = \\ &= \Pr ob(\alpha\sqrt{E_{TX}} + n_0 - n_1 < 0) = \Pr ob(\alpha\sqrt{E_{TX}} + n_0 - n_1 < 0) \end{aligned} \tag{3-31}$$

where:

$$E_{RX} = \alpha^2 E_{TX} \tag{3-32}$$

is the received energy per pulse. Since n_0 and n_1 are independent and equally Gaussian random variables, (3-31) can be rewritten as follows:

$$P_e = \frac{1}{2} erfc\left(\sqrt{\frac{E_{RX}}{2N_0}}\right) \tag{3-33}$$

which represents the average error probability on bit for 2-PPM TH signals.

Results shown above refer to transmissions characterised by one pulse for symbol.

However, in order to improve performance, the transmitter subsystem can introduce redundancy by increasing the number of pulses per symbol.

In soft decision detection, the signal formed by N_s pulses is considered by the receiver as a single multi-pulse signal $s_{mp}(t)$. The received signal is then cross-correlated with a correlation mask, which is matched with the train of pulses representing the entire symbol.

Considering the case of 2PPM TH transmission, in presence of N_s pulses for bit, two possible signals can be generated in the reference bit period [0, T_b]:

$$s_m(t) = \begin{cases} \sqrt{E_{TX}} \sum_{j=0}^{N_s-1} p_0\left(t - jT_s - c_j T_c\right) & for \quad b = 0 \\ \sqrt{E_{TX}} \sum_{j=0}^{N_s-1} p_0\left(t - jT_s - c_j T_c - \delta\right) & for \quad b = 1 \end{cases} \tag{3-34}$$

where:

- $p_0(t)$ is the energy normalized pulse with time duration, T_p;
- E_{TX} is the transmitted energy per pulse;
- T_c is the chip period;
- c_j is the *j-th* coefficient of TH code assigned to *j*-th user;
- δ is the time shift introduced by the PPM modulator.

The multi-pulse signal of (3-34) can be represented as linear combination of two multi-pulse orthonormal functions, $p_{mp0}(t)$ and $p_{mp1}(t)$:

$$s_{mp}(t) = s_{m0} p_{mp_0}(t) + s_{m1} p_{mp_1}(t) \quad m=0,1 \tag{3-35}$$

where:

$$\begin{aligned} p_{mp_0}(t) &= \frac{1}{\sqrt{N_s}} \sum_{j=0}^{N_s-1} p_0\left(t - jT_s - c_j T_c\right) \\ p_{mp_1}(t) &= p_{mp_0}(t - \delta) \end{aligned} \tag{3-36}$$

and:

$$\begin{cases} s_{00} = \sqrt{N_s E_{TX}} = \sqrt{E_b} \\ s_{01} = 0 \\ s_{10} = 0 \\ s_{11} = \sqrt{N_s E_{TX}} = \sqrt{E_b} \end{cases} \tag{3-37}$$

where:

$$E_b = N_s E_{TX} \tag{3-38}$$

is the transmitted energy per bit.

Moreover, the correlation mask, $m(t)$, is a multi-pulse signal defined as follows:

$$m(t) = p_{mp_0}(t) - p_{mp_1}(t) = \frac{1}{\sqrt{N_s}} \sum_{k=0}^{N_s-1} \left(p_0\left(t - jT_s - c_j T_c\right) - p_0\left(t - jT_s - c_j T_c - \delta\right)\right) \tag{3-39}$$

Following the same approach decribed above:

$$P_e = \frac{1}{2} erfc\left(\sqrt{\frac{E_{bRX}}{2N_0}}\right) = \frac{1}{2} erfc\left(\sqrt{\frac{N_s E_{RX}}{2N_0}}\right) \tag{3-40}$$

where:

E_{bRX} represents the received energy per bit;

E_{RX} is the received energy per pulse.

(3-40) shows that by increasing the number of pulses per bit, the received energy is increased by a factor, N_s, with a consequent reduction in the bit error probability. Note that is achieved without increasing the average transmitted power:

$$\mathrm{P}_{av} = \frac{E_{RX}}{\mathrm{T}_s} \tag{3-41}$$

Following an approach based on hard decision detection one, the receiver implements N_s indipendent decisions over N_s pulses that represent one bit. The final decision is achieved by applying a simple majority criterion. Given the number of pulses over a threshold and comparing it with the number of pulses falling below the same threshold, the estimated bit corresponds to the highest of two numbers.

An error occurs if more than the half of pulses are misinterpreted, and the symbol error probability is given by:

$$P_e = \sum_{j=\frac{N_s}{2}}^{N_s} \binom{N_s}{j} P_{eo}^{\,j} \left(1 - P_{eo}\right)^{N_s - j} \tag{3-42}$$

where P_{e0} is the error probability on the single decision (i.e. the error probability for an isolated pulse receiver as derived above).

3.3.5.1 Correlator and Optimum Detector Subsystems for Multi-User Performance

This section is devoted to derive Multi-User performance in terms of bit error probability considering IR-UWB transmission. The results shown in this paragraph are achieved under the following hypotheses:

1. all sources generate binary sequences *b* which consist of indipendent and identically distributed random variables with equally probable symbols 0 and 1;
2. all sources use the same pulse repetition frequency $1/T_s$;
3. codes are indipendent and equally probable. Each code is randomly generated and corresponds to a PN sequence;
4. for each link between a reference transmitter and a reference receiver, the reference transmitter/receiver pair uses a specific code known at the receiver;
5. the pulse is assumed to have limited duration T_p and a symmetrical shape around its central value;
6. radio waves propagate over a multi-path-free channel. The multi-path free impulse response of the channel for the link between user *n* and a reference receiver is a function of $\alpha^{(n)}$ and $\tau^{(n)}$, which are the path gain and time delay for the *n*-th user. The time delays are assumed to be indipendent and identically uniformly distributed random variables over [0, T_s]. The impulse response can be written as follows:

$$h^{(n)}(t) = \alpha^{(n)}\delta\left(t - \tau^{(n)}\right) \tag{3-43}$$

7. the channel output is corrupted by thermal noise $n(t)$, characterized by a double-sided spectral density $N_0/2$ (in W/Hz);
8. the receiver implements a single-user coherent correlation structure with soft decision followed by a ML detector. The received signal is thus analyzed over T_b by considering all N_s pulses composing each bit;
9. the system is asynchronous, but reference transmitter and receiver of a reference link are supposed to be perfectly synchronized under the coherent detection hypothesis.

The binary PPM-THMA signal transmitted by *n-th* user expressed by (3-1) can be rewritten as follows:

$$s_{TX}^{(n)}(t) = \sum_{j=-\infty}^{\infty} \sqrt{E_{TX}^{(n)}}\, p_0\left(t - jT_s - c_j^{(n)} T_c - a_j^{(n)}\delta\right) \tag{3-44}$$

where:

- $p_0(t)$ is the energy normalized pulse with time duration, T_p;
- $E_{TX}^{(n)}$ is the transmitted energy per pulse;
- T_c is the chip period;
- $c_j^{(n)}$ is the *j-th* coefficient of TH code assigned to *n-th* user;
- δ is the time shift introduced by the PPM modulator;
- $a_j^{(n)}\varepsilon$ represents the time shift introduced by PPM modulation (ε is the PPM shift and $a_j^{(n)}$ is the binary value, 1 or 0, conveyed by pulse *j* of *n-th* user).

Given the channel model of (3-43) and the presence of thermal noise at the channel output, the received signal at a reference receiver is given by the sum of all signals originating from the N_u transmitters and can be written as follows:

$$r(t) = \sum_{n=1}^{N_u} \sum_{j=-\infty}^{\infty} \sqrt{E_{RX}^{(n)}}\, p_0\left(t - jT_s - c_j^{(n)} T_c - a_j^{(n)}\delta - \tau^{(n)}\right) + n(t) \tag{3-45}$$

where:

$$E_{RX}^{(n)} = E_{TX}^{(n)}\left(\alpha^{(n)}\right)^2 \tag{3-46}$$

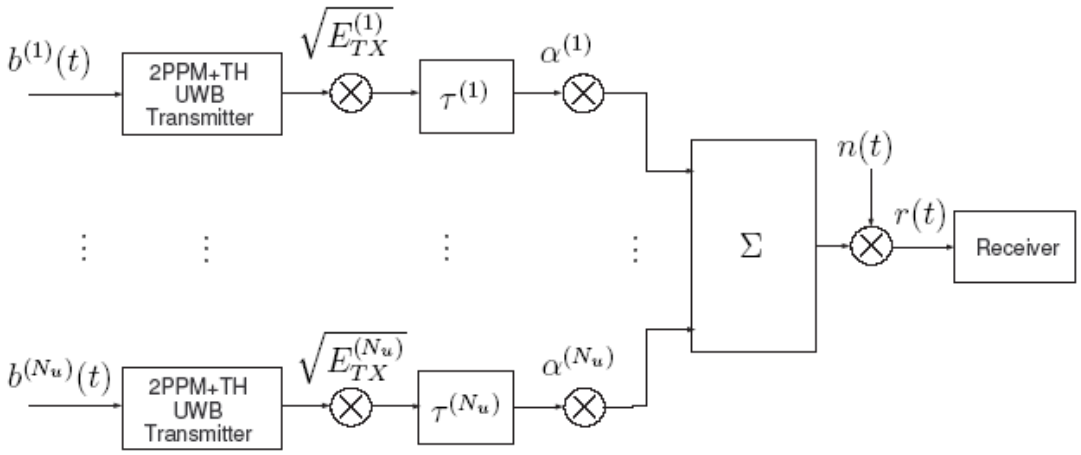

Figure 3-24: 2 PPM-TH Multi-User IR-UWB Scheme (based on ML criterion)

Given the symmetry of the model, we can focus the analysis on one active link. Suppose the reference receiver is listening to the first transmitter (Tx1). Under the hypothesis of

perfect synchronization between the Tx1 and reference receiver, the time delay $\tau^{(1)}$ is known by the receiver, and one can assume $\tau^{(1)} = 0$, given that only relative delays and phases are relevant.

The received signal can thus be rewritten as follows:

$$r(t) = r_u(t) + r_{mui}(t) + n(t) \tag{3-47}$$

where:

- $r_u(t)$ is the useful signal at the receiver input;
- $r_{mui}(t)$ is the Multi-User Interference (MUI) contributions at receiver input.

With soft decision at the receiver, the analysis focuses on a bit time interval of duration T_b. Given again the symmetry of system, the analysis can be focused on the interval [0, T_b]. The $r_u(t)$ and $r_{mui}(t)$ contributions can be written as follows:

$$r_u(t) = \sum_{j=1}^{N_s-1} \sqrt{E_{TX}^{(1)}}\, p_0\left(t - jT_s - c_j^{(1)}T_c - a_j^{(1)}\delta\right) \tag{3-48}$$

$$r_{mui}(t) = \sum_{n=2}^{N_u} \sum_{j=-\infty}^{\infty} \sqrt{E_{RX}^{(n)}}\, p_0\left(t - jT_s - c_j^{(n)}T_c - a_j^{(n)}\delta - \tau^{(n)}\right) \tag{3-49}$$

with $t \in [0, T_b]$.

The soft decision correlation output receiver can be expressed as follows:

$$Z = \int_0^{T_b} r(t)m(t)dt \tag{3-50}$$

where $m(t)$ is the correlation receiver mask and is defined as follows:

$$m(t) = \sum_{j=0}^{N_s-1} v\left(t - jT_s - c_j^{(1)}T_s\right) \tag{3-51}$$

with:

$$v(t) = p_0(t) - p_0(t-\delta) \tag{3-52}$$

The ML decision rule can thus be expressed as follows:

ML Receiver Decision Rule:

$$\text{If} \quad \begin{cases} Z > 0 \Rightarrow \hat{b} = 0 \\ Z < 0 \Rightarrow \hat{b} = 1 \end{cases} \tag{3-53}$$

where $\hat{b}$ indicates the estimated bit. By combining (3-47) with (3-50):

$$Z = Z_u + Z_{mui} + Z_n \tag{3-54}$$

where Z_u, Z_{mui} and Z_n indicate a useful signal, MUI noise and thermal noise at the receiver output.

The *Standard Gaussian Approximation* (*SGA*) hypothesis assumes that Z_{mui}, as well as Z_n, is a zero-mean Gaussian random process characterized by variance σ_{mui}^2, and σ_n^2 is the variance of thermal noise. Under the SGA hypothesis, one can write the relation between P_e and SRN as following:

$$P_e = \frac{1}{2} erfc\left(\sqrt{\frac{SNR}{2}}\right) \tag{3-55}$$

where SNR accounts for both thermal and interference noise contributions.

The useful signal contribution is the bit energy, E_b, and therefore one can write:

$$SNR = \frac{E_b}{\sigma_n^2 + \sigma_{mui}^2} \tag{3-56}$$

By isolating thermal and MUI contributions, (3-56) can be written as follows:

$$SNR = \left((SNR_n)^{-1} + (SNR_{mui})^{-1}\right)^{-1} = \left(\left(\frac{E_b}{\sigma_n^2}\right)^{-1} + \left(\frac{E_b}{\sigma_{mui}^2}\right)^{-1}\right)^{-1} \tag{3-57}$$

where:

SNR_n is the signal to thermal noise ratio;

SNR_{mui} is the signal to MUI ratio.

$$\begin{aligned} E_b = (Z_u)^2 &= \left(\sqrt{E_{RX}^{(1)}} \sum_{j=0}^{N_s-1} \int_{jT_s + c_j^{(1)}T_c}^{jT_s + c_j^{(1)}T_c + T_c} p_0\left(t - jT_s + c_j^{(1)}T_c\right) v\left(t - jT_s + c_j^{(1)}T_c\right) dt\right)^2 = \\ &= E_{RX}^{(1)} \left(N_s \int_0^{T_c} p_0(t)\left(p_0(t) - p_0(t-\delta)\right) dt \right)^2 = \\ &= E_{RX}^{(1)} N_s^{(2)} \left(\int_0^{T_c} p_0(t) p_0(t) dt - \int_0^{T_c} p_0(t) p_0(t-\delta) dt \right)^2 = E_{RX}^{(1)} N_s^2 \left(1 - R_0(\delta)\right)^2 \end{aligned} \tag{3-58}$$

where $R_0(t)$ is the autocorrelation function of the pulse waveform, $p_0(t)$.

The variance of thermal noise at the 2-PPM receiver output, σ_n^2:

$$\delta_n^2 = N_s N_0 \left(1 - R_0\left(1 - \delta\right)\right) \tag{3-59}$$

which leads to the following expression for SNR_n:

$$SNR_n = \frac{N_s E_{RX}^{(1)}}{N_0}\left(1 - R_0\left(1-\delta\right)\right) = \\ = \frac{E_b}{N_0}\left(1 - R_0\left(1-\delta\right)\right) \tag{3-60}$$

This equation shows that SNR_n is maximum when $R_0(\delta)$ is minimum, and can therefore be maximized by selecting an optimal ε value. This procedure leads to optimal 2-PPM. Let us now characterize MUI. Since the system is asynchronous, we need to consider as 'interfering events' all cases where an alien pulse, or a pulse originating by any of the transmitters but TX1, is detected by the receiver.

Figure 3-25 shows the effect on the presence of an alien pulse originating from Tx_n in the receiver, which results in an interference noise amplitude.

The interference noise caused by the presence of one alien pulse at the output of the receiver can be written as follows:

$$mui_p^{(n)}\left(\tau^{(n)}\right) = \sqrt{E_{RX}^{(n)}}\int_0^{2T_M} p_0\left(t-\tau^{(n)}\right)v(t)dt \tag{3-61}$$

We can now find the variance of the interference noise in (3-60). Assuming that the delay, $\tau^{(n)}$ is uniformly distributed over [0, T_s]:

$$\sigma^2_{mui_p^{(n)}} = \frac{1}{T_s}\int_0^{T_s}\left(\left(\sqrt{E_{RX}^{(n)}}\right)^2\int_0^{2T_M} p_0\left(t-\tau^{(n)}\right)v(t)dt\right)^2 d\tau^{(n)} = \\ = \frac{E_{EX}^{(n)}}{T_s}\int_0^{T_s}\left(\int_0^{2T_M} p_0\left(t-\tau^{(n)}\right)v(t)dt\right)^2 d\tau^{(n)} \tag{3-62}$$

The total MUI energy on bit, considering N_s pulses, can be written:

$$\sigma^2_{mui} = \sum_{n=2}^{N_u}\left(\frac{N_s}{T_s}E_{RX}^{(n)}\int_0^{T_s}\left(\int_0^{2T_M} p_0\left(t-\tau^{(n)}\right)v(t)dt\right)^2\right)d\tau^{(n)} \tag{3-63}$$

Since all delays are equally distributed, (3-62) becomes:

$$\sigma^2_{mui} = \frac{N_s}{T_s}\left(\int_0^{T_s}\left(\int_0^{2T_M} p_0\left(t-\tau\right)v(t)dt\right)^2 d\tau\right)\sum_{n=2}^{N_u} E_{RX}^{(n)} = \\ = \frac{N_s}{T_s}\sigma_M^2\sum_{n=2}^{N_u} E_{RX}^{(n)} \tag{3-64}$$

for τ uniformly distributed over [0, T_s].

The term σ_M^2 of (3-64) can be written as follows:

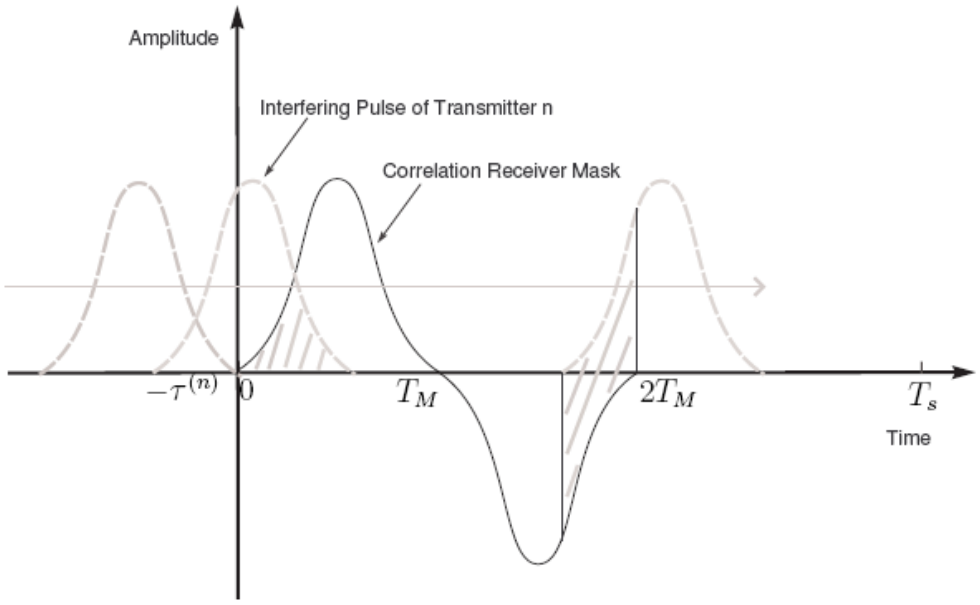

Figure 3-25: Graphical Representation of the presence of an Interfering Pulse at the Reference Receiver Input

$$\begin{aligned}
\sigma_M^2 &= \int_0^{T_s}\left(\int_0^{2T_M} p_0(t-\tau)v(t)dt\right)^2 d\tau = \int_0^{T_s}\left(\int_0^{2T_M} p_0(t-\tau)\left(p_0(t)-p_0(t-\delta)\right)dt\right)^2 d\tau = \\
&= \int_0^{T_s}\left(\int_0^{T_M} p_0(t-\tau)p_0(t)dt - \int_{\delta}^{\delta+T_M} p_0(t-\tau)p_0(t-\delta)dt\right)^2 d\tau = \\
&= \int_{T_M}^{2T_M}\left(\int_0^{T_M} p_0(t-\tau)p_0(t) - \int_{\delta}^{\delta+T_M} p_0(t-\tau)p_0(t-\delta)dt\right)^2 d\tau = \\
&= \int_{T_M}^{2T_M}\left(R_0(\tau)-R_0(\tau+\delta)\right)^2 d\tau
\end{aligned} \tag{3-65}$$

Referring back (3-57), we can express SNR_{mui}:

$$\begin{aligned}
SNR_{mui} &= \frac{E_{RX}^{(1)} N_s^2 \left(1-R_0(\delta)\right)^2}{N_s\sigma_M^2}\left(\frac{1}{\mathrm{T}_s}\sum_{n=2}^{N_u} E_{RX}^{(n)}\right)^{-1} = \\
&= \frac{\left(1-R_0(\delta)\right)^2}{\sigma_M^2} N_s T_s \left(\sum_{n=2}^{N_u}\frac{E_{RX}^{(n)}}{E_{RX}^{(1)}}\right)^{-1} = \frac{\left(1-R_0(\delta)\right)^2}{\sigma_M^2}\gamma_R\left(R_b\sum_{n=2}^{N_u}\frac{E_{RX}^{(n)}}{E_{RX}^{(1)}}\right)^{-1}
\end{aligned} \tag{3-66}$$

which, in the case of orthogonal pulses, reduces to:

$$SNR_{mui} = \frac{\gamma_R}{\sigma_M^2}\left(R_b\sum_{n=2}^{N_u}\frac{E_{RX}^{(n)}}{E_{RX}^{(1)}}\right)^{-1} = \gamma_R\left(2\int_{-T_M}^{T_M} R_0^2(\tau)d\tau\cdot R_b\sum_{n=2}^{N_u}\frac{E_{RX}^{(n)}}{E_{RX}^{(1)}}\right)^{-1} \tag{3-67}$$

(3-66) and (3-67) indicate that, for a given interference scenario, the MUI term can be monitored by controlling the bit rate used by all transmitters. Under the hyphotesis of the perfect power control, i.e. all terms $E_{RX}^{(i)}$ are equal for i = 1,... N_u, we can evaluate the maximum allowed bit rate, R_b, to be used by any of N_u users, for a given SNR_{mui}:

$$R_b\left(SNR_{mui}, N_u\right) = \frac{\left(1-R_0(\delta)\right)^2 \gamma_R^2}{\sigma_M^2}\left(SNR_{mui}\left(N_u-1\right)\right)^{-1} \tag{3-68}$$

By combining (3-68) with (3-66), the P_e for a 2PPM-THMA system based on SGA is:

$$P_e = \frac{1}{2} erfc\left(\sqrt{\frac{1}{2}\left[\left(\frac{E_b^{(1)}}{N_0}\left(1-R_0(\delta)\right)\right)^{-1} + \left(\frac{\left(1-R_0(\delta)\right)^2 \gamma_R}{\sigma_R^2 R_b \left(\sum_{n=2}^{N_u} \frac{E_{RX}^{(n)}}{E_{RX}^{(1)}}\right)}\right)^{-1}\right]^{-1}}\right) \tag{3-69}$$

In the case of PPM, (3-69) becomes:

$$P_e = \frac{1}{2} erfc\left(\sqrt{\frac{1}{2}\left[\left(\frac{E_b^{(1)}}{N_0}\right)^{-1} + \left(\frac{\gamma_R}{\left(2R_b \sum_{n=2}^{N_u} \frac{E_{RX}^{(n)}}{E_{RX}^{(1)}} \int_{-T_M}^{T_M} R_0^2(\tau) d\tau\right)}\right)^{-1}\right]^{-1}}\right) \tag{3-70}$$

$$P_e = \frac{1}{2} erfc\left(\sqrt{\frac{1}{2}\left[\left(\frac{E_b^{(1)}}{N_0}\left(1-R_0(\delta)\right)\right)^{-1} + \left(\frac{\left(1-R_0(\delta)\right)^2 \gamma_R}{\sigma_R^2 R_b \left(N_u-1\right)}\right)^{-1}\right]^{-1}}\right) \tag{3-71}$$

$$P_e = \frac{1}{2} erfc\left(\sqrt{\frac{1}{2}\left[\left(\frac{E_b^{(1)}}{N_0}\right)^{-1} + \left(\frac{\gamma_R}{\left(2R_b\left(N_u-1\right) \int_{-T_M}^{T_M} R_0^2(\tau) d\tau\right)}\right)^{-1}\right]^{-1}}\right) \tag{3-72}$$

(3-71) and (3-72) have been derived considering the hyphotesis of the perfect power control.

3.3.6 UP-FREQUENCY AND DOWN-FREQUENCY CONVERTER SUBSYSTEMS

The base-band output signal of the shaping filter is then up-converted to W band frequencies (i.e. 85 GHz) by using a mixer with a local oscillator. This paragraph is dedicated to the analysis and modeling of the up-frequency converter subsystem, whose block diagram is shown in Figure 3-26.

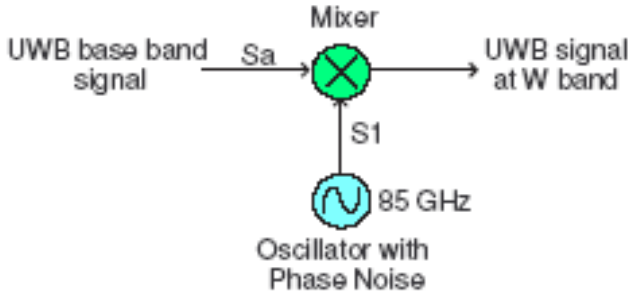

Figure 3-26: Up-Frequency Converter Subsystem Block Diagram

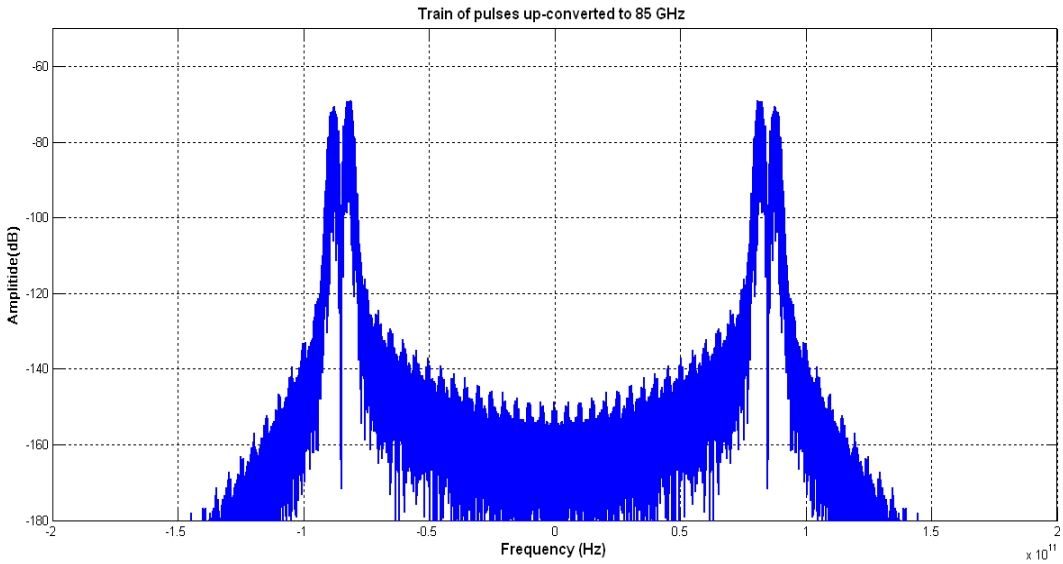

Figure 3-27: Double Side Spectrum of Train of 0.825 ns Pulses up-converted at 85 GHz

A mixer is generally a three-port device that uses a nonlinear or time-varying element to achieve frequency conversion. An ideal mixer produces an output consisting of the sum and difference frequencies of its two input signals. Operation of practical RF and microwave mixers is usually based on the non linearity provided by either a diode or a transistor. A non linear component can generate a wide variety of harmonics and other

products of input frequencies, so filtering must be used to select the desired frequency components. Modern microwave systems typically use some mixer and filter stages to perform the functions of frequency up-conversion and down-conversion between baseband signal frequencies and RF carrier frequencies. Some of the important characteristics of mixers, such as image frequency, conversion loss, noise effects, and intermodulation distortion have to be included in the model of a mixer in order to simulate the real performance of an IR-UWB transceiver operating at W band. On the other hand, mixer design requires impedance matching at three ports, complicated by the fact that several frequencies and their harmonics are involved. Ideally, each mixer port would be matched at its particular frequency (RF, LO, or IF), and undesired frequency products would be absorbed with resistive loads, or blocked with reactive terminations. However, resistive loads increase mixer losses, and reactive loads can be very frequency sensitive. In addition, there are inherent losses in the frequency conversion process because of the generation of undesired harmonics and other frequency products.

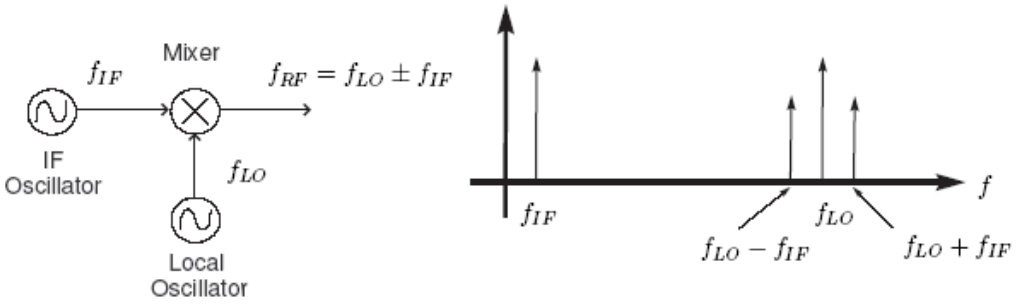

Figure 3-28: Common Up-Frequency Converter Stage

An important figure of merit for a mixer is therefore the conversion loss, which is defined as the ratio of available RF input power to the available IF output power, expressed in dB (relatively to a down-frequency converter stage):

$$L_c = 10\log\frac{available\,RF\,input\,power}{available\,IF\,output\,power} \geq 0\,dB \tag{3-73}$$

Since the RF stages of receivers operate at much lower power levels than do transmitters, minimum conversion loss is a more critical parameter for receivers because of the importance of minimizing losses in the RF stages to maximize receiver noise figure.

Moreover, some intermodulation products are generated by mixers because of their non-linearity characteristics. Another significant mixer parameter is represented by the isolation between the RF and LO ports. Ideally, the LO and RF ports would be decoupled, but

internal impedance mismatches and limitations of coupler performance often result in some LO power being coupled out of the RF port. This is a potential problem for receivers that drive the RF port directly from the antenna, since LO power coupled through the mixer to the RF port will be radiated by the antenna. Since such signals will likely interfere with other services or users, the FCC sets stringent limits on the power radiated by receivers. This problem can be largely alleviated by using a bandpass filter between the antenna and mixer, or by using an RF amplifier ahead of the mixer.

3.3.6.1 Choice of The Image Reject Mixer Circuit for Up And Down Frequency Stages in a W band IR-UWB transceiver

It is well known that two distinct RF input signals at frequencies $\omega_{RF} = \omega_{LO} \pm \omega_{IF}$ down-convert to the same IF frequency when mixed with ω_{LO}. These two frequencies are the upper and lower sidebands of a double-sideband signal. The desired response can be arbitrarily selected as either the LSB ($\omega_{LO} - \omega_{IF}$) or the USB ($\omega_{LO} + \omega_{IF}$), assuming a positive IF frequency. The image reject mixer, shown in Figure 3-29, can be used to isolate these two responses into separate output signals. The same circuit can also be used for up-conversion, in which case it is usually called a single-sideband modulator. In this case, the IF input signal is delivered to either the LSB or the USB port of the IF hybrid, and the associated single sideband signal is produced at the RF port of the mixer. We can analyse the image reject mixer using the small-signal approximation.

Let the RF input signal be expressed as:

$$v_{RF}(t) = V_U \cos(\omega_{LO} + \omega_{IF})t + V_L \cos(\omega_{LO} - \omega_{IF})t \tag{3-74}$$

where V_U and V_L are the amplitudes of the upper and lower sidebands, respectively.

Using the S-matrix for the 90° hybrid:

$$\mathrm{S} = -\frac{1}{\sqrt{2}} \begin{pmatrix} 0 & j & 1 & 0 \\ j & 0 & 0 & 1 \\ 1 & 0 & 0 & j \\ 0 & 1 & j & 0 \end{pmatrix} \tag{3-75}$$

gives the RF voltages at the diodes as:

$$v_A(t) = \frac{1}{\sqrt{2}}[V_U \cos(\omega_{LO}t + \omega_{RF}t - 90^\circ) + V_L \cos(\omega_{LO}t - \omega_{IF}t - 90^\circ)] \tag{3-76}$$

$$
\begin{aligned}
&= \frac{1}{\sqrt{2}}[V_U \sin(\omega_{LO}+\omega_{IF})t + V_L \sin(\omega_{LO}-\omega_{IF})t] \\
v_B(t) &= \frac{1}{\sqrt{2}}[V_U \cos(\omega_{LO}t+\omega_{IF}t-180°) + V_L \cos(\omega_{LO}t-\omega_{IF}t-180°)] \\
&= \frac{1}{\sqrt{2}}[V_U \cos(\omega_{LO}+\omega_{IF})t + V_L \cos(\omega_{LO}-\omega_{IF})t]
\end{aligned}
\tag{3-77}
$$

After mixing with the LO signal:

$$v_{LO}(t)V_{LO}\cos\omega_{LO}t \tag{3-78}$$

and low-pass filtering, the IF inputs to the IF hybrid are:

$$v_{IF}^{A}(t) = \frac{KV_{LO}}{2\sqrt{2}}(V_U - V_L)\sin\omega_{IF}t \tag{3-79}$$

$$v_{IF}^{B}(t) = -\frac{KV_{LO}}{2\sqrt{2}}(V_U + V_L)\cos\omega_{IF}t \tag{3-80}$$

where K is the mixer constant for the squared term of the diode response. The phasor representation of the IF signals of two last equations is:

$$V_{IF}^{A} = \frac{jKV_{LO}}{2\sqrt{2}}(V_U - V_L) \tag{3-81}$$

$$V_{IF}^{B} = -\frac{jKV_{LO}}{2\sqrt{2}}(V_U + V_L) \tag{3-82}$$

Combining these voltages in the IF hybrid gives the following outputs:

$$V_1 = -j\frac{V_{IF}^{A}}{\sqrt{2}} - \frac{V_{IF}^{B}}{\sqrt{2}} = \frac{KV_{LO}V_L}{2} \quad (LSB) \tag{3-83}$$

$$V_2 = -j\frac{V_{IF}^{A}}{\sqrt{2}} - \frac{V_{IF}^{B}}{\sqrt{2}} = -\frac{KV_{LO}V_U}{2} \quad (USB) \tag{3-84}$$

These outputs can be expressed in time-domain form as:

$$V_1(t) = \frac{KV_{LO}V_L}{2}\cos\omega_{IF}t \tag{3-85}$$

$$V_2(t) = \frac{KV_{LO}V_U}{2}\sin\omega_{IF}t \tag{3-86}$$

which clearly shows the presence of a 90° phase shift between the two side-bands. Also note that the image rejection mixer does not incur any additional losses beyond the usual conversion losses of the single rejection mixer.

A practical difficulty with image rejection mixers is in fabricating a good hybrid at the relatively low IF frequency. Losses, and hence noise figure, are also usually greater than for a simpler mixer. However, an image rejection mixer has been used in order to simulate the direct conversion architecture adopted for the receiver chain.

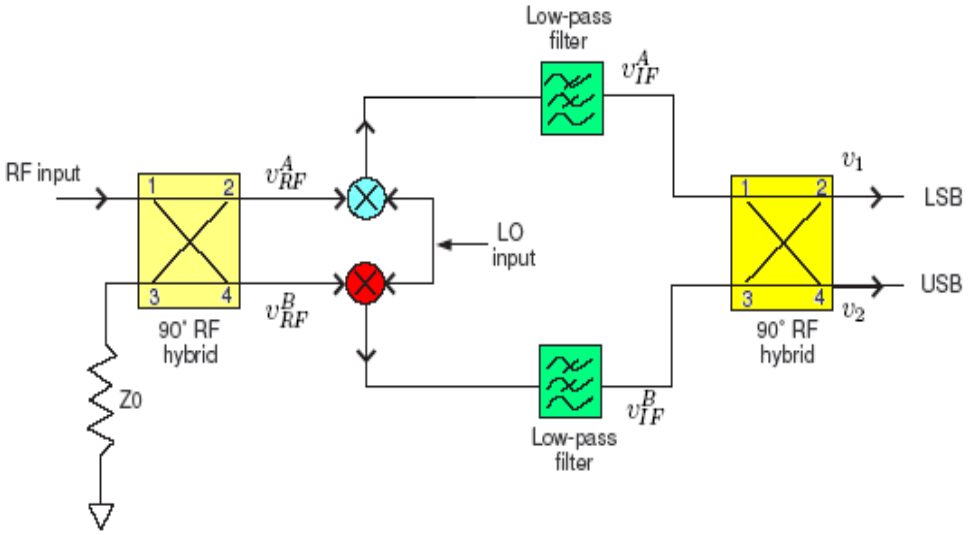

Figure 3-29: Common Image Reject Mixer Circuit

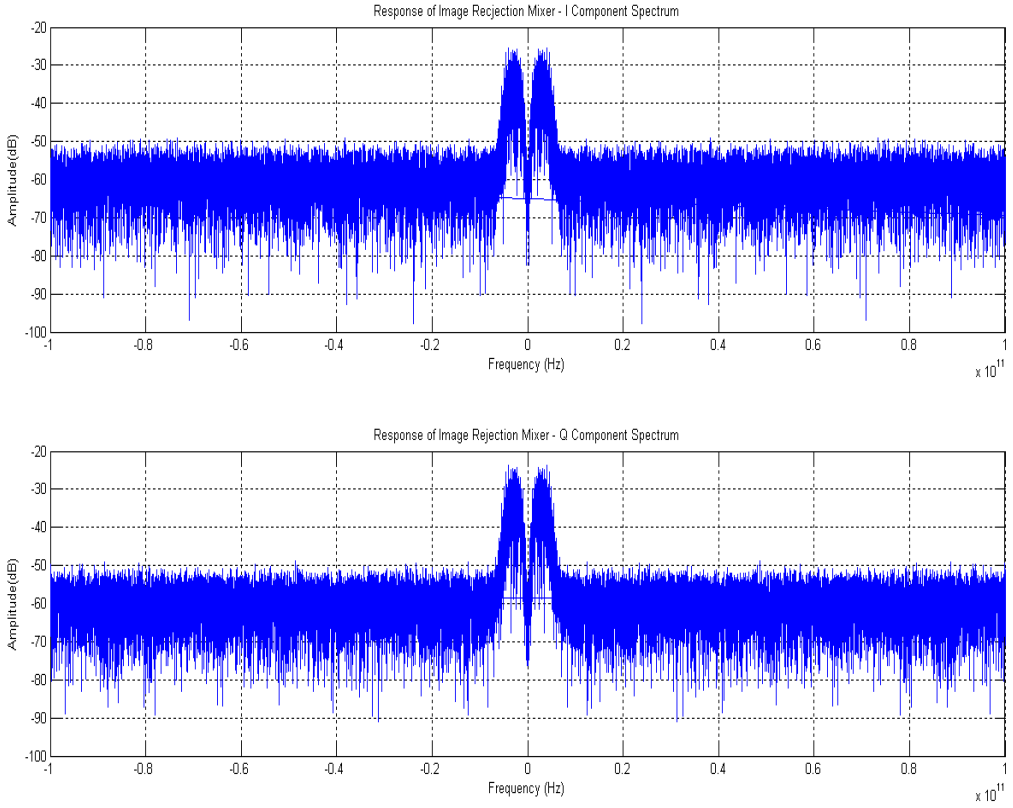

Figure 3-30: I&Q Cmponents Spectrum after down-conversion stage using Image Rejection Mixer

3.3.7 FREQUENCY GENERATOR SUBSYSTEM

The noise produced by an oscillator or other signal source is very important in practice because it may severely degrade the performance of communication receiver system [3-22], [3-27]. Phase noise refers to the short-term random fluctuation in the frequency (or phase) of an oscillator signal. Phase noise also introduces uncertainty during the detection of digitally modulated signals. An ideal oscillator would have a frequency spectrum consisting of a single delta function at its operating frequency, but a realistic oscillator will have spectrum more like that shown in Figure 3-31. Spurious signals due to oscillator harmonics or intermodulation products appear as discrete spikes in the spectrum. Phase noise, due to random fluctuations caused by thermal and other noise sources, appears as a broad continuous distribution localized about the output signal. Phase noise is defined as the ratio of power in one phase modulation side-band to the total signal power per unit bandwidth (one Hz) at a particular offset, f_m, from the signal frequency, and is denoted as £(f_m). It is usually expressed in decibels relative to the carrier power per Hertz of bandwidth (dBc/Hz). The aim of this paragraph is to use a proper model of the power spectral density of phase noise in oscillators in order to examine the phase noise effect on BER performance of W band UWB-IR transceiver.

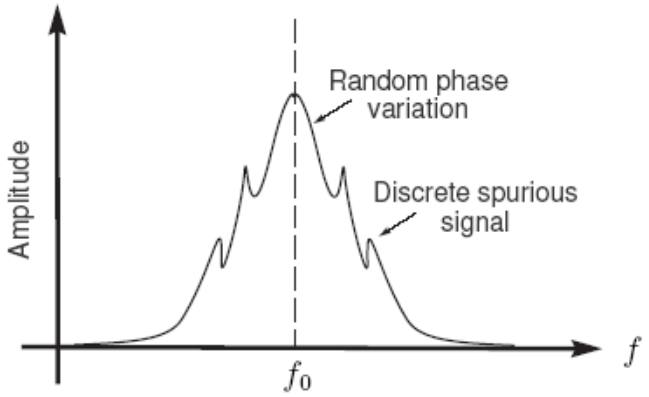

Figure 3-31: Output Spectrum of a Common Oscillator

In general, the output voltage of an oscillator can be written as

$$v_0(t) = V_0[1 + A(t)]\cos(\omega_0 t + \vartheta(t)) \tag{3-87}$$

where:

- $A(t)$ represents the amplitude fluctuations of the output;

- $\vartheta(t)$ represents the phase variation of the output waveform.

Amplitude variations can usually be well controlled, and generally have less impact on system performance. Phase variations may be discrete (due to spurious mixer products or harmonics), or random in nature (due to thermal or other random noise sources).

Note from (3-15) that an instantaneous phase variation is indistinguishable from a variation in frequency.

Small changes in the oscillator frequency can be represented as a frequency modulation of the carrier by letting:

$$\vartheta(t) = \frac{\Delta f}{f_m}\sin(\omega_m t) = \vartheta_p \sin(\omega_m t) \tag{3-88}$$

where $f_m = \frac{\omega_m}{2\pi}$ is the modulating frequency. The peak phase variation:

$$\vartheta_p = \frac{\Delta f}{f_m} \tag{3-89}$$

also called the modulation index. Substituting (3-88) into (3-87):

$$v_0(t) = V_0\left[\cos(\omega_0 t)\cos\left(\vartheta_p \sin(\omega_m t)\right) - \sin(\omega_0 t)\sin\left(\vartheta_p \sin(\omega_m t)\right)\right] \tag{3-90}$$

where we set $\mathrm{A}(t) = 0$ to ignore amplitude fluctuations.

Assuming the phase deviations are small, so $\vartheta_p << 1$, the small argument expressions that $\sin(x) \cong x$ and $\cos(x) \cong 1$ can be used to simplify (3-18) to:

$$\begin{aligned} v_0(t) &= V_0\left[\cos(\omega_0 t) - \vartheta_p \sin(\omega_m t)\sin(\omega_0 t)\right] = \\ &= V_0\left\{\cos(\omega_0 t) - \frac{\vartheta_p}{2}\left[\cos(\omega_0 + \omega_m)t - \cos(\omega_0 - \omega_m)t\right]\right\} \end{aligned} \tag{3-91}$$

This expression shows that small phase or frequency deviations in the output of an oscillator result in modulation sidebands at $\omega_0 + \omega_m$, located on either side of the carrier signal at ω_0.

When these deviations are due to random changes in temperature or device noise, the output spectrum of the oscillator will take the form shown in Figure 3-31. According to the definition of phase noise as the ratio of noise power in a single sideband to the carrier power, the waveform of (3-91) has a corresponding phase noise of:

$$\xi(f)=\frac{\mathrm{P}_n}{\mathrm{P}_c}=\frac{\frac{1}{2}\left(\frac{V_0\vartheta_p}{2}\right)^2}{\frac{1}{2}V_0^2}=\frac{\vartheta_p^2}{4}=\frac{\vartheta_{rms}^2}{2} \tag{3-92}$$

where:

$$\vartheta_{rms}=\frac{\vartheta_p}{\sqrt{2}} \tag{3-93}$$

is the *rms* value of the phase deviation. The two-sided power spectral density associated with phase noise includes power in both sidebands:

$$S_\vartheta(f_m)=2\xi(f_m)=\frac{\vartheta_p^2}{2}=\vartheta_{rms}^2 \tag{3-94}$$

The existence of this perturbation leads to a mismatched up/down-conversion of the signal: hence the phase noise is a particularly sensitive factor that increases the error probability of the communication link.

Another effect of phase noise is to introduce some uncertainty in the modulated signal.

There are several ways of modeling the phase noise process such as an AR (AutoRegressive) filter based model, or by shaping the frequency response of phase noise according to some practical measurements using Leeson's noise spectrum model described in [3-28], [3-29].

The Phase Noise Model used by us to simulate BER vs Eb/No performance for the W band UWB transceiver consists of the Leeson equation for single sideband phase noise density as reported as following [3-29]:

$$L(f_m)=10\log_{10}\left\{\frac{FkT}{2P_{avs}}\cdot\left[\left(1+\frac{f_c}{f_m}+\left(\frac{f_0}{2f_mQ_L}\right)^2\cdot\left(1+\frac{f_c}{f_m}\right)\right)\right]\right\}\ \text{dBc/Hz} \tag{3-95}$$

where F is noise factor of the active device, k is the Boltzmann Constant, T is temperature (K), P_{avs} is the Average Power in Resonator (W), f_c represents Flicker Corner Frequency of the active device , f_m is Carrier Frequency, f_0 is centre carrier frequency, Q_L is the loaded resonator quality factor. The measured phase noise values (considered in simulations) are [-100.2 dBc/Hz, -209.9 dBc/Hz] in correspondence of carrier offset

frequencies range [1 MHz, 10 MHz]. Table 3-2 shows the main parameters used in order to simulate Phase Noise Effect on BER performance of IR-UWB Transceiver operating at 85 GHz.

Input Parameters	Values
f_c	*85 GHz*
f_m	*[1 MHz, 10 MHz]*
P_{avs}	*5 dBm*
Q_L	*100*
T_p	*0.825 ns*
N_s	*2*
N_p *(TH Code)*	*7*
Users	*7*
δ	*0.1648 ns*
T_c *(Chip Time)*	*1.2 ns*

Table 3-2: Simulation Parameters used to evaluate the Phase Noise Effect on BER performance of IR-UWB Transceiver operating at 85 GHz

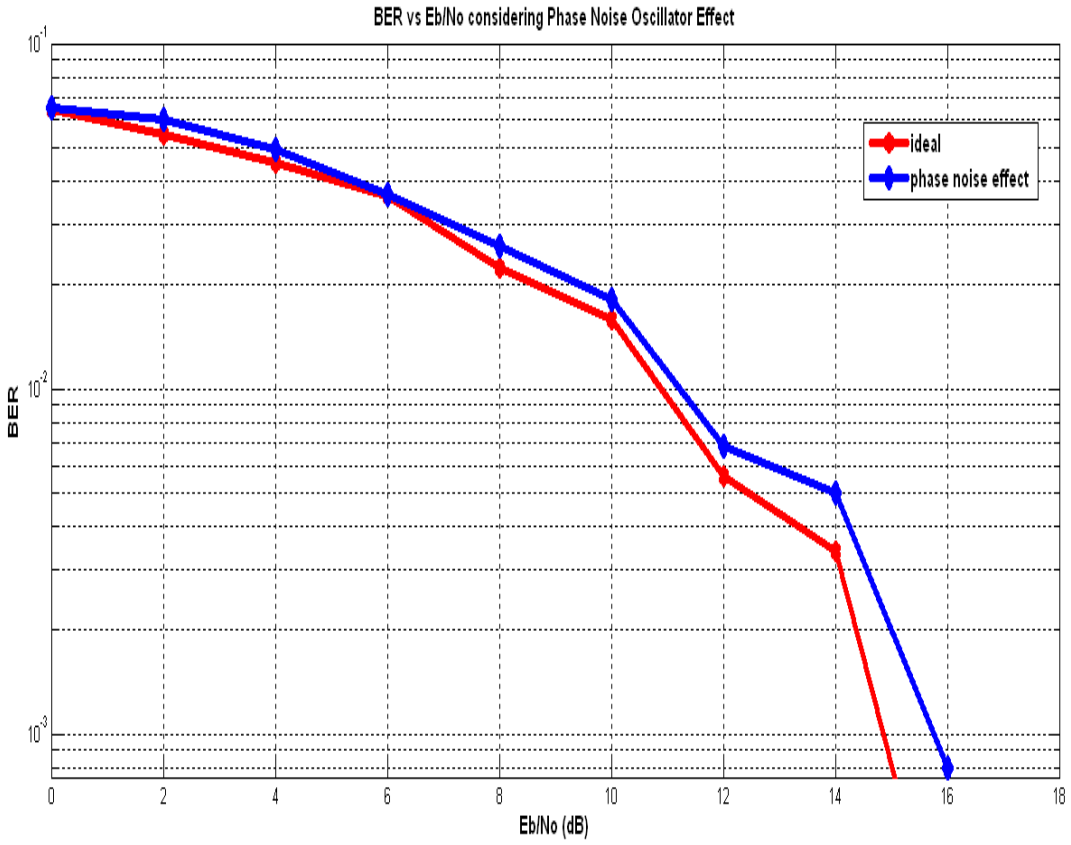

Figure 3-32: BER versus Eb/N0 considering Phase Noise effect

Figure 3-32 shows the phase noise effect on BER vs. Es/No performance. It is clear as the IR-UWB architecture is robust to phase noise effect. The blue curve is referred to real case, while the red one to ideal case. The degradation due to phase noise effect introduced by oscillators and mixers is up to 1 dB.

Compact, reliable and low mass sources are the key components in future millimeter-wave and submillimeter-wave applications as high-resolution, biological and chemical sensors and wide bandwidth communication satellite systems [3-27]. MMICs can obtain the required performance for most of these systems combined with small sizes, low weight and high reliability. Traditionally at these frequencies microwave tubes and microwave diodes have been used. However, nowadays the advances in transistor technologies allow to realise transistor based millimeter wave oscillators. While at first mainly III/V semiconductor transistors have reached the millimeter wave frequency range, the latest developments in SiGe HBTs [3-22], [3-23], [3-24] allow the SiGe technology to compete now with III/V based technologies at these frequencies. The low noise level at low frequencies (LF), and resulting low oscillator phase noise are areas in which SIGe HBTs generally outperform III/V HBTs or HEMTs. The significant lower costs of SiGe chip area can reduce the price of millimeter-wave systems and thus it has the potential to open mass markets for consumer systems at these frequencies. Phase noise is of one of most essential criteria whether a specific oscillator can be used in an intended application. The push-push VCO is the most suitable configuration that allows to achieve the best performance in terms of larger available gain of active devices, potentially less power consumption, higher Q-factor, pulling effect minimization and especially reduced phase noise. A push-push VCO is formed by combining two equal sub-oscillators in such a way that the fundamental signals are cancelled out whereas the second harmonic components are delivered to a load. The noise sources in the two sub-oscillators can be regarded as uncorrelated as they are originated from different, independent devices. At the output terminal of the push-push oscillator the second harmonic carrier powers add up while the uncorrelated noise power remains constant [3-25], [3-26]. This results in a single sideband phase noise reduction by 3 dB with respect to the total signal power at the second harmonic frequency. Due to the halved oscillator frequency of the sub-oscillators, the phase noise of the fundamental frequency is $(6 + \alpha)$ dB lower, with $\alpha > 0$, and the phase noise of the second harmonic frequency is α dB lower than for a fundamental frequency oscillator. The summation of the sub-oscillator signals results in a decrease of the phase noise level with respect to the carrier by 3 dB. Thus, the complete phase noise reduction of a push-push oscillator

compared to a conventional oscillator is (3 + α) dB. Compared to solutions using frequency multipliers or doublers, a push-push oscillator is generally less space consuming, a lower sensitivity temperature and a reduced phase noise. These characteristics make the push-push configuration the best candidate for W band frequency generator subsystems. Moreover, the push-push configuration implemented in SiGe HBT technology looks like the most suitable one for the application of UWB technique to EHF communications thanks to its characteristics of larger available gain of active devices together with lower 1/f noise characteristics shown by HBT compared to HEMT. On basis of these considerations, we supposed for our UWB system a W band frequency generator subsystem scheme, as shown in Figure 3-33.

It consists in an integrated solution that employs a 85 GHz push-push VCO, with a low frequency reference source at 160 MHz. The oscillator is integrated with a buffer amplifier and 8:1 frequency divider on a single MMIC, while a commercial PLL chip and a loop filter can be mounted on an external PCB.

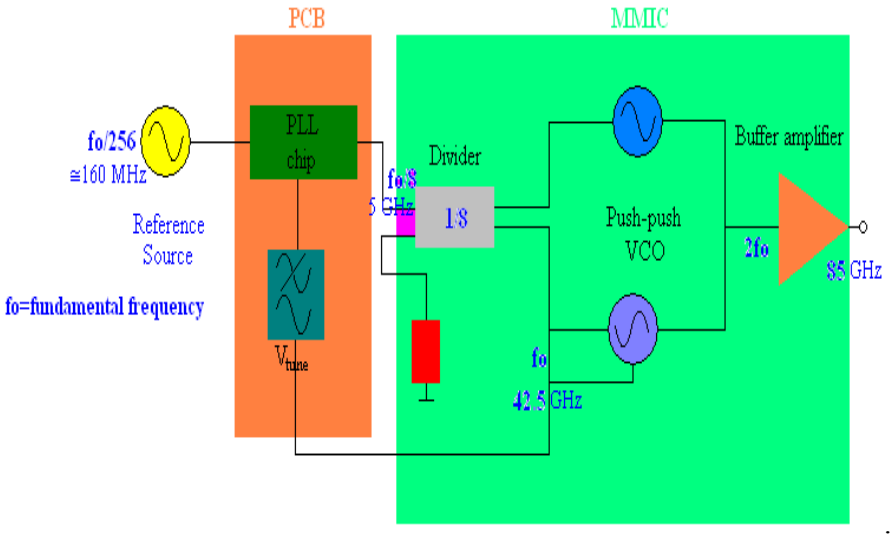

Figure 3-33: 85 GHz Oscillator Scheme for IR-UWB Transceiver

3.3.8 LNA SUBSYSTEM MODELING

The first stage of a receiver is typically a LNA, whose main function is to provide enough gain to overcome the noise of subsequent stages (such as mixer). It is designed to increase the power of the received signal which is usually very weak. LNAs are designed to add as

little noise as possible, such that the SNR is above the minimum required one of the receiver. Every receiver has a minimum SNR at its input, if the SNR drops below this value, the error in the received signal will be high. Therefore, beside stability and gain, the noise figure for a LNA is the most important design parameter since it, according to the well known Friis equation, decides the overall noise figure of the front-end. Moreover, it is not possible to get good gain (gain matching) and good noise figure (noise matching) simultaneously so some compromise must be made while designing the input matching circuit.

On the other hand, nonlinear LNA characteristics can lead to undesired responses such as gain compression and the generation of spurious frequency components. These effects may produce increased losses, signal distortion, and possible interference with other radio channels or services.

The output response of a nonlinear LNA can be modeled as a Taylor series in terms of the input signal voltage v_i:

$$v_0 = a_0 + a_1 v_i + a_2 v_i^2 + a_3 v_i^3 + \ldots \tag{3-96}$$

where the Taylor coefficients are defined as:

$$a_0 = v_0(0) \text{ (DC Output)} \tag{3-97}$$

$$a_1 = \frac{dv_0}{dv_i}\Big| v_i = 0 \text{ (Linear Output)} \tag{3-98}$$

$$a_2 = \frac{d^2 v_0}{dv_i^2}\Big| v_i = 0 \text{ (Squared Output)} \tag{3-99}$$

Firstly, the case where a single frequency sinusoid is applied to the input of a LNA is considered:

$$v_i = V_0 \cos(\omega_0 t) \tag{3-100}$$

Then, (3-96) becomes:

$$\begin{aligned} v_O = a_0 + a_1 V_0 \cos(\omega_0 t) + a_2 V_0^2 \cos^2(\omega_0 t) + a_3 V_0^3 \cos^3(\omega_0 t) + \ldots = \left(a_0 + \frac{1}{2} a_2 V_0^2\right) + \\ \left(a_1 V_0 + \frac{3}{4} a_3 V_0^3\right)\cos(\omega_0 t) + \frac{1}{2} a_2 V_0^2 \cos(2\omega_0 t) + \frac{1}{4} a_3 V_0^3 \cos(3\omega_0 t) + \ldots \end{aligned} \tag{3-101}$$

This result leads to the voltage gain of the signal component at frequency ω_0:

$$G_v = \frac{v_0^{(\omega_0)}}{v_i^{(\omega_0)}} = \frac{a_1 V_0 + \frac{3}{4} a_3 V_0^3}{V_0} = a_1 + \frac{3}{4} a_3 V_0^2 \tag{3-102}$$

The result of this equation shows that the voltage gain is equal to the a_1 coefficient, as expected, but with an additional term proportional to the square of the input voltage gain. Generally, a_3 is negative, so the gain of LNA tends to decrease for large values of V_0. This effect is called gain compression, or saturation. Physically, it is usually due to the fact that the instantaneous output voltage of an amplifier is limited by the power supply voltage used to bias the active device. Smaller values of a_3 will lead to higher output voltages. A typical amplifier response is shown in Figure 3-34.

For an ideal linear amplifier, a plot of the output power versus input power is a straight line with a slope of unity. The not ideal amplifier response tracks the ideal response over a limited range, then begins to saturate, resulting in reduced gain.

To quantify the linear operating range of the amplifier, the 1 dB compression point is defined as the power level for which the output power has decreased by 1 dB from the ideal characteristic. This power level is usually denoted by P1, and can be stated in terms of either input power or output power. For amplifiers P1 is usually specified as an output power.

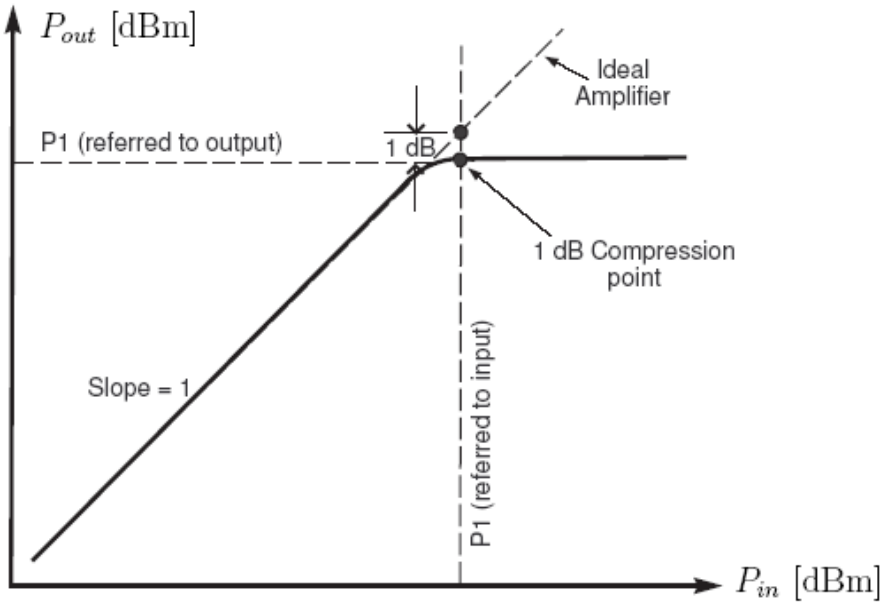

Figure 3-34: Not Ideal Amplifier 1 dB Compression Point

Observing from the expansion of (3-101), a portion of the input signal at frequency ω_0 is converted to other frequency components. For a single input frequency, or tone, ω_0, the

output will in general consist of the input frequency of the form $n\omega_0$ for n =0, 1,2,... Usually these harmonics lie outside the pass-band of the amplifier, and so do not interfere with the desired signal at frequency ω_0.

The situation changes, however, when the input signal consists of two closely spaced frequencies. Consider a two-tone input voltage, consisting of two closely spaced frequencies, ω_1 and ω_2:

$$v_i = V_0\left[\cos(\omega_1 t) + \cos(\omega_2 t)\right] \tag{3-103}$$

From (3-96), the output is:

$$\begin{aligned}
&v_0 = a_0 + a_1 V_0\left[\cos(\omega_1 t) + \cos(\omega_2 t)\right] + a_2 V_0^2\left[\cos(\omega_1 t) + \cos(\omega_2 t)\right]^2 + \\
&a_3 V_0^3\left[\cos(\omega_1 t) + \cos(\omega_2 t)\right]^3 + \ldots = a_0 + a_1 V_0\cos(\omega_1 t) + a_1 V_0\cos(\omega_2 t) + \\
&\frac{1}{2}a_2 V_0^2\left(1 + \cos(2\omega_1 t)\right) + \frac{1}{2}a_2 V_0^2\left(1 + \cos(2\omega_2 t)\right) + a_2 V_0^2\cos(\omega_1 - \omega_2)t + \\
&a_2 V_0^2\cos(\omega_1 + \omega_2)t + a_3 V_0^3\left[\frac{3}{4}\cos(\omega_1 t) + \frac{1}{4}\cos(3\omega_1 t)\right] + \\
&a_3 V_0^3\left[\frac{3}{4}\cos(\omega_2 t) + \frac{1}{4}\cos(3\omega_2 t)\right] + \\
&a_3 V_0^3\left[\frac{3}{2}\cos(\omega_2 t) + \frac{3}{4}\cos(2\omega_1 - \omega_2)t + \frac{3}{4}\cos(2\omega_1 + \omega_2)t\right] + \\
&a_3 V_0^3\left[\frac{3}{2}\cos(\omega_1 t) + \frac{3}{4}\cos(2\omega_2 - \omega_1)t + \frac{3}{4}\cos(2\omega_2 + \omega_1)t\right] + \ldots
\end{aligned} \tag{3-104}$$

where standard trigonometric identities have been used to expand the initial expression. It is possible to see that the output spectrum contains of harmonics of the form: $m\omega_1 + n\omega_2$ with $m, n = 0, \pm1, \pm2, \pm3$.

These combinations of the two input frequencies are called inter-modulation products, and the order of a given product is defined as $|m| + |n|$. For example, the squared term of (3-96) gives rise to the following four inter-modulation products of second order, as shown in Table 3-3:

$2\omega_1$	(second harmonic of ω_1)	$m = 2$	$n = 0$	order= 2
$2\omega_2$	(second harmonic of ω_2)	$m = 0$	$n = 2$	order= 2
$\omega_1 - \omega_2$	(difference frequency)	$m = 1$	$n = -1$	order= 2
$\omega_1 + \omega_2$	(sum frequency)	$m = 1$	$n = 1$	order= 2

Table 3-3: Inter-Modulation Products of second order given a two-tone input voltage

All of these second-order products are undesired in an amplifier; if ω_1 and ω_2 are close, all the second order products will be far from ω_1 or ω_2, and can easily be filtered (either passed or rejected) from the output of the component. The cubed term of (3-104) leads to six third-order inter-modulation products: $3\omega_1$, $3\omega_2$, $2\omega_2+\omega_1$, $2\omega_1+\omega_2$, $2\omega_1-\omega_2$, $2\omega_2-\omega_1$. The first four of these will again be located far from ω_1 or ω_2,and will typically be outside the pass-band of the amplifier.

But the two difference terms produce products located near the original input signals at ω_1 and ω_2, and so cannot be easily filtered from the pass-band of an amplifier. Figure 3-35 shows a typical spectrum of the second- and third-order two tone inter-modulation products. For an arbitrary input signal consisting of many frequencies of varying amplitude and phase, the resulting in-band intermodulation products will cause distortion of the output signal. This effect is called third-order intermodulation distortion.

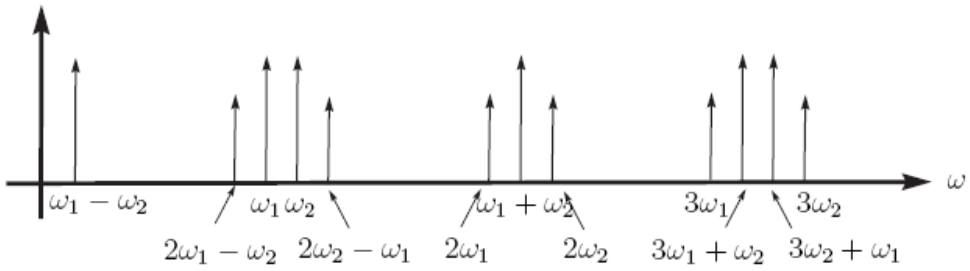

Figure 3-35: Output Spectrum of Second- and Third-Order Two Tone Inter-modulation Products, assuming $\omega_1 < \omega_2$

(3-104) shows that as the input voltage V_0 increases, the voltage associated with the third-order products increases as V_0^3. Since power is proportional to the square of voltage, we can also say that the output power of third-order products must increase as the cube of the input power. So far small input powers the third-order intermodulation products must be very small, but will incrase quickly as input power increases. We can view this effect graphically by plotting the output power for the first- and third-order products versus input power on log-log scales (or in dB), as shown in Figure 3-36.

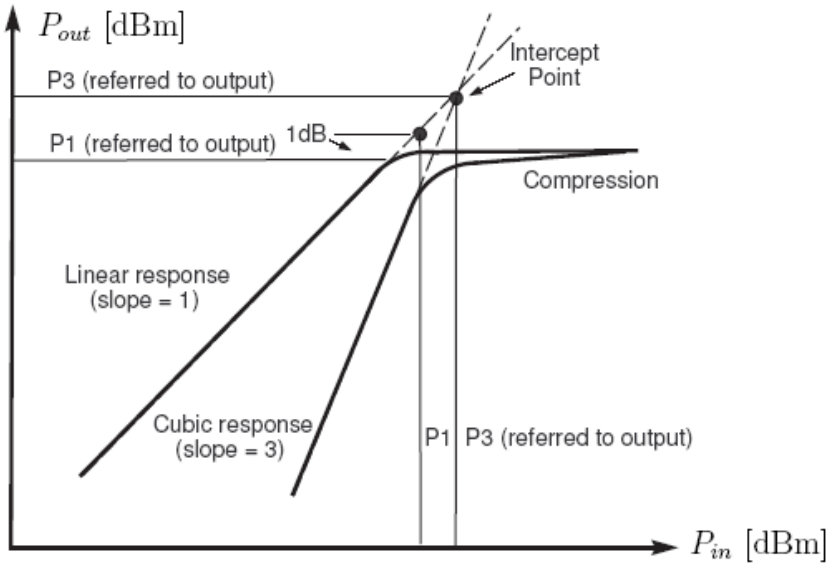

Figure 3-36: Third-Order Intercept for a non-linear LNA

The output power of the first-order, or linear, product is proportional to the input power, so the line describing this response has a slope of unity (before the onset of compression). The line describing the response of third order products has a slope of 3. Both the linear and third-order responses will exhibit compression at high input powers, so we show the extension of their responses with dotted lines. Since these two lines have different slopes, they will intersect, typically at a point above the onset of compression, as shown in Figure 3-36. The hypothetical intersection point, where the first-order and third-order powers are equal, is called the third-intercept point, denoted as P_3, and specified as either an input or an output power. Usually, P_3 is referenced at the output for an amplifier. As depicted in Figure 3-36, P_3 generally occurs at a higher power level than P_1, the 1 dB compression point. We can express P_3 in terms of the Taylor coefficients of the expansion of (3-104) as follows. Define $P_{\omega 1}$, as the output power of the desired signal at frequency ω_1. Then from (3-104) we have:

$$P_{\omega 1} = \frac{1}{2} a_1^2 V_0^2 \tag{3-105}$$

$$P_{2\omega \to \omega_{21}} = \frac{1}{2}\left(\frac{3}{4} a_3 V_0^3\right)^2 = \frac{9}{32} a_3^2 V_0^6 \tag{3-106}$$

By definition these two powers are equal at the third-order intercept point. If we define these input signal voltage at the intercept point as V_{IP}, then equating the last equations gives:

$$\frac{1}{2}a_1^2 V_{IP}^2 = \frac{9}{32}a_3^2 V_{IP}^6 \tag{3-107}$$

Solving for V_{IP} yields:

$$V_{IP} = \sqrt{\frac{4a_1}{3a_3}} \tag{3-108}$$

Since P_3 is equal to the linear response of $P_{\omega 1}$, at the intercept point, we have from (3-105) and (3-108) that:

$$P_3 = P_{\omega_1}\Big|_{V_0 = V_{IP}} = \frac{1}{2}a_1^2 V_{IP}^2 = \frac{2a_1^3}{3a_3} \tag{3-109}$$

where P_3 in this case is referred to the output port.

The model synoptic used in order to evaluate BER performance for the transceiver based on IR-UWB interface operating at W band, is presented in Figure 3-37.

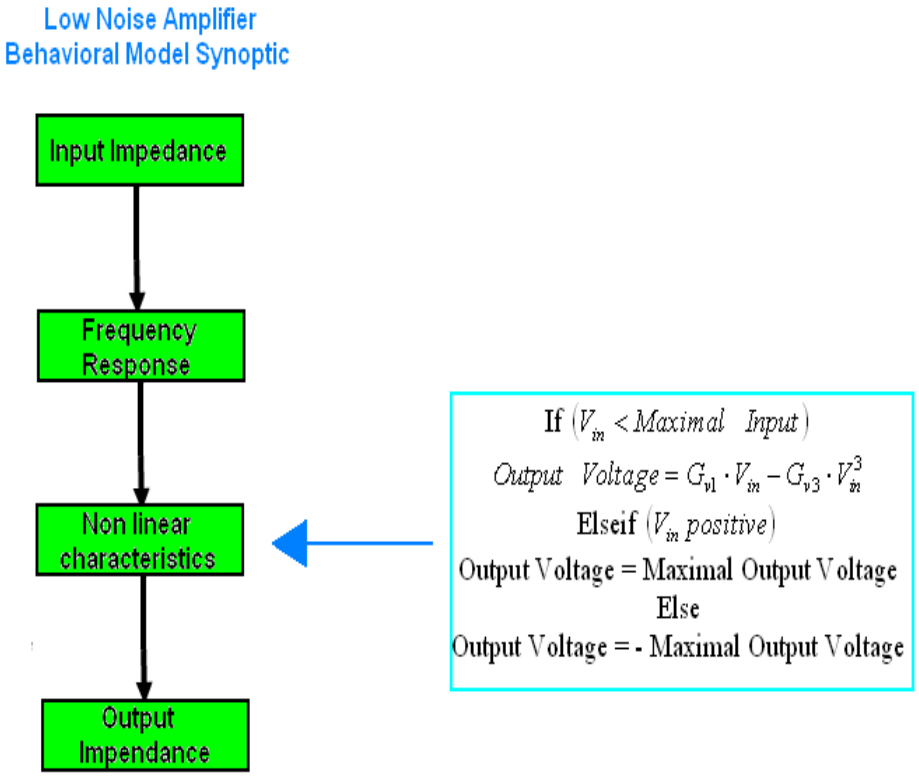

Figure 3-37: 85 GHz LNA Behavioral Synoptic Model

The input parameters are Power Gain, Intercept Point of the Third Order (IP3), Input and Output Impedances (Zin, Zout) and Noise Figure. The corresponding characteristics are computed from those parameters using the classical LNA equations, as it follows:

$$A_v = \sqrt{10^{\frac{A_p}{10}} \cdot \frac{Z_0}{Z_i}} \tag{3-110}$$

$$IIP3_v = \sqrt{2 \cdot Z_i \cdot 10^{\frac{IIP3_{dBm} - 30}{10}}} \tag{3-111}$$

$$V_{s\max} = \frac{2}{3} \cdot A_v \cdot \sqrt{\frac{G_{V1}}{3 \cdot G_{v3}}} \tag{3-112}$$

This model is considered as the block level LNA core.

In the following simulations, 85 GHz LNA with A_p = 22 dB, F = 5.5 dB, IP3 = 13 dBm, Zin=49.98Ω, Zout=50.09Ω is considered.

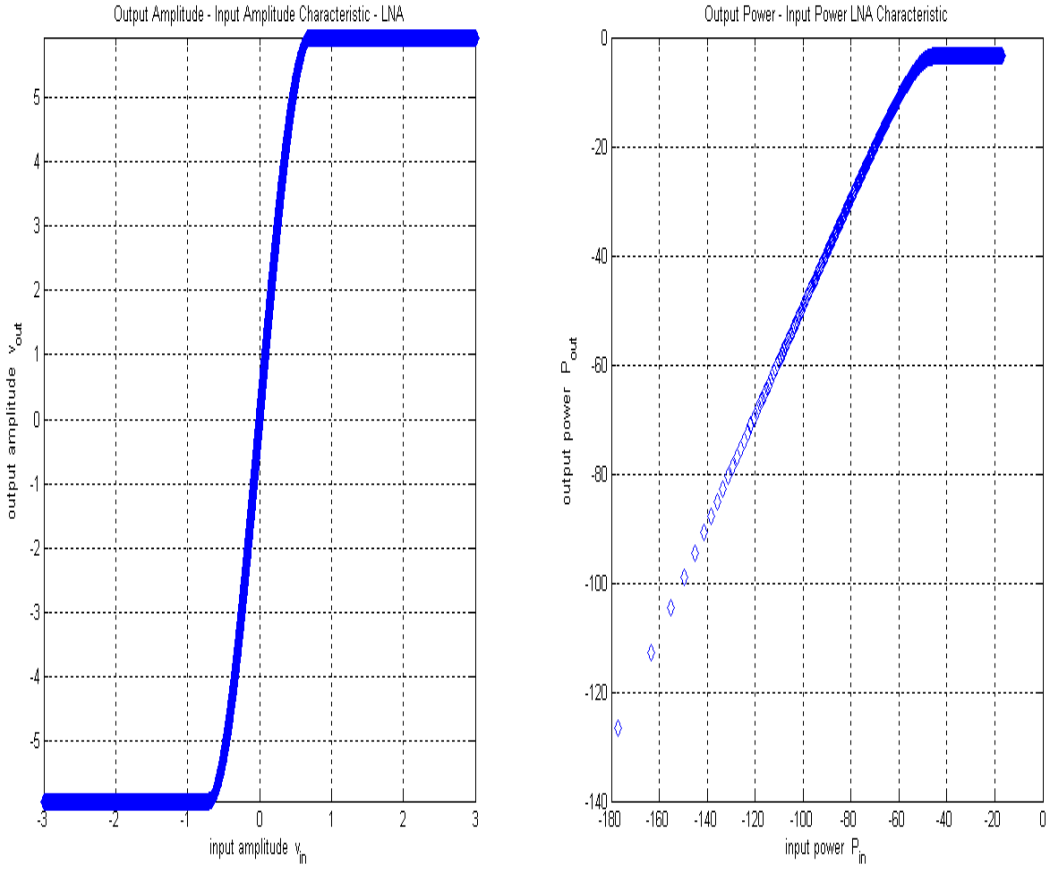

Figure 3-38: 85 GHz LNA Output Amplitude – Input Amplitude Characteristic and 85 GHz LNA Output Power – Input Power Characteristic considering an input signal of a 0.825 ns pulse

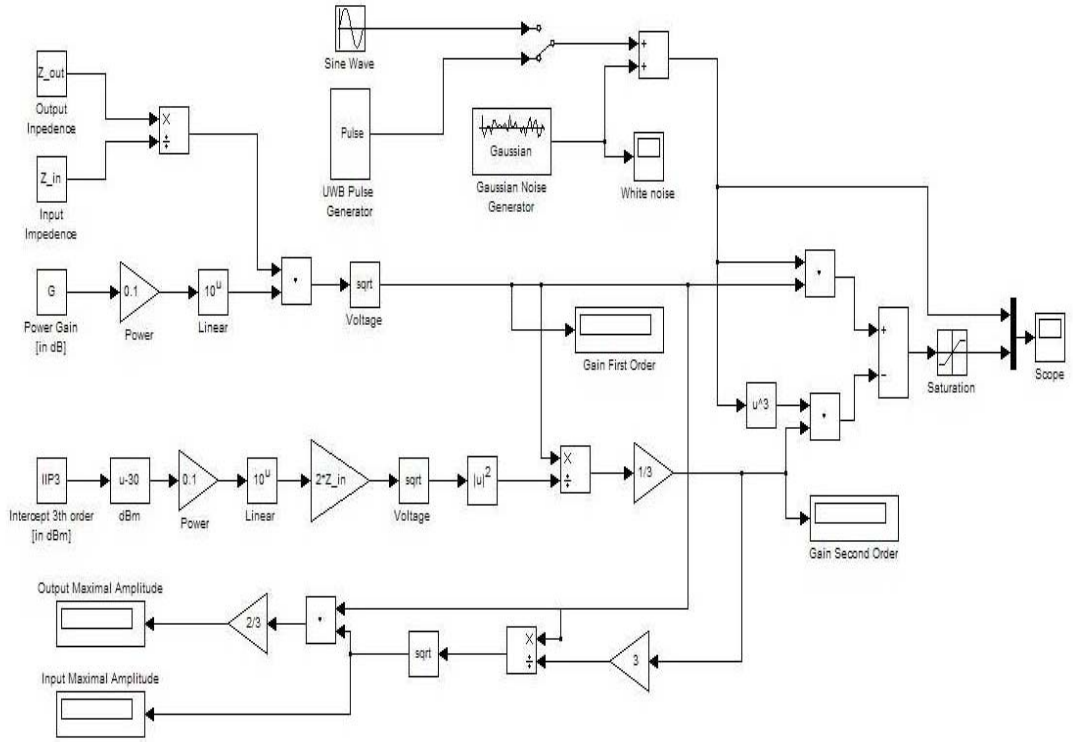

Figure 3-39: LNA Simulink Model

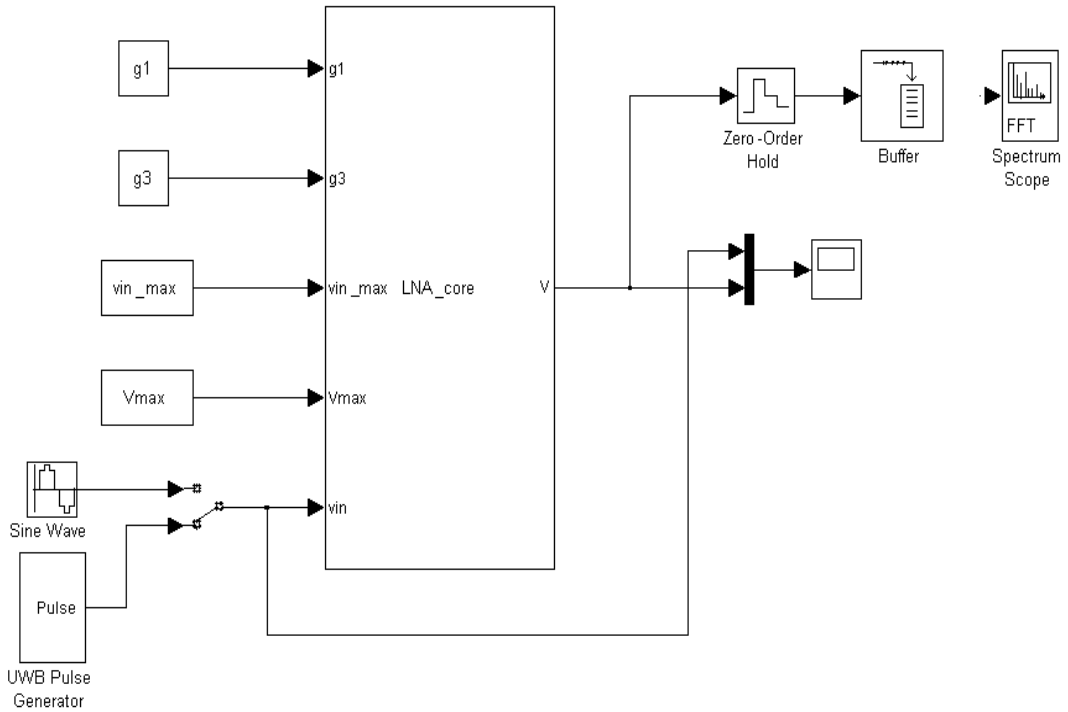

Figure 3-40: UWB Pulse Generator and LNA Simulink Subsystems

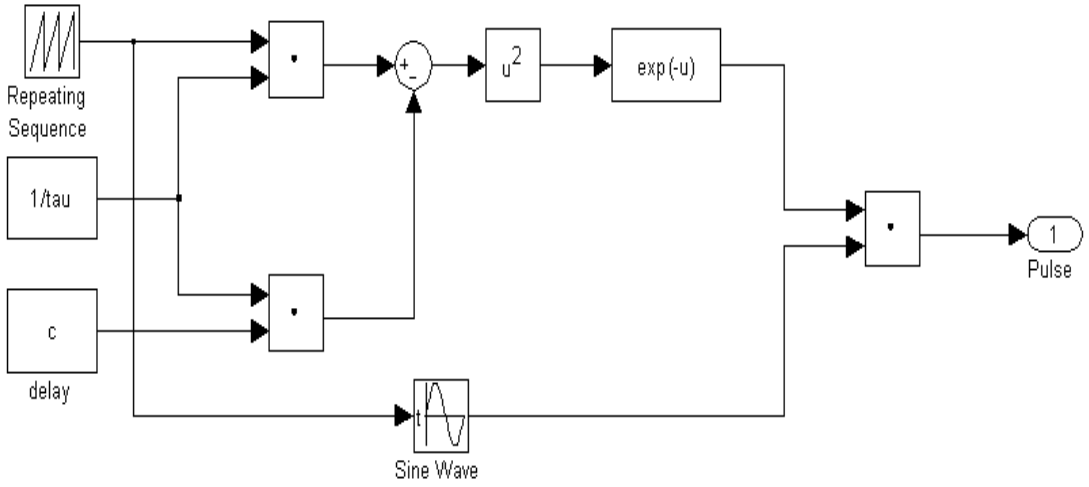

Figure 3-41: Pulse Generator Simulink Model

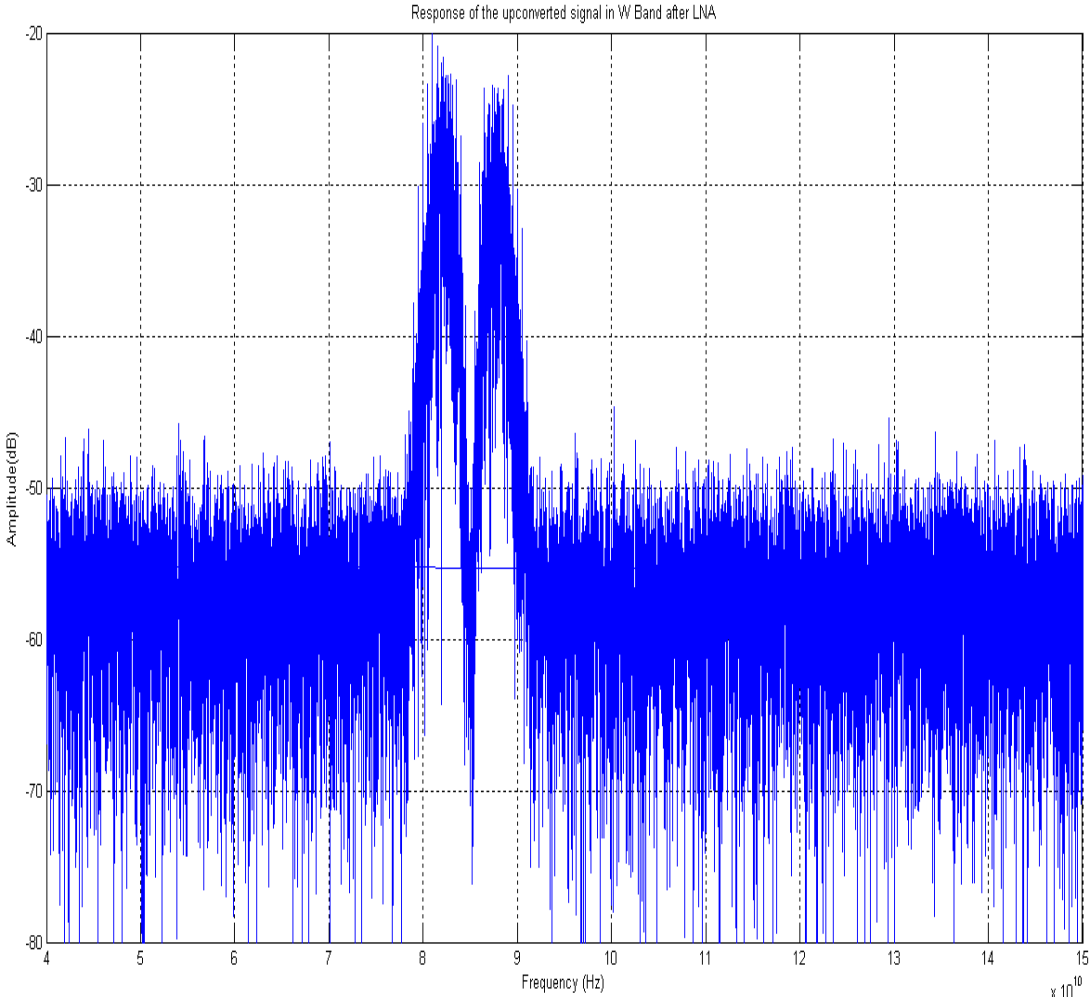

Figure 3-42: Up-Converted Signal at 85 GHz after LNA

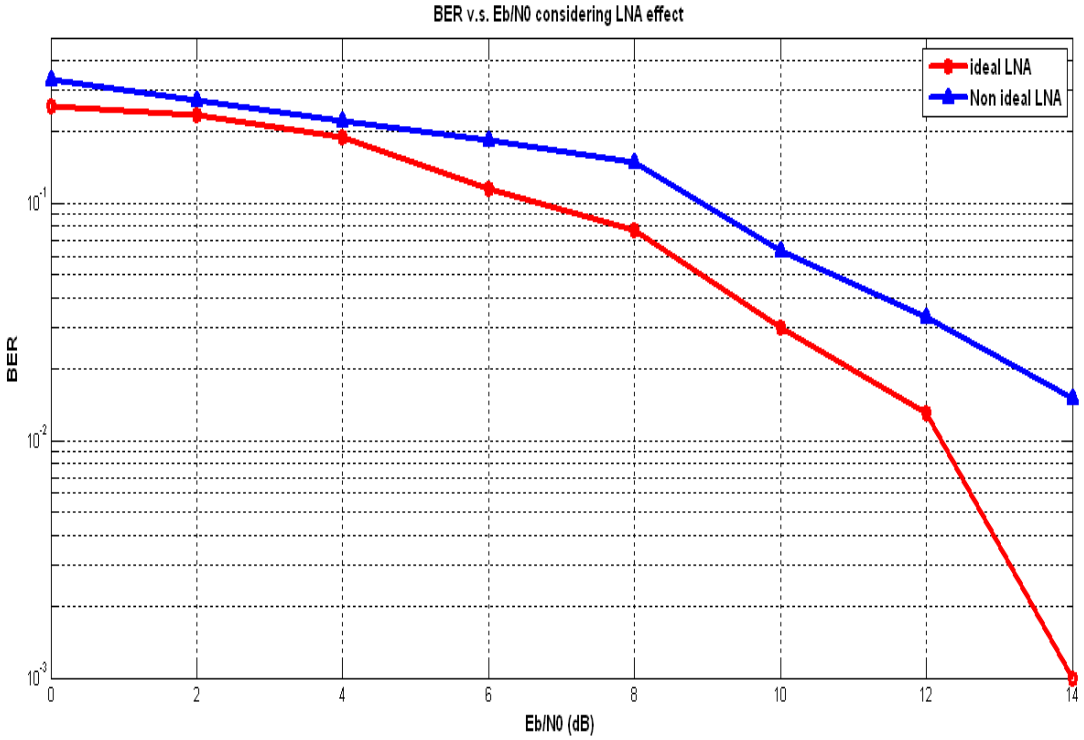

Figure 3-43: BER v.s. Eb/N0 considering ideal case and only LNA effect (Ns=3)

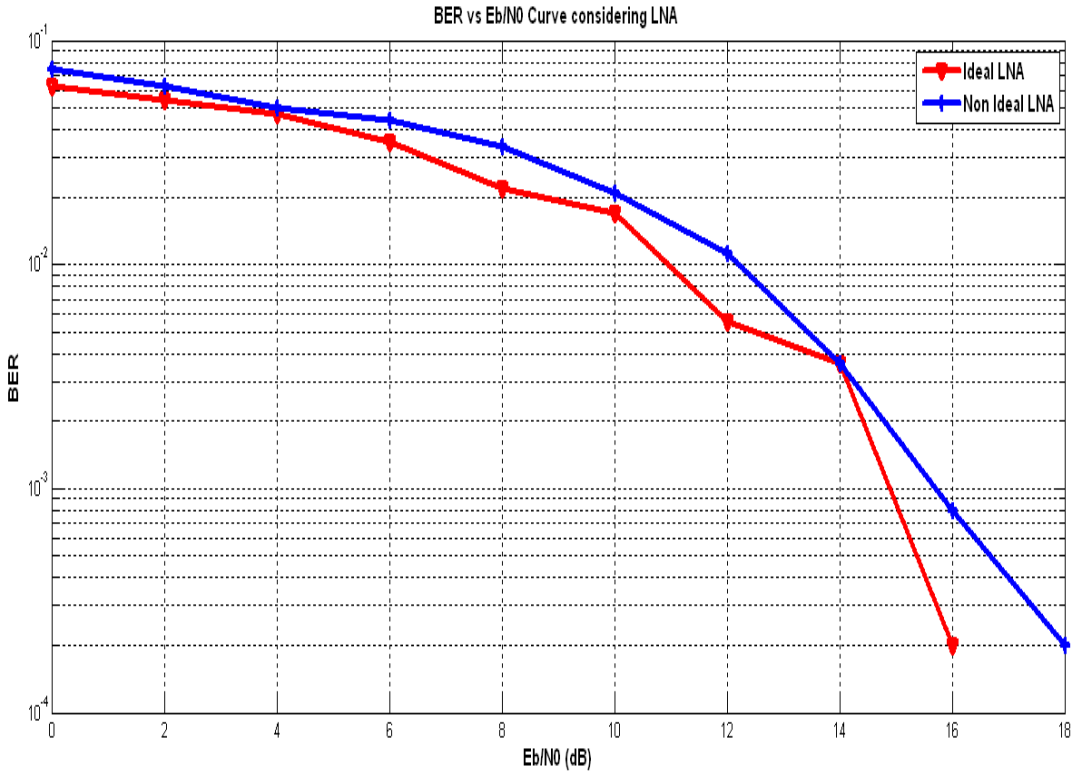

Figure 3-44: BER v.s Eb/N0 considering ideal case and only LNA effect (Ns=5)

3.3.9 HPA SUBSYSTEM

The effects of AM-to-AM (amplitude distortion, or AM-AM) and AM-to-PM (phase distortion, or AM-PM) conversions caused by HPA, such as SSPAs or TWTAs, are major concerns to communication systems engineers [3-30], [3-31]. These effects introduce inter-modulation (IM) components and spectral regrowth, which are undesirable to system designs. Moreover, the effects of AM-AM and AM-PM can also cause power loss and the signal distortion that can degrade the BER performance.

PA modeling has been a popular topic of research in the last few decades. Substantial efforts have been invested in the modeling of memoryless nonlinear PAs. A widely accepted SSPA model [3-32] encompassing amplitude clipping and phase distortion is the Rapp Model, where amplified signal and amplifier gain can be expressed as:

$$u(t) = s(t) \cdot G\left[\left|s(t)\right|\right] \tag{3-113}$$

$$G\left[\left|s(t)\right|\right] = \frac{\mathrm{A}\left[\left|s(t)\right|\right] \cdot e^{j\Phi\left[\left|s(t)\right|\right]}}{\left|s(t)\right|} \tag{3-114}$$

with the following related non linear transformations:

$$A\left[\left|s(t)\right|\right] = \frac{\mathrm{K}_1 \cdot \left|s(t)\right|}{\left[1 + \left(\frac{\mathrm{K}_1 \cdot \left|s(t)\right|}{\mathrm{A}_0}\right)^{2p}\right]^{\frac{1}{2p}}} \tag{3-115}$$

$$\Phi\left[\left|s(t)\right|\right] = \alpha_\varphi \cdot \left(\frac{\mathrm{K}_1 \cdot \left|s(t)\right|}{\mathrm{A}_0}\right)^4 \tag{3-116}$$

where A_0 is the saturating amplitude, K_1 is the small signal gain, *s(t)* is the complex envelope of the input signal, *p* is a parameter which controls the smoothness of the transition from the linear region to the saturation region, α_φ is typically set to zero, meaning SSPA adds no phase distortion.

Figure 3-45 represents the Input v.s. Output Curves for a common PA based on Rapp model in terms of parameter p.

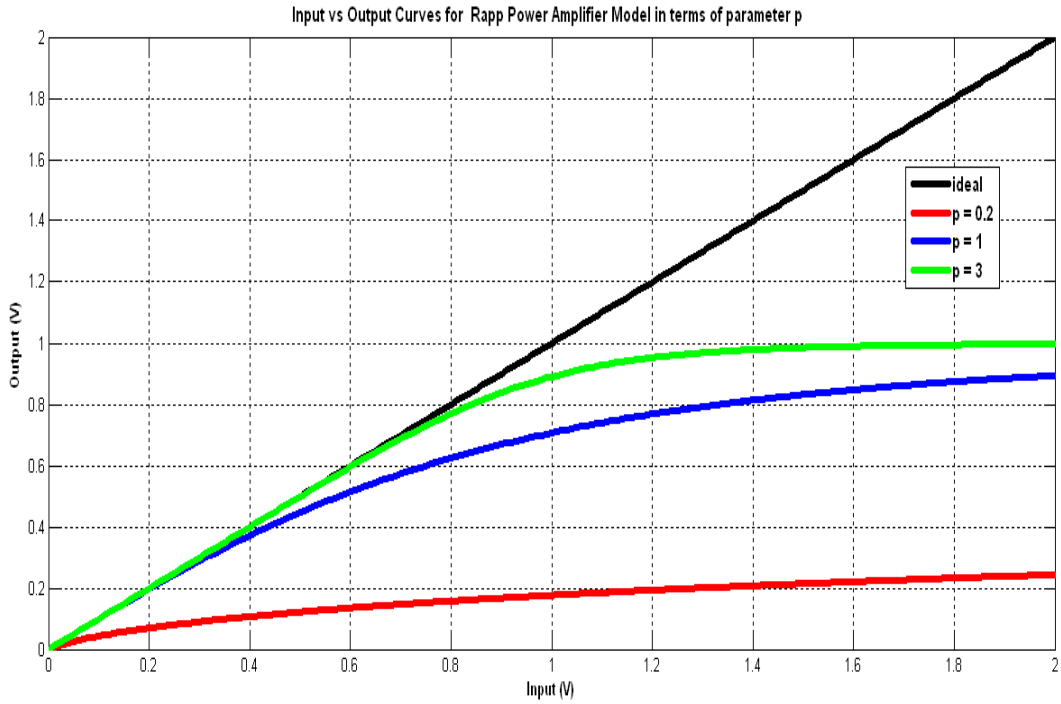

Figure 3-45: AM/AM Amplifier Characteristics (Rapp Model)

For our simulations, we considered a TWTA with the AM/AM and AM/PM characteristics modeled by using Saleh's memory-less model [3-33]. Saleh's model is based on a class of nonlinear functions of the following kind:

$$f(r) = \frac{\kappa r^{n}}{\left(1+\zeta r^{2}\right)^{\nu}} \tag{3-117}$$

where n and ν are assigned integer values, κ and ζ are generally derived from the experimental data obtained by Least-Square curve fitting method and r is the signal amplitude. The functions belonging to this class are general-purpose, meaning that they can be used both for AM/AM and AM/PM characteristics.

In order to consider the HPA effect on BER performance of our transceiver architecture, we used the extended Saleh's Model.

Let $\mathrm{Y}(t)$ be the input of the HPA. The complex baseband representation for the HPA input signal is: $\mathrm{Y}(t) = \rho_{y(t)} e^{j\vartheta_{y(t)}}$, where $\rho_{y(t)}$ and $\vartheta_{y(t)}$ are amplitude and phase of the complex signal, $\mathrm{Y}(t)$, respectively. $\left(\mathrm{M}\rho_{y(t)}\right)$ and $\left(\Phi\rho_{y(t)}\right)$ are the normalized AM-AM and AM-PM responses of the HPA due to input signal $\mathrm{Y}(t)$, respectively. We extended Saleh's Model

for HPA by including four extra parameters (a_0, a_1, b_0 and b_1), resulting in the following generalized equations for $\left(\mathrm{M}\rho_{y(t)}\right)$ and $\left(\Phi\rho_{y(t)}\right)$:

$$\mathrm{M}\left(\rho_{y(t)}\right)=\frac{\alpha_0\rho_y(t)}{a_0+\beta_0\left(\rho_{y(t)}+b_0\right)^2} \tag{3-118}$$

$$\Phi\left(\rho_{y(t)}\right)\equiv\frac{\alpha_1\rho_y^2(t)}{a_1+\beta_1\left(\rho_{y(t)}+b_1\right)^2} \tag{3-119}$$

In order to derive a more realistic nonlinear amplifier simulation, we started from some real AM/AM and AM/PM characteristics contained in confidential data sheets related to commercial TWTA devices working in W-band.

Therefore, we derived the values of a_0, a_1, b_0, b_1, α_0, α_1, β_0 and β_1 using the Nelder-Mead Method fitting the experimental data. The resulting AM/AM and AM/PM characteristics used for our simulations have been depicted in Figure 3-46.

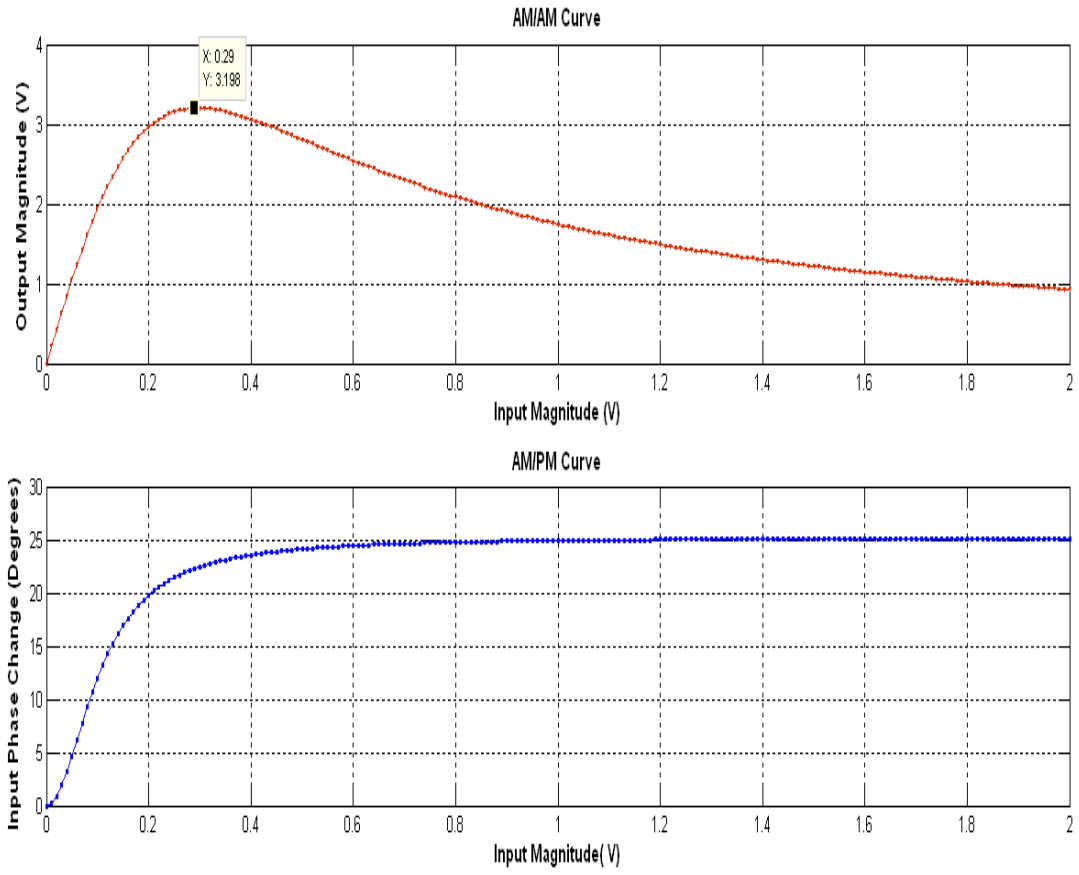

Figure 3-46: AM/AM and AM/PM Amplifier Characteristics (Extended Saleh Model)

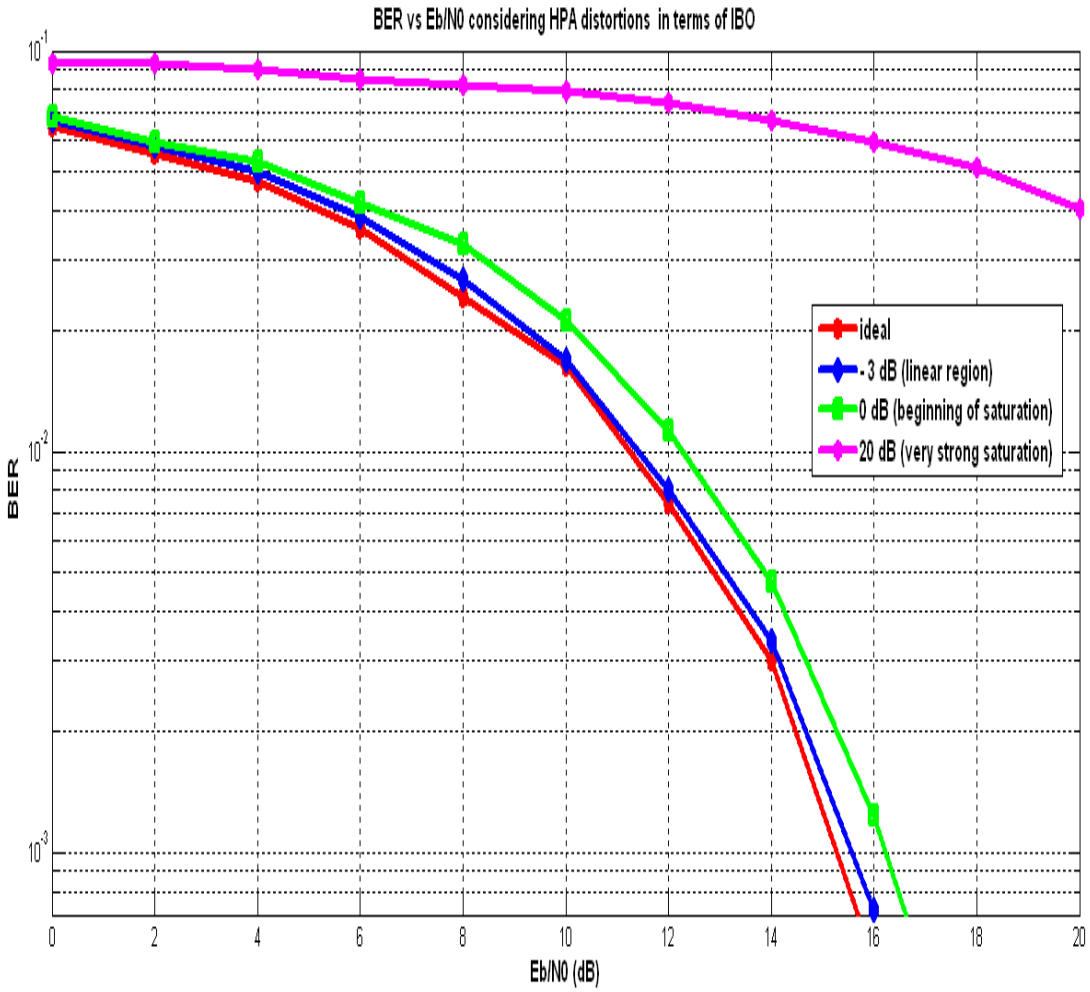

Figure 3-47: BER v.s. Eb/N0 considering HPA distortions in terms of IBO

The operation point of HPA is usually determined by the IBO (Input Back Off), defined as the ratio of the saturation input power, where the output power begins to saturate, to the average input power:

$$IBO_{[dB]} = 10 \cdot \log_{10}\left(\frac{P_{inSAT}}{P_{inAVG}}\right) \tag{3-120}$$

where P_{inSAT} is the input saturated power, and P_{inAVG} is the average input power. Figure 3-47 shows the HPA distortions effect on BER vs. Es/No performance considering P_{inSAT} = 30 dBm. It is evident as the IR-UWB architecture is robust to HPA distortions: an Eb/No of up to17 dB is needed to reach a BER of 10^{-3} considering real scenario, while an Eb/No of 15 dB in ideal case.

3.3.10 TIMING JITTER

Timing jitter results because of the presence of non-ideal sampling clocks in practical receivers. This distortion affects the correlation of signals at the receiver and thus the signal detection ability of the UWB system. The fact that impulse radio employs pulses with very narrow width (typically, less than one ns) makes the sensitivity to timing jitter more significant.

Timing jitters produce a noisy sequence at the receiver, which can be substantially large and result in a bad communication system unless measures are taken to mitigate this effect. The specific effect of timing jitter on an impulse radio system depends on the modulation scheme being used.

However, underlying effect is that timing jitter distorts the correlation property of the basis signal, thereby resulting in a term called "jitter noise". For instance, when the PPM modulation scheme is used, timing jitter distorts the correlation at the optimal modulation index. The modulation index has therefore a grea role in determining the BER performance of IR-UWB. Without loss of generality, consider the basic Gaussian pulse function with c = 0:

$$p(t) = -\frac{\mathrm{A}t}{\sigma^2} e^{-\frac{t^2}{2\sigma^2}} \tag{3-121}$$

If we use *p(t)* to represent '0' and *p(t+δ)* to represent '1' for binary data, the normalised correlation function of the basic pulse over a frame duration becomes:

$$R_1(\delta) = \frac{1}{\mathrm{E}_p} \int_{-\frac{T_f}{2}}^{+\frac{T_f}{2}} p(t)p(t-\delta)dt \approx \frac{1}{\mathrm{E}_p} \int_{-\infty}^{+\infty} p(t)p(t-\delta)dt = \frac{A^2\sqrt{\pi}}{\vartheta \mathrm{E}_p}\left(0.5 - \pi^2\alpha^2\right)e^{-\pi^2\alpha^2}$$

$$p(t) \approx 0 \text{ for } |t| \in \left(\frac{\mathrm{T}_f}{2}, \infty\right) \tag{3-122}$$

where $\delta = 2\pi\sigma\alpha$ has been substituted and E_p is the energy for pulse defined as:

$$\mathrm{E}_p = \int_{-\frac{T_f}{2}}^{\frac{T_f}{2}} |p(t)|^2 dt \tag{3-123}$$

Assuming AWGN and single-user environment, the problem of reducing the BER becomes one of finding δ that reduces the correlation in (3-122). The modulation index that yields the least possible correlation is called the *optimum modulation index,* δ_{opt} .

To obtain δ_{opt}, (3-122) is differentiated and set zero:

$$R_1^{'}(\delta)=\frac{dR_1(\delta)}{d\delta}\Big|\delta=2\pi\sigma\alpha=\frac{\mathrm{A}^2\sqrt{\pi}}{\sigma\mathrm{E}_p}\left(-2\pi^2\alpha\cdot e^{-\pi^2\alpha^2}\right)\cdot\left(\frac{3}{2}-\pi^2\alpha^2\right)=0 \tag{3-124}$$

Further simplification shows that for the solution is the first-order Gaussian monocycle:

$$\alpha_{opt}=\frac{\sqrt{6}}{2\pi}\Rightarrow\delta_{opt}=\sqrt{6}\sigma\approx 0.38985(2\pi\sigma) \tag{3-125}$$

The derivation above is for the first-order Gaussian monocycle. The same technique can be used on a higher order Gaussian monocycle by finding the modulation index that minimizes the normalised correlation of the *k-th order* Gaussian pulse, $p_k=\frac{d^k}{dt^k}p(t)$, given by:

$$\alpha_{opt}=\frac{\sqrt{6}}{2\pi}\Rightarrow\delta_{opt}=\sqrt{6}\sigma\approx 0.38985(2\pi\sigma) \tag{3-126}$$

$$R_k(\delta)=\frac{1}{\mathrm{E}_p}\int_{-\frac{T_f}{2}}^{+\frac{T_f}{2}}p_k(t)p_k(t-\delta)dt \tag{3-127}$$

A recursive formula can be used instead of (3-126) to obtain the correlation formula [32]:

$$R_k(\delta)=-R_{k-1}^{''}(\delta)=(-1)^{k-1}R_1^{(2k-2)}(\delta) \tag{3-128}$$

Solving these recursive equations for the second-, third-, and fourth-order Gaussian monocycles gives the result summarised in Table 3-4.

As seen from the table, the higher order Gaussian monocycles at their optimum modulation indexes achieve lower normalised correlation. In other words, the higher the Gaussian monocycle order, the lower the achievable BER.

However, this comes at the expense of higher time-sensitivity to receiver synchronization and clock sampling jitters. This jitter sensitivity is obvious from the higher level of steepness in the correlation functions for the higher-order Gaussian monocycles as shown in Figure 3-48.

Under the given optimal conditions, that is, when the modulation indexes are chosen to correspond to the point of minimum correlation values, the performance of the fourth-order Gaussian pulse obviously performs better than the lower orders. It is important to note that these results do not accommodate for the inevitable timing jitter that occurs at the receiver's clock sampling.

Pulse Order	α_{opt}	Normalized Correlation, $R_{\min}$
First	0.3899	-0.4463
Second	0.3051	-0.6183
Third	0.2599	-0.7086
Fourth	0.2304	-0.7644

Table 3-4: Optimum modulation indices $\delta_{opt} = 2 \cdot \pi \cdot \sigma \cdot \alpha_{opt}$ and corresponding normalised correlation for various orders of Gaussian monocycle

Using the data obtained from the design of the 0.825 ns pulse generator, it is derived an optimum delta PPM Modulation, for the considered pulse width ($\approx$0.8 ns), of 0.1624 ns, as shown in Figure 3-49. Figure 3-50 shows BER performance respect to modulation index. Using the optimum modulation index calculated for the second derivative of the pulse shown in Figure 3-50 yields a 2 dB improvement compared with typically used modulation index = 0.3051*Tp, where Tp is the width pulse [3-36].

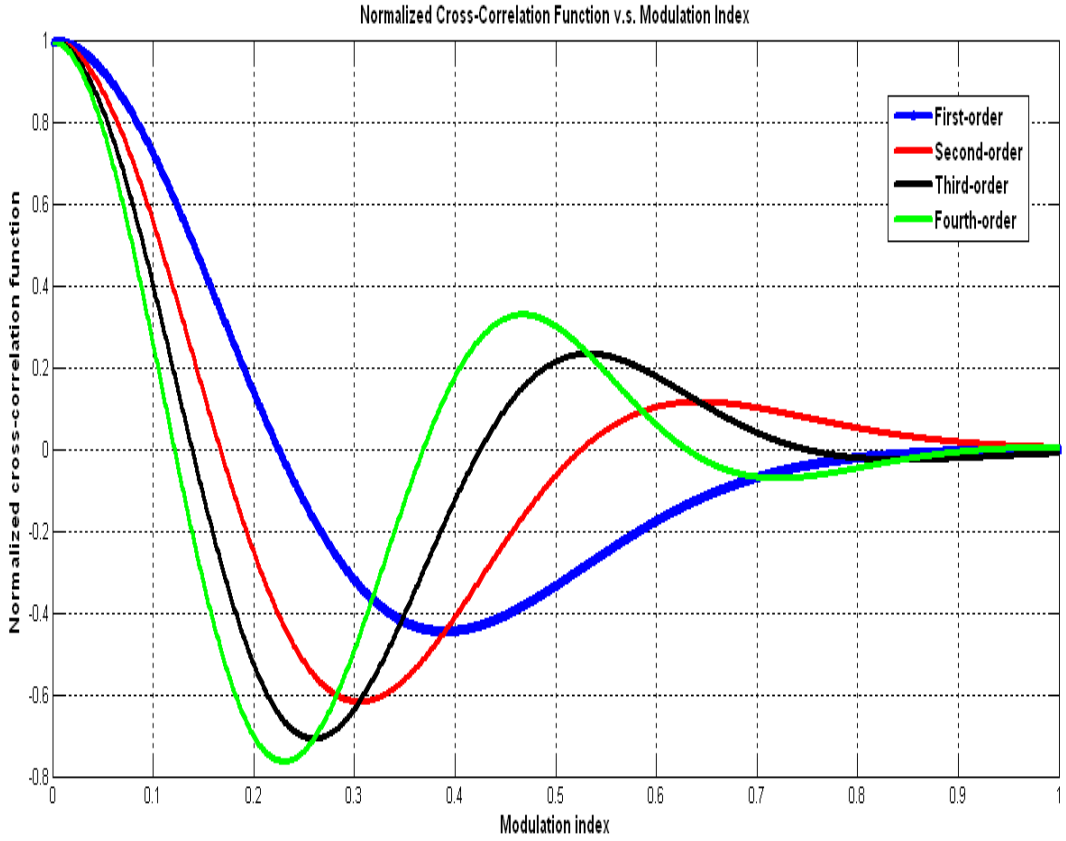

Figure 3-48: Correlation Dependency on modulation index, δ, for various orders of classical Gaussian monocycle

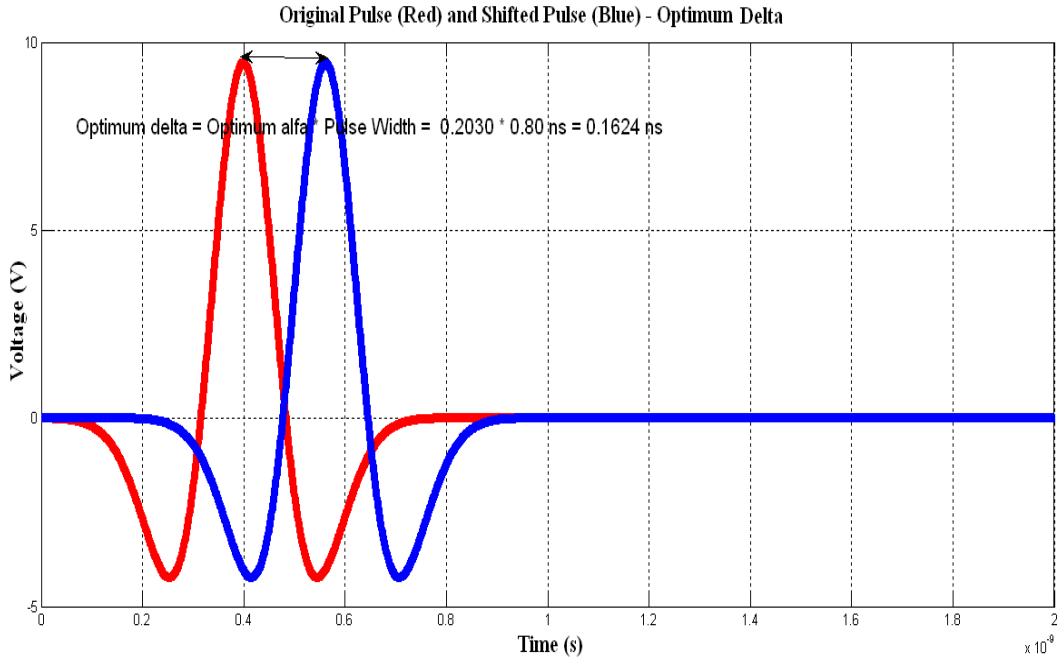

Figure 3-49: Correlation Dependency on modulation index, δ

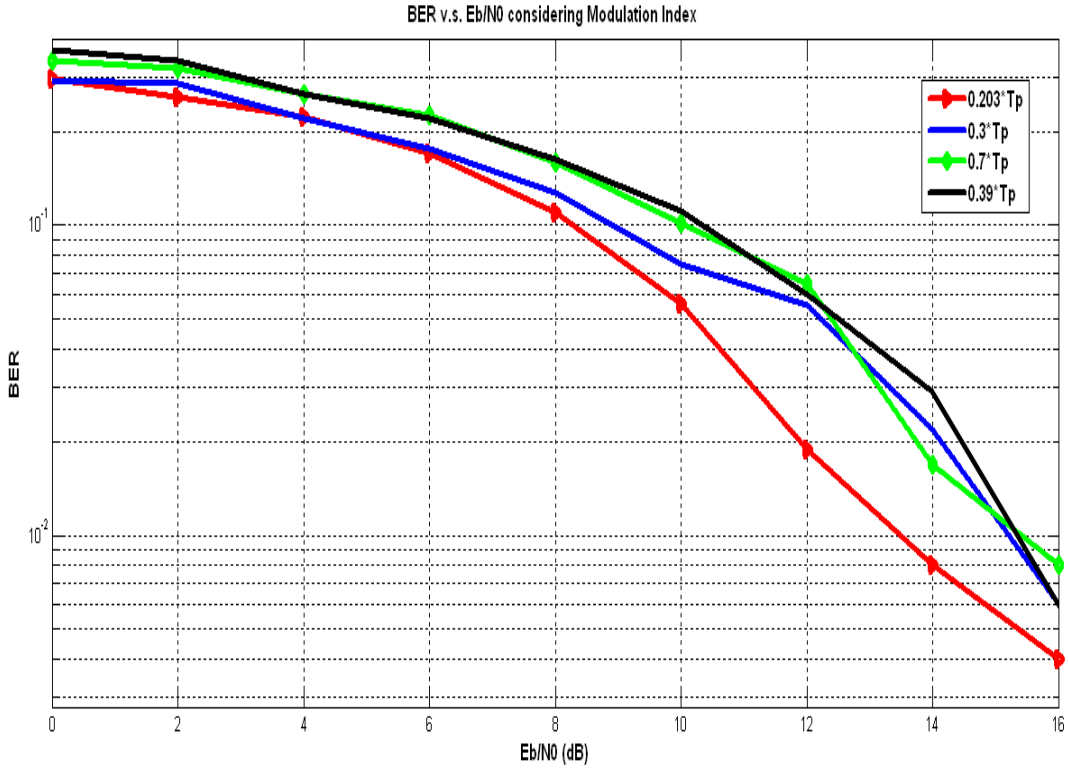

Figure 3-50: BER performance respect to modulation index, δ

The following part is devoted to investigate the timing jitter in IR-UWB and its influence on BER performance. For the sake of description, we consider the first-order Gaussian monocycle previously described.

$$p(t) = \frac{\mathrm{A}}{\sigma}\left(c - \frac{t}{\sigma}\right)e^{-0.5\left(\frac{t}{\sigma}-c\right)^2} \tag{3-129}$$

Suppose the sampling interval is Δ_s, then the received samples processed (ignoring the additive noise), is:

$$p\left(n\Delta_s + \varepsilon\right) = \frac{\mathrm{A}}{\sigma}\left(c - \frac{n\Delta_s + \varepsilon}{\sigma}\right)e^{-0.5\left(\frac{n\Delta_s+\varepsilon}{\sigma}-c\right)^2} \tag{3-130}$$

where ε is the white timing jitter and n is the sampling epoch.

This timing jitter is often modeled as wide sense stationary Gaussian process with zero mean and variance σ_j^2 [3-37]. As indicated in [3-36], [3-38] the RMS of timing jitter, σ_j^2, typically ranges from 10 to 150 ps in UWB receivers.

The effects of white jitter in our communication system are shown in Figure 3-51.

It is seen that for less amount of white jitter (variance in the order of delta/10 where delta is the optimum PPM shift) the effects are negligible, but when the white jitter variance becomes higher (in the order of delta/5) significant performance degradation is observed. These simulations have been performed for the second derivative of the pulse shown in Figure 3-51 with width of 0.825 ns, which means timing jitter RMS of $\delta_{opt}/5$ and $\delta_{opt}/10$ correspond to RMS of about 30 ps and 20 ps respectively. This shows that timing jitter RMS of 30 ps can result in a loss of up to 6 dB in SNR at a BER of 10^{-3}.

The following part investigates the colored timing jitter on BER performance of our transceiver architecture. In practical systems, the system clock is a frequency synthesizer implemented in the form of a hybrid of closed-loop VCO and PLL.

Such a clock exhibits colored instead of white timing jitter. In other words, its phase noise is not flat over all offset frequencies and successive jitter samples are correlated. The extent of the correlation is related to the PLL bandwidth, which would affect the BER performance. A VCO-PLL frequency synthesizer phase noise model is adopted to model the colored timing jitter:

$$S_\varepsilon(f) = \frac{\mathrm{K}}{f_L^2 + f^2} \tag{3-131}$$

where $S_\varepsilon(f)$ is the Power Spectral Density of the modeled phase jitter, $\varepsilon_{n,i}$ (in unit of radians), f_L is the 3dB bandwidth, and K is a constant related to the jitter RMS value, τ_{rms}.

The colored time jitter, $\varepsilon_{n,i}$, can be obtained by filtering Gaussian noise through a digital filter designed from the phase noise model (3-131).

Denote the sampling frequency of the digital filter by f_s. Using the Impulse Invariant Transformation, a time-domain model of colored jitter can be expressed as:

$$\varepsilon_{n,0} = (1-\rho)\omega_0 + \rho\varepsilon_{n-1,N_{f-1}} \tag{3-132}$$

and

$$\varepsilon_{n,i} = (1-\rho)\omega_i + \rho\varepsilon_{n,i-1} \tag{3-133}$$

For i =1, 2, $N_f - 1$, where $\rho = \exp\left(-2\cdot\pi\cdot\frac{f_L}{f_S}\right)$ and ω_i for i = 0,1, … $N_f - 1$ is a zero-mean Gaussian random variable with variance:

$$\sigma_\omega^2 = \frac{f_S}{\pi f_L}\tau_{RMS}^2 \tag{3-134}$$

In accordance with (3-132) and (3-134) the jitter variance is:

$$\sigma_\omega^2 = \frac{(1-\rho)f_S}{(1+\rho)\pi f_L}\tau_{RMS}^2 \tag{3-135}$$

Comparing Figure 3-51 and Figure 3-52 clearly shows that the performance degradation due to colored jitter is much more severe with respect to that of white jitter with the same variance (of the order of delta/5, where delta is the optimum PPM shift) e considering a 3 dB bandwidth of 1 GHz.

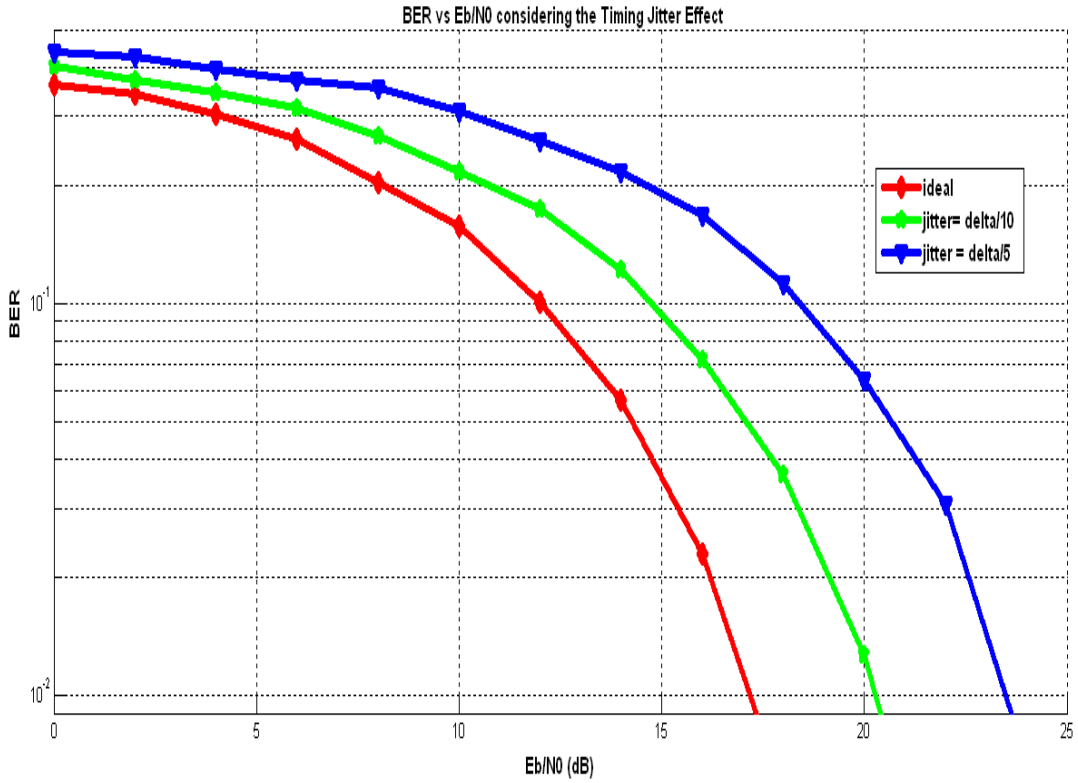

Figure 3-51: Effect of White Timing Jitter on BER performance

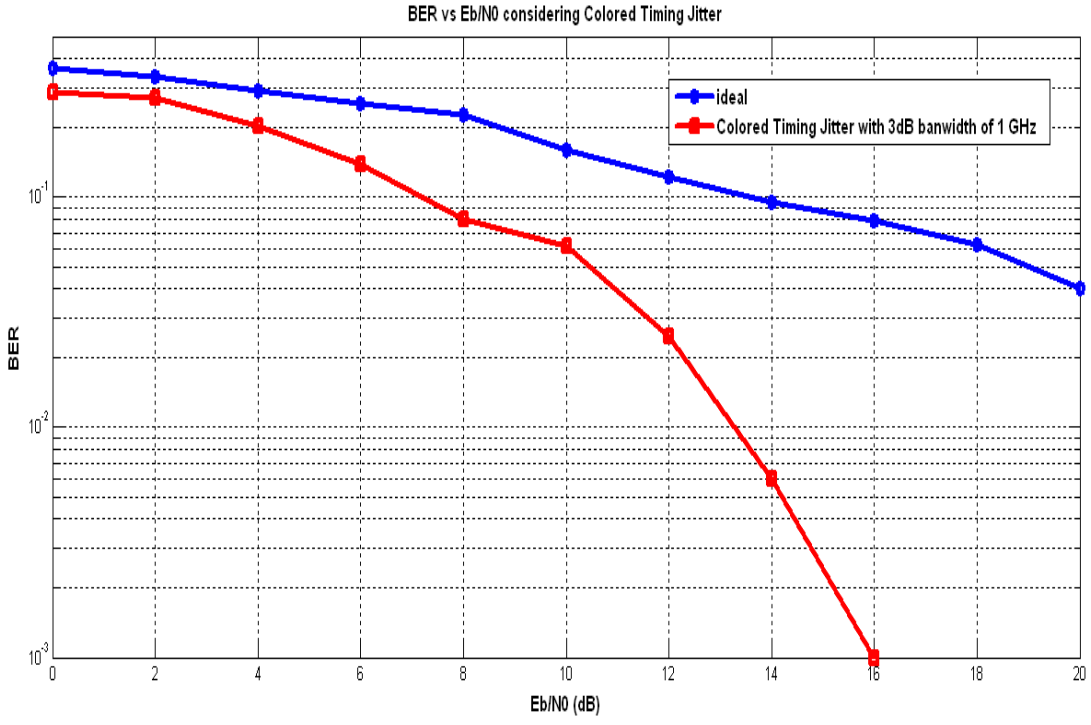

Figure 3-52: Effect of Colored Timing Jitter on BER performance

3.3.11 PERFORMANCE COMPARISON WITH W BAND BFSK TRANSCEIVER

In this paragraph we compare the BER performance respect to E_b / N_0 for an IR-UWB scheme and single 2-FSK architecture (with same data rate, i. e. 725 Mb/s) implemented in W band.

We choose for the IR-UWB scheme the following parameters, as shown below:

- Users = 7;
- Data Rate = 725 Mb/s;
- T_c (Chip Time)=0.06896 ns;
- N_s (Number of Pulses per bit)=2;
- N_p =3;
- δ (PPM shift)= 0.206*40 ps;
- T_p (Pulse width) = 40 ps.

The results of BER performance respect to E_b / N_0 are respectively reported in Figure 3-53 and Figure 3-54: Simulation results show that BER performance for IR-UWB architecture operating in W band are better than a 2-FSK scheme operating at same frequencies range considering Dirty RF effects, while they are worse considering the ideal case.

Parameters	PPM UWB
Users	7
T_c	68,96 ps
N_s	2
N_p	3
δ	0.206*40ps
T_p	40ps
IBO	-1 dB
P_{sat}	30 dBm

Table 3-5: PPM TH-IR UWB Interface Simulation

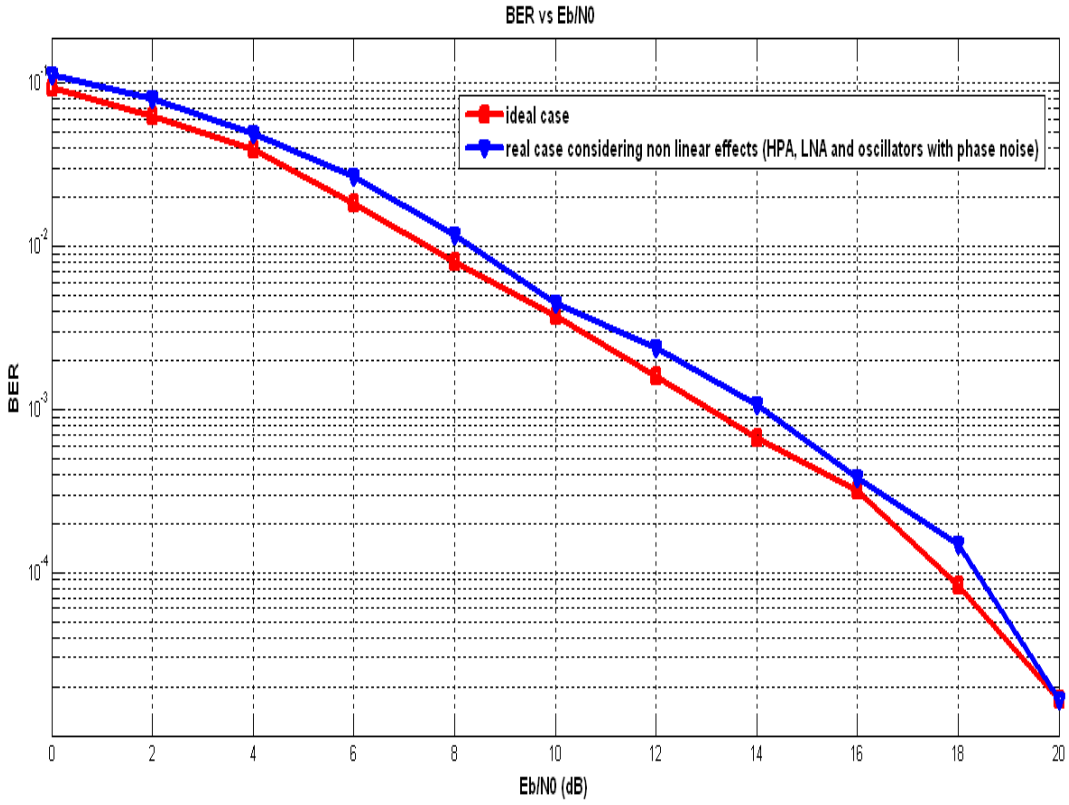

Figure 3-53: BER vs Eb/N0 for PPM TH-IR UWB Transceiver operating at 85 GHz

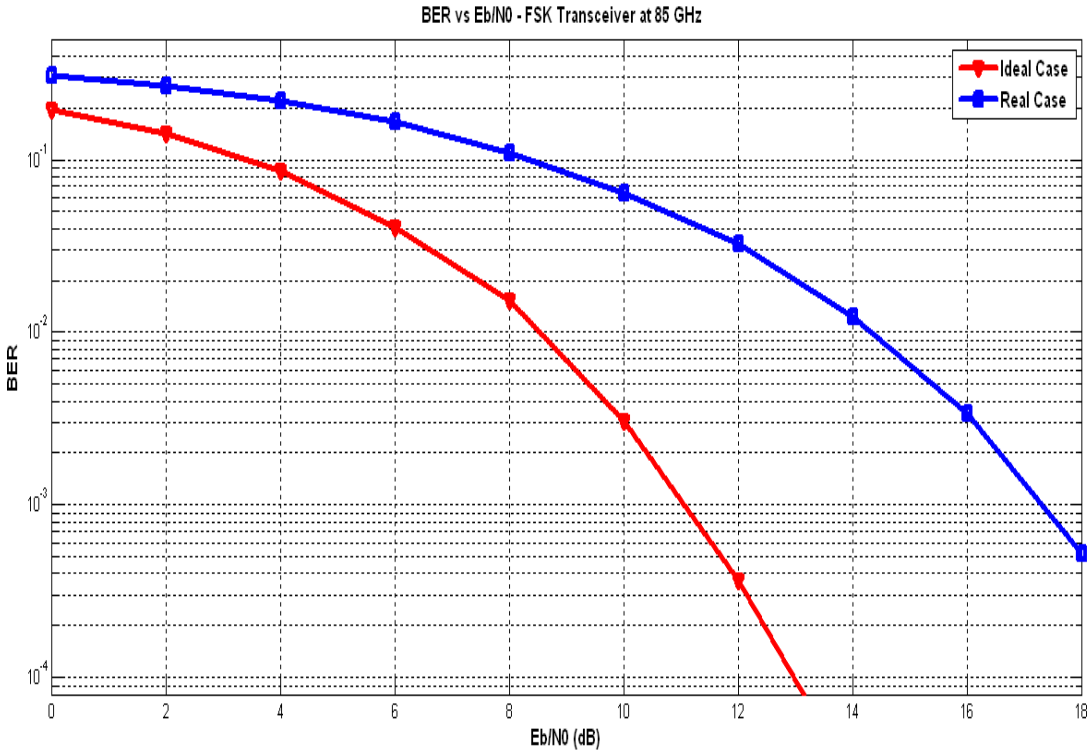

Figure 3-54: BER v.s. Eb/N0 for FSK Transceiver operating at 85 GHz

3.3.12 DESIGN ISSUES ON UWB ANTENNAS

Research and development in UWB-based systems has been increased and significant effort has been placed in facing open issues since the FCC, an independent US government agency charged with regulating interstate and international communications, released the spectrum with emission masks for UWB applications in 2002. So far different topics have been addressed: transmitter/receiver architectures, channel modeling and simulations, pulse source, etc.

However, in addition to issues related to UWB transceivers, a very important item to be considered is the antenna design. Basically, the main characteristics of UWB transmission technology, i.e. the high operating bandwidth, constraints strongly the feasibility of antennas suitable to be used with these systems since antenna parameters become frequency-dependent making analysis and design more complicated. Actually, typical parameters used to characterize antennas for traditional systems such as gain, polarization and impedance matching are not enough to evaluate performance in UWB systems [3-39].

Moreover, with respect to traditional systems, UWB antennas introduce significant distortions in waveforms, therefore such an item cannot be assumed negligible as for carrier-based systems. In particular, considering the antenna as a linear time-invariant system, the spectrum of the radiated pulse is obtained by multiplying the spectrum of the source pulse by the system function in frequency domain, which is frequency-dependent and source-independent. In case of UWB systems therefore, both the transmitting antenna and the source pulse with similar role contribute to shape the emitted pulse and hence the emission spectrum. The same happens at receiver-side adding further distortion and resulting in a final tailoring of radiated/received pulses [3-39], [3-40]. Specifically, in UWB systems transmitting/receiving antennas act as temporal differentiators/integrators or spectral/spatial filters [3-41]. This implies that design of pulse generator and transmitting/receiving antennas need to be carried out together and both have to be optimized for the overall system performance.

Moreover, antenna design is strongly affected by the application and the modulation scheme employed by the UWB system considered. Different issues need to be faced depending on the UWB type. Basically, two types can be identified: pulse-based systems in which pulses fill the UWB available bandwidth and carrier-based systems with OFDM technique. The latter one presents design requirements similar to broadband wireless systems adding a very

important increase in the required bandwidth. Further attention needs to be paid to pulse-based systems in which the antenna operates as a band-pass filter and tailors spectra of radiated/received pulses, as reported above. Hereafter is reported a comparison of design considerations for UWB antennas [3-39] for pulse-based and carrier-based systems. Table 3-6 reports the comparison of design considerations for UWB antennas for pulse-based and carrier-based systems.

Constituent	MB-OFDM	Pulse-based
Electrical	- Wide Impedance bandwidth covering all operating sub-bands - Steady radiation patterns - Constant Gain at directions of interest - Constant desired polarization - High radiation efficiency	- Wide Impedance bandwidth covering the bandwidth where majority of the source pulse energy falls - Constant gain at desired directions - Linear Phase response - Constant desired polarization - High radiation efficiency
Mechanical	- Small size/low profile/embeddable/easy-integrated for portable devices - Compact but robust especially for fixed devices - Low cost	- Small size/low profile/embeddable/easy-integrated for portable devices - Compact but robust especially for fixed devices Low cost

Table 3-6: Comparison of design considerations for UWB antennas [3-39] for pulse-based and carrier-based systems

Then, applications will drive antenna requirements, for example, in terms of size and volume, but also in terms of gain and beamwidths. Hence, characteristics will be different depending on UWB type such as telecommunication transceivers for portable devices, imaging systems, location systems and radar systems.

3.3.13 Design Issue on High Speed ADC for Multigigabit Communication Systems

One of the main problems of IR-UWB is that the over-sampling of such pulses requires extremely high-speed ADCs. For this reason, all existing UWB receivers for high data rate rely on analog correlators [3-42]. However, the time domain processing using analog correlators prevents the receiver from fully exploiting the advantages of digital communications and results in a low data rate. Therefore, several all-digital architectures

have been proposed in order to overcome the problem of the ADC. The digital UWB receiver in [3-43] proposes a parallel ADC structure to over-sample received signals within the time period of the interest. This approach requires a large number of ADCs and it suffers from a timing-jitter problem, since multiple clocks driving the ADCs are skewed by a fine increment of delay and distribution of such clocks is problematic. A sampling rate conversion technique using multi- channel ADCs was proposed in [3-43]. The approach requires low speed ADCs, but needs a large number of ADCs for high data rate. In [3-44] authors proposed a frequency domain approach to address the problem which involves parallel downconversions and filtering operations to channelize and then other upconversion operations in the digital domain (after the ADC) to recombine the signals. This solution has been shown to have several advantages over the previous ones [3-44]. Nevertheless, it seems the less appropriate for the application to EHF as it noticeably increase the cost and complexity of the system for the need of this mixing operation. Hybrid analog/digital or time domain ADC parallelization is more appropriate for EHF applications. About the downconversion at the receiver, most of the published UWB system solutions [3-45], [3-46] have adopted a direct-conversion radio architecture. The direct-conversion architecture utilizes two paths (I and Q) of Local Oscillator (LO), frequency synthesizer and mixer to down-convert the passband signal to baseband prior to the ADCs. However, as for the transmitter side also at the receiver side, the H/W elimination of mixers and local oscillators for mixing would imply a much lower complexity cost in the implementations.

In [3-47], [3-48] a subsampling approach for the downconversion is proposed. The idea is to sample the passband signal at frequency slightly higher than twice the signal bandwidth instead of the Nyquist frequency. As shown in Figure 3-55, the spectrum of the sampled signal will be the periodical repetition of the original spectrum. With the mentioned choice of the sampling frequency, those replicas of the spectrum will not overlap and some of them will also fall around zero. Therefore by using a low-pass filter with a bandwidth equal to the bandwidth of the signal, the transmitted signal is reported in baseband. This dramatically reduces the component counts compared to direct-conversion architecture. The remaining analog blocks prior to ADC are amplifiers and bandpass filters. The sampled data are processed by a digital matched filter in order to reach the matched filter bound for optimal detection. The proposed system avoids wideband analog processing by adding more processing to the digital backend, which results in a more efficient solution.

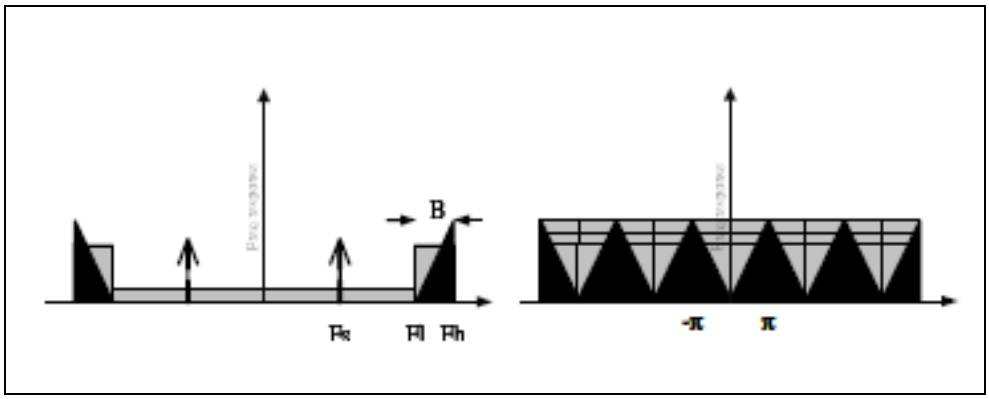

Figure 3-55: Signal and Noise Spectrum before and after subsampling

Nevertheless, this technique offers some challenges: firstly, all the thermal noise in the frequencies less than the lowest frequency content of the initial BPF folds back to the signal band; secondly, the design of a RF BPF is harder than in IF or in baseband; finally, it requires tighter sampling jitter.

In the following paragraphs, we analyse performance for an analog and *n* bit digital UWB receiver and compare them. These considerations are useful in order to identify the most suitable ADC configurations to realise multi-gigabit/s communications in W band.

3.3.13.1 Performance comparison for an analog and n bit digital UWB Receivers

A digital architecture means low cost, ease-of-design and it allows to exploit most of the associated advantages of CMOS technology scaling. Furthermore, a digital system guarantees considerable flexibility. A single receiver could support different modulation schemes, bit-rates, qualities of service and operating ranges, and change these parameters dynamically. The vision of fully-configurable software radios is an exciting one, and the UWB technology may be more amenable to such a realization than conventional, narrowband systems. Figure 3-56 shows a generic block diagram for a digital UWB receiver. A key component of such a system is represented by the ADC. In accordance with the Nyquist theorem, the ADC sampling rate for digitizing a UWB signal must be on the order of a few gigasamples/s. Even with the most modern process technologies, this constitutes a serious challenge. Most reported data converters operating at this speed employ interleaving [3-49] [3-50], with each channel typically based on a FLASH converter. The latter is the architecture of choice for high-speed designs, but is not suitable for high-resolution applications [3-51]. An *n* bit FLASH converter uses 2*n* comparators so its power and area scale exponentially with resolution. Among recently reported high-speed

ADCs (>1 Gigasample) representing the state of the art [3-50], [3-52], none has a resolution exceeding 8 bits. The minimum number of bits needed for reliable detection of a UWB signal is, therefore, a critical parameter. If excessively large, it can render an "all-digital" receiver infeasible.

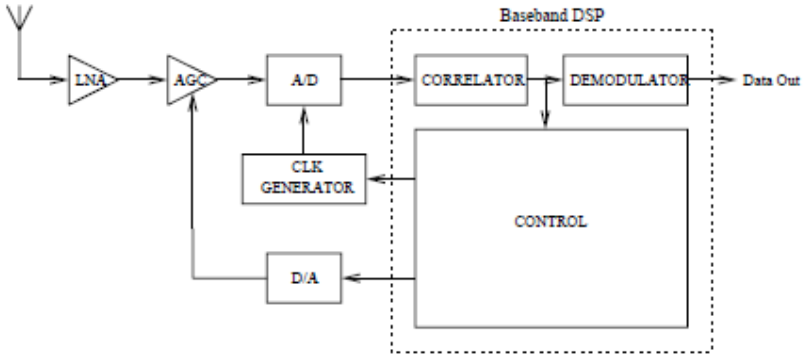

Figure 3-56: Basic Digital UWB Receiver

3.3.13.2 Basic Architecture of Analog IR-UWB Receiver

UWB systems generally employ the following modulation schemes:

- BPSK. Here a binary one is denoted by a normal pulse where as a binary zero is denoted by an inverted pulse.
- OOK. Here a binary one is denoted by a normal pulse where as a binary zero is denoted by the absence of a pulse.
- PPM. Here a binary one is denoted by a normal pulse,where as a binary zero is denoted by the time shifted version of the same pulse. The amount of time shift is often critical and depends on the shape of the pulse [3-38].

Suppose there is a bit-stream b_j (with values zero or one) for $j \in (-\infty,+\infty)$. For BPSK and OOK the modulated pulse can be given as [3-59]:

$$s^k(t) = \sum_j b_{\frac{j}{N_s}} w\left(t - jT_f - c_j^k T_c\right) \tag{3-136}$$

and for PPM it is given by:

$$s^k(t) = \sum_j w\left(t - jT_f - c_j^k T_c - \delta d_{\frac{j}{N_s}}^k\right) \tag{3-137}$$

In (3-136) and (3-137), $w(t)$ is the pulse used, which can be expressed as:

$$w(t) = A\left(1 - 4\pi\left(\frac{t}{\tau}\right)^2\right)e^{-2\pi\left(\frac{t}{\tau}\right)^2} \tag{3-138}$$

For BPSK modulation scheme, b_j in (3-136) can be represented as +1 and -1, while for OOK b_j can be +1 and 0. At receiver side, the input signal is multiplied with:

$$s_{temp}^{k}(t) = \sum_j \Delta\left(t - jT_f - c_j^k T_c\right) \text{ for BSPK and OOK} \tag{3-139}$$

$$s_{temp}^{k}(t) = \sum_j \left(\Delta\left(t - jT_f - c_j^k T_c\right) - \Delta\left(t - jT_f - c_j^k T_c - \delta\right)\right) \text{ for PPM} \tag{3-140}$$

(where, $\Delta(t)$ is 1 for $t = 0$, and 0 for all other values of t) and the product is summed over an entire chip. Figure 3-49 shows as there is substantial overlapping between the two pulses. So when the pulse representing binary zero reaches its top, the pulse representing binary 1 reaches its bottom (and viceversa).

Let us assume that, the top of pulse is A volts (where $A > 0$) and bottom of the pulse is B volts (where $B < 0$) and $A > |B|$.

If no noise is present and a binary zero is transmitted, at the receiver side we have $A(1) + B(-1) = A - B$ (V), and assuming a binary one that is transmitted we have $B(1) + A(-1) = B - A$ (V).

Since $A > 0$ and $B < 0$, both $A - B$ and $|B - A|$ are greater than A.

Depending on this sum, it is decided whether the received bit is a binary one or a binary zero. For example, in PPM case, if the sum is greater than or equal to zero, the incoming bit is taken as one, else the bit is taken as zero. After N_s number of bits are decoded in this way, a final decision is made in favour of the majority. It can be shown that in the presence of a AWGN channel with zero mean and variance σ^2, the probability of error for detection of a single chip can be given by:

$$p_e = Q\left(\sqrt{SNR}\right) \tag{3-141}$$

where SNR is given by $SNR = \frac{A^2}{\sigma^2}$ (a) for BPSK, $SNR = \frac{A^2}{4\sigma^2}$ (b) for OOK, and $SNR = \frac{(A-B)^2}{2\sigma^2}$ (c) for PPM.

Comparing (a), (b) and (c), clearly BPSK is a superior modulation scheme than OOK, and if $|B| > 0.414A$, then PPM outperforms BPSK. In this paragraph, only BPSK and PPM will be considered. The probability of error of detection of a bit is given by:

$$P_e = \sum_{k=1}^{\frac{N_s+1}{2}} {}^{N_s}C_{\frac{N_s+2k-1}{2}} p_e^{\frac{N_s+2k-1}{2}} (1-p_e)^{\frac{N_s-2k+1}{2}} \tag{3-142}$$

Figure 3-57 compares the probability of error calculated from (3-139), (c) and (3-140) for a PPM IR-UWB communication system and BER curve (in blue) for the same system.

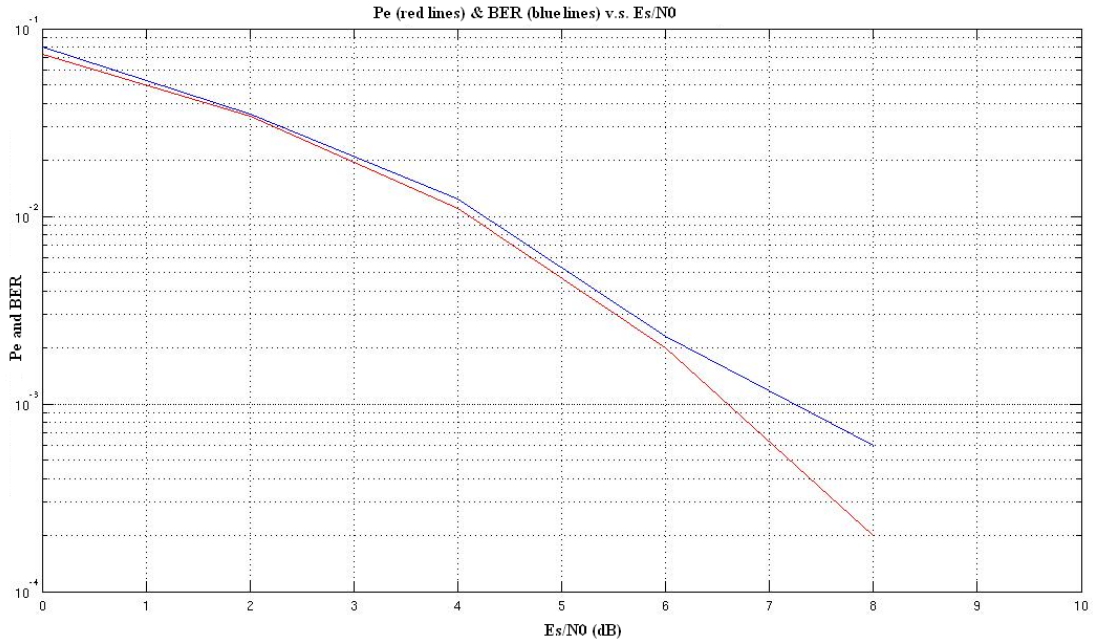

Figure 3-57: Comparison between Pe and BER curves for a IR-UWB communication system using PPM modulation

3.3.13.3 Basic Architecture of a 1-bit Digital UWB Receiver

A basic digital UWB receiver for PPM is shown in Figure 3-58. The optional analog processing contains the LNA, and if necessary mixer and local oscillators for the frequency downconverter section. This signal (with or without analog processing) is sampled by the 1 bit receiver. Ignoring attenuation and if initially we assume that the channel is noiseless, the sampled signal must lie between *B* (V) and *A* (V), where *A* and *B* have been introduced above.

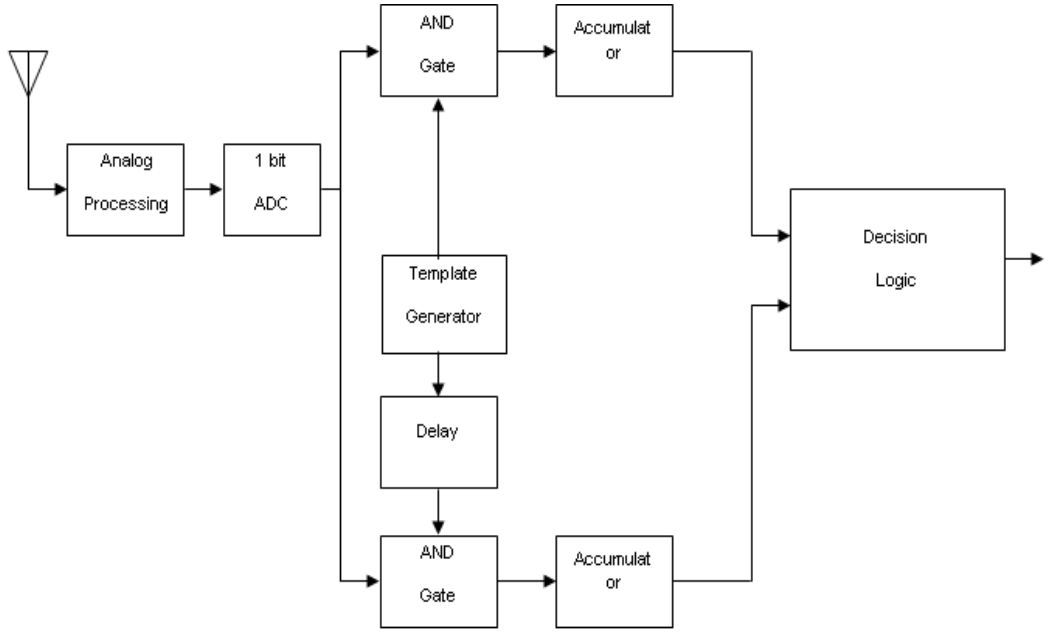

Figure 3-58: 1 bit Digital UWB Receiver for PPM Scheme

The response of the ADC is given as:

$$y(t) = 1 \text{ for } x(t) > 0.5(A + B) \tag{3-143}$$

$$y(t) = 0 \text{ for } x(t) \leq 0.5(A + B) \tag{3-144}$$

The template generator generates pulses with $s_{temp}^{k}(t) = \sum_{j} \Delta\left(t - jT_f - c_j^k T_c\right)$ and the delay circuit delays the same by an amount equal to δ. The upper and lower AND gates are used to multiply the ADC output with the non-delayed signal (in order to search binary zero) and delayed one (in order to search binary one) respectively. Then, the outputs of the AND gates are added in an accumulator, which is resetted after each chip. The decision circuit compares the outputs of two accumulators and decides for a binary zero and binary one according to the following table:

Output of the Upper Accumulator	Output of the lower Accumulator	Decision
0	1	0
1	0	1

Table 3-7: Truth table for decision in a 1-bit digital UWB system assuming noiseless channel

Now, we assume that a AWGN channel with mean 0 and variance σ^2 is present. Eight different possibilities can be identified, as shown in Table 3-8:

Serial Number	Transmitted Data	Output of the upper accumulator	Output of the lower accumulator	Decision
1	0	0	0	?
2	0	0	1	1
3	0	1	0	0
4	0	1	1	?
5	1	0	0	?
6	1	0	1	1
7	1	1	0	0
8	1	1	1	?

Table 3-8: Truth Table for decision in a 1-bit digital UWB system considering AWGN channel

Observing Table 3-8, we can see that in cases 3 and 6 correct decision is taken, in cases 2 and 7 wrong choice is made, and in the remaining cases the receiver fails to make any reliable decision.

Let us compute the probability of each case.

Case 1. The transmitted data is 0, the probability of which is 0.5. In this case, the ADC receives a random variable with mean A and variance σ^2 in the first sampling instant, and another random variable with a mean B and variance σ^2 in the second sampling interval. To have a zero in the first sample the instantaneous value of it should be less than or equal to $(A + B)/2$, its probability is:

$$p_{11} = \frac{1}{\sqrt{(2\pi\sigma^2)}} \int_{-\infty}^{\frac{(A+B)}{2}} e^{\frac{-(x-A)^2}{2\sigma^2}} dx \tag{3-145}$$

taking $(x - A)/\sigma$ as y we get:

$$p_{11} = \frac{1}{\sqrt{(2\pi)}} \int_{-\infty}^{\frac{(B-A)}{(2\sigma)}} e^{\frac{-(y)^2}{2}} dy \tag{3-146}$$

which can be expressed as:

$$p_{11} = \left(\frac{1}{2}\right)\left(1 + erf\left(\frac{(B-A)}{(2\sqrt{2}\sigma)}\right)\right) \tag{3-147}$$

To have a zero in the second sample it should also be less than or equal to $(A + B)/2$, its probability is:

$$p_{12} = \frac{1}{\sqrt{(2\pi\sigma^2)}} \int_{-\infty}^{\frac{(A+B)}{2}} e^{\frac{-(x-B)^2}{2\sigma^2}} dx \tag{3-148}$$

taking $(x - B)/\sigma$ as y we get:

$$p_{12} = \frac{1}{\sqrt{(2\pi)}} \int_{-\infty}^{\frac{(A-B)}{(2\sigma)}} e^{\frac{-(y)^2}{2}} dy \tag{3-149}$$

which can be expressed as:

$$p_{12} = \left(\frac{1}{2}\right)\left(1 + erf\left(\frac{(A-B)}{(2\sqrt{2}\sigma)}\right)\right) \tag{3-150}$$

Therefore, the overall probability of case 1 is:

$$p_1 = \left(\frac{1}{2}\right)p_{11}p_{12} = \left(\frac{1}{8}\right)\left(1 + erf\left(\frac{(B-A)}{(2\sqrt{2}\sigma)}\right)\right)\left(1 + erf\left(\frac{(A-B)}{(2\sqrt{2}\sigma)}\right)\right) \tag{3-151}$$

Case 2. The transmitted data is 0, its probability is 0.5. In this case, the ADC receives a random variable with mean A and variance σ^2 in the first sampling instant, and another random variable with a mean B and variance σ^2 in the second sampling interval. To have a zero in the first sample the instantaneous value of it should be less than or equal to $(A + B)/2$, its probability can be calculated from (3-147), and to have a 1 from the second sample the instantaneous value should be greater than $(A + B)/2$:

$$p_{22} = \frac{1}{\sqrt{(2\pi\sigma^2)}} \int_{\frac{(A+B)}{2}}^{\infty} e^{\frac{-(x-B)^2}{2\sigma^2}} dx \tag{3-152}$$

taking $(x - B)/\sigma$ as y we get:

$$p_{22} = \frac{1}{\sqrt{(2\pi)}} \int_{\frac{(A-B)}{(2\sigma)}}^{\infty} e^{\frac{-(y)^2}{2}} dy \tag{3-153}$$

which can be expressed as:

$$p_{22} = \left(\frac{1}{2}\right)\left(1 - erf\left(\frac{(A-B)}{(2\sqrt{2}\sigma)}\right)\right) \tag{3-154}$$

Hence, the overall probability may be given by:

$$p_2 = \left(\frac{1}{8}\right)\left(1+erf\left(\frac{(B-A)}{(2\sqrt{2}\sigma)}\right)\right)\left(1-erf\left(\frac{(A-B)}{(2\sqrt{2}\sigma)}\right)\right) \tag{3-155}$$

Case 3. The transmitted data is 0, its probability is 0.5. In this case, the ADC receives a random variable with mean A and variance σ^2 in the first sampling instant, and another random variable with a mean B and variance σ^2 in the second sampling interval.

To have a one in the first sample the instantaneous value of it should be greater than $(A + B)/2$:

$$p_{31} = \frac{1}{\sqrt{(2\pi\sigma^2)}} \int_{\frac{(A+B)}{2}}^{\infty} e^{\frac{-(x-A)^2}{2\sigma^2}}\, dx \tag{3-156}$$

taking $(x - A)/\sigma$ as y we get:

$$p_{31} = \frac{1}{\sqrt{(2\pi)}} \int_{\frac{(B-A)}{(2\sigma)}}^{\infty} e^{\frac{-(y)^2}{2}}\, dy \tag{3-157}$$

To have a zero in the second sample the instantaneous value of it should be less than or equal to $(A + B)/2$, its probability can be calculated from (3-150). Hence, the overall probability may be given by:

$$p_3 = \left(\frac{1}{8}\right)\left(1-erf\left(\frac{(B-A)}{(2\sqrt{2}\sigma)}\right)\right)\left(1+erf\left(\frac{(A-B)}{(2\sqrt{2}\sigma)}\right)\right) \tag{3-158}$$

Case 4. The transmitted data is 0, its probability is 0.5. In this case, the ADC receives a random variable with mean A and variance σ^2 in the first sampling instant, and another random variable with a mean B and variance σ^2 in the second sampling interval.

The overall probability is:

$$p_4 = \left(\frac{1}{8}\right)\left(1-erf\left(\frac{(B-A)}{(2\sqrt{2}\sigma)}\right)\right)\left(1-erf\left(\frac{(A-B)}{(2\sqrt{2}\sigma)}\right)\right) \tag{3-159}$$

Case 5. The transmitted data is 1, its probability is 0.5. In this case, the ADC receives a random variable with mean B and variance σ^2 in the first sampling instant, and another random variable with a mean A and variance σ^2 in the second sampling interval.

To have a zero in the first sample, its instantaneous value should be less than or equal to ($A + B$)/2, so the probability is:

$$p_{51} = \frac{1}{\sqrt{(2\pi\sigma^2)}} \int_{-\infty}^{\frac{(A+B)}{2}} e^{\frac{-(x-B)^2}{2\sigma^2}} dx \tag{3-160}$$

taking (x - B)/ σ as y we get:

$$p_{51} = \frac{1}{\sqrt{(2\pi)}} \int_{-\infty}^{\frac{(A-B)}{(2\sigma)}} e^{\frac{-(y)^2}{2}} dy \tag{3-161}$$

which can be expressed as:

$$p_{51} = \left(\frac{1}{2}\right)\left(1 + erf\left(\frac{(A-B)}{(2\sqrt{2}\sigma)}\right)\right) \tag{3-162}$$

To have a zero in the second sample it should also be less than or equal to ($A + B$)/2, probability of which is

$$p_{52} = \frac{1}{\sqrt{(2\pi\sigma^2)}} \int_{-\infty}^{\frac{(A+B)}{2}} e^{\frac{-(x-A)^2}{2\sigma^2}} dx \tag{3-163}$$

taking (x - B)/ σ as y we get:

$$p_{52} = \frac{1}{\sqrt{(2\pi)}} \int_{-\infty}^{\frac{(B-A)}{(2\sigma)}} e^{\frac{-(y)^2}{2}} dy \tag{3-164}$$

which can be expressed as:

$$p_{52} = \left(\frac{1}{2}\right)\left(1 + erf\left(\frac{(B-A)}{(2\sqrt{2}\sigma)}\right)\right) \tag{3-165}$$

Hence, the overall probability of case 5 is:

$$p_5 = \left(\frac{1}{2}\right)p_{51}p_{52} = \left(\frac{1}{8}\right)\left(1 + erf\left(\frac{(A-B)}{(2\sqrt{2}\sigma)}\right)\right)\left(1 + erf\left(\frac{(B-A)}{(2\sqrt{2}\sigma)}\right)\right) \tag{3-166}$$

Case 6. The transmitted data is 1, its probability is 0.5. In this case, the ADC receives a random variable with mean B and variance σ^2 in the first sampling instant, and another random variable with a mean A and variance σ^2 in the second sampling interval. To have a zero in the first sample, its instantaneous value should be less than or equal to ($A + B$)/2, so

the probability is given by (3-162). On the other hand, to have a one in the second sample it should be greater than $(A + B)/2$, so its probability is:

$$p_{62} = \frac{1}{\sqrt{(2\pi\sigma^2)}} \int_{\frac{(A+B)}{2}}^{\infty} e^{\frac{-(x-A)^2}{2\sigma^2}} dx \tag{3-167}$$

taking $(x - A)/\sigma$ as y we get:

$$p_{62} = \frac{1}{\sqrt{(2\pi)}} \int_{\frac{(B-A)}{(2\sigma)}}^{\infty} e^{\frac{-(y)^2}{2}} dy \tag{3-168}$$

which can be expressed as:

$$p_{62} = \left(\frac{1}{2}\right)\left(1 - erf\left(\frac{(A-B)}{(2\sqrt{2}\sigma)}\right)\right) \tag{3-169}$$

So the overall probability is:

$$p_6 = \left(\frac{1}{8}\right)\left(1 + erf\left(\frac{(A-B)}{(2\sqrt{2}\sigma)}\right)\right)\left(1 - erf\left(\frac{(B-A)}{(2\sqrt{2}\sigma)}\right)\right) \tag{3-170}$$

Case 7. The transmitted data is 1, its probability is 0.5. In this case, the ADC receives a random variable with mean B and variance σ^2 in the first sampling instant, and another random variable with a mean A and variance σ^2 in the second sampling interval.

To have a one in the first sample its instantaneous value should be greater $(A + B)/2$, its probability:

$$p_{71} = \frac{1}{\sqrt{(2\pi\sigma^2)}} \int_{\frac{(A+B)}{2}}^{\infty} e^{\frac{-(x-B)^2}{2\sigma^2}} dx \tag{3-171}$$

taking $(x - B)/\sigma$ as y we get:

$$p_{71} = \frac{1}{\sqrt{(2\pi)}} \int_{\frac{(A-B)}{(2\sigma)}}^{\infty} e^{\frac{-(y)^2}{2}} dy \tag{3-172}$$

which is given as:

$$p_{71} = \left(\frac{1}{2}\right)\left(1 - erf\left(\frac{(A-B)}{(2\sqrt{2}\sigma)}\right)\right) \tag{3-173}$$

On the other hand, to have a zero in the second sample, it should be less than or equal to ($A + B$)/2, so its probability is given by (3-165). The overall probability is:

$$p_7 = \left(\frac{1}{8}\right)\left(1 - erf\left(\frac{(A-B)}{(2\sqrt{2}\sigma)}\right)\right)\left(1 + erf\left(\frac{(B-A)}{(2\sqrt{2}\sigma)}\right)\right) \tag{3-174}$$

Case 8. The transmitted data is 1, its probability is 0.5. In this case, the ADC receives a random variable with mean B and variance σ^2 in the first sampling instant, and another random variable with a mean A and variance σ^2 in the second sampling interval.

To have a one in the first sample, its instantaneous value should be greater ($A + B$)/2, so its probability is given by (3-173). On the other hand, the probability of getting a one in the second sample is given by equation (3-169). Therefore, the overall probability is:

$$p_8 = \left(\frac{1}{8}\right)\left(1 - erf\left(\frac{(A-B)}{(2\sqrt{2}\sigma)}\right)\right)\left(1 - erf\left(\frac{(B-A)}{(2\sqrt{2}\sigma)}\right)\right) \tag{3-175}$$

It can be verified that:

$$p_1 + p_2 + p_3 + p_4 + p_5 + p_6 + p_7 + p_8 = 1 \tag{3-176}$$

The probability of error is equal to:

$$p_{error} = p_2 + p_7 = \left(\frac{1}{4}\right)\left(1 - erf\left(\frac{(A-B)}{(2\sqrt{2}\sigma)}\right)\right)\left(1 + erf\left(\frac{(B-A)}{(2\sqrt{2}\sigma)}\right)\right) \tag{3-177}$$

The probability of indecision is:

$$p_{indecision} = p_1 + p_4 + p_5 + p_8 = \left(\frac{1}{2}\right)\left(1 + erf\left(\frac{(A-B)}{(2\sqrt{2}\sigma)}\right)erf\left(\frac{(B-A)}{(2\sqrt{2}\sigma)}\right)\right) \tag{3-178}$$

There are some methods of tackling indecision. If indecision occurs the receiver can:

- Flip a fair coin and decide whether it is a zero or one. In this case, the probability of error increases to:

$$p_{errornew} = p_{errorold} + 0.5\mathrm{p}_{indecision} = \left(\frac{1}{4}\right)\left(2 - erf\left(\frac{(A-B)}{(2\sqrt{2}\sigma)}\right) + erf\left(\frac{(B-A)}{(2\sqrt{2}\sigma)}\right)\right) \tag{3-179}$$

- Request a retransmission of the data (ARQ).

Therefore, the probability of error calculated from (3-177) or (3-179) must be put into (3-142) to get the final probability of error.

The error probability calculated by (3-179) and (3-142) have been plotted (in red) and compared with the simulated results using MATLAB (in blue). The comparison is shown in Figure 3-59.

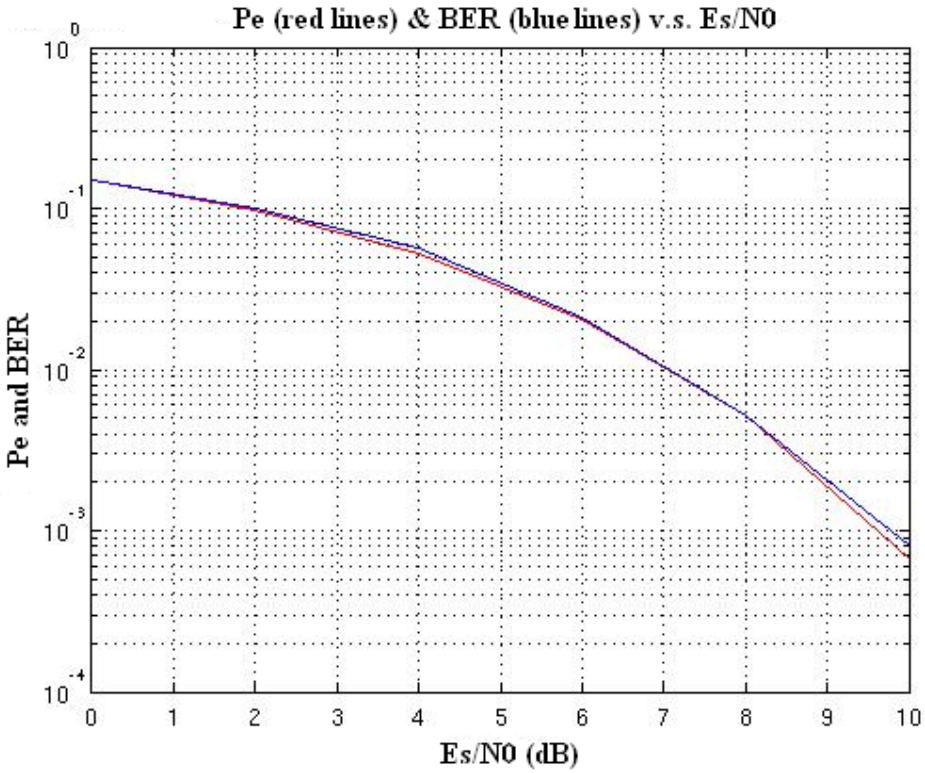

Figure 3-59: Comparison between BER and Pe for a 1 bit digital UWB receiver (Ns = 5)

3.3.13.4 Basic Architecture of an N-bit Digital UWB Receiver

The analysis done above can be generalized for a *N*-bit receiver. A *N*-bit receiver is essentially same as that of 1 bit receiver only the 1 bit ADC is now replaced by a *N*-bit ADC, and all other 1 bit digital components have been replaced by the *N*-bit types. In Figure 3-60 basic architecture of a *N*-bit receiver is described.

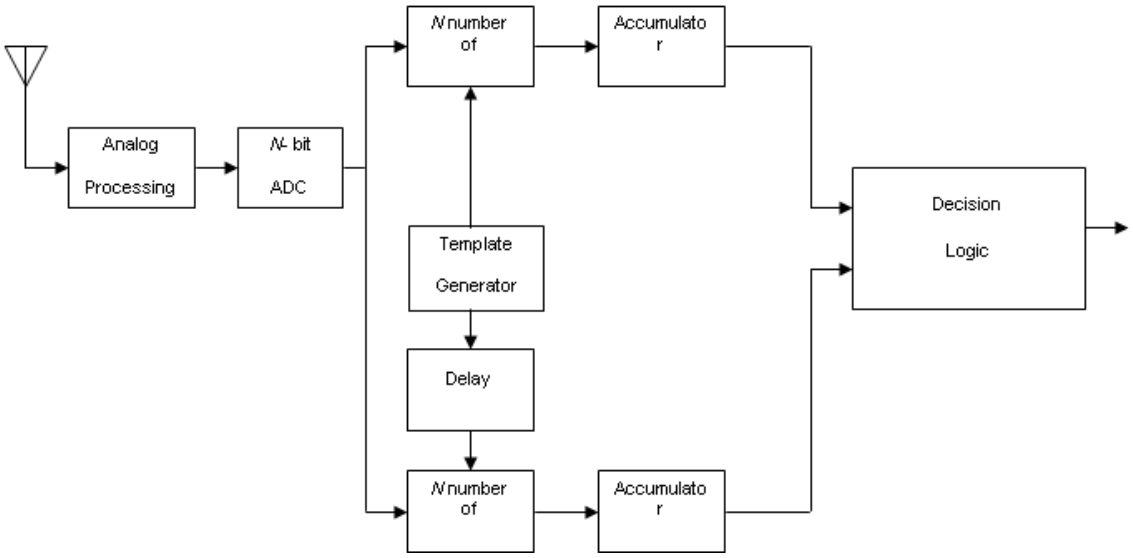

Figure 3-60: Block diagram of a N-bit UWB Receiver

The system function for a *N*-bit ADC is given by:

$$y(t) = 0 \text{ for } x(t) \leq B + (A - B)/2^N \tag{3-180}$$

$$y(t) = 1 \text{ for } B + (A - B)/2^N < x(t) \leq B + 2(A - B)/2^N \tag{3-181}$$

$$y(t) = n \text{ for } B + n(A - B)/2^N < x(t) \leq B + \{(n+1)(A - B)\}/2^N \tag{3-182}$$

$$y(t) = 2^N - 1 \text{ for } B + \{(2^N-1)(A - B)\}/2^N < x(t) \tag{3-183}$$

It can be easily verified that for $N = 1$ (3-180), (3-181), (3-182) and (3-183) reduce to (3-143) and (3-144) for 1 bit ADC.

The template generator produces pulses with: $s_{temp}^{k}(t) = \sum_{j} \Delta\left(t - jT_f - c_j^k T_c\right)$ and the delay circuit delays the same by an amount equal to δ.

The upper and lower *N*-bit AND gates are used to multiply the ADC output with the non-delayed (in order to search binary zero) signal and delayed one (in order to search binary one) respectively.

The outputs of the AND gates are added in an accumulator, which is resetted after each chip.

Assuming that the signal is propagated through an AWGN channel with mean zero and variance σ^2, the decision circuit compares the outputs of two accumulators and decides for a binary zero and binary one according to the following table:

Serial Number	Transmitted Data	Output of the upper accumulator	Output of the lower accumulator	Decision
1	0	Greater than the output of the lower accumulator	Less than the output of the upper accumulator	0
2	0	Equal to the output of the lower accumulator	Equal to the output of the upper accumulator	?
3	0	Less than the output of the lower accumulator	Greater than the output of the upper accumulator	1
4	1	Greater than the output of the lower accumulator	Less than the output of the upper accumulator	0
5	1	Equal to the output of the lower accumulator	Equal to the output of the upper accumulator	?
6	1	Less than the output of the lower accumulator	Greater than the output of the upper accumulator	1

Table 3-9: Truth table for decision in a N-bit digital UWB system in AWGN channel

Again we can see how correct decision is made in cases 1 and 6, wrong decision in cases 3 and 4, and the decision logic fails to arrive in a decision in the case of 2 and 5. Just like the previous section, we start to calculate the probability of each case.

Case 1. The transmitted data is 0, its probability is 0.5. In this case, the ADC receives a random variable with mean A and variance σ^2 in the first sampling instant, and another random variable with a mean B and variance σ^2 in the second sampling interval. If the output of the first accumulator is n_1 (then, clearly $0 < n_1 \leq 2^N - 1$), and the output of the second accumulator is n_2 where $0 \leq n_2 < n_1$, the probability that the output of the first accumulator is n_1 (where $n_1 < 2^N - 1$) is given by:

$$\left(p_{11}\right)_{(n_i)} = \frac{1}{\sqrt{\left(2\pi\sigma^2\right)}} \int_{B+\frac{n_1(A-B)}{2^N}}^{B+\frac{(n_1+1)(A-B)}{2^N}} e^{\frac{-(x-A)^2}{2\sigma^2}} dx \qquad (3\text{-}184)$$

Taking $(x - A)/\sigma = y$ we get:

$$(p_{11})_{(n_i)} = \frac{1}{\sqrt{(2\pi)}} \int_{\frac{(B-A)}{\sigma}(1-\frac{n_1}{2^N})}^{\frac{(B-A)}{\sigma}(1-\frac{n_1+1}{2^N})} e^{\frac{-y^2}{2}} dy \tag{3-185}$$

which can be expressed as:

$$(p_{11})_{(n_i)} = \left(\frac{1}{2}\right)\left(erf\left(\frac{(B-A)}{(\sqrt{2}\sigma)}\times\left(1-\frac{(n_1+1)}{2^N}\right)\right)-erf\left(\frac{(B-A)}{(\sqrt{2}\sigma)}\times\left(1-\frac{n_1}{2^N}\right)\right)\right) \tag{3-186}$$

This formula is valid for all n_1 which are less than $2^N - 1$, if $n_1 = 2^N - 1$, then (3-184) can be modified as:

$$(p_{11})_{(2^N-1)} = \frac{1}{\sqrt{(2\pi\sigma^2)}} \int_{B+\frac{(2^N-1)(A-B)}{2^N}}^{\infty} e^{\frac{-(x-A)^2}{2\sigma^2}} dx \tag{3-187}$$

again taking $(x - A)/\sigma = y$ we get:

$$(p_{11})_{(2^N-1)} = \frac{1}{\sqrt{(2\pi)}} \int_{\frac{(B-A)}{2^N\sigma}}^{\infty} e^{\frac{-y^2}{2}} dy \tag{3-188}$$

which can be expressed as:

$$(p_{11})_{(2^N-1)} = \left(\frac{1}{2}\right)\left(1-erf\left(\frac{(B-A)}{(2^N\sqrt{2}\sigma)}\right)\right) \tag{3-189}$$

The probability that the output of the second accumulator to be less than n_1 is given by:

$$(p_{12})_{(n_1)} = \frac{1}{\sqrt{(2\pi\sigma^2)}} \int_{-\infty}^{B+\frac{(n_1(A-B))}{2^N}} e^{\left(\frac{-(x-B)}{(2\sigma^2)}\right)} dx \tag{3-190}$$

Taking $(x - B)/\sigma = y$ we get:

$$(p_{12})_{(n_i)} = \frac{1}{\sqrt{(2\pi)}} \int_{-\infty}^{\frac{(n_1(A-B))}{2^N}} e^{\left(\frac{-y^2}{2}\right)} dy \tag{3-191}$$

which can be expressed as:

$$(p_{12})_{(n_i)} = \left(\frac{1}{2}\right)\left(1+erf\frac{(n_1(A-B))}{(2^N\sqrt{2}\sigma)}\right) \tag{3-192}$$

and when $n_1 = 2^N$ -1, (3-192) becomes:

$$(p_{12})_{(2^N-1)} = \left(\frac{1}{2}\right)\left(1 + erf\frac{\left((2^N-1)(A-B)\right)}{\left(2^N\sqrt{2}\sigma\right)}\right) \tag{3-193}$$

Hence, the overall probability is:

$$p_1 = \left(\frac{1}{2}\right)\cdot\sum_{n_1=1}^{2^N-1}\left((p_{11})_{(n_i)}(p_{12})_{(n_i)}\right) + \left(\frac{1}{2}\right)(p_{11})_{(2^N-1)}(p_{12})_{(2^N-1)} \tag{3-194}$$

The additional factor (½) comes from the fact that probability of transmission of a zero by the transmitter is 0.5.

It can be verified that for $N = 1$, (3-194) reduces to (3-158), which gives the probability of decoding a 0 in the 1-bit receiver when a 0 was transmitted.

Case 2. The transmitted data is 0, the probability of which is 0.5. In this case the ADC receives a random variable with mean A and variance σ^2 in the first sampling instant, and another random variable with a mean B and variance σ^2 in the second sampling interval. Both accumulators will have equal values if only both the random variables lie in the same interval.

This can be divided into three sub cases:

Case 2a: $n_1 = n_2 = 0$

The Probability of this event can be given as:

$$p_{20} = \left(\left(\frac{1}{\sqrt{(2\pi\sigma^2)}}\right)\int_{-\infty}^{B+\frac{(A-B)}{2^N}} e^{\frac{-(x-A)^2}{(2\sigma^2)}}dx\right)\left(\left(\frac{1}{\sqrt{(2\pi\sigma^2)}}\right)\int_{-\infty}^{B+\frac{(A-B)}{2^N}} e^{\frac{-(x-B)^2}{(2\sigma^2)}}dx\right) \tag{3-195}$$

taking $y_1 = (x- A)/\sigma$ and $y_2 = (x- B)/\sigma$ we get:

$$p_{20} = \left(\left(\frac{1}{\sqrt{(2\pi)}}\right)\int_{-\infty}^{\frac{(B-A)}{\sigma}\frac{(2^N-1)}{2^N}} e^{-y_1^2/2}dy_1\right)\left(\left(\frac{1}{\sqrt{(2\pi)}}\right)\int_{-\infty}^{\frac{(A-B)}{\sigma}\frac{(1)}{2^N}} e^{-y_2^2/2}dy_2\right) \tag{3-196}$$

which can be written as:

$$p_{20} = \left(\frac{1}{4}\right)\left(1 + erf\left(\left(\frac{(B-A)}{\left(\sqrt{2}\sigma\right)}\frac{(2^N-1)}{2^N}\right)\right)\right)\left(1 + erf\left(\left(\frac{(A-B)}{\left(\sqrt{2}\sigma\right)}\frac{(1)}{2^N}\right)\right)\right) \tag{3-197}$$

Case 2b: $n_1 = n_2 = 2^N - 1$

The probability of this event is:

$$p_{(2\infty)} = \left(\left(\frac{1}{\sqrt{(2\pi\sigma^2)}} \right) \int_{B+\frac{((2^N-1)(A-B))}{2^N}}^{\infty} e^{\frac{-(x-A)^2}{(2\sigma^2)}} dx \right) \left(\left(\frac{1}{\sqrt{(2\pi\sigma^2)}} \right) \int_{B+\frac{((2^N-1)(A-B))}{2^N}}^{\infty} e^{\frac{-(x-B)^2}{(2\sigma^2)}} dx \right) \quad (3\text{-}198)$$

taking $y_1 = (x\text{- } A)/\sigma$ and $y_2 = (x\text{- } B)/\sigma$ we get:

$$p_{(2\infty)} = \left(\left(\frac{1}{\sqrt{(2\pi)}} \right) \int_{\frac{(B-A)}{\sigma}\frac{(1)}{2^N}}^{\infty} e^{-y_1^2/2} dy_1 \right) \left(\left(\frac{1}{\sqrt{(2\pi)}} \right) \int_{\frac{(A-B)}{\sigma}\frac{(2^N-1)}{2^N}}^{\infty} e^{-y_2^2/2} dy_2 \right) \quad (3\text{-}199)$$

which can be written as:

$$p_{(2\infty)} = \left(\frac{1}{4} \right) \left(1 - erf\left(\left(\frac{(B-A)}{(\sqrt{2}\sigma)} \frac{(1)}{2^N} \right) \right) \right) \left(1 - erf\left(\left(\frac{(A-B)}{(\sqrt{2}\sigma)} \frac{(2^N-1)}{2^N} \right) \right) \right) \quad (3\text{-}200)$$

Case 2c: $0 < n_1 = n_2 < 2^N - 1$

The probability of that event can be represented by:

$$p_{(2n_1)} = \left(\left(\frac{1}{\sqrt{(2\pi\sigma^2)}} \right) \int_{B+\frac{(n_1(A-B))}{2^N}}^{B+\frac{((n_1+1)(A-B))}{2^N}} e^{\frac{-(x-A)^2}{(2\sigma^2)}} dx \right) \cdot \left(\left(\frac{1}{\sqrt{(2\pi\sigma^2)}} \right) \int_{B+\frac{((n_1)(A-B))}{2^N}}^{B+\frac{((n_1+1)(A-B))}{2^N}} e^{\frac{-(x-B)^2}{(2\sigma^2)}} dx \right) \quad (3\text{-}201)$$

taking $y_1 = (x\text{- } A)/\sigma$ and $y_2 = (x\text{- } B)/\sigma$ we get:

$$p_{(2n_1)} = \left(\left(\frac{1}{\sqrt{(2\pi)}} \right) \int_{\frac{(B-A)}{\sigma}\frac{(2^N-n_1-1)}{2^N}}^{\frac{(B-A)}{\sigma}\frac{(2^N-n_1)}{2^N}} e^{-y_1^2/2} dy_1 \right) \bullet \left(\left(\frac{1}{\sqrt{(2\pi)}} \right) \int_{\frac{(A-B)}{\sigma}\frac{(n_1)}{2^N}}^{\frac{(A-B)}{\sigma}\frac{(n_1+1)}{2^N}} e^{-y_2^2/2} dy_2 \right) \quad (3\text{-}202)$$

which is given by:

$$p_{(2n_1)} = \left(\frac{1}{4}\right)\left(erf\left(\begin{array}{l} \left(\left(\frac{(B-A)}{\left(\sqrt{2}\sigma\right)} \right) \frac{\left(2^N - n_1 - 1\right)}{2^N} \right) - \\ erf\left(\left(\frac{(B-A)}{\left(\sqrt{2}\sigma\right)} \right) \frac{\left(2^N - n_1\right)}{2^N} \right) \end{array} \right) \left(erf\left(\left(\frac{(A-B)}{\left(\sqrt{2}\sigma\right)} \right) \frac{(n_1+1)}{2^N} \right) \right) - erf\left(\left(\frac{(A-B)}{\left(\sqrt{2}\sigma\right)} \right) \frac{(n_1)}{2^N} \right) \right) \right) \quad (3\text{-}203)$$

Hence, the overall probability of case 2 can be given by:

$$p_2 = \left(\frac{1}{2}\right)\left(p_{20} + p_{(2\infty)} + \sum_{j=1}^{j<2^N-1} p_{\left(2n_j\right)} \right) \quad (3\text{-}204)$$

The additional (½) comes from the fact that probability of the transmitter to transmit a zero is 0.5. Moreover, it is interesting to note that for $N = 1$, (3-204) reduces to (3-159) and (3-145), which gives the probability of indecision in the receiver when a 0 was transmitted.

Case 3. The transmitted data is 0, the probability of which is 0.5. In this case, the ADC receives a random variable with mean A and variance σ^2 in the first sampling instant, and another random variable with a mean B and variance σ^2 in the second sampling interval. Now, we have to consider the case that the output of the first accumulator is smaller than the output of the second accumulator. If the output of the first accumulator is n_1 (then, clearly $0 \le n_1 < 2^N - 1$), and the output of the second accumulator is n_2 then $0 \le n_1 < n_2$. The probability that the output of the first accumulator is n_1 (where $n_1 > 0$) is given by:

$$\left(p_{31}\right)_{(n_i)} = \frac{1}{\sqrt{\left(2\pi\sigma^2\right)}} \int_{B+\frac{n_i(A-B)}{2^N}}^{B+\frac{(n_i+1)(A-B)}{2^N}} e^{\frac{-(x-A)^2}{2\sigma^2}} dx \quad (3\text{-}205)$$

Taking $(x - A)/\sigma = y$ we get:

$$\left(p_{31}\right)_{(n_i)} = \frac{1}{\sqrt{(2\pi)}} \int_{\frac{(B-A)}{\sigma}\left(1-\frac{n_i}{2^N}\right)}^{\frac{(B-A)}{\sigma}\left(1-\frac{n_i+1}{2^N}\right)} e^{\frac{-y^2}{2}} dy \quad (3\text{-}206)$$

which can be expressed as:

$$\left(p_{31}\right)_{(n_i)} = \left(\frac{1}{2}\right)\left(erf\left(\frac{(B-A)}{\left(\sqrt{2}\sigma\right)} \times \left(1 - \frac{(n_i+1)}{2^N}\right) \right) - erf\left(\frac{(B-A)}{\left(\sqrt{2}\sigma\right)} \times \left(1 - \frac{n_i}{2^N}\right) \right) \right) \quad (3\text{-}207)$$

This formula is valid for all n_1 which are greater than 1, if $n_1 = 0$, then (3-207) can be modified as:

$$(p_{31})_{(0)} = \frac{1}{\sqrt{(2\pi\sigma^2)}} \int_{-\infty}^{B+\frac{(A-B)}{(2^N)}} e^{\left(\frac{-(x-A)^2}{(2\sigma^2)}\right)} dx \tag{3-208}$$

again taking $(x - A)/\sigma = y$ we get:

$$(p_{31})_{(0)} = \frac{1}{\sqrt{(2\pi)}} \int_{-\infty}^{\left(\frac{(B-A)}{\sigma}\right)\left(1-\frac{1}{(2^N)}\right)} e^{\left(\frac{-y^2}{(2)}\right)} dy \tag{3-209}$$

which can be expressed as:

$$(p_{31})_{(0)} = \left(\frac{1}{2}\right)\left(1 + erf\left(\frac{(B-A)(2^N-1)}{(2^N\sqrt{2}\sigma)}\right)\right) \tag{3-210}$$

The probability that the output of the second accumulator is greater than n_i is given by:

$$(p_{32})_{(n_i)} = \frac{1}{\sqrt{(2\pi\sigma^2)}} \int_{B+\frac{((n_i+1)(A-B))}{2^N}}^{\infty} e^{\left(\frac{-(x-B)^2}{(2\sigma^2)}\right)} dx \tag{3-211}$$

Taking $(x - B)/\sigma = y$ we get:

$$(p_{32})_{(n_i)} = \frac{1}{\sqrt{(2\pi)}} \int_{\frac{((n_1+1)(A-B))}{(2^N\sigma)}}^{\infty} e^{\left(\frac{-y^2}{2}\right)} dy \tag{3-212}$$

which can be expressed as:

$$(p_{32})_{(n_i)} = \left(\frac{1}{2}\right)\left(1 - erf\frac{((n_i+1)(A-B))}{(2^N\sqrt{2}\sigma)}\right) \tag{3-213}$$

when $n_i = 0$, then (3-213) reduces to

$$(p_{32})_0 = \left(\frac{1}{2}\right)\left(1 - erf\left(\frac{(A-B)}{(2^N\sqrt{2}\sigma)}\right)\right) \tag{3-214}$$

Hence, the overall probability is:

$$p_3 = \left(\frac{1}{2}\right)\left(\left(\sum_{n_i=1}^{n_i<2^N-1}(p_{31})_{(n_i)}(p_{32})_{(n_i)}\right) + (p_{31})_0(p_{32})_0\right) \tag{3-215}$$

It can be observed that for $N = 1$ (3-215) reduced to (3-155) which is the probability of receiving a 1 when a zero was transmitted.

Case 4. The transmitted data is 1, the probability of which is 0.5. In this case, the ADC receives a random variable with mean B and variance σ^2 in the first sampling instant, and another random variable with a mean A and variance σ^2 in the second sampling interval.

If the output of the first accumulator is n_1 (then, clearly $0 < n_1 \leq 2^N - 1$), and the output of the second accumulator is n_2, then $0 \leq n_2 < n_1$.

The probability that the output of the first accumulator is n_1 (where $n_1 < 2^N - 1$) is given by:

$$\left(p_{41}\right)_{(n_i)} = \frac{1}{\sqrt{\left(2\pi\sigma^2\right)}} \int_{B+\frac{n_1(A-B)}{2^N}}^{B+\frac{(n_1+1)(A-B)}{2^N}} e^{\frac{-(x-B)^2}{2\sigma^2}} dx \tag{3-216}$$

Taking $(x - B)/\sigma = y$ we get:

$$\left(p_{41}\right)_{(n_i)} = \left(\frac{1}{2}\right)\left(erf\left(\frac{(A-B)}{\left(\sqrt{2}\sigma\right)}\frac{(n_1+1)}{\left(2^N\right)}\right) - erf\left(\frac{(A-B)}{\left(\sqrt{2}\sigma\right)}\frac{(n_1)}{\left(2^N\right)}\right)\right) \tag{3-217}$$

The probability that the first accumulator has an output of $2^N - 1$ is given by:

$$\left(p_{41}\right)_{\left(2^N-1\right)} = \frac{1}{\sqrt{\left(2\pi\sigma^2\right)}} \int_{B+\frac{(2^N-1)(A-B)}{2^N}}^{\infty} e^{\frac{-(x-B)^2}{2\sigma^2}} dx \tag{3-218}$$

taking $(x - B)/\sigma = y$ we get:

$$\left(p_{41}\right)_{\left(2^N-1\right)} = \frac{1}{\sqrt{(2\pi)}} \int_{\frac{(2^N-1)(A-B)}{2^N\sigma}}^{\infty} e^{\frac{-(y-B)^2}{2\sigma^2}} dy \tag{3-219}$$

which can be expressed as:

$$\left(p_{41}\right)_{\left(2^N-1\right)} = \left(\frac{1}{2}\right)\left(1 - erf\left(\frac{\left(2^N-1\right)}{2^N}\frac{(A-B)}{\left(\sqrt{2}\sigma\right)}\right)\right) \tag{3-220}$$

The probability that the output of the second accumulator is less than n_1 is given by:

$$\left(p_{42}\right)_{(n_i)} = \frac{1}{\sqrt{\left(2\pi\sigma^2\right)}} \int_{-\infty}^{B+\frac{\left(n_1(A-B)\right)}{\left(2^N\right)}} e^{\frac{-(x-A)^2}{\left(2\sigma^2\right)}} dx \tag{3-221}$$

taking $(x - A)/\sigma = y$ we get:

$$\left(p_{42}\right)_{(n_i)} = \frac{1}{\sqrt{(2\pi)}} \int_{-\infty}^{\frac{(B-A)}{\sigma}\left(1-\frac{n_1}{2^N}\right)} e^{\frac{-y^2}{(2)}}\, dx \tag{3-222}$$

which can be given by:

$$\left(p_{42}\right)_{(n_1)} = \left(\frac{1}{2}\right)\left(1+erf\left(\frac{\left(2^N-n_1\right)}{2^N}\frac{(B-A)}{\left(\sqrt{2}\sigma\right)}\right)\right) \tag{3-223}$$

when n_1 is $2^N - 1$ (3-223) becomes:

$$\left(p_{42}\right)_{\left(2^N-1\right)} = \left(\frac{1}{2}\right)\left(1+erf\left(\frac{1}{2^N}\frac{(B-A)}{\left(\sqrt{2}\sigma\right)}\right)\right) \tag{3-224}$$

Then the overall probability is given by:

$$p_4 = \left(\frac{1}{2}\right)\left(\left(p_{41}\right)_{\left(2^N-1\right)}\left(p_{42}\right)_{\left(2^N-1\right)} + \sum_{n_i=1}^{n_i<2^N-1}\left(p_{41}\right)_{(n_i)}\left(p_{42}\right)_{(n_i)}\right) \tag{3-225}$$

It can be verified that for $N = 1$ (3-225) becomes (3-174).

Case 5. The transmitted data is 1, the probability of which is 0.5. In this case, the ADC receives a random variable with mean B and variance σ^2 in the first sampling instant, and another random variable with a mean A and variance σ^2 in the second sampling interval. If the outputs are equal, it is clearly the same case as that of case 2 so $p_5 = p_2$.

Case 6. The transmitted data is 1, the probability of which is 0.5. In this case, the ADC receives a random variable with mean B and variance σ^2 in the first sampling instant, and another random variable with a mean A and variance σ^2 in the second sampling interval. If the output of the second accumulator is n_2 (then, clearly $0 < n_1 \leq 2^N - 1$), and the output of the first accumulator is n_1 then $0 \leq n_1 < n_2$. The probability that the output of the first accumulator is n_1 (where $n_1 > 0$) is given by:

$$\left(p_{61}\right)_{(n_i)} = \frac{1}{\sqrt{\left(2\pi\sigma^2\right)}} \int_{B+\frac{n_i(A-B)}{2^N}}^{B+\frac{(n_i+1)(A-B)}{2^N}} e^{\frac{-(x-B)^2}{2\sigma^2}}\, dx \tag{3-226}$$

Taking $(x - B)/\sigma = y$ we get:

$$\left(p_{61}\right)_{\left(n_i\right)}=\frac{1}{\sqrt{\left(2\pi\right)}}\int_{\frac{\left(n_i\right)}{2^N}\frac{\left(A-B\right)}{\sigma}}^{\left(\frac{\left(n_i+1\right)}{2^N}\frac{\left(A-B\right)}{\sigma}\right)}e^{\frac{-y^2}{2}}dy \tag{3-227}$$

which can be expressed as:

$$\left(p_{61}\right)_{\left(n_i\right)}=\left(\frac{1}{2}\right)\left(erf\left(\frac{\left(A-B\right)}{\left(\sqrt{2}\sigma\right)}\times\left(\frac{\left(n_i+1\right)}{2^N}\right)\right)-erf\left(\frac{\left(A-B\right)}{\left(\sqrt{2}\sigma\right)}\times\left(\frac{n_i}{2^N}\right)\right)\right) \tag{3-228}$$

when $n_1 = 0$, the probability becomes:

$$\left(p_{61}\right)_0=\frac{1}{\sqrt{\left(2\pi\sigma^2\right)}}\int_{-\infty}^{B+\frac{\left(A-B\right)}{2^N}}e^{\frac{-\left(x-B\right)^2}{\left(2\sigma^2\right)}}dx \tag{3-229}$$

Taking $(x - B)/\sigma = y$ we get:

$$\left(p_{61}\right)_0=\frac{1}{\sqrt{\left(2\pi\right)}}\int_{-\infty}^{\frac{\left(A-B\right)}{\left(2^N\sigma\right)}}e^{\frac{-y^2}{2}}dy \tag{3-230}$$

which can be given as:

$$\left(p_{61}\right)_0=\left(\frac{1}{2}\right)\left(1+erf\left(\frac{1}{2^N}\frac{\left(A-B\right)}{\left(\sqrt{2}\sigma\right)}\right)\right) \tag{3-231}$$

The probability that the output of the second accumulator is greater than n_1:

$$\left(p_{62}\right)_{\left(n_i\right)}=\frac{1}{\sqrt{\left(2\pi\sigma^2\right)}}\int_{B+\frac{\left(\left(A-B\right)\left(n_i+1\right)\right)}{2^N}}^{\infty}e^{\frac{-\left(x-A\right)^2}{\left(2\sigma^2\right)}}dx \tag{3-232}$$

Taking $(x - A)/\sigma = y$ we get:

$$\left(p_{62}\right)_{\left(n_i\right)}=\frac{1}{\sqrt{\left(2\pi\right)}}\int_{\left(\frac{\left(B-A\right)}{\sigma}\right)\left(1-\frac{\left(n_i+1\right)}{2^N}\right)}^{\infty}e^{\frac{-y^2}{2}}dy \tag{3-233}$$

which can be given as:

$$\left(p_{62}\right)_{\left(n_i\right)}=\left(\frac{1}{2}\right)\left(1-erf\left(\left(1-\frac{\left(n_i+1\right)}{2^N}\right)\frac{\left(B-A\right)}{\left(\sqrt{2}\sigma\right)}\right)\right) \tag{3-234}$$

when $n_1 = 0$, (3-234) becomes:

$$(p_{62})_0 = \left(\frac{1}{2}\right)\left(1 - erf\left(\left(1 - \frac{1}{2^N}\right)\frac{(B-A)}{(\sqrt{2}\sigma)}\right)\right) \tag{3-235}$$

The overall probability is:

$$p_6 = \left(\frac{1}{2}\right)\left((p_{61})_0(p_{62})_0 + \sum_{n_i=1}^{n_i < 2^N - 1}(p_{61})_{(n_i)}(p_{62})_{(n_i)}\right) \tag{3-236}$$

It can be clearly verified that for $N = 1$, (3-236) becomes (3-173).

Using MATLAB it can be verified:

$$p_1 + p_2 + p_3 + p_4 + p_5 + p_6 = 1 \tag{3-237}$$

The probability of error is given by:

$$p_{error} = p_3 + p_4 \tag{3-238}$$

while the probability of indecision is:

$$p_{indecision} = p_2 + p_5 \tag{3-239}$$

In case of indecision we can flip a fair coin and decide in favour of zero or one, so overall probability of error is:

$$p_{errornew} = p_{errorold} + 0.5\mathrm{p}_{indecison} \tag{3-240}$$

Using (3-240) and (3-142), we can calculate the final probability of error. The probability of error analytically calculated was compared with the simulated values of BER achieved using MATLAB considering various values of N. In Figure 3-61, the solid lines give the simulated values of BER and the dashed lines give the calculated values of Probability of Error.

3.3.13.5 Comparison of ADC Effects in Continuous Wave BPSK and PPM IR-UWB Systems

Figure 3-62 shows the comparison of performance degradation in a PPM IR-UWB architecture and a conventional continuous wave BPSK communication system. The data rate of transmission for both systems has been fixed to 10 Mbps. Considering a fixed E_s/N_0 for the UWB system, the corresponding SNR of the BPSK system is given by:

$$log_{10}(SNR) = log_{10}(E_s/N_0) - 0.5 \times T_{symbol} \times f_{sampling} \tag{3-241}$$

where T_{symbol} is the symbol time and $f_{sampling}$ is the sampling frequency.

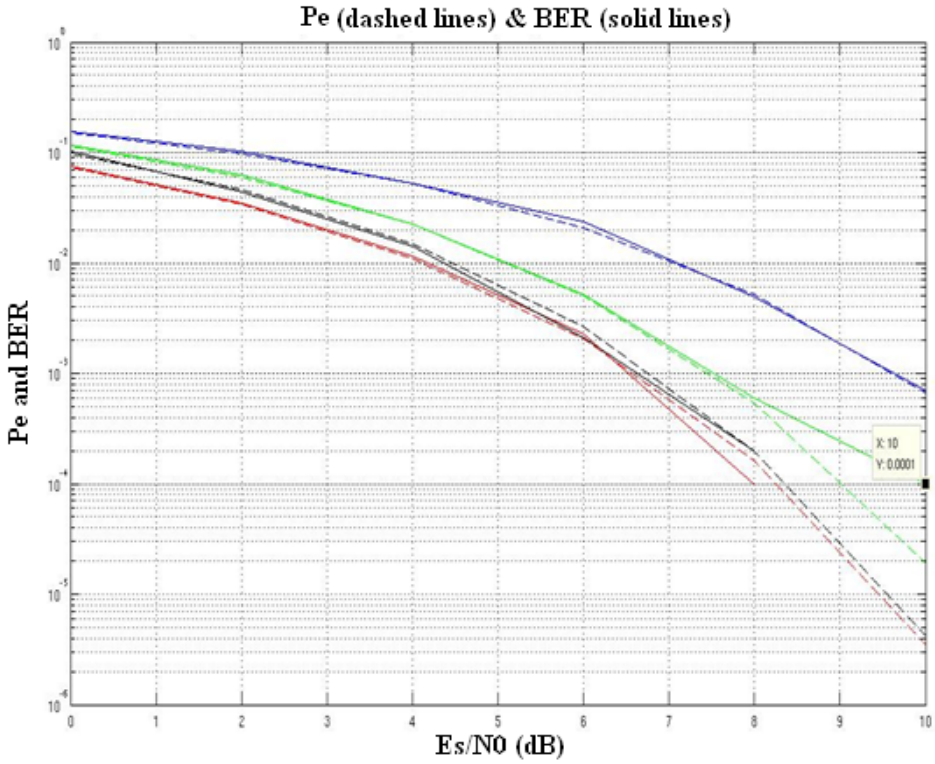

Figure 3-61: Performance Comparison for an analog (in red), 1 bit digital (in blue), 2 bit digital (in green) and 4 bit digital (in black) UWB receivers

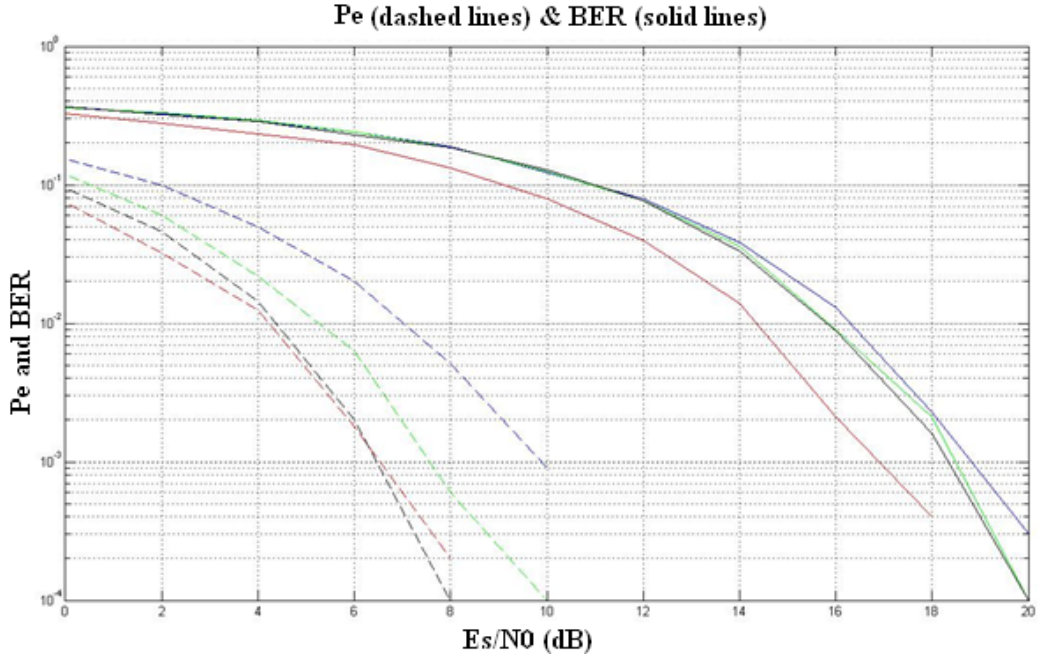

Figure 3-62: Performance Comparison between UWB (shown in dashed lines) and BPSK (shown in solid lines) for analog (red line), 1 bit digital (blue line) 2 bit digital (green line) and 4 bit digital (black line) receivers

Observing Figure 3-62 it is clear that, although the BPSK error performance is poorer than that of UWB, its performance degradation due to low resolution ADC is less severe.

3.3.13.6 Performance Improvement for a 1-bit Digital UWB Receiver

The ubiquitous adoption of WLANs and cellular networks over the last decade has been propelled by the economies of scale associated with digital receiver architectures that leverage Moore's law for low power, low-cost implementations. An integral component of such receiver architectures is the ADC, which converts the received signal into digital format, typically with a precision of 8-12 bits. Operations such as synchronization, equalization, demodulation and decoding are then performed in the digital domain, greatly enhancing the flexibility available to the designer. We would like to scale this "mostly digital" paradigm to multi-Gigabit speeds, in order to enable mass market multi-Gigabit WLANs and WPANs based on large amounts of unlicensed bandwidth available for communications beyond 60 GHz. The bottleneck in such scaling becomes the ADC: high-speed, high-precision ADC is either unavailable, or is too costly and power-hungry.

To counteract this problem, high speed but low precision ADCs are widely used. However, it has been seen that using low precision ADCs (1 bit in the worst case) results in severe degradations of the system performance. In this paragraph, two solutions are proposed based on the results described in 3.3.13.5 in order to improve the performance of the system with 1 bit ADC.

3.3.13.6.1 Ignoring indecision bit(s)

In the case of indecision, instead of tossing a fair coin, we can ignore the bit(s) which cannot be decided, and make the final decision based on remaining bit(s).

We try to calculate the probability of error and measure the probability of error in this case. We assume out of N_s bits (N_s is odd), N_d (where clearly, $0 \leq N_d \leq N_s$) bits are undecided by the receiver.

So out of the remaining $N_s - N_d$ bits the probability of correct decision is:

$$p_c^{'} = \frac{p_c}{(1 - p_d)} \tag{3-242}$$

and probability of wrong decision is:

$$p_w^{'} = \frac{p_w}{(1-p_d)} \tag{3-243}$$

Case 1. We assume N_d is even, then we can write $N_d = 2k$ where $0 \leq k \leq (N_s - 1)/2$. So probability of having $2k$ bits falling in the indecision region out of N_s is given by:

$$^{N_s}C_{(2k)}(p_d)^{(2k)}(1-p_d)^{(N_s-2k)} \tag{3-244}$$

and the probability of error in this case can be written from (3-141):

$$P_e = \sum_{k=1}^{\frac{N_s+1}{2}} {}^{N_s}C_{\frac{N_s+2k-1}{2}} p_e^{\frac{N_s+2k-1}{2}} (1-p_e)^{\frac{N_s-2k+1}{2}} \tag{3-245}$$

and the over all probability is given by:

$$P_1 = \sum_{k=0}^{\frac{N_s-1}{2}} P_{1k} \tag{3-246}$$

Case 2. Now we assume that N_d is odd, we can write $N_d = 2k + 1$, where $0 \leq k \leq (N_s - 1)/2$. This case is more complicated because we can have some interesting subcases.

Case 2a: $N_s = N_d$, the probability of this event is:

$$p_d^{N_s} \tag{3-247}$$

Clearly, in this case none of the bits can be resolved so our only choice is to toss a fair coin, giving a probability of error of 0.5. Hence, the overall probability is:

$$P_{2a} = 0.5 \cdot (p_d)^{N_s} \tag{3-248}$$

Case 2b: $N_d < N_s$, but after decoding we have equal number of 1's and 0's, in other words half of the remaining bits have been erroneously decoded.

The probability of that event is:

$$p_{2bk} = \left({}^{N_s}C_{2k+1} p_d^{2k+1}(1-p_d)^{N_s-2k-1}\right) \cdot \left({}^{(N_s-2k-1)}C_{\left(\frac{N_s-2k-1}{2}\right)} \left(p_w^{'}\right)^{\left(\frac{N_s-2k-1}{2}\right)} \left(1-p_w^{'}\right)^{\left(\frac{N_s-2k-1}{2}\right)} \right) \tag{3-249}$$

As like case 2a here also a fair coin must be tossed to decide the outcome, so the probability of error is 0.5. Therefore, the overall probability is:

$$P_{2b} = \sum_{k=0}^{\frac{N_s-3}{2}} P_{2bk} \tag{3-250}$$

In (3-250), the higher limit of summation is $(N_s - 3)/2$ and not $(N_s - 1)/2$, because if $k = (N_s - 1)/2$, it becomes case 2a.

Case 2c: $N_d < N_s$, but after decoding we have unequal number of 1's and 0's. We assume that k' bits have been erroneously decoded where, for an erroneous decision, clearly $k' > (N_s - 2k - 1)/2$, probability of this event is:

$$p_{2ck} = \left({}^{N_s}C_{2k+1} p_d^{2k+1} (1-p_d)^{N_s-2k-1}\right) \cdot \left(\sum_{k'=\frac{N_s-2k+1}{2}}^{N_s-2k-1} {}^{(N_s-2k-1)}C_{(k')} \left(p_w^{'}\right)^{(k)'} \left(1-p_w^{'}\right)^{(N_s-2k-1-k')} \right) \tag{3-251}$$

Hence, the overall probability is given by:

$$P_{2c} = \sum_{k=0}^{\frac{N_s-3}{2}} P_{2ck} \tag{3-252}$$

The overall probability of error due to indecision is:

$$P_2 = P_{2a} + P_{2b} + P_{2c} \tag{3-253}$$

The total probability of error P_{error} in case of an indecision is given by $P_{error} = P_1 + P_2$.

It was verified using MATLAB that when $N_s = 1$, the probability of error calculated by ignoring the indecision bits and one estimated by tossing a fair coin in case of an indecision (as calculated using (3-142)) are same. The calculated values and the simulated results (using MATLAB) are compared in Figure 3-63.

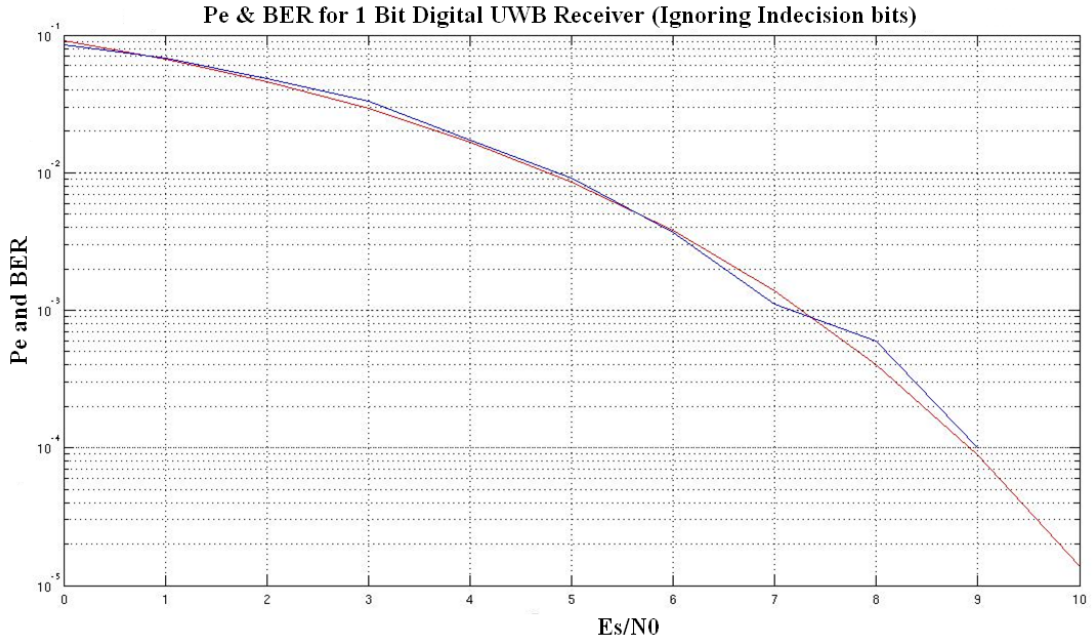

Figure 3-63: Comparison between Pe (in red) and BER (in blue)

Figure 3-63 shows a good resemblance between the simulated and calculated values. Figure 3-64 compares the probability of error calculated by the two methods for $N_s = 5$.

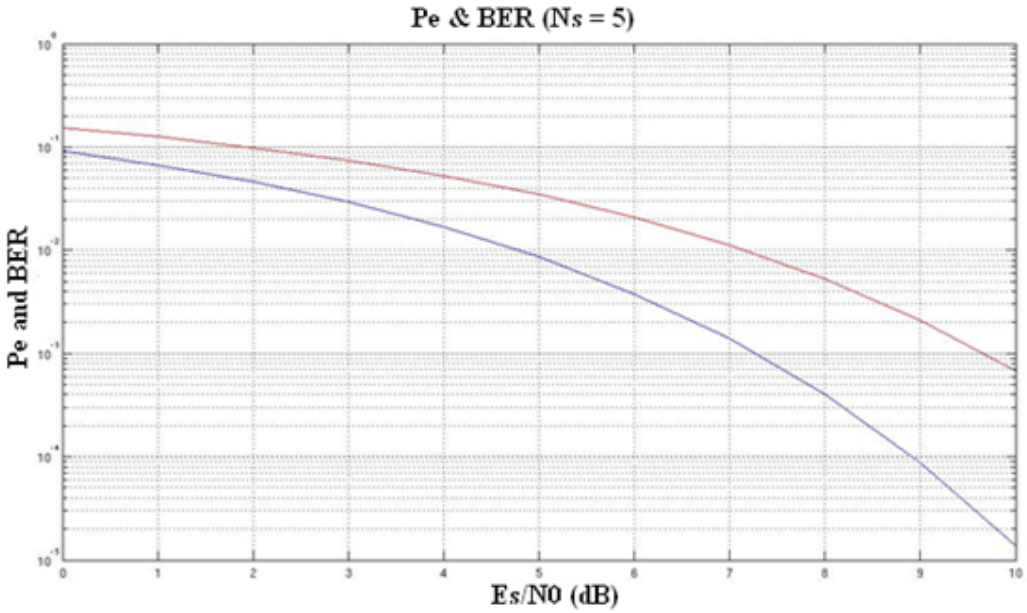

Figure 3-64Comparison of Pe (red lines) and BER (blue lines) for an IR-UWB system with $N_s = 5$ when the indecision bits are ignored and when the decision is made by tossing a fair coin in case of indecision

From Figure 3-64 it can be seen that performance of the system which ignores the indecision bits is better.

3.3.13.6.2 Channel Estimation and Adaptive Coding

If the receiver decodes a 0 or a 1, it could be either received correctly or received with an error. It cannot give us any information about the channel. However, if the receiver arrives at an indecision, the frequency of such arrivals can give us an idea about the channel conditions, because if such indecisions are more frequent the channel is noisy and if they are less frequent (or rare), the channel is good. So, if it is possible to use a stronger code (increasing the value of N_s when number of indecisions are higher and decreasing them when the number is lower), it is theoretically possible to get a BER of any possible value, irrespective of the channel condition. However, we cannot increase N_s as much we want, because a very high value of N_s can reduce the data rate of the system.

This system was simulated according to the following chart and the results are shown in Table 3-10. In Table 3-10, p indicates the ratio of indecisions and N_s. To compare the

performances of this improvement scheme we plot the bit error rates in case of i) an analog receiver ii) a 1 bit digital receiver without performance enhancing technique iii) a 1 bit digital receiver using technique in section 2 and iv) a 1 bit digital receiver using the combined techniques described in sections 2 and 3.

p > 0.4	$N_s = 13$
0.3≤p<0.4	$N_s = 11$
0.2≤p<0.3	$N_s = 9$
0.1≤p<0.2	$N_s = 7$
0.01≤p<0.1	$N_s = 5$
p<0.01	$N_s = 3$

Table 3-10: Table to select N_s according to the indecision

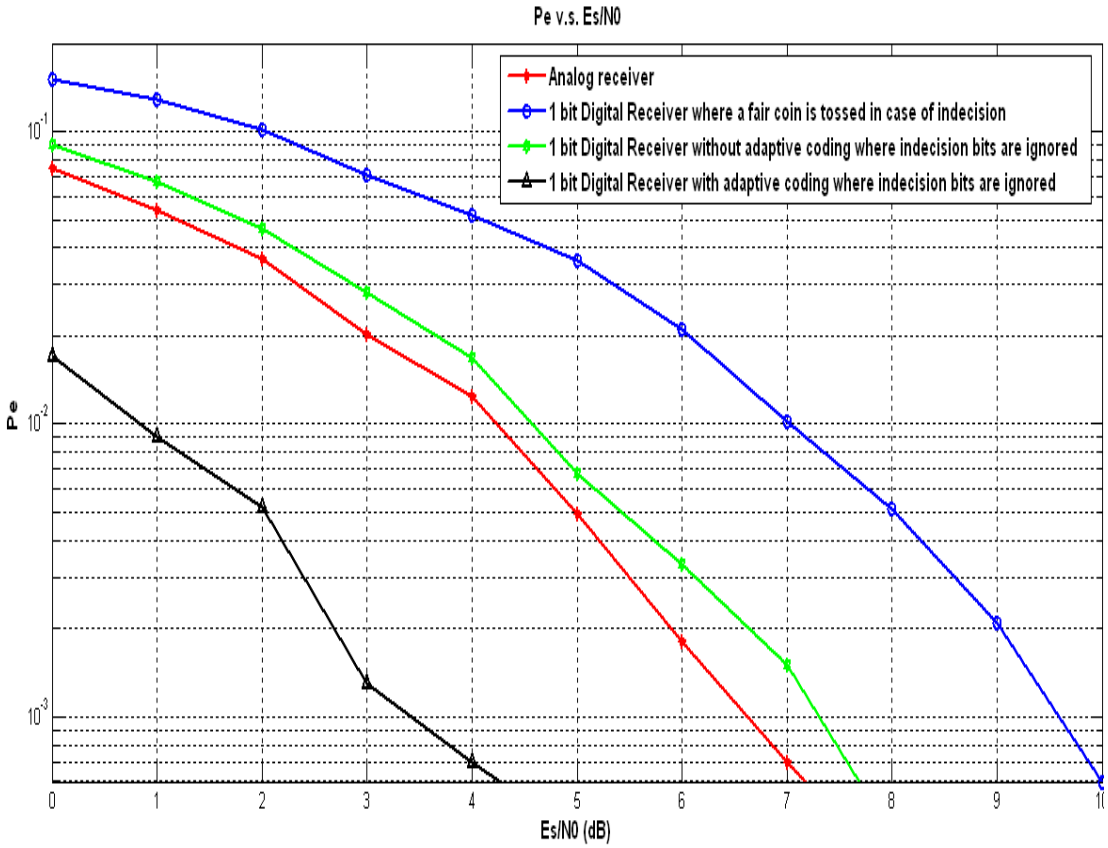

Figure 3-65: Comparison between the performance of an analog receiver, a 1 bit digital receiver where a fair coin is tossed in case of an indecision, a 1 bit digital receiver without adaptive coding where the indecision bits are ignored and a 1 bit digital receiver with adaptive coding where the indecision bits are ignored

We see that there is a significant performance improvement if we ignore the indecision bits instead of tossing a fair coin and if we use variable N_s then the performance of the 1 bit digital receiver way exceeds that of the analog receiver. The following figures illustrate the average values of N_s and p as a function of E_s/N_0 in case of a receiver using adaptive coding.

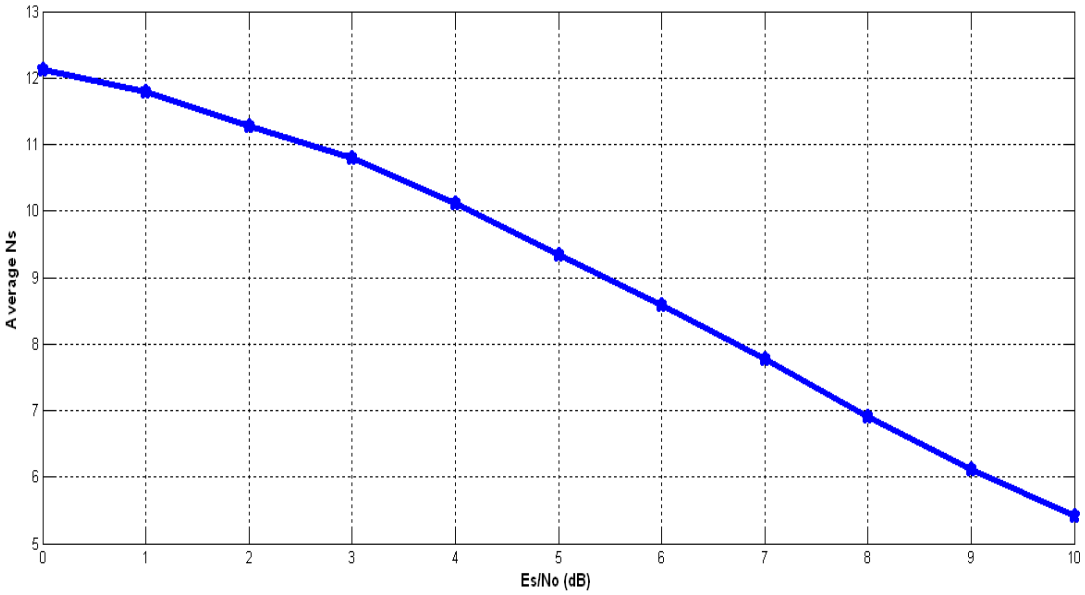

Figure 3-66: Variation of N_s with E_s/N_0

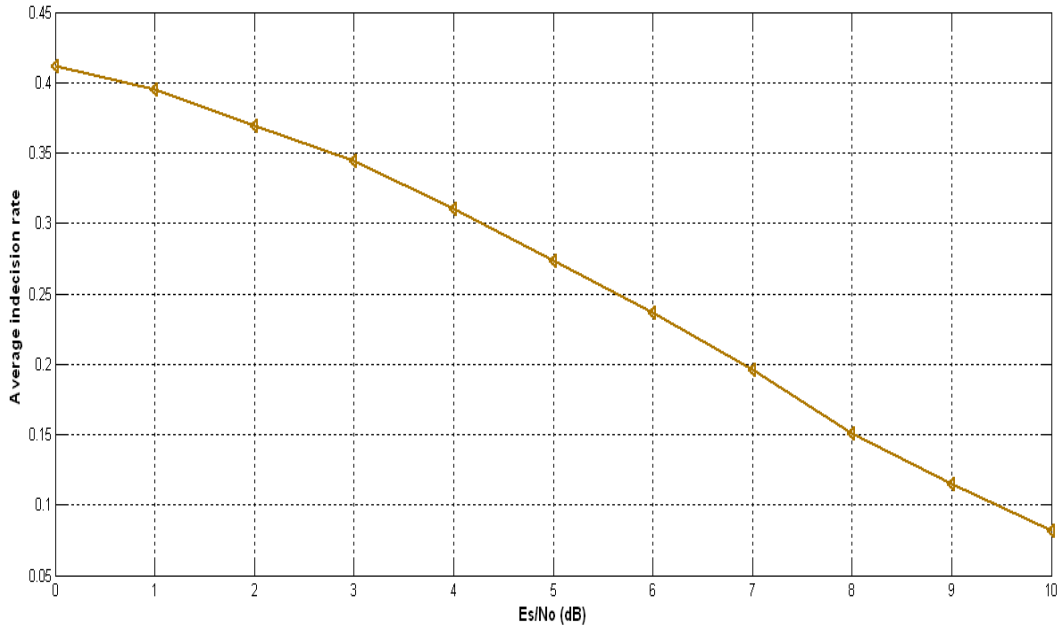

Figure 3-67: Variation of p with E_s/N_0

In this paragraph, two methods of improving the performance of a system using 1 bit ADC have been described. We see that using adaptive coding by estimating the channel according to the number of indecisions, the performance of the receiver using just 1 bit ADC way exceeds that of the analog receiver, thus showing the power of digital processing.

The effects of a low resolution Analog to Digital Converter in an UWB communication system was considered, and the performance degradations were analysed using simulations and analytical calculations. It is seen that the performance of a 4 bit digital UWB receiver is more or less the same as that of an analog receiver in the presence of AWGN noise.
During this work some further areas of research have been found out, some of them are:

- Possibility of better resolution of in the indecision state, for better results some algorithms like Automatic Repeat Request (ARQ) can be used to improve the BER, rather than just wildly guessing the output.
- BER (or Probability of Error, in case of analytical calculations) has been considered as the primary performance index. Similar analysis can be done with more information theoretical approach.
- This analysis has been carried out in baseband, in RF frequencies a similar analysis can be carried out, considering effects of different RF components like oscillators, mixers, amplifiers, filters etc.
- In these considerations only AWGN channel has been considered, it may be possible to extend this work for satellite or outdoor channels.

Finally, two solutions are proposed based on the results described in 3.3.13.5 in order to improve the performance of the system with 1 bit ADC.

3.3.13.7 Modeling Time Interleaved ADCs in IR UWB Systems

3.3.13.7.1 Non-idealities in Time Interleaved ADCs

Four major non-idealities have been modeled in this paragraph:

a) Gain Mismatch. We can assume that the signal amplitude is multiplied by a channel dependent term [3-53], [3-54]. This mismatch value does not change with time and is given by $(1+g)$. We model g using a Gaussian random, variable with a mean of 0

and variance of σ_g^2. Gain mismatch can be modeled as shown in Figure 3-68 [3-55].

b) Offset Voltage. We assume that in each channel a random value of offset voltage is introduced which changes with time and is given by V_{off}. We model V_{off} using a Gaussian random variable with a mean of 0 and variance of σ_0^2 [3-54]. Offset mismatch can be modeled as shown in Figure 3-69 [3-55].

c) Clock Skew. We assume that the clock for each channel is delayed or advanced by an amount r_m. This parameter does not change with time and is modeled by a Gaussian random variable with mean 0 and variance σ_s^2 [3-54]. Clock skew mismatch can be modeled as shown in Figure 3-70 [3-55].

d) Timing Jitter. We assume that there is a timing jitter which varies with time, which is modeled by a Gaussian random variable of mean 0 and variance σ_j^2 and is denoted by ε, we assume that $\varepsilon << r_m$.

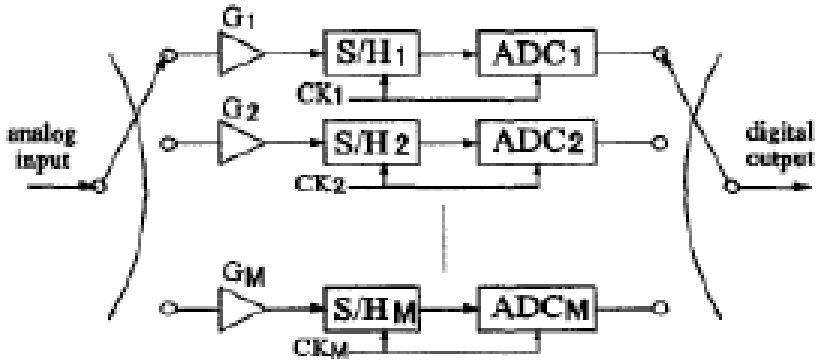

Figure 3-68: Gain mismatch effects in a TI ADC

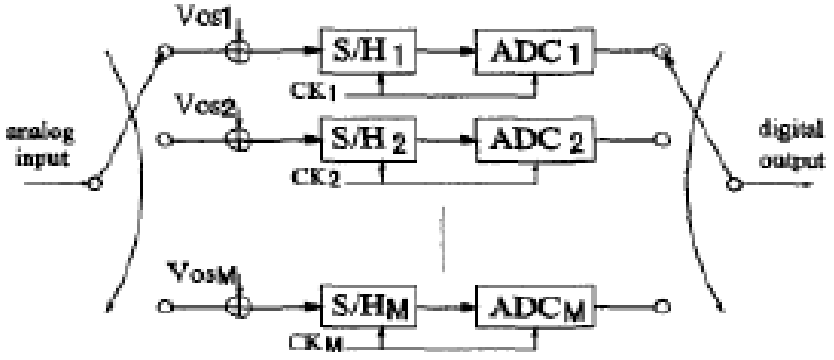

Figure 3-69: Offset mismatch effects in a TI ADC

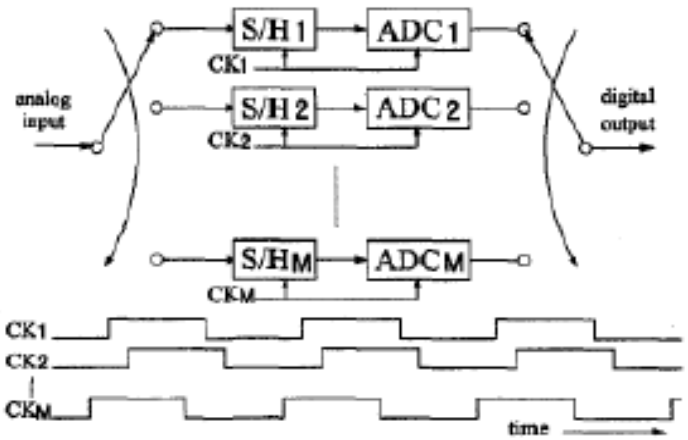

Figure 3-70: Clock Skew effects of a TI ADC

3.3.13.7.2 BER Calculation for a two channel TI ADC

In this case, the sampling is done for each chip, at two instants, each by one ADC. We assume gain of each ADC is given by $(1+g_1)$ and $(1+g_2)$ respectively, where g_1 and g_2 are Gaussian random variables with zero mean and variance of σ_g^2, whose values do not change with time. We start our analysis, in the same way, as we did for *N* bit non-time interleaved ADCs. We go back to Table 3-11.

Serial Number	Transmitted Data	Output of the upper accumulator	Output of the lower accumulator	Decision
1	0	Greater than the output of the lower accumulator	Less than the output of the upper accumulator	0
2	0	Equal to the output of the lower accumulator	Equal to the output of the upper accumulator	?
3	0	Less than the output of the lower accumulator	Greater than the output of the upper accumulator	1
4	1	Greater than the output of the lower accumulator	Less than the output of the upper accumulator	0
5	1	Equal to the output of the lower accumulator	Equal to the output of the upper accumulator	?
6	1	Less than the output of the lower accumulator	Greater than the output of the upper accumulator	1

Table 3-11: Truth table for decision for an N-bit ADC in AWGN channel

3.3.13.7.2.1 Effect of Gain Mismatch

- Case a. The transmitted data is 0, the probability of which is 0.5, in this case the ADC receives a random variable with mean $A(1+g_1)$ and variance $(1+g_1)^2\sigma^2$ in the first sampling instant, and another random variable with a mean $B(1+g_2)$ and variance $(1+g_2)^2\ \sigma^2$ in the second sampling interval.

Now to have the output of the first accumulator larger than the output of the second accumulator, if the output of the first accumulator is n_1 (then, clearly $0 < n_1 \leq 2^N$ - 1), and the output of the second accumulator is n_2 then $0 \leq n_2 < n_1$.

Probability that the output of the first accumulator is n_1 (where $n_1 < 2^N - 1$) is given by:

$$(p_{11})_{(n_i)} = \left(\frac{1}{\sqrt{\left(2\pi\left((1+g_1)\sigma\right)^2\right)}}\right) \int_{B+\frac{(n_1(A-B))}{2^N}}^{B+\frac{(n_1+1)(A-B)}{2^N}} e^{-\frac{(x-A(1+g_1))^2}{\left(2(1+g_1)\sigma^2\right)}} dx \tag{3-254}$$

Assuming $(x - A(1+g_1))/(1+g_1)\sigma = y$ we get:

$$(p_{11})_{(n_i)} = \left(\frac{1}{\sqrt{(2\pi)}}\right) \int_{\left[B+\frac{\frac{(n_1(A-B))}{2^N}-A(1+g_1)}{((1+g_1)\sigma)}\right]}^{\left[B+\frac{\frac{((n_1+1)(A-B))}{2^N}-A(1+g_1)}{((1+g_1)\sigma)}\right]} e^{-\frac{(y)^2}{(2)}} dy \tag{3-255}$$

which can be equated as:

$$(p_{11})_{(n_i)} = \frac{1}{2}\left[erf\left(\frac{\left(B+\frac{(n_1+1)(A-B)}{(2^N)}-A(1+g_1)\right)}{\left(\sqrt{2}((1+g_1)\sigma)\right)}\right) - erf\left(\frac{B+\frac{(n_1(A-B))}{(2^N)}-A(1+g_1)}{\left(\sqrt{2}((1+g_1)\sigma)\right)}\right)\right] \tag{3-256}$$

This formula is valid for all n_1 which are less than $2^N - 1$, if $n_1 = 2^N - 1$, then (3-255) can be modified as:

$$(p_{11})_{(2^N-1)} = \left(\frac{1}{\sqrt{\left(2\pi\left((1+g_1)\sigma\right)^2\right)}}\right) \int_{B+\frac{((2^N-1)(A-B))}{2^N}}^{\infty} e^{-\frac{(x-A(1+g_1))^2}{\left(2(1+g_1)\sigma^2\right)}} dx \tag{3-257}$$

Assuming $(x - A(1+g_1))/(1+g_1)\sigma = y$ we get:

$$(p_{11})_{(2^N-1)} = \left(\frac{1}{\sqrt{(2\pi)}}\right) \int_{\left[B+\frac{\left((2^N-1)(A-B)\right)}{2^N}-A(1+g_1)\right]}^{\infty} e^{-\frac{(y)^2}{(2)}} \, dy \tag{3-258}$$

which can be equated as:

$$(p_{11})_{(2^N-1)} = \frac{1}{2}\left(1 - erf\left(\frac{\left(B+\frac{(2^N-1)(A-B)}{(2^N)}-A(1+g_1)\right)}{\left(\sqrt{2}((1+g_1)\sigma)\right)}\right)\right) \tag{3-259}$$

The probability that the output of the second accumulator to be less than n_1 is given by:

$$(p_{12})_{(n_i)} = \left(\frac{1}{\sqrt{\left(2\pi((1+g_1)\sigma)^2\right)}}\right) \int_{-\infty}^{B+\frac{(n_1(A-B))}{2^N}} e^{-\frac{(x-B(1+g_2))^2}{(2(1+g_2)\sigma^2)}} \, dx \tag{3-260}$$

Assuming $(x - B(1+g_x))/(1+g_2)\sigma = y$ we get:

$$(p_{12})_{(n_i)} = \left(\frac{1}{\sqrt{(2\pi)}}\right) \int_{-\infty}^{\left[\frac{B+\frac{((n_1)(A-B))}{2^N}-B(1+g_2)}{((1+g_2)\sigma)}\right]} e^{-\frac{(y)^2}{2}} \, dy \tag{3-261}$$

which becomes:

$$(p_{12})_{(n_i)} = \frac{1}{2}\left(1 + erf\left(\frac{\left(B+\frac{(n_1(A-B))}{(2^N)}-B(1+g_2)\right)}{\left(\sqrt{2}((1+g_2)\sigma)\right)}\right)\right) \tag{3-262}$$

when n_i is equal to $2^N - 1$, la (3-262) becomes:

$$(p_{12})_{(2^N-1)} = \frac{1}{2}\left(1 + erf\left(\frac{\left(B+\frac{\left((2^N-1)(A-B)\right)}{(2^N)}-B(1+g_2)\right)}{\left(\sqrt{2}((1+g_2)\sigma)\right)}\right)\right) \tag{3-263}$$

$$p_1 = \frac{1}{2}\left\{\sum_{n_1=1}^{2^N-1}\left((p_{11})_{(n_1)}(p_{12})_{(n_1)}\right) + \left((p_{11})_{(2^N-1)}(p_{12})_{(2^N-1)}\right)\right\} \tag{3-264}$$

The additional $\left(\frac{1}{2}\right)$ comes from the fact that the probability of transmission of a zero is 0.5.

- Case b. The transmitted data is 0, the probability of which is 0.5, in this case the ADC receives a random variable with mean $A(1+g_1)$ and variance $(1+g_1)^2\sigma^2$ in the first sampling instant, and another random variable with a mean $B(1+g_2)$ and variance $(1+g_2)^2\sigma^2$ in the second sampling interval. For both accumulators to have equal values both the random variables must lie in the same interval.

This case can be divided into three sub-cases:

Case b-1. $n_1 = n_2 = 0$.

The probability of this event can be expressed by:

$$p_{20} = \left(\frac{1}{\sqrt{\left(2\pi\left((1+g_1)\sigma\right)^2\right)}}\right)\int_{-\infty}^{B+\frac{(A-B)}{2^N}} e^{-\frac{(x-A(1+g_1))^2}{\left(2(1+g_1)\sigma^2\right)}}dx \times \\ \times\left(\frac{1}{\sqrt{\left(2\pi\left((1+g_2)\sigma\right)^2\right)}}\right)\int_{-\infty}^{B+\frac{(A-B)}{2^N}} e^{-\frac{(x-B(1+g_2))^2}{\left(2(1+g_2)\sigma^2\right)}}dx \tag{3-265}$$

Assuming $y_1 = (x - A(1+g_1))/(1+g_1)\sigma$ and $y_2 = (x - A(1+g_2))/(1+g_2)\sigma$ we get:

$$p_{20} = \left(\frac{1}{\sqrt{(2\pi)}}\right)\int_{-\infty}^{\left[\frac{B+\frac{((A-B))}{2^N}-A(1+g_1)}{((1+g_1)\sigma)}\right]} e^{-\frac{y_1^2}{2}}dy_1 \times \left(\frac{1}{\sqrt{(2\pi)}}\right)\int_{-\infty}^{\left[\frac{B+\frac{((A-B))}{2^N}-A(1+g_2)}{((1+g_2)\sigma)}\right]} e^{-\frac{y_2^2}{2}}dy_2 \tag{3-266}$$

which can be written as:

$$p_{20} = \frac{1}{4}\left\{\left(1+erf\left(\frac{\left(B+\frac{(A-B)}{2^N}-A(1+g_1)\right)}{\left(\sqrt{2}(1+g_1)\sigma\right)}\right)\right)\cdot \right. \\ \left.\left(\left(\left(1+erf\left(\frac{B+\frac{(B+(A-B))}{2^N}-B(1+g_2)}{\left(\sqrt{2}(1+g_2)\sigma\right)}\right)\right)\right)\right)\right\} \tag{3-267}$$

Case b-2. $n_1 = n_2 = 2^N - 1$.

The probability of this event can be given by:

$$p_{2N} = \left(\frac{1}{\sqrt{\left(2\pi\left((1+g_1)\sigma\right)^2\right)}}\right)\int_{B+\frac{\left(\left(2^N-1\right)(A-B)\right)}{2^N}}^{\infty} e^{-\frac{(x-A(1+g_1))^2}{\left(2(1+g_1)\sigma^2\right)}}dx \times \tag{3-268}$$

$$\times\left(\frac{1}{\sqrt{\left(2\pi\left((1+g_2)\sigma\right)^2\right)}}\right)\int_{B+\frac{\left|\left(2^N-1\right)(A-B)\right|}{2^N}}^{\infty} e^{-\frac{(x-B(1+g_2))^2}{(2(1+g_2)\sigma^2)}}dx$$

Assuming $y_1=(x-A(1+g_1))/(1+g_1)\sigma$ and $y_2=(x-B(1+g_2))/(1+g_2)\sigma$ we get:

$$p_{2N}=\left(\frac{1}{\sqrt{2\pi}}\right)\int_{\frac{\left[B+\frac{\left(\left(2^N-1\right)(A-B)\right)}{2^N}-A(1+g_1)\right]}{((1+g_1)\sigma)}}^{\infty} e^{-\frac{y_1^2}{2}}dy_1\times \tag{3-269}$$

$$\times\left(\frac{1}{\sqrt{2\pi}}\right)\int_{\frac{\left[B+\frac{\left(\left(2^N-1\right)(A-B)\right)}{2^N}-B(1+g_2)\right]}{((1+g_2)\sigma)}}^{\infty} e^{-\frac{y_2^2}{2}}dy_2$$

which can be written as:

$$p_{2N}=\frac{1}{4}\left\{\left(1-erf\left(\frac{\left(B+\frac{(A-B)\left(2^N-1\right)}{2^N}-A(1+g_1)\right)}{\left(\sqrt{2}(1+g_1)\sigma\right)}\right)\right)\cdot\right.$$
$$\left.\left(\left(1-erf\left(\frac{\left(B+\frac{\left(\left(2^N-1\right)(A-B)\right)}{2^N}-B(1+g_2)\right)}{\left(\sqrt{2}(1+g_2)\sigma\right)}\right)\right)\right\} \tag{3-270}$$

Case b-3. $0<n_1=n_2<2^N-1$.

The probability of this event can be expressed by:

$$p_{(2(n_i))}=\left(\frac{1}{\sqrt{\left(2\pi\left((1+g_1)\sigma\right)^2\right)}}\right)\int_{B+\frac{n_i(A-B)}{2^N}}^{B+\left(\frac{(n_i+1)(A-B)}{2^N}\right)} e^{-\frac{(x-A(1+g_1))^2}{(2(1+g_1)\sigma^2)}}dx\times \tag{3-271}$$

$$\times\left(\frac{1}{\sqrt{\left(2\pi\left((1+g_2)\sigma\right)^2\right)}}\right)\int_{B+\frac{n_i(A-B)}{2^N}}^{B+\left(\frac{(n_i+1)(A-B)}{2^N}\right)} e^{-\frac{(x-B(1+g_2))^2}{(2(1+g_2)\sigma^2)}}dx$$

Assuming $y_1=(x-A(1+g_1))/(1+g_1)\sigma$ and $y_2=(x-A(1+g_2))/(1+g_2)\sigma$ we get:

$$p_{(2(n_i))} = \left(\frac{1}{\sqrt{(2\pi)}}\right) \int_{\left[\frac{B+\left(\frac{n_i(A-B)}{2^N}\right)-A(1+g_1)}{(1+g_1)\sigma}\right]}^{\left[\frac{B+\frac{((n_i+1)(A-B))}{2^N}-A(1+g_1)}{((1+g_1)\sigma)}\right]} e^{-\frac{y_1^2}{2}} dy_1 \times$$
$$\times \left(\frac{1}{\sqrt{(2\pi)}}\right) \int_{\left[\frac{B+\left(\frac{n_i(A-B)}{2^N}\right)-B(1+g_2)}{(1+g_2)\sigma}\right]}^{\left[\frac{B+\frac{(n_i+1)((A-B))}{2^N}-B(1+g_2)}{((1+g_2)\sigma)}\right]} e^{-\frac{y_2^2}{2}} dy_2 \tag{3-272}$$

which can be written:

$$p_{(2(n_i))} = \frac{1}{4} k_1 k_2 \tag{3-273}$$

where:

$$k_1 = erf\left(\frac{\left(B+\left(\frac{(n_1+1)(A-B)}{2^N}\right)\right)-A(1+g_1)}{\left(\sqrt{2}(1+g_1)\sigma\right)}\right) +$$
$$-erf\left(\frac{\left(B+\left(\frac{(n_1+1)(A-B)}{2^N}\right)\right)-A(1+g_1)}{\left(\sqrt{2}(1+g_1)\sigma\right)}\right) \tag{3-274}$$

and:

$$k_2 = erf\left(\frac{\left(B+\left(\frac{(n_1+1)(A-B)}{2^N}\right)\right)-B(1+g_2)}{\left(\sqrt{2}(1+g_2)\sigma\right)}\right) +$$
$$-erf\left(\frac{\left(B+\left(\frac{(n_1)(A-B)}{2^N}\right)\right)-A(1+g_2)}{\left(\sqrt{2}(1+g_2)\sigma\right)}\right) \tag{3-275}$$

Hence, the overall probability is given by:

$$p_2 = \frac{1}{2}\left(p_{20} + p_{2N} + \sum_{i=1}^{2^N-1} p_{(2n_i)} \right) \tag{3-276}$$

- Case c.

  The transmitted data is 0, the probability of which is 0.5, in this case the ADC receives a random variable with mean $A(1+g_1)$ and variance $(1+g_1)^2\sigma^2$ in the first sampling instant, and another random variable with a mean $B(1+g_2)$ and variance $(1+g_2)^2\ \sigma^2$ in the second sampling interval.

Now to have the output of the first accumulator smaller than the output of the second accumulator, if the output of the first accumulator is n_1 (then, clearly $0 < n_1 \le 2^N$ - 1), and the output of the second accumulator is n_2 then $0 \le n_1 < n_2$.

The probability that the output of the first accumulator is n_1 (where $n_1 > 0$) is given by:

$$(p_{31})_{(n_i)} = \left(\frac{1}{\sqrt{\left(2\pi\left((1+g_1)\sigma\right)^2\right)}} \right) \int_{B+\frac{(n_1(A-B))}{2^N}}^{B+\frac{(n_1+1)(A-B)}{2^N}} e^{-\frac{(x-A(1+g_1))^2}{\left(2(1+g_1)\sigma^2\right)}} dx \tag{3-277}$$

Assuming $(x - A(1+g_1))/(1+g_1)\sigma = y$ we get:

$$(p_{31})_{(n_i)} = \left(\frac{1}{\sqrt{(2\pi)}} \right) \int_{\left[\frac{B+\frac{(n_1(A-B))}{2^N}-A(1+g_1)}{((1+g_1)\sigma)}\right]}^{\left[\frac{B+\frac{((n_1+1)(A-B))}{2^N}-A(1+g_1)}{((1+g_1)\sigma)}\right]} e^{-\frac{(y)^2}{(2)}} dy \tag{3-278}$$

which can be written as:

$$(p_{31})_{(n_i)} = \left(erf\left(\frac{\left(B + \frac{(n_1+1)(A-B)}{(2^N)} - A(1+g_1) \right)}{\left(\sqrt{2}\left((1+g_1)\sigma\right)\right)} \right) + \right. \\ \left. - erf\left(\frac{B + \frac{(n_1(A-B))}{(2^N)} - A(1+g_1)}{\left(\sqrt{2}\left((1+g_1)\sigma\right)\right)} \right) \right) \tag{3-279}$$

If $n_1 = 0$:

$$p_{310} = \left(\frac{1}{\sqrt{\left(2\pi\left((1+g_1)\sigma\right)^2\right)}} \right) \int_{-\infty}^{B+\frac{(A-B)}{2^N}} e^{-\frac{(x-A(1+g_1))^2}{\left(2(1+g_1)\sigma^2\right)}} dx \tag{3-280}$$

Assuming $(x - A(1+g_1))/(1+g_1)\sigma = y$ we get:

$$p_{310} = \left(\frac{1}{\sqrt{(2\pi)}}\right) \int_{-\infty}^{\left[\frac{B+\frac{((A-B))}{2^N} - A(1+g_1)}{((1+g_1)\sigma)}\right]} e^{-\frac{(y)^2}{(2)}} dy \tag{3-281}$$

which can be written as:

$$p_{310} = \frac{1}{2} \cdot \left(1 + erf\left(\frac{\left(B + \frac{(A-B)}{(2^N)} - A(1+g_1)\right)}{\left(\sqrt{2}((1+g_1)\sigma)\right)}\right)\right) \tag{3-282}$$

The probability that the output of the second accumulator to be greater than n_i is given by:

$$p_{(32n_i)} = \left(\frac{1}{\sqrt{\left(2\pi((1+g_2)\sigma)^2\right)}}\right) \int_{B+\frac{((n_1+1)(A-B))}{2^N}}^{\infty} e^{-\frac{(x-B(1+g_2))^2}{(2(1+g_2)\sigma^2)}} dx \tag{3-283}$$

Assuming $y = (x - B(1+g_2))/(1+g_2)\sigma$ we get:

$$p_{(32n_i)} = \left(\frac{1}{\sqrt{(2\pi)}}\right) \int_{\left[B+\frac{\frac{((n_1+1)(A-B))}{2^N} - B(1+g_2)}{((1+g_2)\sigma)}\right]}^{\infty} e^{-\frac{(y)^2}{(2)}} dy \tag{3-284}$$

which can be given:

$$p_{(32n_i)} = \frac{1}{2} \cdot \left(1 - erf\left(\frac{\left(B + \frac{(A-B)(n_i+1)}{(2^N)} - B(1+g_2)\right)}{\left(\sqrt{2}((1+g_2)\sigma)\right)}\right)\right) \tag{3-285}$$

when $n_1 = 0$, it can be expressed by:

$$p_{320} = \frac{1}{2} \cdot \left(1 - erf\left(\frac{\left(B + \frac{(A-B)}{(2^N)} - B(1+g_2)\right)}{\left(\sqrt{2}((1+g_2)\sigma)\right)}\right)\right) \tag{3-286}$$

Hence, the overall probability is:

$$p_3 = \frac{1}{2}\left(p_{310}p_{320} + \sum_{n_i=1}^{2^N-1} p_{(32n_i)}p_{(31n_i)}\right) \tag{3-287}$$

- Case d.

The transmitted data is 1, the probability of which is 0.5, in this case the ADC receives a random variable with mean $B(1+g_1)$ and variance $(1+g_1)^2\sigma^2$ in the first sampling instant, and another random variable with a mean $A(1+g_2)$ and variance $(1+g_2)^2\ \sigma^2$ in the second sampling interval.

Now to have the output of the first accumulator smaller than the output of the second accumulator, if the output of the first accumulator is n_1 (then, clearly $0 < n_1 \le 2^N$ - 1), and the output of the second accumulator is n_2 then $0 \le n_1 < n_2$.

The probability that the output of the first accumulator is n_1 (where $n_1 > 0$) is given by:

$$\left(p_{41}\right)_{(n_i)} = \left(\frac{1}{\sqrt{\left(2\pi\left((1+g_1)\sigma\right)^2\right)}}\right) \int_{B+\frac{(n_1(A-B))}{2^N}}^{B+\frac{(n_1+1)(A-B)}{2^N}} e^{-\frac{(x-B(1+g_1))^2}{\left(2(1+g_1)\sigma^2\right)}} dx \tag{3-288}$$

Assuming $y = (x - B(1+g_1))/(1+g_1)\sigma$ we get:

$$\left(p_{41}\right)_{(n_i)} = \left(\frac{1}{\sqrt{(2\pi)}}\right) \int_{\left[B+\frac{\frac{(n_1(A-B))}{2^N}-B(1+g_1)}{((1+g_1)\sigma)}\right]}^{\left[\frac{B+\frac{((n_1+1)(A-B))}{2^N}-B(1+g_1)}{((1+g_1)\sigma)}\right]} e^{-\frac{(y)^2}{(2)}} dy \tag{3-289}$$

which can be written as:

$$\left(p_{41}\right)_{(n_i)} = \frac{1}{2}\left(erf\left(\frac{\left(B+\frac{(n_1+1)(A-B)}{(2^N)}-B(1+g_1)\right)}{\left(\sqrt{2}\left((1+g_1)\sigma\right)\right)}\right) + - erf\left(\frac{B+\frac{(n_1(A-B))}{(2^N)}-B(1+g_1)}{\left(\sqrt{2}\left((1+g_1)\sigma\right)\right)}\right)\right) \tag{3-290}$$

This formula is valid for all n_1 which satisfy this condition: $0 < n_1 < 2^N - 1$, if $n_1 = 2^N - 1$, then (3-290) can be modified as:

$$\left(p_{41}\right)_{(2^N-1)} = \left(\frac{1}{\sqrt{\left(2\pi\left((1+g_1)\sigma\right)^2\right)}}\right) \int_{B+\frac{((2^N-1)(A-B))}{2^N}}^{\infty} e^{-\frac{(x-B(1+g_1))^2}{\left(2(1+g_1)\sigma^2\right)}} dx \tag{3-291}$$

Assuming $y = (x - B(1+g_1))/(1+g_1)\sigma$ we get:

$$\left(p_{41}\right)_{(n_i)} = \left(\frac{1}{\sqrt{(2\pi)}}\right) \int_{\left[B+\frac{\frac{((2^N-1)(A-B))}{2^N}-B(1+g_1)}{((1+g_1)\sigma)}\right]}^{\infty} e^{-\frac{(y)^2}{(2)}} \, dy \tag{3-292}$$

which can be written as:

$$\left(p_{41}\right)_{(2^N-1)} = \frac{1}{2}\cdot\left(1+erf\left(\frac{\left(B+\frac{(A-B)(2^N-1)}{(2^N)}-B(1+g_1)\right)}{\left(\sqrt{2}((1+g_1)\sigma)\right)}\right)\right) \tag{3-293}$$

The probability of the second accumulator to be less than n_1 is:

$$\left(p_{42}\right)_{(n_i)} = \left(\frac{1}{\sqrt{\left(2\pi((1+g_2)\sigma)^2\right)}}\right) \int_{-\infty}^{B+\frac{(n_1)(A-B)}{2^N}} e^{-\frac{(x-A(1+g_2))^2}{(2(1+g_2)\sigma^2)}} \, dx \tag{3-294}$$

Assuming $y = (x - A(1+g_2))/(1+g_2)\sigma$ we get:

$$\left(p_{42}\right)_{(n_i)} = \left(\frac{1}{\sqrt{(2\pi)}}\right) \int_{-\infty}^{\left[\frac{B+n_i\frac{((A-B))}{2^N}-A(1+g_2)}{((1+g_2)\sigma)}\right]} e^{-\frac{(y)^2}{(2)}} \, dy \tag{3-295}$$

which becomes:

$$\left(p_{42}\right)_{(n_i)} = \frac{1}{2}\cdot\left(1-erf\left(\frac{\left(B+\frac{(A-B)(n_i)}{(2^N)}-A(1+g_2)\right)}{\left(\sqrt{2}((1+g_2)\sigma)\right)}\right)\right) \tag{3-296}$$

when $n_1 = 2^N - 1$ it becomes:

$$\left(p_{42}\right)_{(2^N-1)} = \frac{1}{2}\cdot\left(1-erf\left(\frac{\left(B+\frac{(A-B)(2^N-1)}{(2^N)}-A(1+g_2)\right)}{\left(\sqrt{2}((1+g_2)\sigma)\right)}\right)\right) \tag{3-297}$$

Hence, the overall probability is:

$$p_3 = \frac{1}{2}\left(\left(p_{41(2^N-1)}p_{42(2^N-1)}\right)+\sum_{n_i=1}^{2^N-1} p_{(41n_i)}p_{(42n_i)}\right) \tag{3-298}$$

- Case e.

The transmitted data is 1, the probability of which is 0.5, in this case the ADC receives a random variable with mean $B(1+g_1)$ and variance $(1+g_1)^2\sigma^2$ in the first sampling instant, and another random variable with a mean $A(1+g_2)$ and variance $(1+g_2)^2\ \sigma^2$ in the second sampling interval. For both accumulators to have equal values both the random variables must lie in the same interval. This can be divided into three sub-cases:

Case e-1. $n_1 = n_2 = 0$.

The probability of this event can be expressed by:

$$p_{50} = \left(\frac{1}{\sqrt{\left(2\pi\left((1+g_1)\sigma\right)^2\right)}}\right)\int_{-\infty}^{B+\frac{(A-B)}{2^N}} e^{-\frac{(x-B(1+g_1))^2}{\left(2(1+g_1)\sigma^2\right)}}dx \times$$
$$\times\left(\frac{1}{\sqrt{\left(2\pi\left((1+g_2)\sigma\right)^2\right)}}\right)\int_{-\infty}^{B+\frac{(A-B)}{2^N}} e^{-\frac{(x-A(1+g_2))^2}{\left(2(1+g_2)\sigma^2\right)}}dx \tag{3-299}$$

Assuming $y_1 = (x - B(1+g_1))/(1+g_1)\sigma$ and $y_2 = (x - A(1+g_2))/(1+g_2)\sigma$ we get:

$$p_{50} = \left(\frac{1}{\sqrt{(2\pi)}}\right)\int_{-\infty}^{\left[\frac{B+\frac{((A-B))}{2^N}-B(1+g_1)}{((1+g_1)\sigma)}\right]} e^{-\frac{y_1^2}{2}}dy_1 \times \left(\frac{1}{\sqrt{(2\pi)}}\right)\int_{-\infty}^{\left[\frac{B+\frac{((A-B))}{2^N}-A(1+g_2)}{((1+g_2)\sigma)}\right]} e^{-\frac{y_2^2}{2}}dy_2 \tag{3-300}$$

which can be written as:

$$p_{50} = \frac{1}{4}\left\{\left(1+erf\left(\frac{\left(B+\frac{(A-B)}{2^N}-B(1+g_1)\right)}{\left(\sqrt{2}(1+g_1)\sigma\right)}\right)\right)\cdot \left(\left(1+erf\left(\frac{B+\frac{(B+(A-B))}{2^N}-A(1+g_2)}{\left(\sqrt{2}(1+g_2)\sigma\right)}\right)\right)\right)\right\} \tag{3-301}$$

Case e-2. $n_1 = n_2 = 2^N - 1$.

The probability of this event can be expressed by:

$$p_{5N} = \left(\frac{1}{\sqrt{\left(2\pi\left((1+g_1)\sigma\right)^2\right)}}\right)\int_{B+\frac{((2^N-1)(A-B))}{2^N}}^{\infty} e^{-\frac{(x-B(1+g_1))^2}{\left(2(1+g_1)\sigma^2\right)}}dx \times \tag{3-302}$$

$$\times\left(\frac{1}{\sqrt{\left(2\pi\left((1+g_2)\sigma\right)^2\right)}}\right)\int_{B+\frac{\left|\left(2^N-1\right)(A-B)\right|}{2^N}}^{\infty} e^{-\frac{(x-A(1+g_2))^2}{(2(1+g_2)\sigma^2)}}dx$$

Assuming $y_1=(x-B(1+g_1))/(1+g_1)\sigma$ and $y_2=(x-A(1+g_2))/(1+g_2)\sigma$ we get:

$$p_{5\mathrm{N}}=\left(\frac{1}{\sqrt{2\pi}}\right)\int_{\frac{\left[B+\frac{\left(\left(2^N-1\right)(A-B)\right)}{2^N}-B(1+g_1)\right]}{((1+g_1)\sigma)}}^{\infty} e^{-\frac{y_1^2}{2}}dy_1\times$$
$$\times\left(\frac{1}{\sqrt{2\pi}}\right)\int_{\frac{\left[B+\frac{\left(\left(2^N-1\right)(A-B)\right)}{2^N}-A(1+g_2)\right]}{((1+g_2)\sigma)}}^{\infty} e^{-\frac{y_2^2}{2}}dy_2 \tag{3-303}$$

which can be written as:

$$p_{5\mathrm{N}}=\frac{1}{4}\left\{\left(\left(1-erf\left(\frac{\left(B+\frac{(A-B)\left(2^N-1\right)}{2^N}-B(1+g_1)\right)}{\left(\sqrt{2}(1+g_1)\sigma\right)}\right)\right)\cdot\left(\left(1-erf\left(\frac{B+\frac{\left(\left(2^N-1\right)(A-B)\right)}{2^N}-A(1+g_2)}{\left(\sqrt{2}(1+g_2)\sigma\right)}\right)\right)\right)\right\} \tag{3-304}$$

Case e-3. $0<n_1=n_2<2^N-1$

The probability of this event can be expressed by:

$$p_{(5(n_i))}=\left(\frac{1}{\sqrt{\left(2\pi\left((1+g_1)\sigma\right)^2\right)}}\right)\int_{B+\frac{n_i(A-B)}{2^N}}^{B+\left(\frac{(n_i+1)(A-B)}{2^N}\right)} e^{-\frac{(x-B(1+g_1))^2}{(2(1+g_1)\sigma^2)}}dx\times$$
$$\times\left(\frac{1}{\sqrt{\left(2\pi\left((1+g_2)\sigma\right)^2\right)}}\right)\int_{B+\frac{n_i(A-B)}{2^N}}^{B+\left(\frac{(n_i+1)(A-B)}{2^N}\right)} e^{-\frac{(x-A(1+g_2))^2}{(2(1+g_2)\sigma^2)}}dx \tag{3-305}$$

Assuming $y_1=(x-B(1+g_1))/(1+g_1)\sigma$ and $y_2=(x-A(1+g_2))/(1+g_2)\sigma$ we get:

$$p_{(5(n_i))} = \left(\frac{1}{\sqrt{(2\pi)}}\right) \int_{\left[\frac{B+\left(\frac{n_i(A-B)}{2^N}\right)-A(1+g_1)}{(1+g_1)\sigma}\right]}^{\left[\frac{B+\frac{((n_i+1)(A-B))}{2^N}-B(1+g_1)}{((1+g_1)\sigma)}\right]} e^{-\frac{y_1^2}{2}} dy_1 \times$$
$$\times \left(\frac{1}{\sqrt{(2\pi)}}\right) \int_{\left[\frac{B+\left(\frac{n_i(A-B)}{2^N}\right)-B(1+g_2)}{(1+g_2)\sigma}\right]}^{\left[\frac{B+\frac{(n_i+1)((A-B))}{2^N}-A(1+g_2)}{((1+g_2)\sigma)}\right]} e^{-\frac{y_2^2}{2}} dy_2 \tag{3-306}$$

which can be written as:

$$p_{(5(n_i))} = \frac{1}{4} k_1 k_2 \tag{3-307}$$

where:

$$k_1 = erf\left(\frac{\left(B+\left(\frac{(n_1+1)(A-B)}{2^N}\right)\right)-B(1+g_1)}{\left(\sqrt{2}(1+g_1)\sigma\right)}\right) + \\ - erf\left(\frac{\left(B+\left(\frac{(n_1)(A-B)}{2^N}\right)\right)-B(1+g_1)}{\left(\sqrt{2}(1+g_1)\sigma\right)}\right) \tag{3-308}$$

where:

$$k_2 = erf\left(\frac{\left(B+\left(\frac{(n_1+1)(A-B)}{2^N}\right)\right)-A(1+g_2)}{\left(\sqrt{2}(1+g_2)\sigma\right)}\right) + \\ - erf\left(\frac{\left(B+\left(\frac{(n_1)(A-B)}{2^N}\right)\right)-A(1+g_2)}{\left(\sqrt{2}(1+g_2)\sigma\right)}\right) \tag{3-309}$$

Hence, the overall probability is:

$$p_5 = \frac{1}{2}\left(p_{50} + p_{5N} + \sum_{i=1}^{2^N-1} p_{(5n_i)}\right) \tag{3-310}$$

Case f.

The transmitted data is 1, the probability of which is 0.5, in this case the ADC receives a random variable with mean $B(1+g_1)$ and variance $(1+g_1)^2\sigma^2$ in the first sampling instant, and another random variable with a mean $A(1+g_2)$ and variance $(1+g_2)^2\ \sigma^2$ in the second sampling interval. Now to have the output of the first accumulator smaller than the output of the second accumulator, if the output of the first accumulator is n_1 (then, clearly $0 < n_1 \leq 2^N - 1$), and the output of the second accumulator is n_2 then $0 \leq n_1 < n_2$.

The probability that the output of the first accumulator is n_1 (where $n_1 > 0$) is given by:

$$(p_{61})_{(n_i)} = \left(\frac{1}{\sqrt{\left(2\pi\left((1+g_1)\sigma\right)^2\right)}}\right) \int_{B+\frac{(n_1(A-B))}{2^N}}^{B+\frac{(n_1+1)(A-B)}{2^N}} e^{-\frac{(x-B(1+g_1))^2}{\left(2(1+g_1)\sigma^2\right)}} dx \tag{3-311}$$

Assuming $y = (x - B(1+g_1))/(1+g_1)\sigma$ we get:

$$(p_{61})_{(n_i)} = \left(\frac{1}{\sqrt{(2\pi)}}\right) \int_{\left[B+\frac{(n_1(A-B))}{2^N}-B(1+g_1)\right]/((1+g_1)\sigma)}^{\left[B+\frac{((n_1+1)(A-B))}{2^N}-B(1+g_1)\right]/((1+g_1)\sigma)} e^{-\frac{(y)^2}{(2)}} dy \tag{3-312}$$

which can be written as:

$$(p_{61})_{(n_i)} = \left(erf\left(\frac{\left(B+\frac{(n_1+1)(A-B)}{(2^N)}-B(1+g_1)\right)}{\left(\sqrt{2}\left((1+g_1)\sigma\right)\right)}\right) + \right. \\ \left. - erf\left(\frac{B+\frac{(n_1(A-B))}{(2^N)}-B(1+g_1)}{\left(\sqrt{2}\left((1+g_1)\sigma\right)\right)}\right) \right) \tag{3-313}$$

If $n_1 = 0$, then (3-313) becomes:

$$p_{610} = \left(\frac{1}{\sqrt{\left(2\pi\left((1+g_1)\sigma\right)^2\right)}}\right) \int_{-\infty}^{B+\frac{(A-B)}{2^N}} e^{-\frac{(x-A(1+g_1))^2}{\left(2(1+g_1)\sigma^2\right)}} dx \tag{3-314}$$

Assuming $y = (x - B(1+g_1))/(1+g_1)\sigma$ we get:

$$p_{610} = \left(\frac{1}{\sqrt{(2\pi)}}\right) \int_{-\infty}^{\left[\frac{B+\frac{((A-B))}{2^N}-A(1+g_1)}{((1+g_1)\sigma)}\right]} e^{-\frac{y^2}{2}} dy \tag{3-315}$$

which can be written:

$$p_{610} = \frac{1}{2}\left(1 + erf\left(\frac{\left(B+\frac{(A-B)}{(2^N)}-B(1+g_1)\right)}{\left(\sqrt{2}((1+g_1)\sigma)\right)}\right)\right) \tag{3-316}$$

The probability that the output of the second accumulator to be grater than n_i is given by:

$$p_{62(n_i)} = \left(\frac{1}{\sqrt{\left(2\pi((1+g_2)\sigma)^2\right)}}\right) \int_{B+\frac{(n_i+1)(A-B)}{2^N}}^{\infty} e^{-\frac{(x-A(1+g_2))^2}{(2(1+g_2)\sigma^2)}} dx \tag{3-317}$$

Assuming $y = (x - A(1+g_2))/(1+g_2)\sigma$ we get:

$$p_{62(n_i)} = \left(\frac{1}{\sqrt{(2\pi)}}\right) \int_{\left[\frac{B+\left(\frac{(n_i+1)(A-B)}{2^N}\right)-A(1+g_2)}{(1+g)\sigma}\right]}^{\infty} e^{-\frac{y^2}{2}} dy \tag{3-318}$$

which can be given by:

$$p_{62(n_i)} = \frac{1}{2}\cdot\left(1 - erf\left(\frac{\left(B+\frac{(A-B)(n_i+1)}{(2^N)}-A(1+g_2)\right)}{\left(\sqrt{2}((1+g_2)\sigma)\right)}\right)\right) \tag{3-319}$$

If $n_1 = 0$, then (3-319) becomes:

$$p_{620} = \frac{1}{2}\cdot\left(1 - erf\left(\frac{\left(B+\frac{(A-B)}{(2^N)}-A(1+g_2)\right)}{\left(\sqrt{2}((1+g_2)\sigma)\right)}\right)\right) \tag{3-320}$$

Hence, the overall probability is:

$$p_6 = \frac{1}{2}\left(p_{610}p_{620} + \sum_{n_i=1}^{2^N-1} p_{(61n_i)}p_{(62n_i)}\right) \tag{3-321}$$

It was verified using Matlab that:

$$p_1 + p_2 + p_3 + p_4 + p_5 + p_6 = 1 \tag{3-322}$$

The overall probability is given by:

$$p = p_3 + p_4 + 0.5(p_2 + p_5) \tag{3-323}$$

and for N_s (where N_s is odd), the overall probability is:

$$P = \sum_{k=\frac{N_s+1}{2}}^{N_s} (N_s) C_k p^k (1-p)^{N_s-k} \tag{3-324}$$

where C indicates combinations. Figure 3-71 shows good resemblance between the calculated results and the simulated values obtained using Matlab.

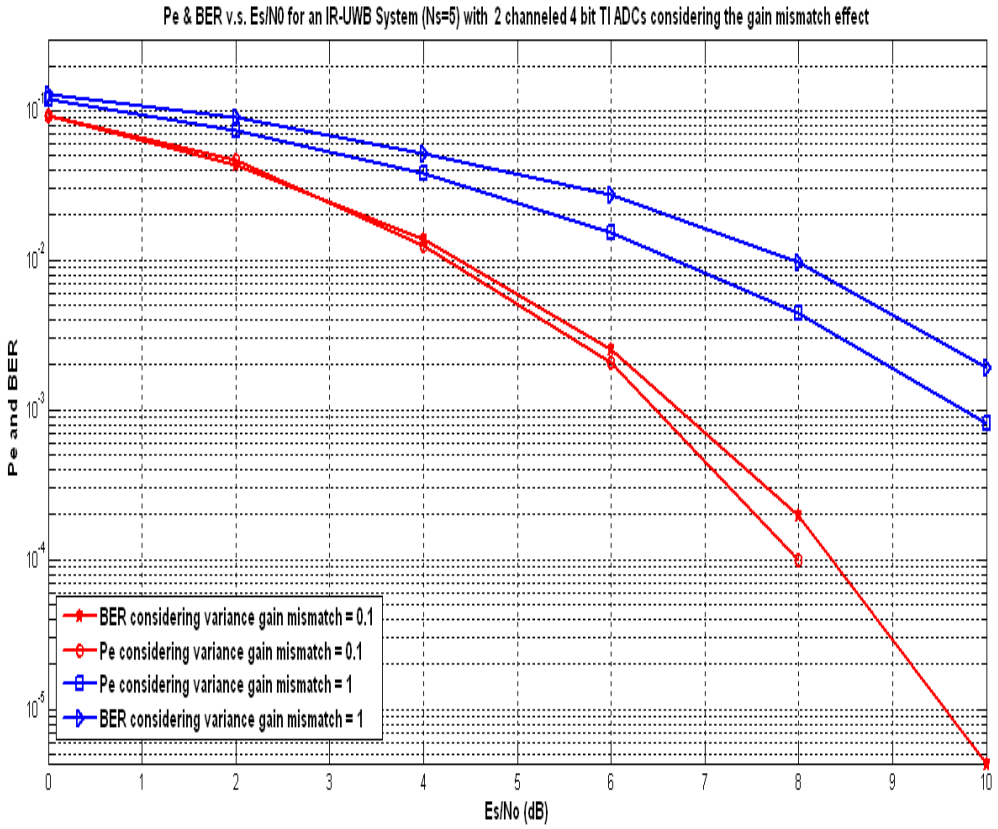

Figure 3-71: Comparison between BER and Pe for an IR-UWB System considering the effect of Gain Mismatch in two channeled 4 bit TI ADCs with variance of mismatch of 0.1 and of 1 respectively

3.3.13.7.2.2 Effect of offset mismatch

In this case, every channel introduces an offset voltage which can be modeled as a Gaussian random variable with mean 0 and variance σ_{off} .

Clearly this effect can be modeled using the same equations ((3-255) to (3-324)) derived above, by just substituting $g_1 = g_2 = 0$, and $\sigma^2 = \sigma_{off}^2 + \sigma_{noise}^2$.

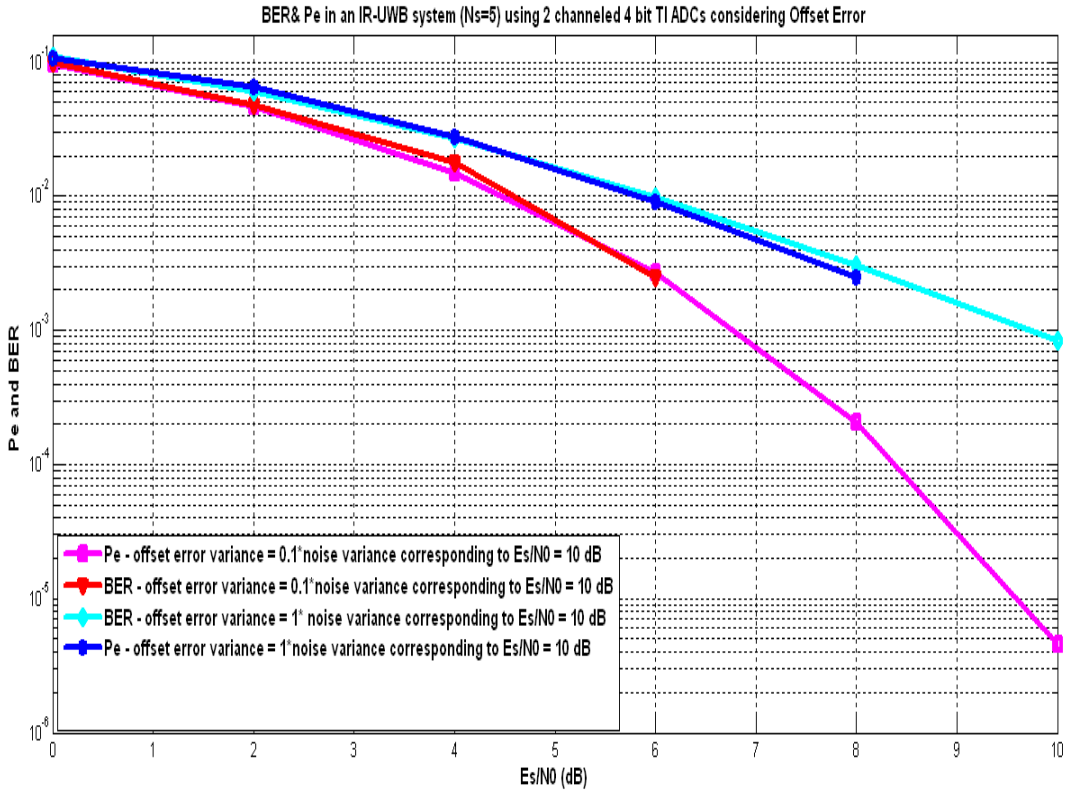

Figure 3-72: Comparison between BER and Pe for an IR-UWB System considering the effect of Offset Error in two channeled 4 bit TI ADCs with a variance of 0.1 time, of 1 times of the noise variance corresponding to a Es/N0 of 10 dB

3.3.13.7.2.3 Effect of Clock Skew

We get the pulse shape as:

$$w(t) = A\left(1 - 4\pi\left(\frac{t}{\tau}\right)^2\right)e^{\left(-2\pi\left(\frac{t}{\tau}\right)^2\right)} \tag{3-325}$$

In order to investigate this effect, we assumed that the clock is shifted such that for the first ADC instead of sampling at t = 0, it is sampled at t = r_1, where r_1 is a Gaussian random variable with mean 0 and variance σ_s^2, and whose value does not change with time. Hence, clearly, the value of the sample (assuming no noise) obtained is:

$$w(r_1) = A\left(1 - 4\pi\left(\frac{r_1}{\tau}\right)^2\right)e^{\left(-2\pi\left(\frac{r_1}{\tau}\right)^2\right)} \tag{3-326}$$

If we assume that this is $(1 + g_1)$ times the original sample, then g_1 can be calculated as:

$$g_1 = \left(1 - 4\left(\frac{r_1}{\tau}\right)^2\right)e^{\left(-2\pi\left(\frac{r_1}{\tau}\right)^2\right)} - 1 \tag{3-327}$$

Also, we assume that for the second ADC, instead of sampling at $t = \sqrt{\left(\frac{3}{4\pi}\right)}\tau$, it samples at $t = \sqrt{\left(\frac{3}{4\pi}\right)}\tau + r_2$, where r_2 is a Gaussian random variable with mean 0 and variance σ_s^2, and whose value does not change with time. Hence, the value of the sample (assuming no noise) obtained is:

$$w\left(\sqrt{\left(\frac{3}{(4\pi)}\right)}\tau + r_2\right) = A\left(1 - 4\pi\left(\frac{\left(\sqrt{\left(\frac{3}{4\pi}\right)}\tau + r_2\right)^2}{\tau}\right)\right)e^{\left(-2\pi\left(\frac{\left(\sqrt{\left(\frac{3}{4\pi}\right)}\tau + r_2\right)^2}{\tau}\right)\right)} \tag{3-328}$$

If we assume that this is $(1 + g_2)$ times the original sample, then g_2 can be calculated as:

$$g_2 = \frac{\left(\left(1 - 4\pi\left(\frac{\left(\sqrt{\left(\frac{3}{4\pi}\right)}\tau + r_2\right)^2}{\tau}\right)\right)\right)\left(e^{-2\pi\left(\frac{\left(\sqrt{\frac{3}{4\pi}}\tau + r_2\right)^2}{\tau}\right)}\right)}{\left(\left(1 - 4\pi\left(\frac{\left(\sqrt{\frac{3}{4\pi}}\tau\right)^2}{\tau}\right)\right)\left(e^{-2\pi\left(\frac{\left(\sqrt{\frac{3}{4\pi}}\tau + r_2\right)^2}{\tau}\right)}\right)\right)} - 1 \tag{3-329}$$

which can be written as:

$$g_2 = -2.24 \times \left(\left(1 - 4\pi \left(\frac{\left(\sqrt{\frac{3}{4\pi}}\tau + r_2 \right)^2}{\tau} \right) \right) \right) e^{\left(-2\pi \left(\frac{\left(\sqrt{\left(\frac{3}{4\pi} \right)}\tau + r_2 \right)^2}{\tau} \right) \right)} - 1 \qquad (3\text{-}330)$$

We cannot put the values of g_1 and g_2 obtained in (3-327) and (3-330) in (3-256) to (3-324) directly, as only the mean value is increased $(1+g_1)$ or $(1+g_2)$ times but not the noise variance. Therefore, we need to recalculate the error probabilities: the calculations will be very similar to those developed in (3-256) up to (3-324), substituting σ_s^2 instead of variance $(1+g_1)^2\sigma^2$ and $(1+g_2)^2\ \sigma^2$. The simulated and calculated data are compared in Figure 3-73.

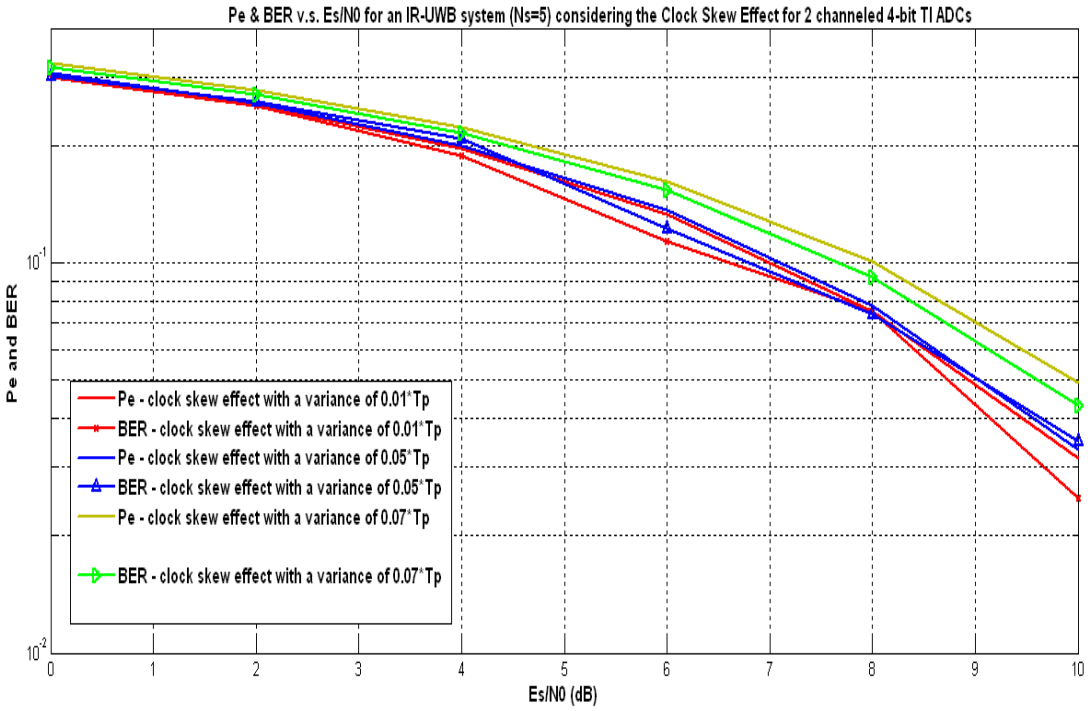

Figure 3-73: Comparison between Pe and BER Curves for an IR-UWB System considering the Effect of Clock Skew in two Channeled 4 bit TI ADCs

3.3.13.7.2.4 Effect of Timing Jitter

Apart from the clock skew, which does not change with time, there is a random white jitter, which is a Gaussian process and whose value is time-invariant.

To model white jitter, we remember that:

$$w(t) = A\left(1 - 4\pi\left(\frac{t}{\tau}\right)^2\right)e^{\left(-2\pi\left(\frac{t}{\tau}\right)^2\right)} \tag{3-331}$$

We model timing jitter by a Gaussian random variable s as it follows:

$$w(t) = A\left(1 - 4\pi\left(\frac{t+s}{\tau}\right)^2\right)e^{\left(-2\pi\left(\frac{t+s}{\tau}\right)^2\right)} \tag{3-332}$$

For the first sample at $t = 0$, (3-332) can be written as:

$$w(0) = A\left(1 - 4\pi\left(\frac{s}{\tau}\right)^2\right)e^{\left(-2\pi\left(\frac{s}{\tau}\right)^2\right)} \tag{3-333}$$

If we assume that s is very small as compared to τ, we can write:

$$e^{\left(-2\pi\left(\frac{s}{\tau}\right)^2\right)} \cong 1 - 2\pi\left(\frac{s}{\tau}\right)^2 \tag{3-334}$$

Inserting (3-333) into (3-332), and neglecting higher terms, we get:

$$w(0) = A\left(1 - 6\pi\left(\frac{s}{\tau}\right)^2\right) = A(1 + g_1) \tag{3-335}$$

where:

$$g_1 = -6\pi\left(\frac{s}{\tau}\right)^2 \tag{3-336}$$

since we assumed that s is a Gaussian distributed, then g_1 must be Chi-Squared distributed [3-55]. For the second sample at $t = \sqrt{\left(\frac{3}{4\pi}\right)}\tau$, we get:

$$w\left(\sqrt{\left(\frac{3}{(4\pi)}\right)}\tau\right) = A\left(1 - 4\pi\left(\frac{\left(\sqrt{\left(\frac{3}{4\pi}\right)}\tau + s\right)^2}{\tau}\right)\right)e^{\left(-2\pi\left(\frac{\left(\sqrt{\left(\frac{3}{4\pi}\right)}\tau + s\right)^2}{\tau}\right)\right)} \tag{3-337}$$

which can be written as:

$$w\left(\sqrt{\left(\frac{3}{(4\pi)}\right)}\tau\right) = A\left(1 - 4\pi\left(\sqrt{\left(\frac{3}{4\pi}\right)} + \frac{s}{\tau}\right)^2\right)e^{\left(-2\pi\left(\sqrt{\frac{3}{4\pi}} + \frac{s}{\tau}\right)^2\right)} \tag{3-338}$$

The effect of timing jitter is shown in Figure 3-74.

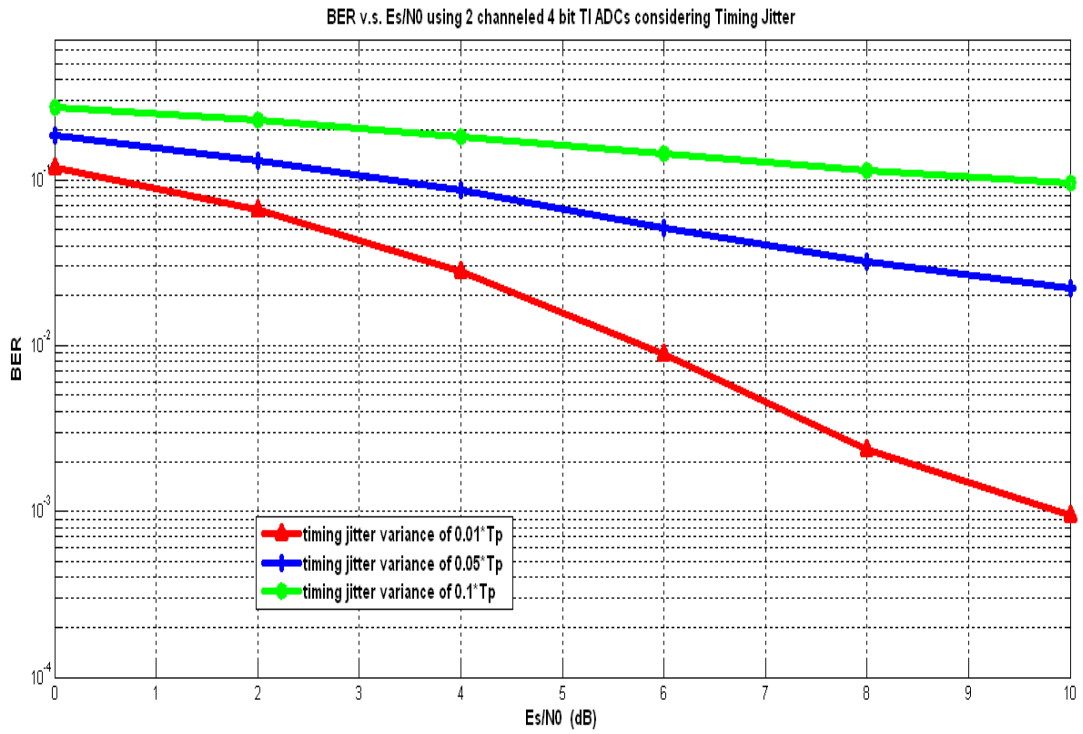

Figure 3-74: BER Curves vs. Es/N0 for an IR-UWB System considering the Timing Jitter effect in two channeled 4 bit TI ADCs with a variance of 0.01*Tp, of 0.05*Tp and 0.1*Tp

3.3.13.7.2.5 Effect of all four non-idealities on an IR-UWB system based on Time Interleaved ADCs

The effects of all four non-idealities considered together on an IR-UWB Communication System based on two channeled 4 bit Time Interleaved ADCs are shown in Figure 3-75.

3.3.13.7.2.6 BER calculations for a M channeled Time Interleaved ADC

The analysis for a 2 channeled Time Interleaved ADC can be extended to a *M* channeled Time Interleaved ADC (where *M* is even). In this case we assume that for each chip two samplings are done by two different ADCs at sampling times. Assuming an user has a time hopping code of cardinality N_c and periodicity N_p. We define the overall chip number (OCN) for a pulse *j* as:

$$OCN = N_p \times (FrameNumber - 1) + c_j \tag{3-339}$$

and this pulse will be sampled by two ADCs which are given by m and $m + 1$, where m is the remainder when $2OCN + 1$ is divided by M.

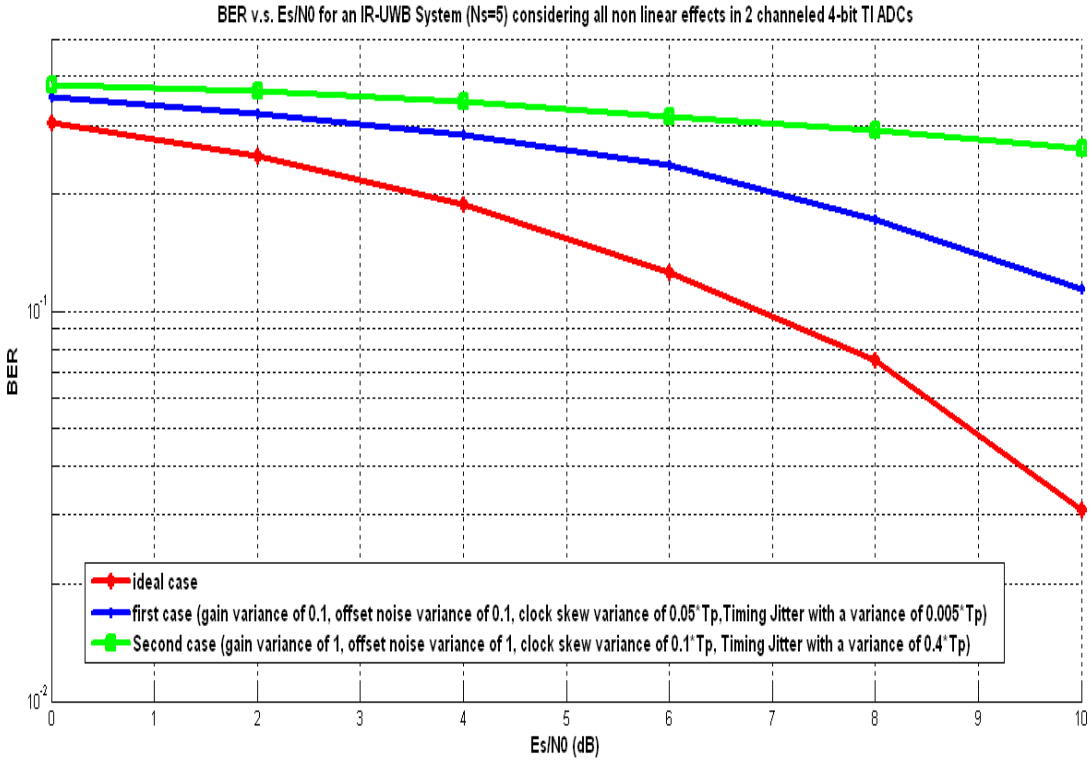

Figure 3-75: BER vs. Es/N0 for an IR-UWB Communication System considering all effects in two channeled 4 bit TI ADCs

- **Effect of gain mismatching**

The basic analysis is same as that done above: we can replace g_1 and g_2 by g_m and g_{m+1} and use equations (3-253) to (3-321) in order to determine p. However, we cannot use (3-322) directly to calculate the overall probability of error since the value of p depends on m and $m+1$, which in turn depend on frame number and c_j. So if there are five frames in one bit, it is possible that all five frames may have different values of p. If we assume that $Ns = 5$, we can write:

$$P = P_1 + P_2 + P_3 \tag{3-340}$$

where:

$$P_1 = p_1 p_2 p_3 p'_4 p'_5 + p_1 p_2 p'_3 p'_4 p_5 + p_1 p'_2 p'_3 p_4 p_5 + p'_1 p_2 p_3 p_4 p'_5 + p_1 p_2 p'_3 p'_4 p_5 + p_1 p'_2 p_3 p'_4 p_5 + p'_1 p_2 p_3 p'_4 p_5 + p'_1 p_2 p'_3 p_4 p_5 + p_1 p'_2 p'_3 p_4 p_5 + p'_1 p'_2 p_3 p_4 p_5 \tag{3-341}$$

and:

$$p' = 1 - p \tag{3-342}$$

$$P_2 = \bar{p}'_1 p_2 \bar{p}_3 p_4 p_5 + p_1 p'_2 p_3 p_4 p_5 + p_1 p_2 p'_3 p_4 p_5 + p_1 p_2 p_3 p'_4 p_5 + p_1 p_2 p_3 p_4 p'_5 \tag{3-343}$$

$$P_3 = p_1 p_2 p_3 p_4 p_5 \tag{3-344}$$

The performance of a 2-channel, 6-channel and 10-channel 4 bit Time Interleaved ADCs are compared in Figure 3-76.

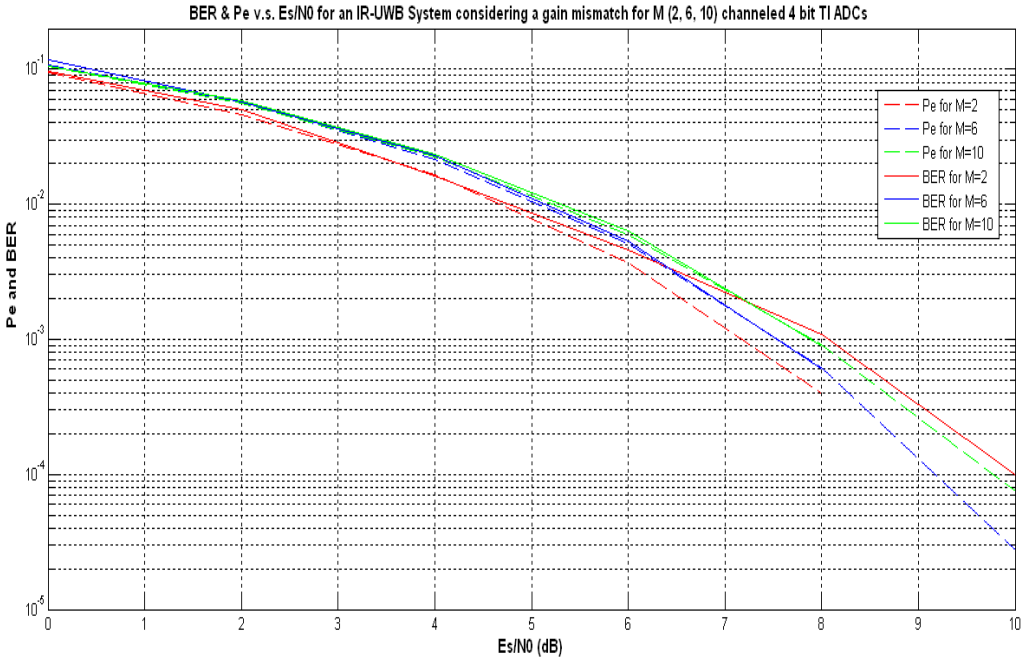

Figure 3-76: Comparison between BER and Pe for a gain mismatched M channeled 4 bit TI ADCs considering M = 2, M = 6 and M = 10

- **Effect of Offset mismatching**

Since offset error is totally random and time changing, it is independent of *M*, and therefore can be treated exactly like above.

- **Effect of Clock skew**

The computation is similar to that described above, only r_1 and r_2 will be replaced by r_m and r_{m+1}. (3-340) should be used instead of (3-324) for Probability of Error calculation. The performance of a 2-channel, 6-channel and 10-channel 4 bit Time Interleaved ADCs are compared in Figure 3-77 considering the clock skew effect.

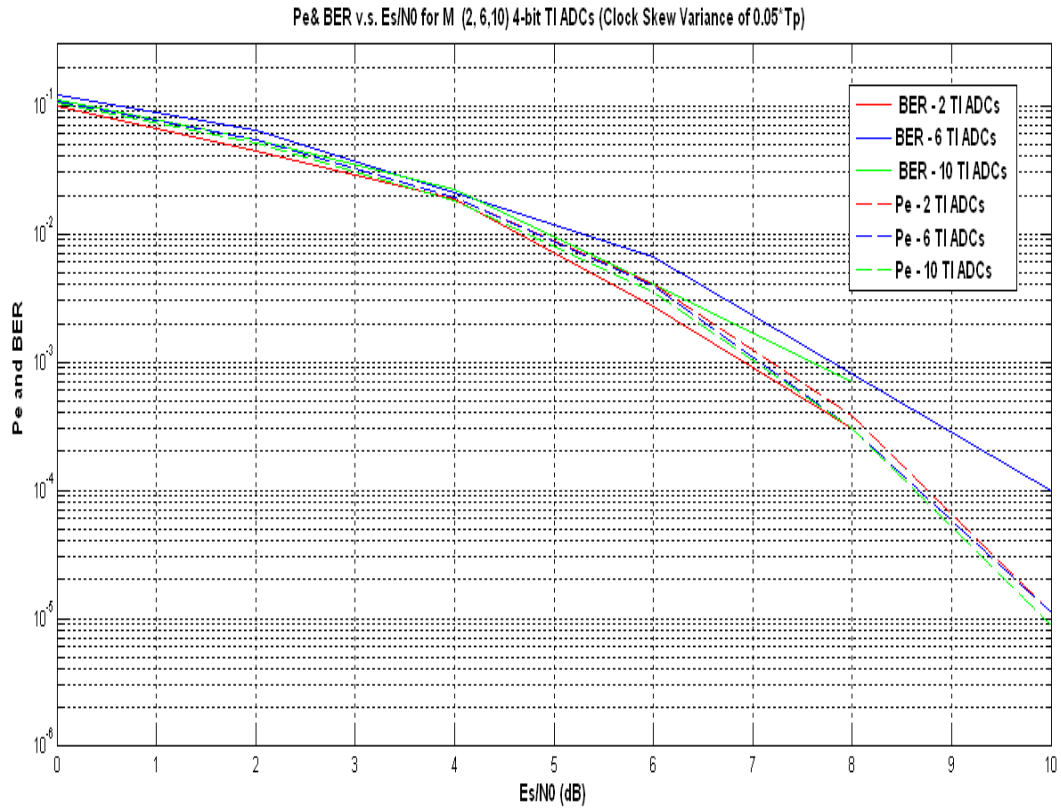

Figure 3-77: Comparison between BER and Pe for an IR-UWB System using a M channeled 4 bit TI ADC considering the clock skew effect

- **Timing Jitter**

Just like offset, timing jitter is also totally random and time changing, so the treatment would be same as done above.

3.4 CONCLUSIONS

Excessive phase noise and I/Q imbalance at frequencies beyond 60 GHz, together with the relatively high cost and difficulties to high component integration at those frequencies, make the design of the RF architecture a challenging topic which cannot be disjoint anymore from the choice of the transmission techniques. IR-UWB provides some degrees of flexibility in the choice of the front-end architecture. Nevertheless, also the alternatives solutions have their drawbacks which must be carefully evaluated before drawing a final conclusion. However, this chapter mainly aimed to focus the attention of the use of UWB in W band as a promising approach. Moreover, a phase noise, LNA and HPA evaluation of

the BER degradation for IR-UWB architecture operating at beyond 60 GHz (in particular, 85 GHz) has been carried out. The evaluations show that IR-PPM-UWB is robust to the additive jitter due to the typical phase noise of oscillators and mixers and distortions due to HPA at W band. Moreover, this sensitivity is less than the one observed in other modulations such as B-FSK considering the same data rate.

Future analyses and developments could be focused also on the antennas to be used relating them to the pulse source employed since both are strictly interlaced and affect the overall system performance.

One of the main problems of IR-UWB applied to beyond 60 GHz is that the over-sampling of such pulses requires extremely high-speed ADCs.

In accordance with the Nyquist theorem, the ADC sampling rate for digitizing a UWB signal at such high frequencies must be on the order of a few gigasamples/s. Even with the most modern process technologies, this constitutes a serious challenge. Most reported data converters operating at this speed employ interleaving [3-49] [3-50], with each channel typically based on a FLASH converter. The latter is the architecture of choice for high-speed designs, but is not suitable for high-resolution applications [3-51]. An n bit FLASH converter uses $2n$ comparators so its power and area scale exponentially with resolution. Among recently reported high-speed ADCs (>1 Gigasample) representing the state of the art [3-50], [3-52], none has a resolution exceeding 8 bits. The minimum number of bits needed for reliable detection of a UWB signal is, therefore, a critical parameter. If excessively large, it can render an “all-digital” receiver infeasible.

On the other hand, operations such as synchronization, equalization, demodulation and decoding are then performed in the digital domain, greatly enhancing the flexibility available to the designer. We would like to scale this “mostly digital” paradigm to multi-Gigabit speeds, in order to enable mass market multi-Gigabit WLANs and WPANs based on large amounts of unlicensed bandwidth available for communications beyond 60 GHz. The bottleneck in such scaling becomes the ADC: high-speed, high-precision ADC is either unavailable, or is too costly and power-hungry.

To counteract this problem, high speed but low precision ADCs are widely used. However, it has been seen that using low precision ADCs (1 bit in the worst case) results in severe degradations of the system performance.

Firstly, this work has analysed performance for an analog and n bit digital UWB receiver and compare them. Secondly, two solutions (i.e. channel estimation and adaptive coding and ignoring indecision bits) have been proposed based on the results described in 3.3.13.5

in order to improve the performance of the system with 1 bit ADC. Finally, four major non-idealities (gain mismatch, offset error, timing jitter and clock skew) have been modeled for M channels TI ADCs solutions in IR-UWB systems.

3.5 REFERENCES

[3-1] [ITURR2008] International Telecommunication Union (ITU), "Radio Regulations", edition of 2008.

[3-2] [ETSI06] ETSI DTR/ERM-RM-049, 'Electromagnetic Compatibility and Radio Spectrum Matters (ERM); System Reference Document; Technical Characteristics of Multiple Gigabit Wireless Systems in the 60 GHz Range', March 2006.

[3-3] [ERC1209] ERC Recommendation 12-09, "Radio Frequency Channel Arrangement for Fixed Service Systems Operating in the Band 57.0 - 59.0 GHz Which Do Not Require Frequency Planning, The Hague 1998 revised Stockholm", October 2004.

[3-4] [ECC0502] ECC Recommendation (05)02, "Use of the 64-66 GHz Frequency Band for Fixed Service", February 2009.

[3-5] [ECC0901] ECC Recommendation (09)01, Use of the 57-64 GHz Frequency Band for Point-to-Point Fixed Wireless Systems, January 2009.

[3-6] [ERC7003] ERC RECOMMENDATION 70-03, "Relating to the use of Short Range Devices (SRD)", Annex 3 Band E, Wideband Data Transmission systems 57-66 GHz.

[3-7] [FCC] Federal Communication Commissions, Code of Federal Regulation, title 47 Telecommunication, chapter 1, part 15.255, October 2004.

[3-8] [ECC0507] ECC Recommendation (05)07, Radio Frequency Channel Arrangements for Fixed Service Systems Operating in the Bands 71-76 GHz and 81-86 GHz, February 2009.

[3-9] Y.Kawano et al, "Sub-10 ps Pulse Generator with Biphase Modulator Function in 0.13 μm InP HEMT", Proceedings of the 3rd European Radar Conference, September 2006, pp. 342-345.

[3-10] Y. Nakasha, Y. Kawano, T. Suzuki, T. Ohki, T. Takahashi, K. Makiyama, T. Hirose, and N. Hara "A W-band Wavelet Generator Using a 0.13-μm InP HEMTs for Multigigabit Communications Based on Ultra-Wideband Impulse Radio," Microw. Symposium Digest, 2008 IEEE MTT-S International Volume, Issue, 15-20 June 2008, pp.109-112.

[3-11] C. Stallo, Lucente, T. Rossi, D. Valente, E. Cianca, M. Ruggieri, S. Barbera, 2009, "UWB concepts applied to W band Telecommunications", IEEE International Siberian Conference on Control and Communications (SIBCON) 2009, Tomsk, Russia, March, 27-28, 2009.

[3-12] M. Morgan, et. al., "Ultra-wideband impulse scattering measurements", IEEE Transactions on Antennas and Propagation, 42, 840-846, 1994.

[3-13] K. Hyunseok, J. Youngjoong, J. Sungyong, "Analytical Model of Pulse Combined UWB Pulse Generator", 4th International Conference on Wireless Communications, Networking and Mobile Computing, 2008 (WiCOM '08), pp. 1-4, 2008.

[3-14] J. Lee, C. Ngyuen and T. Sullicon, "New uniplanar subnanosecond monocycle pulse generator and transformer for time-domain microwave applications", IEEE Transactions on Microwave Theory and Techniques, Vol. 49, no. 6, 2001.

[3-15] C. Zhang, A. E. Fathy, "Reconfigurable Pico-Pulse Generator for UWB Applications", IEEE International Microwave Symposium Digest 2006, pp. 407-410, 2006.

[3-16] J. S. Lee, C. Ngyuen and T. Sullicon, "Novel low-cost ultra-wideband, ultra-short-pulse transmitter with MESFET impulse-shaping circuitry for reduced distortion and improved pulse repetition rate", IEEE Microwave and Wireless Components Letters, Vol. 11, pp. 208-210, 2001.

[3-17] J. W. McCorkle, "Ultra-wideband Communication System, Method, and Device With Low Noise Pulse Formation", World Intellectual Property Organization WO 01/93520 A2.

[3-18] S. Tiuraniemi, "Method and Arrangement For Generating Cyclic Pulses", United States Patent Application 10/304915.

[3-19] J. Li et. al., "A CMOS Ultra-WideBand Impulse Generator for 22-29 GHz Automotive Radar Application", IEEE Radar Conference 2009, pp. 1-4, May 2009.

[3-20] P. K. Saha, N. Sasaki and T. Kikkawa, "A CMOS Monocycle Pulse Generation Circuit in a Ultra-Wideband Transmitter for Intra/Inter Chip Wireless Interconnection", Japanese Journal Applied Physics, Vol. 44, pp. 2104-2108, 2005.

[3-21] G. S. Biradar et all, "Frequency and Time Hopping PPM UWB Multiple Access Communication Scheme", Journal of Communications, Vol. 4, no. 1, February 2009.

[3-22] J. Rutman and G. Gauvage, "Measurement of frequency stability and frequency domains via filtering of phase noise", IEEE Transactions Instrument Measurements, vol. IM-23, Dec. 1974.

[3-23] J. F. Luy, and P. Russer, Eds., "Future Applications in Silicon-Based Millimeter Wave Devices". Springer, Berlin, Germany, 1994.

[3-24] J. Bock et all, "SiGe bipolar technology for automotive radar applications", in Bipolar/BiCMOS Circuits and Technology, 2004. Proceedings of the 2004 Meeting, pp. 84-87.

[3-25] M. Racanalli and P. Kempf, "SiGe BICMOS technology for RF circuit applications", IEEE Transactions on Electron Devices, vol. 52, no. 7, pp. 1259-1270, 2005.

[3-26] G. Freeman, et all, "Transistor Design and application considerations for > 200 GHz SiGe HBTs", IEEE Transactions on Electron Devices, vol. 50, no. 3, pp. 645-655, 2003.

[3-27] B. V. Haaren et all, "Low-frequency noise properties of SiGe HBT's and application to ultra-low phase noise oscillators," IEEE Transactions on Microwave Theory and Techniques, vol. 46, pp. 647-652, May 1998.

[3-28] M. Gris, "Wideband Low Phase Noise Push-Push VCO', Applied Microwave & Wireless, pp. 28-32, Jan 2000.

[3-29] H. C. Chang, et all, "Phase Noise in Coupled Oscillators: Theory and Experiment," IEEE Transactions on Microwave Theory and Techniques, vol. 45, pp. 604-615, May 1997.

[3-30] J. C. FuenZalida, O. Shimbo, and W. L. Cook, "Time domain analysis of intermodulation effects caused by nonlinear amplifiers," COMSAT Technical Review, vol.3, no. 2, Spring 1973.

[3-31] A. N. Andrea, V. Lottici, and R. Reggiannini, "RF power amplifier linearization through amplitude and phase distiortion," IEEE Trans. Commun., vol. 44, no. 11, Nov. 1996.

[3-32] O. Shimbo, "Effects of intermodulation, AM-PM conversion, and additive noise in multicarrier TWT systems," Proc. IEEE, vol. 59, no. 2, Feb. 1971.

[3-33] A. A. M. Saleh, "Frequency-independent and frequency-dependent non linear models of TWT amplifiers", IEEE Trans. Commun., vol. Com-29, no. 11, Nov. 1981.

[3-34] J. K. Cavers, "The effects of Data Modulation Format on Intermodulation Power in Nonlinear Amplifiers", IEEE Transactions on Communications, pp. 489-493, March 1994.

[3-35] A. A. Abidi, "Direct Conversion Radio Transceivers for Digital Communications", IEEE Journal of Solid State Circuits, Vol: 30, Issue: 12, December 1995, pp. 1399-1410.

[3-36] X. Gao, R. Yao, and Z. Feng, "Multi-band uwb system with hadamard coding," IEEE Vehicular Technology Conference, vol. 2, pp. 1288–1292, Oct. 2003.

[3-37] Liu, T. and Wang, C., "A 1-4 GHz DLL based low-jitter multi-phase clock generator for low-band ultra-wideband application," IEEE Asia-Pacific Conference on Advanced Systems Integrated Circuits, pp. 330–333, Aug. 2004.

[3-38] U. Onunkwo, and Y. G. Li, "On the optimum pulse-position modulation index for ultra-wideband communication," in Proceedings IEEE Circuits and Systems Symposium Emerging Technology: Frontiers of Mobile and Wireless Communications, vol. 1, pp. 77–80, May-June 2004.

[3-39] Z. N. Chen, "UWB Antennas: Design and Applications", International Conference on Information, Communications and Signal Processing - ICICS 2007, December 10-13, 2007 – Singapore.

[3-40] X.H.Wu, Z.N.Chen, M.Y.W. Chia, "Note on Antenna Design in UWB Wireless Communication Systems", Dept. of Radio Systems, Institute for Infocomm Research – Dept of Electrical and Computer Engineering.

[3-41] Z. N. Chen et al., "Considerations for Source Pulses and Antennas in UWB Radio Systems", IEEE Transactions on Antennas and Propagation, Vol. 52, n.7, July 2004.

[3-42] O'Donnell, M. Chen, S. Wang and R. W. Brodersen, "An Integrated, Low- Power, Ultra-Wideband Transceiver Architecture for Low-Rate, Indoor Wireless Systems," IEEE CAS Workshop on Wireless Communications and Networking, September 2002.

[3-43] C. Gangyaokuang and S. Zhonglianglu, "A Way of Multichannel AID for UWB Signal,'' IEEE NAECON 1995, Vol. 1, pp. 206-209, May 22-26, 1995.

[3-44] H. J. Lee and D. S. Ha, "Frequency Domain Approach for CMOS Ultra-Wideband Radios," VLSI, 2003 IEEE Computer Society Annual Symposium, pp. 236-237, February 20-21,2003.

[3-45] A. Tanaka et al., "A 1.1v 3.1-to-9.5GHz MB-OFDM UWB transceiver in 90nm CMOS," IEEE International Solid-State Circuits Conference (ISSCC) Dig. Tech. Papers, vol. 49, pp. 120–121, Feb. 2006.

[3-46] C. Sandner et al., "A WidMedia/MBOA-Compliant CMOS RF transceiver for UWB," IEEE International Solid-State Circuits Conference (ISSCC) Dig. Tech. Papers, vol. 49, pp. 122–123, Feb. 2006.

[3-47] M. S. Chen and R. W. Brodersen, "Implementation Considerations for a Sub sampling Impulse Radio", Proceedings of the IEEE International Conference on Ultra Wideband, September, 2006.

[3-48] M. S. Chen and R.W. Brodersen, "A Subsampling Radio Architecture for 3-10 GHz UWB", Berkley Wireless Research Centre.

[3-49] P. P. Newaskar, R. Blazquez and A. P. Chandrakasan, "A/D Precision Requirements for an ultra-wideband radio receiver".

[3-50] W. Ellersick, Chih-Kong Ken Yang, W. Horowitz and W. Dally, "GAD: A 12Gs/s CMOS 4-bit A/D converter for an equalized multi-level link," in Symposium on VLSI Circuits, 1999, Digest of Technical Papers , 1999, pp. 49–52.

[3-51] B. Razavi, Principles of Data Conversion System Design , IEEE Press, 1995.

[3-52] K. Poulton *et al.*, "An 8-G Sample/s 8-bit ADC system," in VLSI Symposium on Circuits , June 1997

[3-53] R. A. Scholtz, "Multiple Access with Time-Hopping Impulse Modulation".

[3-54] G. Leger, E. J. Peralias, A. Rueda and J. L. Huertas, "Impact of Random Channel Mismatch on the SNR and SFDR of Time Interleaved ADCs", IEEE Transactions on Circuits and Systems, Vol. 51, No 1, January 2004, pp. 140-150.

[3-55] N. Kurosawa, K. Maruyama, H. Kobayashi, H. Sugawara and K. Kobayashi, "Explicit Formula for Channel Mismatch Effects in Time Interleaved ADCs", Proceedings of IEEE Instrumentation and Measurement Technology Conference, 2000.

[3-56] J. G. Proakis, "Digital Communications", 3rd Edition, McGraw Hill, 1995.

[3-57] J. Singh, S. Ponnuru and U. Madhow, "Multigigabit Communications: The ADC Bottleneck", ICUWB 2009.

[3-58] R. Walden, "Analog-to-Digital Converter survey and analysis", IEEE Journal on Selected Areas of Communication, 17(4):539–550, April 1999.

[3-59] R. A. Scholtz, "Multiple Access with Time Hopping Impulse Modulation", in Proceedings of IEEE MILCOM 1993, October 1993, Vol. 2, pp.447–450.

4 W BAND TERRESTRIAL RADIO LINK DESIGN

Nowadays W band is an experimental frontier since no satellite telecommunication mission has been developed and the technology at those frequencies is still poor and relatively not ready.

In this framework, a preliminary useful step toward the W band exploitation in satellite telecommunications is represented by the analysis and the validation of a terrestrial link operating at those frequencies with the capability to carry out transmission/reception experiments. Such experiment could give important feedback from the technology point of view and also for the channel characterisation.

In this frame, the University of Rome "Tor Vergata" in collaboration with the company Rheinmetall Italy is carrying out an experiment to investigate a W band terrestrial point-to-point link over a distance of around 7.4 km. Many technological issues have to be faced.

This chapter presents an overview of preliminary design of an experimental W band terrestrial air link between "Tor Vergata" Electronic Department and Villa Mondragone (Frascati) identifying main critical elements.

Since 1998 the University of Rome "Tor Vergata" has been deeply involved in studying and verifying the use and potentialities of EHF in satellite telecommunications. Specifically, the attention has been focused on the lower EHF band, ranging from 75 GHz to 110 GHz, already known as W band. In the last years an increasing interest for such a range has been demonstrated in some intrinsic characteristics such as higher bandwidth availability, minimum oxygen attenuation around 95 GHz (with respect to the absorption peaks), reduced interference, smaller dimensions of antennas. On the other hand, the influence of the atmosphere on signal propagation at those frequencies is considerable and has to be carefully taken into account in systems dimensioning. Actually, the transmitted signal is affected as more as frequency increases (above 10 GHz) by atmosphere (gaseous absorption) and by weather conditions (rain, clouds, fog, snow, etc.). So far, W band has found its main application in radar and radio-astronomy systems. Actually, this frequency range, specifically 94-96 GHz, is currently employed both for terrestrial and space radar applications.

Concerning terrestrial telecommunications, so far some microwave links have been carried out. The Lincoln Laboratory (LL) deployed in the USA a terrestrial link for evaluating dual-polarization techniques in satellite communications [4-1], establishing a link in the range 17-21 GHz which approximately simulates a satellite-to-ground link in terms of many dynamical atmospheric conditions involved in.
In Belfort (France) in collaboration with CNES [4-2] a 800 m terrestrial transmission link operating at 30, 50, 60 and 94 GHz was planned some years ago to better understand the influence of hydrometeors on the propagation in the millimeter wavelength region.
In 90s experiments [4-3] were carried out in Southern part of India to evaluate signal strength fluctuations on 11 GHz line-of-sight microwave link with a hop length of 31.2 km.

Concerning satellite telecommunications, currently no operative mission in W band has been developed for satellite applications (it will be largely shown in the next chapter), but only preliminary studies (up to phase B) [4-4].
Nevertheless, as already reported above, the use of millimeter frequencies could introduce several problems related to the propagation losses caused by atmospheric phenomena (gaseous absorption, rain, snow, clouds, fog, etc.), decreasing the availability of an hypothetic link [4-5].
For the evaluation of these contributions, various theoretical models have been developed. Currently, they do not have practical verification due to the scarce use of such frequencies.

In this scenario, the propagation channel evaluation and technology validation of a terrestrial air link operating at W band can be envisaged as a first step of strategic worth toward a future phase of development of a telecommunication satellite P/L at these frequencies.
Currently, a terrestrial air link at W band can be considered representative of a more challenging satellite-to-ground link. Specifically, a terrestrial link reproduces many of the dynamic atmospheric conditions experienced by a satellite link, allowing to evaluate how atmosphere affects signal propagation and to identify and test possible countermeasures (such as ACM). Consequently, tests conducted on this terrestrial link would allow to quantify how to improve the communications performance of the system. This would constitute an expertise acquired on the field to be potentially extended to future satellite links establishment.

Moreover, in addition to W band channel impairments estimation, technology validation constitutes an additional common item to space link. Actually, besides the components and devices space qualification, the reliability of W band technology, being a “technological frontier”, needs to be proved on the field, especially for long duration missions (as for channel statistics evaluation). A terrestrial link would provide an easy way of testing different equipment (LNA, SSPA, LO, etc.) through a continuous monitoring to derive worth information on their behavior (including also possible commercial components to be used in future satellites).

Further advantages of a terrestrial link are identified by the following points:

- it allows to acquire measurements in a continuous way without suffering from satellite movements (in case of LEO orbits);
- it allows to manage the power without severe constraints (as for satellite transmitters);
- no antenna tracking is required (as for LEO satellites);
- it introduces more flexibility to carry out telecommunications experiment due to the ground based transmitter and receiver (ease of access).

Moreover, a more affordable feasibility is envisaged from the technical point of view and in terms of costs. In fact, a ground-based link also allows a more accessible and less expensive testing facility than a satellite-to-ground system. On the other hand, the link distance and the signal path are different with respect to space links. However, a preliminary understanding of the channel conditions and the selection of the approach to be pursued for future satellite links could be achieved. At the present state of the art, such an experiment would be the first terrestrial characterization of a W band link for telecommunication experiments. Moreover, it will be an important preliminary test of the technology. This section will firstly provide a preliminary orographic analysis of the terrestrial link on 7.4 Km between the Electronic Department of University of Rome “Tor Vergata” and Villa Mondragone. Then, a detailed insight into transmitter and receiver schemes will be reported taking into account constraints related to the characteristic of the available H/W in RHI Italy. Finally, an accurate link budget for dimensioning the system in terms of maximum link capability will be reported. The ongoing activities are focused on testing of the demonstrator with dedicated field trials in order to verify the compliance with theory predictions.

4.1 W BAND RADIO LINK EXPERIMENT DEFINITION

Based on a first idea developed in 2002 [4-5], the University of Rome "Tor Vergata" aims at carrying out and validating an experiment based on the establishment of a W band terrestrial link point-to-point over a distance of some kilometers between two line-of-sight terrestrial sites: the Electronic Department of University of "Tor Vergata" (Rome) and Villa Mondragone (Frascati near Rome). This project is named PERLA-W, which stands for *Propagation Experiment for a Radio-Link Analysis at W band*.

The proposed experiment aims at manifold objectives:

- to demonstrate the theoretical and experimental feasibility of a W band terrestrial link over a significant distance (about 7.4 km);
- to carry out transmission/reception experiments of un-modulated and modulated signals (employing different modulation schemes and evaluating the BER);
- to evaluate attenuation phenomena for different observation times and weather conditions;
- to test W band technology (with special attention to commercial equipment and devices).

The feasibility of the proposed link will be evaluated through a theoretical approach followed by an experimental phase.

From a technological point view, the feasibility of the link presents some criticalities. At first, the microwave technology at W band is currently poor and few developed at applications level, due to the lack of a significant market providing the necessary funding. Therefore, its use is presently limited to the research in radio-astronomy and cosmology, where signals at such frequencies and higher are passively collected to study interstellar and cosmic sources.

Consequently, the technology is just available through ad-hoc (and so, costly) developments at particular frequencies, depending on the research topic (for instance, some specific emission lines by interstellar molecules). However, in the last years an increasing interest has been demonstrated outside the pure research field, converging in radar domain. Actually, exploiting the short wavelength of W band, radars can obtain views of the observed objects with very high resolution, producing a sort of radio images (radar imaging). However, the strong atmosphere absorption, typical at those frequencies, implies to choose specific frequency range. In particular, the frequencies band around 94-96 GHz

has been selected since oxygen absorption shows a minimum in order to properly exploit W band for radar imaging. This aspect inherent to atmosphere impairment is the reason for which the few commercial components operating at W band are available within the range 90-100 GHz. Another item to be considered is the precise pointing requested to align Tx and Rx antenna over a path of 7.4 kilometers and the related logistic problems related to maintain fixed antennas for 3-6 months.

On the basis of the previous considerations and taking into account also the need to maintain costs as low as possible (being the experiment leaded by the University), we decided to approach the test-bed design and development through two drivers:

- trade-off between the scientific objectives and the technological feasibility. It has been based on maximizing reuse of components and devices already developed or purchased, exploiting the long theoretical and experimental expertise and background provided by RHI;
- minimizing the purchase of new components and at the same time assigning priority to European companies.

A preliminary pursued activity has been the definition of the communication link. In most of the communication links the propagation is affected by the presence of Earth, atmosphere, ionosphere and hydrometeors (rain, snow, etc.). Moreover, the propagation of radio-waves depends on the operating frequency, on the antennas directivity and on the antenna height with respect to the ground.

With respect to the previous considerations, to guarantee the transmission of radio-wave signals between two points, it has to be verified that the radio path is not obstructed, checking the area topography and morphology. Specifically, both transmitter and receiver have to be in optical line of sight. First of all, the morphology analysis of the terrain along the line-of-sight has been performed in order to check eventual intersections of Fresnel's ellipsoid along the path between the transmitting site and the receiving site (Electronic Department of University of "Tor Vergata" (in Rome) and Villa Mondragone (near Frascati), about 7,4 km away). Results of this analysis are reported in the next paragraph.

After this phase, on the basis of the drivers before mentioned, a preliminary study has been carried out in order to define the test-bed that will be physically implemented.

Specifically, the transmitter and receiver schemes to be used for the PERLA-W experiment and fitting the philosophy above reported have been identified.

4.1.1 OROGRAPHIC ANALYSIS

The radius of the external surround of an *nth* Fresnel's zone is called *nth Fresnel's radius* and it is indicated as ρ_n. According to Figure 4-1 and considering $d = d_1 + d_2$ as the total distance from T (Transmitter Side) to R (Receiver Side), and H_n the projection of P_n over the $\overline{TR}$ segment, we can write:

$$d = \overline{TH_n} + \overline{H_n R} = d_1\sqrt{1-\left(\frac{\rho_n}{d_1}\right)^2} + \left(d_2 + n\frac{\lambda}{2}\right)\sqrt{1-\left(\frac{\rho_n}{d_2 + n\frac{\lambda}{2}}\right)^2} \qquad (4\text{-}1)$$

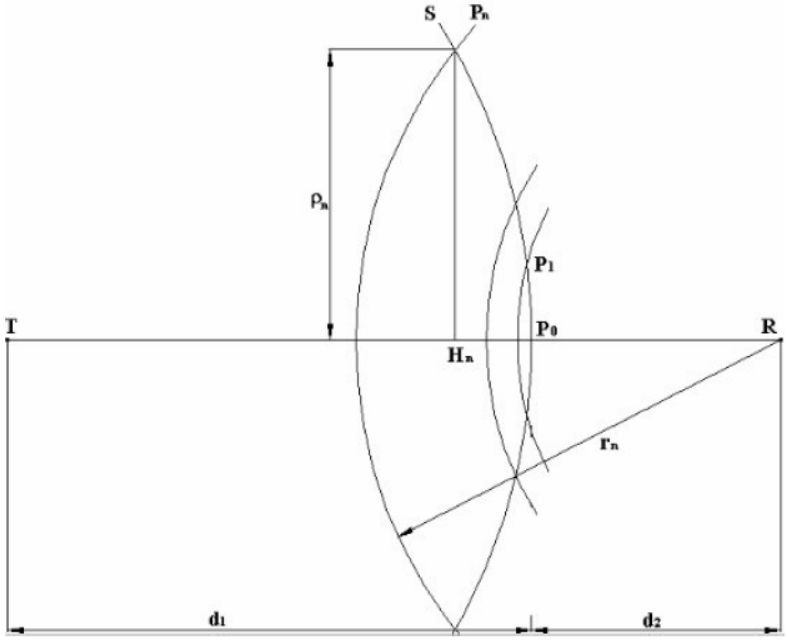

Figure 4-1: Fresnel's Zones

where $\overline{TH_n}$ and $\overline{H_n R}$ are expressed applying the Pythagorean theorem. If the following conditions are satisfied:

$$\rho_n^2 << d_1^2 \qquad (4\text{-}2)$$

$$n\frac{\lambda}{2} << d_2 \qquad (4\text{-}3)$$

the first order of the Taylor's series can be used to approximate the roots square above, achieving a simplified expression for the Fresnel's radius:

$$d = d_1\left(1-\frac{1}{2}\frac{\rho_n^2}{d_1^2}\right)+d_2\left(1+\frac{n}{2}\frac{\lambda}{2}-\frac{1}{2}\frac{\rho_n^2}{d_2^2}\right) \tag{4-4}$$

Solving (4-4) respect to ρ_n, we can write:

$$\rho_n = \sqrt{n\lambda\frac{d_1 d_2}{d_1+d_2}} \tag{4-5}$$

The sum of the distances from T to R, for a given point P_n on the external surround of the nth Fresnel's zone, does not depend from d_1 or d_2, but only from the total distance d between antennas, and the wavelength λ:

$$\overline{TP_n}+\overline{P_nR} = d_1+d_2 = d_2+n\frac{\lambda}{2} \tag{4-6}$$

The collection of points which satisfies the previous (4-6) describes an ellipse in a plane or an ellipsoid in 3-D space.

The range of validity of (4-6) is therefore verified comparing it with the real radius formula obtained by the canonical ellipse equation, as reported below.

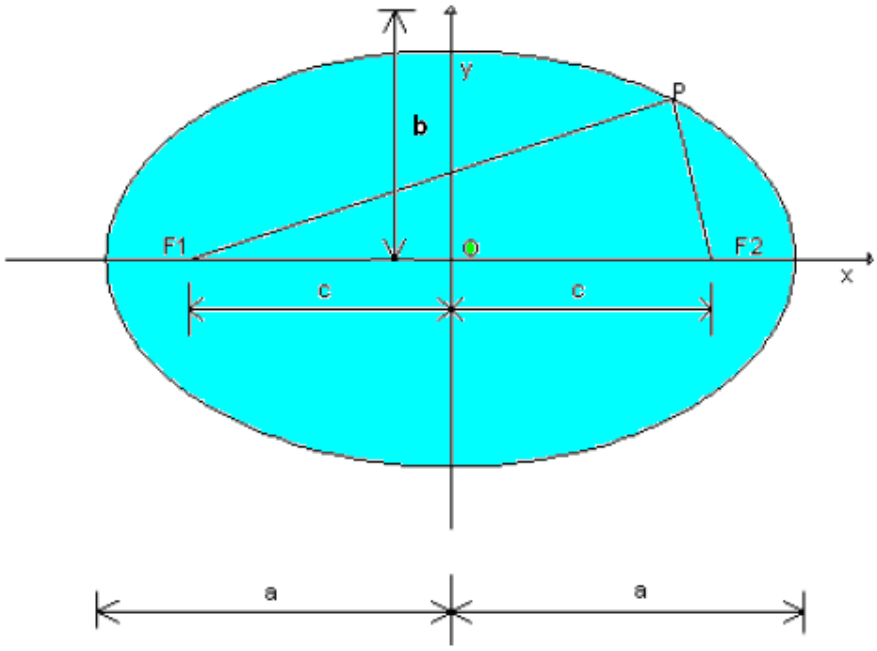

Figure 4-2: Canonical Ellipse

Hence, we consider an ellipse that has the major axis and minor one on the x-asis and y-asis of a Cartesian plane, respectively. Considering the eccentricity, *e*, defined as the ratio between the minor axis and major one, the following relations can be written:

$$\left(\frac{d}{2}\right)^2 + b^2 = a^2, \text{ where } 2c = d \text{ (path length: 7411 [m]) and } b = \rho_{\max} \tag{4-7}$$

$$\frac{d}{2} = \sqrt{a^2 - b^2} = c = e \cdot a \tag{4-8}$$

$$a = \sqrt{\left(\frac{d}{2}\right)^2 + b^2} \tag{4-10}$$

In the center of the path, the approximated formula can be considered valid, thanks to the copiously satisfaction of the conditions (4-2), (4-3), so *b* can be written as:

$$b = \sqrt{\lambda\left(\frac{d}{2}\right)^2 \frac{1}{d}} \tag{4-11}$$

The equation of the ellipse drawn in Figure 4-2 is:

$$\frac{x^2}{a^2} + \frac{y^2}{b^2} = 1 \tag{4-12}$$

substituting the values of *a* and *b* from (4-10) and (4-11), respectively, in (4-12), the following relationship between *x* and *y* is derived:

$$y = \sqrt{b^2 - b^2 \frac{x^2}{a^2}} \tag{4-13}$$

Figure 4-3 shows the absolute error due to use of the approximated formula (4-5). The absolute error increases moving away from the center of the path, where the conditions listed above are widely satisfied, and reachs its maximum value of about 0.04 near both transmitter and receiver antennas. This result allows to use (4-6) with *n=1* for the first Fresnel's ellipse.

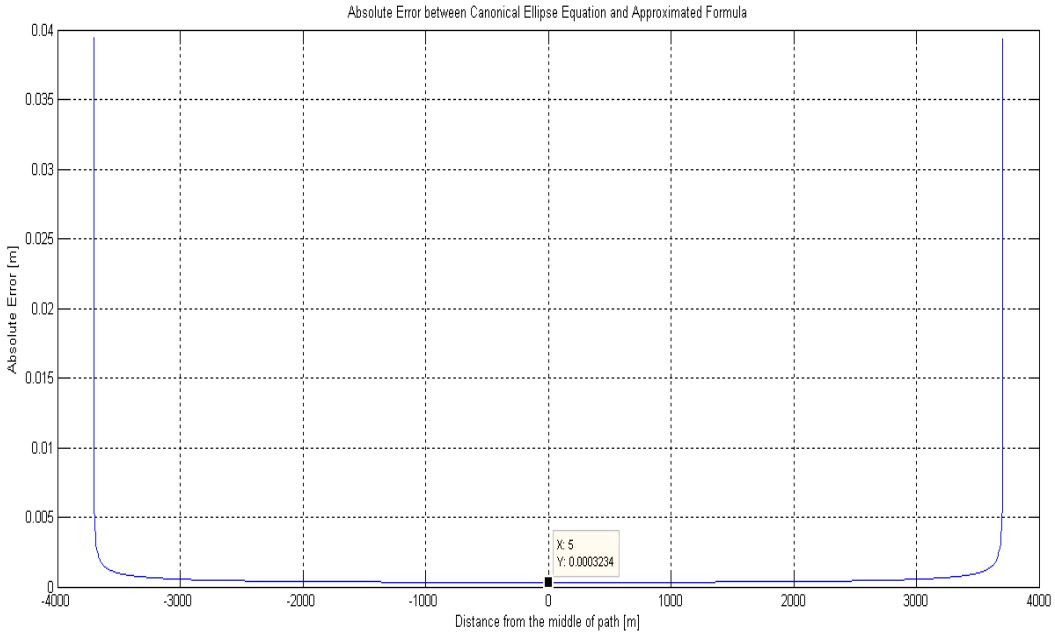

Figure 4-3: Absolute Error between Canonical Ellipse Equation and Approximated Formula (2-5)

In order to indagate the clearance of the first Fresnel's ellipsoid, some information about the environment involved in the propagation has to be well-known. First of all, the heights ((m) from the sea level)) of places located under the straight line between Tx and Rx antennas have to be known. There are several methods to obtain elevation information of a given point on the earth, due to the high number of missions funded by some world's space agencies [4-6]. STR (Shuttle Radar Topography) Digital Elevation Model (DEM) [4-7] has been used in order to derive detailed information about the orographic profile of places along the point-to-point radio-link between Electronic Department of University of Rome 'Tor Vergata' and Villa Mondragone (in Frascati).

SRTM (Shuttle Radar Topography Mission) data products were validated on continental scales through comparison with reserved ground control (i.e. control not used in the mosaicking bundle adjustments).

The best quality control data were the kinematic GPS data acquired by JPL (Jet Propulsion Laboratory) and NGA (National Geospatial-Intelligence Agency) specifically for SRTM validation. Long tracks of GPS estimates were acquired along roads on most major continents. These data were accurate to better than 1 m, and they could characterize SRTM errors on spatial scales from hundreds of meters up to thousands of kilometers. With those data, it was possible to develop a spatial error spectrum and a total absolute error estimate

that has high confidence and are generally applicable away from the kinematic tracks themselves. Using a model based on equivalent heights for all points below the straight line that links the transmitted and receiver antennas, it is easier to carry out a consistent processing of the Digital Elevation Model.

Because of the presence of various gases in the atmosphere, including water vapor, the dielectric constant of the air in the troposphere, ε_r, is slightly greater than the value of the dielectric constant in free space (unity). Since the density of those gases generally decreases with height, ε_r an the refractive index of the air, $n = \sqrt{\varepsilon_r}$, decrease with height. This variation of refractive index gives rise to propagation phenomena such as refraction, reflection, scattering, duct transmission, and fading of signals.

Because of the decrease of the index of refraction with increase in height, the velocity of propagation increases with height in such a way that the radio wave ray paths are very nearly arcs of circles over the distances involved in ground-to-ground mobile communications.

In this scenario, a horizontally emitted ray is curved, bending toward Earth instead of continuing in a straight line, but not intersecting Earth (assumed to be a sphere). Since the radio wave paths are curved, the distance to the horizon for radio signals is larger than the straight-line distance (optical path).

As well known, an electromagnetic ray undergoes a gradual bending during its propagation in proportion with the tropospheric refractivity gradient, G, in accordance with:

$$\frac{1}{R_{Bending}} = -10^{-6}\left(\frac{dN}{dh}\right) = -10^{-6} G \tag{4-14}$$

where:

N is the vertical gradient of refractivity;

h is the altitude over the sea level.

In nearly all common situations, the condition G < 0 is verified.

Observing Figure 4-4, a correction factor, CF1, for the STRM DEM can be evaluated by:

$$CF1 = \frac{\Delta r}{\cos(\alpha_{path})} = \frac{\{[1-\cos(\gamma)]R_{Bending}\}}{\cos(\alpha_{path})} \tag{4-15}$$

$$l_{em} = \gamma_{\max} R_{Bending} \tag{4-16}$$

where:

l_{em} is the effective length of the electromagnetic path;

γ is the angle between the straight lines starting from the center of earth and directed to the transmitter and receiver antennas;

$R_{Bending}$ is the atmospheric bending radius.

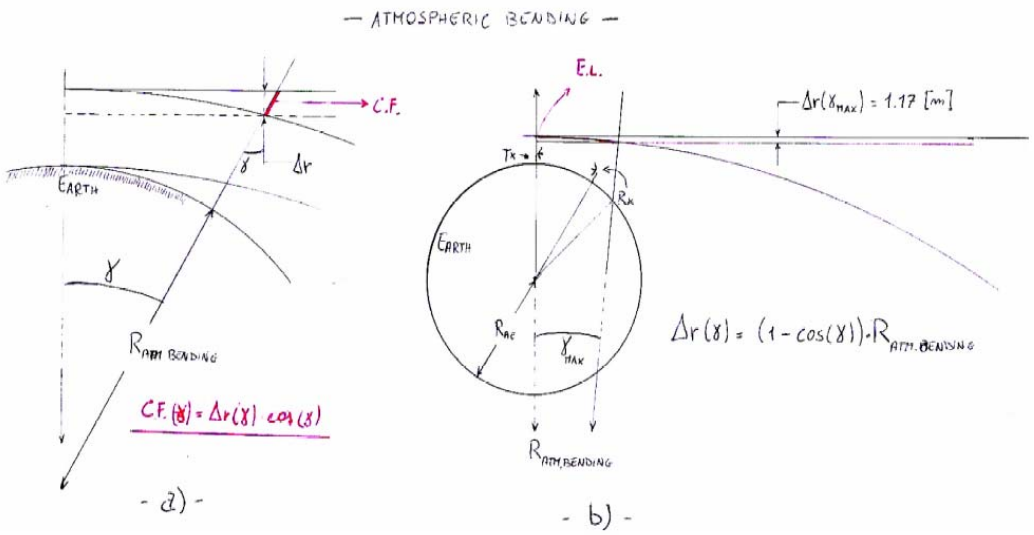

Figure 4-4: Atmospheric Bending and equivalent rapresentation

The estimate of γ_{Max} is mandatory to develop an algorithm which provides a fast method to calculate 1025 correction values, one for each elevation. However, the effective electromagnetic path length has to be known to carry out this step. Since the average distance between rays and ground is seriously smaller than the average earth radius, we could approximate l_{em} with the on-ground path length obtained by the DEM. However, a more accurate estimate could be achieved considering an average altitude between Tx and Rx antennas of about 200 m. In accordance with the assumption made above, which sees Tx antenna located at Tor Vergata and the Rx one at Villa Mondragone, the average height h_M :

$$h_M = h_{Tx} + \left(\frac{h_{Rx} - h_{Tx}}{2} \right) \cong 200(m) \tag{4-17}$$

The effective length of the path related to electromagnetic rays can be written as:

$$l_{em} = \beta\left(\overline{R_T} + h_M\right) = 7411{,}23(m) \tag{4-18}$$

where β is shown in Figure 4-5.

From (4-16) γ_{Max} can be evaluated:

$$\gamma_{\max} = \frac{l_{em}}{R_{Bending}} = 3{,}17 * 10^{-4} (rad) \tag{4-19}$$

and

$$\Delta r_{Max} = R_{Bending} \left[1 - \cos(\gamma_{Max}) \right] \tag{4-20}$$

Although the earth bending could be taken into account only for links of more than 10 km, more accurate considerations have to be carried-out to estimate a second correction:

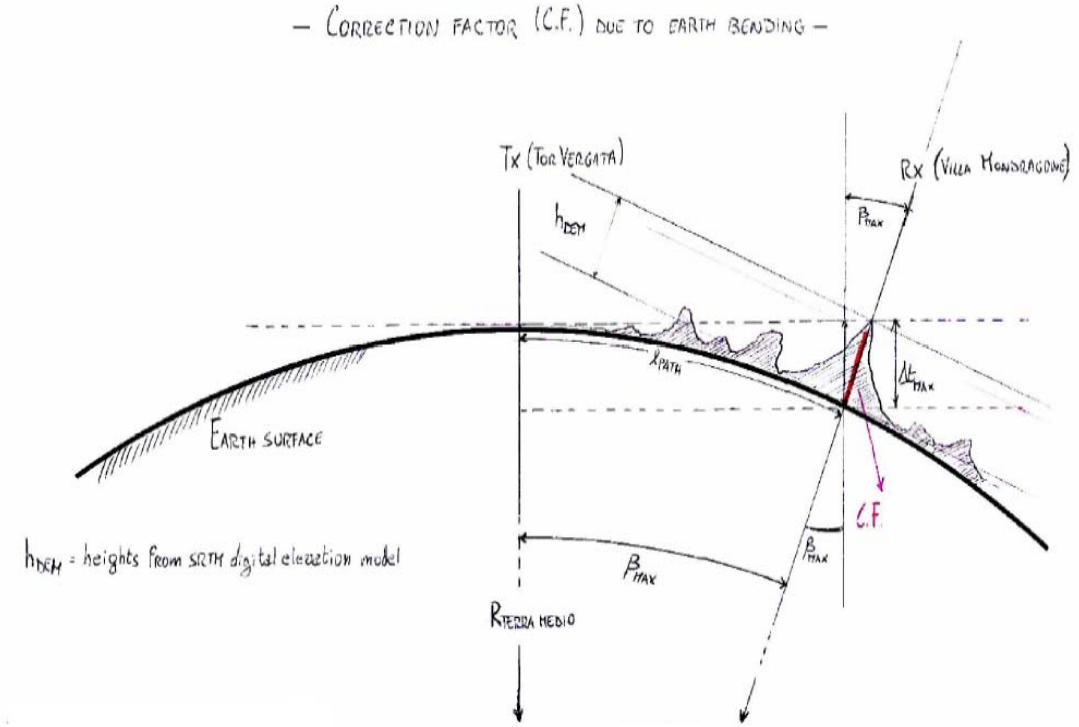

Figure 4-5: Correction Factors of SRTM Data due to Earth Bending

$$CF_2(\beta) = \overline{R}_{Earth} \left[\cos(\beta) + \cos(\beta)^2 \right] \tag{4-21}$$

and the correction factor is related to $\Delta t(\beta)$ by:

$$CF_2(\beta) = \Delta t(\beta) \cos(\beta) \tag{4-22}$$

where β varies from 0 to β_{MAX}:

$$\beta_{MAX} = \frac{l_{path}}{\overline{R}_{Earth}} = 1{,}16 * 10^{-3} (rad) \tag{4-23}$$

Using Matlab, a 1025 elements vector has been obtained and it contains the values of β from 0 to β_{MAX} expressed in radians; an analog procedure has been followed to obtain CF2. The Correction Factor calculated above has to be added to the real elevations data obtained from the SRTM.

ID	X	Y	Elevation	Distance (Segment)	Distance (Total)
1	855.40.00	519.10.00	71589	0	0
2	50.33.00	221.38.00	71611	07.21.00	07.21.00
3	337.40.00	1016.22.00	71601	07.21.00	14.43.00
4	624.47.00	718.49.00	71560	07.21.00	22.04.00
5	911.52.00	421.16.00	71486	07.21.00	29.26.00
6	106.41.00	123.42.00	71381	07.21.00	36.07.00
7	393.45.00	918.24.00	71244	07.21.00	43.28.00
8	680.48.00	620.50.00	71075	07.21.00	50.05.00
9	967.50.00	323.15.00	70874	07.21.00	57.07.00
10	162.35.00	1117.56.00	70642	07.21.00	64.09.00
11	449.36.00	820.21.00	70377	07.21.00	72.01.00
12	736.35.00	522.45.00	70252	07.21.00	79.04.00
13	1023.34.00	225.09.00	70283	07.21.00	86.06.00
14	218.16.00	1019.48.00	70315	07.21.00	93.08.00
15	505.13.00	722.11.00	70346	07.21.00	101
16	792.09.00	424.34.00	70377	07.21.00	108.02.00
17	1079.04.00	126.56.00	70309	07.21.00	115.04.00
18	273.43.00	921.34.00	70176	07.21.00	122.06.00
19	560.36.00	623.55.00	70011	07.21.00	129.08.00
20	847.29.00	326.16.00	69814	07.21.00	137.01.00
21	42.05.00	1120.53.00	69585	07.21.00	144.03.00
22	328.56.00	823.13.00	69324	07.21.00	151.05.00
23	615.46.00	525.33.00	69032	07.21.00	158.07.00
24	902.35.00	227.52.00	68765	07.21.00	165.09.00
25	97.07.00	1022.27.00	68907	07.21.00	173.01.00

Figure 4-6: SRTM Digital Elevation Data

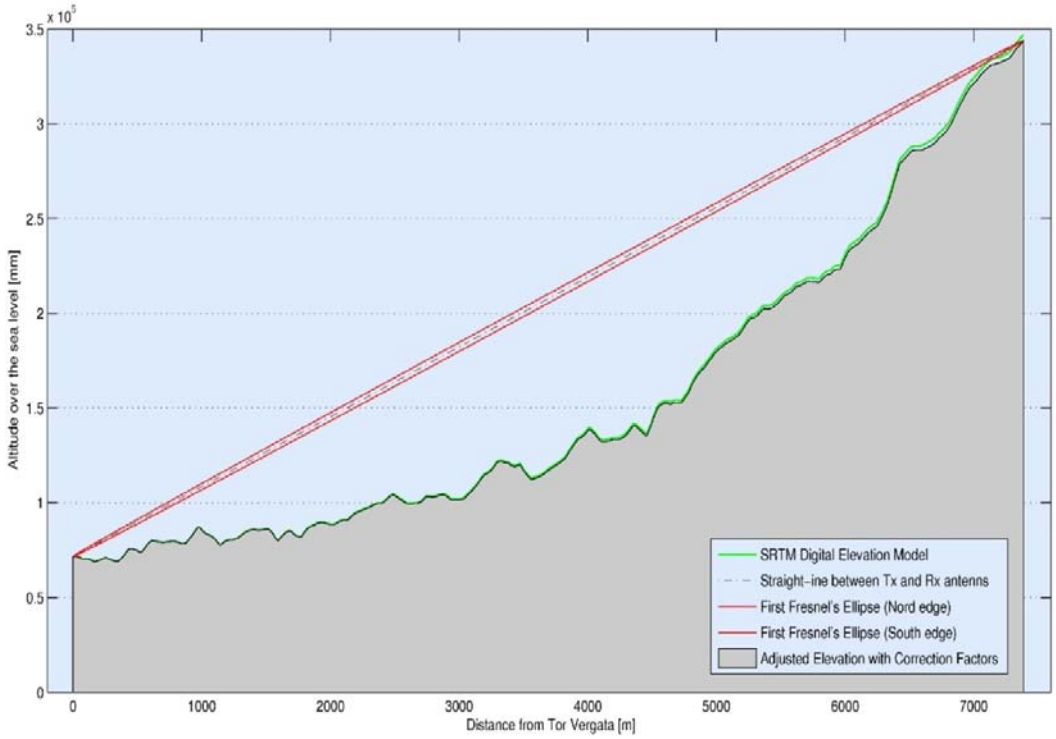

Figure 4-7: Orographic Profile and Straight Line between Tor Vergata and Villa Mondragone

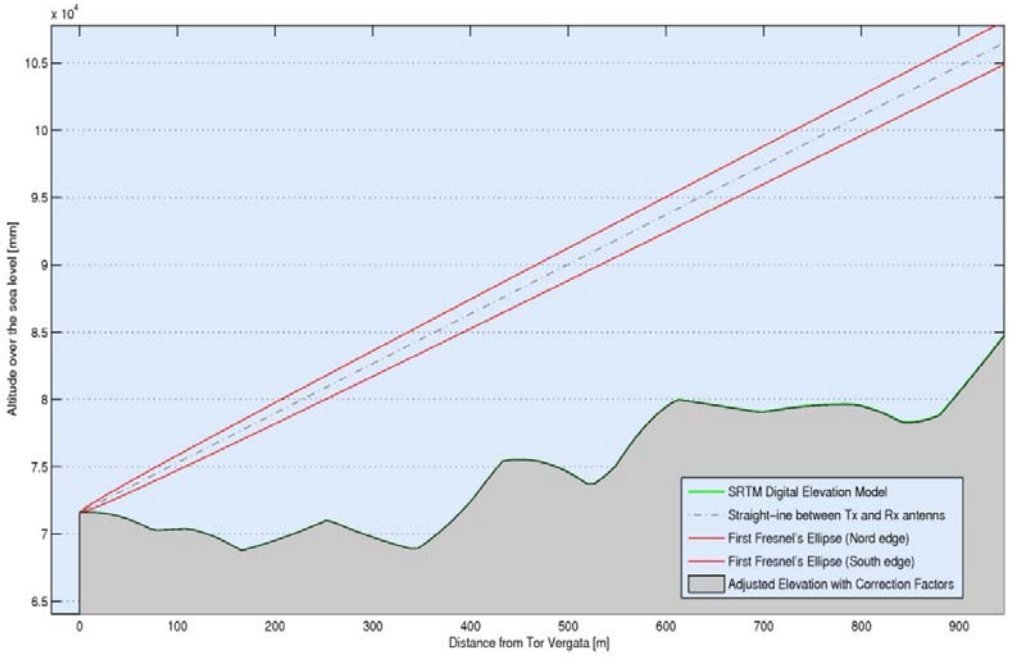

Figure 4-8: Orographic Profile at Tor Vergata Side

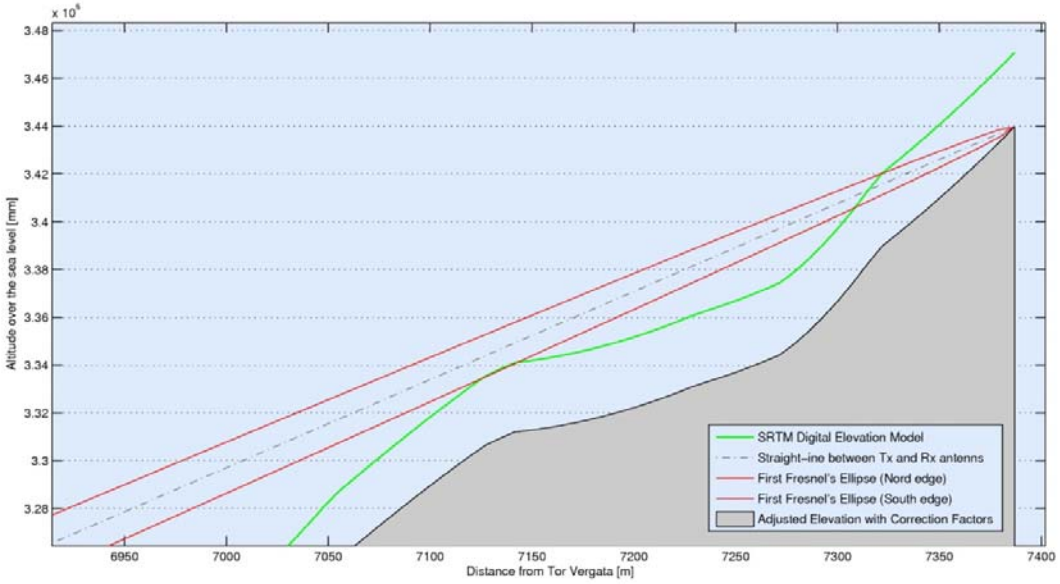

Figure 4-9: Orographic Profile Villa Mondrone Side

On the basis of results shown in Figure 4-7, Figure 4-8 and Figure 4-9, a line-of-sight link (the straight line connecting Tx / Rx) do not cross the red line, which constitutes the estimated height for which the Fresnel ellipsoid is crossed. Moreover, the Fresnel analysis provided that no strict requirements on antenna positioning are necessary. Therefore, it is possible to state that the radio path is not obstructed.

4.1.2 ATTENUATION DUE TO ATMOSPHERIC GASES

The specific attenuation due to dry air and water vapor, from sea level to an altitude of 5 km, can be estimated using the following simplified algorithms [4-8], which are based on curve-fitting to the line-by-line calculation, and agree with more accurate calculations to within an average of about ±15 % at frequencies removed from the centers of major absorption lines. The absolute difference between the results from these algorithms and the line-by-line calculation is generally less than 0.1 dB/Km near 60 GHz. For altitudes higher than 5 Km, and in cases where higher accuracy is required, the line-by-line calculation should be used.

For dry air, the attenuation γ_0 (dB/Km) at frequencies 66 < f < 120 GHz is given by [4-9]:

$$\gamma_0 = \left[\frac{0.2296 d \gamma_0^{'}(66)}{(f-66)^c + d} + \frac{0.286 r_p^2 r_t^{3.8}}{(f-118.75)^2 + 2.97 r_p^2 r_t^{1.6}} \right] f^2 \cdot 10^{-3} \tag{4-24}$$

$$\gamma_0^{'}(66) = 1.935 r_p^{(1.6657)} r_t^{-(3.3714)} e^{[-4.1643(1-r_t)]} \tag{4-25}$$

$$\varepsilon_1 = 6.9575 r_p^{-(0.3461)} r_t^{(0.2535)} e^{[1.3766(1-r_t)]} - 1 \tag{4-26}$$

$$\varepsilon_2 = 42.1309 r_p^{-(0.3068)} r_t^{(0.2023)} e^{[2.5147(1-r_t)]} - 1 \tag{4-27}$$

$$c = \frac{\ln\left(\frac{\varepsilon_2}{\varepsilon_1}\right)}{\ln(3.5)} \tag{4-28}$$

$$d = \frac{4^c}{\varepsilon_1} \tag{4-29}$$

$$r_p = \frac{p}{1013} \tag{4-30}$$

$$r_t = \frac{288}{273 + t} \tag{4-31}$$

where f (GHz), p pressure (hPa), t temperature (°C). The mean temperature values can be obtained from maps given in recommendation ITU-R P.1510, when no adequate temperature data are available.

For water vapour, the attenuation γ_w (dB/Km) at frequencies f < 350 GHz is given by:

$$\gamma_w = \left\{ 3.13 * 10^{-2} r_p r_t^2 + 1.76 * 10^{-3} \rho r_t^{8.5} + \left[r_t^{2.5} (A + B + C) \right] \right\} f^2 \rho * 10^{-4} \tag{4-32}$$

$$A = \left\{ \begin{array}{l} \dfrac{3.84\varepsilon_{w1} g_{22} e^{[2.23(1-r_t)]}}{(f-22.235)^2 + 9.42\varepsilon_{w1}^2} + \dfrac{10.48\varepsilon_{w2} e^{[0.7(1-r_t)]}}{(f-183.31)^2 + 9.48\varepsilon_{w2}^2} + \\ + \dfrac{0.078\varepsilon_{w3} e^{[6.4386(1-r_t)]}}{(f-321.226)^2 + 6.29\varepsilon_{w3}^2} \end{array} \right\} \tag{4-33}$$

$$B = \left\{ \begin{array}{l} \dfrac{3.76\varepsilon_{w4} e^{[1.6(1-r_t)]}}{(f-325.153)^2 + 9.22\varepsilon_{w4}^2} + \dfrac{26.36\varepsilon_{w5} e^{[1.09(1-r_t)]}}{(f-380)^2} + \\ + \dfrac{17.878\varepsilon_{w5} e^{[1.46(1-r_t)]}}{(f-448)^2} \end{array} \right\} \tag{4-34}$$

$$C = \left\{ \frac{883.7\varepsilon_{w5} g_{557} e^{[0.17(1-r_t)]}}{(f-557)} + \frac{302.6\varepsilon_{w5} g_{752} e^{[1.09(1-r_t)]}}{(f-752)} \right\} \tag{4-35}$$

$$\rho = \rho_1 \exp\left(\frac{h_1}{2}\right) \tag{4-36}$$

$$g_{22} = 1 + (f-22.235)^2 / (f+22.235)^2 \tag{4-37}$$

$$g_{557} = 1 + (f-557)^2 / (f+557)^2 \tag{4-38}$$

$$g_{752} = 1 + (f-752)^2 / (f+752)^2 \tag{4-39}$$

$$\xi_{w1} = 0.9544\, r_p\, r_t^{0.69} + 0.0061\, \rho \tag{4-40}$$

$$\xi_{w2} = 0.95\, r_p\, r_t^{0.64} + 0.0067\, \rho \tag{4-41}$$

$$\xi_{w3} = 0.9561\, r_p\, r_t^{0.67} + 0.0059\, \rho \tag{4-42}$$

$$\xi_{w4} = 0.9543\, r_p\, r_t^{0.68} + 0.0061\, \rho \tag{4-43}$$

$$\xi_{w5} = 0.955\, r_p\, r_t^{0.68} + 0.006\, \rho \tag{4-44}$$

Figure 4-10 shows the specific attenuation from 1 to 350 GHz at sea-level for dry air and water vapour with a density of 7.5 g/m^3, while Figure 4-11 reports the Surface water vapour (g/m³) - exceeded for 50% of the year according to ITU-R P.836 [4-10].

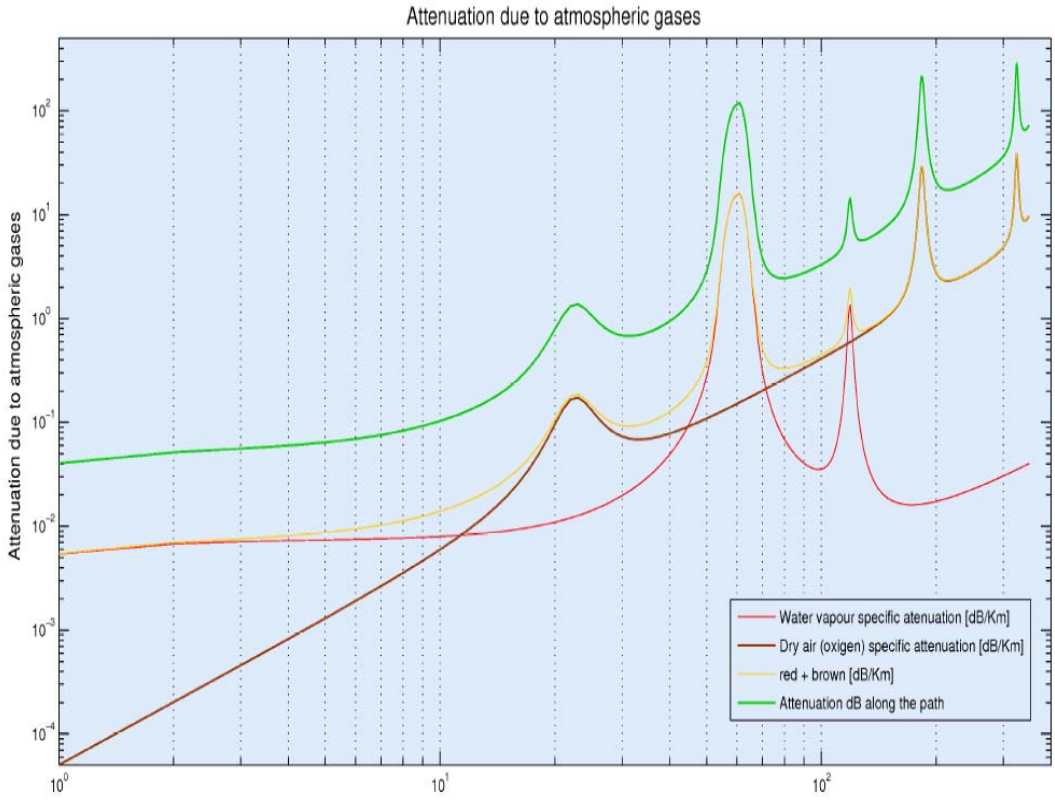

Figure 4-10: Specific attenuation due to Atmospheric Gases from 1 to 350 GHz at sea-level with a density of 7.5 g/m^3

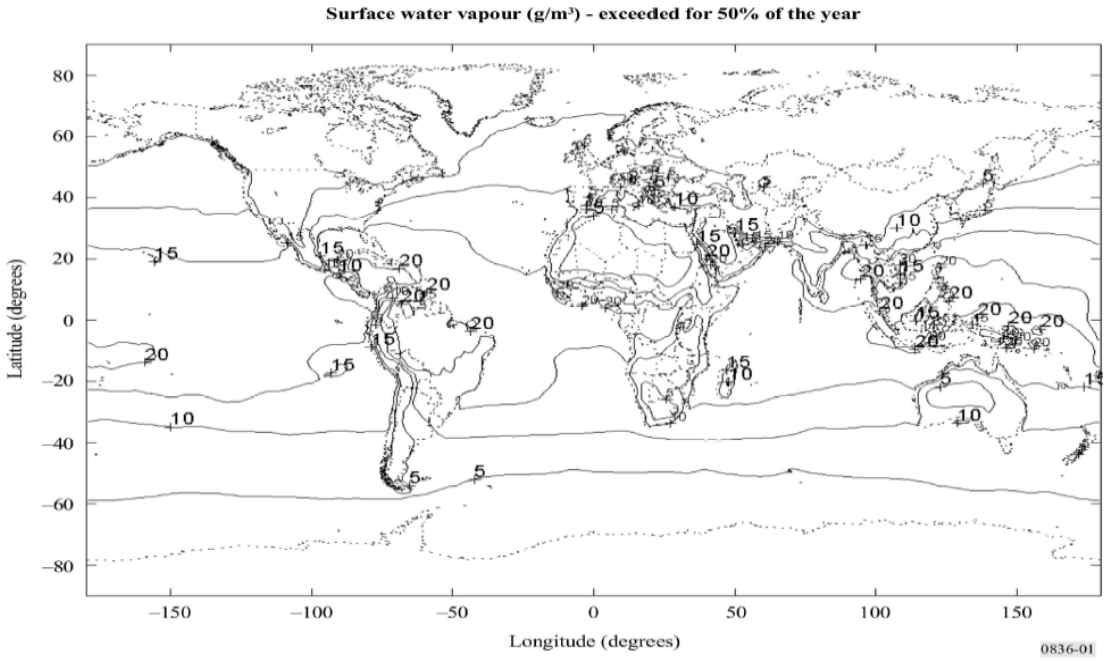

Figure 4-11: Surface water vapour (g/m³) - exceeded for 50% of the year ITU-R P.836

For an horizontal path, or for slightly inclined paths close to the ground, the path attenuation, *A*, may be written as:

$$A = \gamma\, r_0 = (\gamma_O + \gamma_W)\, r_0 \qquad \text{dB} \tag{4-45}$$

Since the elevation angle of the electromagnetic beam considered in this radio-link design is approximately 3.49*10^(-2) rad (nearly 2°), the path should be considered as horizontal, and hence (4-45) should be used. However, the following procedure valid for slant-path has been applied in order to provide more accurate results and to quantify the difference between the procedure indicated by (4-45) and the following one.

This section offers an easy procedure for estimating the gaseous attenuation along slant paths through the Earth's atmosphere, by defining an equivalent height by which the specific attenuation calculated in (4-24) and (4-32) may be multiplied to obtain the zenith attenuation. The resulting zenith attenuations are accurate to within ±10% from sea level up to altitudes of about 2 km, using the pressure, temperature and water-vapour density appropriate to the altitude of interest. For dry air, the equivalent height is given by:

for 1 GHz $\le f \le$ 56.7 GHz

$$h_o = 5.386 - 3.32734\times10^{-2}\, f + 1.87185\times10^{-3}\, f^2 - 3.52087\times10^{-5}\, f^3 + \frac{83.26}{(f-60)^2 + 1.2} \qquad \text{km} \tag{4-46}$$

for 56.7 GHz $< f <$ 63.3 GHz

$$h_O = 10 \text{ km} \tag{4-47}$$

for 63.3 GHz $\le f <$ 98.5 GHz (*our case*)

$$h_o = f\left\{\frac{0.039581 - 1.19751\times10^{-3}\, f + 9.14810\times10^{-6}\, f^2}{1 - 0.028687\, f + 2.07858\times10^{-4}\, f^2}\right\} + \frac{90.6}{(f-60)^2} \qquad \text{km} \tag{4-48}$$

for 98.5 GHz $\le f \le$ 350 GHz

$$h_o = 5.542 - 1.76414\times10^{-3}\, f + 3.05354\times10^{-6}\, f^2 + \frac{6.815}{(f-118.75)^2 + 0.321} \qquad \text{km} \tag{4-49}$$

For water vapour, the equivalent height for $f \le$ 350 GHz is given by:

$$h_w = 1.65\left\{1 + \frac{1.61}{(f-22.23)^2 + 2.91} + \frac{3.33}{(f-183.3)^2 + 4.58} + \frac{1.90}{(f-325.1)^2 + 3.34}\right\} \qquad \text{km} \tag{4-50}$$

The concept of equivalent height is based on the assumption of an exponential atmosphere specified by a scale height to describe the decay in density with altitude. Note that scale heights for both dry air and water vapour may vary with latitude, season and/or climate, and that water vapour distributions in the real atmosphere may deviate considerably from the exponential, with corresponding changes in equivalent heights. The values given above are applicable up to an altitude of 2 km.

The total zenith attenuation is then:

$$A = \gamma_o \, h_o + \gamma_w \, h_w \qquad \text{dB} \tag{4-51}$$

Figure 4-12 reports Specific attenuation due to Atmospheric Gases from 1 to 350 GHz at the zenith from the sea-level with a density of 7.5 g/m^3.

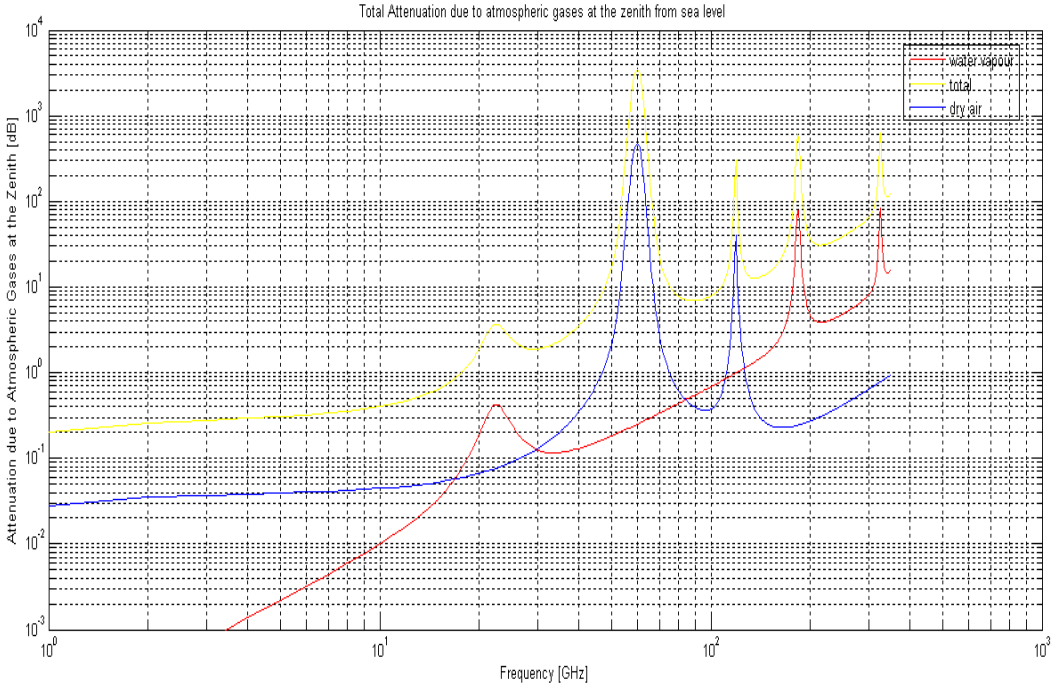

Figure 4-12: Specific attenuation due to Atmospheric Gases from 1 to 350 GHz at the zenith from the sea-level with a density of 7.5 g/m^3

Now the total attenuation over an inclined path, A_{ts}, between a station situated at altitude h_1 and one at altitude h_2 (with $h_2 \geq h_1$ and both altitudes are less than 2000 m above the sea level), can be determined from:

$$\begin{aligned} A_{ts} = {} & \gamma_o \sqrt{h_o} \left[\frac{\sqrt{R_e + h_1} \cdot F(x_1) \, e^{-h_1/h_o}}{\cos \varphi_1} - \frac{\sqrt{R_e + h_2} \cdot F(x_2) \, e^{-h_2/h_o}}{\cos \varphi_2} \right] \\ & + \gamma_w \sqrt{h_w} \left[\frac{\sqrt{R_e + h_1} \cdot F(x_1') \, e^{-h_1/h_w}}{\cos \varphi_1} - \frac{\sqrt{R_e + h_2} \cdot F(x_2') \, e^{-h_2/h_w}}{\cos \varphi_2} \right] \qquad \text{dB} \end{aligned} \tag{4-52}$$

where:

Re: effective Earth radius including refraction, given in Recommendation ITU-R P.834, expressed in km (a value of 8 500 km is generally acceptable for the immediate vicinity of the Earth's surface);

φ_1: elevation angle at altitude h_1;

F: function defined by:

$$\mathrm{F}(x) = \frac{1}{0.661\,x + 0.339\sqrt{x^2 + 5.51}} \tag{4-53}$$

$$\varphi_2 = \arccos\left(\frac{R_e + h_1}{R_e + h_2}\cos\varphi_1\right) \tag{4-54}$$

$$x_i = \tan\varphi_i \sqrt{\frac{R_e + h_i}{h_o}} \qquad \text{for } i = 1, 2 \tag{4-55}$$

$$x_i' = \tan\varphi_i \sqrt{\frac{R_e + h_i}{h_w}} \qquad \text{for } i = 1, 2 \tag{4-56}$$

it being understood that the value ρ of the water vapour density used in equation (4-32) is the hypothetical value at sea level calculated as follows:

$$\rho = \rho_1 \cdot \exp\left(h_1 / 2\right) \tag{4-57}$$

where ρ_1 is the value corresponding to altitude h_1 of the station in question, and the equivalent height of water vapour density is assumed as 2 km (see Recommendation ITU-R P.835). Table 4-1 reports the values of main parameters used for estimating the total attenuation due to atmospheric gases at 96 GHz, whereas Figure 4-13 shows the total attenuation due to atmospheric gaseous over the path from Tor Vergata to Villa Mondragone, which should be considered in the link-budget. It is clearly visible how the attenuation at 96 GHz is approximatively 2.7 (dB), whereas the ones obtained from Figure 4-12 (yellow line) is slightly greater (3.058 dB). This behavior can be considered as a confirm of the theory at the basis of this phenomenon, which foresees a reduction of the atmospheric absorption with the increase of the height over the sea level.

Parameters	Water-vapour Specific Attenuation
$\rho = 7.5\ (g/m^3)$	$\gamma_w = 0.3784(dB/Km)$
$A(96) = 2.353 * 10^{-3}$	
$B(96) = 5.442 * 10^{-4}$	
$C(96) = 7.354 * 10^{-3}$	

Parameters	Parameters	Dry-Air Spacific Attenuation
$f = 96$ (GHz)	$\gamma_0'(66) = 1.9350$	$\gamma_0 = 0.0355(dB/Km)$
$p = 1013$ (hPa) $\simeq 1$(atm)	$\xi_1 = 5.9575$	
$r_p = 1$ (atm)	$\xi_2 = 41.1309$	
$r_t = 1$	$c = 1.5423$	
$t = 15$ (°C)	$d = 1.4239$	

Table 4-1: Main Parameters for Specific Attenuations due to Atmospheric Gases over the path from Tor Vergata to Villa Mondragone at 96 GHz

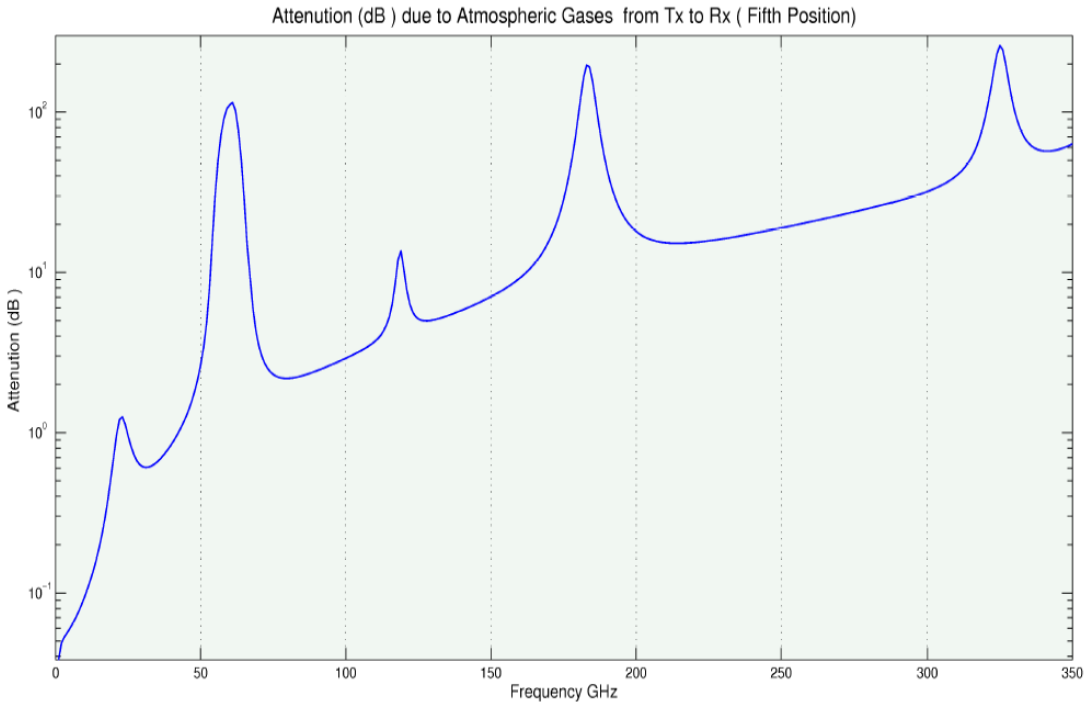

Figure 4-13: Total attenuation due to Atmospheric Gases along the path from Tor Vergata to Villa Mondragone

4.1.3 ATTENUATION DUE TO MULTIPATH

Various clear-air fading mechanisms caused by extremely refractive layers in the atmosphere have to be taken into account in the planning of links of more than a few kilometers in length; beam spreading (commonly referred as defocusing), antenna decoupling, surface multi-path, and atmospheric multi-path. Most of these mechanisms can occur themselves or in combination with each other. A particular severe form of frequency-selective fading occurs when a beam spreading of the direct signal, combines with a surface reflected signal to produce multi path fading. Scintillation-fading, due to smaller scale turbulent irregularities in the atmosphere, always occurs with those mechanisms; at frequency above 40 GHz its effect on the overall fading distribution must be taken into account.

The following method to foresee the single-frequency (or narrow-band) fading distribution at large fade depth, is referred to the average worst month (hence the worst propagation conditions are considered) and provides a percentage of time in which a given value of fading is exceeded. The algorithm starts with evaluation for small percentage of time and obtains more complete results exploiting the previous calculus.

- *Method for small percentage of time:*

Step1: For the path location in question, estimate the geoclimatic factor K for the average worst month from:

$$K = 10^{-3.9-0.003dN_1} s_a{}^{-0.42} \tag{4-58}$$

where:

d_{N1} is the point refractivity gradient in the lowest 65m of the atmosphere exceeded for 1 % in the average year, provided in Recommendation ITU-R P.453 with a graphic representation shown below.

s_a is the area terrain roughness defined as the standard deviation of terrain heights (m) within a 110 Km x 110 Km area with a 30 s resolution (e.g. the Globe "gtopo30" data).

Step 2: From the antenna heights h_r and h_e ((m) above the sea level), calculate the magnitude of the path inclination $|\varepsilon_p|$ (mrad) from:

$$|\varepsilon_p| = \frac{|h_r - h_e|}{d} \tag{4-59}$$

where d is the path length (Km).

Step 3: For detailed link design applications the percentage of time p_w (%) the fade depth A is exceeded in the average worst month is given by:

$$p_w = kd^{3.2}\left(1+|\varepsilon_p|\right)^{-0.97} * 10^{\left(0.032f-0.00085h_L-\frac{A}{10}\right)} \tag{4-60}$$

where:

f is the frequency (GHz);

h_L is the altitude of the lower antenna (i.e. the smaller of h_r and h_e);

K is the geoclimatic factor obtained from (4-58).

- *Method for all percentage of time:*

The method given below for predicting the percentage of time that any fade depth is exceeded combines the deep fading distribution given in the preceding section and an empirical interpolation procedure for shallow fading down to 0 dB.

Step 1: Using (4-60) with A = 0 for calculate the occurrence factor, p_0:

$$p_0 = kd^{3.2}\left(1+|\varepsilon_p|\right)^{-0.97} * 10^{(0.032f-0.00085h_L)} \tag{4-61}$$

Step 2: Calculate the fade depth, A_t (dB), at which the transition occurs between the deep-fading distribution and the shallow-fading distribution as predicted by the empirical interpolation procedure:

$$A_t = 25 + 1.2\log(p_0) \tag{4-62}$$

Step 3a: If the required fade depth, *A*, is equal or grater than A_t, calculate the percentage of time A is exceeded in the average worst month:

$$p_w = p_0 * 10^{-\frac{A}{10}} \tag{4-63}$$

Step 3b: If the required fade depth, A, is less than A_t, calculate the percentage of time, pt, that A_t is exceeded in the average worst month:

$$p_w = p_0 * 10^{-\frac{A_t}{10}} \tag{4-64}$$

Calculate $q_a^{'}$ from the transition fade A_t and transition percentage time p_t:

$$q_a^{'} = \frac{-20 * \log\left\{-\ln\left[\frac{(100 - p_t)}{100}\right]\right\}}{A_t} \tag{4-65}$$

Calculate q_t from $q_a^{'}$ and transition fade A_t:

$$q_t = \frac{\left(q_a^{'} - 2\right)}{\left[\left(1 + 0.3 * 10^{-\frac{A_t}{20}}\right) * 10^{-0.016 A_t}\right]} - 4.3 * \left(10^{-\frac{A_t}{20}} + \frac{A_t}{800}\right) \tag{4-66}$$

Calculate q_a from the required fade A:

$$q_a = 2 + \left[1 + 0.3 \times 10^{-A/20}\right]\left[10^{-0.016\,A}\right]\left[q_t + 4.3\left(10^{-A/20} + A/800\right)\right] \tag{4-67}$$

Calculate the percentage of time, p_w, that the fade depth A (dB) is exceeded in the average worst month:

$$p_w = 100\left[1 - \exp\left(-10^{-\frac{q_a A}{20}}\right)\right] \tag{4-68}$$

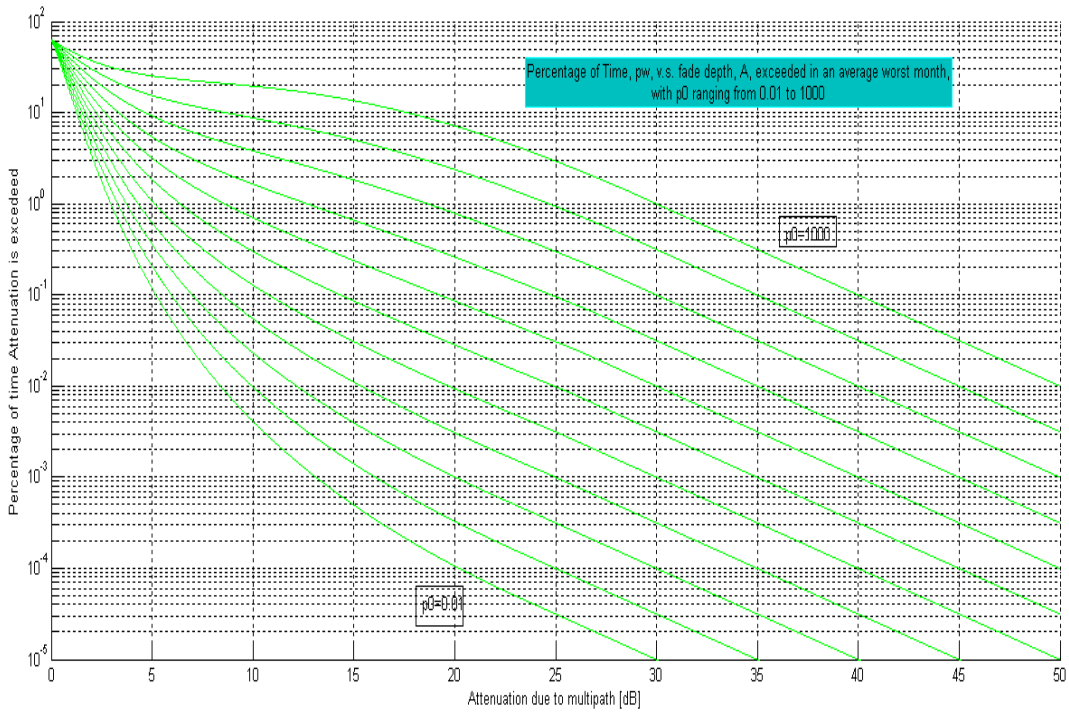

Figure 4-14: Percentage of Time, p_w, respect to fade depth, A, exceeded in an average worst month, with p_0 ranging from 0.01 to 1000

With p_0 as a parameter ranging from 0.01 to 1000, Figure 4-14 gives a family of curves providing a graphical representation of the method.

In order to reach the best behaviour of the link with respect to multipath attenuations and considering also a small value of outage probability, a greater supplementary attenuation due to multipath has to be taken into account. The multipath attenuation not exceeded for 99.9% of time is roughly to be 33 dB. Figure 4-15 shows the probability of time p_w, that the fade depth is exceeded in the average worst month for the radio-link at 96 GHz over path from Tor Vergata to Villa Mondragone.

The experience in development of radio link affected by reflection phenomena teaches that it is very high the probability to have a destructive interference between the rejected beams in place of a constructive effect. However, large enhancement are observed during the same general conditions of frequent ducts that result in multi path fading which we are going to quantify, following the recommendation ITU-R P.530-10. Average worst month enhancement above 10 dB should be predicted using:

$$p_W = 100 - 10^{(-1.7 + 0.2\,A_{0.01} - E)/3.5} \quad \% \quad \text{for} \quad E > 10\ \text{dB} \qquad (4\text{-}69)$$

where E (dB) is the enhancement not exceeded for p% of the time and $A_{0.01}$ is the predicted deep fade depth), as appropriate, exceeded for $p_w = 0.01\%$ of the time.

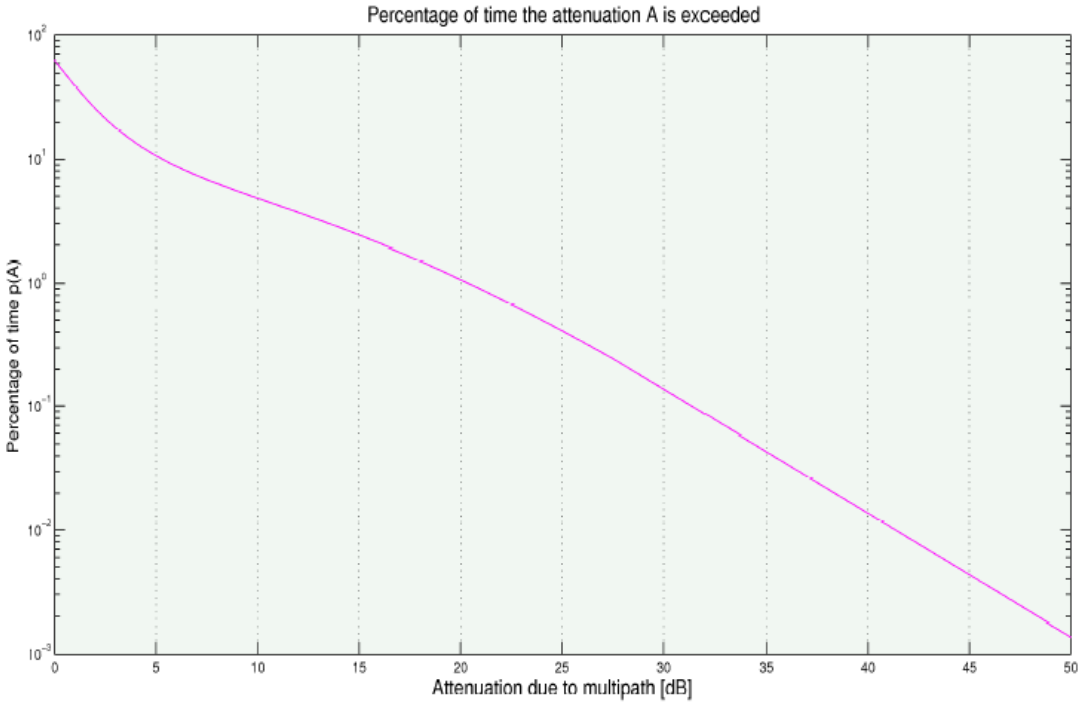

Figure 4-15: Probability of Time that the fade depth is exceeded in the average worst month for the radio-link at 96 GHz over path from Tor Vergata to Villa Mondragone

For the enhancement between 10 and 0 dB use the following step-by-step procedure:

Step 1: Calculate the percentage of time p'_w with enhancement less or equal to 10 dB ($E' = 10$) using equation (4-69).

Step 2: Calculate q'_e using:

$$q'_e = -\frac{20}{E'}\left(\log_{10}\left[-\ln\left(1-\frac{100-p'_w}{58.21}\right)\right]\right) \tag{4-70}$$

Step 3: Calculate q_S using:

$$q_s = 2.05q'_e - 20.3 \tag{4-71}$$

Step 4: Calculate q_e for the desired E using:

$$q_e = 8 + \left[1 + 0.3\times 10^{-E/20}\right]\left[10^{-0.7E/20}\right]\left[q_s + 12\left(10^{-E/20} + E/800\right)\right] \tag{4-72}$$

Step 5: The percentage of time that the enhancement E (dB) is not exceeded is found from:

$$p_w = 100 - 58.21\left[1 - \exp\left(-10^{-q_e E/20}\right)\right] \tag{4-73}$$

The set of curves in Figure 4-16 gives a graphical representation of the method with p_0 as parameter. Each curve in Figure 4-16 corresponds to the curve in Figure 4-14 with the same value of p_0. It should be noted that gives the percentage of time for which the enhancements are exceeded which corresponds to $(100 - p_w)$, with p_w given by equations (4-69) and (4-73).

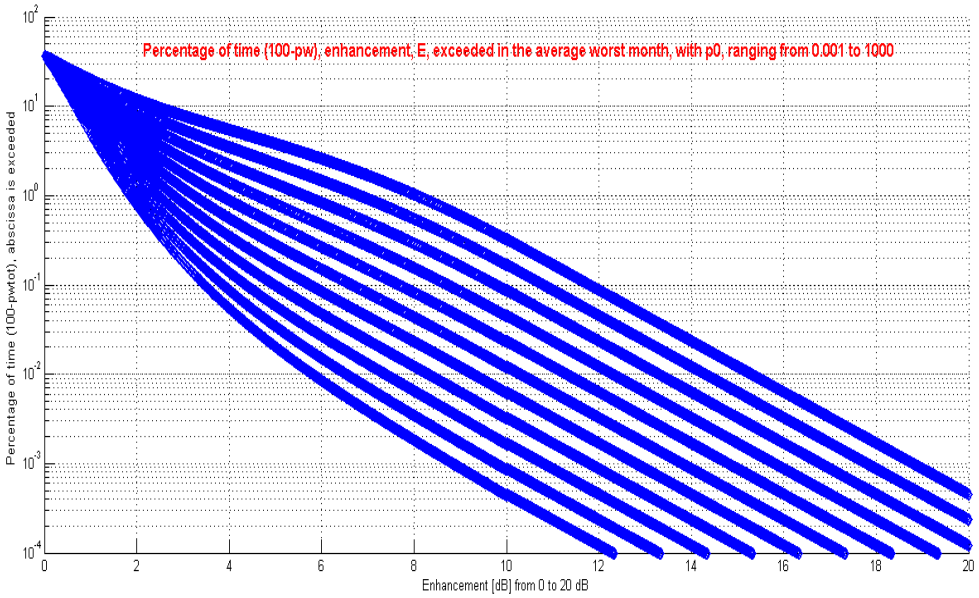

Figure 4-16: Percentage of Time (100-pw), enhancement, E, exceeded in the average worst month, with p0 ranging form 0.001 to 1000

Figure 4-17 shows the enhancement wich should be obtained with probability p; y-axis reports the percentage of time with respect to the enhancement (dB), indicated on x-axis, is not exceeded. Since no one enhancement is shown up to 65% of time, and the knowledgment about the channel behavior at W-band is relatively still poor, the enhancement effects will be not taken into account in link budget.

The trend shown in Figure 4-17 underlines the well known behavior of the constructive and destructive interference of electromagnetic fields on the surface of a receiving antenna, according to that the probability to have a destructive interference is higher than one to have a constructive interference.

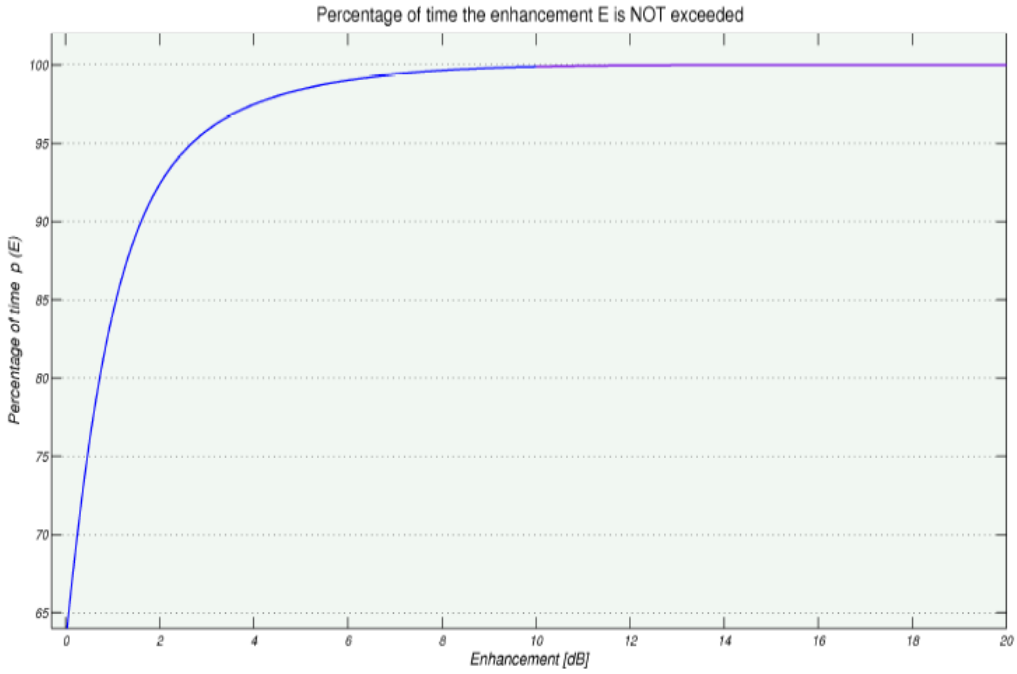

Figure 4-17: Enhancement due to Multipath

4.1.4 ATTENUATION DUE TO HYDROMETEORS

Attenuation can also occur as a result of absorption and scattering by such hydrometeors as rain, snow, hail and fog. Although rain attenuation can be ignored at frequencies below about 5 GHz, it must be included in design calculations at higher frequencies, where its importance increases rapidly. The long-term statistics of rain attenuation for the radio-link at 96 GHz have been estimated using the procedure described below. On paths at high latitudes or high altitude paths at lower latitudes, wet snow can cause significant attenuation over an even larger range of frequencies.

At frequencies where both rain attenuation and multipath fading must be taken into account, the exceedance percentages for a given fade depth corresponding to each of these mechanisms can be added.

4.1.4.1 LONG-TERM STATISTICS OF RAIN ATTENUATION

The following technique has been used for estimating the long-term statistics of rain attenuation:

Step 1: Obtain the rain rate $R_{0.01}$ exceeded for 0.01% of the time (with an integration time of 1 min). If this information is not available from local sources of long-term measurements, an estimate can be obtained from the information given in Recommendation ITU-R P.837.

Step 2: Compute the specific attenuation, γ_R (dB/km) for the frequency, polarization and rain rate of interest using Recommendation ITU-R P.838.

Step 3: Compute the effective path length, d_{eff}, of the link by multiplying the actual path length *d* by a distance factor *r*. An estimate of this factor is given by:

$$r = \frac{1}{1 + d / d_0} \tag{4-74}$$

$$\text{where for } R_{0.01} \leq 100 \text{ mm/h: } \quad d_0 = 35\ e^{-0.015 R_{0.01}} \tag{4-75}$$

while use the value 100 mm/h in place of $R_{0.01}$ for $R_{0.01}$ > 100 mm/h.

Step 4: An estimate of the path attenuation exceeded for 0.01% of the time is given by:

$$A_{0.01} = \gamma_R d_{eff} = \gamma_R d_r \text{ dB} \tag{4-76}$$

Step 5: For radio links located in latitudes equal to or greater than 30° (North or South), the attenuation exceeded for other percentages of time *p* in the range 0.001% to 1% may be deduced from the following power law:

$$\frac{A_p}{A_{0.01}} = 0.12\ p^{-(0.546 + 0.043 \log_{10} p)} \tag{4-77}$$

This formula has been determined to give factors of 0.12, 0.39, 1 and 2.14 for 1%, 0.1%, 0.01% and 0.001% respectively, and must be used only within this range.

Step 6: For radio links located at latitudes below 30° (North or South), the attenuation exceeded for other percentages of time *p* in the range 0.001% to 1% may be deduced from the following power law:

$$\frac{A_p}{A_{0.01}} = 0.07\ p^{-(0.855 + 0.139 \log_{10} p)} \tag{4-78}$$

This formula has been determined to give factors of 0.07, 0.36, 1 and 1.44 for 1%, 0.1%, 0.01% and 0.001%, respectively, and must be used only within this range.

Step 7: If worst-month statistics are desired, calculate the annual time percentages *p* corresponding to the worst-month time percentages p_w using climate information specified in Recommendation ITU-R P.841. The values of *A* exceeded for percentages of the time *p* on an annual basis will be exceeded for the corresponding percentages of time p_w on a worst-month basis. The prediction procedure outlined above is considered to be valid in all

parts of the world at least for frequencies up to 40 GHz and path lengths up to 60 km. However, this procedure has been applied since no models at 96 GHz are available.

Figure 4-18 shows the attenuation due to rain and hydrometeors as a function of the outage probability, referred to long-term statistics. Since a given outage probability has been assumed, the worst propagation conditions have to be considered. The following paragraph is focused on the above mentioned recommendation which provides an easy method to realize the conversion of annual statistics to worst month statistics.

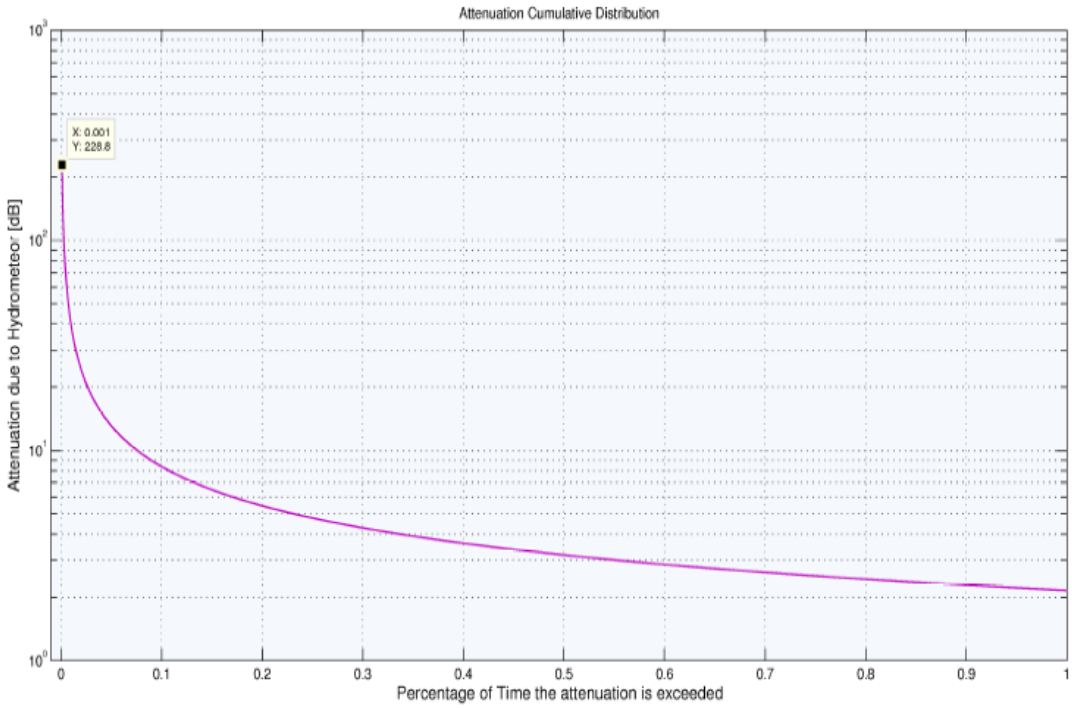

Figure 4-18: Attenuation due to Hydrometeors

4.1.4.2 CONVERSION OF ANNUAL STATISTICS TO WORST-MONTH STATISTICS

The average annual worst-month time percentage of excess, p_w, is calculated from the average annual time percentage of excess p using the conversion factor Q [4-11]:

$$p_w = Q \cdot p \tag{4-79}$$

where 1 < Q < 12, and both p and p_w refer to the same threshold levels. Q is a two parameter (Q_1, β) function of p (%):

$$Q_{(p)} = \begin{cases} 12 & \text{for} \quad p < \left(\frac{Q_1}{12}\right)^{\frac{1}{\beta}} \% \\ Q_1\, p^{-\beta} & \text{for} \quad \left(\frac{Q_1}{12}\right)^{\frac{1}{\beta}} < p < 3\% \\ Q_1\, 3^{-\beta} & \text{for} \quad 3\% < p < 30\% \\ Q_1\, 3^{-\beta} \left(\frac{p}{30}\right)^{\frac{\log\left(Q_1\, 3^{-\beta}\right)}{\log(0.3)}} & \text{for} \quad 30\% < p \end{cases} \tag{4-80}$$

Since the probabilities of interest vary within the range of 0.01% to 3%, the following equation can be used to find the Q factor:

$$Q_{(p)} = Q_1 \cdot p^{-\beta} \tag{4-81}$$

Global values for Q_1, β_1 referred to rain effects for terrestrial attenuation are 0.13 and 2.85 respectively. In the link-budget tool for the design of the 96 GHz radio-link, the outage probabilities are assumed equal to 0.1% and 0.01%.

Exploiting (4-81), the percentage of time p of long-term statistics, related to the same attenuation not exceeded in percentage of time, p_w, can be written as:

$$p_w = pQ_1 p^{-\beta_1} \Longrightarrow p = \left(\frac{p_w}{Q_1}\right)^{\frac{1}{(1-\beta_1)}} \tag{4-82}$$

Table 4-2 shows some relations between p and p_w where A_{pw} is the wrong rain attenuation which could be considered if no conversion is realized.

p_w	p	A_{pw}(dB)	A_p (dB)
0.5%	0.135%	3.18	6.95
0.1%	0.021%	8.38	23.52
0.01%	0.0015%	30.66	≃170

Table 4-2: Relations between annual statistics (year vs worst-month)

4.1.5 REDUCTION OF XPD

The XPD can deteriorate sufficiently to cause co-channel interference and, to a lesser extent, adjacent channel interference. The reduction in XPD that occurs during both clear-air and precipitation conditions must be taken into account.

4.1.5.1 PREDICTION OF XPD OUTAGE DUE TO CLEAR-AIR EFFECTS

The combined effect of multipath propagation and the cross-polarization patterns of the antennas governs the reductions in XPD occurring for small percentages of time. To compute the effect of these reductions in link performance the following step-by-step procedures should be used:

Step 1: Compute:

$$XPD_0 = \begin{cases} XPD_g + 5 & \text{for} \quad XPD_g \le 35 \\ 40 & \text{for} \quad XPD_g > 35 \end{cases} \tag{4-83}$$

where XPD_g is the manufacturer's guaranteed minimum XPD at boresight for both the transmitting and receiving antennas, i.e., the minimum of the transmitting and receiving antenna boresight XPDs.

Step 2: Evaluate the multipath activity parameter:

$$\eta = 1 - e^{-0.2(P_0)^{0.75}} \tag{4-84}$$

where $P_0 = p_w/100$ is the multipath occurrence factor corresponding to the percentage of the time p_w (%) of exceeding $A = 0$ dB in the average worst month, as calculated from equation (4-37) or (4-38), as appropriate.

Step 3: Determine:

$$Q = -10 \log\left(\frac{k_{XP}\ \eta}{P_0}\right) \tag{4-85}$$

where:

$$k_{XP} = \begin{cases} 0.7 & \text{one transmit antenna} \\ 1 - 0.3 \exp\left[-4 \times 10^{-6}\left(\frac{s_t}{\lambda}\right)^2\right] & \text{two transmit antennas} \end{cases} \tag{4-86}$$

In the case where two orthogonally polarized transmissions are from different antennas, the vertical separation is s_t (m) and the carrier wavelength is λ (m).

Step 4: Derive the parameter C from:

$$C = XPD_0 + Q \tag{4-87}$$

Step 5: Calculate the probability of outage P_{XP} due to clear-air cross-polarization from:

$$P_{XP} = P_0 \times 10^{-\frac{M_{XPD}}{10}} \tag{4-88}$$

where M_{XPD} (dB) is the equivalent XPD margin for a reference BER given by:

$$M_{XPD} = \begin{cases} C - \dfrac{C_0}{I} & \text{without XPIC} \\ C - \dfrac{C_0}{I} + XPIF & \text{with XPIC} \end{cases} \quad (4\text{-}89)$$

Here, C_0/I is the carrier-to-interference ratio for a reference BER, which can be evaluated either from simulations or from measurements.

XPIF is a laboratory-measured cross-polarization improvement factor that gives the difference in cross-polar isolation (XPI) at sufficiently large carrier-to-noise ratio (typically 35 dB) and at a specific BER for systems with and without cross polar interference canceller (XPIC). A typical value of XPIF is about 20 dB.

4.1.5.2 PREDICTION OF XPD OUTAGE DUE TO CLEAR –AIR EFFECTS

Intense rain governs the reductions in XPD observed for small percentages of time. For paths on which more detailed predictions or measurements are not available, a rough estimate of the unconditional distribution of XPD can be obtained from a cumulative distribution of the co-polar attenuation (CPA) for rain using the equi-probability relation:

$$XPD = U - V(f)\log CPA \quad \text{dB} \quad (4\text{-}90)$$

The coefficients U and $V(f)$ are in general dependent on a number of variables and empirical parameters, including frequency, f. For line-of-sight paths with small elevation angles and horizontal or vertical polarization, these coefficients may be approximated by:

$$U = U_0 + 30 \cdot \log(f) \quad (4\text{-}91)$$

$$\begin{aligned} V(f) &= 12.8\, f^{0.19} && \text{for} \quad 8 \le f \le 20 \text{ GHz} \\ V(f) &= 22.6 && \text{for} \quad 20 < f \le 35 \text{ GHz} \end{aligned} \quad (4\text{-}92)$$

An average value of U_0 of about 15 dB, with a lower bound of 9 dB for all measurements, has been obtained for attenuations greater than 15 dB.

The variability in the values of U and $V(f)$ is such that the difference between the CPA values for vertical and horizontal polarizations is not significant when evaluating XPD. The user is advised to use the value of CPA for circular polarization when working with equation (4-90).

Long-term XPD statistics obtained at one frequency can be scaled to another frequency using the semi-empirical formula:

$$XPD_2 = XPD_1 - 20\log(f_2/f_1) \quad \text{for} \quad 4 \le f_1, f_2 \le 30 \text{ GHz} \quad (4\text{-}93)$$

where XPD_1 and XPD_2 are the XPD values not exceeded for the same percentage of time at frequencies f_1 and f_2.

The relationship between XPD and CPA is influenced by many factors, including the residual antenna XPD, that has not been taken into account. Equation (4-93) is least accurate for large differences between the respective frequencies. It is most accurate if XPD_1 and XPD_2 correspond to the same polarization (horizontal or vertical).

The following graph shows the cumulative probability function for XPD indicated as F_{XPD}.

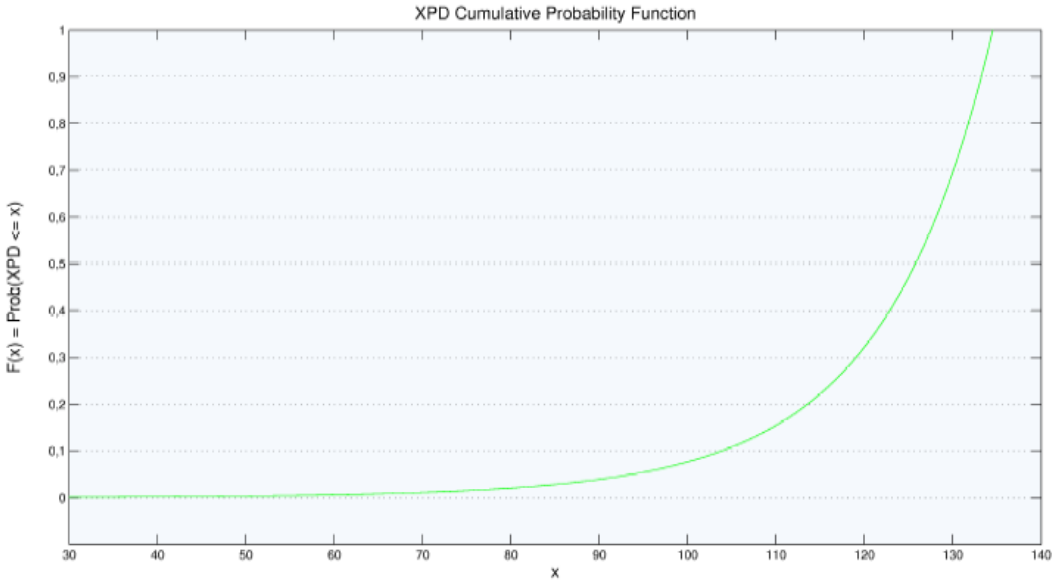

Figure 4-19: XPD Cumulative Probability Distribuition

A maximum value for XPD is assumed be near to 140.

Observing both Figure 4-18 and Figure 4-19, it is clearly visible how if we choose a lower percentage of time for the CPA, (i.e a greater value of attenuation), the probability to find lower values of XPD decreases. In other words, as soon as the co-polar attenuation increases in order to take into account worst meteorological situations, the probability to have bad XPD values decreases.

4.2 TRANSMITTER AND RECEIVER ARCHITECTURES

The PERLA-W transmitter scheme is reported in Figure 4-20. The transmitter is based on the DDS logic which allows to generate signals through the so called Software Defined

Radio, simplifying in this way the signal generation. Moreover, it presents a good flexibility permitting to generate both un-modulated and modulated signals with a large possibility of choice in terms of modulation types and data rate.

This characteristic will be useful during the experimentation of the link on the field. Basically, a reference signal at 100 MHz drives the DDS providing the clock signal at 500 MHz. At the output the DDS, after proper filtering, provides a signal at 136 MHz that is afterwards mixed with another signal at 1300 MHz, generated through a secondary path from the initial signal reference at 100 MHz, creating an output at 1436 MHz signal. The latter one is amplified and then upconverted by mixing it with a local oscillator at 5.2 GHz (PLDRO based). The output signal at 6.65 GHz is then spectrally cleaned from the lower frequencies by using a junction SMA/WR137-WR137/SMA, exploiting the typical cut-off frequency of waveguides.

After a new amplification and filtering, the processed signal is again up-converted by mixing it with a local oscillator at 88.8 GHz and generating a 95.5 GHz output. As before, this local oscillator is based on a basic PLDRO at 14.8 GHz and provides the necessary output through two multipliers. Both PLDROs used are driven by the original reference signal at 100 MHz. Finally, a SSPA provides the needed power to be sent to the antenna. A similar scheme was derived for the receiver, as shown in Figure 4-21. Basically, after signal receiving at 95.5 GHz, the signal is filtered by using a strategy similar to that one used in the transmitter. A junction WR10/WR8-WR8/WR10 allows to eliminate all the higher frequencies exploiting the cut-off frequency of the waveguide WR8.

Afterwards, a LNA amplifies the signal and send it to the mixer where it beats with a local oscillator signal at 88.8 GHz. Then, the signal is amplified at IF frequency 6.65 GHz, filtered and again down-converted through a local oscillator at 7.9 GHz (PLDRO based). At last, the received signal can be analysed by means of a VSA. Considering such schemes, at present the most critical component is represented by the SSPA, while all the other devices can be developed by ourselves or purchased by European companies. In Table 4-3 and Table 4-4, the main components of the PERLA transmitter and receiver are reported respectively.

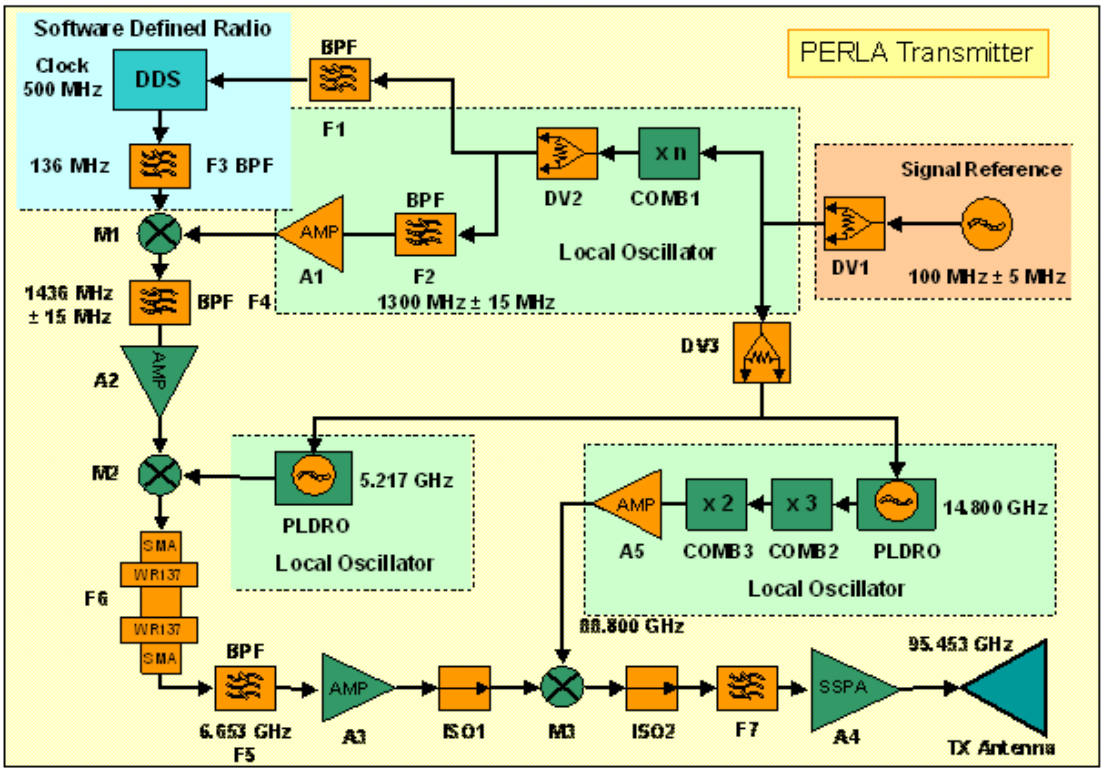

Figure 4-20: PERLA Transmitter

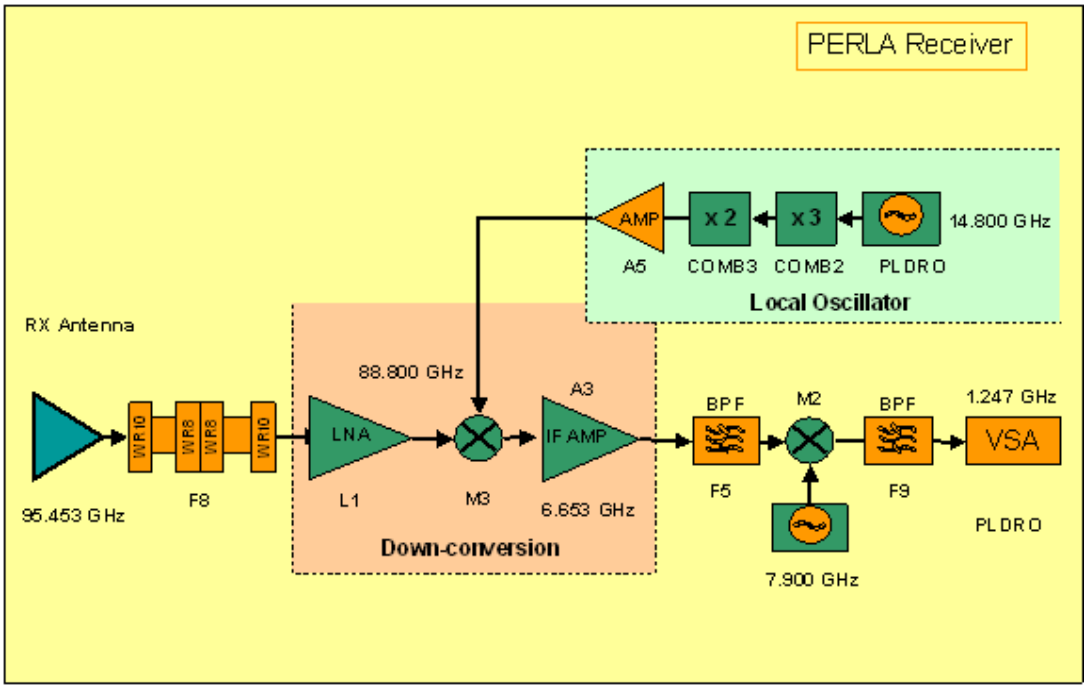

Figure 4-21: PERLA Receiver

Name	Identification	Manufacturer	Description	Gain (dB)	Max Output Power (dBm)	Noise Figure (dB)
A3	ZX60-8008E+	Mini-Circuits	Amplifier	8,20	8,78	4,3
A4	FPA-10-19-21	Farran	SSPA	19	22	5

Name	Identification	Manufacturer	Description	Insertion Loss (dB)
DV1	ZX10-2-12	Mini-Circuits	Power Splitter	3,50
DV2	ZX10-20-20+	Mini-Circuits	Power Splitter	3,80
DV3	ZX10-2-12	Mini-Circuits	Power Splitter	3,50
Comb2	MUT-22	Millitech	Frequency Tripler	20,00
Comb3	MUD-10	Millitech	Frequency Tripler	22,00
F3	AB127B809	AMCrf	Cavity BPF	2,50
F4	AB1542B748	AMCrf	Cavity BPF	2,50
F5	VBFZ-6260+	Mini-Circuits	BPF	1,27
F6	4602	Narda	HPF	
F7	FNP-10	Millitech	BPF	2,20
M1	ZX05-11X+	Mini-Circuits	Mixer	7,25
M2	ZX05-U742MH+	Mini-Circuits	Mixer	7,25
IS01	F2153-0565-12	Wenteq	Isolator	0,40
IS02	FBI-10	Millitech	Isolator	2,50

Table 4-3: PERLA Transmitter Components

Name	Identification	Manufacturer	Description	Gain (dB)	Noise Figure (dB)
L1a	HLNAW-127	HXI	LNA	16	6
L1b	HLNAW-277	HXI	LNA	22	5,5
L1c (considered in Link Budget due to higher gain)	HLNAW-241	HXI	LNA	32	6
A3	ZRON-8G+	Mini-Circuits	MPA	20	4,66

Name	Identification	Manufacturer	Description	Insertion Loss (dB)
Comb2	MUT-22	Millitech	Frequency Tripler	20,00
Comb3	MUD-10	Millitech	Frequency Tripler	22,00
F5	VBFZ-6260+	Mini-Circuits	BPF	1,27
F8	TWT-08, TWT-09	Millitech	HPF	0,4
F9	AB1542B748	AMCrf	Cavity BPF	2,50
M2	ZX05-14LH+	Mini-Circuits	Mixer	5,64
M3	MXP-12-R	Millitech	Mixer	8,50

Name	Identification	Manufacturer	Description	Max Output Power (dBm)	Input Level (dBm)
PLDRO	PLDRO-xxx	Jersey Microwave	Oscillator	13	0±40

Table 4-4: PERLA Receiver Components

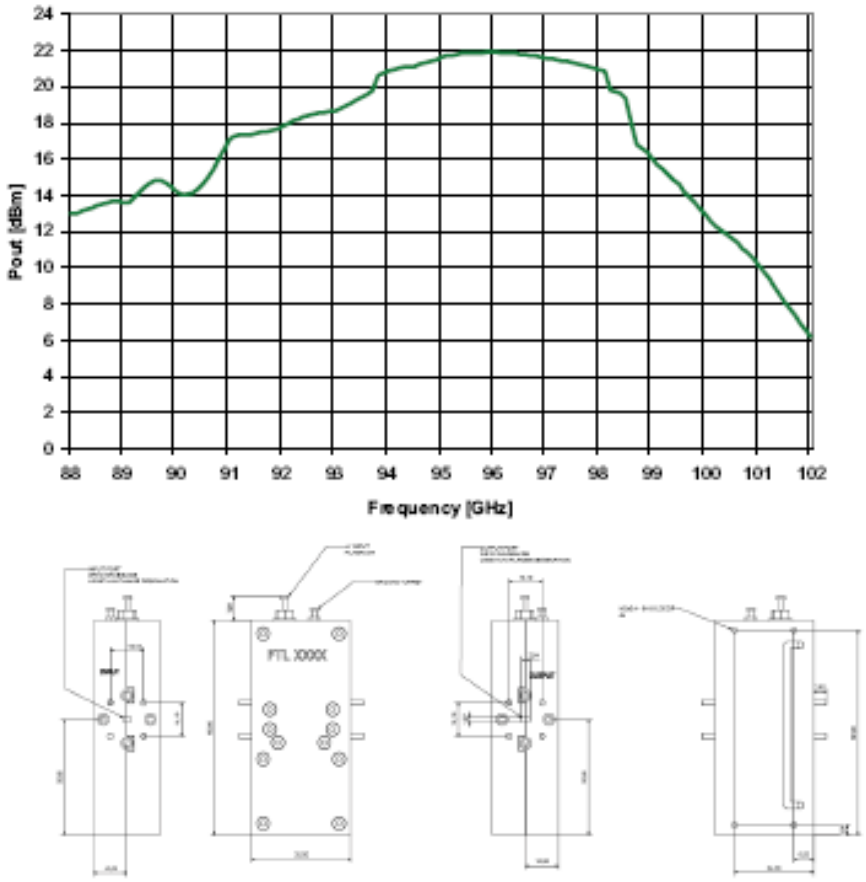

Figure 4-22: FPA-10-19-21 P_{out} - Frequency Characteristic

Figure 4-23 and Figure 4-24 show the link budget for an uncoded Q-PSK with a data rate of modulation considering an availability percentage of time of 99.9%, respectively.

It is clear how the SSPA subsystem is fundamental in order to improve the performance link, together with a suitable coding.

Moreover, using an Horn Antenna at receiver side does not allow to achieve a positive system link Margin.

However, the realisation of a Cassegrain-to-Cassegrain radio link over a distance of more than few Km is a really hard task due to their extremely high values of directivity. Hence, high performance pointing systems are required in order to use Cassegrain reflectors at both Tx side and Rx one: in fact, very small vibrations at the support of the antennas could mean the totality absence of signal at the receiver side.

W band Link Villa Mondragone - Univ. Tor Vergata						
Parameter:	*Value:*	*Units:*	*Comments:*			
Tor Vergata Tx						
Pt (Transmitter Power Output):	0.300	Watts				
In dBW:	-5.23	dBW				
In dBm:	24.77	dBm				
Transmission Line Losses:	0.20	dB				
S/C Connector, Filter or In-Line Switch Losses:	1.50	dB				
Tx Antenna Diameter	0.45	m	Cassegrain	45816H1124		
Efficiency	0.60					
Tx Antenna Gain	50.89	dBi				
TxTheta3dB	0.49	degrees				
Depointing	0.14	degree				
Effective Isotropic Radiated Power (EIRP):	43.96	dBW	Effective Isotropic Radiated Power			
Cross polarization Discrimination (XPD)						
In dBm:	73.96	dBm				
Tor Vergata Tx - Villa Mondragone Rx						
Transmission Antenna Pointing Loss:	1.00	dB				
Antenna Polarization Loss:	0.00	dB				
Frequency (Carrier)	9.60E+10	Hz				
Wavelenght	0.00313	m				
Outage Probability (1-δ(t))	0.01000					
Distance	7.4E+03	m				
Free Space Loss:	149.5	dB				
Atmospheric Loss:	2.60	dB	(1-δ(t)) =0.1 %			
Multipath Loss:	33.89	dB	(1-δ(t)) =0.1 %			
Rain Loss:	23.52	dB	(1-δ(t)) =0.1 %			
Isotropic Signal Level at Ground Station:	-166.50	dBW	EIRP/(Final Att.)			
Villa Mondragone Rx						
Receive Antenna Pointing Loss:	2.03	dB				
Rx Antenna Lunghezza	0.45	m				
Efficiency	0.60					
Rx Antenna Gain	50.89	dBi				
RxTheta3dB	0.49	degrees				
Depointing	0.20	degree				
LNA Noise Temperature:	864.51	K				
Transmission Line Temp.:	290	K				
Antenna Sky Temperature:	100	K				
Transmission Line Coefficient (L):	0.90					
Transmission Line Coefficient (L dB):	-0.46					
Ts System Noise Temperature:	943.40	K	Maral-Bousquet			
G/T (Gain to Noise Temperature Ratio):	20.69	dB/K	M=2 for QPSK			
C/No (Carrier-to-Noise Power Density):	80.76	dBHz	-228.6	dBW/K/Hz		
Bn (PLL Noise Bandwidth):	8.00E+06	Hz				
C/N (Carrier-to-Noise Ratio):	11.72	dB				
			M=2 for QPSK			
Rsource (source bit rate):	8.00E+06	bps				
Tb (source bit duration):	0.0000001250	s				
M (number of bits per modulated symbol):	2					
R1 (inner code rate):	1.0000000000					
R2 (outer code rate):	1.0000000000					
Rb (channel bit rate):	8.00E+06	bit/s				
Rs (channel symbol rate):	4.00E+06	symbol/s	uncoded QPSK			
Eb/No:	11.72	dB				
Es/No:	14.73	dB				
Downlink Required Es/No:	10.5	dB	uncoded QPSK			
System Link Margin:	4.23	dB				

Figure 4-23: Link Budget – Uncoded QPSK - Data Rate 8 Mbps (considering a SSPA subsystem using two 150 mW modules- Output Power = 300 mW (Linear)) – 99.9% Link Availability

W band Link Villa Mondragone - Univ. Tor Vergata						
Parameter:	*Value:*	*Units:*	*Comments:*			
Tor Vergata Tx						
Pt (Transmitter Power Output):	0.300	Watts				
In dBW:	-5.23	dBW				
In dBm:	24.77	dBm				
Transmission Line Losses:	0.20	dB				
S/C Connector, Filter or In-Line Switch Losses:	1.50	dB				
Tx Antenna Diameter	0.45	m	**Cassegrain**	45816H1124		
Efficiency	0.60					
Tx Antenna Gain	50.89	dBi				
TxTheta3dB	0.49	degrees				
Depointing	0.14	degree				
Effective Isotropic Radiated Power (EIRP):	43.96	dBW	Effective Isotropic Radiated Power			
Cross polarization Discrimination (XPD)						
In dBm:	73.96	dBm				
Tor Vergata Tx - Villa Mondragone Rx						
Transmission Antenna Pointing Loss:	1.00	dB				
Antenna Polarization Loss:	0.00	dB				
Frequency (Carrier)	9.60E+10	Hz				
Wavelenght	0.00313	m				
Outage Probability (1-δ(t))	0.01000					
Distance	7.4E+03	m				
Free Space Loss:	149.5	dB				
Atmospheric Loss:	2.60	dB	(1-δ(t)) =0.1 %			
Multipath Loss:	33.89	dB	(1-δ(t)) =0.1 %			
Rain Loss:	23.52	dB	(1-δ(t)) =0.1 %			
Isotropic Signal Level at Ground Station:	-166.50	dBW	EIRP/(Final Att.)			
Villa Mondragone Rx						
Receive Antenna Pointing Loss:	2.03	dB				
Rx Antenna Lunghezza	0.45	m				
Efficiency	0.60					
Rx Antenna Gain	50.89	dBi				
RxTheta3dB	0.49	degrees				
Depointing	0.20	degree				
LNA Noise Temperature:	864.51	K				
Transmission Line Temp.:	290	K				
Antenna Sky Temperature:	100	K				
Transmission Line Coefficient (L):	0.90					
Transmission Line Coefficient (L dB):	-0.46					
Ts System Noise Temperature:	943.40	K	Maral-Bousquet			
G/T (Gain to Noise Temperature Ratio):	20.69	dB/K	M=2 for QPSK			
C/No (Carrier-to-Noise Power Density):	80.76	dBHz	-228.6	dBW/K/Hz		
Bn (PLL Noise Bandwidth):	2.00E+07	Hz				
C/N (Carrier-to-Noise Ratio):	7.74	dB				
			M=2 for QPSK			
Rsource (source bit rate):	2.00E+07	bps				
Tb (source bit duration):	0.0000000500	s				
M (number of bits per modulated symbol):	2					
R1 (inner code rate):	1.0000000000					
R2 (outer code rate):	1.0000000000					
Rb (channel bit rate):	2.00E+07	bit/s				
Rs (channel symbol rate):	1.00E+07	symbol/s	uncoded QPSK			
Eb/No:	7.74	dB				
Es/No:	10.76	dB				
Downlink Required Es/No:	10.5	dB	uncoded QPSK			
System Link Margin:	0.26	dB				

Figure 4-24: Link Budget – Uncoded QPSK- Data Rate 20 Mbps (Max Performance considering a SSPA subsystem using two 150 mW modules - Output Power = 300 mW (Linear)) -99.9% Link Availability

4.3 REFERENCES

[4-1] A. J. Fenn and L. W. Rispin, "A Terrestrial Air Link for Evaluating Dual-Polarization Techniques in Satellite Communications", The Lincoln Laboratory Journal, Vol.9, N.1, 1996.

[4-2] Veyrunes, O.; Le Clerc, P.; Sizun, H "First Results of Precipitation Effects at 30, 50, 60 and 94 GHz on a 800 m Link in Belfort (France)", National Conference on Antennas and Propagation, 1999.

[4-3] D. Narayana Rao, K. Krishna Reddy, K.S. Ravi, S.V.B. Rao, T.G. Faizuddin, M.J. Kesava Murthy, "Study on Rain Attenuation and Fading on a Terrestrial Microwave", SV University, India.

[4-4] M. Ruggieri et al., "Data Collection from the Antarctic Region through a W-band Low Earth Orbit Satellite", International Journal of Satellite Telecommunications, 2001.

[4-5] C. Dainelli, M. Ferri, A. De Fazio, L. Ricci, M. Ruggieri, "W band communication link, design and on ground experimentation", IEEE Aerospace Conference 2005, 5-12 March 2005, pp. 920 – 926.

[4-6] FreeGis italy web site http://www.freegis-italia.org/

[4-7] NASA's official mission website, site http://www2.jpl.nasa.gov/srtm/ srtmBibliography.html/.

[4-8] ITU-R P. 530-10 "Propagation data and predictions methods required for the design of terrestrial line of sight systems".

[4-9] ITU-R P.676-5 "Approximate estimation of gaseous attenuation in the frequency range 1-350 GHz".

[4-10] ITU-R P. 836 "Water vapour: surface density and total columnar content".

[4-11] ITU-R P.841-3 "Conversion of annual statistics to worst-month statistics".

[4-12] ITU-R P.453-9 "The radio refractive index: its formula and refractivity data".

5 MISSIONS DESIGN FOR INNOVATIVE BROADBAND COMMUNICATION SATELLITE SYSTEMS IN W BAND

5.1 STATE OF THE ART OF EHF SATELLITE SYSTEMS

The frequencies allocated for the first satellite commercial services were in C-band (uplink frequencies near 6 GHz, while downlink ones near 4 GHz). These frequencies were selected since the propagation effects were estimated and measured, while the technology was well in hand as a result of earlier work on terrestrial microwave links.

Subsequently, when the C-band became congested, the Ku-band was used (uplink frequencies were near 14 GHz, downlink ones near 12 GHz). Currently the standard is moving towards the Ka-band (uplink frequencies near 30 GHz and downlink ones near 20 GHz). At the end of '90, the encouraging scientific and technical results achieved by the Italian ITALSAT [5-1] [5-2] systems, contributed to the Aerospace Community firm belief in the feasibility of "beyond Ka-band" satellite communication systems. As described in the first chapter, the reason for the large international interest in global EHF satellite systems is led by the future perspectives of the growth in data communications demand. These systems can help national and regional telecommunications service providers to support terrestrial networks. Moreover, they can mitigate the critical issue of Digital Divide in order to provide instant connectivity between disparate networks and instant infrastructure in areas not adequately served by terrestrial systems. During 1990s, the problem of the inhomogeneous development of digital knowledge was firstly identified within different areas of the United States. At the beginning of the new millennium, the same feeling was perceived by United Nation on a larger scale, when differences between technologically advanced countries and poor nations in Africa and Asia were considered. United Nations Organization has thus developed a recovery plan to fill the increasing gap in the use of digital technologies in different areas of the world and issued the Millennium Goals as a roadmap to solve the Digital Divide problem.

On the other hand, European Union with the "eEurope 2002" plan faced the same problem with the aim of reducing the gap in the field of new technologies use among members of the Community.

The Italian Government, taking into consideration European Union recommendations, issued its own plan to promote adequate policies intended to widespread IT culture at every degree of the school institution.

From European Union and Italian standpoints, several objectives have been identified to counteract the increasing Digital Divide. Among others, major points are:

- to develop new techniques for cheap, fast and secure access to the Internet;
- to promote educational goals in order to diffuse the knowledge of new technologies;
- to enhance the use of Internet in the Public Administration;
- to increase the development of e-commerce.

In this context, studies made on possible solution to satisfy the demand of European Union to allow the whole European Society to access the knowledge were carried out. They showed that, despite ADSL, Fiber and Wireless services will cover a large percentage of European Union users, mostly located in urban areas, terrestrial broadband services will still be unavailable by 2013 for about 4 million of possible users in Europe, (30% of which will be business users). These possible clients of broadband access could be interested in the take-up of satellite services.

Forecasts about economical-scale price reduction between terrestrial and satellite service costs showed that satellite solution will be more affordable for rural area users, while being not competitive in those areas covered by the terrestrial service.

Anyway, even though a great number of users in rural areas (maybe about 1 million over 4 millions) could potentially be covered by satellite broadband services, the available capability of actual satellite systems is not able to fulfil the service demand of such a high number of users.

Therefore, new generation of EHF band satellites, with higher intrinsic spectrum availability, could be suitable to mitigate the Digital Divide in rural areas; this is the reason why currently applications in Q/V bands are considered to be the most promising technology for the broadband services distribution.

There are a good number of systems, most of them developed for dual-use (civil and defence) applications, operating in Q/V band (40-75 GHz).

They aim at exploiting the Q/V bands in order to provide broadband services such as: backbone connectivity, high rates broadcasting and multicasting, backbones interconnection trunking and bulk data delivery, and point-to-point intensive communications. However, adequate countermeasures have to be applied in order to compensate the high propagation loss measured for Q/V frequencies, increasing the complexity of the system and in particular of the Earth Stations (both Ground and User Segments).

Following this trend, in the last years, the scientific research has focused its attention on "beyond Q/V-band" systems. In fact, these frequency ranges represent the current technological/scientific frontier. As already explained, in the near future, the need for broadband satellite services and the growing saturation of lower frequency bands will make it mandatory the identification of novel concepts, the design of innovative systems and the development of advanced technological solutions that will lead the change towards "beyond Q/V band" satellite communication systems.

In this scenario, my Ph. D activities have been focused on the study and analysis of W band (75-110 GHz) to use it for satellite communication systems. This frequency band has very interesting features for research purposes, being never used for telecommunication applications but being extensively used (in particular the 90-95 GHz range) in radio-astronomy and radar applications. My work has been carried out with the aim to analyse the interest in future EHF satellite communication systems and evaluate the innovative scientific concepts that arise in this frame.

After an analysis of the global scenario for the future generation of EHF broadband satellite systems, the goal of this section is to carry out the feasibility study of a small P/L satellite in W band.

First of all, the analysis of the state of the art has been carried out in order to identify the proposed, the operative and the discontinued systems operating in Q/V and W-band.

Then, the main EHF satellite propagation issues are described. The design techniques recommended for predicting propagation effects are presented. Rain, atmospheric gases, clouds and scintillation attenuation phenomena are deeply analysed and some simulation results on the use of these models for W band link are provided.

Finally, a development strategy of missions for the future exploitation of W band for satellite communications is shown, principally focusing on the feasibility study of a W band Small P/L satellite, together with main systems and P/L architectures.

5.2 STATE OF THE ART OF Q/V-BAND SATELLITE SYSTEMS

In the last years, several proposals to realise commercial satellite services in the EHF bands have been brought forward, especially in the United States.

At the end of 1997, a request to the United States FCC for licenses to operate commercial satellite services in the 36.1-51.4 GHz bands, was made for seventeen systems [5-3] [5-4] [5-5]. The 17 filers proposed applications ranging from mobile high data rate wireless communication to additional broadcasting capability.

The proposed systems are based on the use of GEO, LEO, MEO and Molniya orbit satellites, and in some cases on the combination of two of these orbits. Moreover, most of these systems foresee to employ new technologies, such as ISL, multiple narrow spot-beam antennas with on-board demodulation and routing of traffic between beams.

As previously discussed in this work, one of the major difficulty involved in fielding systems at these high frequencies arises from the propagation impairments that can be expected and the high cost of solid-state power devices for user terminals, which will drive up costs; on the other hand, the large amount of bandwidth available for these systems is very attractive.

In Table 5-1 the FCC frequency allocation for Q/V band satellite systems is reported, both for GEO and non-GEO satellites.

Satellite Orbit	Uplink Freq. (GHz)	Downlink Freq. (GHz)
GEO	47.2 – 50.2	37.5 – 40.5
Non-GEO	48.2 – 49.2	37.5 – 38.5

Table 5-1: FCC allocated frequencies for Q/V band satellite systems

In Table 5-2 and Table 5-3, some of the most important proposed EHF satellite systems are listed, together with indications about coverage, the type of orbit(s) to be employed, coverage, beams characteristics, TWTA power, EIRP and other P/L characteristics. The GEO results the orbit of choice for most systems; such satellites require no tracking by Earth Station antennas, which greatly simplifies their cost, installation, and maintenance (given that most of the cost of a fully deployed system is due to GS). For GEO EHF satellite systems, RF power generation can be considered one of the most interesting challenges (considering the high requirements in terms of power for a GEO-Earth link); in fact, “beyond Ka-band” HPAs can be identified as the frontier of the space technologies.

Table 5-2: EHF Satellites Filing

Company	System	Orbit	No. of sat.	Coverage	Satellite Capacity (Gb/s)	ISL	Onboard Switching	Capital Investment $B
Denali Telecom	Pentriad	Molniya	9	25° -85° N	≤ 36	No	MS M	1.9
GE Americom	GE* StarPlus	GEO	11	Global	~ 70	No	MS M	3.4
Globalstar L.P.	GS-40	LEO	80	± 70°	~ 1	No	MS M	?
Hughes Comm. Inc.	Expressway	GEO	14	Limited Global	~ 65	Optical 3 (Gbps)	SSTDMA	3.9
Hughes Comm. Inc.	SpaceCast	GEO	6	Limited Global	~ 64	Optical 3 GBps	SSTDMA	1.7
Hughes Comm. Inc.	StarLynx	GEO & MEO	4 20	± 80	≤ 5.9 ≤ 6.3	2 optical	Baseband	2.9
Lockheed Martin	Q/V-Band	GEO	9	Global	≤ 45	3 Optical 2 Radio	ATM Baseband	4.75
Loral Space and Comm. Ltd.	Cyberpath	GEO	10	Global	17.9	2 Radio	ATM Baseband	1.17 (for 4)
Motorola	M-Star	LEO	72	± 60°	~ 36	2 Radio	MSM & SSTDMA	6.4
Orbital Sciences Corp.	Orblink	MEO	7	± 50	~ 75	2 Radio	MS M	0.9
PanAmSat	V-stream	GEO	12	Global	< 3.2	2 Radio	MS M	3.5
Spectrum Astro, Inc.	Aster	GEO	25	Global	~ 10	2 Optical	SSTDMA & Baseband	2.4
Teledesic	VBS	LEO	72	Global	4	4 Optical	Baseband	1.9
TRW	GESN	GEO & MEO	14 15	± 70°	~ 50 ~ 70	10 Optical 4 Optical	Baseband	3.4

Table 5-3: Parameters of U.S. Q/V band Satellite Systems

System	No. of Beams	Beam Size	No. of Earth-Space Transp.	Transponder Bandw. (MHz)	TWTA PW (W)	EIRP (dBW)	Life
Pentriad	80 V-band 12 W-band	~ 0.6° ~ 0.4°	80 12	78	80	73.0 77.7	10
GE* StarPlus	40 V-band	0.3°	400	300	100	59	15
GS-40	30 steered	2°	30	18 / 90	48	52	7.5
Expressway	20 V-band 8 Ku-band	0.5° 1° x 3°	20 8	300 250	100 25	55 48	15
SpaceCast	40 V-band 16 Ku-band	0.15° 1° x 3°	40 16	300 250	100 150	72 55	15
StarLynx	40 GEO 32 MEO	0.15° 0.6°	40 32	270	100 50	70.5 56	15 12
Q/V-Band	9	0.30°	48 user 8 gateway	125	Active phased array	64.2 62.7	15
Cyberpath	100	0.42°	100	142	40	77.5	15
M-Star	32	1.1°	104	90	Active phased array	21-29	8
Orblink	100	0.5°	800 narrow 20 wide	50 1000	25	62 60	9
V-stream	20	1.5°	80	375	75	60	15
Aster	8 spot 8 regional	0.5° 1° - 5°	18	470 spot 980 regional	50	66.7 60.7	15
GESN	32 GEO 48 MEO	32 48	32 48	300 / 3000	Active phased array	83 78	15

LEO systems have been proposed (e.g., by Teledesic at Ka-band) out of concern for the half-second response time encountered over GEO satellites, which can limit the speed of access to the Internet and hinder real-time applications.
All of the systems aim to offer global or nearly global service employing some form of on-board routing. This need comes from the narrow spot beams used in order to overcome propagation effects.
Some of these proposed systems were abandoned during the last years because of the high technological and financial investments required, while some of them will be realised in the near future.
In the following paragraphs of this section, the most important characteristics of the major Q/V-band satellite systems will be reported. The main actors in the field of EHF satellite communications have been identified during this research: Europe (in particular Italy), U. S., and Japan.

5.2.1 ITALSAT

ITALSAT F1 and F2 [5-1], [5-2], [5-7] are two experimental/pre-operative telecommunication GEO satellites built by Alenia Spazio for the ASI.
The first satellite, F1, was launched in January, 16, 1991 and, the second one, F2, was launched in August, 8, 1996. They provided 30 GHz (in up-link) and 20 GHz (in down-link) Italian domestic coverage using six high-directivity spot beams and a "global" national elliptic beam. The F1 spacecraft also carried sophisticated propagation beacons at 40 and 50 GHz, able to provide significant information about satellite channel propagation in EHF bands.
The propagation package included a telemetry-modulated 20 GHz beacon (also used for tracking), a 40 GHz beacon phase modulated by a 505 MHz coherent sub-carrier, and a polarization-switched (but otherwise un-modulated) 50 GHz beacon. It supports attenuation and depolarization measurements at 20, 40, and 50 GHz, as well as measurements of phase and amplitude dispersion. The availability of a polarization-switched signal enabled earth stations to characterize fully the matrix depolarization characteristics of the 50 GHz channel.

The 40 GHz beacon had two side bands at ±0.5 GHz from the carrier. This provided an opportunity to measure the coherence bandwidth and other differential properties of the medium in order to calculate the achievable maximum data rate. Researchers compared the millimetre wavelength beacon measurements with simultaneous measurements at 18.7 GHz and with radiometric brightness temperature measurements at 51 GHz.

The propagation beacons had total European coverage from an orbit position of 13 deg. E, as shown in Figure 5-1 and Figure 5-2. These beacons provided a unique opportunity to obtain propagation data appropriate to the next generation of 40/50 GHz systems. As a matter of fact the scientific results achieved through ITALSAT, in the field of satellite propagation channel characterization, are of paramount importance, being used for the creation of statistical models for each atmospherical impairments (rain, clouds, gas, scintillation, etc.) in EHF (till 50 GHz).

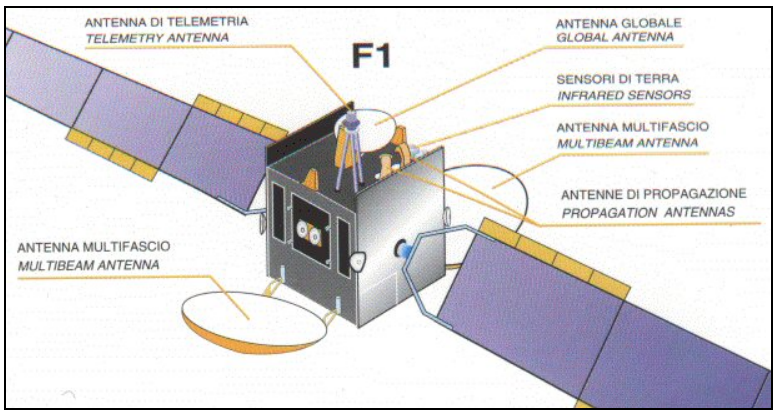

Figure 5-1: Italsat F1 Satellite

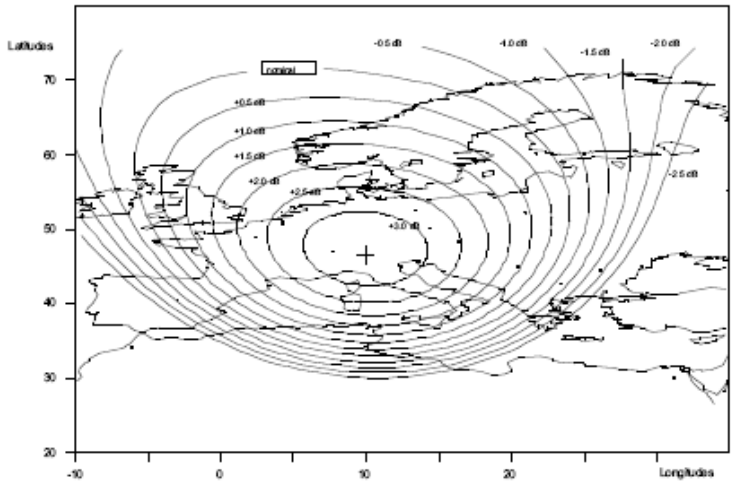

Figure 5-2: Italsat 40 and 50 GHz Propagation Experiment Coverage

5.2.2 SICRAL

SICRAL (Sistema Italiano per Comunicazioni Riservate ed Allarmi) is the first Italian system for secure tactical military communication over national and international areas and for mobile communication with earth, naval, and aerial platforms (Figure 5-3 [5-8]).
The system is in service since May 2001 and operates in three frequency bands (multi-payload and multi-transmission): EHF (20-44 GHz) for infrastructural communications, UHF (260-300 MHz) for mobile tactical communication, SHF (7-8 GHz), that is the main band for high volume data transfer, with a multi-beam reconfigurable antenna. SICRAL is based on innovative technologies that enable the satellite to adapt promptly to changing emergency conditions. It is also highly flexible, with a large capacity and can be used for land, sea and air operations.

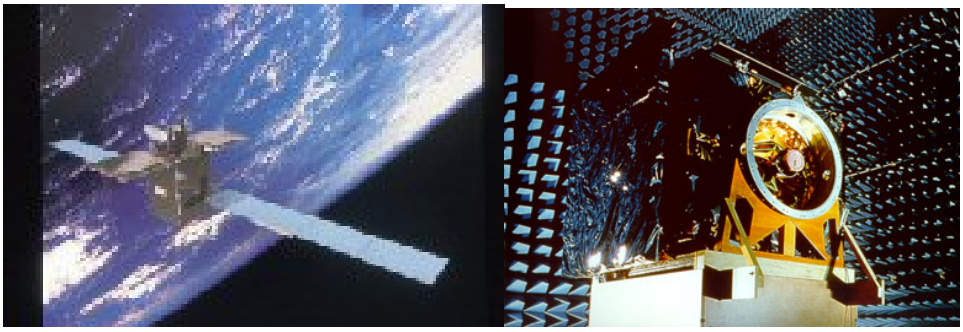

Figure 5-3: Sicral I Satellite

5.2.3 ALPHASAT - TECHNOLOGICAL DEMONSTRATION PAYLOAD #5

ESA is the owner of a satellite platform named Alphabus [5-9]. This platform will be capable of carrying a P/L of about 1000 kg with power consumption up to 16 kW. The Alphabus platform (proto-flight model) will be ready for launch in the end of 2011. ESA, through the Alphasat Mission, will use this platform to offer Operators, Service Providers and Industrial Groups the possibility to fly their P/Ls on board of the Alphabus proto-flight model. The Alphabus platform represents a unique opportunity for demonstrating new technologies, systems and services in-orbit. Some of these P/Ls will be "Technological Demonstration Payloads" (TDPs); among these, the experimental TDP#5, named "Q/V band Payload", will be devoted to the experimentation of Q/V band satellite propagation and communication.
The Q/V Band TDP#5 mission will allow to perform three different experiments:

1. *Communication Experiments* with the aim of assessing, over-the-air, the performance of links operating at Q/V bands in conjunction with IFMT such as ACM. These experiments will be performed in the perspective of deploying future high-capacity systems based on the use of EHF bands for the feeder-link, while the current technology limits the adoption of lower frequencies range for the user link. In order to test the ACM technique, a Q/V band P/L is used for interactive point-to-point communications between two Ground Stations through the use of the DVB-S2 standard, which implements the ACM technique.
2. *Scientific Experiments* with the purpose of obtaining additional Q/V band propagation data, essential for optimising modern satellite systems design, and evaluating the system-level impact of data coming from propagation measurements, database and channel simulators.
3. *Technology Experiments* in order to verify the in-flight performance of innovative Q/V band H/W, with particular attention to devices based on MEMS.

Concerning the TDP#5 mission, the space segment consists of:

- a Q/V band P/L;
- a Q band beacon;
- a Ka band beacon.

The minimum set of ground segment facilities, for the communication experiment, will consist of a couple of TX/RX ground stations each one located in the foot-prints of the beams generated by the TDP#5 P/L and compliant to its space-to-ground interface.

The ground stations are conceived as for operator remotely controlled unit, under the supervision of the dedicated Experiment Control Centre for Communication (ECC-C) which represents the user interface.

The ground segment can be complemented by:

- an auxiliary re-locatable RX only ground station to support the site diversity experiment.
- an additional TX/RX ground station located in Aalborg (DK) (TBC), to be used in alternative to that in Spino d'Adda, thus supporting the experiment between Italy (Rome) and Denmark (Aalborg).

The functional architecture of the Q/V Band TDP system is shown in Figure 5-4.

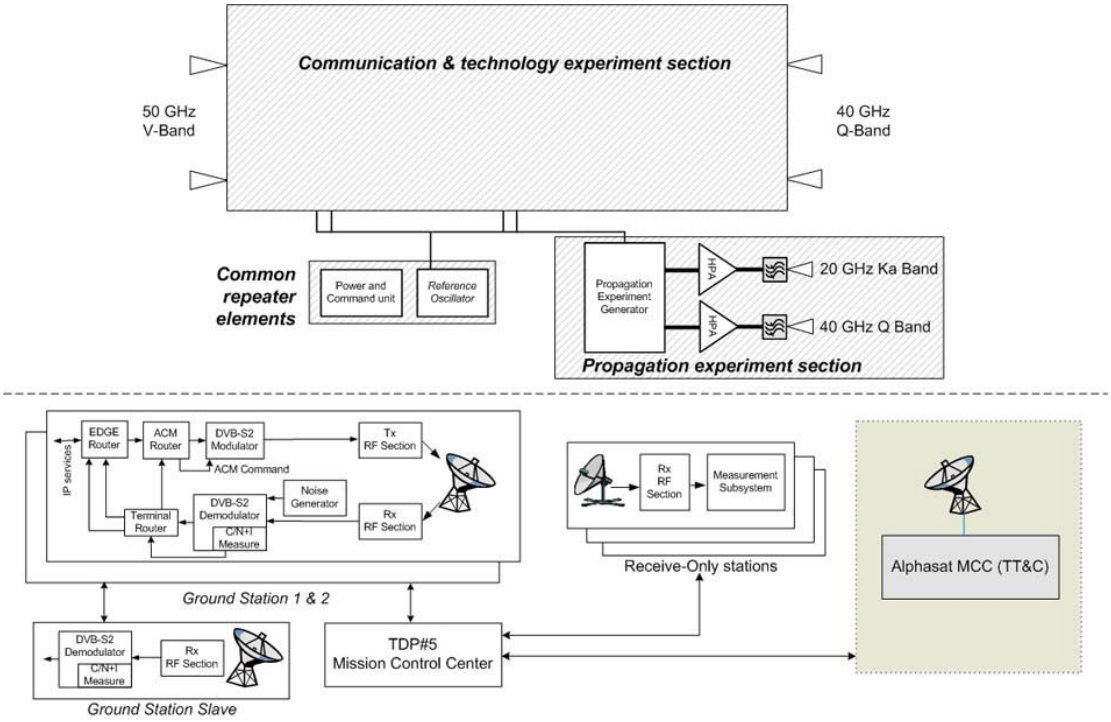

Figure 5-4: Q/V band TDP#5 Functional Architecture

For the *propagation experiment*, the minimum set of Ground Segment facilities will consist of:

- RX-only main ground station, probably embedded in both fixed main telecommunication terminals, compliant to the space-to-ground interface of the TDP#5 P/L beacons operating at Q-Band and Ka-Band. This kind of ground station will be dimensioned in order to have wide margins for the reception of the beacons.
- some unattended RX only terminals (number TBD), to extend the measurements over the Continental Europe. These propagation terminals shall be connected to the main ground station for gathering the local measurement results.

Taking into account the fundamental commonality between the *communication* and the *propagation experiments*, the two parts shall necessarily cooperate in the sense that the results of each experiment shall be available to the other to be integrated in the evaluation.

The space to Earth communication (downlink) will be performed in Q band region: 37.5 ÷ 43.5 GHz (selected center channels frequencies 37.9 and 38.1 GHz). The Earth to space communication (uplink) will be performed in V band region: 47.2 ÷ 50.2 GHz (selected center channels frequencies 47.9 and 48.1 GHz). The centre frequency of the transponders is 200 MHz apart (both at TX and RX side).

The space-borne transponders will be configurable as follows:

- the cross-mode, whereby the receive beam of one repeater serves the same geographical area of the other repeater transmit beam, and vice-versa;
- the loop-back-mode, in which each repeater connected in transmission and reception to the same beam.

The next two paragraphs will be devoted to depict scientific requirements and telecommunication experiments.

5.2.3.1 TDP#5 Scientific Requirements

In order to achieve meaningful data towards the implementation of a real satellite system operating at Q/V bands and to obtain a consistent and valuable feedback for the verification of the effectiveness of IFMT techniques, the TDP#5 system should be capable to support the communication experiments and the propagation one simultaneously.

The knowledge of propagation impairments is required to implement innovative Q/V band satellite systems adopting adaptive techniques.

On the basis of these considerations, the TDP#5 system should be able to log the data related to:

- BER with coding and without coding, PER;
- instantaneous coding/modulation scheme together with MER;
- SNR and C/N;
- throughput;
- received power;
- local attenuation and XPD measurements, radiometric data;
- phase shift of the cross-polar signal;
- meteorological data (ground temperature, pressure, humidity, rain intensity, general status of the atmosphere);
- basic acquisition parameters of propagation signals (acquisition rate filtering, locking status, locked frequency);
- satellite and Earth station health/status data (i.e. satellite position, pointing errors, etc.);
- H/W equipment data (i.e.: satellite/Earth station SSPA transmit power, antennas noise temperature, etc.);
- time (from GPS measurements).

The previously listed parameters should be measured for both links above described. The system should be designed to support the following operative test modes:

- Configured Test: the MODCOD (Modulation and Coding) scheme is chosen in real-time by the scientific user. The manual reconfiguration of the modulation and coding schemes must be achieved in at most 1 minute.
- Automatic Adaptation Test: after a configuration of the MODCOD schemes to be used for a given SNR (or C/N, or BER of the inverse link), the system automatically adapts the MODCOD schemes during the transmission. The automatic configuration of the MODCOD schemes must be achieved in at most 5 seconds.

5.2.3.2 TDP#5 Telecommunication Experiments

In order to verify the effectiveness of IFMT techniques, the TDP#5 P/L will carry out some telecommunication and propagation experiments. Here the analysis will focus just upon the first ones [5-10] [5-11].

The main objective of the envisaged communication experiments is to show the effectiveness of ACM and diversity techniques for improving the achievable throughput in a Q/V band satellite link. In particular, the first years of the experiment, whose duration is currently established to be three years, will be used to optimize the main parameters of the IFMT (ACM and site diversity), which will be tested during the remaining period of the experiment duration.

The experiment foresees two Tx/Rx ground stations: a fixed reference station located at the Engineering Faculty of the University of Rome “Tor Vergata” (central Italy); a second fixed ground station located in Spino D’Adda (Milan, Northern Italy). Moreover, a third relocable Rx-only ground station is foreseen to carry out the site diversity experiment.

The latter one will be performed in the area around Rome and/or Spino D’Adda.

A further option, to be investigated and defined, is to use an additive ground station located in Northern Europe and funded by the host country, acquiring data from a different climatology which would make more reliable the experimentation.

The development of a ground station for the experimentation is under consideration by the University of Aalborg (Northern Denmark). Two experiments are envisaged: ACM and site diversity.

5.2.3.2.1 ACM Experiment

Concerning the ACM experiment, the minimum set of modulation and coding schemes (implemented following the DVB-S2 standard) that the system shall support is listed in Table 5-4.

Mode #	Modulation type	Coding rate	Type of requirement
1	QPSK	1/4	mandatory
2	QPSK	1/3	mandatory
3	QPSK	2/5	mandatory
4	QPSK	1/2	mandatory
5	QPSK	3/5	mandatory
6	QPSK	2/3	mandatory
7	QPSK	3/4	mandatory
8	QPSK	4/5	mandatory
9	QPSK	5/6	mandatory
10	QPSK	8/9	optional
11	QPSK	9/10	optional
12	8PSK	3/5	mandatory
13	8PSK	2/3	mandatory
14	8PSK	3/4	mandatory
15	8PSK	5/6	mandatory
16	8PSK	8/9	optional
17	8PSK	9/10	optional
18	16APSK	2/3	mandatory
19	16APSK	3/4	mandatory
20	16APSK	4/5	mandatory
21	16APSK	5/6	mandatory
22	16APSK	8/9	optional
23	16APSK	9/10	optional

Table 5-4: ACM modes which will be tested in TDP#5 Telecommunication Experiments

The parameters to be optimized include SNR thresholds, shape of the hysteresis and safety margins. SNR thresholds indicate the minimum SNR at which one specific ACM mode can be used to provide the required PER. Those thresholds will drive the selection of the ModCod mode that will used with the measured SNR. Hysteresis and safety margins must be used to avoid too frequent switches among the ModCod modes due to the fast variations of the channel (for instance, due to scintillations). The selection of the thresholds and the experiment schedule are hereafter described. The thresholds choice will be preliminary done off-line, before the experiment starts, by setting up simulations of the physical layer of the DVB-S2 standard (the output of those simulations will be SNR-BER curves), taking into account the already available channel models for Q/V bands satellite links (Italsat). Those thresholds must be further optimized when applied to the real channel, due to the

fact that selected thresholds do not take into account electronic equipments and real channel non-linearities. Therefore, the first year of the experiment will be dedicated to better optimize the selected thresholds. One important issue is to make this selection in one year, in order to verify that for SNR higher than each thresholds, the corresponding ACM mode achieves a PER of 10^{-7}. On the other end, for each ACM mode, it is necessary to show that for lower SNR, the ACM mode does not work. This might require much more time than one year. However, it helps to consider that SNR-BER curve of DVB-S2 standard using LDPC channel codes, are very steep. This means that BER values increase quite rapidly when SNR level goes below the threshold. They might change of several order of magnitude within few tenths of dB, going from BER of 10^{-10} when the SNR is close to the threshold, up to BER of 10^{-2} when the SNR is just fractions of dB below the threshold. Therefore, it is enough to see a BER of 10^{-2}, which requires less than one second of transmission (at 1Mbps) to say that we are above the threshold for that ACM mode. On the other hand, it could be enough to verify that the BER is higher than 10^{-5} (for instance, BER=10^{-6}), which corresponds to around 15 minutes of transmission, to say that we are above the threshold.

An automatic routine will be developed to change the SNR (by changing the added noise in a controlled manner) after 1 second when BER of 10^{-2} or higher are measured, after 15 minutes when lower BER are measured. One hour of experiment for each ACM mode is foreseen per day, in the first year. After each test, one threshold for that ACM mode will be recorded together with the suitable log files. In one hour of experiment the channel condition might change. If the channel becomes worst and it is not possible to test that mode, the experiment will be stopped and another ACM mode will be tested. If the channel becomes better, some noise is added to get the desired SNR close to the threshold we are looking for. After one year, my research group expects to have enough statistics to set the optimum thresholds.

During the second year, the effectiveness of the implementation of ACM techniques (automatic adaptation) without safety margin and setting of the safety margin (together with time hysteresis thresholds) for each mode will be verified. During the third year, the effectiveness of optimized ACM techniques will be tested using automatic system (implementing optimized safety margin and hysteresis time).

In this year the testing of pre-operative services (i.e.: voice and video transmission) should be performed.

5.2.3.2.2 Site Diversity Technique Experiment

Such an experiment will have to demonstrate the effectiveness of the Diversity Technique in presence of ACM, in particular Site Diversity, i.e. diversity based on the selection of a different link geometry using a terminal at a different location and likely with a lower fading when the main site is in outage. It will be implemented through a small Rx-only ground station to be positioned at short distance with respect to the master station (i.e. the University of Rome "Tor Vergata"). The term "short" means a range within 10-30 km from the master station. The experiment shall be carried out through a transportable Rx-only station (i.e. a station that is easily assembled and moved). The experiment strategy foresees to use the transportable station at variable distances (at maximum three different locations), within the range above mentioned, from the master station, with an experiment duration, for each of the distance, that varies according to the availability of positioning site and scientific requirements. Such a variability is envisaged to broaden the base of the diversity statistics and explore extended separation, allowing to evaluate performance of the communication link at different distances. Actually, rain cells that create large attenuation values on an Earth-space link often have horizontal dimensions of no more than a few kilometers. Hence, the evaluation of the link performance at higher and different distances is essential to verify and quantify the improvement in the system reliability. Considering this aspect, two parameters should be measured to evaluate the effectiveness of such a technique:

- the diversity improvement factor, defined as the ratio of the single-site time percentage and the diversity time percentage, at the same attenuation level;
- and the diversity gain, defined as the difference (in dB) between the single-site and diversity attenuation values for the same time percentage. In this context, prediction procedures of such parameters should be foreseen on the basis of ITU-R recommendations (P618-8, [5-12]) as preliminary and rough evaluation (being just tested up to 30 GHz).

The need of using three different locations for the transportable station is justified to achieve significant results for the measured parameters [5-13]. Actually, three locations guarantee three experimental points to be used to identify the theoretical behaviour in terms of better fitting curve for both the parameters above introduced, i.e. the diversity improvement factor and the diversity gain. With respect to the distance variability, the 10-30 km range was chosen on the basis of two arguments. At first, review of past site

diversity experiments showed that at lower frequencies (i.e. 18 GHz) the achievement of a 0.01 % outage was obtained at distances between 32 and 48 km. Moreover, on the basis of ITU-R recommendations above mentioned, it is possible to evaluate diversity between two sites as a function of their distance and of the operating frequency. The procedures have been tested at frequencies between 10 and 30 GHz. Anyway, a preliminary estimate can be achieved extending such procedures up to Q-V bands. It should be highlighted that the diversity prediction procedures are only recommended for time percentages less than 0.1 %. Hence, applying such a strategy is possible to derive the most suitable distance range to be used to carry out the diversity experiment. The result is shown in Figure 5-5.

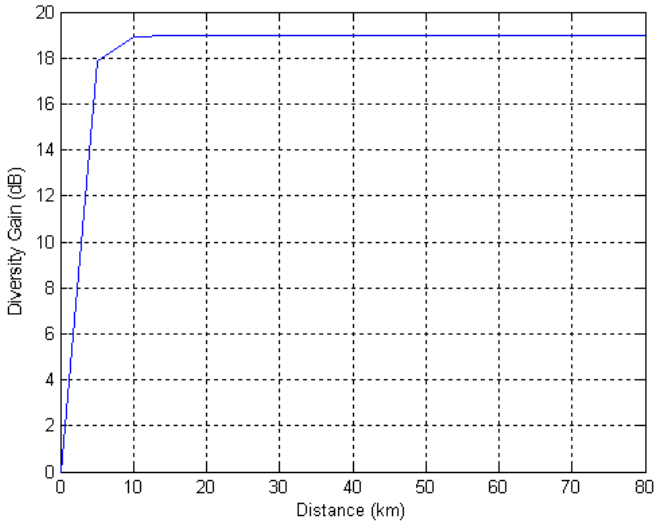

Figure 5-5: Diversity gain between two sites evaluated through ITU-R recommendations P.618-8

The experiment would have major consistency if the measurements were acquired at the same time in all the locations in order to reduce the weather fluctuations between contiguous years. However, this implies three different stations contemporaneously operating and, hence, an increase in costs. Therefore, such a possibility should be evaluated carefully in future phases. However, assuming an uncertainty due to weather variability, the scientific effectiveness of the proposed experiment is still maintained. From the operational point of view, the Site Diversity Experiment foresees the following steps:

- to send a modulated carrier, on the basis of the DVBS2 standard, from the reference station (master station) and to receive the downlink signal both at the secondary station (site diversity station) and at the master station;

- to evaluate power level (attenuation) and SNR at both stations. To this respect, the carrier shall be modulated with a known data pattern and the received pattern at both the receiving stations will be matched to the original one to derive BER and, generally, the SNR;
- to record and storage acquired data on a suitable device (PER, BER, SNR).
- to evaluate an operative mode, identifying a threshold wherein to switch the link on the path less affected by attenuation.

The experimentation will foresee two phases.

The first phase, that will last for the first year of the mission, is completely devoted to characterize the site diversity effectiveness as above illustrated and to evaluate possible strategies to be pursued for the site switching in terms of thresholds on the PER, BER. It will be achieved positioning the Rx-only ground station from the master one at three different distances varying in the range 10-30 km every three months.

The second phase, which will last for the second-third years, is devoted both to continue the characterization and to verify operatively the site switching (thresholds fixing, switching delay tolerance, system reliability, etc.).

5.2.4 TRANSPONDERS

In 2004 ASI funded a feasibility study (phase A), called TRANSPONDERS (**T**ask di **R**icerca, **AN**alisi e **S**tudio su **P**ayload **O**peranti **N**ella banda **D**etta Q/V **E**stesa ai **R**itorni ed agli **S**cenari), Italian acronym for "Research, Analysis and Study of Q/V payloads for telecommunications", aimed at studying and designing a P/L to be used to fully characterize the channel at Q/V bands and to test novel adaptive IFMTs such as ACM. Moreover, this study aims at verifying the feasibility and performance of preliminary broadband services in such frequencies. A new phase of this study has recently finished (April 2009), called TRANSPONDERS-2 and leaded by Space Engineering S.p.A., to continue the achievements gained during the first phase.

In this scenario, it is mandatory to identify pre-operative experimental missions aiming at fully verifying the feasibility of future Q/V bands satellite telecommunication applications. The experimental goals are mainly to test the effectiveness of PIMTs in such frequency bands and the minimization of implementation risks for operative system characterized by a series of technological challenges.

The first phase of this project was focused on the identification of a set of candidate operative missions covering all the types of satellite links (GEO-Earth, NGSO-Earth, ISL – IPL): these missions will be the benchmark for innovative future Q/V band satellite telecommunication applications. A list of possible Q/V band applications identified during this phase of study for all types of satellite links is shown in Table 5-5 [5-14].

Possible Applications	Type of Satellite Link
Broadband Distributed User Access Backbone Connectivity Wideband Broadcasting	GEO-EARTH
Aeronautical Broadband Communications	NGSO-EARTH
Interplanetary High Data Rate Transmission Backbone Connectivity	IPL
Inter-Satellite Links (Sky Nets – Relay)	ISL

Table 5-5: **Possible Applications for all types of satellite links**

However, a key step towards the full exploitation of the Q/V band is represented by the development of a preliminary scientific mission aimed at realizing a full channel characterization and, in general, at constituting a valuable mean to gain insight on the aspects related to the Q/V band propagation which require to be addressed in the design of future commercial systems operating in such a frequency range.

The last studies have identified the BDUA operative mission as the most promising among the candidate ones, since it could guarantee a wideband internet access to disadvantaged European zones, thus fulfilling the European Union requirements [5-15]. However, the feasibility of innovative broadband services in Q/V bands has to be verified analyzing the adaptability of a mission in such a frequency range to very high link impairments and all challenges related to immature technology at these frequencies [5-16].

In this scenario, it is mandatory to carry out research activities on the propagation phenomena at these frequencies aiming at providing a full characterization of the propagation medium parameters. These are fundamental in order to refine and optimize algorithms of the new adaptive access techniques that could allow to realize innovative broadband applications. During the phase A2 of the TRANSPONDERS project, preliminary experimental missions have been identified aiming at establishing the effectiveness of PIMTs in Q/V bands (that should be adopted for the proper operation of

future systems operating at those frequencies), and at identifying technological critical elements related to the design and development of a telecommunication Q/V band P/L.
This paragraph focuses on objectives and the top level system architecture of the operative broadband mission in Q/V bands that the last activities have identified and indicated as BDUA mission. Finally, an overview of the planning of applicative experimental missions is reported focusing on limits and constraints with respect to the final operative mission in Q/V bands.

5.2.4.1 BDUA MISSION

The mission related to the BDUA will consist in a setting up of a BMSS aimed at providing multiple-play services. Multiple-play means the possibility to provide different types of services by the use of a single platform. "Double play" services started in 1990 year when the dial-up internet access was added to the telephone service. "Triple play" services started at the end of 90s when the TV service (video on demand) was added to the voice telephone services and to the internet one. These three different services were delivered by the use of a single broadband connection (multiple-service versus single platform).
However, the potentiality of a broadband connection leads to assume that more and more service can be added to the above remembered three ones, such as: Tele-medicine, Tele-learning, Tele-voting, Tele-banking, Tele-shopping, and Tele-betting (multi-play services).
The BDUA mission is hence in principle associated to the multi-play services, and, in particular, to the “Triple play” ones (Internet Access, Video on-demand, Voice over IP). This means that the possible user class could be: Consumer (Home), B2C (Business to Consumer) market type, Professional (Small Office/Home Office - SOHO) B2C market type, Institutions B2G (Business to Government) market type, Companies B2B (Business to Business) market type.

5.2.4.1.1 BDUA Mission Architecture

The BDUA mission [5-17], [5-18] is based on a geostationary satellite system that foresees a star network with a DVB-S2 like Forward Link and an enhanced version of DVB-RCS standard on the Reverse Link. The system, as shown in Figure 5-6, presents a Feeder Link in Q/V band (Down-link: 37.5 ÷ 39.5 GHz and Up-link: 47.2÷ 49.2 GHz) and a Service

Link in Ka band (Down-link: 19.7.÷ 20.2 GHz and Up-link: 29.5.÷ 30 GHz). The current technology limits the use of Ka frequencies range instead of Q/V bands for the user link. However, the feeder link migration toward Q/V bands fits the main stream evolution of such a multimedia system very well and offers a large degree of freedom in the use of scarce and most valuable Ka band for the user segment. The satellite coverage region is split among a number of beams that share the available bandwidth according to a predefined frequency pattern reuse. The Service Link Satellite Coverage presents spot beams with an approximate beamwidth of 0.5°, so about 64 spot beams may be required to cover Europe and a part of the Mediterranean area. The GW Stations will be distributed in the covered region and the number of them will be defined on the basis of the traffic distribution. The European region can be covered through 8 GWs. The Feeder Link Satellite Coverage foresees one beam per GW with full reuse of the available feeder link beamwidth, assuming that sufficient separation between spots is provided; 8 distant beams (one per GW) constitute the Feeder Link Coverage.

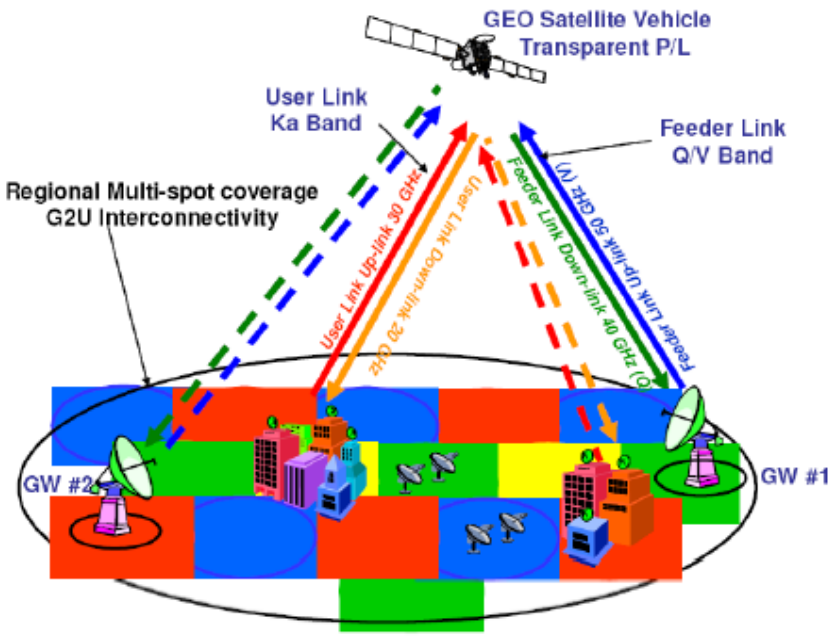

Figure 5-6: BDUA Mission System Architecture

The frequency plan identified for the BDUA mission is reported in Figure 5-7. The possible BDUA mission coverage is shown in Figure 5-8, while Frequency/Polarization Reuse Schemes for Q/V Band (left), Ka-Band (right) are illustrated in Figure 5-9.

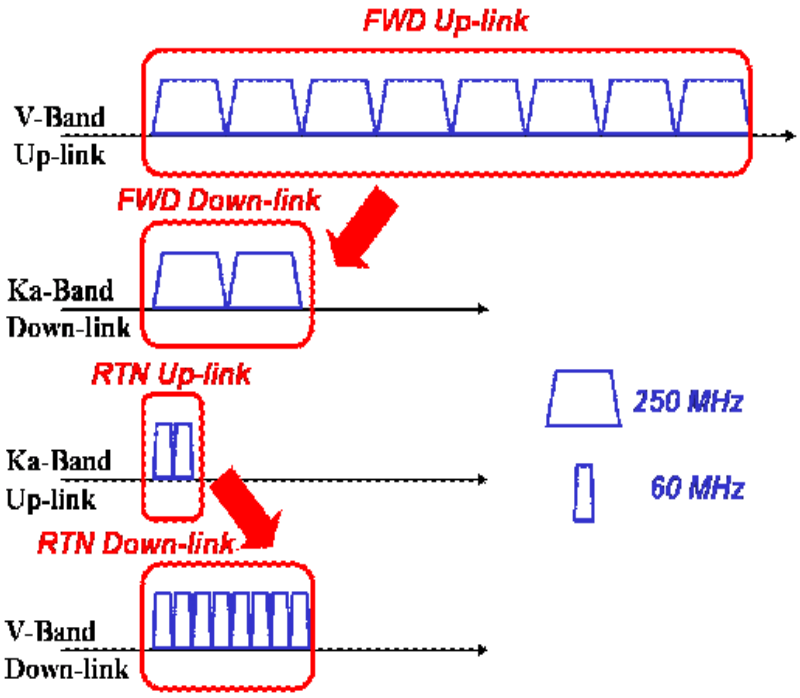

Figure 5-7: BDUA Mission Frequency Plan

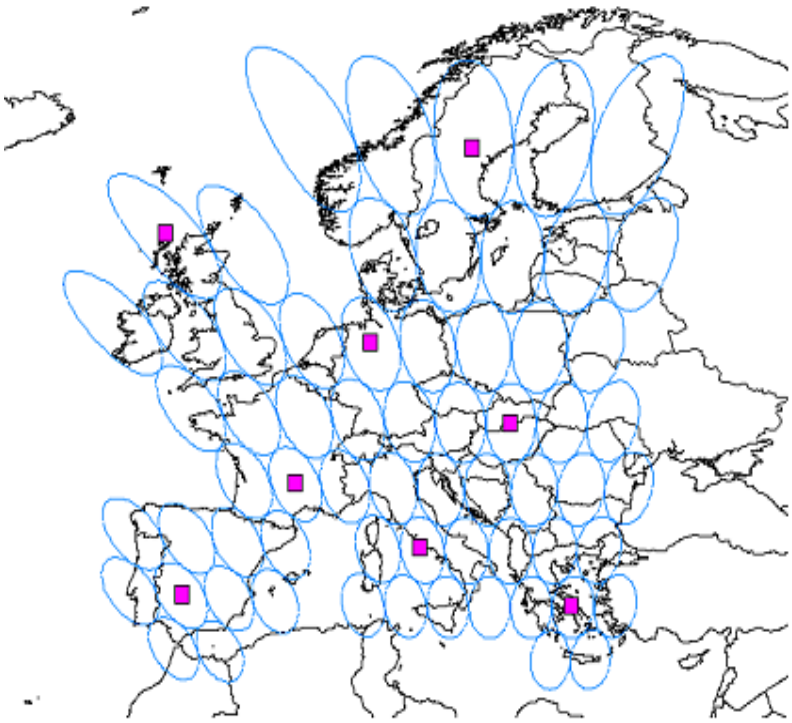

Figure 5-8: BDUA Mission Frequency Plan

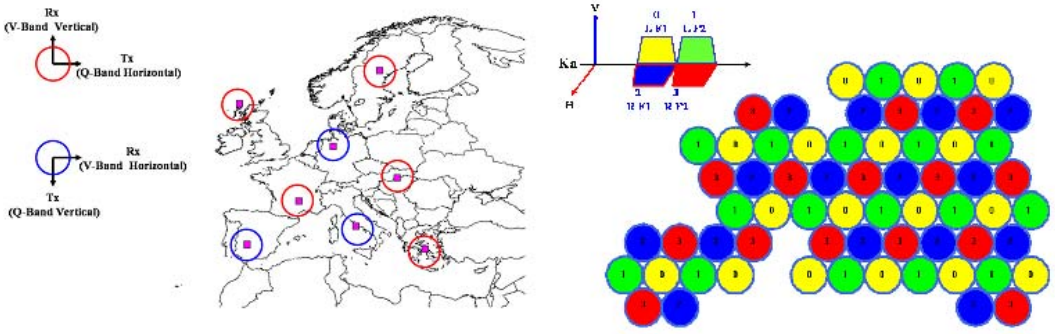

Figure 5-9: Frequency/Polarization Reuse Schemes for Q/V Band (left), Ka Band (right)

In Table 5-6 and Table 5-7 a summary of user link and feeder link characteristics is reported, respectively.

Coverage	Gateway spots (Q/V) (8 Beams ~ 0.5° BW)
Forward Bandwidth	~ 2 GHz per beam
Return Bandwidth	~ .5 GHz per beam
Frequency Polarization	Singular Linear per Gateway Reused in double polarization Reused in space by Gateways

Table 5-6: Feeder Link Characteristics Summary

Coverage	European Coverage Multibeam Cellular-Like (64 Beams ~ 0.5° BW –Ka)
Forward Bandwidth	~ 250 MHz per beam
Return Bandwidth	~ 60 MHz per beam
Frequency Polarization	Four colour patten (2 Frequencies – 2 Polarizations) (500 MHz@20GHz) (125MHz@30 GHz)

Table 5-7: User Link Characteristics Summary

Table 5-8 reports the P/L characteristics for the forward link. The EIRP in the user link is the total EIRP required to feed each user beam with a beamwidth of 250 MHz.

Table 5-9 shows the P/L characteristics for the return link.

In this case, the EIRP is the total EIRP required to the return link in order to cover each GW beam of 500 MHz. Table 5-10 summarizes the P/L performance in terms of total RF power.

Forward Link P/L Parameter	Value	Remarks
G/T (dB/K)	18.2	V band section (receiver); antenna gain @ Beam Center (BC)
EIRP(dBW)	59.5	Ka band section (transmitter); antenna gain @ End of Coverage (EOC) and with Beam Pointing Error (BPE)

Table 5-8: Forward Link – P/L characteristics for each 250 MHz user beam

Return Link P/L Parameter	Value	Remarks
G/T (dB/K)	14	Ka band section (receiver); antenna gain @ EOC and with BPE
EIRP(dBW)	58	Q band section (transmitter); antenna gain @ BE

Table 5-9: Return Link – P/L characteristics for each 250 MHz user beam

Parameter	Value
Forward Link	
GWs	8
User Beam for each GW	8
Carriers per user beam	5
Total Forward Link carriers	320
Satellite RF power for carrier	16 W
Total RF power (Ka Band)	**5120W**
Return Link	
Carriers per user beam	66
User beam for GW	8
Carriers per GW	528
Total Return Link Carriers	4224
Satellite RF power for carrier	0.06 W
Total RF power (Q Band)	**253.4 W**

Table 5-10: Satellite total RF power

The GWs and User Terminal characteristics are described in Table 5-11 and Table 5-12, respectively. In the case of user terminal, the EIRP is associated to a single 0.512 kBaud carrier. The Link refers to 36 MHz channels requiring 10 W at GW side. 2 GHz of GW bandwidth are covered by 40 channels so the total required GW RF power is 400 W. The performance of both the forward link and the return one were evaluated using a link budget tool. The communication link is considered to be affected from the following main aspects:

- Propagation Margin (total attenuation related to a specific level of link unavailability);
- Air Interface based on the DVB-S2 standard in the forward link and on an enhanced version of the DVB-RCS standard in the return link;
- the ACM interference and Fading Mitigation Technique on both links;
- non-linear degradations, as a main channel impairment affecting the link.

	Parameter	Value
Tx antenna	Frequency	48.2 GHz
	Diameter	4 m
	Efficiency	60%
	Gain	63.9 dBi
	EIRP	83.6 dBW
Rx antenna	Frequency	38.5 GHz
	Gain	61.9 dBi
	G/T	33.1 dB/K

Table 5-11: BDUA GW Characteristics

	Parameter	Value
Tx antenna	Frequency	29.75 GHz
	Diameter	1 m
	Gain	47.7 dBi
	EIRP	39.5 dBW
Rx antenna	Frequency	19.95 GHz
	Diameter	1 m
	Gain	44.2 dBi
	G/T	18.4 dB/K

Table 5-12: User Terminal Characteristics

The link budget identifies the available link margin expressed as the difference between the achievable $\frac{E_b}{N_0}$ and the target value as specified by the DVB-S2 standard in the Forward Link and by the DVB-RCS standard in the Return Link. The link budget has been evaluated it for both the forward and the return links:

- for different combination of modulation format and FEC encoding;
- at different user position (EOC and BE) and different BPE;

Further, the performance of both the forward link and the return link have been analyzed in the case of clear sky condition and of rain-induced attenuation on both the up and down links.

From the user position point of view, two interesting cases have been considered:

- worst case: user at EOC with maximum BPE (Pointing Losses equal to 4dB w.r.t. EOC gain);

- best case: user at BC with BPE=0. This case presents the advantage of 7 dB more on the downlink EIRP with respect to the worst case: 3 dB are due to the gain difference between centre to EOC and 4 dB are due to the fact no BPE affects the link.

The Baud Rate considered in the link budgets is 27.5 MBaud for the Forward Link and 512 kBaud for the Return Link. Table 5-13 and Table 5-14 report the results of the link budget in terms of maximum MODCOD at which the system is able to operate in both the best and the worst cases:

- in the Forward Link the system can operate with a maximum MODCOD of 16-APSK $\frac{9}{10}$, taking advantage of a spectral efficiency equal to 3.6 bit/s/Hz and supporting a bit rate of 98.2 Mbit/s;
- in the Return Link the system can operate with a maximum MODCOD of 16-APSK $\frac{3}{4}$, thus presenting a spectral efficiency of 3 bit/s/Hz and supporting a maximum bit rate of 1.5 Mbit/s.
-

	MODCOD	Value [Bit/s/Hz]	Margin [dB]	Bit rate [Mbit/s]
Best case	16 APSK 9/10	3.6	0.6	98.2
Worst case	8 PSK 5/6	2.5	1.2	68.2

Table 5-13: Forward Link Maximum MODCOD (27.5 Mbaud carriers)

	MODCOD	Value [Bit/s/Hz]	Margin [dB]	Bit rate [Mbit/s]
Best case	16 APSK 3/4	3	1.6	1.5
Worst case	8 PSK 2/3	2	0.1	1

Table 5-14: Return Link Maximum MODCOD (512 kBaud carriers)

5.2.4.1.1.1 Experimental Pre-operative Q/V Band Missions

The BDUA mission is characterised by many aspects whose feasibility is not yet completely verified. Experimental missions in Q/V bands are hence necessary in order to reduce the risks of an implementation of an operative system with many technological challenges.

This experimental phase is already started with the ASI Alphasat TDP#5 programme, as already shown above. TDP#5/Alphasat is the initiator of a more comprehensive roadmap that will arrive to a Final Operational Mission (MOR, Italian acronym which stands for "Missione Operativa di Riferimento") consisting in a very large telecommunication infrastructure operating in the Q/V bands for the feeder links, and in Ka band for user links. However, a second experimental phase is necessary with the scope to verify communication and propagation aspects with a pre-operative system implementing the most important functions of the MOR-BDUA. The main objectives of the pre-operative BDUA mission can be classified in three main groups: communication, scientific and technological objectives.

i. Communication Objectives

They are bound to test and evaluate the effectiveness of PIMTs that should be adopted for the proper operation of future Q/V band systems, so allowing to optimise and validate relevant algorithms. These objectives particularly consist of:

- establishing the effectiveness of ACM in very high frequency band operation. In particular, the ACM implementation, as defined in the DVB-S2 standard, will be tested in the experiments;
- testing and establishing the performance of other PIMTs, complementary to ACM, like: site diversity, up-link power control, and the reconfigurable antenna;
- optimising the simultaneous application of the different PIMTs.

ii. Scientific Objectives

Main objective is to improve the knowledge of propagation impairments at Q/V band which is instrumental in the design of satellite communication systems adopting adaptive techniques. A better characterization of 2nd-order statistics is currently required to better exploit the characteristics of the new interference and fading mitigation schemes.

iii. Technological Objectives

Main objective is to test the technologies that are required for implementing a modern communication P/L in Q/V band. This mission aims at realising in flight qualification of an innovative technology that is considered of great interest by a great part of microwave research community. It includes: HPAs, both on board and on ground, with high output power amplifier power level requiring new design and development; MPAs and or/and flexible TWTAs to implement the inter-beam partitioning leading to the

optimization of the on board power consumption with respect to the channel impairments; switches based on MEMS technology. Three different experimental missions have been defined by a down scaling of the MOR-BDUA:

- Large-BDUA (LBDUA);
- Medium-BDUA (MBDUA);
- Small-BDUA (SBDUA).

The down scaling has been based on the reduction of the feeder and user spots, with the scope to have a system attaining the main objectives of the experimental mission listed in Table 5-15 [5-18], [5-19]. After a trade-off among the three different scaled MOR, based on technical, economical and programmatic aspects, the SBDUA has been selected as the experimental (pre-operative) BDUA mission.

	Objectives	Value
OB1	User Link	Ka Band
OB2	Feeder Link	Q/V band
OB3	Number of GW	N≥1
OB4	Number of User Spots	N*8
OB5	Link Dimensioning	
OB6	Baud Rate	27.5 MBaud
OB7	PIMT1	ACM
OB8	PIMT2	ULPC
OB9	PIMT3	Site Diversity
OB10	PIMT4	Inter-Beam Partioning
OB11	Technology 1	On board new design HPA
OB12	Technology 2	On board antenna design
OB13	Technology 3	Ground new design HPA
OB14	Operative Condition	-

Table 5-15: Experimental Mission Main Objectives

The SBDUA mission mainly presents a reduced number of GTWs (1 against 8) and of user spots (8 against 64) with respect to the BDUA one, as shown in Table 5-16. The compliance with the BDUA mission objectives is shown in Table 5-17. The SBDUA is in compliance with all the objectives, but the OB10, OB12 and OB14 [5-20], [5-21], [5-22].
The first two objectives are partially met as explained below:

- OB10: SBUA mission is partially compliant with BDUA one due to two reasons. The first one is related to the PIMTs implementation (through the modification of the channel amplifier output level). The second one is due to the fact that the limitation to just one groups of 8 user spots limits the experiment to one area only;

- OB12: the SBDUA system partial compliance with BDUA one is justified by the fact that the reduced number of GWs and User Spots leads to consider the SBDUA on board antenna little representative of the final one.
- OB14: this objective is no instead met due to the fact that the 8 user spots cannot be representative of the BDUA operative condition. The reduced number of GWs and user spots impacts on the SBDUA P/L in terms of mass and power consumption and the total channel both in forward and return links, as reported in Table 5-18. These characteristics lead to consider viable a piggy-back solution for the P/L embarking [5-23], [5-24], [5-25]. This means that the SBDUA P/L will not be the principal one and hence all the functions relative to the platform management (platform monitor and control) will be in charge to the P/L owner.

Parameter	Value
Gateway	**1**
User Beam	**8**
Q/V Band Antenna	**1**
Ka Band Antenna	**2**
User Ka Coverage	**8 Beams**
SBDUA Centre Frequency	**FWD link:** • **Feeder Link: 48, 2 GHz** • **User Link: 19,95 GHz** • **RTN Link:** • **User Link: 29,75 GHz** • **Feeder Link: 38,5 GHz**
Useful Bandwidth	**FWD link:** • **User Beam: 250 MHz** • **GTW Beam: 2 GHz:** **RTN link:** • **User Beam: 60 MHz** • **GTW Beam: 500 MHz:**
P/L Mass	**183 kg**
P/L Power Consumption	**1.3 kW**
Ka Band EIRP	**61.2 dBW**
Q Band EIRP	**58.5 dBW**

Table 5-16: SBDUA Main Characteristics

Taking into account the considerations above reported, the P/L physical architecture will be downsized as shown in Figure 5-10.

The SBDUA P/L will consist of the following main elements:

- one forward repeater;
- one return repeater;
- one Q/V Rx/Tx antenna (1 beam);
- one Ka Rx antenna (8 beams);
- one Ka Tx antenna (8 beams).

	Objectives	Value	State of Condition	Note
OB1	User Link	Ka Band	Confirmed	-
OB2	Feeder Link	Q/V band	Confirmed	-
OB3	Number of GW	N≥1	Confirmed	1 GTW
OB4	Number of User Spots	N*8	Confirmed	8 User Spots
OB5	Link Dimensioning	As for BDUA	Confirmed	-
OB6	Baud Rate	27.5 MBaud	Confirmed	-
OB7	PIMT1	ACM	Confirmed	-
OB8	PIMT2	ULPC	Confirmed	-
OB9	PIMT3	Site Diversity	Confirmed	-
OB10	PIMT4	Inter-Beam Partioning	Partially confirmed	This PIMT will be verified only from the operational point of view
OB11	Technology 1	On board new design HPA	Confirmed	-
OB12	Technology 2	On board antenna design	Partially confirmed	Limited to the spot number defined in OB3 and OB4
OB13	Technology 3	Ground new design HPA	Confirmed	-
OB14	Operative Condition	More close to BDUA condition	Partially confirmed	Due to the limited number of GTW and User Spots.

Table 5-17: SBDUA Mission Objectives

A preliminary mass and power budget evaluation has been performed with to the following results:

- mass: 172 kg;
- DC Power: 1.700 W.

The above values lead to consider a shared embarking solution having as reference a Space Bus 4000B2 platform class.

Parameter	Value
Forward Link	
GWs	1
User Beam for each GW	8
Carriers per user beam	5
Total Forward Link carriers	40
Satellite RF power for carrier	16 W
Total RF power (Ka Band)	**640W**
Return Link	
Carriers per user beam	66
User beam for GW	8
Carriers per GW	528
Total Return Link Carriers	528
Satellite RF power for carrier	0.06 W
Total RF power (Q Band)	**31.7 W**

Table 5-18: SBDUA satellite RF power

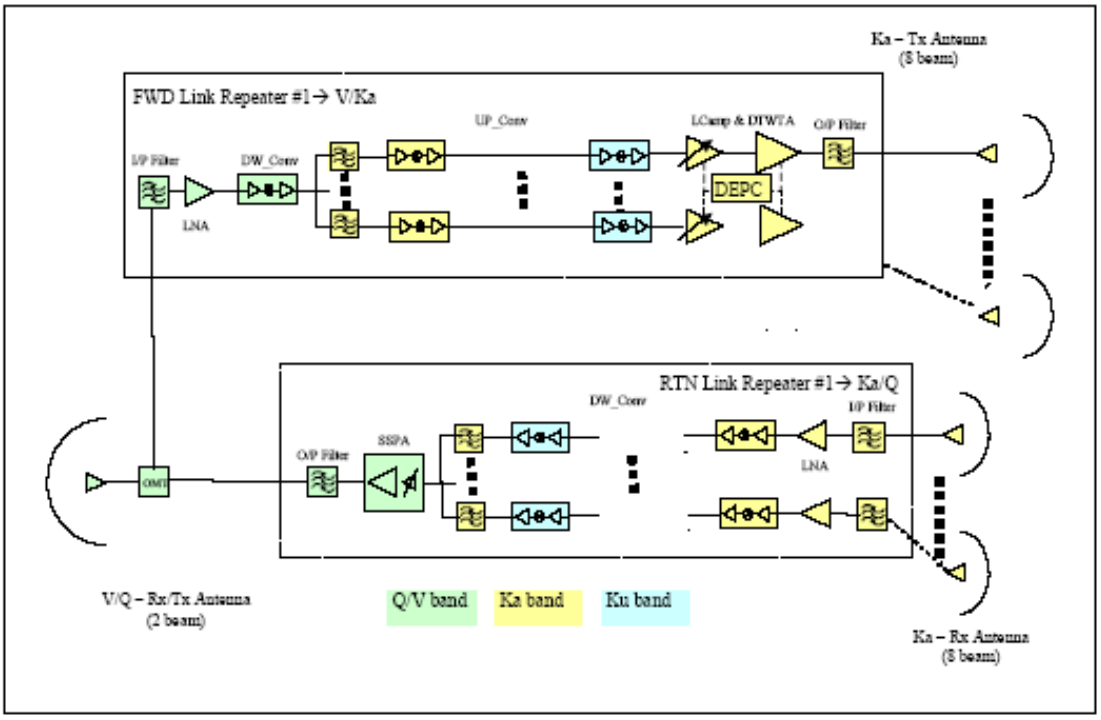

Figure 5-10: SBDUA P/L architecture

5.2.4.1.1.1.1 Q/V Band Technological Challenges

The SBDUA mission is the first step toward the realisation of the full operative one represented by the MOR-BDUA mission. The SBDUA mission development has some critical technological elements represented by the HPA and antenna sections operating at Q/V bands. In the following lines, these two technological issues will be investigated and the results of this analysis will be reported. Finally, a possible implementation based on a flat Ka band antenna configuration is proposed for the SBDUA mobile user terminals.

Due to the "niche" domain of this amplifier type, just few manufacturers in the world are able to provide units with suitable specifications.

According to the results of University of Rome 'Tor Vergata' investigation within the TRANSPONDERS Phase A2, and considering the most important manufacturers of tubes for space applications [5-25], [5-26], three companies have been considered: L3-COM, Thales Electron Devices - hereafter TED -, and the CPI Canada.

It has been verified that there is currently the following scenario:

- **L3-COM** is able to provide a TWT (its model is *999H*) with the following characteristics:

Frequency range	***22-40 GHz***
Sat Gain	***46-56 dB***
Sat Drive	***-3 to 0 dBm***
Size (W×H×L)	***2.7''×2.9''×12.7''***
Weight	***3.8lbs***
Sat Power Range	***20-200 W***
DC in (max)	***380 W***
Dissipation (max)	***290 W***
Size (W×H×L)	***2.7''×2.9''×12.7''***
Weight	***3.8lbs***

Table 5-19: 999H TWT Main characteristics

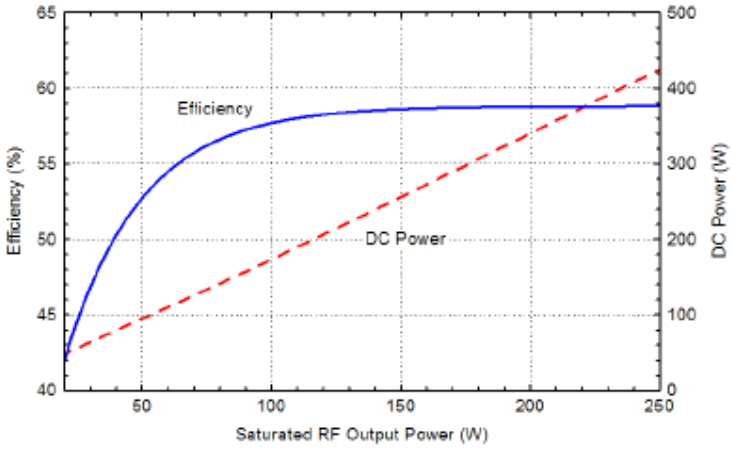

Figure 5-11: 999H TWT Efficiency versus Saturated RF Output Power

Figure 5-12: 999H TWT Image

This component fully satisfies the SBDUA P/L Ka to Q bands Section requirements in terms of CW Saturated Power (30 W).

- **CPI Canada** is able to provide a CW EIK (its model is VKQ2477) with the following characteristics:

Frequency range	***33-50 GHz***
Gain	***30 dB***
Power	***250 W***
-1 dB Bandwidth	***200 MHz***
Cooling	***liquid / air***

Table 5-20: VKQ2477 CW EIK Main characteristics

From the point of view of suppliers of Klystron technology, the only one able to satisfy the strict requirements requested by the design of the SBDUA Ground Station HPA is the Canadian company CPI, Communications and Power Industries, at present worldwide leader in high power amplification based on vacuum technology. Actually, the most advanced HPAs, space qualified and realised in EHF band, specifically in Ka and W bands, are developed by CPI. It is the unique supplier for the EHF missions such as CloudSat, EarthCARE and EGPM.

In particular, CPI realised the first space qualified EIK (pulsed) at W band in 2006 for the Cloudsat mission and is currently developing another equivalent model for the EarthCARE mission.

Currently, CPI is able to provide EIKs that can operate at frequencies from 18 to 280 GHz. The current state of the art is summarised in Table 5-21.

Frequency	Pulsed Power	Average Power
95 GHz	3000 W	400 W
140 GHz	400 W	50 W
183 GHz	50 W	10 W
220 GHz	50 W	6 W
280 GHz	30 W	0.3 W

Table 5-21: CPI EIK performance State of Art

Some examples of EIKs fabricated by CPI operating at EHF frequencies are reported in Figure 5-13, Figure 5-14 and Figure 5-15.

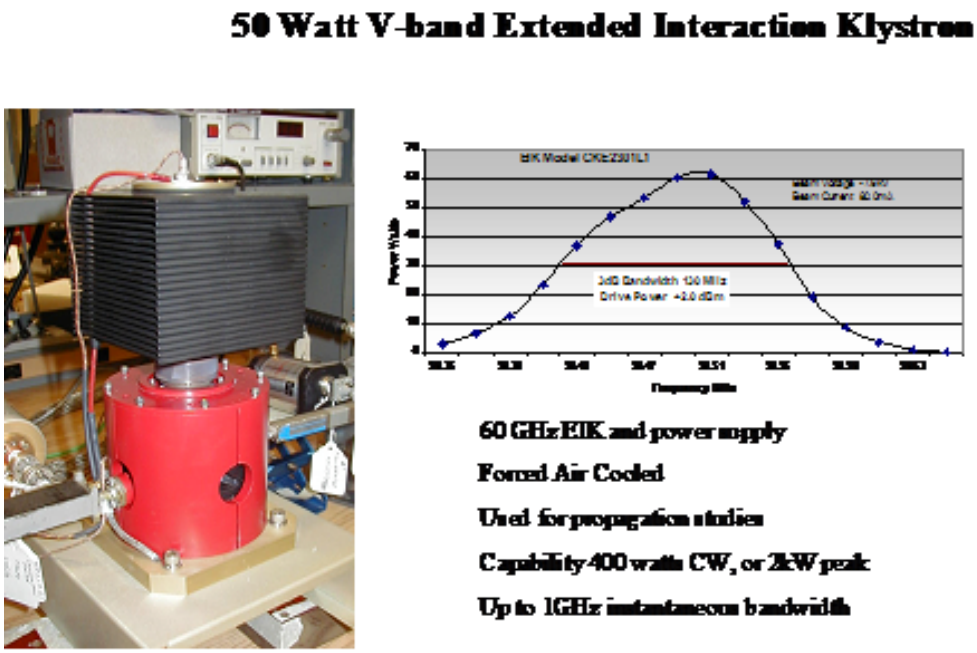

Figure 5-13: 50 W EIK operating at 60 GHz

As it can be observed above, there are very few models of HPA developed by CPI that operate in Q bands. This is due to a strong lack of applications at this frequencies range, so the availability of HPA matching the requirements of Q band Section SBDUA P/L is critical. Paradoxically, there are more advancements and availability at W band, due to the overwhelming present activity in weather and imaging radar, both space and ground-based.

- However, results of our survey in CPI market allowed to identify a solution matching present needs [5-26]. TED is the European Company leader in high power amplification based on vacuum technology. However, they have not shown interest to the issue.

However, the realization of a Q band HPA with 32 W output RF power level and a Q/V band Tx/Rx single beam Antenna for the SBDUA P/L needs a specific development and qualification campaign with the objective of pursuing a first electrical validation and performance evaluation based on a breadboard model.

Once the electrical design is confirmed, it is possible to proceed to the EQM model. This model shall be built with space components in order to undergo the thermal and vibration tests and acceptance and to be space qualified.

Finally, the PFM model shall be manufactured with high reliable space components and shall undergo both the thermal-vacuum and the vibration tests.

The SBDUA GW Station includes the following main elements:

- Antenna subsystem
- Receive subsystem
- Transmit Subsystem
- Inter Facility Link

The GTW RF working frequencies are reported in Table 5-22.

Figure 5-14: 100 W EIK operating at 95 GHz

The overall GTW (Rx and Tx) architecture is shown in Figure 5-16.

The antenna section consists of the following elements:

- Antenna mount;
- Feed and Optical system;

- Servo and Tracking System.

The optical system is based on Cassegrain geometry with main reflector and sub-reflector shaped to the best trade-off between maximum efficiency and low side lobes.

The assembly of 3,5 meter reflector consists of a machined central hub to which are attached the radial trusses and the reflector panels. The antenna diameter has been chosen in order to guarantee the required EIRP (83,6 dBW at 48,2 GHz) and G/T (33,1 dB/K at 38,5 GHz) performance.

The servo control system provides the capability of driving the antenna axes in all operational modes under the requirements needed to perform tracking operation as well as manual pointing on GEO satellites.

The antenna control system provides the following modes of operation:

- Manual Rate;
- Position Designate;
- Step track (with capability of tracking inclined orbit satellites);
- Remote Control (interfaced with the station Monitor and Control);
- Stand by;
- Memory track.

According to the considerations, the Q/V Band SBDUA GTW antenna requires ad hoc development.

A preliminary planning for the design and development of the Q/V band antenna for the SBDUA GW is shown in Table 5-23. The overall timeline is preliminarily estimated in 16 months.

Based on the fact that a 25 W Q band HPA requires 36 months for its fabrication, the realization of the HPA for the SBDUA P/L at least requires 3 years [5-26].

The risk related to Q/V band single-beam antenna development instead is lower than a multi-beam solution operating at the same frequency bands due to high heritage for the first alternative.

A total time of about 58 months is necessary to carry out all the activities related to the SBDUA P/L development and to embark it on the Spacebus 4000B2 platform as piggy-back solution, as shown in Figure 5-17 [5-26].

A possible implementation of a flat Ka band antenna for SBDUA mobile user terminals is reported in the following lines of paragraph.

The specifications of the antenna are recalled in Table 5-24.

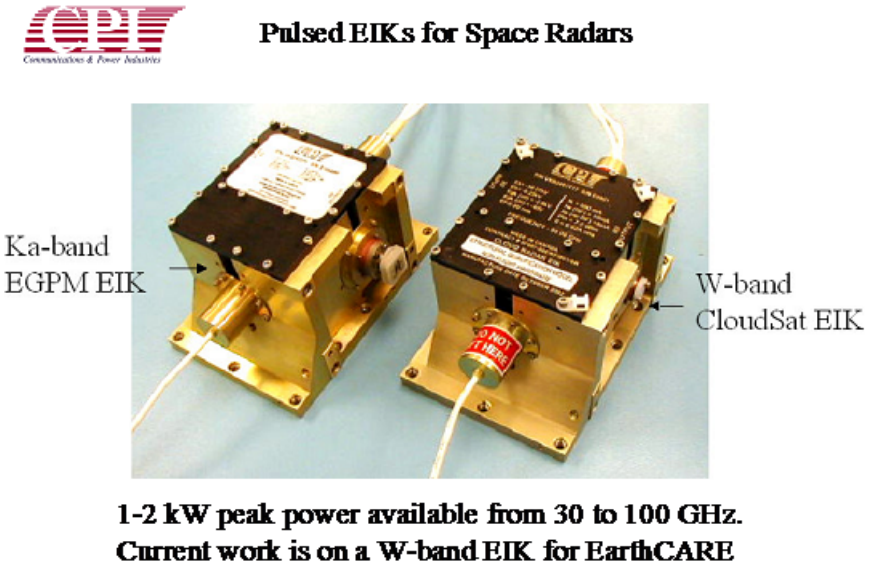

Figure 5-15: pulsed EIKS for space radars

Parameter	Value	Units
Return Link Q Band (Down)	37.5 ÷ 39.5	GHz
Forward Link V Band (Up)	47.2 ÷ 49.2	GHz

Table 5-22: GTW Q/V working frequencies

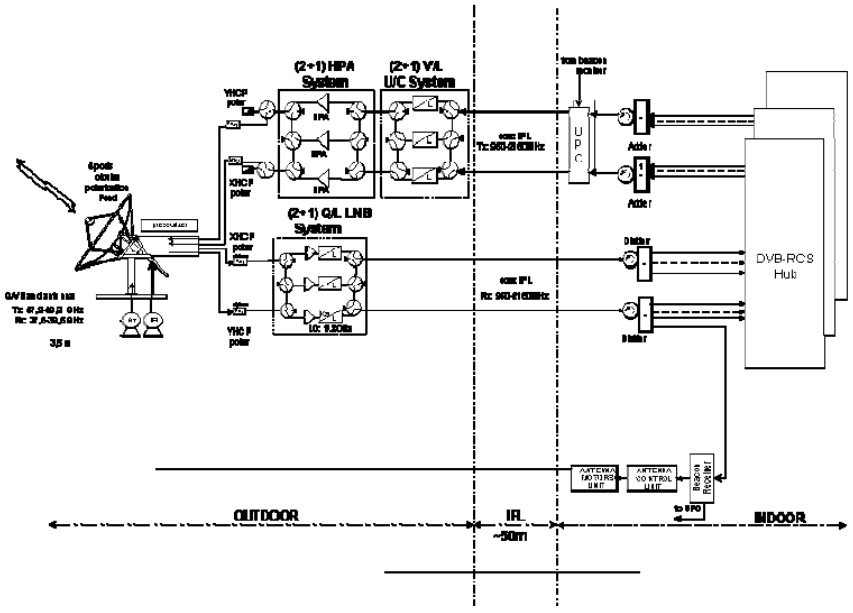

Figure 5-16: Full GTW Rx and Tx Architecture

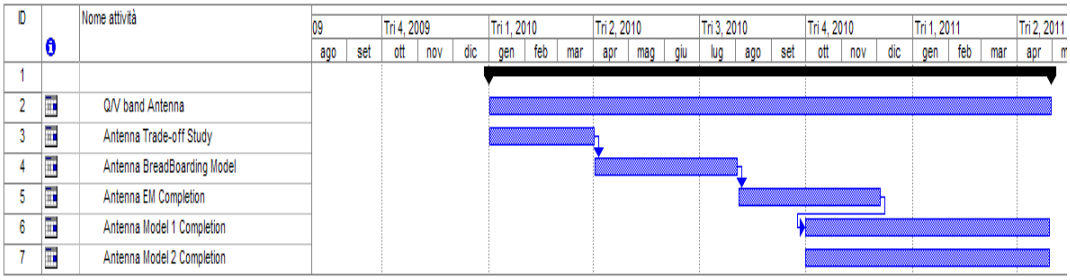

Table 5-23: Plan of Development of the SBDUA GW Antenna in Q/V Band

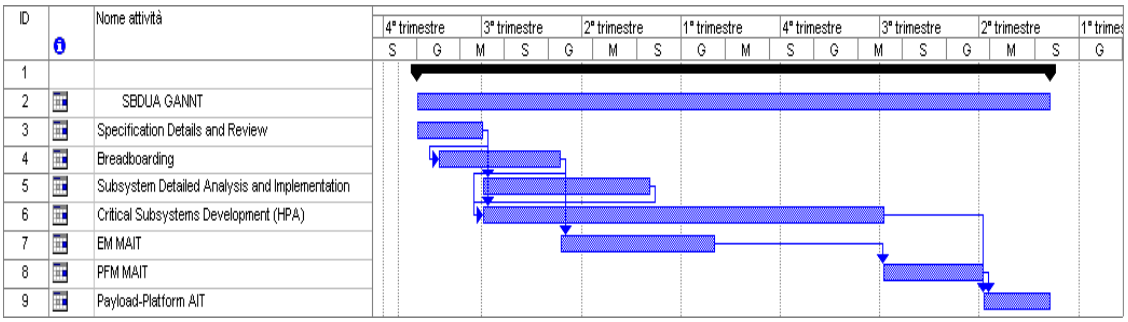

Figure 5-17: SBDUA Mission Plan Development

Parameter	Value	Units
TX Antenna	29.75	GHz
Bandwidth	500	MHz
Gain	43.6	dBi
EIRP	38.1	dBW
Rx Antenna	19.95	GHz
Gain	41.1	dBi

Table 5-24: Requirements of User terminal at Ka band

The use of a flat antenna (i.e. a *phased array*) is of fundamental importance whenever the service is to be furnished to users on the move. A compact size is needed for an easy placement on mobile vehicles. Moreover, for many applications, a flat profile is mandatory to maintain aerodynamic properties of a vehicle as well as to allow the integration of the antenna itself (for instance, in high speed trains).

The most critical issue for an effective design of a phased array achieving such stringent requirements is indeed the identification of the most suitable technology. The development of high-performance and low-cost critical components (such as LNAs, rotary joint, radiating element, etc.) is essential, as well as the implementation of a cost-effective architecture for the BFN and control system.

The major limiting factor for mobile terminal development is represented by the beam steering approach and the number of electronic components employed.

An alternative approach for beam steering, not employing phase shifters, has recently proposed. It is based on switched beam architecture to obtain electronic beam steering in the elevation plane, whereas mechanical beam steering is performed in the azimuthal plane.

This approach allows a considerable reduction of the overall system complexity and fabrication costs, being the BFN realized in microstrip technology in the form of a Rotman lens, still maintaining extremely high performance through the use of LNAs.

The use of COTS in this case is the most convenient solution due to the extremely wide market of such components.

The radiating elements technology and architecture represent another critical issue: a suitable solution has to be identified in order to maintain a flat profile and guarantee high performance at low cost. For services operating in linear polarization, the slotted SIW approach is one of the most efficient and cost-effective solution [5-27].

This innovative technique consists of the realization of waveguides into a dielectric substrate by means of rows of plated via-holes that realize the lateral walls of the waveguide, as shown in Figure 5-18.

This technology has been already experimented up to millimeter wave frequencies and retains the same high performance of a classical dielectric filled waveguide with much lower fabrication costs, being the complete circuit compatible with standard PCB processes [5-28].

Concerning the BFN subsystem, it has strong impact on the overall system cost, mainly because of high costs associated with the many phase shifters needed if a standard phased array architecture is adopted.

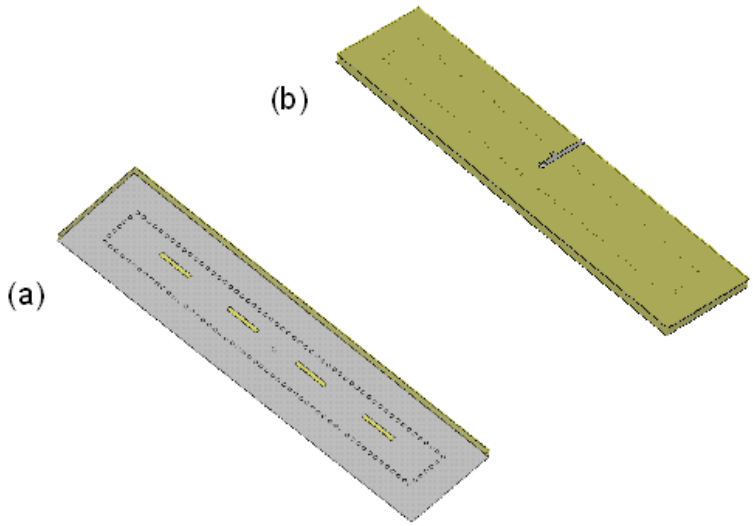

Figure 5-18: Slotted Substrate Integrated Waveguide: top view (a), slots are realized with standard printed circuit technology; bottom view (b), the transition between the BFN and the antenna is realized with a post that connects the microstrip line to the opposite wall of the waveguide

Multi-beam BFN architectures appear therefore as a viable solution for beam steering in the elevation plane, performed with a switched beam approach. The schematic of Antenna based on Multi-Beam BFN architecture is shown in Figure 5-19. Among many possible solutions (Buttler Matrix, Blass Matrix, Rotman lens), a Rotman lens fabricated in microstrip technology combined with active elements (LNAs) is one of the lowest cost approach exhibiting the best performance [5-29].

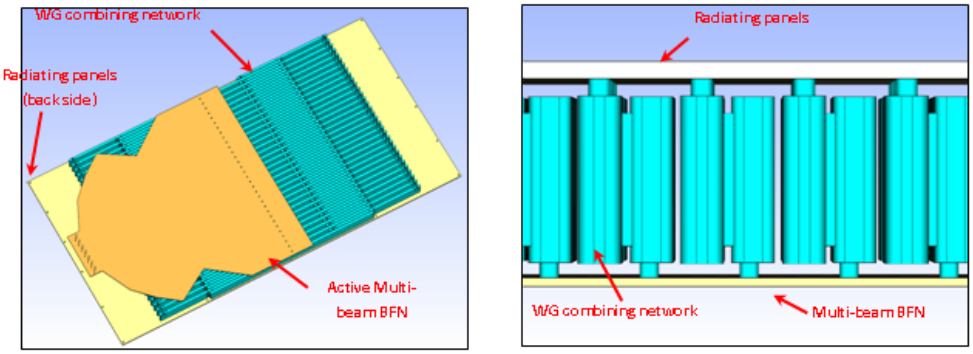

Figure 5-19: Schematic of the Final Antenna: 3D view (sx) and cross-section view (dx)

Figure 5-20 and Figure 5-21 show a possible implementation of this architecture [5-26], in which two antennas, TX and RX, are realized as separate section in a single flat dish with

thickness 5cm. Azimuth tracking is realized mechanically throughout a dish rotation, while elevation tracking is obtained electronically.

This approach can be easily extended at Ka band (Rx bandwidth of 2.5%, Tx bandwidth of 1.6%), and especially designed for the working frequencies of the SBDUA User Terminals.

However, by considering a flat antenna horizontally placed (with no tilting), the effective area is much lower than the actual one reported in [5-29]. In order to maintain the same requirements given in Table 5-24, the area of RX antenna should be at least:

$$A_{RX} = \frac{G_{RX} \cdot \lambda^2}{4\pi \cdot \eta \cdot \sin(\theta)} \tag{5-1}$$

where η is the antenna efficiency (estimated around 70%), θ is the elevation angle of the satellite with respect to the horizon (from Italy, around 40°) and λ is the centre wavelength. By substituting the above values, a required area for the Rx Ka antenna is of 0.5 m². For the Tx antenna, the required area results 0.4 m². Therefore a total area of 0.9 m², divided in TX and RX parts, would satisfy the requirements, this implying the use of a dish with a radius of 0.54 m in which 45% of the area is assigned to the TX section, whereas 55% to the RX one.

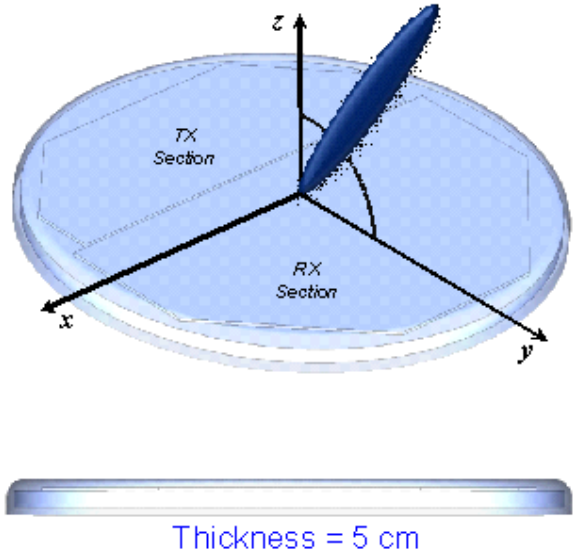

Figure 5-20: Implementation of the phased array into the same dish 5 cm thick. Part of the dish contains the TX section, the other part the RX one. The diameter can be set in order to give the required gain

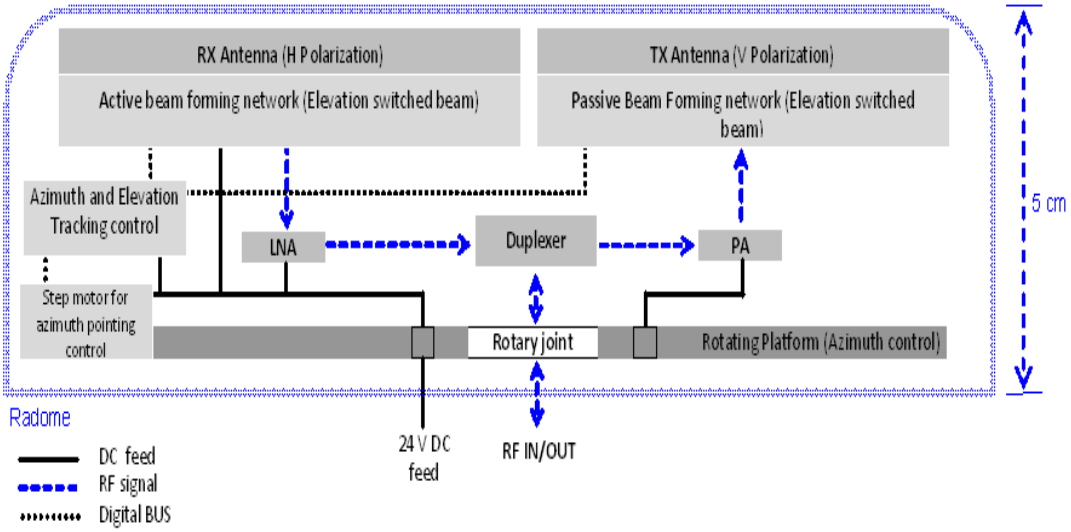

Figure 5-21: Sketch of the structure, with RX and TX antenna and step motors for azimuth controls [5-29]

5.2.5 MILSTAR

Hughes Space and Communications Company (HSC), now known as Boeing Satellite Systems, Inc. (BSS), is the major part of the Milstar (Military Strategic & Tactical Relay) system team [5-30] [5-31].

The Milstar system is a tactical and strategic multi-service program involving the U.S. Air Force, Army, Navy, and other agencies. Milstar provides protected communications for command and control of the United States war-fighting forces. These include the National Command Authority (NCA), military tactical and strategic forces, Air Force Space Command (AFSPC), and other users. The Program is managed by the U.S. Air Force Space and Missile Systems Center.

Milstar is a constellation of GEO satellite that provides uplink communications at EHF (44 GHz), and UHF (300 MHz), and downlink communications at SHF (20 GHz), and UHF (250 MHz).

Moreover, it provides survivable medium data rate (MDR, in the range from 4.8 kbps to 1.5 Mbps), at 44 GHz uplink and 20 GHz downlink, and low data rate (LDR, at 2.5 kbps) communications services between terminals worldwide. It uses cross-links between Milstar satellites (both for the MDR and LDR payloads) operating in the 60 GHz region.

Survivability requirements are satisfied by anti-jam, hardening, and system autonomy features. A pictorial view of Milstar 2 satellite is shown in Figure 5-22.

Figure 5-22: Milstar 2 Satellite

5.2.6 AEHF

Lockheed Martin Space and Strategic Missiles is the prime contractor of the AEHF (Advanced Extreme High Frequency Satellite), a.k.a. AWS (Advanced Wideband Satellite), program [5-32][5-33]. AEHF is the next generation of highly secure, high capacity, survivable communications to the U.S. warfighters during all levels of conflict, and will become the protected backbone of the Department of Defense's military satellite communications architecture. The AEHF system will be integrated into the legacy Milstar constellation, and will be backward compatible with Milstar's low data rate and medium data rate capabilities, while providing extreme data rates (XDR) and larger capacity at substantially less cost than the Milstar system.

Advanced EHF satellites will provide 10 times greater total capacity and offer channel data rates six times higher than that of Milstar II communications satellites. The higher data rates allow transmission of tactical military communications such as real-time video, battlefield maps and targeting data. As previously introduced, AEHF adds new higher data rate modes to the low data rate and medium data rate modes of Milstar II satellites. The higher data rate modes will provide data rates up to 8.2 million bits of data per second (Mbps) to future Advanced EHF Army terminals (the system will be able to support 6000 terminals). That rate is more than 150 times faster than the 56 kilobit-per-second modems of today's personal computers. Each Advanced EHF satellite employs more than 50 communications channels via multiple, simultaneous downlinks. For global

communications, the Advanced EHF system uses ILs, eliminating the need to route messages via terrestrial systems.

The first three satellites will be launched on an Evolved Expendable Launch Vehicle (EELV) in 2010-2012. On-board signal processing will provide protection and ensure optimum resource utilization and system flexibility among the Armed Forces and other users who operate terminals on land, sea and air.

A pictorial view of AEHF 1 Satellite is shown in Figure 5-23.

Figure 5-23: AEHF Satellite

5.2.7 COMETS

The COMETS (Communication and Broadcasting Engineering Test Satellite) project was jointly developed by the National Space Development Agency (NASDA) and Ministry of Post and Telecommunications / Communications Research Laboratory (MPT/CRL) [5-34][5-35][5-36]. This GEO three-axis stabilized satellite was placed at 121° E by the NASDA H-II rocket in 1998 with an expected mission life of three years. Due to a launch vehicle failure, the satellite was not injected in the GEO-transfer orbit. Then the satellite has been moved to recurrent orbit thanks to successful orbital manoeuvres. COMETS has three deployable antennas and a 32 m long solar paddle. It has three mission P/Ls. The first is an advanced mobile satellite communications system using both Q-band and Ka-band, which was developed by CRL. The second is a 21 GHz band advanced broadcasting system developed by CRL and NASDA. The third is an inter-satellite communications system developed by NASDA using the S and Ka-bands.

The objective of the first mission is to study the feasibility of advanced mobile satellite communications at Q-band (47/44 GHz) and Ka-band (31/21 GHz). The P/L consists of a multi-beam antenna, Q-band and Ka transmitters and receivers, an IF filter bank and a regenerative repeater, which enables the use of a 2 x 2 matrix switch for beam interconnections. COMETS terminated its operations on 1999.

5.3 DISCONTINUED Q/V-BAND SYSTEMS

5.3.1 ASTER

Spectrum Astro Inc. applied to the FCC to license a five-slot GEO V-band constellation, named Aster [5-37], with five satellites per orbital slot, using the following frequencies: 36 GHz for uplink and 51.4 GHz for downlink. Each slot should had to provide coverage through 48 spot beams, eight regional beams and 2 steerable beams; connections between the slots were supplied by optical ILS. Initial service was targeted for 2002 with single cast and multicast communications up to 622 Mbps. The target markets included tele-medicine and tele-learning, private intranets and extranets, corporate training, video conferencing and business video, broadcast broadband multimedia, and software and entertainment transactions.

5.3.2 M-STAR

M-star was the Motorola follow up to Iridium, until Celestri was announced [5-38][5-39]. Motorola asked for FCC approval, and they thought it would take four years from getting approval and six billion dollars to build this 72-active-satellite constellation with laser ILS and V-band, rather than Ka-band, to ground. This wasn't a global scheme - it's between 57 degrees of latitude only. It was aimed at providing wireless connectivity to mobile base stations. The network was planned to offer speeds of up to 1 Gbit for satellite-to-satellite laser communications and 155 Mbit for satellite-to-earth transmissions. M-Star was restored and remarketed as the LEO component of Celestri**.**

Before merging with Teledesic, Motorola's Celestri incorporated Motorola's previously planned 72 LEO satellites M-Star with the scope of transmitting voice, video and data

worldwide and Millennium constellations, with Celestri satellites carrying a dual Ka and V-band payload. The V-band payload was to be used primarily for high-bandwidth applications such as trunking.

5.3.3 STENTOR

The STENTOR experimental program was constructed by Alcatel and supported by CNES (French Space Agency), France Telecom (French Telecommunications Operator) and DGA (Ministry of Defence) to validate advanced technologies in flight. It was a GEO satellite to be located at13°E and to provide onboard multiplexing of digital TV channels [5-40], [5-41]. The transmission subsystem was constituted by a transparent repeater divided into two 40 MHz channels separated by 1 GHz; up-link is between 44 and 45 GHz and down-link between 20.2 and 21.2 GHz.

The propagation experimental P/L was formed by two propagation beacons at 20.7 GHz and 41.4 GHz. The 20.7 GHz beacon was common to both missions and one of its goals was to improve the antenna pointing at 44 GHz. The lunch process of this satellite failed on December, 11, 2002 when the French Ariane 5 launcher was blown up by the Range Safety Officer, shortly after take-off from Kourou in French Guiana due to flight malfunction. Stentor satellite was destroyed in the ensuing explosion.

5.3.4 PENTRIAD

Pentriad was a Denali Telecom V-band constellation using 13 satellites in Molniya HEO over the Northern Hemisphere. They also aimed at providing wireless infrastructure for *HALO*, a stratospheric broadband data and communication system.

5.3.5 V-STREAM

In September 1997, the U.S. based PanAmSat (81% owned by HUGHES Electronics Corporation.) requested authorization from the FCC to construct, launch and operate a series of 12 V-band geostationary satellites called V-stream for high-power, flexible broadcast and telecommunications services [5-42]. The system was planned to use 3 GHz of spectrum in the 50/40 GHz frequencies band. Key components of the system included

ILS, on-board processing and high-powered spot beams. In 2005 PanAmSat was acquired by Intelsat Ltd. and the project was quitted.

5.4 STATE OF THE ART OF W-BAND SATELLITE SYSTEMS

Currently no operative W band satellite communication system has been developed, only experimental trials over short horizontal terrestrial links have been performed. In this frame, W band can be considered as a frontier for space telecommunication applications.
However, there are some missions in the development phase conceived to perform telecommunication links in W-band. In the following sections the main characteristics of these missions are reported and analysed.

For what concerns the regulatory aspects, the ITU frequency allocations for W band spectrum are reported in Table 5-25. For FSS the allocated frequency bands are 71-76 GHz for downlink and 81-86 GHz for uplink. For Mobile Satellite Services the allocated frequency are 71-74 GHz for downlink and 81-84 GHz for uplink and for BSS the allocated frequencies are 74-76 GHz.

Table 5-25: ITU W band frequencies allocation

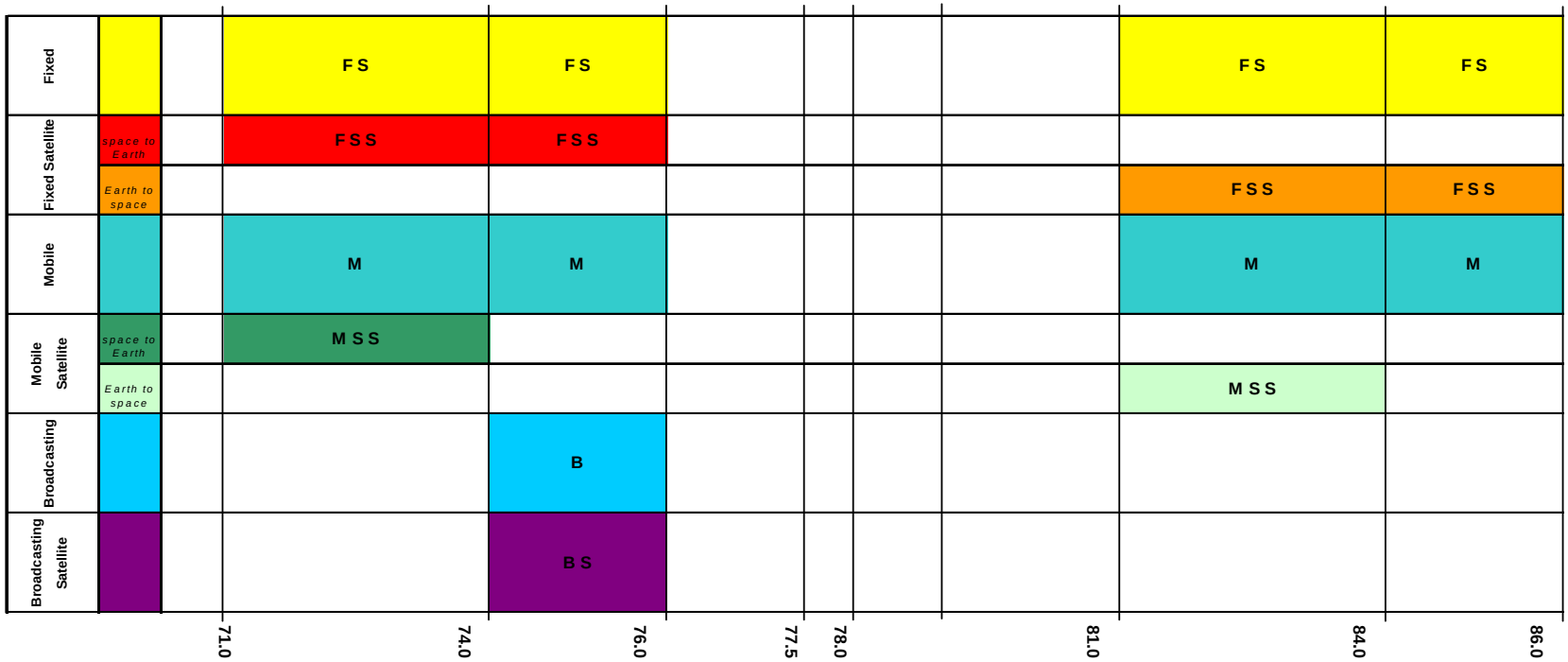

5.4.1 DAVID

DAVID is a satellite scientific mission of the ASI [5-43][5-44][5-45]. The B phase of the DAVID Mission was completed and the C/D proposal has been delivered to ASI.
The DAVID satellite is planned to be located in a Sun-synchronous LEO at about 570 km, ensuring the re-visitation of the same sites at the same hour every day. The DAVID mission is composed by two main experiments, which aim at:

- exploring the W-band channel for a high capacity data transfer (DCE);
- test dynamic resource sharing techniques (RSE) for the optimal exploitation of the EHF satellite channel.

In Figure 5-24 it is shown the DAVID DCE experiment.

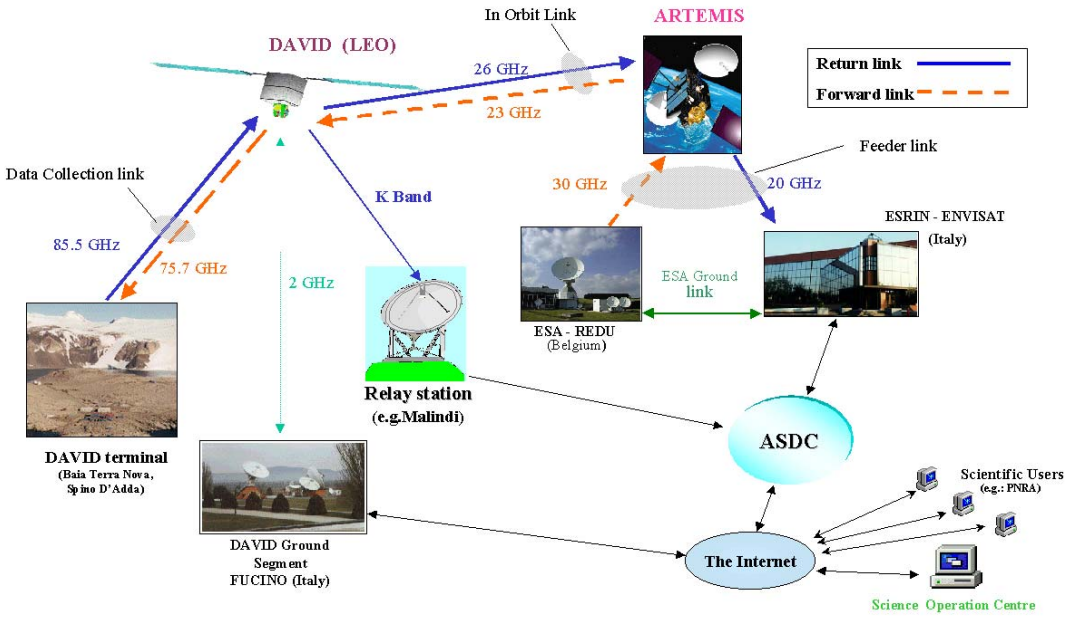

Figure 5-24: DAVID DCE Experiment

The DCE aim is to prove the feasibility of a high speed data collection from CPSs via a W-band link at 84.5 GHz. Since this frequency band is still unused for satellite communications, a large portion of the spectrum is available. It will lead to the possibility of collecting data at about 100 Mbit/s practically "error free" (BER of $6 \cdot 10^{-11}$), so allowing to upload on the on-board memory at least 1 Gbyte of net data (i.e. after regeneration and decoding of the received data) during the short visibility time window of

each passage over the CPS locations (about 3 minutes, considering antennas and attitude constraints).

The data will be stored on-board thanks to the regenerative capability of the payload and to the presence of an on-board memory. Then they will be relayed to earth exploiting the space and ground segments of the ESA's satellite ARTEMIS (Inter Orbit Link between DAVID and ARTEMIS and Feeder Link between ARTEMIS and the ground station) and gathered at the ASI Scientific Data Centre premises located in Frascati (Italy). This centre will act as Mirror Provider, allowing to collect rough data. Then they will be processed and made them available to scientific users connected to Internet.

The envisaged CPSs, at present, are Spino d'Adda (Italy) and the PNRA's Antarctic base at Baia Terra Nova (BTN), a truly remote site, both for its location that for the existing communication facilities (only an Immarsat link allows daily data exchange of limited entity). To provide interactivity for the system, also a small flux of data will be carried in the opposite direction, i.e. from fixed users to CPSs via ARTEMIS and DAVID, and a data rate of 1 Mbit/s should be sufficient. The TT&C service will be performed through an S-band link with the Telespazio station in Fucino (Italy).

5.4.2 QZSS

This JAXA project is a feasibility study for a 3 GEO synchronous satellites constellation. Each satellite has 45° of inclination. Moreover, this constellation aims at achieving a near-continuous coverage over Japan and Australia with a quasi-zenithal elevation angle (greater than 70°) [5-46].

The system will be used as an augmentation of GPS and as backbone for VSAT-VSAT links, as a secondary service.

The proposed operative frequencies for telecommunications application are 84 GHz for the uplink and 74 GHz for the downlink. The system will provide a link data rate of 45 Mbps, and it will allow to achieve a good coverage of polar regions. This satellite system will provide good propagation performance for what concerns urban mobile telecommunication services; in fact, it allows a strong reduction of the shadowing in metropolitan areas because of its elevation angle greater than 70°.

As previously introduced, the system is also expected to enhance accuracy and availability of the GPS service over Japan.

The use of the quasi-zenith satellite at high elevation angles in combination with GPS improves the availability of satellite positioning for areas where GPS signals could not be received such as urban canyon and mountain terrain.

In order to facilitate GPS availability enhancement, the navigation signals and messages of the QZSS have complete interoperability with those of GPS. Users can receive advanced positioning service combining GPS and QZSS without being aware of the difference between the two systems.

The GPS Performance Enhancement ensures high accuracy by transmitting position correction data, and it achieves high reliability by sending integrity data that enable users to rely on the positioning signals, thus improving the use of GPS.

5.4.3 IIN

NASA and other Space Agencies is involved in the design of a space infrastructure able to support the future solar system exploration missions, both manned and unmanned ones. This infrastructure, called IIN, will be able to relay data from landers, satellites, rovers, etc. to the Earth.

Moreover, it will consist of a fleet of data relay satellites positioned through the solar system to support space exploration activities [5-47].

The IIN will be gradually deployed, positioning the first two key nodes (DRS) around Earth and Mars. Hence, a telecommunication infrastructure will be developed around Mars in order to provide data relay and navigation services.

The space network will be developed adding other satellites that can be considered as the communication nodes, as additional needs arise.

An example of IIN possible configuration is shown in Figure 5-25. The IIN requires great technology development that can support the transfer of high volumes of scientific and communication data. In this frame, W band can be considered as a key enabling technology for ISL links between space nodes of the infrastructure, due to the absence of additional atmospheric attenuation. W band will be useful in order to realise reliable, high bandwidth, space trunk lines.

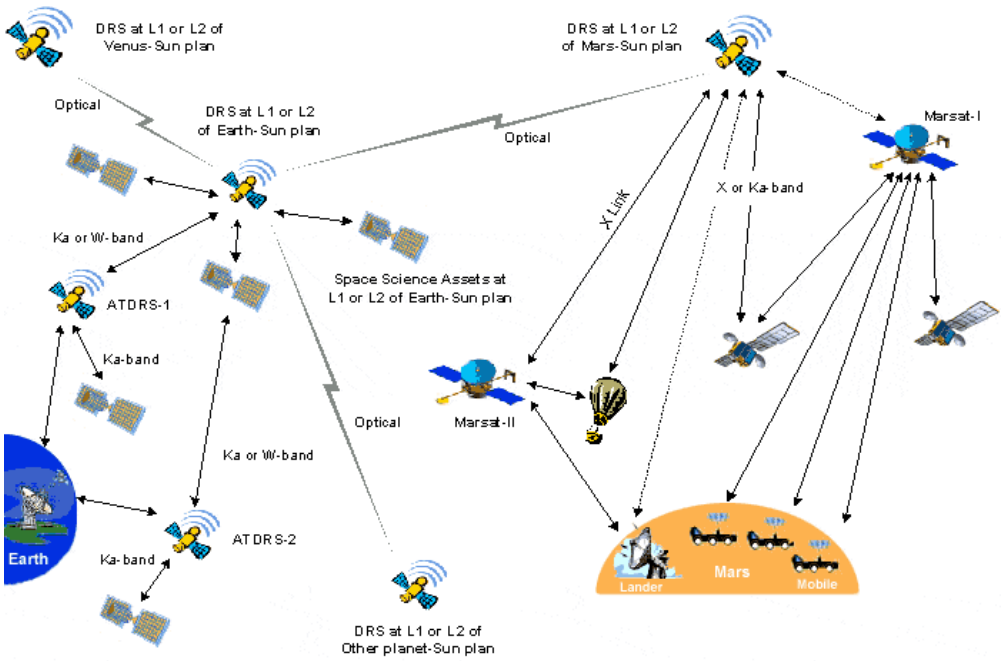

Figure 5-25: Integrated Interplanetary Network Scheme

5.5 EHF PROPAGATION EVALUATION

This paragraph is devoted to the analysis of EHF satellite propagation. Some propagation models, providing first order statistics, have been used in order to perform some simulations able to identify and analyze the major characteristics of additional attenuation for EHF satellite links [5-48]. As largely described above, the current scientific research is pointing toward the exploitation of frequency ranges beyond the Q/V bands. W band is considered as the new frontier of satellite communications. The large bandwidth availability in W band allows to conceive and propose many advanced and innovative services that need high-volume data transfers without tight interactivity constraints for future scenarios. Therefore, such a frequencies range could be exploited in order to meet the high-quality data transmission requirements for a large number of end users and data-oriented services. The most important benefits provided by such frequency range are not only in terms of available bandwidth, with respect to saturated lower frequency band; as a matter of fact there are a large number of advantages and opportunities provided by EHF [5-49]. One of the most important advantages is represented by the very high security level (both for commercial and dual applications) in terms of:

- increased protection due to use of very narrow spot beams;

- improved anti jammer protection thanks to wider available spreading bandwidth and more limited jammer capability.

Antennas operating at those bands have a higher directivity than ones (of the same size) operating at lower frequencies, so the interference between adjacent satellite position is reduced. Furthermore, this high directivity allows to use high-gain spot beam satellite antennas, increasing down-link power flux density and saving satellite power (one of the most important resource of the platform). Hence, an efficient capitalization of the bandwidth resource can be achieved if a high frequency reuse is applied.

Finally, the innovative W band technology involves a high security standard. Another important improvement provided by EHF consists of the reduction of all RF hardware equipment. This makes the use of EHF especially attractive with respect to development of portable terminals and smaller satellite P/Ls, for example in the scenario of space exploration, where mass and size are one of the most important mission drivers.

The main drawback of these satellite links is the large atmospheric fade experienced when rainfall occurs along the path, in addition to the gaseous atmospheric absorption by oxygen and water vapour. Due to the fact that Q/V bands have been extensively analysed through the Italsat satellites and propagation models have been created using the collected data, the current research activity has to be pointed toward W band. The experimentation of the channel at those frequencies represents the first preliminary step in order to exploit the novel W-band frequency range for advanced satellite applications.

This paragraph deals with the preliminary evaluation of W band propagation impairments. The development of future broadband communication satellite systems will be driven by the need for reconfigurability techniques at physical, access, transport and application levels in order to provide QoS (Quality of Service) multimedia services. The satellite network will be integrated with the terrestrial one in order to create a cooperative environment for the provision of high level services to the customer. In this frame, an overview of the most promising PIMTs, that could be used in the future broadband EHF satellite communications, will be introduced together with some preliminary simulation for performance evaluation.

5.5.1 ATTENUATION PREDICTION MODELS, FIRST ORDER STATISTICS

As previously introduced, no scientific experiments and measurements on the signal propagation through an Earth-satellite link operating in W-band exist.

However, some satellite systems in W-band have been proposed, such as:

- the ASI's experimental satellite DAVID [5-50], which is a 570 km LEO (85.5/75.7 GHz);
- the ASI WAVE Project, aiming at developing a complete line of W band demonstrative and pre-operative payloads [5-51], [5-52], [5-53], [5-54];
- the Japanese QZSS, composed of 3 GEO orbit satellites separated by 120° with inclination angle of 45°(81-84/71-74 GHz), for VSAT and mobile applications.
- A study for interplanetary link (IIN) was also proposed by NASA, for data relay services in space exploration missions.

In order to get reliable measurements on the channel behaviour at this frequency bands and evaluate the influence of rain drops, clouds and scintillation, 3-5 years of studies are required. Then, the data gathered with the experiments are used as input for propagation models that help to predict the attenuation levels on signal, such as different releases of Millimetre Propagation Model (MPM) by H. J. Liebe [5-55][5-56].

In order to realise a first model for the behaviour of the channel in W band, known statistics and models for lower frequencies are needed; from these ones some estimates about the channel attenuation can be gleaned. For instance, it is well known that rain attenuation has the stronger contribution at these frequencies with values of the order of tens dB, which will lead to large link margins. As far as the contribution of others atmospheric agents is considered, the database of ESA for climatic data and ITU-R recommendations [5-57] can be used for estimating the attenuation. By using them, it is possible to get the contribution of various effects to the total attenuation, hence the total attenuation value at a fixed probability and the cumulative distribution of atmospheric attenuation for a set of locations. In order to have a preliminary evaluation of W band atmospheric attenuation, in the following section, the procedure to obtain first order statistics will be described and some results achieved through simulations will be shown.

5.5.1.1 Propagation in W band

Increasing frequency means stronger impact of the atmosphere on the radio-wave propagation. In particular, the impairments due to the presence of the atmosphere cause a signal attenuation (referred to as "additive attenuation"), which has to be added to the free space losses and carefully taken into account in the system design. Generally a "worst case" approach is considered, that brings to the introduction of a system margin. Therefore,

by means of cumulative distribution of expected attenuation, the time percentage of system outage during a year may be estimated.

The atmosphere may be divided in several different layers, according to their properties. There are two main layers that relate to radio-waves propagation: the troposphere that has impact on frequencies above 30 MHz; the ionosphere that crosses the boundaries of the meteorological layers and extends from around 60 km up to 700 km. In this region, the air tends to ionise, yielding ions and free electrons. The free electrons have an impact on radio-waves at frequencies below 1 GHz, often bending them back to Earth so that they can reach wide distances around the world. Therefore, the ionospheric attenuation will not be considered for EHF propagation impairments evaluation.

The propagation loss on the Earth-space path is the sum of different contributions as follows:

- absorption of atmospherical gases (oxygen and water vapour);
- absorption, scattering and depolarization due to rain and other precipitations;
- attenuation due to clouds;
- noise emission due to atmospherical absorption;
- fast fading, scintillation and others related to variations of refraction index.

Each of these contributions has its own characteristics as a function of different parameters such as frequency, geographic location and elevation angle.

5.5.1.2 Parameters and prediction models

The required parameters to work out the additional attenuation for the Earth-Satellite path could be divided into two categories: the first addicted to Earth stations and geometry of the system, the second one strictly linked to radio-electric parameters. Some examples for the first one are:

- satellite coordinates;
- geographical coordinates and climate of the receiving stations.

Those information allow to determine the elevation angles and the altitude; both of them contribute to determine the length of the tropospheric link. Examples of radio-electric parameters are:

- frequency;
- polarization;
- antenna diameter.

Moreover, the knowledge of the atmospheric status along the link is required to create a prediction model for the additional attenuation. For analysis purpose, in this work three main prediction algorithms, developed by ITU, are used: the ones described in ITU-R P676 ("Attenuation by atmospheric gases"), P840 ("Attenuation due to clouds and fog") and P618 ("Propagation data and prediction methods required for the design of Earth-space telecommunication systems") [5-58][5-59][5-60]. The attenuation contributions that most heavily impact on the capacity of the model prediction are those closely depending from the climatic situation, such as raindrop, hydrometeors in general, presence of clouds, tropospheric scintillations, atmospheric pressure and humidity. All these contributions can only be evaluated in statistical terms, and their interdependence is not easily estimated since they might combine in a non-linear way.

5.5.1.2.1 Atmospheric gases

The atmosphere basically consists of gases and water droplets. When only gases are present, the atmosphere is commonly defined clear and the non-scattering assumption is correct. In clear sky condition, the troposphere composition could be roughly divided in a humid part, due to the presence of water vapour, and a dry part, formed by other gases. Due to different climatic conditions, the water vapour concentration is highly variable. Dry air is mainly composed by Nitrogen (78%) and Oxygen (21%), with traces of other gases (1%), and its composition is quite stable. At microwave frequencies, the absorbing gases are represented by oxygen and water vapour that are generally present in any situation. The absorption effect of other gases, such as ozone, is negligible with respect to oxygen and water vapour in the 1-300 GHz frequency range. The microwave absorption spectrum of oxygen has a complex resonance centered around 60 GHz and extended in the range between 50 and 70 GHz, and an isolated weaker line at 118.8 GHz. Being the oxygen concentration roughly constant, the oxygen absorption depends only on the profiles of temperature and pressure and its calculation is rather straightforward. Water vapour absorption results from the superposition of two terms: one linearly related to the water density and the other is a quadratic function of the density. In the microwave and millimeter-wave regions, a weak absorption line occurs at 22.235 GHz and much stronger lines at 183.3 GHz and 324.4 GHz. The total absorption due to gases is shown in Figure 5-26. Blue curve represents the average value on annual scale of the total absorption as a function of the water vapour content, while red curve displays the same but only for the dry season. The estimation of the atmospheric gaseous absorption could be performed

through the MPM by H. J. Liebe [5-55]-[5-56], which was found to have good match with experimental results in both horizontal and vertical links test trials. However, this is a physical model, which requires accurate measurements of the main meteorological parameters (pressure, temperature, and humidity percentage) along the vertical path. On a statistical basis, those information can be obtained relying on existing meteorological databases. Equipment should be used to characterise the actual channel such as weather balloon or multi-frequency radiometers, which are able to retrieve the vertical profiles of the quantities of interest. For each single component of the radio refractivity, the relationship to meteorological parameters is defined by MPM.

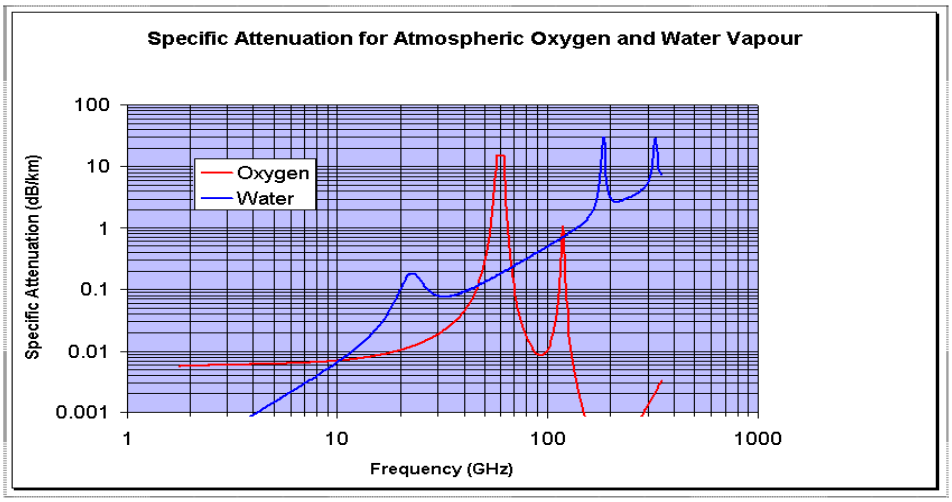

Figure 5-26: Specific attenuation due to oxygen and water vapour [dB/Km] in function of frequency

The gaseous attenuation can be calculated using ITU-R P.676 [5-58], that has been created on the basis of Liebe models. The specific gaseous attenuation γ, can be calculated by:

$$\gamma = \gamma_0 + \gamma_w = 0.1820 f N''(f) \tag{5-2}$$

where γ_0 and γ_w are the specific attenuations (dB/km) due to dry air and water vapour respectively, and where f is the frequency (GHz) and $N''(f)$ is the imaginary part of the frequency-dependent complex refractivity:

$$N''(f) = \sum_i S_i F_i + N''_D(f) + N''_w(f) \tag{5-3}$$

S_i is the strength of the *i*-th line, F_i is the line shape factor and the sum extends over all the lines; $N''_D(f)$ and $N''_w(f)$ are dry and wet continuum spectra. The line strength is given by:

$$\begin{aligned} S_i &= a_1 \times 10^{-7}\, p\theta^3 \exp\left[a_2(1-\theta)\right] \quad \text{for oxygen} \\ &= b_1 \times 10^{-1}\, e\theta^{3.5} \exp\left[b_2(1-\theta)\right] \quad \text{for water vapour} \end{aligned} \tag{5-4}$$

where:

p: dry air pressure (hPa), e: water vapour partial pressure (hPa), $\theta = 300/T$, T: temperature (K). Local values of p, e and T measured profiles should be used. However, in the absence of local information, the reference standard atmospheres described in Recommendation ITU-R P.835 ("Reference standard Atmosphere") could be used [5-60]. The water-vapour partial pressure, e, may be obtained from the water-vapour density ρ using the expression:

$$e = \frac{\rho T}{216.7} \tag{5-5}$$

The coefficients a_1, a_2 for oxygen and b_1, b_2 for water vapour are given in [5-58]. The line-shape factor is given by:

$$F_i = \frac{f}{f_i}\left[\frac{\Delta f - \delta(f_i - f)}{(f_i - f)^2 + \Delta f^2} + \frac{\Delta f - \delta(f_i + f)}{(f_i + f)^2 + \Delta f^2}\right] \tag{5-6}$$

where f_i is the line frequency and Δf is the width of the line:

$$\begin{aligned} \Delta f &= a_3 \times 10^{-4}\left(p\theta^{(0.8-a_4)} + 1.1\mathrm{e}\theta\right) \quad \text{for oxygen} \\ &= b_3 \times 10^{-4}\left(p\theta^{b_4} + \mathrm{b}_5\mathrm{e}\theta^{b_6}\right) \quad \text{for water vapour} \end{aligned} \tag{5-7}$$

and δ is a correction factor which arises due to interference effects in oxygen lines:

$$\begin{aligned} \delta &= \left(a_5 + a_6\theta\right) \times 10^{-4}\mathrm{p}\theta^{0.8} \quad \text{for oxygen} \\ &= 0 \quad \text{for water vapour} \end{aligned} \tag{5-8}$$

All the spectroscopic coefficients a_i are given in [5-58]. The dry air continuum arises from the non-resonant Debye spectrum of oxygen below 10 GHz and the pressure-induced nitrogen attenuation above 100 GHz.

$$N_D''(f) = fp\theta^2\left[\frac{6.14\times10^{-5}}{d\left[1+\left(\frac{f}{d}\right)^2\right]} + 1.4\times10^{-12}\left(1-1.2\times10^{-5}f^{1.5}\right)p\theta^{1.5}\right] \tag{5-9}$$

where d is the width parameter for the Debye spectrum:

$$d = 5.6\times10^{-4}\left(p + 1.1e\right)\theta \tag{5-10}$$

The wet continuum $N''_W(f)$ is included to account for the fact that measurements of water-vapour attenuation are generally in excess of those predicted using the theory described by previous equations, plus a term to include the effects of higher-frequency water-vapour lines not included in the reduced line base:

$$N''_W(f) = f\left(3.57\theta^{7.5}e + 0.113p\right)10^{-7}e\theta^3 \tag{5-11}$$

The total slant path attenuation, $A(h,\varphi)$, from a station with altitude, h, and elevation angle, φ, can be calculated using the following formula (when $\varphi \geq 0$):

$$A(h,\varphi) = \int_h^{\infty} \frac{\gamma(H)}{\sin\Phi} dH \tag{5-12}$$

where the value of Φ can be determined as follows, based on Snell's law in polar coordinates:

$$\Phi = ar\cos\left(\frac{c}{(r+H)\times n(H)}\right) \tag{5-13}$$

where:

$$c = (r+h)\times n(h)\times\cos\varphi \tag{5-14}$$

$n(h)$ is the atmospheric radio refractive index, calculated from pressure, temperature and water-vapour pressure along the path (as defined in Recommendation ITU-R P.835) using Recommendation ITU-R P.453 [5-61].

On the other hand, when $\varphi < 0$, there is a minimum height, $h_{\min}$, at which the radio beam becomes parallel with the Earth's surface. The value of $h_{\min}$ can be determined by solving the following transcendental equation:

$$(r+h_{\min})\times n(h_{\min}) = c \tag{5-15}$$

This can be solved by repeating the following calculation, using $h_{\min} = h$ as an initial value:

$$h'_{\min} = \frac{c}{n(h_{\min})} - r \tag{5-16}$$

Therefore, $A(h,\varphi)$ can be calculated as follows:

$$A(h,\varphi) = \int_{h_{\min}}^{\infty} \frac{\gamma(H)}{\sin\Phi} dH + \int_{h_{\min}}^{h} \frac{\gamma(H)}{\sin\Phi} dH \tag{5-17}$$

A numerical solution for the attenuation due to atmospheric gases can be implemented with the following algorithm. To calculate the total attenuation for a satellite link, it is

necessary to know not only the specific attenuation at each point of the link, but also the length of path that has that specific attenuation. To derive the path length it is also necessary to consider the ray bending that occurs in a spherical Earth.

Using Figure 5-27 as a reference, a_n is the path length through layer n with thickness δ_n that has refractive index n_n, α_n and β_n are the entry and exiting incidence angles, r_n are the radii from the centre of the Earth to the beginning of layer n. a_n can then be expressed as:

$$a_n = -r_n \cos\beta_n + \frac{1}{2}\sqrt{4r_n^2 \cos^2\beta_n + 8r_n\delta_n + 4\delta_n^2} \tag{5-18}$$

The angle α_n can be calculated from:

$$\alpha_n = \pi - ar\cos\left(\frac{-a_n^2 - 2r_n\delta_n - \delta_n^2}{2a_n r_n + 2a_n\delta_n}\right) \tag{5-19}$$

β_1 is the incidence angle at the ground station (the complement of the elevation angle θ). β_{n+1} can be calculated from α_n using Snell's law that in this case becomes:

$$\beta_{n+1} = \arcsin\left(\frac{n_n}{n_{n+1}}\sin\alpha_n\right) \tag{5-20}$$

where n_n and n_{n+1} are the refractive indexes of layers n and $n+1$. The remaining frequency dependent (dispersive) term has a marginal influence on the result (around 1%) but it can be calculated from the method shown in the ITU-R Handbook on Radiometeorology. The total attenuation can be derived using:

$$A_{gas} = \sum_{n=1}^{k} a_n \gamma_n \tag{5-21}$$

To ensure an accurate estimate of the path attenuation, the thickness of the layers should increase exponentially, from 10 cm at the lowest layer (ground level) to 1 km at an altitude of 100 km, according to the following equation:

$$\delta_i = 0.0001\exp\left(\frac{i-1}{100}\right) \tag{5-22}$$

from $i = 1$ to 922, noting that $\delta_{992} \cong 1.0$ km and $\sum_{i=1}^{992}\delta_i \cong 100$ km.

For Earth-to-space applications, the integration should be performed at least up to 30 km, and up to 100 km at the oxygen line-centre frequencies.

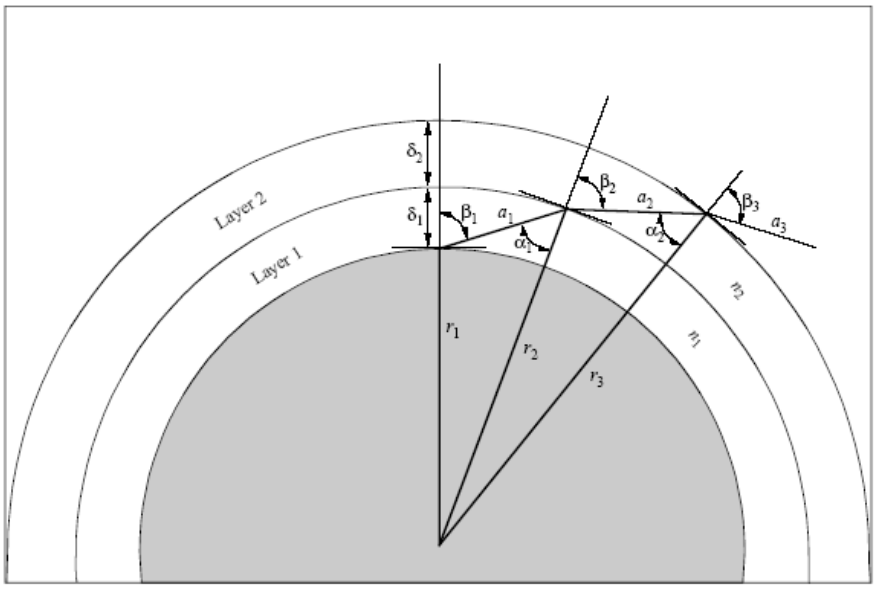

Figure 5-27: Gaseous attenuation slant path geometry

5.5.1.2.2 Rain

Rain is the phenomena that is responsible of the highest contribution to the total additive attenuation above 10 GHz (an exception occurs for frequencies near oxygen resonance peak and low elevation angles). When the rain droplets are smaller than the wavelength (i.e. below 20 GHz), the rain rate is sufficient statistics to estimate rain attenuation. On the other hand, with higher operating frequencies, Drop Size Distribution (DSD) can no longer be neglected. Raindrops have very variable size and shape. When the diameter exceeds 4 mm, they become hydro-dynamically unstable and break. Above 1 mm diameter, the shape tends to become spheroidal with a flat basis. Therefore, usually it is called radius of the raindrop the radius of the sphere that has the same volume. The different DSD is due to the warm rain processes:

- condensation of water vapour;
- coalescence between raindrops;
- break of the raindrops.

Various semi-empirical models have been developed for estimating drop-size distribution. Among them, the most relevant are:

- Law-Parsons model;
- Marshall-Palmer model;

In order to calculate rain attenuation, the Dissanayake-Haidara-Allnutt (DHA) method [5-62] is used, as recommended by ITU [5-57]. The main input to this model is the raindrop intensity not exceed for 0.01% of time, $R_{0.01}$ (mm/h). The DHA method assumes a log-normal distribution for rain. Horizontal and vertical dis-homogeneity that characterise different types of precipitations (stratiform or convective) have been taken into account. Other required inputs are:

- latitude of the reference site, φ and its altitude above sea level, h_s (useful for calculation of the highest altitude of raining layer);
- θ, elevation angle of hearth antenna (for calculating path distance);
- polarization angle, ζ and operational frequency, f (for calculating the coefficients used to derive, for a given *R*, the attenuation given by the rain);
- R_e, effective radius of the Earth (8500 km).

A schematic presentation of the Earth-space path geometry is presented in Figure 5-28: A is the frozen precipitation layer, B is the rain height, C is the liquid precipitation, D is the Earth-space path.

In the following lines, the main steps for rain attenuation evaluation are reported. First of all the rain height, h_R (km), has to be calculated using the procedure presented in ITU-R P.839 [5-63].

For $\theta \geq 0.5$, the slant-path length L_s (km) below the rain height:

$$L_s = \frac{(h_R - h_s)}{\sin\theta} \text{ (km)} \tag{5-23}$$

For $\theta < 0.5$, the following formula is used:

$$L_s = \frac{2(h_R - h_s)}{\left(\sin^2\theta + \frac{2(h_R - h_s)}{R_e}\right)^{1/2} + \sin\theta} \text{ (km)} \tag{5-24}$$

The horizontal projection of the slant-path length L_G (Km), has to be calculated as:

$$L_G = L_s \cos\theta \text{ (km)} \tag{5-25}$$

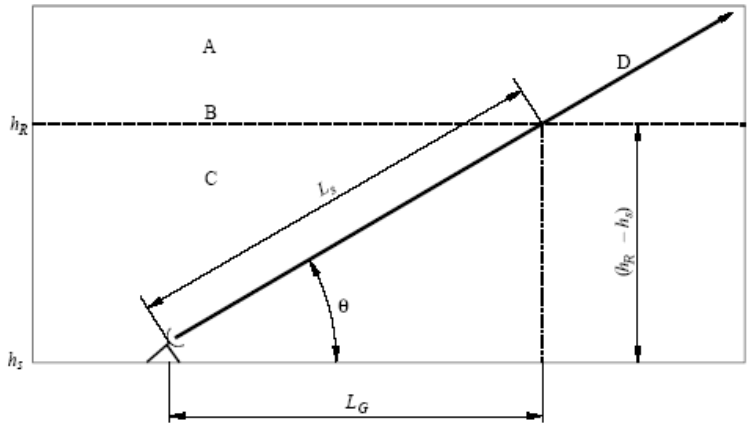

Figure 5-28: Schematic presentation of Earth-space path geometry

The rainfall rate exceeded for 0.001% of an average year, $R_{0.01}$, can be obtained from local data sources or using the maps reported in ITU-R P.837 [5-64].

Once the rainfall rate $R_{0.01}$ that is exceeded for 0.01% is achieved, the specific attenuation γ_R (dB/km) can be calculated according to the Mie formulation, which is modified by considering oblate spheroid instead of spherical shape for rain drops and also assuming a Marshall-Palmer drop-size distribution:

$$\gamma_R = k\left(R_{0.01}\right)^{\alpha} \tag{5-26}$$

where values of k and α for different frequencies and polarization are reported in Recommendation ITU-R P.838 [5-65]. An horizontal reduction factor for 0.01% of time, $r_{0.01}$, has to be calculated as:

$$r_{0.01} = \frac{1}{1 + 0.78\sqrt{\frac{L_G \gamma_R}{f}} - 0.38\left(1 - e^{-2L_G}\right)} \tag{5-27}$$

A vertical adjustment factor for 0.01% of time, $v_{0.01}$, has to be calculated using the following procedure:

$$\zeta = \tan^{-1}\left(\frac{h_R - h_s}{L_G r_{0.01}}\right) \text{ degrees,} \tag{5-28}$$

$$\text{for } \zeta > \theta,\ L_R = \frac{L_G r_{0.01}}{\cos\theta} \text{ km,} \tag{5-29}$$

$$\text{else } L_R = \frac{\left(h_R - h_s\right)}{\sin\theta} \text{ km.} \tag{5-30}$$

$$\begin{aligned} &\text{If } |\varphi| < 36°,\ \chi = 36 - |\varphi| \text{ degrees,} \\ &\text{else } \chi = 0. \end{aligned} \tag{5-31}$$

$$v_{0.01} = \frac{1}{1 + \sqrt{\sin\theta}\left(31\left(1 - e^{-(\theta/(1+\chi))}\right)\frac{\sqrt{L_R \gamma_R}}{f^2} - 0.45\right)} \tag{5-32}$$

The effective path length is:

$$L_E = L_R v_{0.01} \text{ (km)} \tag{5-33}$$

The predicted attenuation exceeded for 0.01% of an average year can be obtained from:

$$A_{0.01} = \gamma_R L_E \text{ (dB)} \tag{5-34}$$

The estimated attenuation to be exceeded for other percentages of an average year, in the range 0.001% to 5%, can be determined from the attenuation to be exceeded for 0.01% for an average year:

$$\begin{aligned} &\text{if } p \geq 1\% \text{ or } |\varphi| \geq 36°: && \beta = 0 \\ &\text{if } p < 1\% \text{ and } |\varphi| < 36° \text{ and } \theta \geq 25°: && \beta = -0.005\left(|\varphi| - 36\right) \\ &\text{otherwise:} && \beta = -0.005\left(|\varphi| - 36\right) + 1.8 - 4.25\sin\theta \end{aligned} \tag{5-35}$$

$$A_p = A_{0.01}\left(\frac{p}{0.01}\right)^{-\left(0.655 + 0.033\ln(p) - 0.045\ln(A_{0.01}) - \beta(1-p)\sin\theta\right)} \text{ (dB)} \tag{5-36}$$

Using this method an estimate of the long-term statistics of attenuation due to rain can be obtained.

5.5.1.2.3 Tropospheric Scintillations

Scintillations are rapid fluctuations of signal amplitude, phase or angle of arrival of radio waves. They are produced by small-scale refractive index variations. Tropospheric scintillations are produced in the first kilometres of Earth atmosphere and depend on season, local climate, frequency and elevation angle. In general, tropospheric amplitude scintillation magnitude increases with increase in radio frequency, reduction in elevation angle and antenna diameter and increase in temperature humidity and wind velocity.

At W-band frequencies, tropospheric scintillations may cause a heavy degradation of the transmitted signals, especially when the dimensions of the antennas are small. Locally, scintillations are due to variations of refraction index values; in particular, the amplitude and level of scintillations depend from the structure of the refraction index, and they are

proportional to the entity of its variations. In other words, more refraction index gradient is high and discontinuous, higher will be scintillation entity.

The tropospheric scintillations are determined by atmospheric phenomena such as strong winds, which affect the atmosphere and contribute to air mixing, causing loss of stratification. The turbulence gives rise to rapid variations of the refractive index.

As previously introduced, tropospheric scintillation intensity is proved to increase by increasing the carrier frequency, beamwidth and average temperature, along with decreasing the elevation angle and antenna size. In particular, when operating at high frequencies and low elevation angles (propagation path covers most of the atmosphere), the contribution of scintillation to the total fade can be comparable to the one of the rain.

Tropospheric scintillations are essentially a non-absorptive effect. In fact, the mean level of the signal does not change significantly when compared to the peak-to-peak amplitude excursion. Theoretical studies of the atmospheric turbulence-induced scintillation have been carried on by Tatarskii [5-65]. Results from his study and from experimental trials confirm that over relatively short time periods, where the meteorological conditions could be assumed constant, scintillation amplitude (in dB) follows a Gaussian distribution around the mean signal level, which is zero.

Therefore, the most significant parameter to characterize the phenomena it is the variance σ^2 or the standard deviation σ (which is commonly referred to as "scintillation intensity"). For finding the appropriate statistics that describe the phenomenon, it is important to obtain and suitably interpret some input data, such as annual and/or monthly average site temperature, T (°C), and relative humidity, H, which reflect important meteorological characteristics of the area. In fact, correlation has been found between the standard deviation of the scintillation amplitude and the long-term average of these meteorological parameters. As the averages values of T and H are subject to changes with seasons, the distribution of the attenuation given by scintillations changes as well. In particular, σ is correlated with the wet term of tropospheric refractivity N_{wet}, which is a function of ground temperature and relative humidity (when reliable measurements are not available, long term statistics could be inferred from ITU recommendation).

The most used method to predict long term statistics of scintillation related attenuation is the ITU-R 618 [5-57]. It relies on long term statistics of ground based measurements of temperature and humidity for the site of interest. In the following it is shown the computation of monthly and long-term statistics of amplitude scintillations at elevation

angles greater than 4°. The procedure has been tested at frequencies between 7 and 14 GHz, but it is truly trustable for applications at higher frequencies.

Parameters involved in the model include:

- T: average surface ambient temperature (°C) at the site for a period of one month or longer;
- H: average surface relative humidity (%) at the site for a period of one month or longer;
- f: frequency;
- θ: path elevation angle, $\theta \geq 4°$;
- D: physical diameter (m) of the earth-station antenna;
- η: antenna efficiency; if unknown, $\eta = 0.5$ is a conservative estimate.

The predicted standard deviation is given by:

$$\sigma = \sigma_{ref} f^{7/12} \frac{g(x)}{\sin\theta} \tag{5-37}$$

where

$$\sigma_{ref} = 3.6 \cdot 10^{-3} + 10^{-4} \cdot N_{wet} \tag{5-38}$$

The antenna averaging factor $g(x)$ is related to antenna parameters (such as antenna efficiency and geometrical diameter):

$$g(x) = \sqrt{3.86 \cdot \left(x^2 + 1\right)^{11/12} \cdot \sin\left(\frac{11}{6} arctg \frac{1}{x}\right) - 7.08 \cdot x^{5/6}} \tag{5-39}$$

with x given by:

$$x = 1.22 \cdot D_{eff}^2 \cdot \left(\frac{f}{L}\right) \tag{5-40}$$

whereas D_{eff} is the effective antenna diameter:

$$D_{eff} = \sqrt{n} \cdot D \tag{5-41}$$

Defining the time percentage factor $a(p)$ for the time percentage p:

$$a(p) = -0.061\left(\log_{10} p\right)^3 + 0.072\left(\log_{10} p\right)^2 - 1.710 \cdot \log_{10} p + 3.0 \tag{5-42}$$

The scintillation fade depth for the time percentage p could be obtained by:

$$A_{sc}(p) = a(p) \cdot \sigma \tag{5-43}$$

5.5.1.2.4 Clouds

Clouds are composed by very small raindrops or ice crystals of variable size (up to hundreds of micrometer). The clouds can be classified in two main subsets: stratified clouds and vertical clouds, subdivided in ten main types according to their composition, shape and altitude with respect to the Earth surface [5-59]:

- cirro: is the prefix for the high altitude clouds, such as cirrus, cirrocumulus and cirrostratus;
- alto: is the prefix for medium height clouds, such as altocumulus, altostratus and nimbostratus.

At lower altitude there are clouds such as stratocumulus and stratus; cumlus and cumulonimbus have a higher vertical extension, and could spread across all the troposphere. Clouds identification and classification is very helpful in the estimation of clouds related attenuation. The contribution of attenuation from clouds can be evaluated through new recent prediction models [5-66][5-67]. The different clouds considered in these models are divided in four types: nimbocumulus, cumulus, nimbostratus, and stratus. Their properties are shown in Table 5-26; the main data are vertical height, horizontal length and water content.

Cloud Type	Vertical Extent (km)	Horizontal Extent (km)	Water content (g/m^3)
Cumulonimbus	3.0	4.0	1.0
Cumulus	2.0	3.0	0.6
Nimbostratus	0.8	10.0	1.0
Stratus	0.6	10.0	0.4

Table 5-26: Average properties of the four cloud types used in the cloud attenuation model

The cloud attenuation is considered only in non-rainy conditions since during rain events it is not possible to separate the two contributions. Moreover, it is derived assuming the average cloud properties of four cloud types and a log-normal statistic distribution of clouds attenuation. The hypothesis that there is not overlap among different clouds is taken on, so there is a direct correspondence between the distribution and the type of cloud.

The specific attenuation for each of the cloud type could be evaluated by [5-69], [5-59]:

$$\gamma_c = K_l \cdot M \tag{5-44}$$

where:

K_l is specific attenuation coefficient ((dB/km)/(g/m^3));

M is liquid water density in the cloud or fog (g/m^3).

Using the Rayleigh approximation for cloud drops scattering and the double-Debye model for the dielectric permittivity $\varepsilon(f)$ of water, K_l could be calculated as follows:

$$K_l = \frac{0.189 \cdot f}{\varepsilon''\left(1+\eta^2\right)} \tag{5-45}$$

where f is the frequency in GHz and

$$\eta = \frac{2+\varepsilon'}{\varepsilon''} \tag{5-46}$$

Expressions for the real ε' and imaginary ε'' part of the dielectric permittivity are provided in [5-70]:

$$\varepsilon'(f) = \frac{\varepsilon_0 - \varepsilon_1}{\left[1+\left(f/f_p\right)^2\right]} + \frac{\varepsilon_1 - \varepsilon_2}{\left[1+\left(f/f_s\right)^2\right]} + \varepsilon_2 \tag{5-47}$$

$$\varepsilon''(f) = \frac{f\left(\varepsilon_0 - \varepsilon_1\right)}{f_p\left[1+\left(f/f_p\right)^2\right]} + \frac{f\left(\varepsilon_1 - \varepsilon_2\right)}{f_s\left[1+\left(f/f_s\right)^2\right]} \tag{5-48}$$

where: $\varepsilon_0 = 77.6 + 103.3\left(\theta - 1\right)$, $\varepsilon_1 = 5.48$, $\varepsilon_2 = 3.51$, $\theta = 300/T$ (K).

The principal and secondary relaxation frequencies are:

$$f_p = 20.09 - 142\left(\theta - 1\right) + 294\left(\theta - 1\right)^2 \tag{5-49}$$

$$f_s = 590 - 1500\left(\theta - 1\right) \tag{5-50}$$

To obtain the attenuation due to clouds for a given probability value, the statistics of the total columnar content of liquid water L (kg/m^2) or, equivalently, mm of precipitable water for a given site has to be known yielding:

$$A = \frac{LK_l}{\sin\theta} \text{ dB, for } 90° \geq \theta \geq 5° \tag{5-51}$$

Figure 5-29 shows the values of K_l at frequencies from 5 to 200 GHz and temperatures between –8° C and 20° C. For cloud attenuations, the curve corresponding to 0° C should be used. The path attenuation due to each cloud types is calculated assuming that the cloud shape is a vertical cylinder with vertical and horizontal dimension H_c and L_c, respectively.

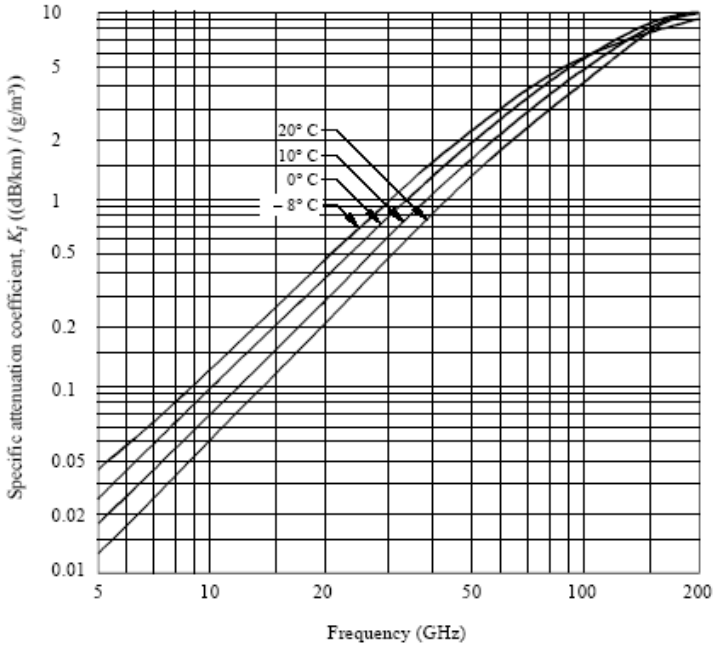

Figure 5-29: Specific attenuation by water droplets at various temperatures as function of frequency

5.5.1.2.5 Combination of effects and results

All the phenomena described above are strongly interdependent. For instance, cumulus clouds can produce both attenuation and scintillations, whereas gaseous absorption increases during rain due the increased water vapour content in the atmosphere. Therefore, after the contribution of different phenomena has been calculated, it is necessary to combine them in order to estimate total attenuation. This means to combine the cumulative distributions of all contributions in a suitable way.

The total attenuation, A_T (dB), represents the combined effect due to gases, clouds, rain and tropospheric scintillations. Fixed a p level of probability, $A_T(p)$ is composed by some terms:

- $A_R(p)$, attenuation due to rain;
- $A_C(p)$, attenuation due to clouds;
- $A_S(p)$, attenuation due to tropospheric scintillations;
- $A_{WV}(p)$, attenuation due to water vapour;
- $A_O(p)$, attenuation due to oxygen.

The ITU-R P618 [5-57] recommendation contains information about the combination method to use in order to calculate the total attenuation. There are three possible methods [5-71] [5-72]:

- simple sum, assuming equiprobability of single contribution;
- weighted sum, assuming equiprobability of single contribution;
- square root of the simple sum.

These methods range from total correlation condition to the statistic independence, with the intermediate case of weighted contributions. A general method exists to calculate the total attenuation at a fixed value of probability, $A_T(p)$:

$$A_T(p) = A_G(p) + \sqrt{\left(A_R(p) + A_C(p)\right)^2 + A_S^2(p)} \tag{5-52}$$

The following equations take into account the fact that a large part of the cloud attenuation and gaseous attenuation is already included in the rain attenuation prediction for time percentages below 1%:

$$A_C(p) = A_C(1\%) \text{ for } p < 1.0\% \text{ and } A_G(p) = A_G(1\%) \text{ for } p < 1.0\%. \tag{5-53}$$

The final formula that combines all the contributions is:

$$A_T(p) = A_O(p) + A_{WV}(p) + \sqrt{\left(A_R(p) + A_C(p)\right)^2 + A_S^2(p)} \tag{5-54}$$

In the following figures, the results for the total attenuation obtained from the simulation done during the WAVE A2 Project study are shown. These curves represent the total attenuation (x-axis, dB) not exceeded for a time percentage (y-axis %).

The frequencies used for the simulation are 86 GHz for the uplink and 76 GHz for the downlink. The two locations considered are Rome and Spino D'Adda (Milan). In these figures different curves are reported as function of the elevation angles.

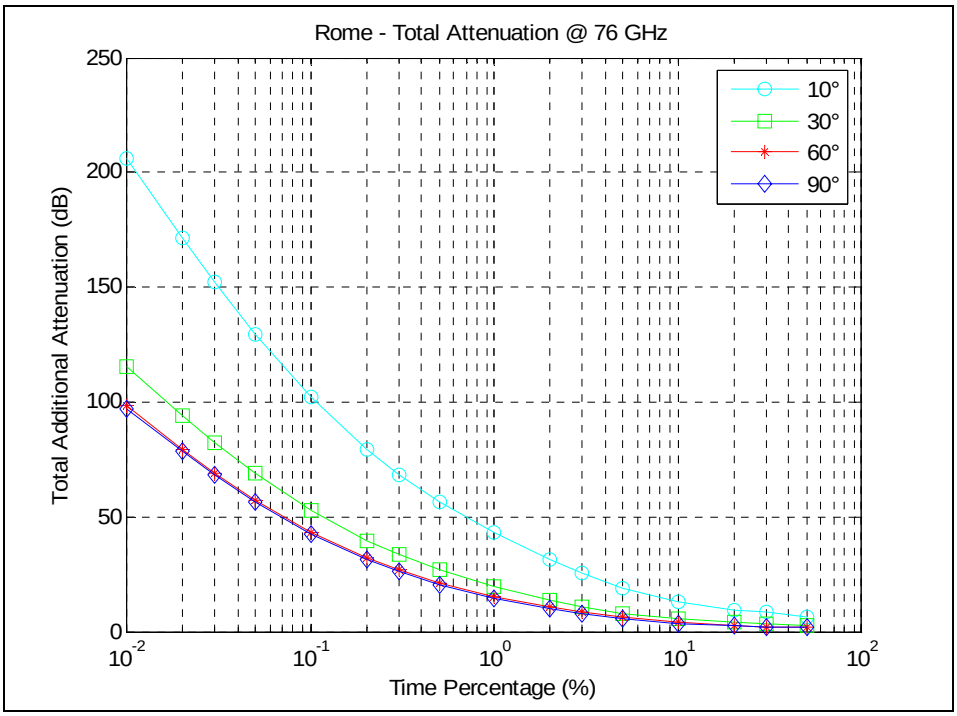

Figure 5-30: Total additional attenuation estimated at 76 GHz (Rome)

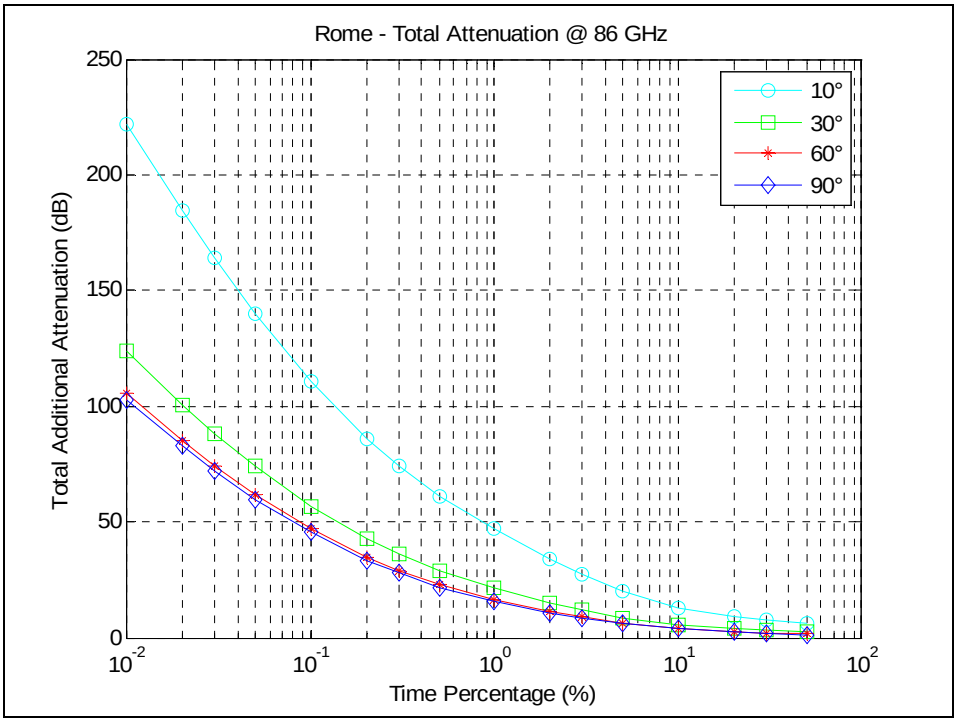

Figure 5-31: Total additional attenuation estimated at 86 GHz (Rome)

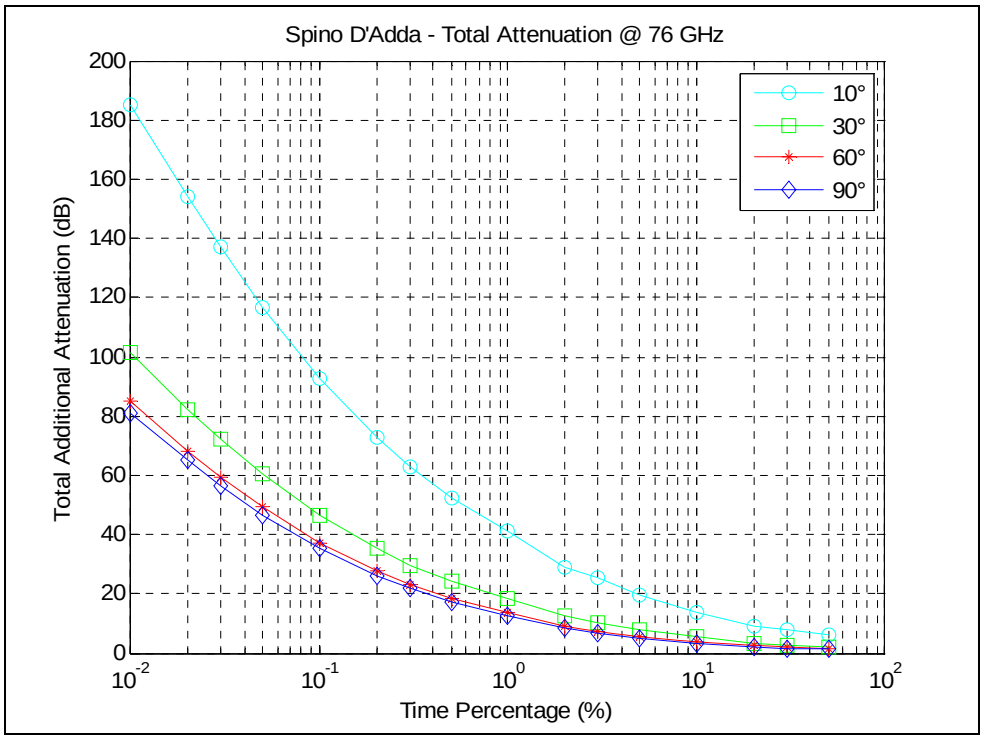

Figure 5-32: Total additional attenuation estimated at 76 GHz (Spino D'Adda)

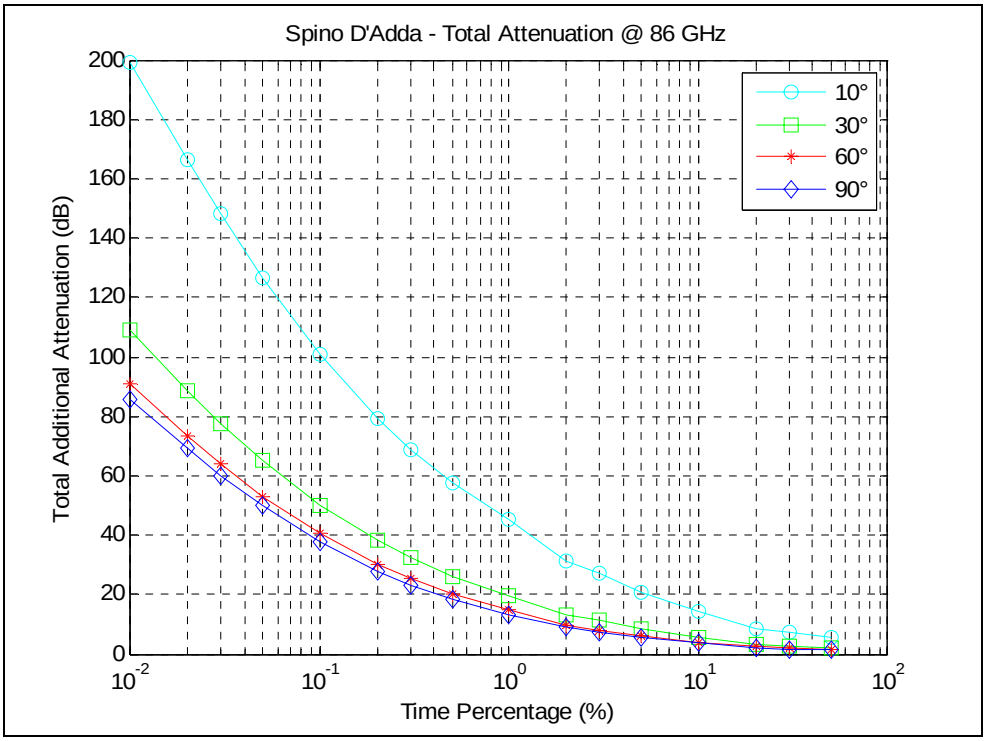

Figure 5-33: Total additional attenuation estimated at 86 GHz (Spino D'Adda)

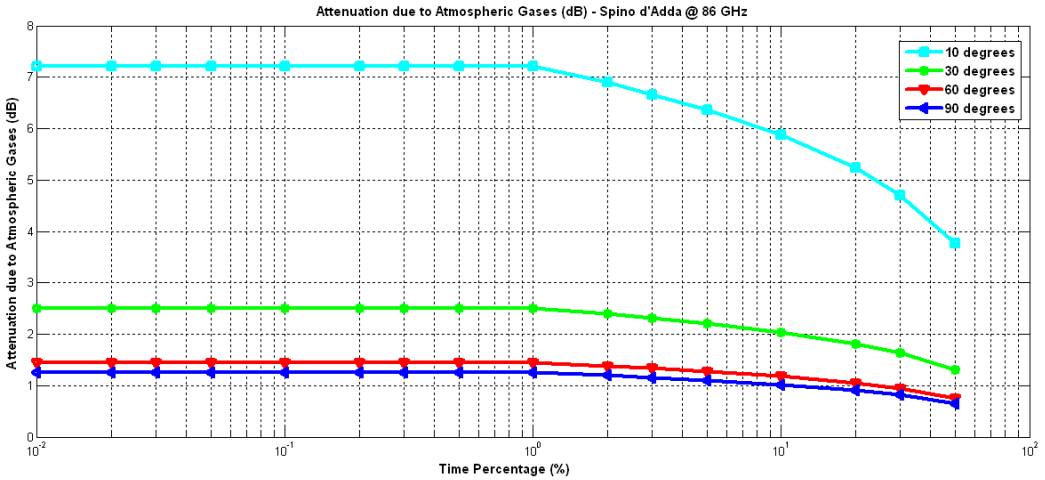

Figure 5-34: Attenuation due to Atmospheric Gases estimated at 86 GHz (Spino D'Adda)

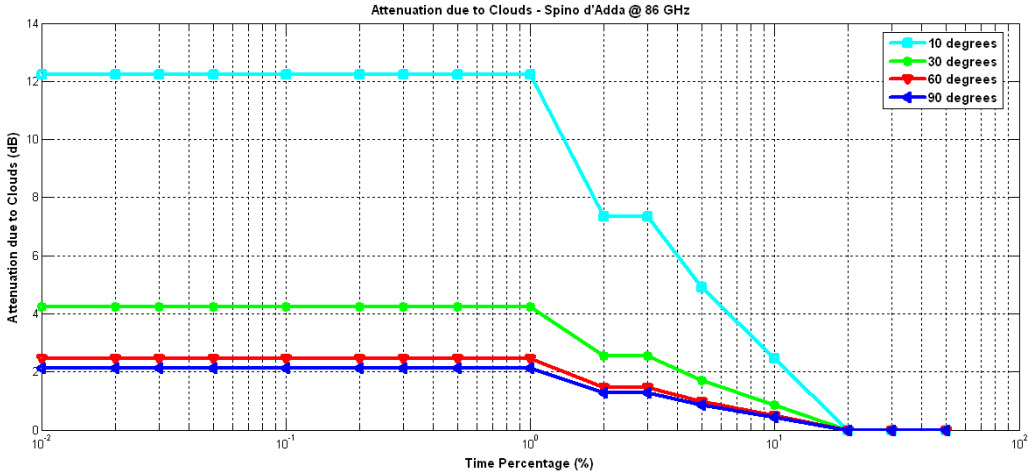

Figure 5-35: Attenuation due to Clouds estimated at 86 GHz (Spino D'Adda)

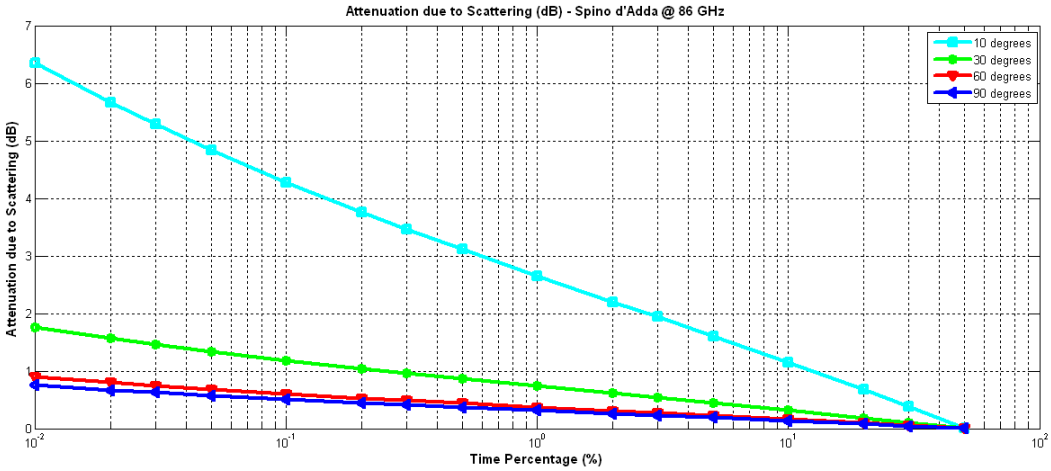

Figure 5-36: Attenuation due to Scattering estimated at 86 GHz (Spino D'Adda)

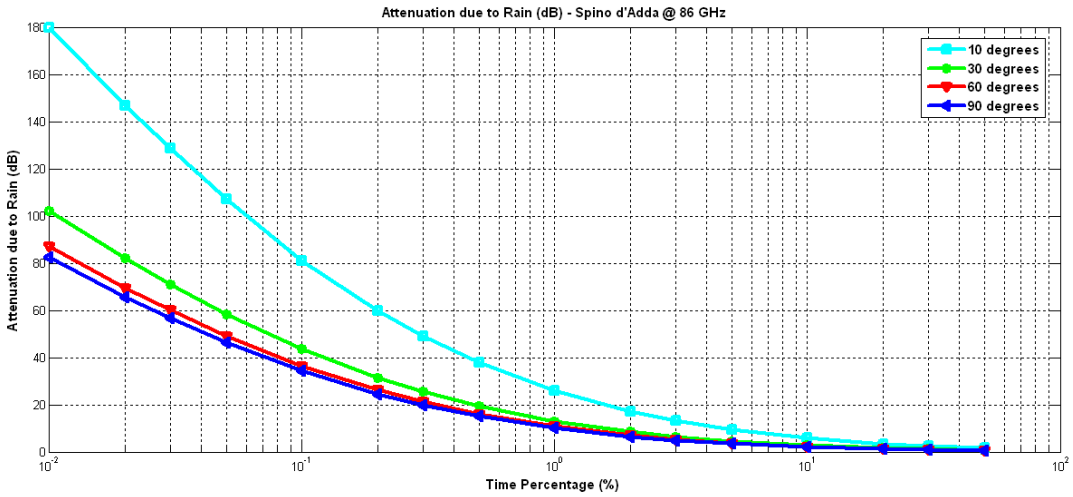

Figure 5-37: Attenuation due to Rain estimated at 86 GHz (Spino D'Adda)

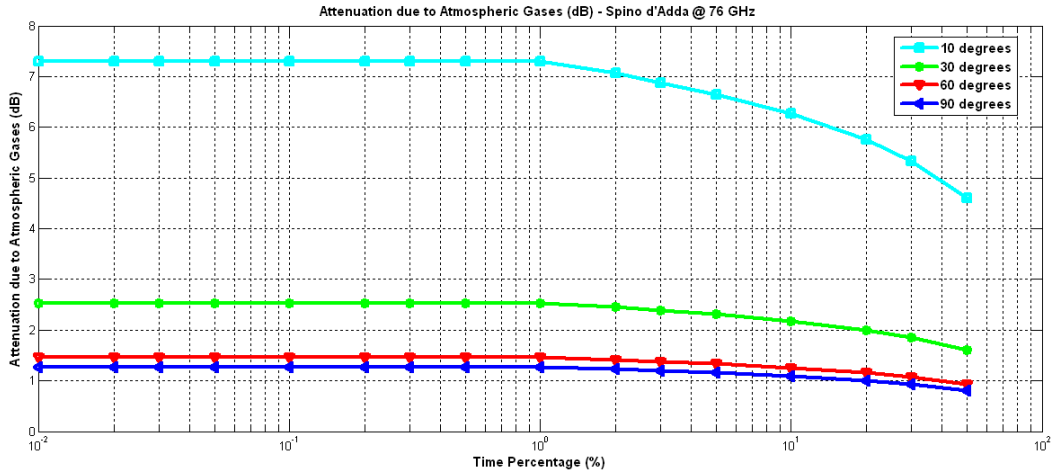

Figure 5-38: Attenuation due to Atmospheric Gases estimated at 76 GHz (Spino D'Adda)

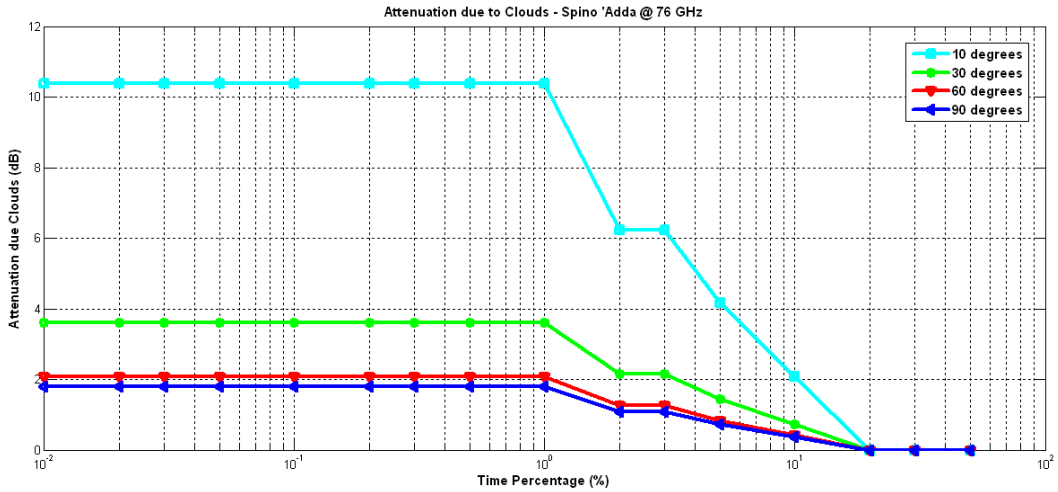

Figure 5-39: Attenuation due to Clouds estimated at 76 GHz (Spino D'Adda)

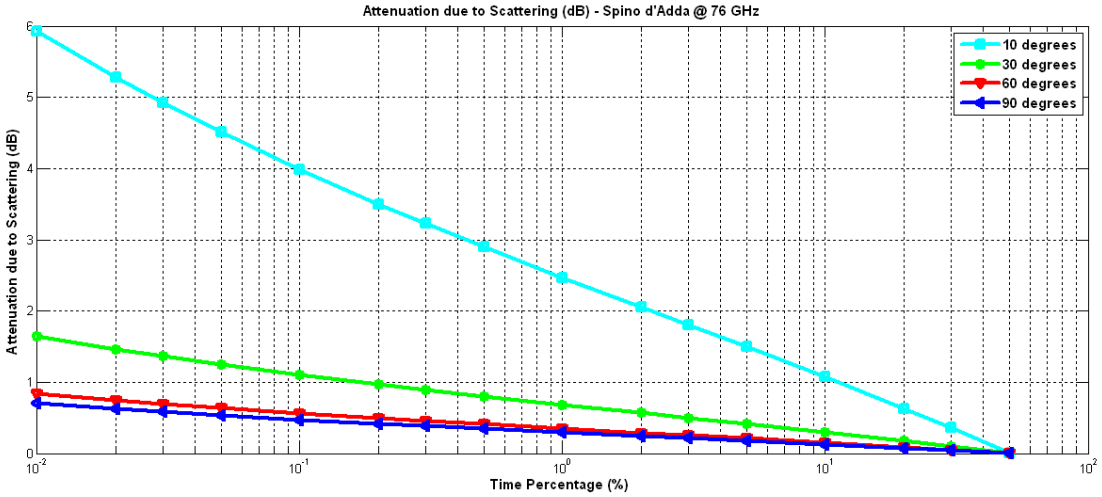

Figure 5-40: Attenuation due to Scattering estimated at 76 GHz (Spino D'Adda)

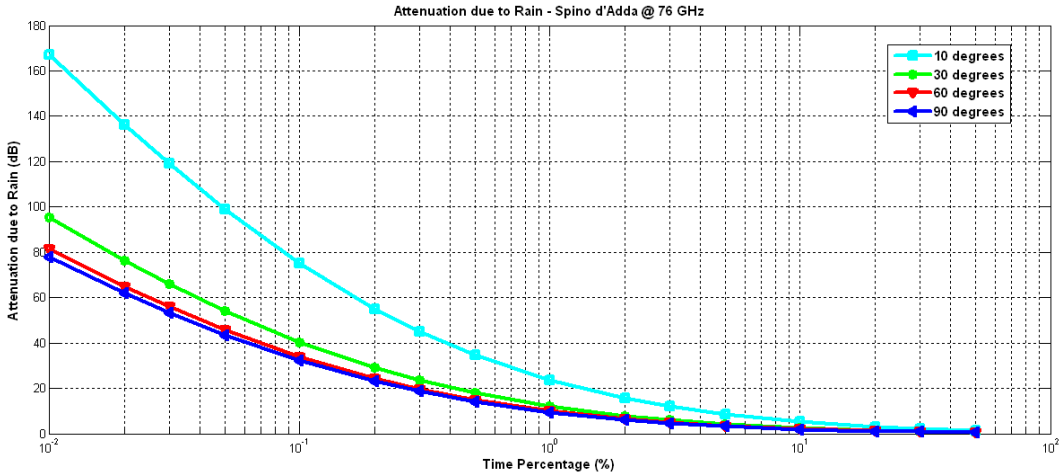

Figure 5-41: Attenuation due to Rain estimated at 76 GHz (Spino D'Adda)

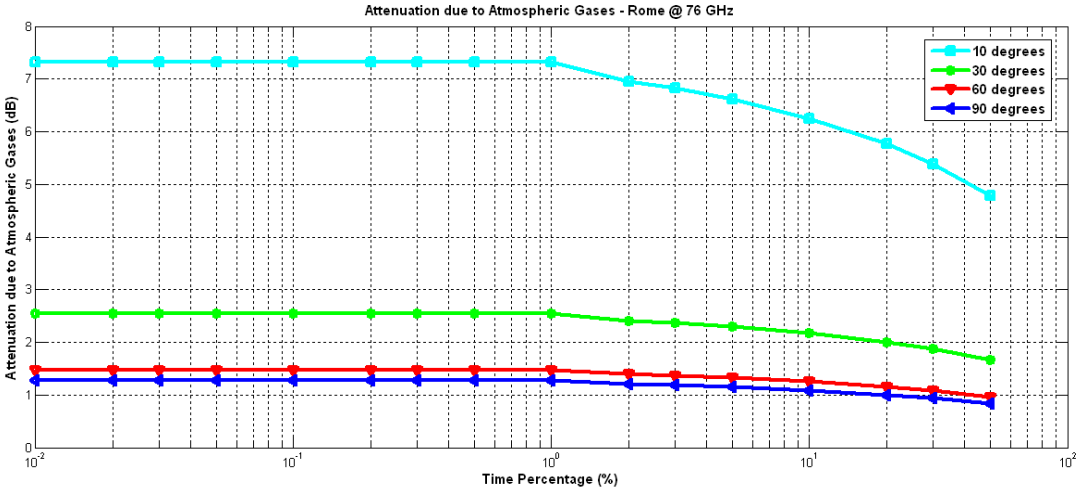

Figure 5-42: Attenuation due to Atmospheric Gases estimated at 76 GHz (Rome)

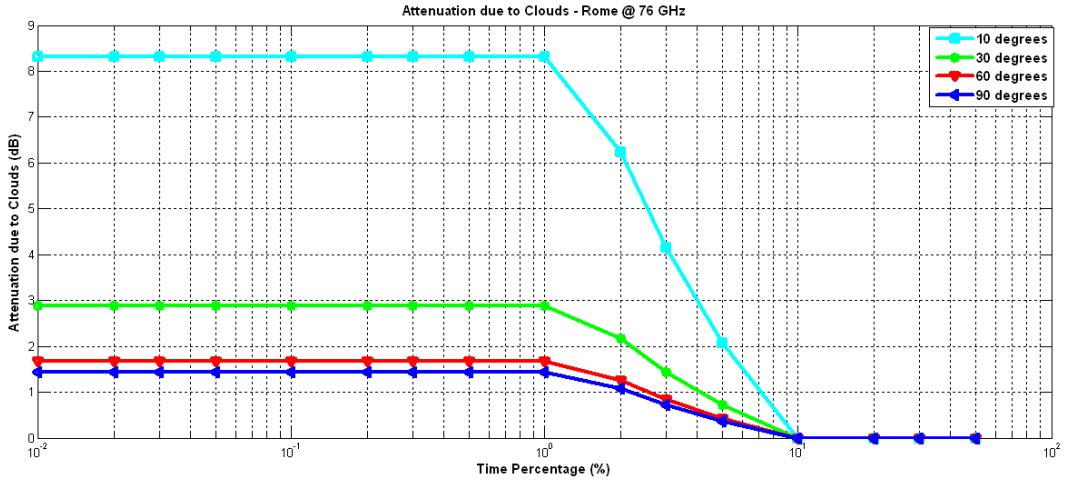

Figure 5-43: Attenuation due to Clouds estimated at 76 GHz (Rome)

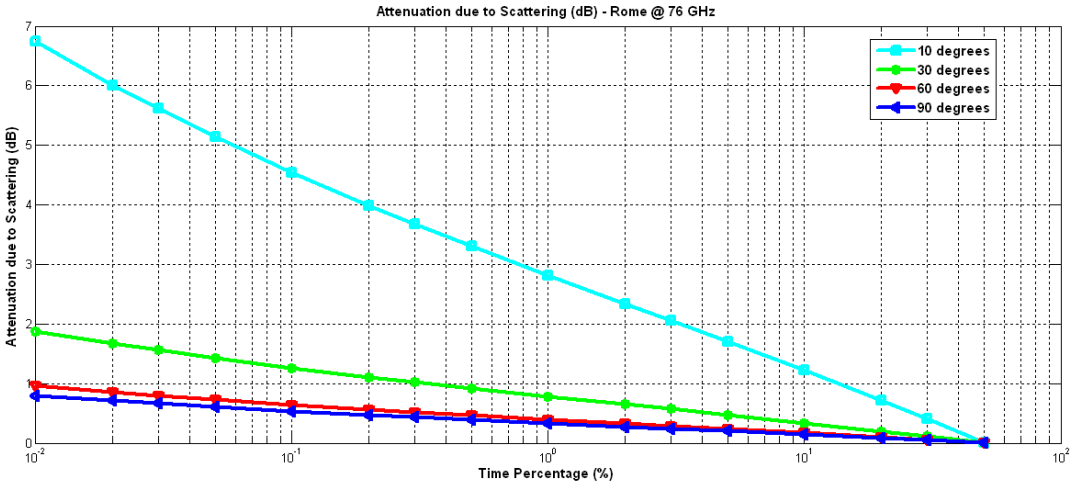

Figure 5-44: Attenuation due to Scattering estimated at 76 GHz (Rome)

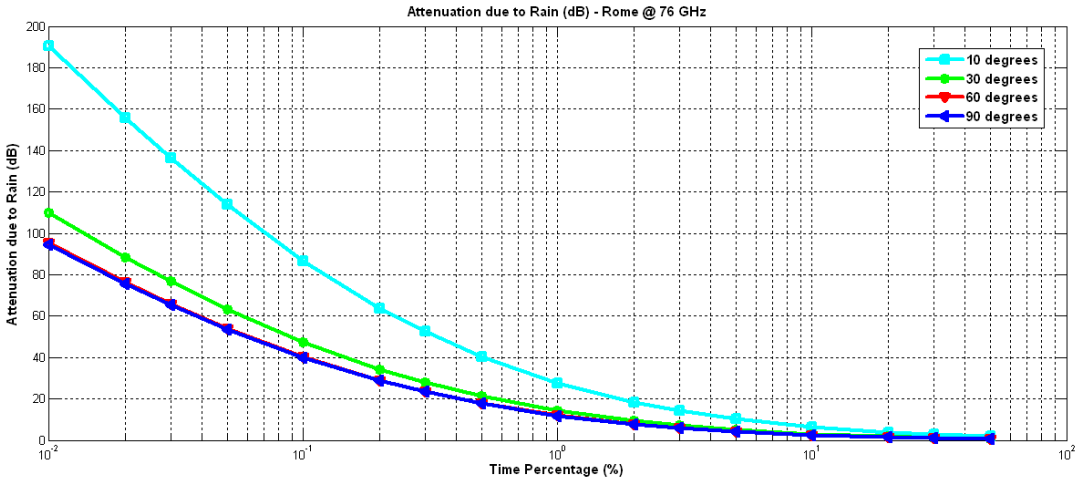

Figure 5-45: Attenuation due to Rain estimated at 76 GHz (Rome)

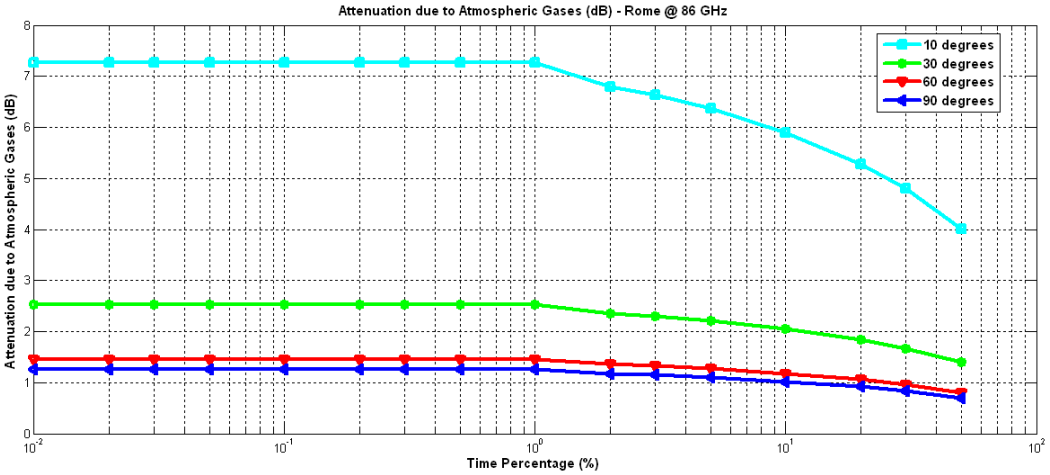

Figure 5-46: Attenuation due to Atmospheric Gases estimated at 86 GHz (Rome)

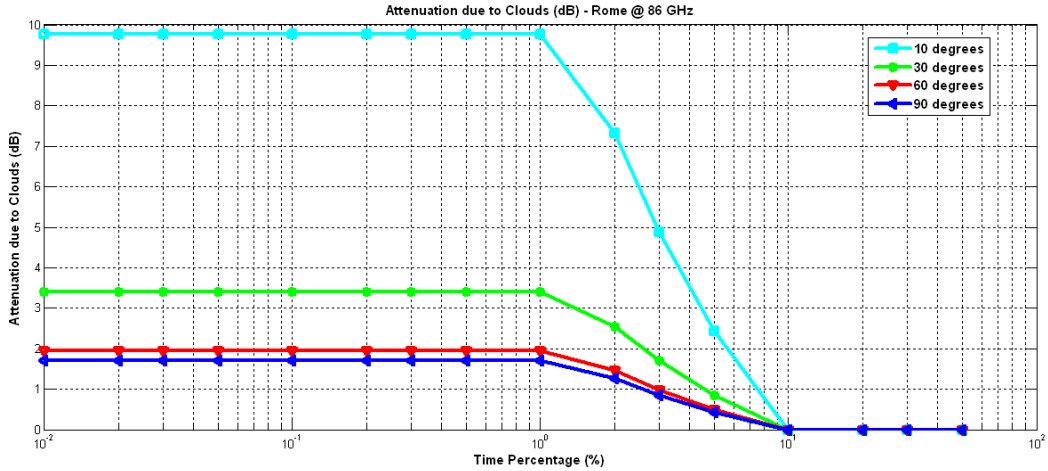

Figure 5-47: Attenuation due to Clouds estimated at 86 GHz (Rome)

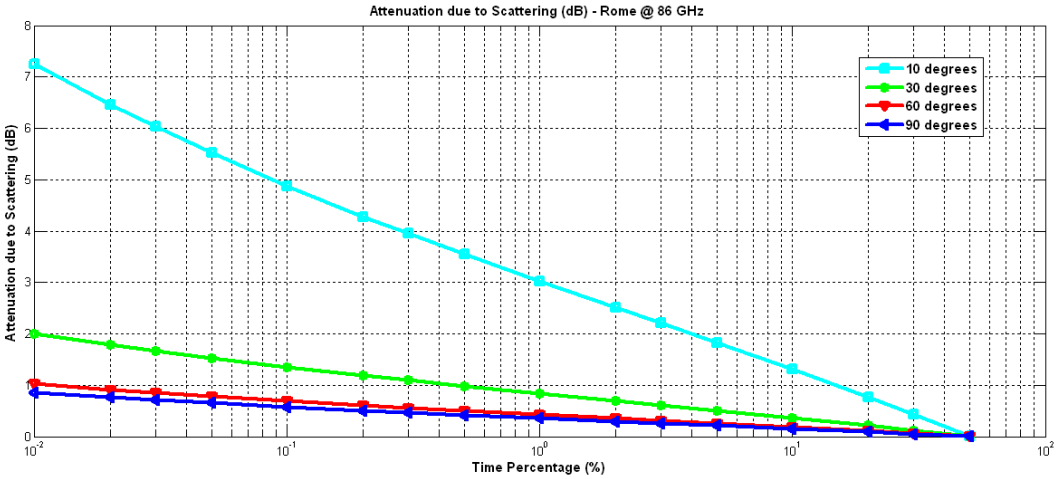

Figure 5-48: Attenuation due to Scattering estimated at 86 GHz (Rome)

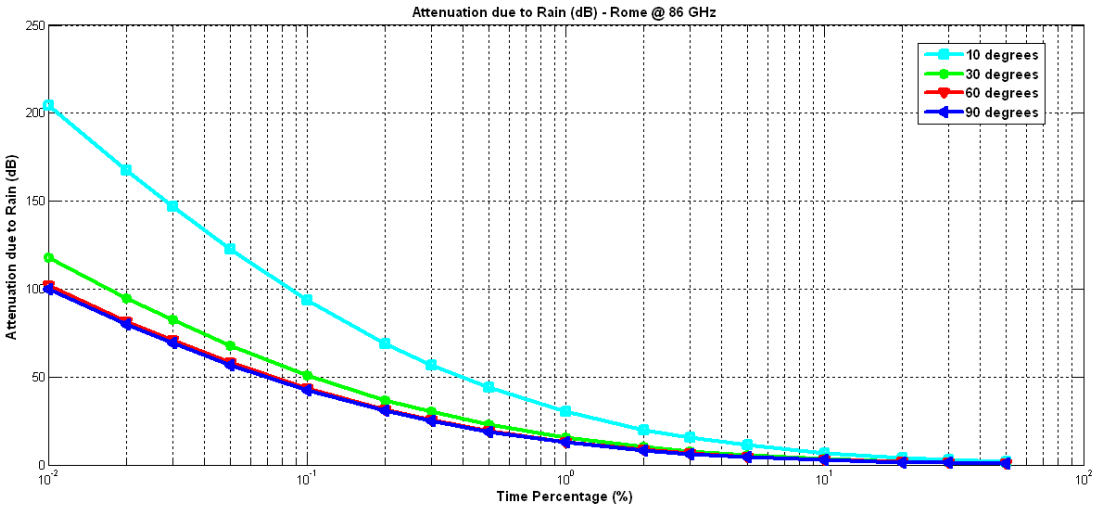

Figure 5-49: Attenuation due to Rain estimated at 86 GHz (Rome)

5.6 PROPAGATION IMPAIRMENTS MITIGATION TECHNIQUES

As introduced in previous section, EHF satellite communications are very attractive because of very huge frequency bandwidth. However, some important limitations arise from the high propagation impairments. In this frame, techniques able to improve system availability and throughput have to be developed.

In order to counteract atmospheric attenuation, high system static link margins should be implemented in order to insure minimum outage duration of the services. Fixing high static link margins is in contrast with technology limitations, both on space and ground segments, and with efficiency of the system. In fact, because of the large attenuation variation due to the presence of rain, fixing static link margins brings to a tremendous waste of resource of the system for a great time percentage of the system. As shown above, attenuation greater than 10 dB is foreseen only for 5% of the total link time. Therefore, a system dimensioning using a fixed margin (i.e. to operate for 99.5% of the service) brings to a great inefficiency.

In order to deal with high atmospheric fading PIMTs have to be implemented. These techniques aim at compensating for the fade, while at the same time minimising the disruption to other services and misuse of system resources [5-73], [5-74], [5-75], [5-76], [5-77]. These techniques allow to design systems with rather small static margin, while

overcoming in real time cloud attenuation, some fraction of rain attenuation, scintillation, and depolarisation events.

Three main categories of PIMT can be identified:

- Diversity Techniques;
- Adaptive Techniques;
- Signal Processing Techniques.

The first ones include time, frequency and spatial diversity, and mainly deal with the problem of a fade by moving around it. This can be done either in space, by sending the information on a different route to the one that is suffering a high fade, or similarly in the time or frequency domains. Another solution consists of transmitting at a different time or in a different frequency band in order to render statistically uncorrelated the probabilities of each signal being affected by a fade.

Adaptive techniques involve changing some aspect of the system set-up to compensate for the fade. For instance, in adaptive power control, the transmit power is increased to compensate for the effects of a fade.

These two techniques work at physical layer, while the last technique, signal processing, works at the data layer, compensating the fade by a more efficient coding or modulation scheme. In terms of spectrum efficiency, these techniques aim at keeping the same basic amount of spectrum constant and altering the rate at which the data is sent through that amount of bandwidth, in order to compensate for a fade. In situations where the data throughput must be kept constant, the amount of bandwidth used may be modified to compensate for a fade. Signal processing techniques allow the performance of individual links to be optimised, and the transmission characteristics to be adapted to the propagation channel conditions and to the service requirements for the given link.

Combining the previous described techniques, hybrid PIMT can be obtained; these PIMT take aspects from all three categories, such as adaptive space time coding.

In the following section the most promising PIMTs for EHF satellite communications will be presented.

5.6.1 ADAPTIVE POWER CONTROL

Adaptive Power Control (APC) [5-78] involves increasing the transmit power in order to be able to compensate for fades. Transmitter power is increased to counteract fade or

decreased when more favourable propagation conditions are retrieved. Hence, interference is limited in clear sky conditions and therefore the satellite capacity is optimised.

Given a reliable power control system, it could be possible to reduce the fixed fade margin during clear sky conditions, thereby improving the rate of frequency reuse in the geographical area of the link. This is because lower fade margins mean less transmit power, which lessens the interference on adjacent links. Adaptive power control can be divided into: Up-Link Power Control (ULPC), End-to-End Power Control (EEPC), Down-Link Power Control (DLPC) and On-Board Beam Shaping (OBBS).

APC can be implemented using:

- open loop schemes, that relies on estimating the fade by an independent means, such as radiometry or monitoring the satellite beacon;
- closed-loop schemes, in which the transmitting section uses its own transpond carrier to estimate the fade.

Currently DLPC cannot be efficiently used for Q/V and W bands due to the fact that power generation at these frequencies is one of the main technological challenge. On the other hand, ULPC and EEPC could be effectively used as a promising PIMT.

In particular, the ULPC can greatly reduce the co-channel interference on the up-link. Assuming an on-board transparent bent-pipe repeater, up-link power control could be operated according to several strategies:

- estimation of up-link fading based on the SNR measurement of a beacon. This approach is affected by the frequency scaling error, being the beacon frequency likely in a different frequency band, (e.g. at the edge of the Rx band segment);
- measurement of the resulting down-link signal through a collocated station. This method has the drawback that the measured attenuation is the sum of both up- and down-link attenuation. Then, frequency scaling error would also result;
- on-board measurement of the received level. This measurement could be done indirectly through the status (gain) of the AGC amplifier which is likely to be employed to stabilize the HPA output power even in presence of strongly attenuated up-link signal. Such status could be inserted in the telemetry stream forwarded to ground. The precision of such measurement is not very good also because it is affected by the gain instabilities of the transponder receiver chain. Further, these measurements would need to be reported to GW very frequently. This could cause too much load on the telemetry channel.

According to the above discussion, the approach based on the SNR measurement of a beacon appears the best approach in this case. This would also result in the absence of any power control supporting signalling. The instantaneous frequency scaling error at EHF band is difficult to predict. Measurements with fixed frequency scaling ratio has shown that errors up to 4 dB could be expected at Ka-band during strong raining events. At Q/V band and beyond much higher frequency scaling error is to be expected.

Anyway, the presence on-board of an AGC makes such error tolerable, being the purpose of ULPC that of minimizing unwanted interference towards other GWs co-channel beams more than stabilizing the output power of the on-board HPA.

With regard to the problem of interference minimization, each GW should regulate its transmit power in order that the PFD produced at the satellite antenna interface is the same for all GWs.

5.6.2 ADAPTIVE CODING AND MODULATION

ACM has already been proposed several years ago as fading countermeasure in the satellite telecommunication field, although technology complexity has, up to recently, prevented a widespread diffusion of such techniques.

ACM is a sophisticated form of data rate control in which information rate is adapted by changing modulation and coding rate whilst maintaining a constant symbol rate on the channel. This technique can both increment the system capacity and increase the link availability [5-79].

As far as modulation formats are concerned, preference to QPSK or BPSK has been always given in the satellite communication systems for the higher power efficiency of such modulation formats and the high-cost of the on-board power. This justification, however, does not hold any more for Q/V band systems because their design foresees a significant power margin for counteracting fading events. For most of the time, propagation conditions are good and better use of the on-board power could be made in such conditions. In particular, more bandwidth efficient modulation and coding modes could be employed for most of the time without requiring to increase the power budget with reference to conventional systems. We have assumed with power control that the transmitted power is changed to compensate for the estimated attenuation on the up-link. Actually, instead of changing this parameter, the power control feedback signal may well

be used for adapting the data rate (through adaptive modulation and coding). Clearly, rate control (by either ACM or techniques also adapting the signal bandwidth) is the only possibility when the user is running out of power. Moreover, according to the previous discussion on power control, rate control is the only possibility for counteracting down-link attenuation in selected reference scenarios. The strategy of allocating a fixed on-board power to the users and then playing with the modulation/coding to adapt the data rate to the user propagation and interference conditions, is a good compromise between the wish to improve the overall system throughput, which would lead instead to privilege the links which are not affected by fading and are in better coverage/interference conditions, and the wish to be fair with respect to SIT in non good geographic and / or propagation conditions. Finally, rate control could be preferred to power control even to counteract up-link fading, if the objective is that of decreasing as much as possible the cost of the SITs by avoiding any power margin. Appropriate work should be done to select optimal signal constellation taking into account the peak power limit of HPA and the requirement for operating very close to saturation.

5.6.3 LAYER 2 TECHNIQUES

Layer 2 techniques do not properly mitigate the fade event but rely on the re-transmission of the data. These techniques can be divided into: Automatic Repeat Request (ARQ) and Time Diversity (TD). ARQ foresees a regular or a random message re-sending until it reaches successfully the receiver. Time diversity aims at re-sending the data when the propagation channel state is in good transmission conditions. In this case, there is no need to receive the data in real time, for the user point of view it is acceptable to wait for the end of the propagation event or for a decrease of channel traffic. This technique can be effectively used together with propagation mid-term prediction model in order to estimate the most appropriate time to re-sent the message.

5.6.4 DIVERSITY TECHNIQUES

The basic principle used in diversity techniques [5-80], [5-81] is the concept of re-routing the radio path around the source of the fading, whether this occurs in the space, time or frequency domains. In order to understand how these techniques work, it has to be pointed out that rain is a phenomenon spatially and temporally intermittent and inhomogeneous. As

shown above, rain is the major cause of fading for EHF links. Rain cells that cause extreme attenuation often have horizontal dimensions of only few kilometres [5-82], using spatial diversity the transmitted information can be routed along the path experiencing the least fading. The performance gains achieved using spatial diversity are dependent on the space and time correlation of rain events, i.e. the distance that one has to have between two points before the behaviour of the rain at both points is completely uncorrelated. Site diversity is applied only for fixed satellite link, being based on the change of the network routes. Site diversity technique is based on the fact that two fades experienced by two Earth stations separated by a distance higher than the size of a convective rain cell (of the order of 10 km), are statistically independent. The Earth station affected by a weaker event is used and the information is routed to the original destination through a separated terrestrial network, switching to the site experiencing the least fading improves system performance considerably. Another diversity technique, named satellite diversity, is based on the possibility, for the Earth station, to select between different satellite to realise the link. If two different frequency are available on the satellite payload, a further diversity technique can be applied (frequency diversity); when fade occurs links are re-routed using the lowest frequency band payload. These diversity techniques are very expensive, being based on redundancy, but are very promising with respect to fade mitigation. In Table 5-27 a comparison between various IPMTs carried out during the phase A of TRANSPONDERS Study is shown [5-83].

	Complexity/Cost	**Throughput Increase**	**Availability Increase**
Frequency Diversity	High	Low	Medium
Slow Frequency Hopping	Low	Very low	Very low
Fast Frequency Hopping	High	Low	Low
Polarization Restoration	High	Low	Low
Interference Cancellation	High	Low	Low
Power Control	Low/Medium	Medium	Medium
Site Diversity	High	Low	Medium
ACM	Medium	Very High	Very High
Data Rate Control	Low	High	High
Hybrid ARQ	Medium	Low	Low

Table 5-27: Performance comparison between IFMTs applied to Q/V bands and beyond

5.6.5 SITE DIVERSITY PERFORMANCE EVALUATION FOR A W BAND LINK

Some simulations have been made in order to evaluate the performance of a site diversity technique applied to a W band Earth satellite link operating at 76 GHz downlink frequency. The system architecture has been designed after the evaluation of the diversity gain curves, as a function of the separation between two sites for a W band link, using [5-57]. The results are shown in Figure 5-50. The plateau of the diversity gain is obtained for distances greater than 12 km, therefore this is the minimum distance between two points in order to consider the behaviour of the rain fading (for a W band link) at both points completely uncorrelated.

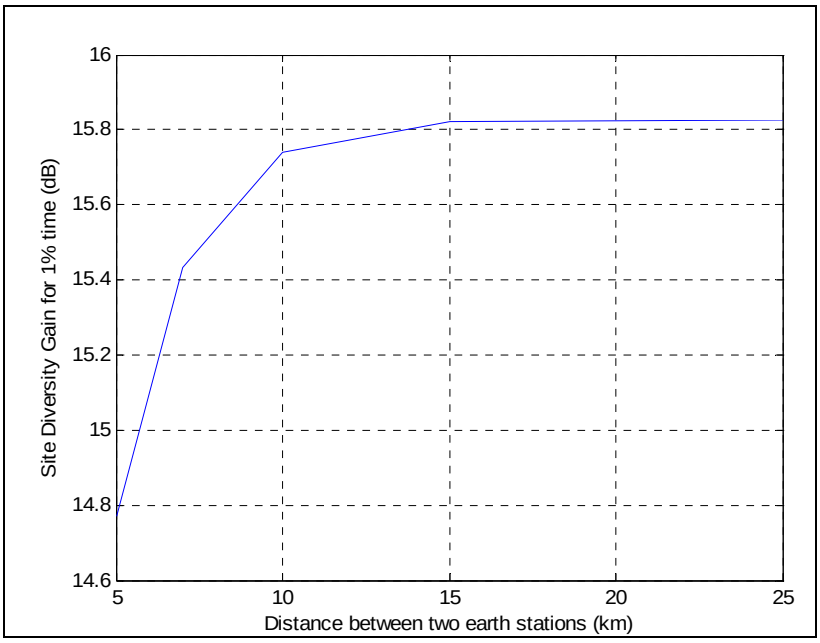

Figure 5-50: Diversity gain as a function of Earth station distance for a W band link

The site diversity simulations have been performed considering two Earth stations separated by 12 km, in the area around Rome (latitude 42°, longitude 12°), in order to consider the rain events on the two stations uncorrelated.

The Earth station switching control logic strategy is based on the following assumptions:

- "alternate prime logic": in which no diversity path is considered as a primary path; as a consequence once a path has been selected it continues to be operative until the signal attenuation is below a certain threshold, T_0 [5-80];
- the possible excessive switch-over caused by scintillations, fast fluctuation of rain attenuation or noise in the fade detection system is prevented inserting an hysteresis

threshold T_H. The switching between the two stations is performed if the attenuations in the sites differ by an amount larger than T_H.

5.7 REFERENCES

[5-1] R. Polonio, C. Riva, "ITALSAT propagation experiment at 18.7, 39.6 and 49.5 GHz at Spino D'Adda: three years of CPA statistics", IEEE Transactions on Antennas and Propagation, Volume 46, Issue 5, May 1998, Pag. 631-635.

[5-2] M. Mauri, A. Paraboni, A. Pawlina, "The OLYMPUS and ITALSAT propagation programs of the Italian Space Agency: an overview of the first experimental results in the 12 to 50 GHz frequency bands", Third European conference on Satellite Communications, 2-4 Nov 1993, Pag. 263-268.

[5-3] J. Evans, A. Dissanayake, "Prospects for Commercial Satellite Services at Q/V-band", IEEE Transactions vol. 0-7803-4506-1/98, 1998.

[5-4] J. Freitag, P. Hadinger, H. Ho, E. Wiswell, "Global EHF satellite network for delivering fiber optic capacity worldwide", 4th Ka-band Utilization Conference, Venice Italy, Nov. 2-4, 1998.

[5-5] J. V. Evans, "Proposed US global satellite systems operating at Ka band", IEEE Aerospace Conference, Snowmass, CO, 1998.

[5-6] J. Farserotu, R.Prasad, "A Survey of Future Broadband Multimedia Satellite Systems, Issues and Trends", IEEE Communications Magazine, June 2000.

[5-7] Italian Space Agency official site: www.asi.it.

[5-8] Italian Defence Department web site: http://www.difesa.it/.

[5-9] European Space Agency web site: http://www.esa.int.

[5-10] European Space Agency, "Q/V band P/L Phase A study Final Report", ESTEC contract 19680/NL/AD, 2006.

[5-11] "Scientific operational requirements" ALPHASAT TDP#5, October 2008.

[5-12] ITU-R P618-8 Recommendation "Propagation data and prediction methods required for the design of Earth-space telecommunication systems".

[5-13] T. Rossi, E. Cianca, C. Stallo, M. Lucente, M. De Sanctis, M. Ruggieri, A. Paraboni, A. Vernucci, L. Zuliani, L. Bruca, G. Codispoti, "Experimental Italian Q/V Band Satellite Network", IEEE Aerospace Conference 2009, Big Sky, Montana, March, 7-14, 2009.

[5-14] TRANSPONDERS– Phase A2, Allegato Tecnico Gestionale, ASI, Italy, 2008.

[5-15] TRANSPONDERS – Phase A, Final Technical Report, ASI, Italy, 2004.

[5-16] L. Castanet, J. Lemorton, M. Bousquet, "Fade Mitigation Techniques for New SatCom services at Ku-band and above: a Review" 4th Ka Band Utilization Conference, Venice, 2-4 November 1998.

[5-17] TRANSPONDERS – Phase A, Interference and Fading Mitigation Techniques: Final Technical Report, ASI, Italy, 2004.

[5-18] C. Stallo, M. Lucente, T. Rossi, E. Cianca, M. Ruggieri, A. Paraboni, C. Cornacchini, A. Vernucci, M.T. Nocerino, A. Ceccarelli, L. Bruca, G. Codispoti, M. De Sanctis, 2009, "TRANSPONDERS: Research and Analysis for the Development of Telecommunication Payloads in Q/V Bands", IEEE Aerospace Conference 2009, Big Sky, Montana, March, 7-14, 2009.

[5-19] C. Stallo, E. Cianca, T. Rossi, M. De Sanctis, A. Vernucci, C. Cornacchini, L. Bruca, M. Lucente, "TRANSPONDERS: Effectiveness of Propagation and Impairments Mitigation Techniques at Q/V Band", Globecom 2008 – IEEE Workshop/EHF -AEROCOMM, "Exploitation of Higher Frequency Bands in Broadband Aerospace Communications", November 30 – December 4, 2008, New Orleans, LA, USA.

[5-20] C. Stallo et. al., "Transponders-2 ASI Project: WP TR2-MSP-URM-RT-1A-AD133 – Implicazioni Economico-Programmatiche".

[5-21] C. Stallo et. al., "Transponders-2 ASI Project: WP TR2-MSC-URM-RT-1A-AD133 – Implicazioni Economico-Programmatiche".

[5-22] C. Stallo et. al., "Transponders-2 ASI Project: WP TR2-MSC-URM-RT-1A-AD133 – Impatti Economico-Programmatici".

[5-23] C. Stallo et. al., "Transponders-2 ASI Project: WP TR2-MSC-URM-RT-1A-AD2123 – Impatti Economico-Programmatici".

[5-24] C. Stallo et. al., "Transponders-2 ASI Project: WP TR2-MSC-URM-RT-1A-AD133 – Impatti Economico-Programmatici".

[5-25] C. Stallo et. al., "Transponders-2 ASI Project: WP TR2-MSC-URM-RT-1A-AD41 – Sviluppo Elementi Critici".

[5-26] C. Stallo et. al., "Transponders-2 ASI Project: WP TR2-MSP-URM-RT-1A-AD133 – Sviluppo Elementi Critici".

[5-27] X. C. Zhang et. al., "Novel Band-pass Substrate Integrated Waveguide (SIW) Filter Based on Complementary Split Ring Resonators (CRSS)", Progress In Electromagnetics Research, PIER 72, 39–46, 2007.

[5-28] Yu J. Chang et. al., "Substrate Integrated Waveguide (SIW) Rotman Lens and Its Ka-Band Multibeam Array Antenna Applications" IEEE Transaction on Antennas and Propagation, Volume 56, Issue 8, August 2008 pp.2504 – 2513.

[5-29] L. Marcaccioli, et. al. "Flat Array Antennas for Ku-Band Mobile Satellite Terminals", International Journal of Antennas and Propagation, Vol. 2009.

[5-30] United State Air Force web site: http://www.af.mil/

[5-31] Boeing web site: http://www.boeing.com/defense-space

[5-32] Lockheed Martin web site: http://www.lockheedmartin.com

[5-33] The Aerospace Corporation web site: http://www.aero.org/

[5-34] Y. Hase, "Propagation experiment of COMETS Ka/Q-band Communication Link for future satellite cellular system", CRL publications, vol. ACTS-95-029, 1995.

[5-35] M. Ohkawa, T. Takahashi, H-B. Li, K. Ilgusa, H. Wakana, "Comets 21GHz advanced satellite broadcasting experiments", Microwave Conference Asia-Pacific, Pag.1539-1542, 2000.

[5-36] H. Wakana, H. Saito, S. Yamamoto, M. Ohkawa, N. Obara, H-B. Li, M. Tanaka, "COMETS experiments for advanced mobile satellite communications and advanced satellite broadcasting", International Journal of Satellite Communications, Vol.18, Issue 2, Pag.63-85, Apr. 2000.

[5-37] General Dynamics C4 Systems web site: http://www.gdc4s.com/

[5-38] "Application of Motorola Satellite Systems, Inc. for Authority to Construct, Launch and Operate The M-Star System", Federal Communication Commission (FCC) file no. 157-SAT-P/LA-96(72), Washington, D.C., September 1996.

[5-39] H. Keller, H. Salzwedel, “Comparison of the probability of visibility of new planned mobile satellite systems (M-star, Celestri, SkyBridge)”, 48th IEEE Vehicular Technology Conference, Vol. 1, Pag.81-85, May 1998.

[5-40] D. Rogues, H. Chane-Kee-Sheung, F. Dubos, B. Cogo, J.L. Cazaux, “Ku-band Quadri-SSPA for Stentor satellite transmit active antenna”, IEEE International Microwave Symposium Digest, Vol. 2, Pag.657-660, 2001.

[5-41] J. Lemorton, L. Castanet, T. Marsault, F. Destruhaut, S. Grély, “Recent developments concerning the EHF propagation experiment with STENTOR satellite”, First COST 255 Workshop, Noordwijk, The Netherlands, 28-29 October 1998.

[5-42] Intelsat web site: http://www.intelsat.com/.

[5-43] C. Bonifazi, M. Ruggieri, A. Paraboni, “The DAVID mission in the heritage of the SIRIO and ITALSAT satellites”, IEEE Transaction on Aerospace and Electronic Systems, Volume 38, Issue 4, Pag.1371-1376, Oct. 2002.

[5-44] M. Ruggieri, S. De Fina, M. Pratesi, A. Salomè, E. Saggese, C. Bonifazi, “The W-band Data Collection Experiment of the DAVID Mission”, Special Section of IEEE Transactions on AES on “The DAVID Mission of the Italian Space Agency”, vol. 38, no. 4, pp. 1377-1387, Oct. 2002.

[5-45] S. De Fina, M. Ruggieri, A. Bosisio, “On the Exploitation of the W-Band for High-Capacity Satellite Communications”, IEEE Transactions on AES, vol. 39, no. 1, January 2003.

[5-46] T. Takahasha, Y. Konishi, T. Noguchi, N. Futagawa, “Payload configuration study for Quasi Zenith Satellite System”, 22nd AIAA International Communications Satellite Systems Conference 2004, Monterey, California, May 2004.

[5-47] B. Younes, “White paper on Integrated Interplanetary Network (IIN)”, NASA Publications and Reports, Nov. 2000.

[5-48] R. Polonio, C. Riva, “ITALSAT propagation experiment at 18.7, 39.6 and 49.5 GHz at Spino D'Adda: three years of CPA statistics”, IEEE Transactions on Antennas and Propagation, Volume 46, Issue 5, May 1998, Pag. 631-635.

[5-49] V. Dainelli, E. Limiti, M. Ruggieri, "Innovative Technologies for the Development of W-band Radars and Communication Payloads", IEEE Aerospace Conference 2006, Big Sky, Montana, March 2006.

[5-50] C. Bonifazi, M. Ruggieri, A. Paraboni, "The DAVID mission in the heritage of the SIRIO and ITALSAT satellites", IEEE Transaction on Aerospace and Electronic Systems, Volume 38, Issue 4, Pag.1371-1376, Oct. 2002

[5-51] T. Rossi, M. Lucente, C. Stallo, E. Cianca, M. Ruggieri, G. Codispoti, L. Zuliani, "EHF Systems: Experimental Missions for Broadband Communications", European Conference on Antennas and Propagation (EuCAP), Berlin, Germany, March, 23-27, 2009.

[5-52] M. Lucente, C. Stallo, E. Re, T. Rossi, E. Cianca, M. Ruggieri, A. Jebril, C. Dionisio, G. Codispoti, L. Zuliani, "IKNOW Mission: Payload Design for In Orbit Test of W Band Technology", IEEE Aerospace Conference, Big Sky, 1-8, March, 2008.

[5-53] E. Cianca, M. Lucente, E. Re, T. Rossi, M. Ruggieri, C. Stallo, V. Dainelli, G. Codispoti, F. Marzano, G.Belyaev, "Aero-WAVE: A First Step Towards the Characterization of W Band", IEEE Aerospace Conference, Big Sky, March, 1-8, 2008.

[5-54] M. Lucente, T. Rossi, C. Stallo, M. Ruggieri, A. Iera, A. Molinaro, S. Pulitanò, 2008, "IKNOW: a Small LEO Satellite for W Band Experimentation", 26th International Communications Satellite Systems Conference (ICSSC), 10 - 12 June 2008, San Diego, CA.

[5-55] H. Liebe, "MPM89 An atmospheric mm-wave propagation model, Int. J. IR & MM Waves", vol. 10, no. 6, pp. 631-650, June 1989.

[5-56] H. Liebe, G. Hutford, M. Cotton, "Propagation modeling of moist air and suspended water/ice particles at frequencies below 1000 GHz", Proc. AGARD Conf. Paper 3/1-10, Palma De Mallorca, Spain, May 1993.

[5-57] ITU-R P.618, "Propagation data and prediction methods required for the design of Earth-space telecommunication systems".

[5-58] ITU-R P.676, "Attenuation by atmospheric gases".

[5-59] ITU-R P.840-3, "Attenuation due to clouds and fog".

[5-60] ITU-R P.835, Reference standard atmosphere.

[5-61] ITU-R P.453, The radio refractive index: its formula and refractivity data.

[5-62] A. Dissanayake, F. Haidara, J. Allnut, "A Prediction Model that Combines Rain Attenuation and other Propagation Impartirments Along Earth-Satellite Paths", IEEE Trans. Antennas and Propagation., vol. 45, pp. 1546-1558, Oct 1997.

[5-63] ITU-R P.839, "Rain height model for prediction methods".

[5-64] ITU-R P.837, "Characteristics of precipitation for propagation modelling".

[5-65] ITU-R P.838, "Specific Attenuation Model for Rain for Use in Prediction Methods".

[5-66] V.I. Tatarskii, "Wave propagation in a turbulent medium", Dover Edition, New York, 1961.

[5-67] E.Salonen, "Prediction models of atmospheric gases and clouds for slant path attenuation", in Proceedings of the Olympus Utilization Conference, Seville (Spain), pp. 615- 622, April 1993.

[5-68] E. Solonen, S. Uppala, "New prediction method of cloud attenuation", Electronics Letters, vol.27, pp.1106-1108, 1991.

[5-69] A. Paraboni, M. Ruggieri, C. Bonifazi, C. Capsoni, M. Pratesi, "Assessment of Joint Scientific Experiments in the DAVID Mission", 7th Ka Band Utilization Conference, pp. 43-50, S. Margherita Ligure, Italy, September 2001.

[5-70] H.J. Liebe, G.A. Hufford, T. Manabe "A model for the complex permittivity of water at frequencies below 1 THz", International Journal of Infrared and Millimeter Waves, n.12, pp.659-675, 1991.

[5-71] M. Ruggeri, S. De Fina, A. V. Bosisio, "Exploitation of the W-band for High Capacity Satellite Communication", IEEE Transactions on Aerospace and Electronic System Vol. 39, No.1, Jan. 2003.

[5-72] A. De Luise, A. Paraboni, M. Ruggieri, "Satellite communications in W-band: experimental set-up for channel characterization", IEEE Aerospace Conference 2004, Big Sky, Montana, March 2004.

[5-73] ITU-R P.1623, Prediction method of fade dynamics on Earth-space path.

[5-74] J. Lemorton, L. Castanet, F. Lacoste, MMJL Van de Kamp, C. Riva, E. Matricciani, U-C Fiebig, “Development of propagation models for telecommunication satellite systems”, Final Report of ESA study no.1685/03/NL/EC, Sep. 2004.

[5-75] U-C Fiebig, “Channel modelling for Ka-band and above”, Personal Indoor Mobile Radio Conference, Osaka, Japan, 1999.

[5-76] A. Paraboni, C. Riva, “A new method for the prediction of fade duration statistics in satellite links above 10 GHz”, IEEE International Journal on Satellite Communications, Vol.12, Pag.387-394, 1994.

[5-77] MMJL Van de Kamp, “Statistical analysis of rain fade slope”, IEEE Transaction on Antennas and Propagation, Vol.51, no.8, 2003.

[5-78] L. Castanet, A. Bolea-Alamanac, M. Bousquet, “Interference and fade mitigation techniques for Ka and Q/V band satellite communication systems”, International Workshop on Satellite Communications from Fade Mitigation to Service Provision, Noordwijk, The Netherlands, May 2003.

[5-79] G. Albertazzi et al., WP 131 “Contribution for IFMT algorithm design justification”, Report of University of Bologna in the frame of ESTEC Contract N. 16532/02/NL/EC, Adaptive Coding Modulation Techniques for Ka / Q Band Systems, 25 July 2003.

[5-80] E. Russo, “Implementation of a space diversity system for Ka-band satellite communications”, IEEE International Conference on Telecommunications, Geneva, Switzerland, 1993.

[5-81] A. Paraboni, A. Bosisio, C. Capsoni, F. Protto, G.E. Corazza, F. Vatalaro, "Study on Site Diversity for 20/30 GHz Earth Stations”, in ESOC Contract n.9805/92/D/DK, Final Report, July 1993.

[5-82] M. Luglio, C. Riva, A. Paraboni, F. Barbaliscia, “The Use of Large Scale Site Diversity to Improve Availability for Satellite Systems”, 8th Ka Band Utilization Conference, Baveno, September 2002.

[5-83] TRANSPONDERS – Phase A, “Interference and Fading Mitigation Techniques”, Intermediate Technical Report, ASI, Italy, 2004.

6 W BAND ANALYSIS AND VERIFICATION (WAVE) FOR SATELLITE COMMUNICATIONS

In this section the first part of my Ph.D activities is reported: the analysis carried out in the frame of the WAVE (W band Analysis and VErification) Project. The work has been pointed towards the definition of architectures for innovative missions for the development of experiments able to sound the W band channel for satellite telecommunications purposes, together with some preliminary missions and payloads design activities. The year 2007 can be considered as a pivotal year for satellite broadband communication in Europe, thanks to a great technology improvement and a high user broadband services demand. In this framework, the Ka-band can be considered as the current standard for broadband satellite services. As outlined above, some systems operating in V-band are currently in an operative phase (i.e. the Italian military satellite Sicral) and under development (also with ASI and ESA support, i.e.: Alphasat TDP#5). One of the most important issue for the exploitation of such high frequencies is the knowledge of the satellite propagation channel. Important propagation experiments in Q/V-band frequencies have been performed (Italsat F1) together with the development of technologies. Therefore, Q/V-band can be considered as a current industrial research topic for the short term implementation of satellite operative systems, while W-band can be considered as the most important scientific research frontier for broadband satellite communications. Investments in W-band could turn broadband satellite communications into a strong reality, creating a new market rich in commercial returns. Both industrial and scientific community should aim to gain a stronger know-how in this innovative sector. In this framework, Italy has a proven and remarkable experience in the exploration of high frequency ranges in satellite communications through the Sirio and Italsat [6-1] missions. Furthermore, in the last years some effort has been dedicated in conceiving and developing a scientific satellite project in W-band named DAVID (DAta and Video Interactive Distribution) [6-2], [6-3]. This project has been developed till the B-Phase and allowed Italy to gain a pioneer position in the field of high frequency satellite communications. As a matter of fact, making investments in innovative W-band technologies could bring important returns both to the scientific and industrial communities. The scientific sector will be enriched with new research opportunities; there will be great international returns

for Italy for the maintenance of a pioneer position in this field. For the European industrial community, it is a key element for gaining and maintaining a competitive commercial position with respect to the U.S. industrial market [6-4]. In this framework, the WAVE-A2 project has been conceived with the goal to make possible the deployment of operative LEO/GEO satellite in W-band for commercial use in 10 years. More specifically, the WAVE-A2 project aimed at designing and developing a complete line of W-band communication satellite payloads [6-5], [6-6].

The project includes two demonstrative missions and two pre-operative missions. The demonstrative missions are needed to characterize the channel and test the technology in-orbit:

1) Aero-WAVE mission, which is based on COTS hardware and High altitude Platform (HAP), will give preliminary results on the channel characterization;
2) the IKNOW mission, based on a small LEO, which will be the first W-band telecommunication satellite mission. It will provide the first order statistics of satellite channel additional attenuation.

Finally, two pre-operative missions, one over a LEO and the other one over a GEO, will exploit the results achieved from the demonstrative missions for performing preliminary tests for the commercial/operative use of W-band.

Since the results from the demonstrative missions are preparatory to the correct design of the pre-operative ones, design choices, development plans and level of details take strictly into account the time constraints. It should be possible to launch the demonstrative missions in the short term (~ two years), especially the IKNOW mission. It will provide the first characterisation of W-band satellite channel together with the first in-orbit test of W-band RF innovative technologies and thus more complete results with respect to the Aero-WAVE mission, for enabling the future pre-operative missions.

It is important to outline that the scientific and technological results achieved by the demonstrative missions will play a key role in an international environment, enabling Italy to play a major role in the field of broadband satellite communications.

Figure 6-1 shows the WAVE A2 P/L development timeline: the two demonstrative line of study missions have been conceived in order to be mutually independent, while the two pre-operative missions are strictly dependant on the IKNOW mission. This one can be considered as the pivotal mission for the evolution towards W-band satellite communication systems.

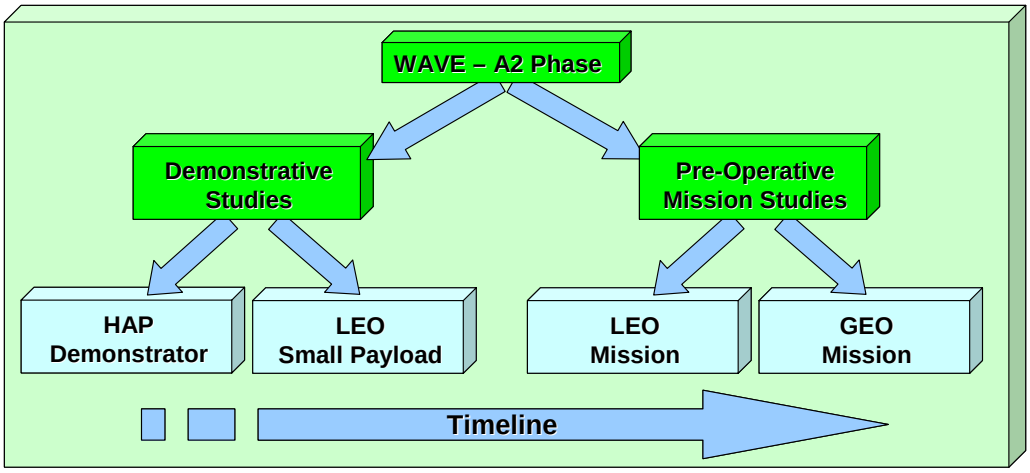

Figure 6-1: WAVE A2 lines of study

Time is a crucial issue for the project: W-band has to be practically investigated in a short time in order to have the preliminary channel characterisation results, fundamental for the pre-operative missions. In the following paragraphs, the main results achieved for the two demonstrative lines of study are reported, focusing the attention on the IKNOW scientific mission that can be considered the nodal point of the entire project.

6.1 IKNOW MISSION

IKNOW P/L will be used for a first uplink-downlink in-orbit validation of W band technology and space qualification processes [6-7], [6-8]. This mission will be a crucial point for the future exploitation of W band. Its aim is to provide a first evaluation of the W band satellite channel in order to verify the feasibility of more complex missions and the possibility for an operational use of W band satellite TLC, in addition there are other main objectives that will be addressed in following sections. The timeline for the development of the IKNOW payload is one of the central issues of the activity.

6.1.1 MISSION OBJECTIVES / NEEDS

The activities within the IKNOW program focus on the development of a P/L carried on a LEO platform. As previously outlined, this will be a demonstrative mission with the aim to realise the first satellite W-band link in order to collect the preliminary experimental W-

band satellite propagation data. Before making great investments in W-band, a demonstrative mission is needed in order to evaluate if this could be a promising field of research and development. Being a demonstrative study, clearly the IKNOW mission definition is driven by the need to realise a low cost system that could be developed in a short time and could provide the required proof of concept. In addiction, considering the high strategic relevance of W band application for space communications, the time constraints are a crucial point that will address all project activities.

In this frame, the mission general objectives can be divided in two different categories:

- *Scientific objectives*:
    - W band satellite channel tropospheric attenuation characterisation;
    - W band satellite channel quality measurements (secondary).
- *Technological objectives*:
    - In-orbit validation of W band hardware and space qualification methodologies.

With regards to the first scientific objective, the IKNOW mission has to realise a propagation preliminary channel assessment. As a matter of fact, considering the pioneering nature of the W band experiment, the main aspect that should be investigated concerns the troposphere attenuation.

Other phenomena of potential interest could be the depolarization, the increase of noise due to thermal emission and the interference. It is thought that in the IKNOW Mission these more ambitious phenomena may be neglected. Measures with dual polarization could be useful in order to assess future utilization of dual polarization in W-band but it could have strong impacts in terms of required margin. Currently, no W-band tropospheric measurement have been performed and no “additional attenuation” statistical or empirical models are available (it is possible to obtain a preliminary order of attenuation levels using the models validated at lower frequencies, i.e. ITU ones). In this frame, the IKNOW mission should provide the preliminary information that will be helpful for the creation of empirical models or for the validation of physically-based electromagnetic models. One of the most important requirement of the Mission will be the collection of attenuation measurements in order to realise a preliminary database whereby modelling the most relevant propagation impairments phenomena [6-10].

Attenuation is a phenomenon mainly induced by rain, humidity, clouds and scintillations. Rain is certainly the dominant phenomenon (for frequencies greater than 10 GHz) for time percentages less than the 1% of the time.

However, the following two considerations have to be carried out:

- the investigation of channel statistical nature can be hardly pursued taking into account the limited available connection time due to the LEO orbit and the limited number of ground stations;
- the demanding availability objectives are not foreseen by the IKNOW phase being more than sufficient a loss of observation time not exceeding a few days per year (the scientific nature of IKNOW does not pursue operative objectives like availability).

On the basis of these two considerations, it is thought that the system design should be carried out taking into account attenuation levels exceeded for no more than 1% of the time, which includes humidity, clouds and scintillations but only light rain.

It will be meaningless to realise only attenuation measurements without the concurrent collection of meteorological data. These data are mandatory in order to correlate the propagation attenuation phenomena with their causes and create valid attenuation models.

Some of the most important additional meteorological data required for the W band channel assessment are: meteorological radar measurements in order to evaluate the rain/clouds characteristics, radiometric measurements in order to estimate water vapour and liquid water content, pluviometric measurements in order to estimate the rain rate on ground. A complete list of required meteo instruments is provided in following sections. In conclusion, with respect to the channel measurements, the main mission requirement will consist in the possibility of observing, both for uplink and downlink, the W band signal level variations for the maximum allowed time. This has to be compatible with the inherent system limitations and with the very severe conditions posed by the tropospheric attenuation for low percentages of time, together with the collection of meteorological data.

Therefore, it is assumed that the system operations are designed to measure the channel characteristics:

- for a tropospheric attenuation not higher than ~16 dB;
- at a satellite altitude of ~600 km as reference;

- with angles of view: along track 90+/-20°(+/-47.5° with an antenna pointing system); cross track 90°+/-20° (+/-47.5° with an antenna pointing system).

The system under investigation has to guarantee the fulfilment of the following goals:

- tracking and keeping the track of the W band carrier in various tropospheric conditions for most of the satellite passes so ensuring a preliminary channel assessment, even not on statistical basis.
- assessment of the dependence of frequency attenuation with observation angle.
- assessment of the signal dynamics so demonstrating the possibility (or the conditions under which this possibility exists) to design a variable transmission rate system by adapting the channel capacity to the actual tropospheric conditions and, especially, the capability to operate in difficult condition of transmission time and space relocation.

For what concerns the second scientific objective, it has to be outlined that channel quality measurements are not a primary issue of the mission. In order to fulfil this second goal, the IKNOW Mission has to realise a database of BER measurements both for uplink and downlink (or for the complete ground-satellite-ground chain). In this frame, the P/L has to be able to send and receive a modulated W band signal for the realisation of a preliminary pre-operative channel assessment. A specific modulation (or a restrict set of modulations) has to be selected and its main features, with respect to W band satellite system issues, have to be investigated. Some information on propagation impairments could be acquired exploiting BER measurements. These one could be useful in the frame of the first mission scientific objective. Anyhow it has to be underlined that channel quality measurements are not a baseline for IKNOW mission (secondary objective).

Regarding the technological objectives, the mission aims at the two following goals:

- to realise the P/L using both COTS (Commercial Off The Shelf) and innovative hardware (on the basis of mission constraints);
- to perform hardware in-flight test.

In fact, being IKNOW the first satellite mission with a W band P/L, to take advantage of it, making in-orbit test of hardware that will be employed in the GEO/LEO future missions, is mandatory.

The P/L will send on ground (through the TT&C) a rich set of subsystems health/status and RF signal data in order to perform hardware in-flight test. Some of the most important H/W information are:

- W band LO time stability and phase noise;
- RF Tx power measurements;
- currents for all active devices (as LNA), etc.

All these data will be monitored, collected and analysed on-ground.

Due to the fact that IKNOW is a demonstrative mission that should meet low-cost and short development-time requirements, the P/L will have a very simple architecture and will be embarked on a dedicated nano-platform.

However, in order to relax the tight time constraints that drive the IKNOW project, a secondary mission P/L has been designed and analysed, removing all the previous identified regulatory constraints that are an heritage of the DAVID project. Moreover, being the channel quality measurements a secondary objective that will lead up to a more complex P/L architecture and long development time, it is not considered as baseline for the Basic Mission but only for a Full Mission. In this frame the second mission (the "Full" one) will be defined on the following basis:

- an orbit (different from the one scheduled for the DAVID mission) optimized for the coverage of the ground segment;
- a P/L able to perform a more complete W-band satellite channel characterization, performing the channel quality measurements as a baseline;

Moreover, the Full P/L will use a set of ad-hoc hardware developments larger than the Basic one.

In Table 6-1 all the objectives are summarised both for the Basic and Full Mission.

Objectives		Basic	Full
Scientific	W band satellite channel tropospheric attenuation characterisation	Applicable	Applicable
	W band satellite channel quality measurements	Not applicable	Applicable
Technological	In-orbit validation of W band hardware and space qualification methodologies.	Applicable - few technological developments	Applicable - medium level of technological developments
Regulatory	DAVID frequencies maintaining	Applicable	Not applicable

Table 6-1 : IKNOW Basic and Full Missions objectives Summary

6.1.2 ADDITIONAL ATTENUATION PRELIMINARY EVALUATION

The results achieved from a preliminary analysis of W band additional attenuation are reported in Figure 6-2 and Figure 6-3, using the two central frequencies identified for DAVID Mission (75.7 and 85.5 GHz, respectively) for a site located in the area of Rome. In order to obtain the probability density curves, the ITU propagation models (validated at lower frequencies) have been used.

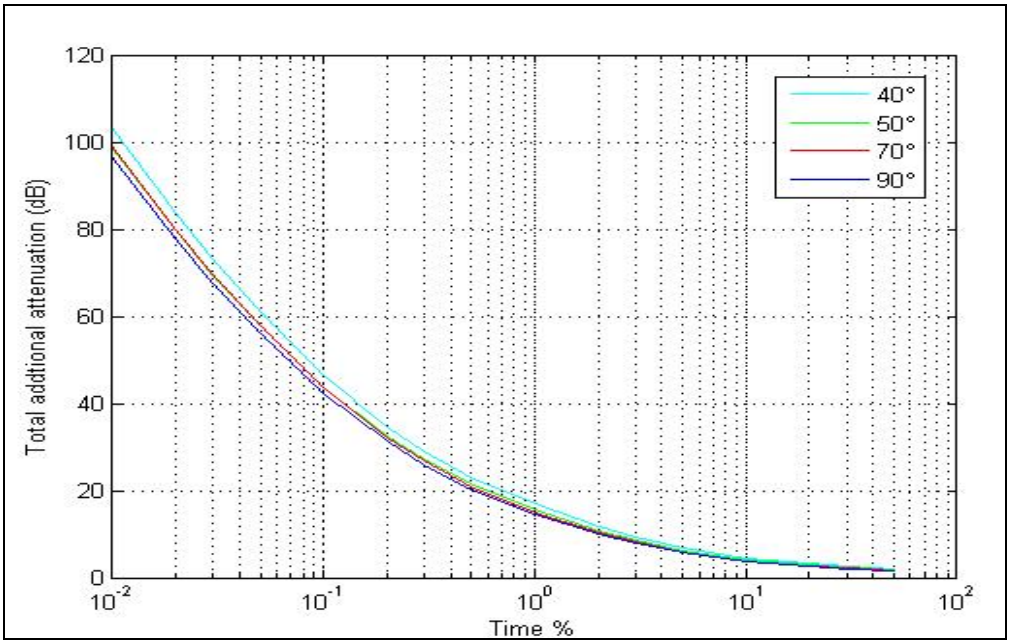

Figure 6-2: Additional attenuation for Rome site at 75.7 GHz

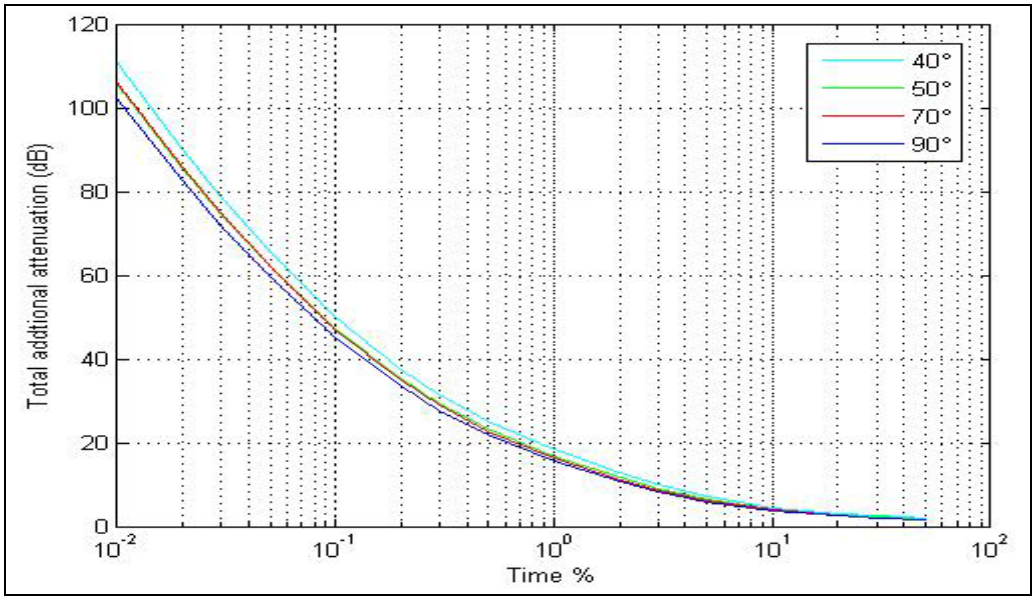

Figure 6-3: Additional attenuation for Rome site at 85.5 GHz

For 1% of time the total attenuation does not exceed 15.5 dB, for an inclination of 50° using the 75.7 GHz link (decreasing the inclination of 10° increases the attenuation of ~1.3dB). For 1% of time the total attenuation does not exceed 16.8 dB, for an inclination of 50° using the 85.5 GHz link (decreasing the inclination of 10° increases the attenuation of ~1.4dB).

6.1.3 IKNOW BASIC MISSION DEFINITION

As already explained, one of the main goals of the Basic IKNOW mission is to maintain the frequencies requested by ASI during the DAVID project, while performing some preliminary channel experimentation. Thus, this mission has to use both the uplink and downlink. The used frequency range will be the same requested for the DAVID project: 85.25-85.75 GHz for the uplink, 75.6-75.8 GHz for the downlink. The satellite orbit will be optimized with respect to the ground segment, in order to ensure the best coverage performance.

In order to fulfil scientific objectives the IKNOW P/L has to include:

- a W band beacon transmitting section, for the downlink power measurements data collection realised by the ground terminal;
- and a W band beacon receiving section that has to perform the uplink power measurements.

Considering the targets of IKNOW Basic Mission (scientific, technological and regulatory) it seems reasonable to identify the following baseline assumptions:

a) Downlink: unmodulated carrier (only the central frequency of 75.7 GHz is here considered).
b) Uplink: unmodulated carrier (at central frequency of 85.5 GHz).
c) Downlink: modulated signal for channel quality evaluation.
d) Uplink: modulated signal for channel quality evaluation.
e) Optimised orbit.
f) “Today available” state of the art RF source.
g) Programmable ground station antenna tracking.

Assumptions a) and b) leaves apart the possible use of modulated bit sequences to measure the BER. The carrier tracking needs to keep at minimum the receiver bandwidth: the

minimum is determined by the phase locked loop optimization and is of the order of 1 kHz, thus not allowing any reasonable measurement of BER.

Assumption c) is imposed by the need of having the same orbit identified for DAVID Mission, designed to have two passes per day guaranteed over the Station of Spino d' Adda (that was one of the ground station of DAVID Mission and will be part of IKNOW Earth segment) with the satellite at zenith (relaxing this requirement would impose to account for unacceptably large attenuations due to the long tropospheric paths that would happen with passages far apart).

Assumption d) is a prudential requirement ensuring, already today, the availability of enabling technologies realised in Italy.

Assumption e) allows to avoid expensive and risky technological developments of monopulse systems in W bands.

The basic configuration of IKNOW mission is shown in Figure 6-4. The main components are a W band P/L carried on-board the LEO satellite and some Ground stations (fixed and/or transportable).

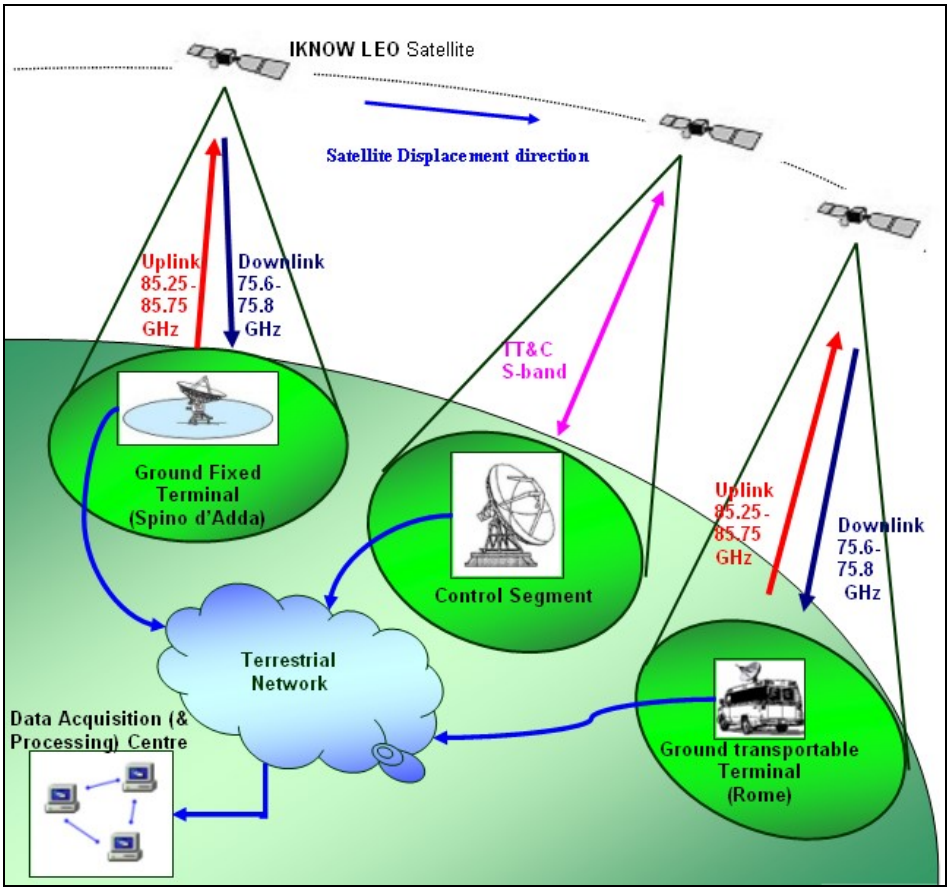

Figure 6-4: IKNOW LEO mission

Both the satellite and the ground station must be able at least to transmit a radio beacon and to detect the incoming signal power and to transmit and receive a modulated signal for the BER measurement experiment. For the Ground Terminals, it will also be mandatory to collect meteorological data and relate them to the power measurement carried out at the same time.

Those measurements should be continuously collected in fixed intervals. The recording of meteorological data has be synchronized with the power measurements recording.

Those information are collected, stored and processed in a Data Acquisition (& Processing) Centre. In order to realise the tropospheric attenuation characterisation, it is required a 2 years database of measurements.

Hence, the results obtained will not have a statistical validity comparable with the ones that could be obtained using a GEO satellite (5 years of near-continuous data), but they will still be very useful for the preliminary channel evaluation and for the realisation of the first attenuation models. The on-board P/L could reuse the signal integrator device on uplink signal in order to realise a passive measurement system (total power radiometer). The P/L informs the Control Centre of the signal measurements acquisition through the TT&C channel. These will contain ancillary information in order to calibrate and process the gathered measurements. Then, the Control Centre delivers the information to the Data Acquisition Centre through a terrestrial network. Ground Stations can send measurement data (and optionally power measurements), acquired directly through a terrestrial network, to the Data Acquisition Centre where they are stored.

With respect to the ground station, it will be very useful to have both a fixed and a transportable one, being the outage probability at W band significantly affected by the site and its climatology.

The expected additional attenuation for Milan and Rome sites, which are Alps-dominated and Coastline-dominated meteorological regions respectively, have been evaluated.

This reflects into a different climatology which is mid-continental for Milan and typically Mediterranean for Rome with very different cloudy and precipitation regimes. In this respect, it is considered essential to acquire data from both sites to characterize the site diversity from a radiometeorological point of view at W band. It also has to be underlined that, in order to meet the tight time (and cost) constraints, part of the IKNOW P/L H/W will be COTS (as already introduced).

6.1.4 IKNOW FULL MISSION DEFINITION

The Full Mission definition is based on the previous introduced Basic Mission concept, but some elements will change. In particular, the satellite orbit will be optimized with respect to the ground segment, in order to ensure the best coverage performance. In addition, the P/L could be more complex with respect to the receiving chain. Relaxing mission launch time constraint will lead to the development of a more complex P/L; the H/W COTS will be less with respect to Basic Mission, for some critical elements, an accurate design and development phase including space qualification could be envisaged. A demodulation and modulation section could be foreseen, in order to realize uplink channel BER measurements. Being the channel quality measurements a requirement for both uplink and downlink the P/l should have a W band modulated signal Tx section. In this frame, also the ground terminal should have both a modulated signal Tx and Rx section. This backup mission will still remain a demonstrative study; as a consequence (even if more relaxed) the targets of low cost and fast development time will remain a nodal point of the study (but will not be so tight as primary mission ones). In this frame, most of the considerations will be the same identified for the primary mission, but platform requirements could change.

6.1.5 IKNOW MISSION ARCHITECTURE

The mission infrastructure is composed by the following elements:

- Space Segment;
- Ground Segment, constituted by:
    - Signal Ground Stations/Terminals;
    - Mission and Satellite Control Center;
    - Data Acquisition & Processing Centre.

The following sub-sections describe each of these segments that constitute the preliminary mission architecture.

6.1.5.1 Space Segment

The space segment is represented by the satellite. It can be conceived as the combination of a supporting platform and the P/L. In the following the two subsystems are described.

6.1.5.2 On-board P/L

As introduced, the Basic Mission P/L has a simple configuration and should be developed to fly in the optimised foreseen orbit (or a launch opportunity) for 2011.
Basically, the P/L transmits an unmodulated carrier in the range between 75.6-75.8 GHz and detects an incoming signal carrier in the range between 85.25-85.75 GHz.

6.1.5.2.1 The Transmitting Chain

The transmitter chain for the propagation experiment consists of a frequency generator subsystem and a PA. The first part of the transmitter is a critical issue for IKNOW mission, and it has been defined during the project on the basis of the W band technology state of the art and available equipments. The PA could be chosen between a HPA or a SSPA on the basis of the power requirements. However, as already stated, it can be preliminary assumed that the most suitable solution is a SSPA (GaAs PHEMT) in order to maintain the weight constraint on-board the nano-satellite. From a preliminary link analysis, the Tx power generated by the SSPA should be 100mW minimum (300mW goal). A Tx dedicated antenna is then used in order to simplify the overall design.
Of key importance is the power monitor function, whose scope is to measure the P/L transmitted power that is sent to ground by the telemetry link. In addition, it is also important as housekeeping function.

6.1.5.2.2 The Receiving Chain

For what concerns the Rx chain of the propagation experiment P/L, the signal received from the Rx dedicated antenna subsystem, goes into a filter, a RF detector that detects the incoming signal (and the noise) and integrate it. A high dynamic AD converter (12/14 bits) produces the data to be recovered and transmitted to ground (through the TT&C channel).
The same Rx chain can be applied to a radiometer function, being the only difference between the two applications the presence of a dedicated filtering function and the optimization of the integration time interval. In other words, the RX chain can operate as a radiometer, in the full BW, when the P/L is not receiving the signal from ground. This can be done before and after the ground connection or in a stand-alone configuration to get more information about the Earth albedo in that frequency range. The basic concept

envisages to reuse the same H/W in exclusive modes, but it is also possible to operate the two modes in parallel.

The radiometer function will extend the scientific objectives of the first P/L with minimum addition of components (not increasing P/L costs). Due to the fact that the up and down links have the same BW, in principle, the same detector could be used for Rx signal and the power monitor function. But this, of course, limits the possibility to operate separately the two on-board chains.

The antenna subsystem has been investigated in depth during the project.

Due to the low orbit of the satellite and to the small beamwidth, the visibility window during each pass would be only few seconds long without the implementation of the platform or antenna steering. Thus, it is mandatory to use a pointing system both in the ground and on-board antennas considering also as a target the absence of the platform propulsion subsystem. This demonstrative mission should be embarked on a dedicated low cost nano-platform; the satellite antenna pointing could be realised using only the attitude control of the platform, maintaining the antenna fixed, or rather including a steering subsystem that will make the P/L system more complex. The overall pointing error should be in the order of 0.5°-1°.

As previously outlined, the second scientific objective is to perform channel quality measurements; in this frame the system has to be able to perform uplink and downlink BER measurements.

Because of wide bandwidth available in the W region in comparison with the limited capability of H/W equipments, it would be more suitable to select simple modulation schemes (FSK and PSK at first), instead of using more complex ones with better spectral efficiency.

Due to the fact that the main goal of the IKNOW mission is to test the channel operative usability using, firstly, a simple baseband transmission scheme as experimentation preliminary step, we propose the use of a Split-Phase (SP) Manchester-coded BPSK modulation, already considered for the W-band collection link of DAVID project [6-11]. The reason of such a technical choice is related to the reduction of the complexity of the carrier recovery operation performed at receiver level.

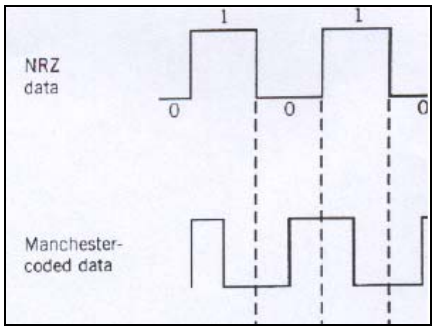

Figure 6-5: Manchester coded signal

As depicted in Figure 6-5, a bit at "1" level is encoded with a transition from a positive amplitude value to a negative amplitude value, and a bit "0" level is encoded with a transition from a negative amplitude value to a positive amplitude value. The bit duration time T_b is so split into two-pulse interval of duration $T_b/2$, so the bandwidth occupied by the Manchester-coded signal is doubled with respect to the one occupied by a classical polar NRZ signal.

The modulation index Φ_m for the Manchester-coded SP scheme is equal to 60°, so such a phase shift is attributed to the modulated carrier in case of positive pulse amplitude; otherwise a phase shift of -60° is attributed to the modulated carrier. The constellation is shown in Figure 6-6.

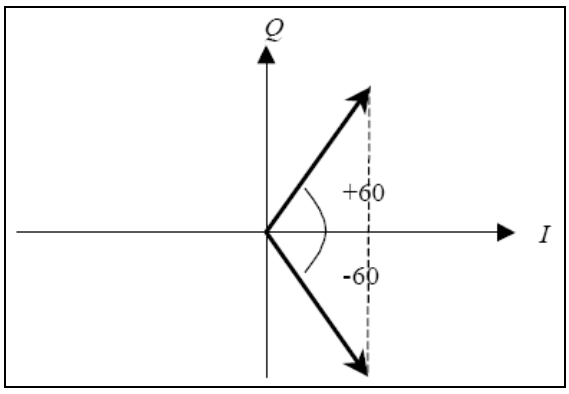

Figure 6-6: BPSK with modulation index 60°

As a result of this choice, we obtain an amplitude spectrum of the modulated signal with two main lobes and a carrier pulse at the central frequency, as shown in Figure 6-7.

A coherent demodulation with matched filter receiver can be employed at the receiver. Decision about transmitted bits is kept on the basis of the difference between two consecutive demodulated symbols of duration $T_b/2$, so to decide for a "1" bit if a transition

from a positive amplitude pulse to a negative amplitude pulse is detected, and for a "0" bit if vice-versa. The presence of the carrier peaking the signal spectrum due to the unbalanced signal configuration implies a not optimal spectral efficiency of the Manchester-coded BPSK. In fact, the modulation loss is 1.25 dB.

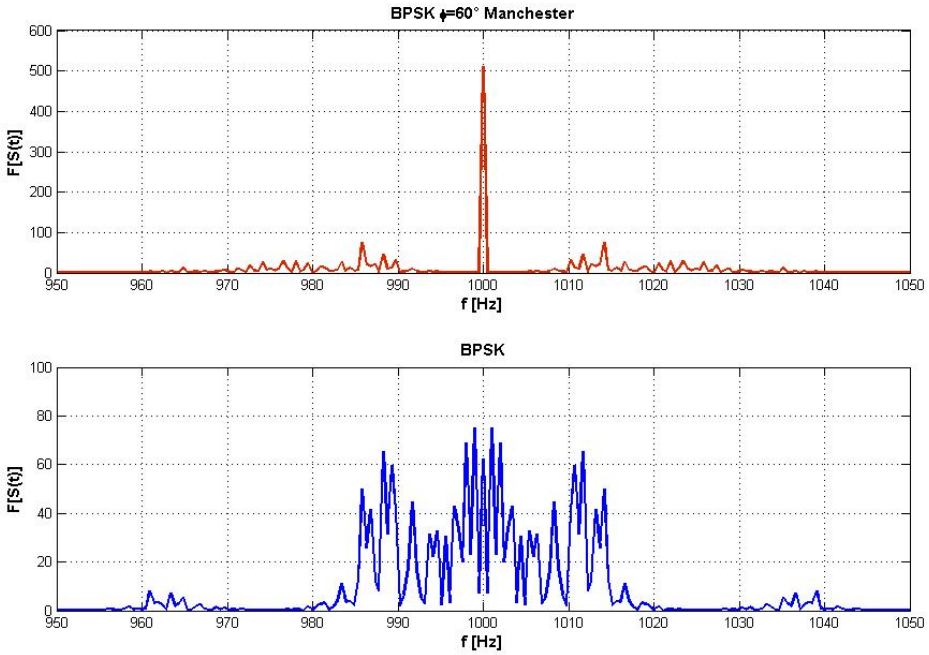

Figure 6-7: Comparison between the Amplitude spectrum of the Manchester-coded 60° BPSK and simple BPSK modulated signal

The BER provided by a SP- Manchester-coded BPSK over an AWGN channel can be computed as:

$$P_b = Q\left(\sqrt{2 \cdot \frac{E_b}{N_0} \cdot \sin^2(\phi_m)}\right) \tag{6-1}$$

where $\frac{E_b}{N_0}$ is the energy per bit-to-noise ratio, *Q(x)* is the Gaussian error function, and $\sin^2(\phi_m)$ is the term related to modulation loss with respect to an antipodal BPSK scheme. Therefore, the performance in terms of BER are lower than a simple BPSK assuming the same transmission power. Nevertheless, the presence of an unmodulated carrier in the centre of the signal spectrum allows to simplify the carrier recovery operation, which is one of the most critical issues when facing the real applications. In the IKNOW context,

high level of phase noise due to imperfections of high frequency oscillators and high value of Doppler shift can make such a modulation scheme the most suitable. The BER versus the E_b/N_0 for the two modulation schemes is shown in Figure 6-8.

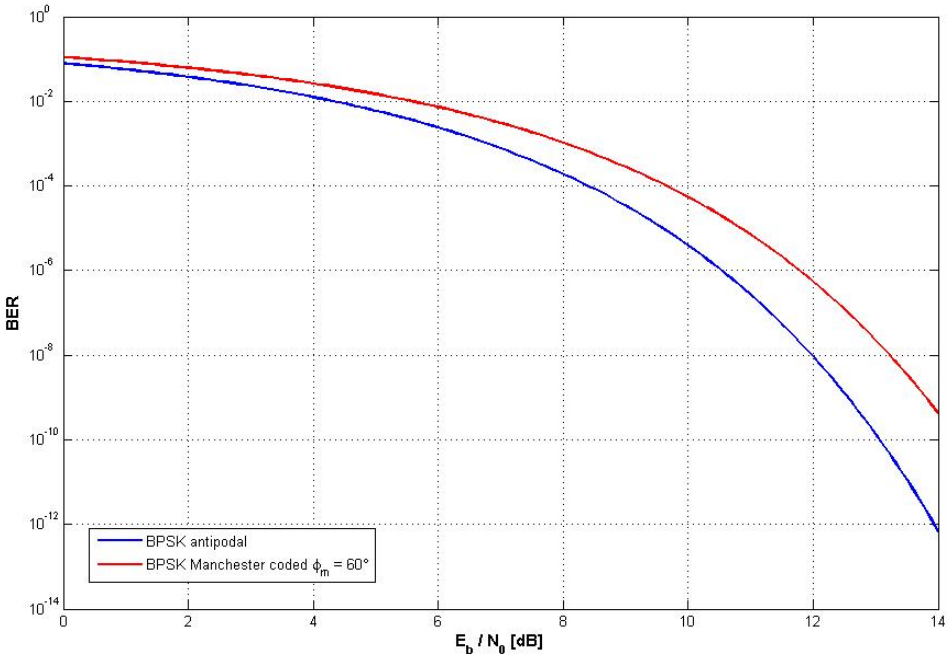

Figure 6-8: Comparison of BER versus E_b/N_0 curves for an antipodal BPSK and a Manchester-coded Φ_m=60° BPSK

Finally, at the receiver end, the signal is demodulated and the resulting baseband bit stream is compared with that of the originally transmitted (saved in a memory) in order to determine the erroneous bits and hence, the BER value.

The data rate will be established by the technology and link budget more than ex-ante decision. As previously introduced, the data transmission experiment for BER measurement is performed both for the uplink and the downlink; in the Figure 6-9 the IKNOW Mission P/L is shown. The MOD/DEMOD functions could be carried out by SW if the data rate is relative low.

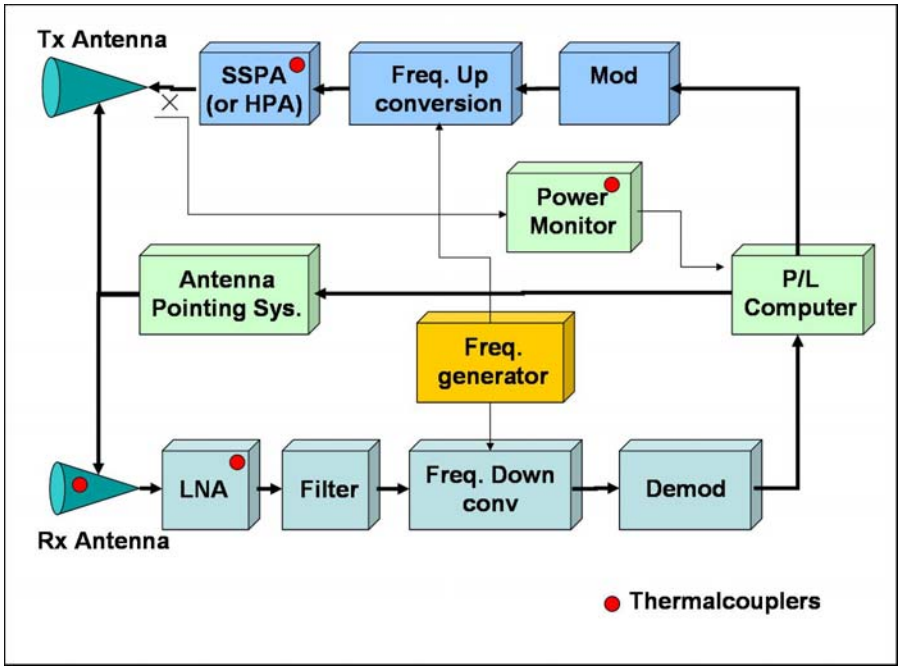

Figure 6-9: IKNOW Mission Operational Architecture

6.1.5.3 IKNOW Platform / Orbit

Being IKNOW a demonstrative Mission with a characteristic of cost/time-effectiveness, and considering that the P/L will have to carry out simplified channel measurements, a target weight can be identified for the platform: a nano-satellite in the range of 20-50 kg could be suitable for the mission objectives.

In fact, from a preliminary P/L weight estimation, it could be foreseen a target of 10-20 kg.

In order to obtain a meaningful W band satellite channel characterisation, it will be satisfactory the realisation of a 2 years measurements database. In this frame, operating a trade-off with the identified target of using nano-platform, the mission operating life should be in the order of 2 years (being this life period, as a matter of fact, the average lifetime of a micro/nano-platform).

The required visibility for each passage is in the order of some minutes for the realisation of a channel attenuation measurements database. In this frame, taking into account the lack of an orbit maintenance system (because the nanosat cannot embark a propulsion system), it could be foreseen a pointing system based on platform attitude or based on a steering antenna subsystem.

The latter solution is clearly more complex with respect to P/L realisation. In order to select a preliminary orbit for the IKNOW satellite, a genetic algorithm has been used to

determine the best orbital parameters that maximise a cost function based on coverage evaluation over Rome and Spino D'Adda (equally weighted). Moreover, the fitness function considers the elevation angles statistics as well (taking into account time access percentage for any given elevation angle).

The coverage has been evaluated using J4 perturbation for a two years mission.

Some "solutions bounds" have been chosen in order to make the algorithm working in the most efficient way:

- the orbit inclination has been restricted to angles between 35° and 145° in order to focus coverage on latitudes of ground segment;
- the orbit altitude has been restricted from 500km to 700km in order to relax control commands related to atmospheric drag and maintain a good link budget margin. Moreover, the maximum altitude has been set to 700 km in order to avoid the satellite to pass into Van Allen's inner belt;
- the eccentricity has been set equal to 0 (simple circular orbit).

The results of this preliminary optimisation are reported into the Table 6-2 and are shown in Figure 6-10 and Figure 6-11.

Height (km)	**692**
Inclination (deg)	**47**
Argument of Perigee (deg)	**0**
RAAN (deg)	**294**
Period (hours)	**1.64338**
Number of orbits per day	**14.6041**

Table 6-2: Optimised orbit characteristics

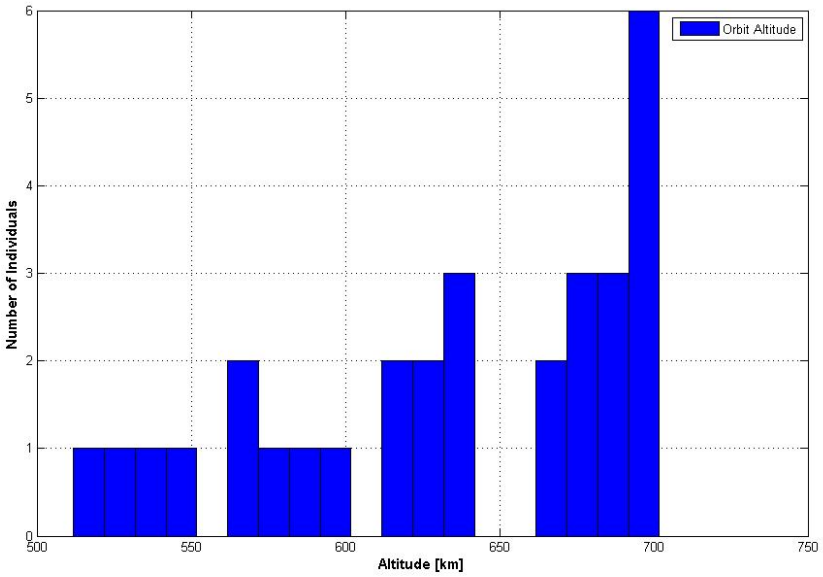

Figure 6-10: Statistics of Best Orbits Altitude

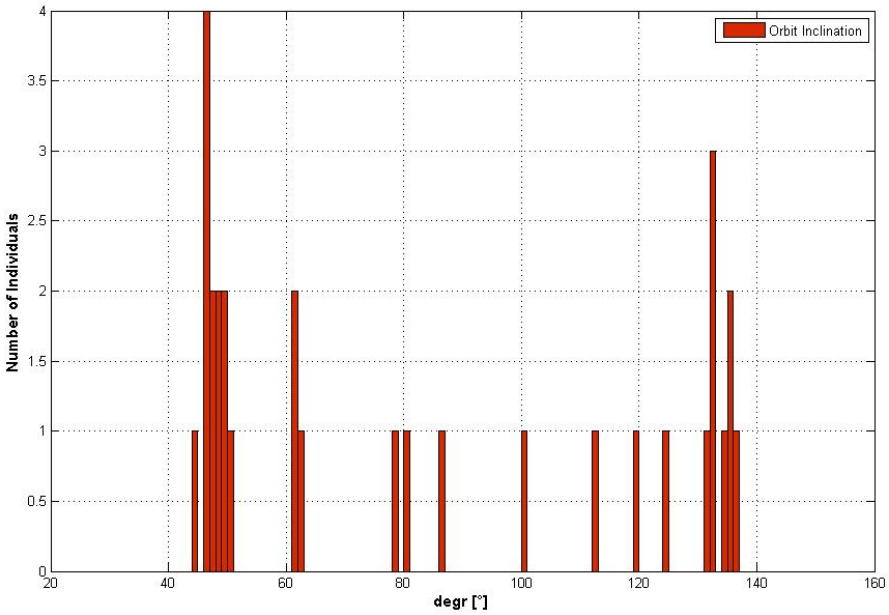

Figure 6-11: Statistics of Best Orbits Inclination

These orbital parameters concern the "best one" of the population obtained in the last generation of the genetic algorithm. In order to create a "statistical evaluation" of the best orbital parameters, all the features of the best 20% of last generation "population" providing a low cost-function value have been analysed.

6.1.5.3.1 Orbital analysis

An analysis activity on the optimised orbit has been carried out in order to evaluate the perturbations that will affect the IKNOW Mission satellite and the visibility window between the satellite's antenna and the ground antennas located in Rome and Spino d'Adda.

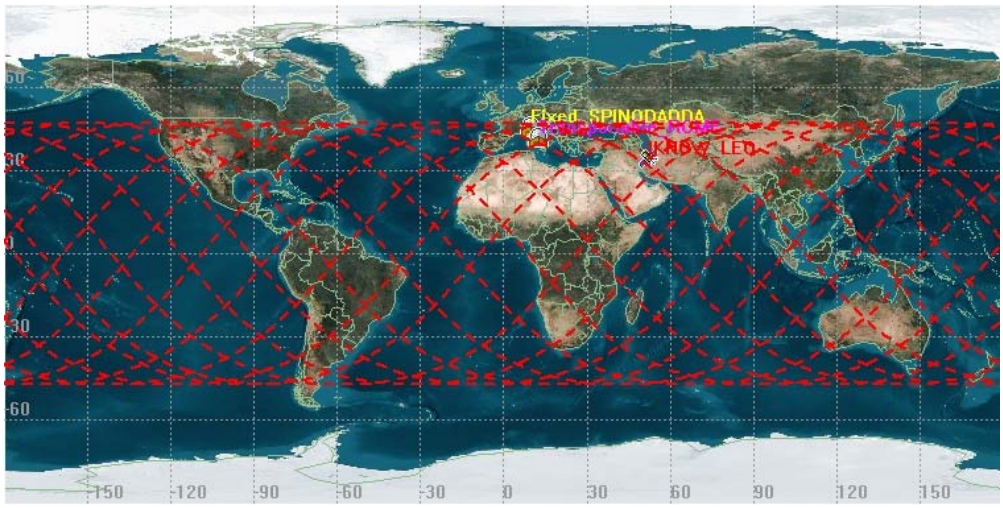

Figure 6-12: Optimised Orbit ground track

Figure 6-13: IKNOW – Spino D'Adda access

Some simulations have been performed in two years of satellite propagation. From this preliminary analysis an orbital altitude decay of ~20 km is expected at the end of the

mission. The other five orbital parameters (eccentricity, inclination, RAAN, argument of perigee, true anomaly) variations are, in first instance, periodical with slow drifts. They are shown in Figure 6-14, Figure 6-15, Figure 6-16, Figure 6-17 and Figure 6-18.

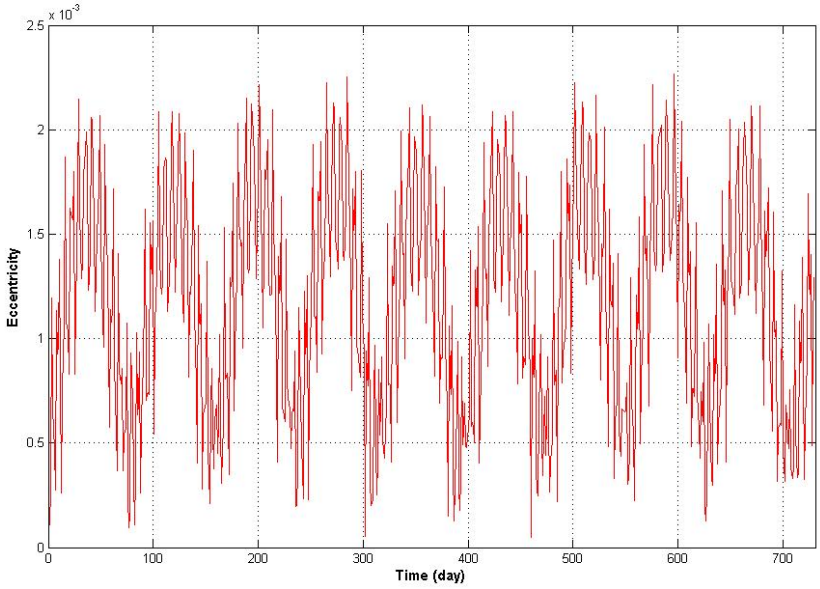

Figure 6-14: IKNOW Optimised Orbit eccentricity time variations

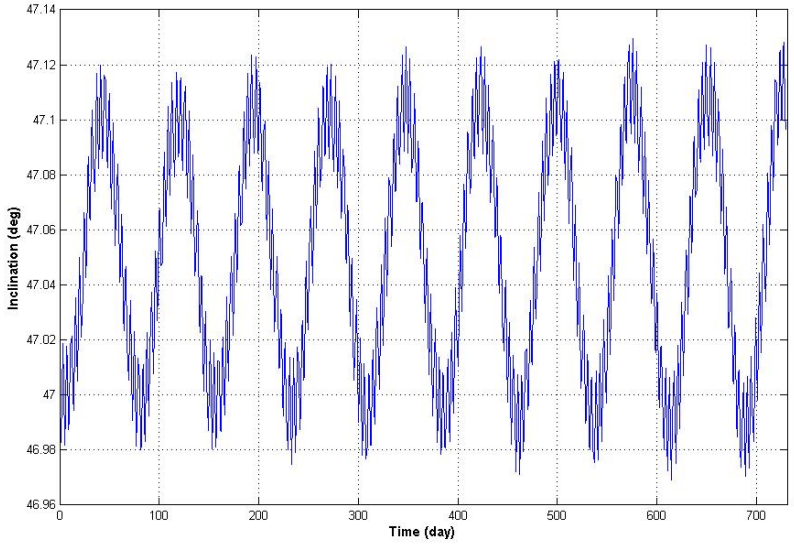

Figure 6-15: IKNOW Optimised Orbit inclination time variations

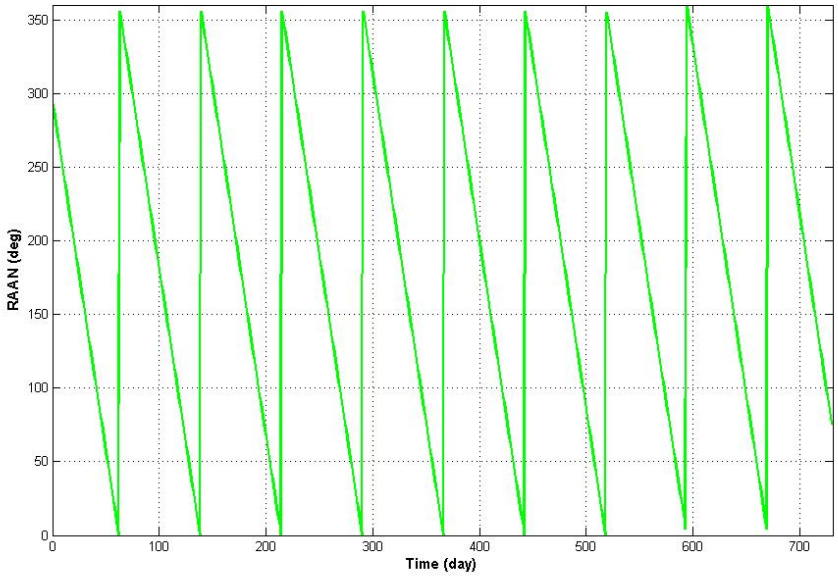

Figure 6-16: IKNOW Optimised Orbit RAAN time variations

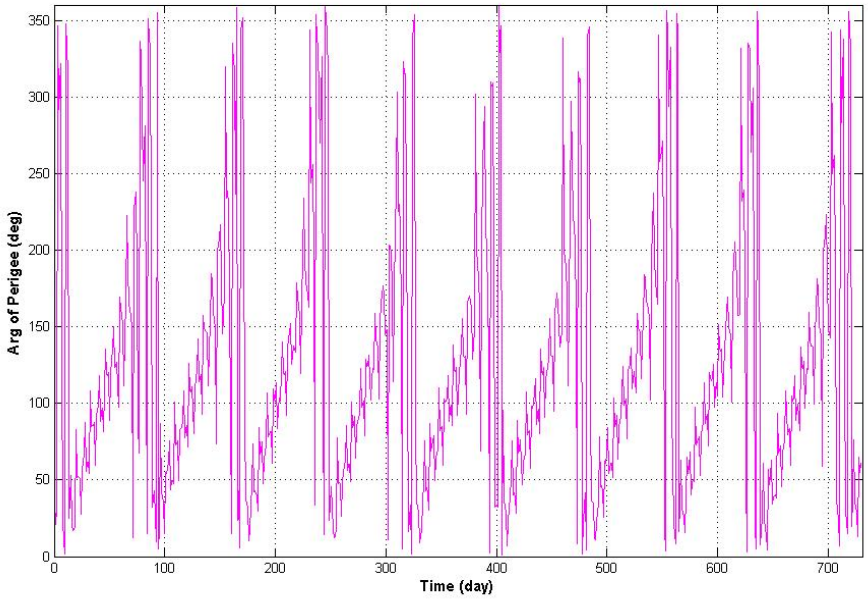

Figure 6-17: IKNOW optimised orbit Argument of Perigee time variations

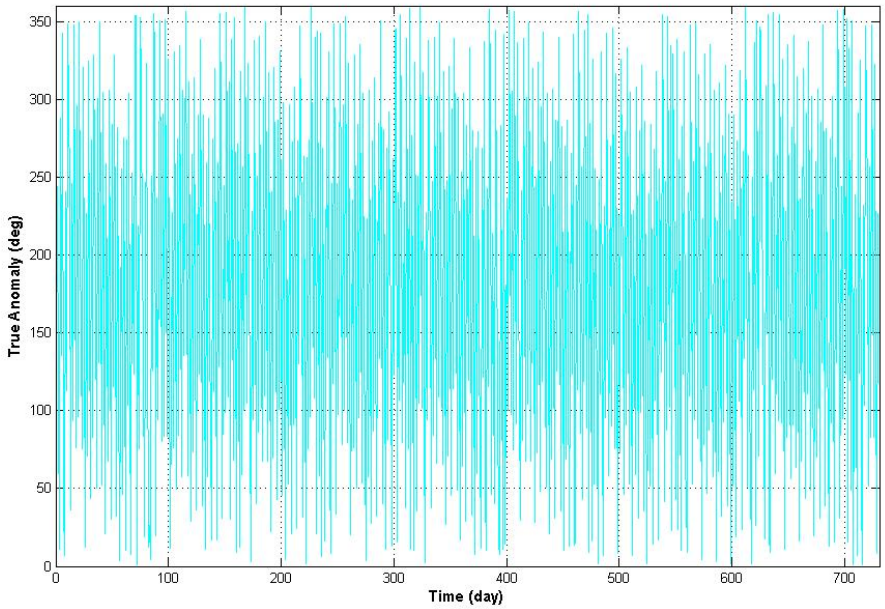

Figure 6-18: IKNOW optimised Orbit True Anomaly time variations

Concerning the visibility analysis, two different configurations have been analysed:

- the first one considers the use of a steerable antenna, allowing a maximum off-nadir angle equal to 47.5°.

Global Statistics	
Min Duration (s)	**4.951**
Max Duration (s)	**257.387**
Mean Duration (s)	**226.974**
Total Duration (hrs)	**165.7**

Table 6-3: Rome to IKNOW Access Summary Report (first configuration)

Global Statistics	
Min Duration (s)	**1.490**
Max Duration (s)	**241.328**
Mean Duration (s)	**195.339**
Total Duration (hrs)	**160.6**

Table 6-4: Spino d'Adda to IKNOW Access Summary Report (first configuration)

- the second one considers to point the on-board antenna towards the ground stations through the asset control system.

Global Statistics	
Min Duration (s)	3.820
Max Duration (s)	78.742
Mean Duration (s)	62.562
Total Duration (hrs)	29.9

Table 6-5: Rome to IKNOW Access Summary Report (second configuration)

Global Statistics	
Min Duration (s)	7.572
Max Duration (s)	78.543
Mean Duration (s)	60.982
Total Duration (hrs)	14.5

Table 6-6: Spino d'Adda to IKNOW Access Summary Report (second configuration)

Figure 6-19 and Figure 6-20 show the statistics of the elevation angle, respectively, for the transportable station in Rome and for the fixed station located in Spino d'Adda. These statistics represent the time percentage each ground station sees the satellite with a certain elevation angle interval with respect to the visibility time in the overall mission operations (2 years).

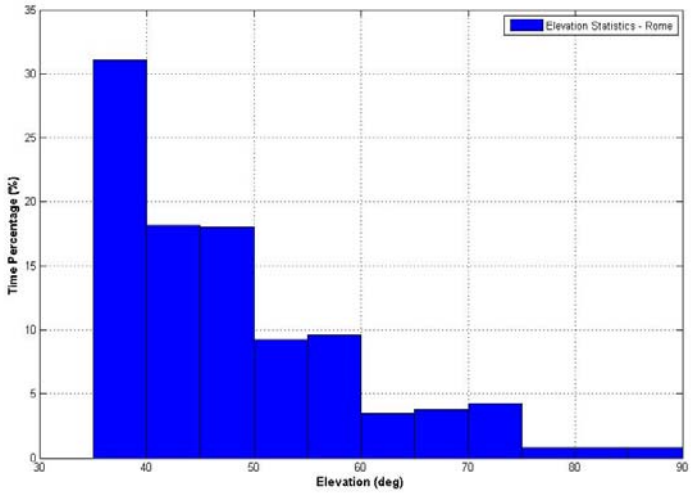

Figure 6-19: Optimised Orbit Elevation Statistics over Rome Transportable Station

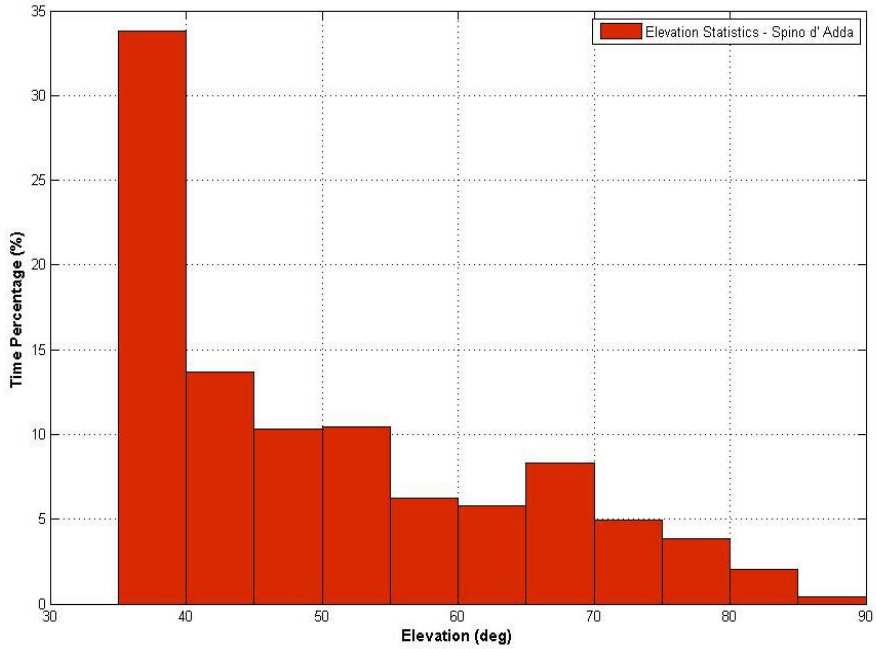

Figure 6-20: Optimised orbit elevation statistics over Spino d'Adda Fixed Station

6.1.5.3.2 Doppler Shift

In this section a first characterisation of the expected Doppler shift (and Doppler rate) of the carrier in both the uplink and downlink is provided.

Global Statistics	
UPLINK	
Min value (Hz)	**0**
Max value (MHz)	**1.3**
Mean value (MHz)	**0.6**
DOWNLINK	
Min value (Hz)	**0**
Max value (MHz)	**1.1**
Mean value (MHz)	**0.5**

Table 6-7: Expected Values of Doppler Shift for IKNOW Optimised Orbit

6.1.5.3.3 IKNOW Platform

As already stated, since IKNOW is a scientific/technological demonstrator, it is not possible to propose a high-performance (hence high-cost) platform of the order of 10^2-10^3 kg. In this frame, the IKNOW platform will not embark the propulsion subsystem (or will embark a low-cost, low-performance one) and therefore it will not be possible to guarantee the station-keeping in the DAVID orbit, and in general any manoeuvre to reach specific orbit position. According to the analysis carried out above, the approach to use this kind of platform is adequate in order to satisfy all mission objectives/requirements.
Moreover, the selection of the launcher will be based on opportunity and not on a dedicated mission. The satellite life time is constrained from consumable like fuel (not for IKNOW) and solar panel and material (blankets, etc) degradation. These parameters, in turn, are depending on the selected orbit. As already stated for this mission, a minimum life time of two years is requested.

For what concerns the platform:

- it will be fully steerable over all the axes (two mandatory);
- the platform pointing accuracy will be better than 0.5° (3 sigma) for all the axes (two mandatory);
- the pointing knowledge will be better than 0.1° for all the axes;
- it will provide a mass memory of ~1Gbits EOL;
- it will provide a TT&C capability (1 Mbps down, 100 kbps up);
- it will provide 15 W average for payload operations for an orbit duty cycle of 10% in about five orbits per day.

The identified target for TT&C data rate has been selected on the basis of a preliminary analysis considering:

- command: 2 - 8 kbps , 4 kbps typical;
- health & status telemetry: 40 -10000 bps, 8 kbps common;
- mission / scientific data: <1 kbps.

The evaluation of TT&C requirement for scientific data has been performed under the following assumptions:

- in each passage over a ground station, the P/L Rx chain collects a 24 bit data each second;
- the duration of each passage visibility over ground station is ~10 min (for the propagation experiment);
- the TT&C has to download the data stored for 2 satellite previous passes;
- the TT&C link duration of each passage over the ground station is ~10 min (this value should be greater than the one identified for the W band link, but here is considered the same in order to maintain a conservative budget).

The scientific data that the TT&C has to download during the satellite pass is in the order of 30 Kbits. In this frame, the considered TT&C total data rate values of 1 Mbps for downlink and 100 kbps for uplink represent a good conservative assumption.
The identified target for satellite power requirements has been selected on the basis of a preliminary analysis considering the following assumptions:

- P/L - 15 W;
- spacecraft bus subsystems:
    - propulsion - 0 W,
    - attitude control - 3 W,
    - communications - 1,5 W,
    - command and data handling - 1,5 W,
    - power - 9 W,
    - thermal - 0 W,
    - structure - 0 W.

The total satellite required power is in the order of 30 W. In this frame, small Si (COTS technology) solar arrays could be used (~0.3-0.4 m²: this surface value is compliant with the identified target of a nano-platform). It has to be underlined that this is only a preliminary power budget: in the payload architecture activities, more punctual requirements have been identified.
In order to facilitate the mission operation, the platform will embark a GPS receiver and an orbit propagator.

6.1.5.3.4 Embark Analysis

6.1.5.3.4.1 Basic Mission

The requirements used for the selection of the primary bus for the basic mission are mainly given by the characteristics of the orbit that should be maintained (the sun-synchronous DAVID orbit).

Primary Bus

The primary bus is selected under the assumption that the satellite requires a small amount of orbital correction during its lifetime (however not an orbit transfer). The technological research performed during project activities allows to identify the most suited platform as follows:

- Microsat 100

Secondary Buses

The secondary bus is selected under the assumption that the satellite does not need any orbital correction manoeuvre. Possible candidates are listed in the following:

- Microsat 70
- Tubsat-C
- NADIR

6.1.5.3.4.2 Full Mission

The satellite platform requirements for the full mission depend on the selected orbit (that should be defined) and, hence, in a first approximation, the primary buses and secondary ones selected for the basic mission are suited also for the full mission.
In Table 6-8, a list of the main characteristics of the secondary buses is reported.
Due to the pioneer nature of the P/L, it is recommended the use of a full space qualified platform, already in-orbit tested. Moreover, considering that the price of the platforms is similar, Microsat 70 or 100 could be the most qualified choices.

6.1.5.4 Additional considerations

Instead of the up and down BER measurements experiments defined in this section, it could be possible to realise a transparent transponder that creates a transparent ground-satellite-ground link over the same terminal station. This could be interesting in order to test different types of modulations and coding schemes for channel quality measurements collection. On the other hand, the introduction of a transparent transponder could not be a good choice being the connection time of the LEO P/L very low and being the overall mission lifetime of two years (too low for testing of different modulation/coding schemes, considering also that this will be the first W band demonstrative satellite mission). In addiction, the transparent link could give only information on the complete up-down link and is not possible to separate the analysis of the two links.

Characteristics	NADIR	TUBSAT	MICROSAT 70
Delivery Time	24 months	18-24 months	19 months
Price (without launch) for 1 flight model	800 K€	> 1 M€	> 1 M€
Mechanical interface:	Good	Medium (it will be same adjustment to the platform)	Good
Electrical interface:	Good	Good	Good
Thermal Interface:	Passive	Passive	Passive
Power availability	Solar panel during sun-light phase	Battery source in all cases (sunlight and eclipse)	Solar panel during sun-light phase
Mission Lifetime	> 3 years	> 3 years	>3 years
Attitude accuracy	0.5 ° @ 3-sigma	0.5 ° @ 3-sigma	0.5° @ 3-sigma
Propulsion unit	None	Can be added (in function of DV required)	None
Launcher compatibility	PSLV, Dnepr, VEGA	PSLV recommend	Zenit, Kosmos, Tsyklon, Athena and Dnepr
Country	ITALY – Rome – IMT srl	Germany - Berlin - Berlin university	United Kingdom - Guildford - SSTL

Table 6-8: Possible IKNOW Platforms Comparison

Another important issue that can be analysed consists of the possibility to use a second modulation scheme, in addition to the SP-BPSK (or BPSK) one, in order to preliminarily

test adaptive techniques. A good choice for the second modulation could be the QPSK. However, the addiction of a second modulator/demodulator will increase P/L complexity.
This issue has the same drawbacks with respect to the mission complexity/time requirements previously introduced.

6.1.6 GROUND COMMUNICATION STATIONS

The IKNOW mission includes some Earth terminals, both fixed and transportable. Currently, two Ground stations are proposed:

- a fixed ground terminal located at Spino D'Adda site, used previously in various propagation measurements and proposed for DAVID and WAVE phase A. This station is equipped to achieve low attenuation levels even in poor channel conditions;
- a transportable ground terminal mostly located in the area around Rome. The implementation of such a station increases the complexity of the P/L with respect to the antennas, but at the same time it allows a particularly broad collection of propagation measurements in various places and weather conditions, giving the ability to change locations (latitudes) in the ranges established by regulatory aspects (about 50-100 km around the area of Rome). In addiction, this station could be shared with other European partners encouraging international cooperations. The transportability allows to use high-resolution weather forecasts in order to relocate the station in relation with scientific experimentation measurements requirements (clear sky, light or heavy rain, different clouds types, etc.).

For the propagation experiment each ground terminal transmits an unmodulated carrier in the range between 85.25-85.75 GHz and detects an incoming signal carrier in the range between 75.6-75.8 GHz.
The PA has be chosen between a HPA or a SSPA on the basis of the power requirements. This requirement is mainly related with the sensitivity of the on-board RF detector. We can expect that its quality will be worse than the ground station detector due to the weight constraint. Moreover, we must take into account the fact that the use of a HPA on ground is much less critical since the weight constraint is relaxed and the existing devices do not need a development related to the space qualification process. Hence, a trade-off analysis can be performed.

The antenna subsystem has been investigated in depth during the project activities and the results of the trade-off analysis will be shown in 6.2.9.1.

After the antenna subsystem, the incoming signal goes to a RF Detector. On ground, this section could be more complex than that one on-board the LEO satellite.

All the stations must have the capability of detecting the sinusoidal signals transmitted from the satellite (and they might be able to measure the power of the incoming signals).

It is appropriate to combine power measurements with some radiometric equipment in the Earth terminal, operating at lower frequencies, typically in Ka band, in order to perform the so-called "bias removal", specifically to estimate the "zero dB" attenuation level. This measurement technique, derived and validated in previous propagation experiments (Olympus and Italsat), allows the estimation and calibration of the channel power, considering the clear-air attenuation due to presence of gases in atmosphere, which also affects the attenuation of transmitted beacon signal.

Power measurements are performed in order to estimate the tropospheric attenuation in the vertical satellite link. Therefore, they have to be related to simultaneous meteo data acquisition. The measurements data should be continuously collected during the satellite connection time interval.

Thus, it should be envisaged the installation of a weather station situated next to the receivers. This station should be equipped with sensors for temperature, humidity, pressure, wind speed, wind direction, precipitation and solar irradiance, and sensor to monitor visibility and present weather. In particular, the ancillary data needed to realise a meaningful W band additional attenuation database are:

- atmospheric measurements (pressure, temperature, specific humidity, wind and possibly cloud sizes and content) at ground derived from weather stations and cloud particle probes;
- availability of high-resolution three-dimensional mesoscale meteorological forecast and analysis;
- rain cloud coverage and estimate from ground-based weather radars and Meteosat satellite infrared radiometer;
- availability of ground-based microwave radiometers to estimate integrated water vapor and cloud liquid contents;

Both W band beacon power and meteorological data will be stored and processed in a Data Acquisition and Processing Centre.

Spino d'Adda station, located close to Milan, includes some radio equipments that allow to perform advanced telecommunications and propagation experiments in the EHF range. Spino d'Adda was built about 30 years ago mainly in the frame of SIRIO experiment. Later, it was enhanced with instruments for meteorological measurements allowing the experiments of OLYMPUS and ITALSAT. Telespazio leads the management of propagation experiments, while "INGEGNERIA DELLE FREQUENZE" leads the management of the meteorological radar.

Table 6-9 shows a list of facilities included in the station.

Propagation Station ITALSAT	Receiver, 20, 40, 50 GHz, antenna 3.5 m	ASI Property
Propagation Station OLYMPUS	Receiver, 12. 20, 30 GHz, antenna 3.5 m	ASI Property
Communications station ITALSAT	Receiver-Transmitter , 20, 30 GHz, antenna 5 m	ASI Property
Radiometer V band	20, 30 and 50 GHz	ASI Property
Radiometer ka band	12, 20 and 30 GHz	ASI Property
Meteo Radar	2.7 GHz, antenna 3m	CNR Property
Meteo equipment	Rain gauge, humidity, pressure, temperature	ASI Property
Motor generator and UPS	50 kW	ASI Property
Walls and open air	3000 m^2	Politecnico Property

Table 6-9: Main facilities of Spino d'Adda station

There are other useful ancillary measurement instruments that can be used in order to monitor the weather situation such as:

- Meteosat data;
- radioprobes (available by the Linate Aeroport, near Spino d' Adda).

For what concerns facilities that could be complementary to the transportable ground station test site, TOR manages, in the Engineering Faculty (located in Rome), an analog X band non-coherent weather radar called Meteor 200. This radar is operative since 1997 for cooperative research of CNR and University of Rome "Tor Vergata" and is placed on the "Ingegneria Dell'Informazione" building [6-12].

Moreover, the Engineering Faculty of Tor Vergata manages a meteosolar station, named UTVES and located in the Faculty, Figure 6-21. This station could provide accurate and

punctual measurements of temperature, humidity, pressure, rainfall rate, wind speed and direction and all components of solar radiation.

Figure 6-21: University of Rome "Tor Vergata" meteosolar station

The area of Rome is also covered, since 2006, from the C-band weather radar data, located at M. Midia near Avezzano (AQ) and managed by CETEMPS, University of L'Aquila on the behalf of Region Abruzzo. The research centre CETEMPS also performs a daily high-resolution meteorological forecast at 9 km in Central Italy providing all meteorological fields, including cloud and rain products (see http://cetemps.aquila.infn.it).

As an example, Figure 6-22 shows the coverage of the C-band weather radar data (in false colours) in Central Italy, superimposed to the cloud coverage (in back/white) derived from Meteosat-8 image on July 23, 2006.

Moreover, ULS manages in Rome at the Engineering Faculty a radio-meteorological test site which includes the instrumentation listed in Table 6-10.

Meteo Radar	9.6 GHz, antenna 1 m	ELDES Property
Meteo station equipment	3 Raingauges, humidity, pressure, temperature	ULS Property
Ku and Ka Radiometer	13, 23 and 31 GHz	ASI Property
Ceilometer Lidar	0.9 micron – Mini-Lidar	ULS Property
Propagation Station	Receiver 20 GHz, antenna 1.5 m	ASI Property

Table 6-10: Main facilities of Rome ULS station

All the previously described test sites might be exploited in addition to the transportable station measurements in synergy with all other ancillary data to characterize the W-band satellite channel experiment.

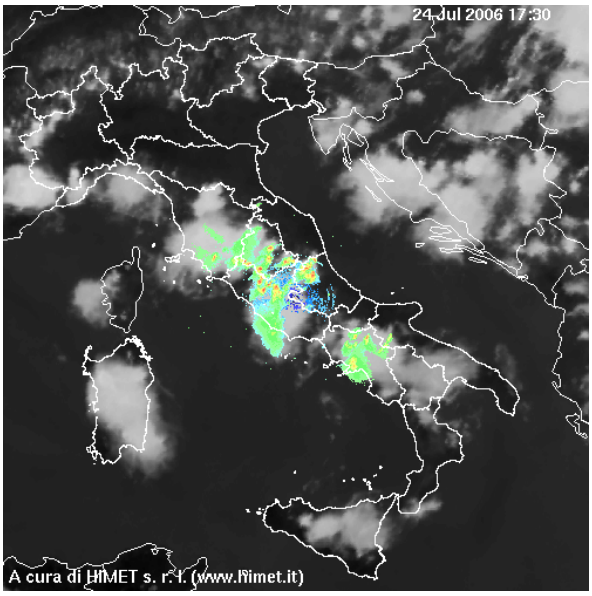

Figure 6-22: Coverage of the C-band weather radar data located at M. Midia in Central Italy

6.1.7 CONTROL SEGMENT AND DATA ACQUISITION AND PROCESSING CENTRE

The IKNOW control segment can be divided into a Mission Control and Planning Centre (MCC) and a Satellite Control Centre (SCC). The latter can be further divided into a P/L control station and a platform control station. The P/L and platform operational manoeuvres that have to be performed in the IKNOW Mission are strictly related to the needs of the scientific data users. In order to meet these needs, the mission control segment and the satellite control centre should be located within the same area. In this framework, it could be very useful to foresee a control station (both for mission and satellite) located in the Engineering Faculty of the University of Rome "Tor Vergata", together with the acquisition and processing centre. The P/L control station will consist of a computer station which will enable the definition of the satellite mission planning according to the user requests coming from the User interface. The User Interface is based on a second work station and it is fully dedicated to the Web connection with the scientific mission users. Most of the mission control activities will be performed inside this centre, which is

also responsible for the preparation of MCMDs (Macro-Commands) and satellite status control.

The satellite control station is a computer station which only transmits and receives telemetries. As already introduced it could be located in the University of Rome Tor Vergata. This class of satellites in fact has no critical control issues and there are other examples of scientific satellites (of the same IKNOW class) controlled by Universities. Alternatively, the platform control centre may be located within the Fucino Control Centre while maintaining the satellite control centre in Tor Vergata.

The presence of other stations located at different latitudes would allow the optimization of satellite resources. This is valid only in case that:

- the telemetry link needs same pointing to ground (because during measurement the satellite is pointed toward the ground station),
- the satellite resources (mostly power can't permit simultaneous operations).

A "training time period" of about 6 months could be scheduled, in which expert industrial Companies like TPZ could skill Tor Vergata engineers in control and operational manoeuvres. Then, in the latter 18 months of the P/L lifetime, the University of Rome Tor Vergata could control and maintain the IKNOW satellite. This kind of approach will guarantee a high reliability standard for the first and more crucial activities (the first 6 months) and it will heavily reduce the overall mission operational costs thanks to the moderate-cost of the University engineering staff. It is evident that during the "training time period" the IKNOW Mission will be fully operative. Basically, the function of the control station is monitoring the status of the satellite and tracking the precise position of the satellite through TT&C channel. The TT&C subsystem will operate in the "standard" S frequency band (during the future phase A2 activities transmitter and receiver central frequencies and bands will be defined). Other alternatives can be explored ranging from UHF to X-band. This latter would be very useful in order to reduce the "crowd" on the S frequency. The same channel is also used to send the information about the reception on the satellite of the signal transmitted by the ground station. After that, those information are sent from the Control Station to the Data Acquisition Centre. The overall system operational picture is provided in Figure 6-23. The picture summarises all the previously introduced functionalities and relations between the system elements.

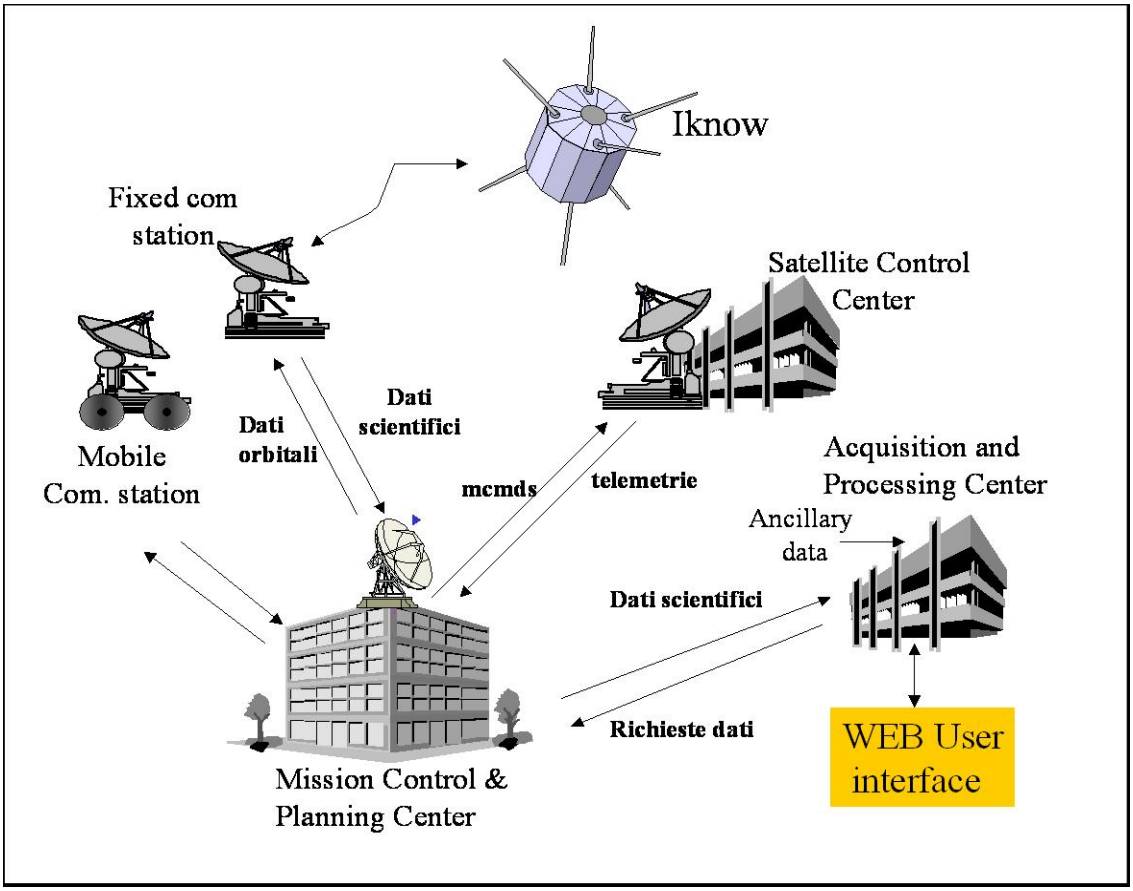

Figure 6-23: IKNOW System Architecture

6.1.8 DATA PROCESSING CONSIDERATIONS

As previously introduced, the Data Acquisition Centre basically collects and stores all the information coming from:

- the control station about the reception on the satellite of the beacon coming from the ground stations;
- the ground stations about the reception of the beacon coming from the satellite (and power measurements);
- ancillary data collection. The collection of ancillary data like meteo data, atmospheric data, etc. is essential to better evaluate and process the scientific data.

As mentioned, the state of the atmosphere can be estimated from a synergic use of weather observation instruments such as weather stations, radio soundings, ground-based microwave radiometers, ground-based microwave radars, aircraft cloud probes and

satellite-based microwave and infrared radiometers coupled with numerical weather forecast model outputs. Data from both models and instruments should be processed in the APS as follows:

- numerical weather forecast model outputs are acquired for the area of interest and for the season of the experimental campaign in order to construct a significant METEO archive of space-time atmospheric variables;
- a propagation model is developed and set up to derived path attenuation, phase shift and noise temperature at W band from the METEO archive data;
- from the coupled METEO-PROP archive and from the specification of the W-band experimental channels, the space-time mapping of C/N is derived in terms of first- and second-order statistics conditioned to surface conditions, cloud coverage and rainfall;
- during the planned experimental campaigns:
    - measurements of available weather stations and radiosoundings are processed to acquire surface and vertical profiles of pressure, temperature and humidity ;
    - measurements of available ground-based weather radars are processed to estimate range-resolved rainfall and hail;
    - measurements of available ground-based microwave radiometers are processed to estimate integrated water vapour and cloud liquid water ;
    - measurements of available satellite-based microwave and infrared radiometers are processed to estimate cloud coverage and rainfall;
    - measurements of available aircraft cloud probes are processed to estimate cloud particle size distributions;
    - data of numerical weather forecast model outputs are processed to plan the campaign and to compare with available measurements;
    - the METEO-PROP model at W band is applied to weather forecast numerical outputs to derive radiometeorological maps;
- the available W-band channel measurements, taken from ground receivers during the campaign, are compared with the results of METEO-PROP models in terms of:
    - statistical prediction of path attenuation, phase shift and noise temperature based on available meteorological measurements;

- deterministic prediction based on the METEO-PROP model applied to available weather forecast numerical outputs;

- error budget of both statistical and deterministic prediction is analyzed and W-band METEO-PROP model eventually refined.

6.1.8.1 Meteorological data considerations

In this section, the primary meteorological data needed for channel characterization are defined, providing also a priority assessment.

Then, the eventual costs of utilization of the instruments/equipment previously identified are preliminarily derived.

Among the meteorological data needed to set up a robust propagation model at W band, we can list in possible order of priority:

1. measurements of weather stations and radiosoundings to derive surface and vertical profiles of pressure, temperature and humidity ;
2. measurements of ground-based weather radars to estimate range-resolved rainfall and hail;
3. measurements of ground-based microwave radiometers to estimate integrated water vapor and cloud liquid water ;
4. measurements of satellite-based microwave and infrared radiometers to estimate cloud coverage and rainfall;
5. measurements of aircraft cloud probes to estimate cloud particle size distributions;
6. data of numerical weather forecast model outputs to derive pressure, temperature, humidity, water content spatial distribution fields.

The costs of each source are dictated mainly by:

- period interval of requests;
- type of product and processing level;
- availability and delivery.

In a schematic way it can be indicated that, apart from the person-months needed to process and deliver data:

1. radiosounding data are provided by the Italian Air Force and may be available at a free cost under a ASI agreement;

2. ground-based radar data can be acquired at a cost of about 3-5000 Eu/month or for a dedicated portable system at 15-20000 Eu/month;
3. microwave radiometer data may be obtained within the project by financing the system operations of the involved groups ;
4. satellite data may be obtained by Eumetsat at a cost of about 3-5000 Eu/month; ;
5. dedicated numerical outputs may be acquired at a cost of about Eu 10-15000 Eu/month.

Of course, this estimate does not include:

- costs for the processing and integration of overall data;
- costs for W-band propagation model set up;
- error budget evaluation and model refinents;
- activity coordination

6.2 IKNOW P/L DESIGN

Next sections will detail the IKNOW P/L design and architecture and will provide a detailed and updated review of the P/L technical requirements [6-8], [6-13] and [6-14].
The IKNOW basic configuration is composed of four main subsystems:

- Tx chain;
- Rx chain;
- P/L controller;
- P/L power supply.

These subsystems are described in the following sections. In Figure 6-24, the functional block diagram is provided.

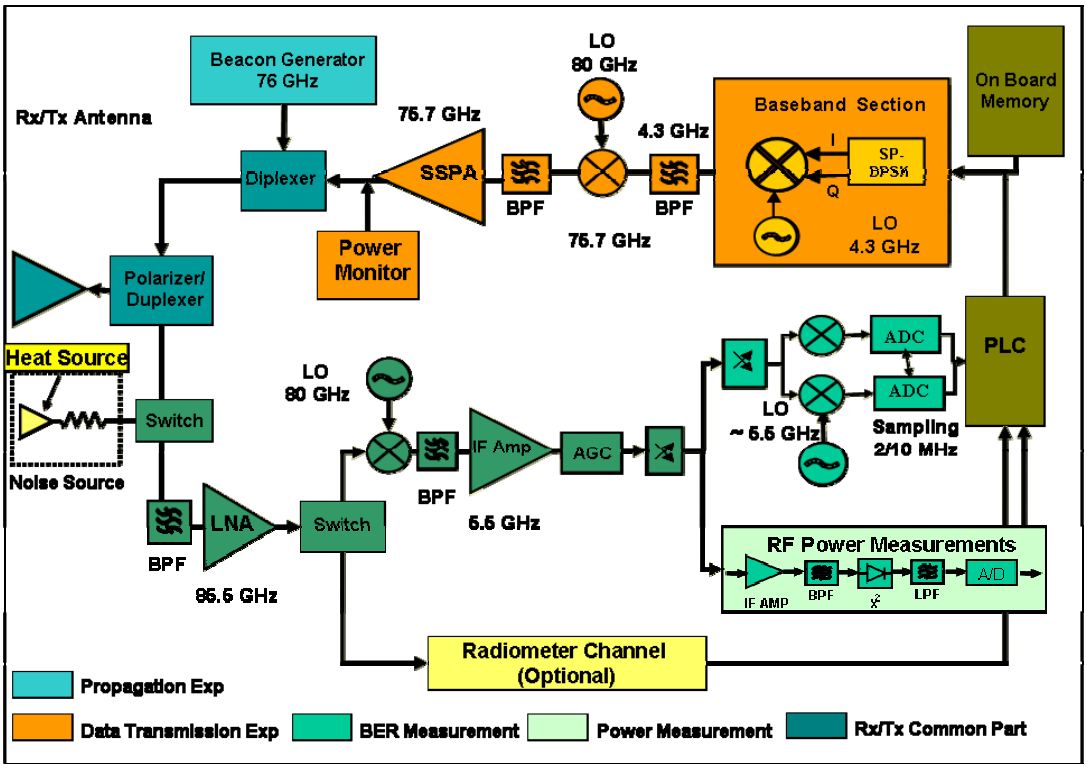

Figure 6-24: IKNOW P/L functional diagram

It can be noted the modulator in the transmission chain and a full heterodyne chain in reception. A I & Q approach has been selected in order to down the ADC sampling frequency. The idea is to transmit the signal from ground in packets that are received and sampled from the Rx chain and stored into the PLC. Then the PLC, by suitable SDR (Sequence Determined Redundancy) technique, will process in batch time the data extracting all the scientific information as:

- BER;
- Signal E_b/N_o and C /N_o;
- Statistical evaluation;
- Samples of data stream;
- Etc.

The synthesis of all those information will be later sent to ground for further evaluation. Let's consider that the P/L operation time will be no more than few minutes per day and therefore the PLC has a long time to process the data. The important aspect is the availability of an on-board memory to store the packets received from ground but, even in

case of the adoption of an analogical demodulator, the matter remains unchanged with a reduced flexibility to change the modulation scheme. The system frequency plan have been optimised and, through the use of a two basic local oscillator at 80 GHz and one at 4.3 GHz, we can reduce the number of devices employed, lowering on-board mass and power consumption. Finally, image rejection mixer is still applicable in the second down-conversion to reduce the complexity of IF filters.

6.2.1 TX CHAIN

The propagation experiment transmitting chain is devoted to the generation and transmission of a W band beacon.
It basically implements the following functions:

- Beacon generation at ~ 75.7 GHz;
- Beacon signal power amplification;
- Beacon transmission by antenna;
- Tx power measurement by power monitor circuit.

The power monitor is an essential element for getting the measurement accuracy since it measures the SSPA output power. In addition, several temperature measurement devices will be properly placed in the most sensitive points. Those measurements will be characterised on ground as function of transmitting power variation with temperature.
From a physical point of view, the transmitting chain is based on:

- Antenna;
- SSPA that includes PA and EPC (Electronic Power Conditioner);
- Beacon generator;
- Waveguide coupler;
- Waveguides;
- Power monitor circuit with thermal stabilisation.

In addition, the Tx chain has to perform the SP-BPSK signal generation for the channel quality evaluation experiment.

6.2.2 RX CHAIN

The modulated signal Rx chain implements the following functions:

- signal reception at 85.5 GHz;
- signal low noise amplification;
- signal filtering at +/-250 MHz around central frequency;
- signal beacon filtering at 10 MHz (nominal);
- signal AGC;
- signal down-conversion and detection;
- signal ADC;
- digital signal transmission to the PLC;
- coupling radiometer channel;
- radiometer signal detection;
- radiometer signal integration with selectable time constant;
- noise/gain calibration.

The propagation experiment Rx chain, devoted to the reception of W band beacon and radiometry function, implements the following functions:

- signal beacon reception at 85.5 GHz;
- signal low noise amplification;
- signal filtering at +/-250 MHz around central frequency;
- signal beacon filtering at 100 kHz;
- signal beacon AGC (Automatic Gain Control);
- signal beacon detection;
- signal beacon integration with selectable time constant;
- integrated signals (both beacon and radiometer) digital conversion;
- digital signal transmission to the PLC;
- switch radiometer channel;
- radiometer signal detection;
- radiometer signal integration with selectable time constant;
- noise/gain calibration.

The receiver calibration is performed by switching the RF device (a wave-guide switch or a latching circulator, to be decided during next phases), placed just before of the LNA, to the load. This is an attenuator connected to a noise source. Such a configuration will allow to carry out a three-points calibration. In fact, the receiver can alternatively receive signals

from the space (the cosmic microwave background at 2.7 K), from a matched load and from a heat source when switched on. So it is possible to use the calibration path both with and without the noise source creating two reference points for gain and noise figure calculation. In addition, as mentioned before, there will be the external calibration based on known target (2.7 K).

An AGC function is requested to cope with the signal dynamic and the Rx chain gain variation to properly setting the signal into the detector and the ADC (Analog Digital Converter) dynamics.

The signal dynamics is influenced by:

- Atmospheric conditions (~12-16 dB expected additional attenuation, for 1% of total time);
- Satellite altitude (~700 km with an orbit decay estimated of about 20 km);
- Angle of view (+/- 20° both in elevation and azimuth);
- Gain variation due to temperature (2-5 dB expected in OFTR, Over Full Temperature Range, without temperature compensation);
- Noise figure variation (expected limited to 0.1/0.2 dB).

A total value of ~24 dB dynamic range is considered reasonable at this stage of the project. Without the AGC at least two bit of ADC dynamics would be lost. The AGC setting step will be 1 dB.

The very strict requirement imposed to signal power measurement accuracy leads to envisage the need of the Rx chain temperature stabilisation. However, values the few tenths of dB requested for measurement accuracy can not be reasonable maintained without same in-flight calibration procedure. On the other hand, the total power radiometer accuracy is strongly affected by the lack of a noise/gain calibration.

The Rx gain variation and setting can be computed by Rx noise integration over suitable time interval by combining the integrator measurement and PLC average computation. Of course, the measurement accuracy is a function of the integration time. It should be noted that, during the P/L operation, particularly for the radiometer, it is important to consider the position of the angle of sun with respect to the P/L antenna.

In fact, sun ray can reach the Rx antenna and might affect P/L noise figure. Because the radiometer does not work simultaneously with the beacon reception, only one AD converter is used.

The integration constants will be selectable in a range of values. It is worth to mention that anyway a second integration can be done in the PLC so reducing the data rate to ground. The Rx chain will be able to operate independently from the Tx chain so improving the overall system reliability and reducing the power consumption when the radiometer mode is used.

6.2.3 P/L CONTROLLER (PLC)

The P/L controller is devoted to the control and management of the IKNOW P/L.
The functions of PLC are:

- to receive commands from OBC (On-Board Computer);
- to switch on/off IKNOW payload equipment by commanding PSU (Power Supply Unit);
- to control and implement operative modes;
- to collect science data and telemetries;
- to transmit science data and telemetries to OBC;
- to buffer science and telemetries data for one orbit pass;
- to control telemetries and communicate to OBC outages;
- reprogrammability.

During the P/L contact operation, the PLC will store the data in its memory than the Tx and Rx chains are switched off and the data processing begins.

6.2.4 POWER SUPPLY UNIT

The Power Supply Unit (PSU) is devoted to the generation of suitable supply voltages for the P/L operations. Functions of PSU are identified in the following items:

- to receive unregulated bus from platform;
- to receive commands from the PLC;
- to regulate voltage;
- to generate the IKNOW P/L supply voltages;
- to implement protections (over-voltage, short-circuit, etc.);
- to provide power consumption and status telemetries to the PLC.

The PSU is designed as single element and it can be accommodated behind the PLC.

6.2.5 PROPAGATION EXPERIMENT P/L REQUIREMENT

In this section an updated and detailed list of the main requirements of the propagation experiment payload are reported on the basis of the following items:

- Tx chain;
- Rx chain;
- Common requirements;
- P/L design.

6.2.5.1 TX CHAIN

The Tx W-band signal beacon to ground will have a CW frequency in the range 75.7 GHz +/-100 MHz, the frequency stability has to be less than 10-7 OFTR, EOL. The Tx EIRP has to be greater than 23.5 dBW, qith a stability > 0.1 dB OFTR. The antenna beamwidth is 3°, while the power meter measurement accuracy is set to 0.1 dB OFTR.

6.2.5.2 RX CHAIN

For the Radiometer mode the BW is set to 500 MHz (TBC), while the integration time will be selectable 10-1000 ms / with step 10 ms (TBC). The same ADC of the signal beacon could be used: 12/14.

The Rx beacon mode will have a CW frequency in the range 85.5 GHz+/- 250 MHz, with an input signal level of -174.5 –154.5 dBW. The Rx gain knowledge/stability should be greater than 0.15 dB OFTR. The Rx figure of merit will be greater than 2.8 dB/K OFTR. The antenna beamwidth is 3°. The detected signal integration time will be selectable: 10-1000 ms/ step 10ms (TBC). For the Calibration mode a noise source of 130 dBm (TBC) has been identified.

6.2.5.3 COMMON REQUIREMENTS

In this section the main common requirements are summarised:

1. P/L operative temperature range (OFTR): 0-50 °C;
2. power supply: un-regulated bus (24-37 V);
3. power consumption: < 10 W during operation, 3 in warm-up, 0 in off;
4. P/L mass: < 10 kg (TBC);

5. maximum size: 400 mm x 400 mm x 150 mm;
6. temperature telemetries accuracy: 0.1°(TBC) OFTR;
7. CAN bus or equivalent;
8. mission scientific data rate: < 1 kbits.

6.2.5.4 P/L DESIGN

In the P/L design one of the major requirements is the maximum reuse of existing HW or COTS, in order to reduce the technological developments. Moreover, no redundancy is requested (Rx and Tx chain should be decoupled and commanded separately from the operation point of view).

6.2.6 CHANNEL QUALITY EXPERIMENT P/L REQUIREMENTS

In this section a detailed list of main requirements of the channel quality experiment payload are reported on the basis of the following items:

- Tx chain;
- Rx chain;
- Common requirements;
- P/L design.

6.2.6.1 TX CHAIN

The Tx W-band signal beacon to ground will have the same characteristics of the propagation experiment.
Tx W band modulated signal will have a central frequency selectable in the range: 75.7 GHz+/- 100 MHz; the modulation type used is BPSK/SP-BPSK.

6.2.6.2 RX CHAIN

For the Radiometer and Rx beacon mode the same characteristics of the propagation experiments have been defined. For the Rx modulation mode the harmonic and sporious is set to -60 dBc, while the maximum input signal BW is 10 MHz. The ADC has 4 bits.

6.2.6.3 COMMON REQUIREMENTS

In this section the main common requirements are summarised:

1. P/L operative temperature range (OFTR): 0-50 °C;
2. Power supply: un-regolated bus (24-37 V);
3. power consumption: < 25 W during operation, 3 in warm-up, 0 in off;
4. P/L mass: < 15 kg;
5. maximum dimension: 400 mm x 400 mm x 150 mm;
6. temperature telemetries accuracy: 0.1°(TBC) OFTR;
7. CAN bus or equivalent;
8. mission scientific data rate: < 1 kbits.

6.2.6.4 P/L DESIGN

The P/L design requirements are the same identified for the propagation experiment.

6.2.7 OPERATIVE MODES

The IKNOW P/L operative modes are depicted in Figure 6-25.

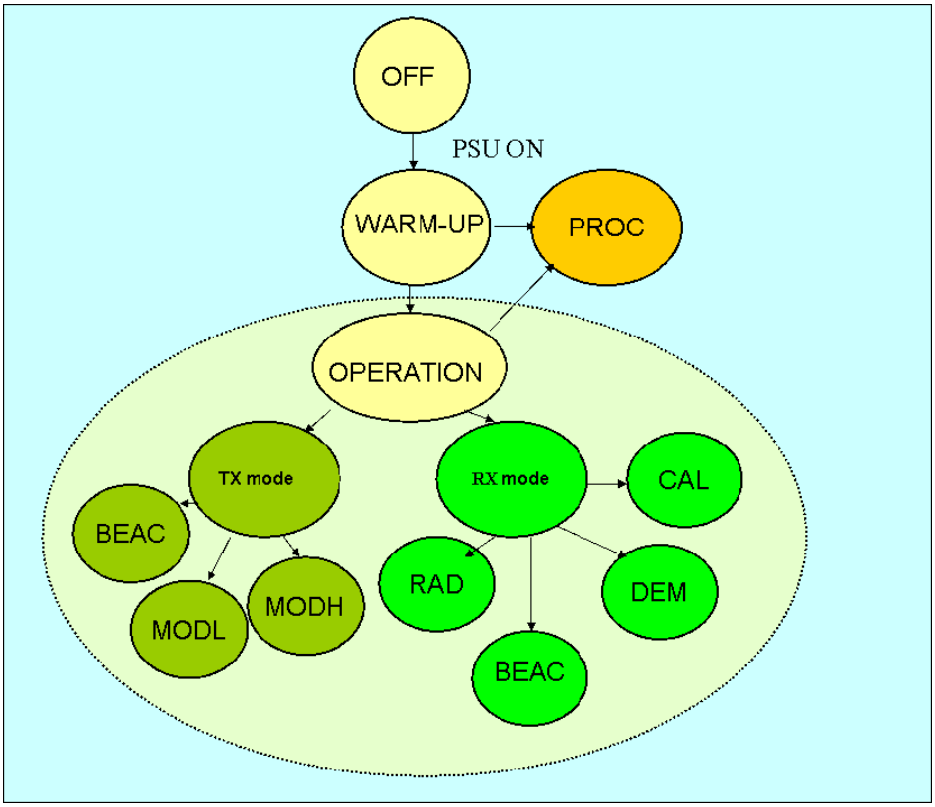

Figure 6-25: Operative Modes for the Full Configuration

The Rx data could be sent to ground by the platform for further processing. During the warm-up phase, it will be possible to reprogram the P/L controller. Basically, during the warm-up, only the computer and the frequency oscillators, needing same warm-up time, will be switched-on.

6.2.8 P/L TRADE–OFFS

Potential trade-offs, that will be evaluated during the following phases of the project, are:

1. one or two antennas;
2. radiometer scheme: homodyne or heterodyne;
3. number of frequency conversions;
4. power supply concentrated or distributed;
5. type of processor: DSP or FPGA or CPU;
6. RF switch or latching circulator for Rx calibration.

The following considerations can be highlighted for each item:

1. The Tx and Rx antennas can be combined in a single equipment and the separation of the two chains is made by a circulator or diplexer or can be completely separated. The selection is based on cost and volume trade-off of the two antennas with respect to a single one.
2. The radiometer detection can be implemented at W band or after the first conversion. The second solution should be preferred considering the components availability.
3. There are several technical considerations to be done. It is possible to have one, two or three frequency conversions. Two conversions should be the preferred solution. Generally, a higher number is selected to keep at minimum the RF distortions. The PLL to track the Rx frequency can be implemented in W or by software as it is chosen here. A digital PLL/NCO is embedded into the software to recover and to annul the Doppler frequency.
4. There are main design options for the power supply. Basically, a design with one converter to regulate the primary supply voltage and several voltage regulators, one for each unit (Tx chain, Rx chain, controller) will be selected.
5. The Processor selection will be based on cost and availability of the components.

6. The Latching circulator is faster and probably more reliable, however is more expensive.

6.2.9 P/L EQUIPMENT PRELIMINARY SPECIFICATIONS

This section is devoted to provide preliminary technical specifications of the main P/L equipment.

6.2.9.1 Antenna Specifications

On the basis of the trade-off carried out during project activities among different types of configurations (direct radiating array antenna, reflector antenna, lens antenna) and considering the present technological state of the art in W-band, the most adequate antenna configuration for spatial application at these high frequencies seems to be a reflector antenna. The main reasons of this choice are: technological maturity, costs, weight, robustness, sub-system complexity, electrical performances at W-band. The single reflector antenna is preferred respect to the dual reflector, because of its low architectural complexity and losses (alignment and blockage). Therefore, the candidate baseline configuration foresees a single reflector-type antenna (suitable both for receiving and transmitting sections), onset or offset (to be defined in following phases of the study) fed by a single feed.

The main specifications of the antenna in receiving and transmitting mode are reported in Table 6-11.

Parameter	Rx	Tx
Frequency (GHz)	85.5	75.7
Diameter (mm)	110	110
Bandwidth	TBD	TBD
Minimum Gain (dBi)	36.4	35.3
Efficiency	65 %	60%
HPBW (°)	2.2	2.4
Side Lobe Isolation	> 25 dB (TBC)	> 20 dB (TBC)
Cross-polarization Isolation	> 15 dB (TBC)	> 15 dB (TBC)

Table 6-11: Specifications of the IKNOW Single Antenna

6.2.9.1.1 Preliminary Antenna Electrical Design

In this paragraph, both offset and onset configurations for the single reflector antenna fed by a single feed have been investigated and illustrated. The selected optic presents a reflector with an aperture diameter of 110 mm and an F/D of 0.5.

6.2.9.1.1.1 Antenna Reflector Offset Configuration

Main geometrical characteristics of antenna offset configuration are illustrated in Figure 6-26 and summarized in Table 6-12.

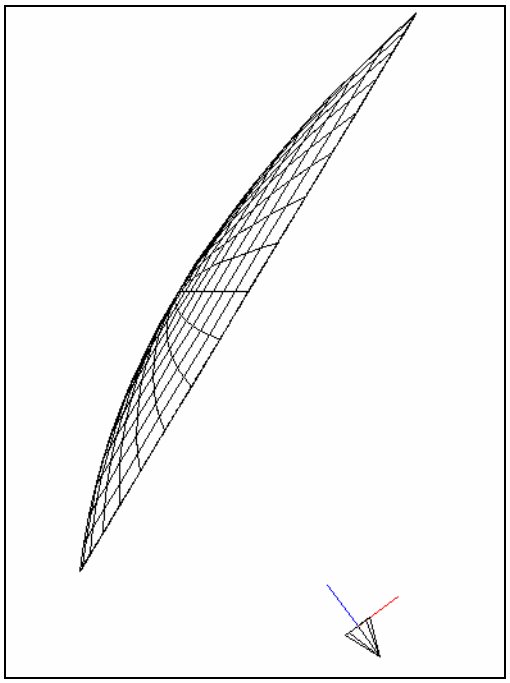

Figure 6-26: Single Reflector Offset Antenna Configuration

Aperture Diameter [mm]	**110.0**
Focal Length [mm]	**55.0**
Clearance [mm]	**11.0**
Feed Diameter [mm]	**6.0**
Feed Type	**Potter Horn**
Feed Polarization	**LHCP**

Table 6-12: Single Reflector Offset Antenna Main Geometrical Parameters

A theoretical feed model has been selected to perform preliminarly antenna analysis. It is a Potter Horn with circular aperture of about 6 mm, working in LHCP. Theoretical feed pattern cuts, respectively at 85.5 GHz and 75.7 GHz, are shown in Figure 6-27.

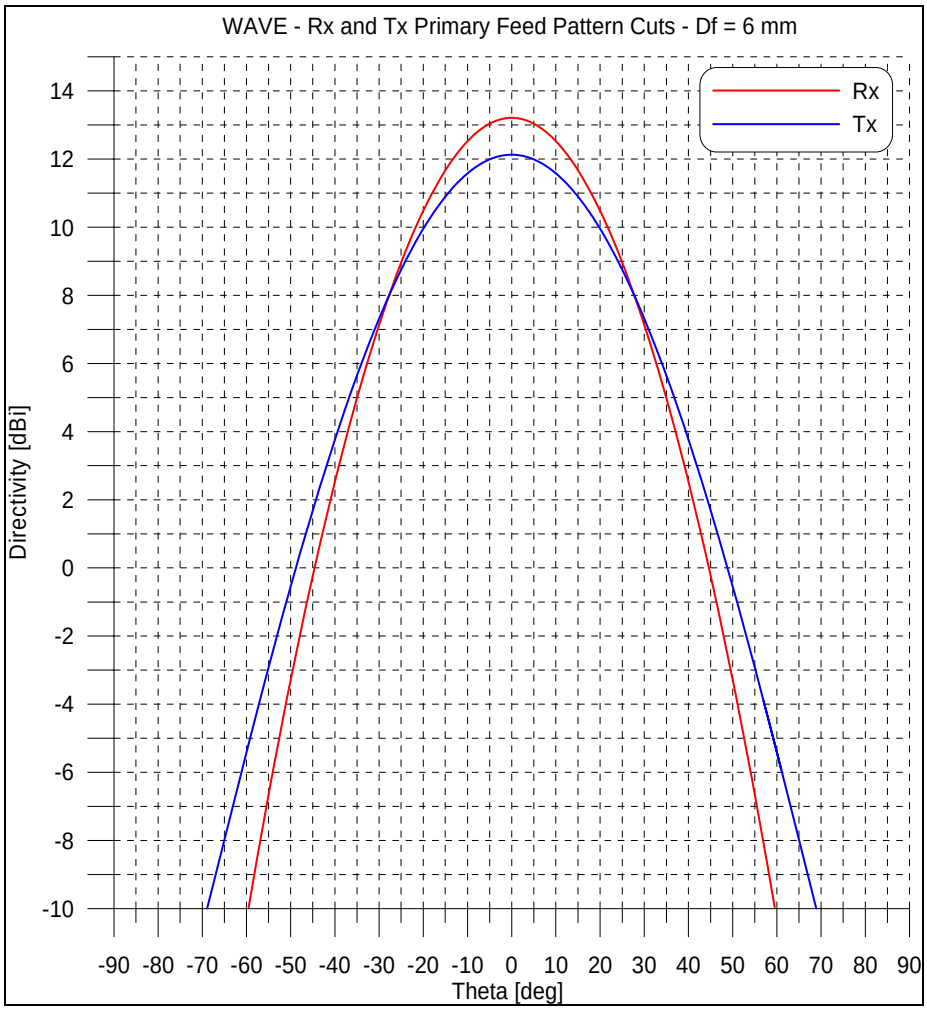

Figure 6-27: Rx and Tx Primary Feed Pattern Cuts – Onset Configuration

In Table 6-13, antenna electrical performance at Tx and Rx bands are reported.

Parameters	Tx	Rx
Frequency [GHz]	75.7	85.5
Directivity Peak [dBi]	37.5	38.6
HPBW [deg]	2.4	2.2
SLL [dB]	26.5	30.6

Table 6-13: Single Reflector Offset Antenna Electrical Performance

In Table 6-14, preliminary antenna loss budget has been carried out. Losses items, reported in the budget, are based on performance of commercial products currently on international market.

Parameters	Tx	Rx
Frequency [GHz]	75.7	85.5
DIRECTIVITY PEAK [dBi]	37.5	38.6
Pointing Losses	0.50	0.60
MINIMUM DIRECTIVITY [dBi]	**37.00**	**38.00**
FEED SYSTEM (RF chain: OMT + Polarizer)	0.80	1.00
REFLECTOR (Ohmic)	0.10	0.10
SUBTOTAL OHMIC LOSSES	0.90	1.10
THERMAL+ MANUFACTURING+ DESIGN (SUBTOTAL RSS)	0.30	0.35
TOTAL LOSSES	**1,20**	**1,45**
MINIMUM GAIN [dBi]	**35.80**	**36.55**
Requested Minimum Gain [dBi] (Spec.)	35.30	36.40

Table 6-14: W-band Antenna Loss Budgets – Offset Configuration

In Figure 6-28, the antenna pattern cuts are illustrated, respectively, at 75.7 and 85.5 GHz. Directivity contour plots for the proposed single reflector offset antenna configuration are reported in Figure 6-29 and Figure 6-30.

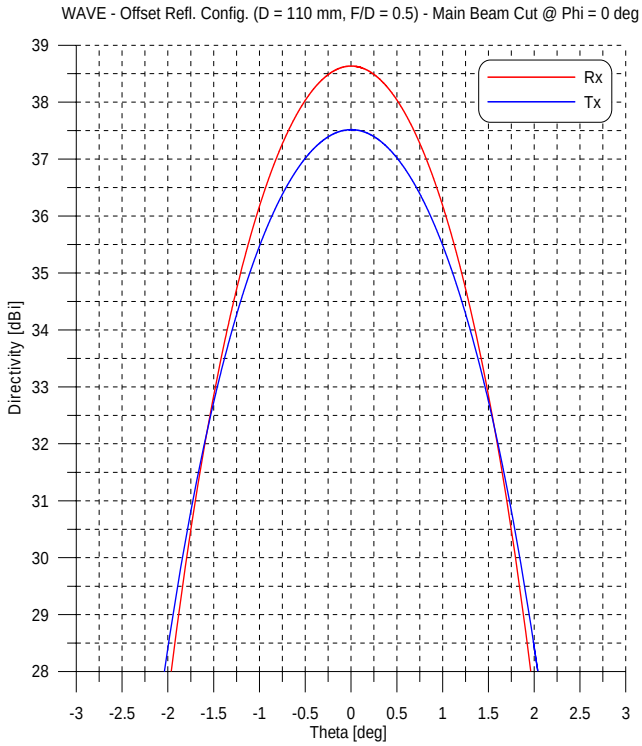

Figure 6-28: Rx and Tx Antenna Reflector Offset Configuration Pattern Cuts @90 deg

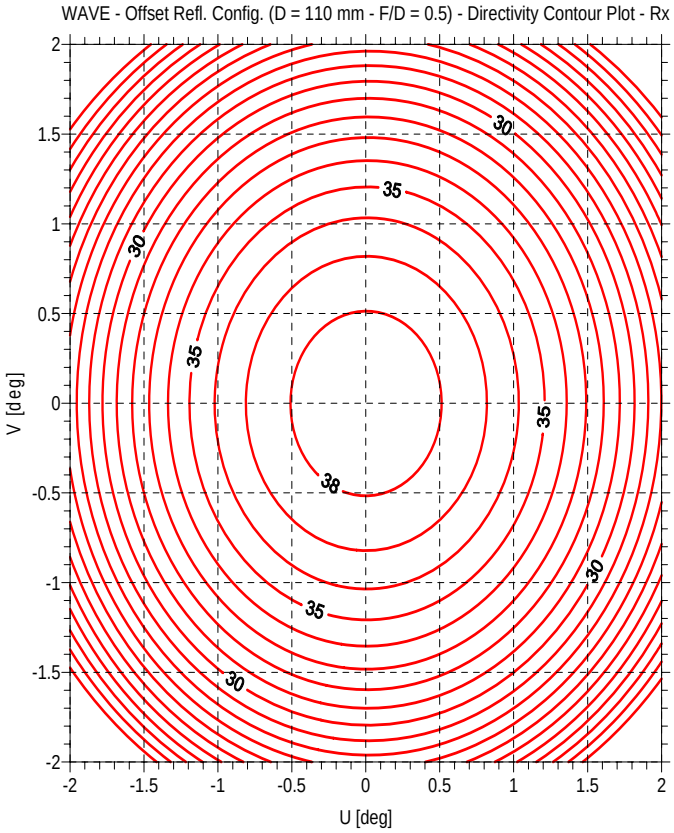

Figure 6-29: Single Reflector Offset Antenna Directivity Contour Plot @ 85.5 GHz

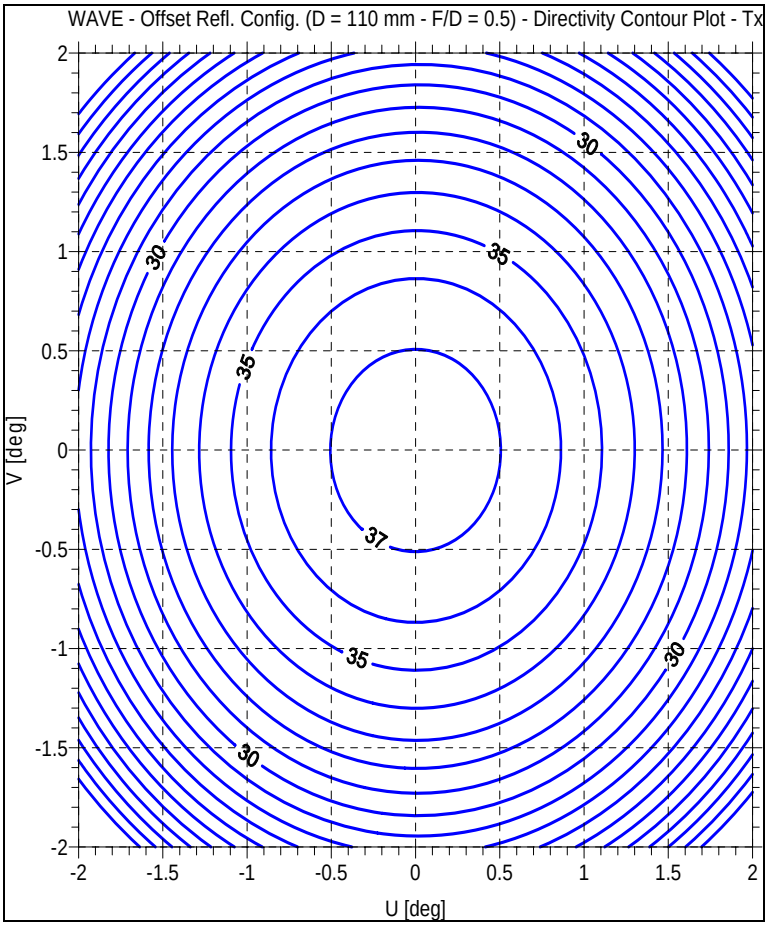

Figure 6-30: Single Reflector Offset Antenna Directivity Contour Plot @ 75.7 GHz

6.2.9.1.1.2 Antenna Reflector Onset Configuration

Main geometrical characteristics of antenna offset configuration are illustrated in Figure 6-31 and summarized in Table 6-15.

Aperture Diameter [mm]	110.0
Focal Length [mm]	55.0
Feed Diameter [mm]	4.8
Feed Type	Potter Horn
Feed Polarization	LHCP

Table 6-15: Single Reflector Onset Antenna Main Geometrical Parameters

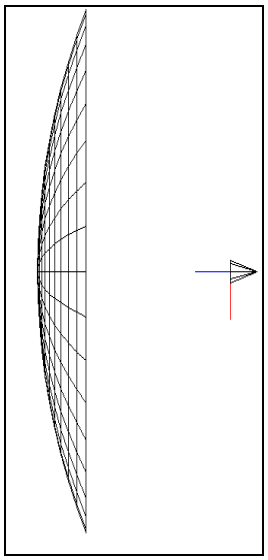

Figure 6-31: Single Reflector Onset Antenna Configuration

A theoretical feed model has been selected to perform preliminary antenna analyses. It is a Potter Horn with circular aperture of about 6 mm, working in LHCP. Theoretical feed pattern cuts, respectively at 85.5 GHz and 75.7 GHz, are shown in Figure 6-32.

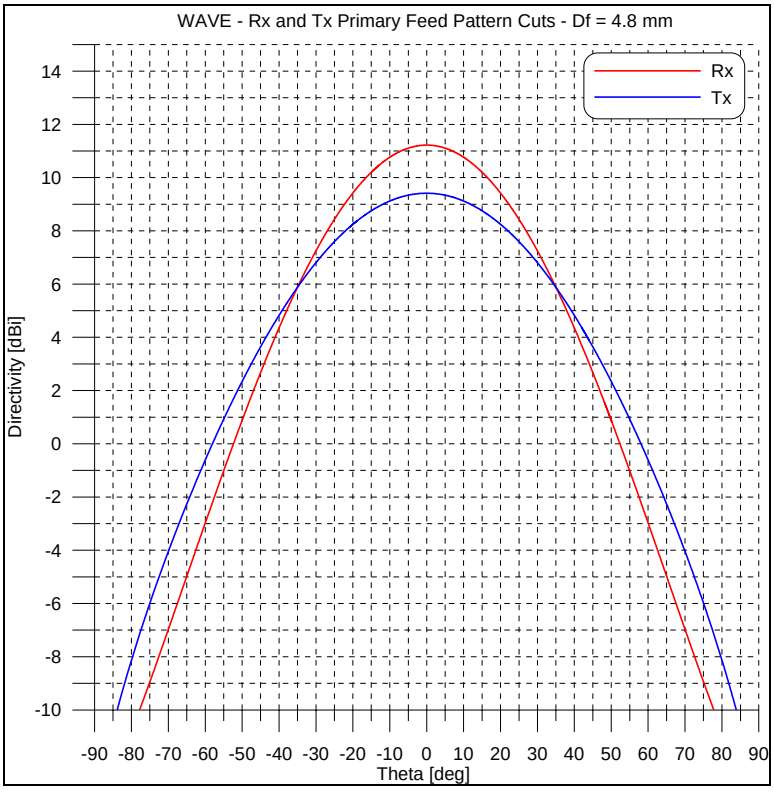

Figure 6-32: Rx and Tx Primary Feed Pattern Cuts – Onset Configuration

In Table 6-16, antenna electrical performances in Tx and Rx bands are reported.

Parameters	Tx	Rx
Frequency [GHz]	75.7	85.5
Directivity Peak [dBi]	37.4	38.6
HPBW [deg]	2.4	2.2
SLL [dB]	24.4	29.6

Table 6-16: Single Reflector Onset Antenna Electrical Performance

In Table 6-17, preliminary antenna loss budget has been carried out. Losses items presented in the budget are based on performance of commercial products currently presented on international market.

Parameters	Tx	Rx
Frequency [GHz]	75.7	85.5
DIRECTIVITY PEAK [dBi]	37.4	38.6
Pointing Losses	0.50	0.60
MINIMUM DIRECTIVITY [dBi]	**36.90**	**38.00**
FEED SYSTEM (RF chain: OMT + Polarizer)	0.80	1.00
REFLECTOR (Ohmic)	0.10	0.10
SUBTOTAL OHMIC LOSSES	0.90	1.10
THERMAL+ MANUFACTURING+ DESIGN (SUBTOTAL RSS)	0.30	0.35
TOTAL LOSSES	**1,20**	**1,45**
MINIMUM GAIN [dBi]	**35.70**	**36.55**
Requested Minimum Gain [dBi] (Spec.)	35.30	36.40

Table 6-17: W-band Antenna Loss Budgets – Onset Configuration

In Figure 6-33 the antenna pattern cuts are illustrated at 75.7 and 85.5 GHz. Directivity contour plots for the proposed single reflector onset antenna configuration are reported in Figure 6-34 and Figure 6-35.

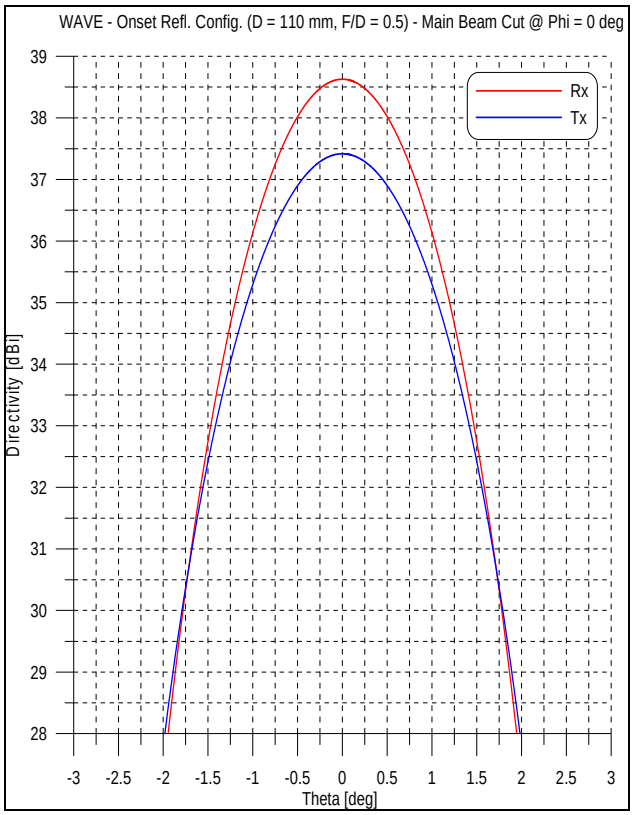

Figure 6-33: Single Reflector Onset Antenna Pattern Cut

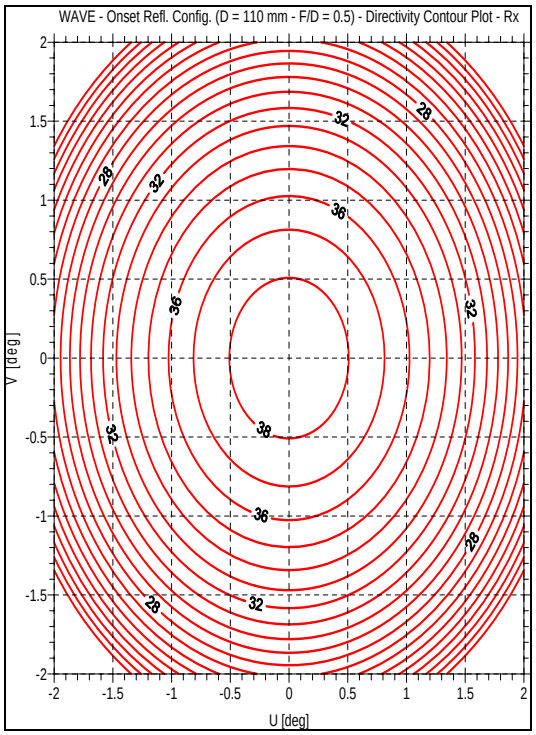

Figure 6-34: Single Reflector Onset Antenna Directivity Contour Plot @ 85.5 GHz

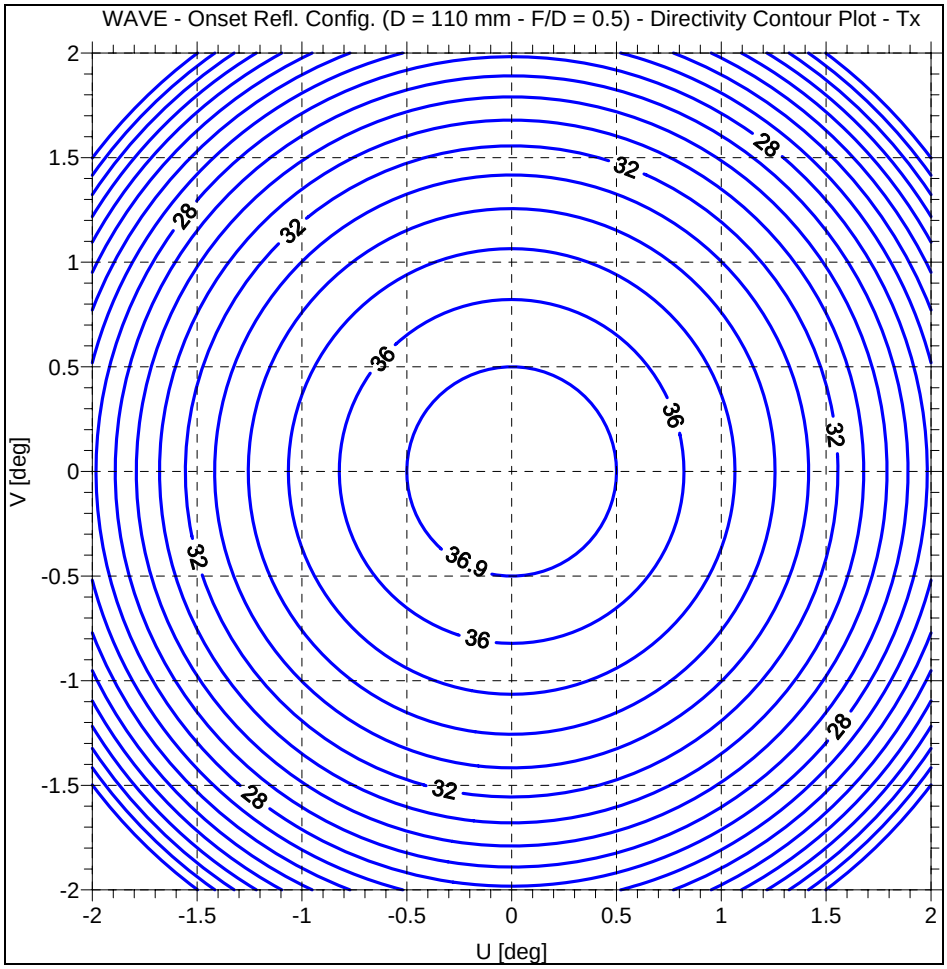

Figure 6-35: Single Reflector Onset Antenna Directivity Contour Plot @ 75.7 GHz

The carried out design activities underlines the fact that, even if the onset configuration performs better than the offset one, it presents more blockage losses.

The wavelength at W-band is much lower than that of the microwaves thus requiring tight tolerances to achieve the desired performance.

Typical dimension and alignment tolerances for W band could be considered +12 μm on waveguide, and surface finish of 0.25 micrometer Ra (source: DRDO, Ministry of Defence, India). The manufacturing is, then, the critical item to achieve excellent performance and, currently, only Electrical Discharge Machining and Electroforming are techniques to be used with success.

In our case, Electroforming seems to be the most promising technology for the primary source (feeds and/or waveguides) with Electrolytic copper used as a tool electrode material. On the contrary, Electrical Discharge Machining could represent a suitable solution for the reflector manufacturing.

6.2.9.2 Pointing System Specifications

Due to the low orbit of the satellite and to the small beamwidth, the visibility window during each pass would be only few seconds long without the implementation of the platform or antenna steering. Thus, it is mandatory to use a pointing system both in the ground and on-board antennas. The satellite antenna pointing could be realised using only the attitude control of the platform, maintaining the antenna fixed. Main pointing system specifications are reported in Table 6-18.

Pointing Specifications	
Pointing knowledge	0.01° pitch and roll, 0.05° yaw
Pointing accuracy	0.5° three axis (1° acceptable) (P/L included);
Platform stability	0,005° rms/s (TBC) all axes

Table 6-18: Specifications of the IKNOW Antennas

Anyway, during next more detailed study phases, also the possibility of using a pointing system capable of steering the antenna will be again taken into account, in order to better evaluate advantages and disadvantages of both configurations in terms of mass, performance and costs.

6.2.9.3 P/L Controller Specifications

The P/L controller, for both the configurations, should have, as preferred option, the following minimum characteristics:

- Clock: 100 MHz (typical);
- Radiation hardening (not mandatory, eventually, already space tested in other missions);
- Temperature operating range: -55 °C / + 125 °C;
- Interfaces for commands.

Specifically, on the basis of these elements, a suitable solution could be a modified version of the evaluation kit of the LEON2 Atmel ASIC, shown in Figure 6-36.

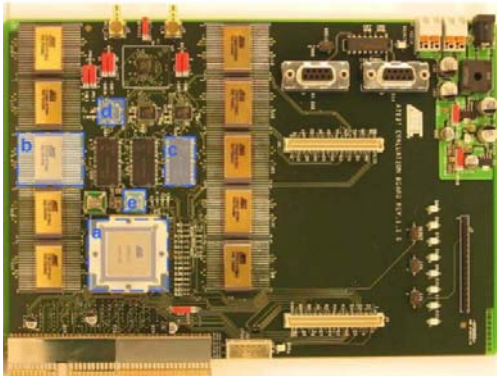

Figure 6-36: Atmel AT697 Evaluation Board

Main characteristics are hereafter reported:

- Main processor: Atmel AT697 (dimensions are 2.5 x 2.5 cm^2);
- Rad-Hard 512K x 8 Low Power CMOS SRAM, Atmel AT60142F, in 4+1 configuration for the checkbit (dimensions are 2.7 x 2.1 cm^2);
- 16 M x 16 (4M x 16 x 4 banks) Micron MT48LC16M16 SDRAM in 2+1 configuration for the checkbit (dimensions are 2.2 x 1.1 cm^2);
- 8-Mb (512 K x 16, 1M x 8) 3V Flash Memory, Atmel AT49BV802A, in two possible configurations: 1 M x 8 bit (1 chip), or 512 k x 40 bit (3 chip);
- Master clock, 25 MHz resonator connected in 4*F configuration (100 MHz).

The above board dimensions are 17 x 22 cm^2.
The board shall be completed with interfaces for commands and the bus connecting it to the OBC.

6.2.9.4 Receiver Specifications

The Rx chain is composed of the following elements:

- Antenna;
- Noise source;
- LNA;
- First down-conversion section (mixer and local oscillator);
- Filters;
- Couplers (two, at least);
- IF Amplifier (two);

- AGC;
- ADC;
- Second down-conversion section (90 degrees hybrid, mixer and local oscillator);
- Radiometer, optional (detector+ integrator+ ADC);
- Power monitor;
- Waveguides.

The receiver configuration is shown in Figure 6-23. The uplink signal is at first used to calibrate the receiver through the use of a noise source. In fact, a switch in the front-end, located before the LNA, allows to characterise gain and noise of the receiver. Such a section is designed as for the basic configuration. After the calibration stage, the signal is coupled in two chains: a first chain is devoted to carry out BER measurements in addition to detect signal power, a second chain is devoted to gather measurements through a radiometer channel. Such a second chain is optional for the full payload configuration. Both chains are filtered through a band-pass filter centred at 85.5 GHz and with a 500 MHz bandwidth. A switch in the chain allows for alternatively delivering the signal to the first or to the second chain, depending on the mission phase and in agreement with measurement modes. Such a switch could be operated by ground control or on the basis of time tag pre-defined and on-board stored.

Figure 6-37 shows these measurement modes for the P/L full configuration.

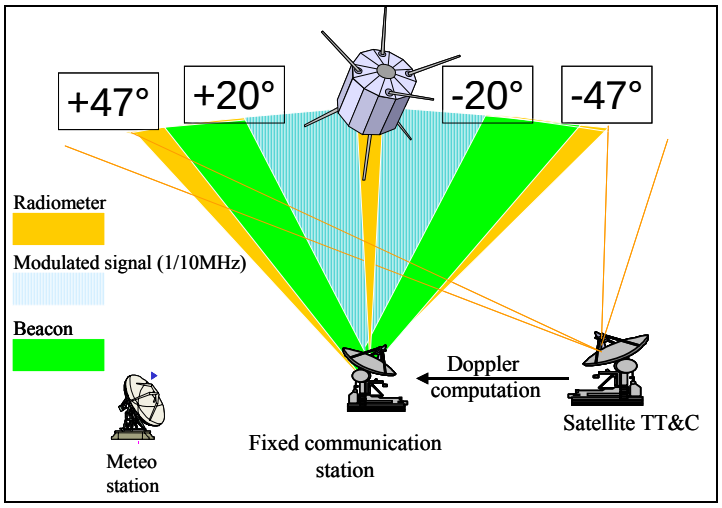

Figure 6-37: Ground Station Tracking and Measurement Modes for IKNOW Full Configuration

The first chain is basically composed by a down-conversion section (LNA, mixer, local oscillator) which amplifies and then down-converts the 85.5 GHz uplink signal at 5.5 GHz by using a mixer and a local oscillator centred at 80 GHz (the same frequency will be used for the transmitting section in order to simplify the on-board hardware).

The output is then again filtered and amplified at IF frequency (5.5 GHz). A further stage, the Automatic Gain Control (AGC), is inserted into the chain, after the IF amplifier, in order to cope with the signal dynamic and the receiving chain gain variation. After the AGC, a 90 degrees hybrid coupler acts as power divider (3 dB) on two channels.

First channel sends the signal through a second hybrid 3 dB which feeds two mixers. Such a section is basically a demodulator which consists of two separate mixers that are driven 90° out of phase with each other to generate quadrature (I and Q) signals. In this block, a second down-conversion is used to lower the input frequency (5.5 GHz) through the use of a local oscillator at about 5.5 GHz in order to create an output with a magnitude order of tenths of MHz. Such a frequency is suitable to be used as input to the following Analog to Digital Converter. This second down-conversion subsystem works as demodulator in order to extract the I and Q components of the modulated signal.

Second channel feeds the RF power measurement section. Such a block is basically constituted by an IF logarithmic amplifier (due to the large input dynamic), a square detector (e.g. diode) and an Analog to Digital Converter (ADC).

On the basis of that configuration, the receiver specifications are shown in Table 6-19.

The second chain is constituted by a radiometer, a total power radiometer has been chosen. Finally, all the measurements are coordinated and collected by a payload controller computer.

Concerning the receiving section, in this case the signal is SP-BPSK modulated occupying a bandwidth of 7.2 MHz and the system data rate is 6 Mbps, according to the link budget later on shown.

On the basis of the configuration shown in Figure 6-23, the receiver noise and signal cascade have been derived for the receiver chain; they are shown in Table 6-20 and Table 6-21. Two different tables are provided: the difference is related to consider maximum and minimum gain for the AGC, respectively. The choice of the AGC configuration has been carried out taking into account that the signal level at the output of the receiver chain should be in the range allowed by the RF power measurement unit (-58 dBm minimum, typically).

Receiving Section Specifications		
Dynamic Range	≥ 24 dB	
IPFD	≥ -153.9 dBW/m^2	
G/T	> 6.35 dB/K (OFTR)	
Noise Source	Output Power	130 dBm (TBC)
LNA Specifications	Noise Figure	3.5 dB
	Gain	15 dB
	RF Operating Frequency Range	85.25 -85.75 GHz
	RF Connection Port	WR-10
Mixer Specifications	RF Operating Frequency Range	85.25 -85.75 GHz
	IF Frequency Range	5.5 GHz
	Conversion Loss	< 10 dB
	LO-RF Isolation	>15 dB
	LO-IF Isolation	> 20 dB
	Breakdown Power	+ 15 dBm CW /+ 25 dBm pulsed
	RF Connection Port	WR-10
LO Specifications	Central Frequency	80 GHz
	Output Power	> 10 dBm
Radiometer	Bandwidth	500 MHz
	Integration time	Selectable, 10-1000 ms / step 10 ms (TBC)
	Detector type	TBD
ADC	Number of bit	12/14

Table 6-19: Specifications of the Receiving Section

IKNOW Receiver - Full Configuration	Signal Cascade												
Parameter	Waveguide	Polarizer/Duplexer	Switch	BPF	LNA	Switch	Mixer	BPF	IF Amp	AGC	Hybrid1	Hybrid2	Cable
Gain (dB)	-0,50	-2,00	-3,00	-1,60	15,00	-3,00	-7,00	-1,60	20,00	65,00	-3,20	-3,20	-0,50
NF (dB)	0,50	2,00	3,00	1,60	3,50	3,00	10,00	1,60	4,00	4,03	3,20	3,20	0,50
Cumulative Gain (dB)	-0,50	-2,50	-5,50	-7,10	7,90	4,90	-2,10	-3,70	16,30	81,30	78,10	74,90	74,40
Cumulative NF (dB)	0,50	2,50	5,50	7,10	10,60	10,66	11,63	11,84	12,75	12,75	12,75	12,75	12,75
Output Noise Floor (dBm)	-174,24	-174,24	-174,24	-174,24	-155,74	-158,68	-164,71	-166,10	-145,19	-80,19	-83,39	-86,59	-87,09
Output MDS Level (dBm)	-161,99	-163,99	-166,99	-168,59	-153,59	-156,59	-163,59	-165,19	-145,19	-80,19	-83,39	-86,59	-87,09
Output Signal With Margin (dBm)	-154,99	-156,99	-159,99	-161,59	-146,59	-149,59	-156,59	-158,19	-138,19	-73,19	-76,39	-86,59	-80,09
Notes	Margin	7,00											
	Input noise Power (dBm)	-174,24											

Table 6-20: Receiver Noise and Signal Cascade Normalised to a 1 Hz Bandwidth for IKNOW P/L (AGC Maximum Gain)

IKNOW Receiver - Full Configuration	Signal Cascade												
Parameter	Waveguide	Polarizer/Duplexer	Switch	BPF	LNA	Switch	Mixer	BPF	IF Amp	AGC	Hybrid1	Hybrid2	Cable
Gain (dB)	-0,50	-2,00	-3,00	-1,60	15,00	-3,00	-7,00	-1,60	20,00	45,00	-3,20	-3,20	-0,50
NF (dB)	0,50	2,00	3,00	1,60	3,50	3,00	10,00	1,60	4,00	7,01	3,20	3,20	0,50
Cumulative Gain (dB)	-0,50	-2,50	-5,50	-7,10	7,90	4,90	0,90	-0,70	19,30	64,30	61,10	57,90	57,40
Cumulative NF (dB)	0,50	2,50	5,50	7,10	10,60	10,66	11,63	11,84	12,75	12,77	12,77	12,77	12,77
Output Noise Floor (dBm)	-174,24	-174,24	-174,24	-174,24	-155,74	-158,68	-161,71	-163,10	-142,19	-97,17	-100,37	-103,57	-104,07
Output MDS Level (dBm)	-158,97	-160,97	-163,97	-165,57	-150,57	-153,57	-160,57	-162,17	-142,17	-97,17	-100,37	-103,57	-104,07
Output Signal With Margin (dBm)	-151,97	-153,97	-156,97	-158,57	-143,57	-146,57	-153,57	-155,17	-135,17	-90,17	-93,37	-96,57	-97,07
Notes	Margin	7,00											
	Input noise Power (dBm)	-174,24											

Table 6-21: Receiver Noise and Signal Cascade Normalised to a 1 Hz Bandwidth for IKNOW P/L (AGC Minimum Gain)

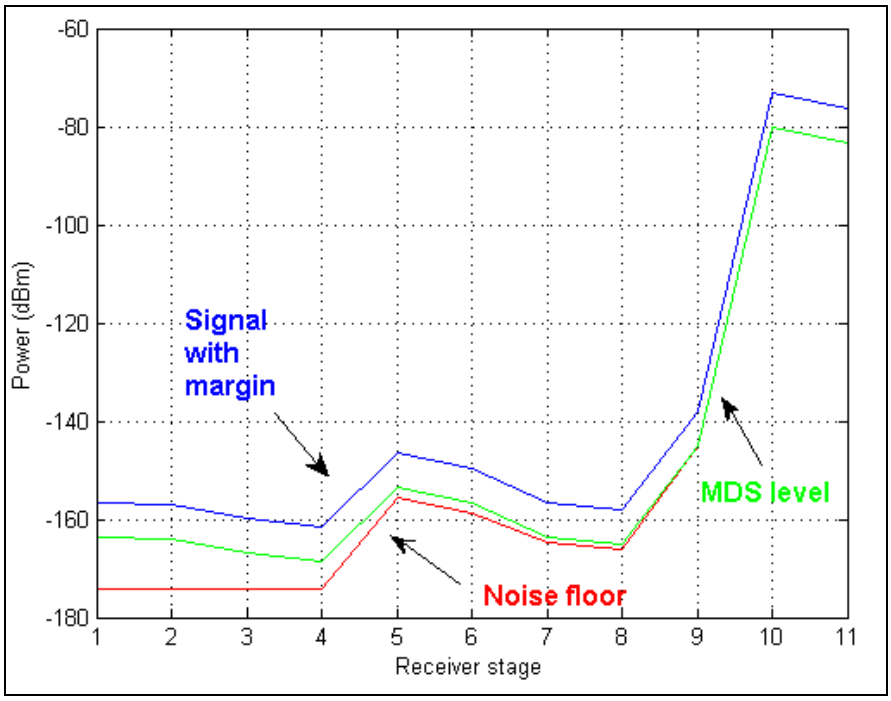

Figure 6-38: Diagram of the Receiver Noise and Signal Cascade Normalised to a 1 Hz Bandwidth for IKNOW P/L (AGC Maximum Gain)

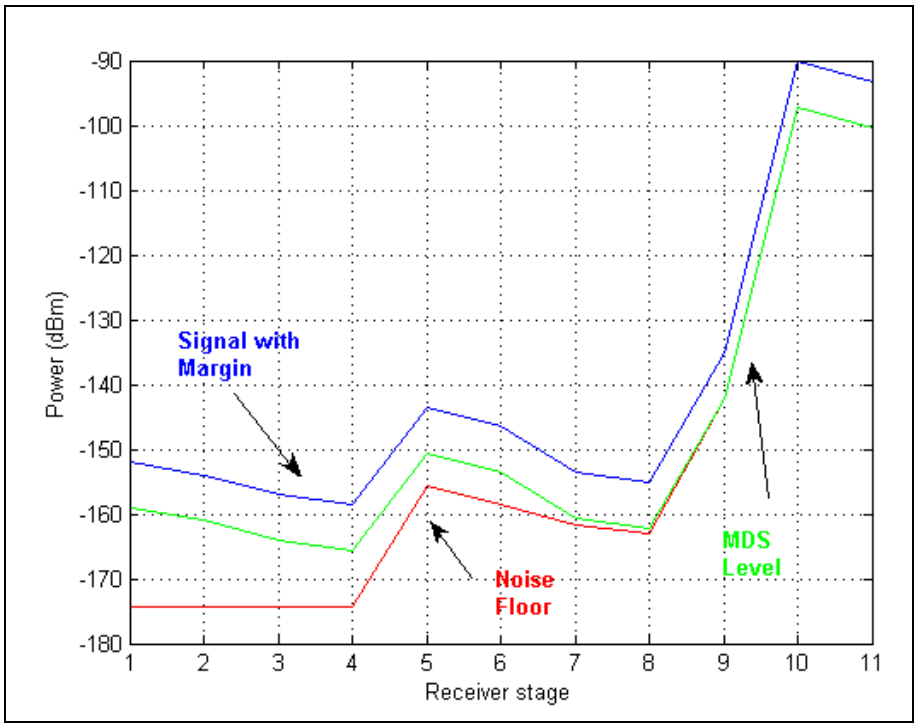

Figure 6-39: Diagram of the Receiver Noise and Signal Cascade Normalised to a 1 Hz Bandwidth for IKNOW P/L (AGC Minimum Gain)

Some preliminary simulations have been carried out in order to evaluate performance of the P/L. In this section, some results are reported related to simulate the P/L and specifically the receiving chain through ADS software. In the design of a communication system the use of CAD/CAE software to simulate RF/microwave and signal processing components is a powerful tool. The ADS from Agilent provides this RF analog/digital simulation capability, enabling such things as time-saving trade-off studies for the performance requirements on each side of a communications system.

Hereafter, ADS software is employed in order to simulate the performance of the IKNOW P/L receiving chain.

Three types of simulations have been carried out:

1. Power Budget Analysis;
2. Small Signal Sweep Analysis;
3. Harmonic Balance Analysis.

The first simulation illustrated is relative to a power budget analysis, which is suited for evaluating absolute power levels at specific point in the transmitter/receiver chain. Then, the linear swept frequency response of the subsystem has been simulated using the small signal sweep bench.

Finally, non linear effects are also analyzed employing the harmonic balance bench, in which a multi-tone excitation is demonstrated.

In order to analyze and verify the performance and the principal parameters, which are typical of a receiving chain, the IKNOW P/L receiver scheme, which is shown in Figure 6-24, has been employed for ADS simulations. In the receiving subsystem, the RF input stage consists of a 85.5 GHz band-pass filter with a bandwidth of 500 MHz, followed by a low noise amplifier with 15 dB of gain. Then, there is a single down-conversion stage, which is comprised of an on-board Voltage Controlled Oscillator to provide the 80 GHz LO signal, and a Double-Balanced Mixer. At the output there are a 5.5 GHz band-pass filter with a bandwidth of 110 kHz and a 20 dB gain IF amplifier. In addition to the components listed above, the scheme includes two attenuators in the receiver subsystem. The input pad (5.5 dB insertion loss) is used to represent cable, connector, waveguide, ortho-mode transducer and switch losses present in the receiver subsystem. The output pad (1.5 dB insertion loss) is used to take in account waveguide, cable and connector losses.

1. Power budget

The power budget analysis is useful for assessing the power flow through the system. Figure 5 illustrates the schematic used for the power budget analysis. Table 6-22 shows the

power budget results for a single 85.5 GHz tone. The chosen input power to the receiver subsystem during measurement is fixed at -1 15 dBm. The output power delivered to the receiver output is -83.2 dBm. Convenient calculation of the internal power levels is important for maintaining linear operation of the active components of the system, namely LNA amplifier, mixer and IF amplifier.

2. Small Signal Sweep

An efficient way to simulate the frequency-dependent, small-signal behavior of the system is with small signal sweep. The simulated results are reported in Figure 6-41. The simulation shows a pass-band centred on the desired 85.5 GHz, with a much lower amplitude response when RF is at image frequency of 74.5 GHz.

3. Harmonic Balance Simulation

A harmonic balance simulation can be used to investigate the non-linear performance of a subsystem at user-specified input power levels. Results of the simulation are shown in Figure 6-42.

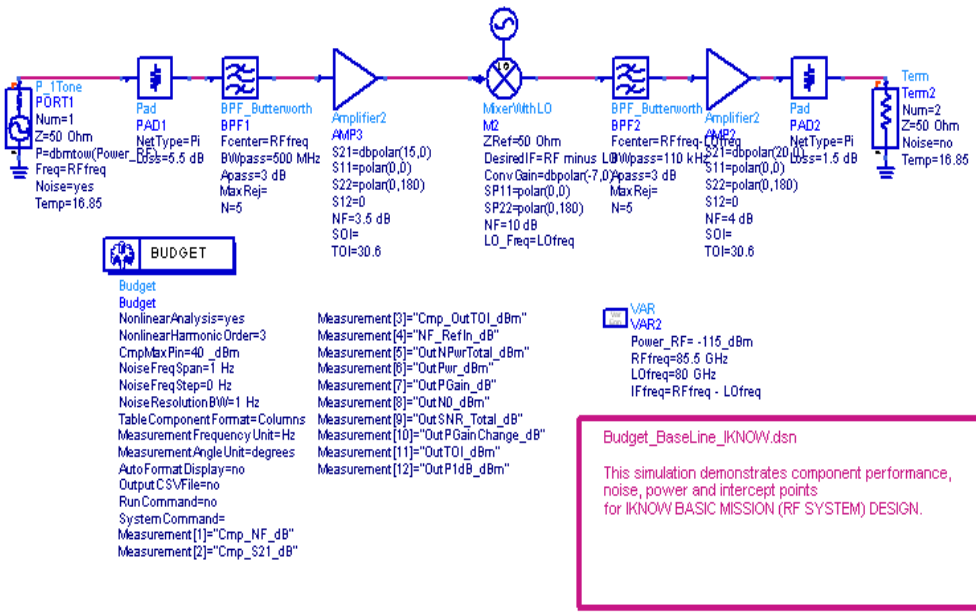

Figure 6-40: Schematic used for the IKNOW P/L Receiver Chain Power Budget Analysis Simulation

Meas_Name	BPF1	AMP3	M2	BPF2	AMP2
Cmp_NF_dB	1.600	3.500	10.000	1.600	4.000
Cmp_S21_dB	-1.600	15.000	-7.000	-1.600	20.000
Cmp_OutTOI_dBm	1000.000	30.600	1000.000	1000.000	30.600
NF_Refln_dB	7.100	10.600	13.171	13.320	13.985
OutNPwrTotal_dBm	-173.975	-155.475	-159.904	-161.355	-140.690
OutPwr_dBm	-122.100	-107.100	-114.100	-115.700	-95.700
OutPGain_dB	-7.100	7.900	0.900	-0.700	19.300
OutN0_dBm	-173.975	-155.475	-159.904	-161.355	-140.690
OutSNR_Total_dB	51.875	48.375	46.804	45.655	44.990
OutPGainChange_dB	0.000	0.000	0.000	0.000	0.000
OutTOI_dBm	1000.000	30.600	23.600	22.000	30.296
OutP1dB_dBm	1000.000	19.962	12.962	11.362	19.737

Table 6-22: IKNOW P/L Receiver Chain Power Budget Analysis Results

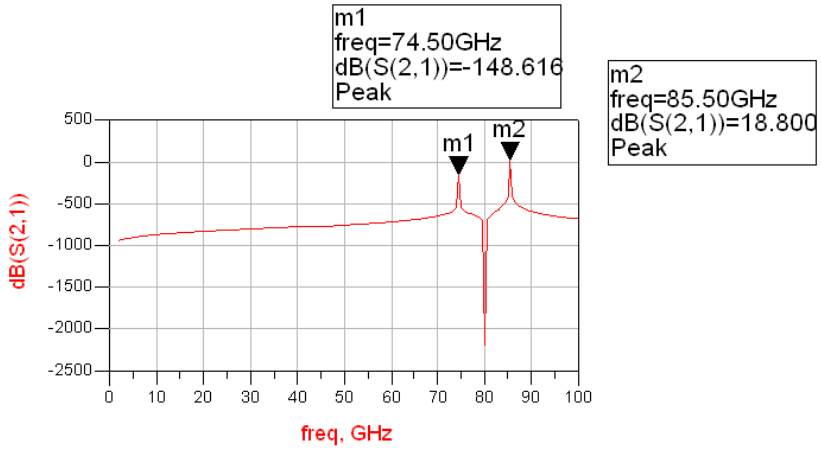

Figure 6-41: IKNOW P/L Receiver Chain Small Signal Sweep Results

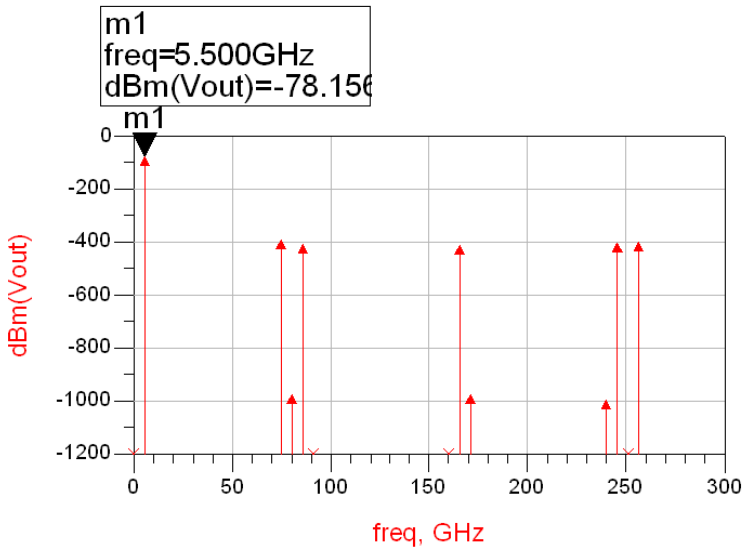

Figure 6-42: IKNOW P/L Receiver Chain Harmonic Balance Results

In order to preliminarily investigate on the performance and the behavior of IKNOW P/L, the IKNOW receiving chain performance was simulated using a standard QPSK modulated

signal input. ADS scheme employed is shown in Figure 6-43. In the receiving subsystem, the RF input stage is composed of a 85.5 GHz BPF with a bandwidth of 500 MHz, followed by a LNA with 15 dB of gain. Then, there is a single down-conversion stage, which includes an on-board voltage controlled oscillator to provide the 80 GHz LO signal, and a double-balanced mixer. At the output there are a 5.5 GHz band-pass filter with a bandwidth of 110 kHz and a 20 dB gain IF amplifier. In order to generate an RF QPSK signal suitable for simulating IKNOW receiving chain performance, a pseudorandom bit sequence, a QPSK modulator and two raised-cosine base-band filters to generate the base-band I and Q were used. A symbol rate of 100 kHz has been assumed for the performed simulations.

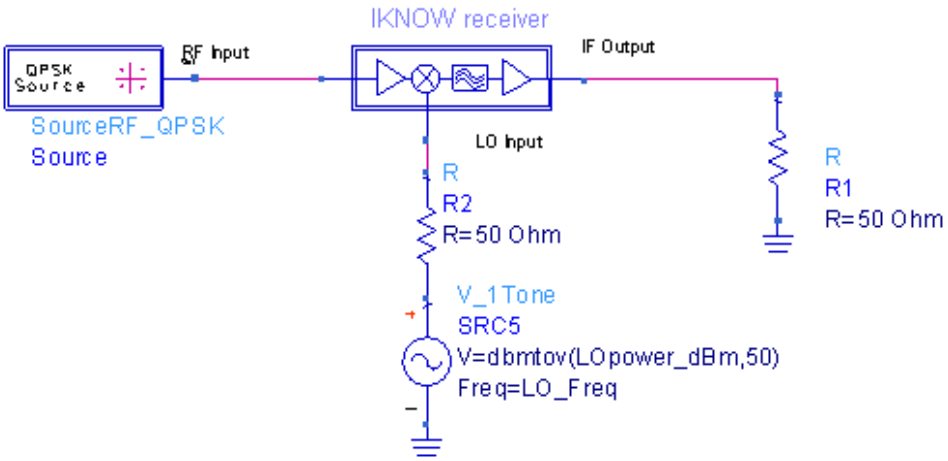

Figure 6-43: IKNOW P/L Receiver Chain with QPSK signal source

Results related to P/L simulations through the ADS Circuit Envelope Simulator are shown in Figure 6-44. This tool was used for efficiently simulating the performance of the IKNOW receiving chain with a digitally modulated input signal in terms of spectrum of generated signal, error vector magnitude, output constellations and trajectory diagrams.

Figure 6-45 shows the trajectory diagram, which plots the instantaneous relative phase and amplitude of the IF signal versus time, and the constellation diagram, as well as the calculated error vector magnitude.

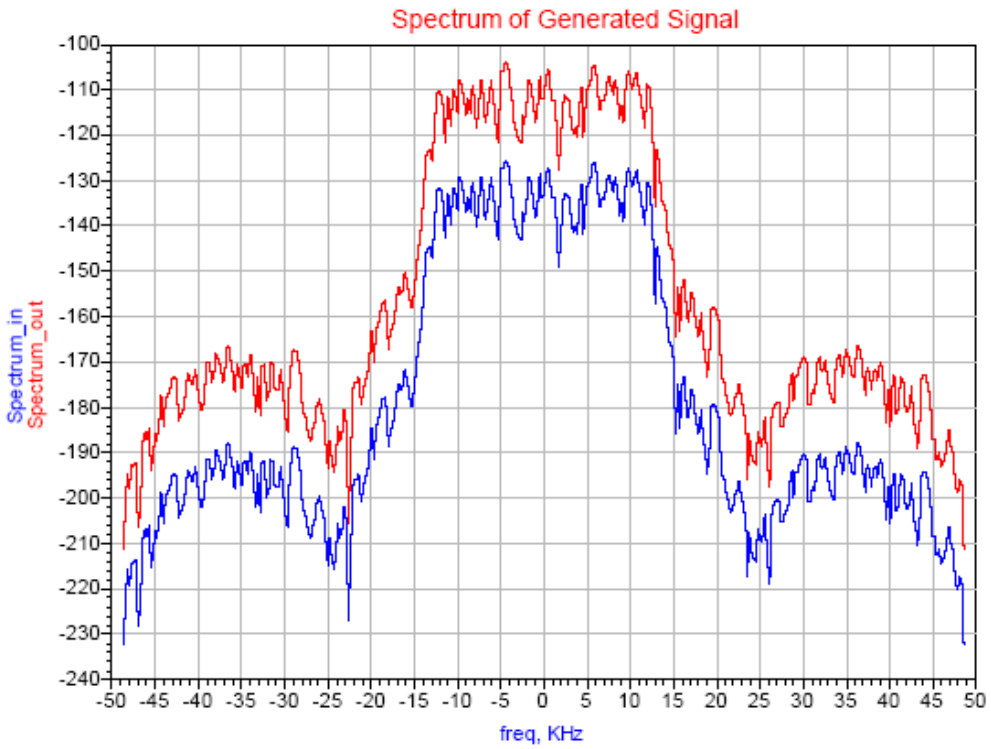

Figure 6-44: Spectrum at the IKNOW Receiving Chain as an Offset from the IF Signal Frequency

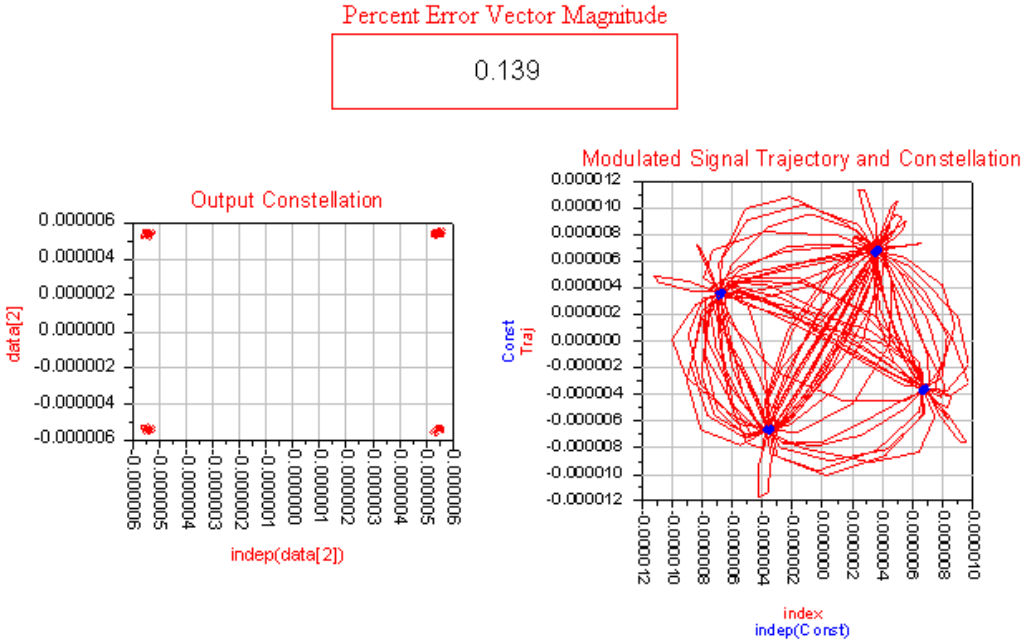

Figure 6-45: Percent EVM, Constellation and Trajectory Diagrams

6.2.9.5 Transmitter Specifications

Concerning the transmitting section, the P/L has to perform two tasks:

1. transmission of a modulated signal;
2. transmission of a beacon.

The above mentioned tasks are realised by two transmitting sections, both transmitting through the same antenna.

The first section consists of a base-band section with a signal generator at 4.3 GHz, SP-BPSK modulated, an up-conversion section at 75.7 GHz and a PA section based on a SSPA to reach the requested EIRP. The signal is generated at 4.3 GHz and at first filtered with a band-pass filter centred at this frequency. Then, the signal is up-converted at 75.7 GHz by using a mixer with a local oscillator at 80 GHz. The output is sent to a SSPA in order to acquire the needed power gain to be delivered to the transmitting antenna.

The second section consists of a beacon generator at 76 GHz. Such a section shares the transmitting antenna with the modulated section through a diplexer which has two pass-bands centred respectively at 76 GHz and 75.7 GHz. Hence, the P/L transmits to ground at the same time a beacon (propagation experiment) and a modulated signal (data transmission).

Therefore, the Tx chain for the full configuration is composed of the following elements:

- Beacon generator;
- Diplexer;
- Base-band section (signal generator, SP-BPSK modulator);
- Up-conversion section (mixer and local oscillator);
- Filter;
- SSPA;
- Power Monitor;
- OMT;
- Antenna.

We distinguish between propagation experiment and data transmission one in the following specifications.

Propagation Experiment

Beacon Generator Specifications – Full Configuration		
Transmitter	Central Frequency	76 GHz
	EIRP	$\geq$ 22.5 dBW
	EIRP stability	± 1 dB over 12 months
	P_{out}	> 20 dBm
	Frequency stability	< 10^{-7} over 12 months
	Phase Noise	< -105 dBHz @ 100 kHz
Antenna	Central Frequency	75.7 GHz
	Diameter	110 mm
	Minimum Gain	35 dBi
	Beamwidth	2.5 °

Table 6-23: Specifications of the Beacon Generator Section

Such specifications are compliant with the link budget and an un-modulated signal and 0.1 W of power output.

Data Transmission Experiment

Transmitting Section Specifications – Full Configuration		
Transmitter	Central Frequency	75.7 GHz
	EIRP	$\geq$ 31.3 dBW
	EIRP stability	± 1 dB over 12 months
	P_{out}	> 13 dBm (LO generator)
	Frequency stability	< 10^{-7} over 12 months
	Phase Noise	< -105 dBHz @ 100 kHz
SSPA Specifications	Central Frequency	75.7 GHz
	P_{out} (1 dB cp)	> 24 dBm
	Gain (linear)	> 20 dB
Antenna	Central Frequency	75.7 GHz
	Diameter	110 mm
	Minimum Gain	37 dBi
	Beamwidth	2.5°

Table 6-24: Specifications of the Transmitting Section

Such specifications are compliant with the link budget and a SP-BPSK modulated signal with 2.4 MHz of bandwidth, considering a system data rate of 2 Mbps on downlink and 0.3 W of power output.

6.2.9.6 On-board Memory

The scientific measurement that the P/L has to operate requires the availability of an on-board memory to be used to collect measured data, and to store on-board the pre-defined data to be transmitted to ground. Moreover, the on-board memory has to store on-board the pre-defined data to be compared to those received (for BER evaluation) and, generally, the information collected from on-board devices (power levels, voltages, temperatures, etc.). Therefore, it is foreseen the use of an on-board memory with a available capacity of at least 1 Gb.

6.3 TECHNOLOGICAL FEASIBILITY

Concerning the technology to be implemented, the most promising approach in terms of performance and mass and volume saving is based on the use of MMIC technology, in which passive elements and interconnects are fabricated on the same semiconductor substrate as the active devices. All the critical, microscopic circuit elements are defined on-chip through photolithography from a scaled-up mask. This eliminates the parasitics associated with component packages, leads, and solder pads. Some advantages of this technology consist of reduced mass and volume with respect to conventional circuit assemblies, highly repeatable performance, and low-cost fabrication in large-quantities.

Currently, the growth in the number of systems using the millimetre-wave region of the electromagnetic spectrum is partially founded on the development, in the last years, of low cost and high performance MMIC circuits.

The approach identified for IKNOW foresees the development of both receiver and transmitter in MMIC technology.

It has to be outlined that MMICs designed and realised to operate in space environment require several specialize test in order to assure, for this products, quality and reliability levels compatible with space requirements. Taking into account only the frequency requirements, it highlights that only one process by OMMIC foundry is qualified for space

applications. The typical space qualification of MMIC requires the satisfaction of several tests, synthesized in Figure 6-46.

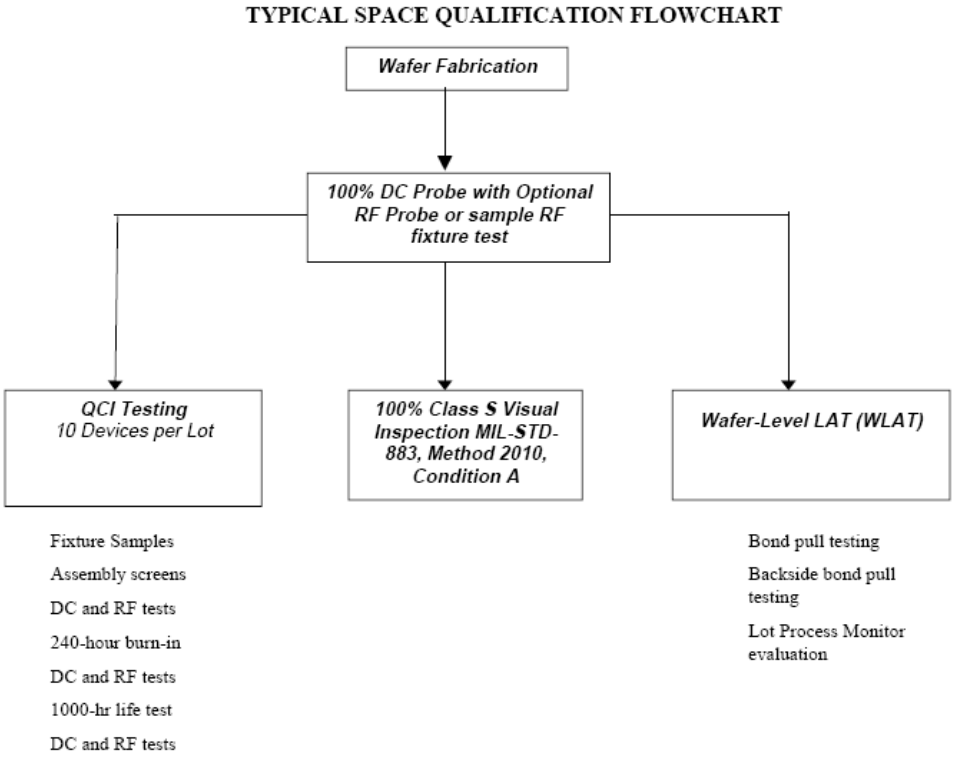

Figure 6-46: MMIC Space Qualification Flowchart

Concerning the reliability of the P/L, the use of on-board spares (redundancy) would allow to enhance the P/L safety and maintenance. On the other hand, such a choice would introduce a higher complexity on-board due to the use of supplementary equipment and related switches. This implies an increase in the final mass budget and in the final cost of the P/L. However, a minimum redundancy should be foreseen at least for the LNA and for the SSPA (both the configurations).

A complete technological state of the art survey for each of the main IKNOW P/L subsystems has been performed during the WAVE A2 project activities. In the following sections, the main characteristics of the identified equipment are reported.

The main identified foundries are from the United States, but also some European ones have been identified.

Concerning the Italian market, two main companies are involved in this area, Thales Alenia Space [6-16] and Rheinmetall Italy [6-17].

6.3.1.1 SSPA

This section presents the W-band SSPA equipment already available (or in development phase). It must be highlighted that all the products listed below are COTS and are not qualified for space applications.

From the analysis performed on European foundries, it has been found that only three foundries or research Institutes are active in this area:

- UMS(F) [6-18];
- OMMIC(F) [6-19];
- IAF(D) [6-20].

Among the three companies, IAF seems to be the more advanced and completed offering both LNAs and MPAs.

The best IAF available product characteristics are shown in Figure 6-50, Figure 6-51 and Table 6-25 for MPA (model IAF MDMAW01BM).

Figure 6-47: W band dual gate MPA Module

Operatine Frequency Range	80-100 GHz
Small Signal Gain	13 dB
RF output power, saturation	15 dBm
P_{in} max	6 dBm
DC power consumption	2000 mW
Supply Voltage	5 V
Drain Current	450 mA
Module size	30 x 30 x 20 mm^3
Note	Electrostatic sensitive

Table 6-25: Main Features- IAF MPA Module

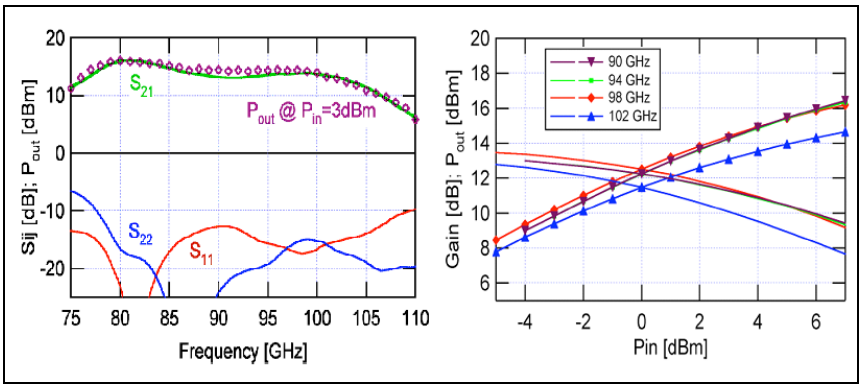

Figure 6-48: S Parameters and Gain – IAF MPA Module

For what concerns the U.S. market, four great companies are active in this area:

- QuinStar [6-21]
- Millitech [6-22]
- Northrop Grumman [6-23]
- WiseWave Technologies Inc. [6-24]

Each one of these companies fabricates SSPA that matchs IKNOW P/L requirements. Howeverm the products with the best performance can be provided only by QuinStar and Millitech.

6.3.1.2 LNA

This section shows the W-band LNA equipment already available (or in development phase). It must be highlighted that all the products listed below are COTS and are not qualified for space applications. The European identified main foundry is IAF (as for the SSPA). The considered module is identified by the MDLAW336M part number, and the electrical and mechanical features of the MDLAW336M module are summarized in Figure 6-49 and Table 6-26.

Operating Frequency Range	80-100 GHz
Small Signal Gain	18 dB
Noise Figure	4 dB
DC power consumption	350 mW
Supply Voltage	5 V
Drain Current	75 mA
Max. input power	-15 dBm
Module size	28 x 28 x 20 mm^3

Table 6-26: LNA Module Main Features

Figure 6-49: IAF MDLAW336M Module Photo

The detailed performance of the LNA module are reported in Figure 6-50 and Figure 6-51.

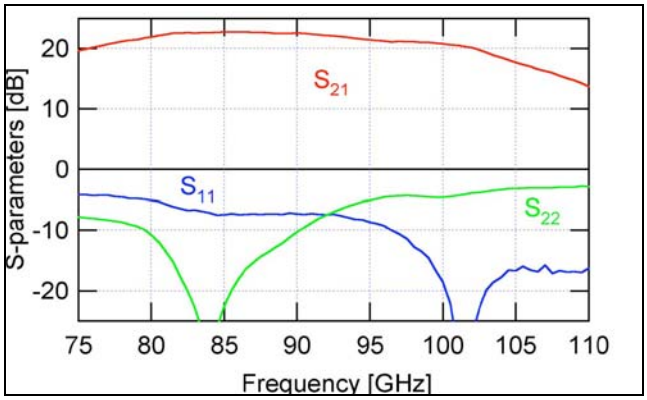

Figure 6-50: IAF MDLAW336M Module - Scattering Parameters

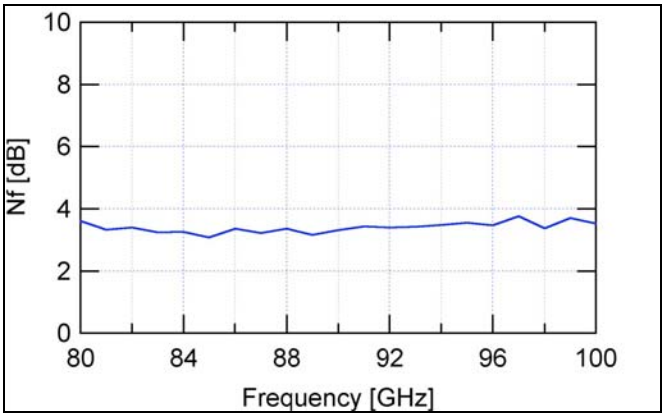

Figure 6-51: IAF MDLAW336M Module - Noise Figure

For what concerns the United States market, three great possible suppliers have been identified:

- QuinStar
- Millitech
- Northrop Grumman

However, the products with the best performance can be provided only by Northrop Grumman.

6.3.1.3 Up/Down-conversion and frequency generation

For the frequency conversion design activities of the project has been pointed out that the IKNOW Up/Down Converter can be designed in the following way: a monolithic three-stage LNA, a monolithic image rejection mixer and a hybrid IF 90° coupler with an IF amplifier. The functional architectures are shown in Figure 6-52 and Figure 6-53.

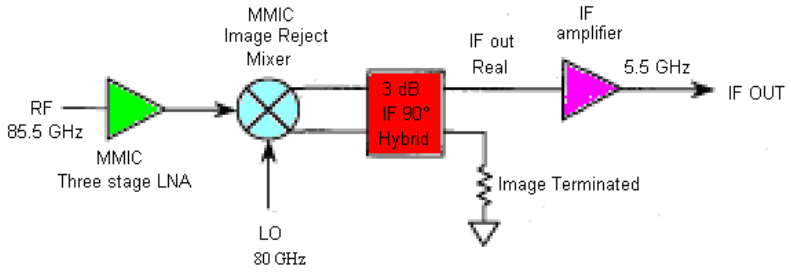

Figure 6-52: Functional Architecture of IKNOW Down Converter based on Image Rejection Mixer

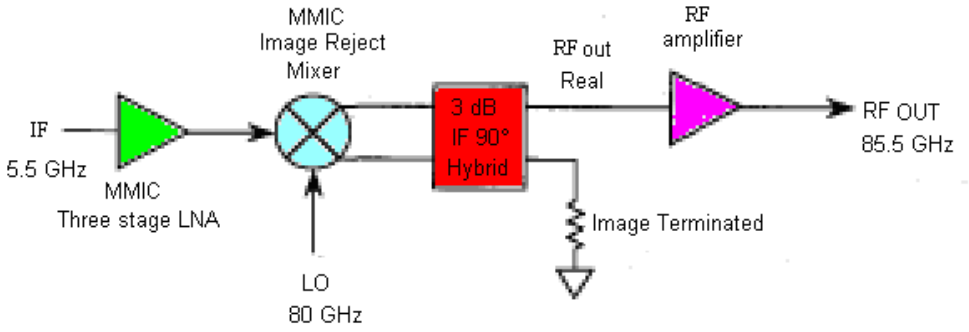

Figure 6-53: Functional Architecture of IKNOW Up Converter based on Image Rejection Mixer

For the design of IKNOW frequency generator, it is suitable to employ the push-push VCO design approach based upon InP HBT technology. Then, the design of the IKNOW frequency generator consists in an integrated solution that employs a 80 GHz VCO, with a low frequency reference source at 160 MHz. The use of push-push principle is a practical solution with good frequency stability and low phase noise, and thus allows the tension of the usable frequency range.

Moreover, as operating frequency increases, it becomes very difficult to implement an inductor and a varactor with a high quality factor.

It is possible to integrate a push-push oscillator with buffer amplifier and 8:1 frequency divider on a single MMIC, while a commercial PLL chip and a loop filter can be mounted on an external PCB. In Figure 6-54, the functional architecture of the IKNOW frequency generator is shown.

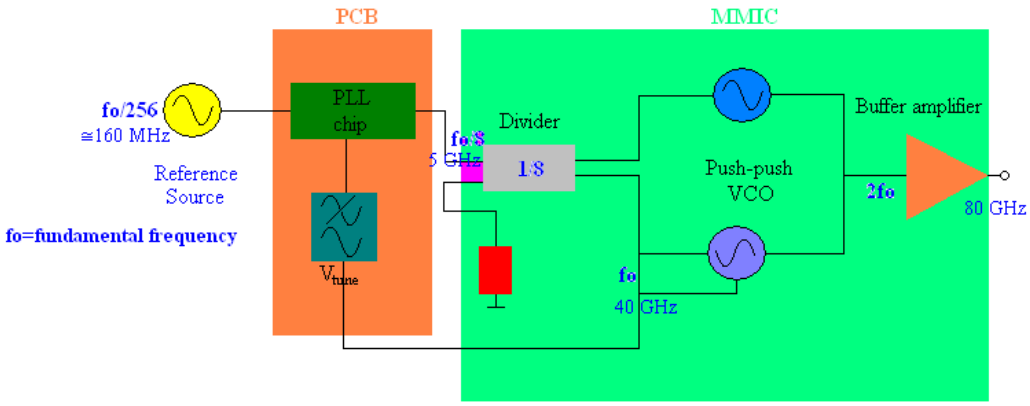

Figure 6-54: Functional Architecture of the IKNOW Frequency Generator

Since the first stage of any frequency divider has to operate at the same high frequency as the VCO, a high speed frequency divider is required. The frequency divider can be designed in source coupled FET logic (SCFL) to divide the fundamental frequency of the VCO by a factor of eight. The schematic block of the frequency divider is shown in Figure 6-55. There are many advantages using SCFL logic [6-25]:

1. a wide allowable threshold voltage range for FET's;
2. an excellent fan-out capability;
3. a small input capacitance;
4. a high input sensitivity.

These characteristics make the SCFL logic ideal to implement the frequency divider for such a range of frequency.

The divide-by-four static frequency divider circuit can be implemented in SCFL logic using two divide-by-two stages based on master-slave toggle flip-flops.

In the design of the dynamic frequency divider it is fundamental to minimize parasitic capacitances to increase the speed of circuit. The most effective way to obtain this objective is to reduce the number of the fan-out and fan-in.

In the design of the static frequency divider, the function of the latches of the MS-TFF is to maintain a constant output voltage and to isolate the output from the input if the input signal changes during the positive (or negative) clock period.

However, if the clock signal is too fast for the input signals to change during the positive (or negative) clock period, the latches can be omitted. The result consists in a reduction of the number of fan-out and fan-in of the data path to merely one. Furthermore, the load of the input clock signal is also half of the static divider.

The buffer amplifier at the harmonic output increases the output signal and minimizes the effects of the measurement setup on the oscillation frequency and the phase noise behaviour. It is suitable using a FET single stage buffer amplifier in cascode configuration.

To vary the oscillation frequency, it is appropriate to integrate HEMT diodes in parallel configuration within a series-feedback network. Moreover, the matching networks will be optimised to maximize the output signal at the fundamental output port.

To ensure this operation, it is necessary to supply enough power to the frequency divider. A commercial PLL chip can be used to design a stabilization circuit on a printed circuit board [6-26].

The scheme of the PLL for IKNOW frequency generator is shown in Figure 6-56. To ensure the stabilization of the millimeter wave VCO, the reference frequency of 160 MHz can be chosen. It leads to an output frequency of 80 GHz from the frequency generator and an output frequency of 5 GHz from the PLL chip.

The loop filter can be realized using a resistor in series with a capacitor and it is suitable to put a capacitor in parallel with them to smooth the output signal from the charge pump (CP). Finally, it is suitable to shift the tuning voltage towards negative values to generate the whole tuning voltage swing. The Phase Frequency Detector (PFD) works at half of the reference frequency, therefore the input frequency of the PLL circuit is divided by a factor of 64.

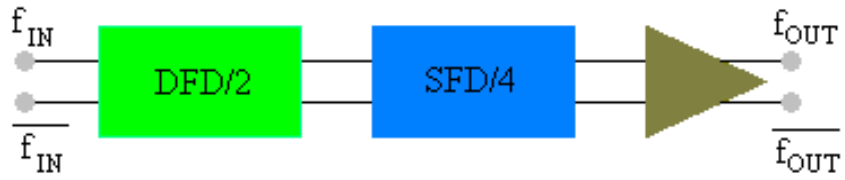

Figure 6-55: Schematic Block of the Frequency Divider for IKNOW Frequency Generator

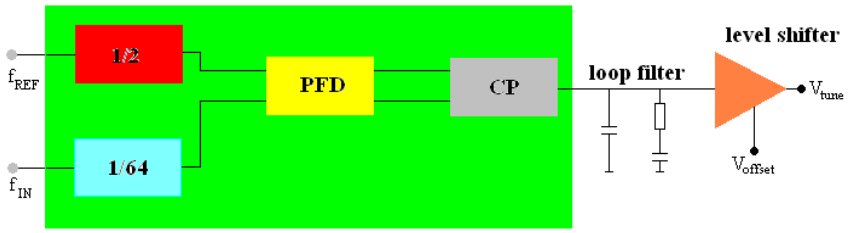

Figure 6-56: Schematic Block of the PLL for IKNOW Frequency Generator

The same considerations reported for SSPA equipment suppliers still stands for frequency generation equipment (both for European and U.S. suppliers).

6.3.2 P/L BUDGETS

In the following paragraphs, some P/L budgets related to mass and power are shown. In addition, link budgets for both the configurations have been reported. All these budgets have been carried out on the basis of the P/L configurations above discussed.

6.3.2.1 Mass Budget

In Table 6-27 preliminary mass budget of the IKNOW P/L is reported.

Mass Budget IKNOW Payload - Full Configuration					
Payload Element	**Quantity**	**Unit Mass (kg)**	**Total Mass (kg)**	**Margin (%)**	**Total with Margin (kg)**
W band Antenna	1	0,70	0,70	20,00	0,84
Polarizer	1	0,10	0,10	20,00	0,12
Duplexer	1	0,10	0,10	20,00	0,12
WR-10 Coupler	1	0,05	0,05	20,00	0,06
WR-10 Switch	1	0,05	0,05	20,00	0,06
Noise Source	1	0,10	0,10	20,00	0,12
W band LNA	1	0,10	0,10	20,00	0,12
W band Mixer	5	0,10	0,50	20,00	0,60
W band LO	4	0,10	0,40	20,00	0,48
W band Filter	4	0,03	0,12	20,00	0,14
Power Detection	1	0,05	0,05	20,00	0,06
Hybrid	2	0,10	0,20	20,00	0,24
IF Amplifier	1	0,10	0,10	20,00	0,12
AGC	1	0,35	0,35	20,00	0,42
ADC	2	0,03	0,06	20,00	0,07
SP-BPSK Modulator	1	0,10	0,10	20,00	0,12
W band SSPA	1	0,10	0,10	20,00	0,12
Power monitor	1	0,20	0,20	20,00	0,24
Diplexer	1	0,15	0,15	20,00	0,18
Beacon Generator	1	0,25	0,25	20,00	0,30
On-board Memory	1	0,20	0,20	20,00	0,24
Payload Controller	1	0,70	0,70	20,00	0,84
Radiometer Section (optional)	1	0,20	0,20	20,00	0,24
WR-10 Switch (optional)	1	0,05	0,05	20,00	0,06
Power Supply	1	1,00	1,00	20,00	1,20
WR-10 Waveguides	15	0,03	0,45	20,00	0,54
Harness	1	0,40	0,40	20,00	0,48
Mechanical structure	1	1,00	1,00	20,00	1,20
		Payload Total Mass	7,78	Payload Total Mass with margin	9,34
			7,53		9,04

Table 6-27: Mass Budget for IKNOW P/L Full Configuration

6.3.2.2 Power Budget

In Table 6-28 preliminary power budget of the IKNOW P/L is shown.

Power Budget IKNOW Payload - Full Configuration					
Payload Element	**Quantity**	**Unit Power (W)**	**Total Power (W)**	**Margin (%)**	**Total with Margin (W)**
W band LNA	1	0,35	0,35	20,00	0,42
Frequency Generation Unit	4	1,10	4,40	20,00	5,28
Power Detection Unit	1	0,35	0,35	20,00	0,42
IF Amplifier	1	0,30	0,30	20,00	0,36
ADC	2	2,00	4,00	20,00	4,80
AGC	1	0,60	0,60	20,00	0,72
Baseband Section	1	1,50	1,50	20,00	1,80
W band SSPA	1	2,00	2,00	20,00	2,40
Beacon Generator	1	2,00	2,00	20,00	2,40
Radiometer Section (optional)	1	0,20	0,20	20,00	0,24
On-board Memory	1	2,50	2,50	20,00	3,00
Payload Controller	1	3,00	3,00	20,00	3,60
		Payload Total Power	21,20	Payload Total Power with margin	25,44
			21,00		25,20

Table 6-28: Power Budget for IKNOW P/L Full Configuration

6.3.3 LINK BUDGETS

Hereafter, link budgets related to the IKNOW mission links are reported in Table 6-29, Table 6-30, Table 6-31, and Table 6-32.

WAVE		
Parameter:	*Value:*	*Units:*
Ground Station:		
Transmitter Power Output:	0,25	W
In dBW:	-6,02	dBW
In dBm:	23,98	dBm
Transmission Line Losses:	2,0	dB
S/C Connector, Filter or In-Line Switch Loss	0,0	dB
Antenna Gain:	51,2	dBi
EIRP:	43,2	dBW
Uplink Path:		
Ground Station Antenna Pointing Loss:	1,7	dB
Antenna Polarization Loss:	0,5	dB
Frequency	85500,0	MHz
Distance	1109,0	km
Free Space Loss	192,0	dB
Atmospheric Loss:	19,5	dB
Ionospheric Loss:	0,0	dB
Spacecraft:		
------- C/N Method -------		
Satellite Power Flux Density	-170,5	dBW/m2
Antenna Pointing Loss:	0,62	dB
Antenna Polarization Loss:	0,5	dB
Antenna Gain:	36,4	dBi
Antenna Noise Temperature	290	K
Transmission Line Losses:	2	dB
LNA Noise Figure	3,5	dB
LNA Noise Temperature:	359,23	K
Transmission Line Temp.:	290	K
Sky Temperature:	273	K
Transmission Line Coefficient:	0,6310	
Satellite Effective Noise Temperature:	639	K
Satellite Figure of Merit, G/T:	5,2	dB/K
S. Carrier-to-Noise Power Density (C/No):	62,7	dBHz
PLL Noise Bandwidth	200000	Hz
Uplink C/N:	9,7	dB
Uplink Required C/N:	7	dB
System Link Margin:	**2,7**	dB
Receiver Input Levels:		
Input Signal Power (C)	-104,71	dBm
Noise Spectral Density (N0 = k*T)	-174,24	dBm/Hz
Noise Power (N = k*B*T = N0*B)	-121,23	dBm
Number of Carriers	1	

Table 6-29: Uplink Budget (1 % unavailability), un-modulated signal

WAVE		
Parameter:	*Value:*	*Units:*
Spacecraft:		
Spacecraft Transmitter Power Output:	0,30	W
In dBW:	-5,20	dBW
In dBm:	24,80	dBm
Spacecraft Transmission Line Losses:	2,5	dB
S/C Connector, Filter or In-Line Switch Losses:	0,0	dB
Spacecraft Antenna Gain:	39,0	dBi
Spacecraft EIRP:	31,3	dBW
In dBm:	61,3	dBm
Downlink Path:		
Spacecraft Antenna Pointing Loss:	0,52	dB
Antenna Polarization Loss:	0,5	dB
Frequency	75700,0	MHz
Distance	1109,0	km
Path Loss:	190,9	dB
Atmospheric Loss:	17,9	dB
Ionospheric Loss:	0,0	dB
Input Power Flux Density at Ground Station:	-178,5	dBW/m2
Ground Station:		
------- C/N Method -------		
Ground Station Antenna Pointing Loss:	1,0	dB
Ground Station Antenna Gain:	52	dBi
Ground Station Transmission Line Losses:	2	dB
Receiver NF	12,06	dB
Ground Station Transmission Line Temp.:	290	K
Ground Station Sky Temperature:	100	K
G.S. Transmission Line Coefficient:	0,6310	
Ground Station Effective Noise Temperature:	4542	K
Ground Station Figure of Merit (G/T):	13,4	dB/K
Total Input Noise Power	-143,5	dBW
G.S. Carrier-to-Noise Power Density (C/No):	62,5	dBHz
Noise Bandwidth	200000	Hz
Downlink C/N:	9,5	dB
Downlink Required C/N:	7	dB
System Link Margin:	**2,5**	dB
Input Noise Power=k*B*T	-125,5897	dBm
Transmitter Output Levels:		
Output Signal Power (C)	60,28	dBm
Noise Spectral Density (N0 = k*T)	-208,60	dBm/Hz
Noise Power (N = k*B*T = N0*B)	-155,59	dBm
Number of Carriers	1	

Table 6-30: Downlink Budget (1 % unavailability), un-modulated signal

WAVE		
Parameter:	*Value:*	*Units:*
Ground Station:		
Transmitter Power Output:	0,50	W
In dBW:	-3,01	dBW
In dBm:	26,99	dBm
Transmission Line Losses:	2,0	dB
S/C Connector, Filter or In-Line Switch Loss	0,0	dB
Antenna Gain:	53,0	dBi
EIRP:	48,0	dBW
Uplink Path:		
Ground Station Antenna Pointing Loss:	1,7	dB
Antenna Polarization Loss:	0,5	dB
Frequency	85500,0	MHz
Distance	1109,0	km
Free Space Loss	192,0	dB
Atmospheric Loss:	7,72	dB
Ionospheric Loss:	0,0	dB
Spacecraft:		
------- C/N Method -------		
Satellite Power Flux Density	-153,9	dBW/m2
Antenna Pointing Loss:	0,6	dB
Antenna Gain:	36,4	dBi
Antenna Noise Temperature	300	K
Transmission Line Losses:	2	dB
LNA Noise Figure	3,5	dB
LNA Noise Temperature:	359,23	K
Transmission Line Temp.:	290	K
Sky Temperature:	273	K
G.S. Transmission Line Coefficient:	0,63	
Satellite Effective Noise Temperature:	638,50	K
Satellite Figure of Merit, G/T:	6,35	dB/K
S. Carrier-to-Noise Power Density (C/No):	80,4	dBHz
System Desired Data Rate:	6000000	bps
Baseband scheme Spectral efficiency	1,20	
In dBHz:	68,57	dBHz
System Eb/No:	11,86	dB
System Required Bit Error Rate:	1,00E-06	
System Required Eb/No:	10,00	dB
System Link Margin:	**1,9**	dB

Table 6-31: Uplink Budget (5 % unavailability), SP-BPSK modulated signal

WAVE		
Parameter:	*Value:*	*Units:*
Spacecraft:		
Spacecraft Transmitter Power Output:	0,30	W
In dBW:	-5,20	dBW
In dBm:	24,80	dBm
Spacecraft Transmission Line Losses:	2,5	dB
S/C Connector, Filter or In-Line Switch Losses:	0,0	dB
Spacecraft Antenna Gain:	39,0	dBi
Spacecraft EIRP:	31,3	dBW
In dBm:	61,3	dBm
Downlink Path:		
Spacecraft Antenna Pointing Loss:	0,52	dB
Antenna Polarization Loss:	0,5	dB
Frequency	75700,0	MHz
Distance	1109,0	km
Path Loss:	190,9	dB
Atmospheric Loss:	7,34	dB
Ionospheric Loss:	0,0	dB
Input Power Flux Density at Ground Station:	-168,0	dBW/m2
Ground Station:		
------- C/N Method -------		
Ground Station Antenna Pointing Loss:	1,0	dB
Ground Station Antenna Gain:	52	dBi
Ground Station Transmission Line Losses:	2	dB
Receiver NF	12,75	dB
Ground Station Transmission Line Temp.:	290	K
Ground Station Sky Temperature:	100	K
G.S. Transmission Line Coefficient:	0,6310	
Ground Station Effective Noise Temperature:	5343	K
Ground Station Figure of Merit (G/T):	12,7	dB/K
G.S. Carrier-to-Noise Power Density (C/No):	72,3	dBHz
System Desired Data Rate:	2000000	bps
Baseband scheme Spectral efficiency	1,20	
In dBHz:	63,80	dBHz
System Eb/No:	8,54	dB
System Required Bit Error Rate:	1,00E-06	
System Required Eb/No:	7,00	dB
System Link Margin:	**1,5**	dB

Table 6-32: Downlink Budget (5 % unavailability), SP-BPSK modulated signal

6.3.4 TECHNOLOGY CRITICAL ELEMENTS IDENTIFICATION

This section summarizes the technological critical elements for the IKNOW P/L. Some considerations have to be addressed in order to define the critical technologies.

IKNOW is the first satellite mission devoted to the W band among all the development lines. This implies the need to take into account some constraints in designing and developing the P/L. These constraints concern the employed frequencies and the extra-European W band technology manufacturers.

Considering the frequency ranges to be used, U/L: 85.2-85.7 GHz, D/L: 75.6-75.8 GHz, they are not currently employed in the commercial market. Currently, the existing commercial hardware components (COTS) are developed only around 94-96 GHz, frequencies at which radar applications exist [6-27][6-28].
Considering W band technology, at present most of the manufacturing companies are from the U.S... Therefore, criticalities could derive from the procurement of components and devices beyond the Atlantic Ocean, in terms of security and/or strategic technology constraints.

Focusing on specific critical elements, we identified the following challenging issues:

- development/change of RF devices: LOs, LNAs, SSPAs, mixers, filters working at the requested frequencies;
- carrier recovery and tracking, due to the high value of Doppler shift and Doppler rate;
- antenna pointing system (if the outcome of the project will outline the necessity of such a system in order to increase the visibility period).

For what concerns the antennas, the use of high frequency ranges such those of the W band, allows to achieve some advantages related mainly to smaller dimensions, on-board and on ground, and the beam-widths. These elements guarantee a clear saving in terms of mass and volume, strictly severe for space applications.
However, some critical issues have to be considered:

- high accuracy in manufacturing antennas surface due to the use of higher frequency;
- better integration of subsystems: antennas, waveguide paths, LNA;
- pointing systems and RF sensors;
- development of RF chains and microwave components with realisation tolerances of about 10 μm.

However, issues related to technology critical elements have been also faced into the design and development plan, identifying the more suited and applicable development philosophy.

6.3.5 IKNOW P/L DEVELOPMENT PLAN AND COSTS

On the basis of the ECSS model philosophy and of the qualification status of the equipment, the IKNOW P/L H/W development matrix is shown in Table 6-33.

	Sub-system	Qual. status	BB	EM	PFM	Notes
Rx and Tx	Rx/Tx Antenna	D	X	X	X	BB is restricted to technological aspects relevant to surface Plating
Tx	Duplexer	B	X	X	X	WG Technology
	Transmit Path Power Monitor	B		X	X	
	SSPA	D	X	X	X	Technology develop and functionally validation
	BPF 75.7 GHz	C	X→		X	High stability filters
	BPF 4.3 GHz	A				
	Signal Generator	A		X	X	
Rx	Heat Source	B		X	X	
	Switch 85.5 GHz	B	X	X	X	
	BPF	A		X	X	
	LNA	D	X→		X	MMIC technology, based on IAF
	Switch	B		X	X	WG Technology
	BPF at 5.5 GHz	B		X	X	
	IF Amplifier	B		X	X	
	AGC	B		X	X	
	RF power measurement	B		X	X	
	Radiometer channel	B		X	X	
Common	P/L Controller	A		X	X	
	Local Oscillator	D	X→		X	MMIC technology, NG, IAF
	Mixer	D	X→	X	X	MMIC technology, NG (BB model to be use for EM plus another)
	Power supply			X	X	
	On board Memory			X	X	Simulation Test Bed
Note	IAF: Institute of Fraunhofer					

Table 6-33: H/W Matrix for IKNOW P/L

Equipment are typically classified according to the following categories:

- ✓ **Category A:** off-the-shelf equipment requiring no modification which has been subjected to a qualification test programme.
- ✓ **Category B:** off-the-shelf equipment requiring no modifications that have already been tested and qualified, but subjected to a different qualification programme or to a different environment. A delta qualification test programme shall be decided and performed case by case.
- ✓ **Category C:** off-the-shelf equipment requiring minor design modifications. A delta or full qualification test programme shall be decided on a case-by-case basis depending on the impact of the required modification.
- ✓ **Category D:** newly designed and developed equipment or existing equipment requiring major re-design. A full qualification test programme shall be imposed.

6.3.6 ACTIVITIES TIME PLANNING

In this section, a preliminary time planning of the foreseen activities of detailed design, development, integration and test for IKNOW P/L is provided on the basis of the design and development plan and of the integration, test and verification activities outlined in previous section.

Considering the preliminary phase of study, time planning showed has to be considered as a baseline to be verified during next deepened study phases. Figure 6-57 shows the Gantt diagram for IKNOW P/L, applicable for all the configurations. (time planning has been estimated from January 2008 to September 2009, where a next WAVE phase is possible). The overall design, development, integration, test and verification timeline has been estimated in about 21 months, divided in system requirements and analysis (6), bread-boarding (7), system detailed analysis and implementation (15), EM MAIT (6, Manufacturing, Assembly, Integration, Test), EM testing (3), PFM MAIT (5.5).

ID	Nome attività
1	**IKNOW - Overall Design and Development Timeline**
3	System Requirements and Analysis
4	Breadboarding
5	Subsystem Detailed Analysis and Implementation
6	EM MAIT
7	EM Testing
8	PFM MAIT
9	
10	
11	
12	
13	
14	
15	
16	

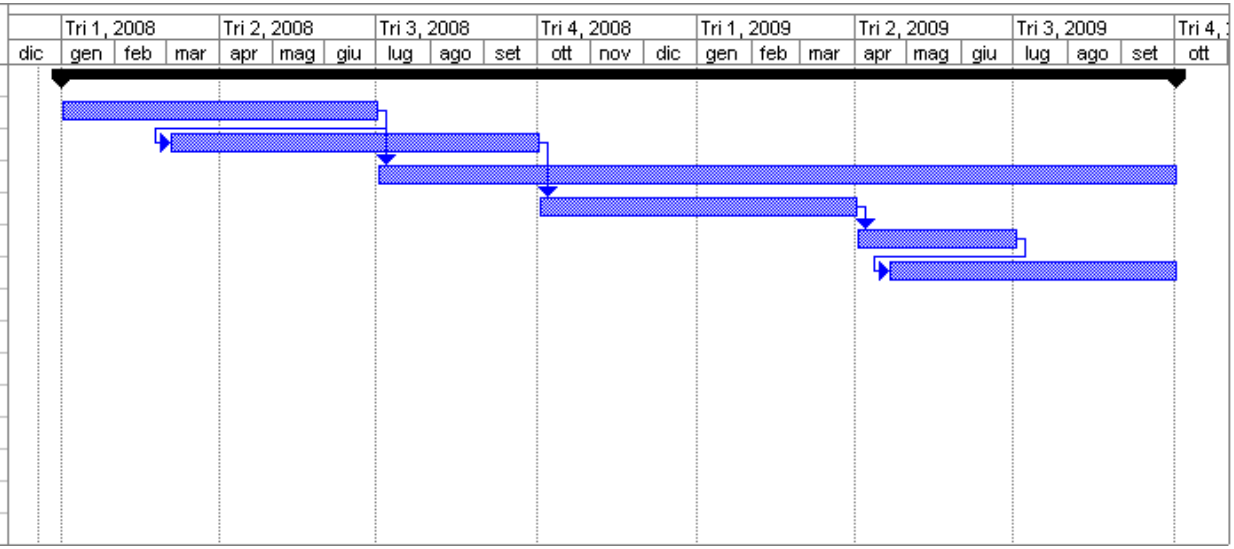

Figure 6-57: IKNOW Development Plan Gantt

6.4 AERO-WAVE MISSION

Even if the full W band satellite channel characterization will be carried out through the LEO mission (IKNOW), preliminary significant results are expected by the shorter-term HAP mission. In fact, since the main phenomenon that could limit the exploitation of this frequency band is the troposphere attenuation due to rain, clouds, fog, gaseous absorption and scintillation, measurements collected by the HAP experiment could already give important highlights to the future work on W band propagation. Time constraints on the development of the P/L to be embarked on a HAP, limits on the flying time of the HAP, and hence on the period of time available for the measurements, poses many challenges to the mission definition and payload design.

The activities within the Aero-WAVE program focus on the development of a P/L carried on-board a High Altitude Platform [6-29][6-30]. This first preliminary mission aims at demonstrating the effectiveness of W band technology in Earth-to-Space communications. The heritage that will be gained through Aero-WAVE mission will be useful for the more complex in-orbit demonstrative mission (IKNOW).

The P/L designing and developing time will be very tight in order to gather in a little time the first results obtained on channel characteristics. In this frame no ad-hoc technological development are foreseen and all the hardware used for P/L development will be COTS (Commercial Off The Shelf).

The P/L will perform experimental measurements on W band channel embarked on-board a HAP. The stratospheric platform is a high altitude aircraft known as the M-55 Geophysica, as shown in Figure 6-58, a Russian aircraft well known in the atmospheric research environment and the European scientific community since 1996 [6-31]. The M-55 Geophysica will be equipped with the P/L instrumentation to carry out the measurements. These measurements and the resulting data provided throughout the Aero-WAVE mission will give important indications of the channel behaviour at different weather conditions and at different locations.

Figure 6-58: Geophysica M55 Aircraft

The mission aims at the following goals:

- In-flight test of W band technology;
- W band satellite channel measurements.

For what concerns the in-flight test at present, most of the commercial W band H/W available has been developed mainly for radar and radio astronomy applications. It should be noted that these are both terrestrial applications. Hence, Aero-WAVE represents a chance to test for the first time some COTS hardware in-flight. This first test is also helpful for the IKNOW mission and for the two pre-operative missions, identifying the critical technologies that need to be developed to be suitable for space applications. In fact, at least for the IKNOW mission, also the use of not space qualified hardware is foreseen. Concerning the latter objective, at present the factor that could potentially limit the exploitation of this frequency band is the troposphere attenuation due to rain, clouds, fog, gaseous absorption and scintillation. Currently, the impact of these phenomena on W band signal propagation is still unknown (from an empirical point of view) because of the pioneering state of W band communications.

6.4.1 AERO-WAVE EXPERIMENTS ARCHITECTURE

Specifically, the project aims at analyzing the W band channel through two different experiments:

1. Channel propagation experiment, including power measurements in order to create a first troposphere attenuation model (on both uplink and downlink);
2. Data transmission experiment, including BER measurements in order to evaluate the W band channel quality (on downlink).

While the first experiment is mandatory, the feasibility of the latter one (matching the project policy) will be investigated during the project.

From the point of view of the time evolution before mentioned, the Aero-WAVE demonstrator constitutes a preliminary step to the development and deployment of IKNOW.

The mission shall be composed by two flight campaigns; one around Rome, and another one over Spino d'Adda. Each campaign shall have a duration of 2 weeks-2 months depending on the number of M-55 flights and on logistic issues (aircraft basing management, man-power costs). As above mentioned, the mission is composed of two different experiments, based on a W band P/L with two RF transmitting channels on-board the Geophysica M-55 aircraft:

- a *beacon transmission and reception section* operating at frequencies in the band of 92-96 GHz, used to provide the necessary signal reception experiments in W band at the fixed ground station in Spino d'Adda, and the transportable station around Rome (channel propagation experiment). The ground segment is the same identified in the phase A. The received signals will provide the necessary elements to analyze the channel behavior at different weather conditions. The operative frequency comes as an output of a preliminary technological market analysis.
- a *data transmission section* operating at a frequency around 94 GHz, used to transmit a known bit stream saved in the on-board memory. Ground stations will be able to perform BER measurements by a simple comparison between the transmitted bit sequence (known a-priori) and the received one, in order to evaluate the W band channel quality.

One of the objectives of Aero-WAVE is to evaluate the troposphere attenuation and to use the acquired knowledge for the development of a W band satellite communication P/L. ITU allocated the 71-76 / 81-86 frequency bands for satellite communications in W band, respectively for downlink and uplink.

One of the requirement of the Aero-WAVE mission is the use of COTS H/W, so the recommended operating frequency range is 92-95 GHz (where most of the COTS hardware components developed for radar and radio astronomy systems operates). Using a recently developed mm-wave radiative model, called SNEM (Sky Noise Eddington Model), it can be noted a high correlation between path attenuation in W band, even though beam filling problems and horizontal atmospheric inhomogeneity are not here considered [6-32]. These results suggest that an instantaneous frequency scaling between link path attenuation at 75/85 GHz (satellite foreseen operative

frequencies) and 92 / 95 GHz (Aero-WAVE foreseen operative frequencies) may be theoretically foreseen as a power law regression.

It is worth mentioning that these model-based results are fairly consistent, in terms of dynamic range and correlation behaviour, with the experimental results obtained for a 1-km terrestrial link at 30, 50, 60 and 94 GHz in France by Veyrunes et al.

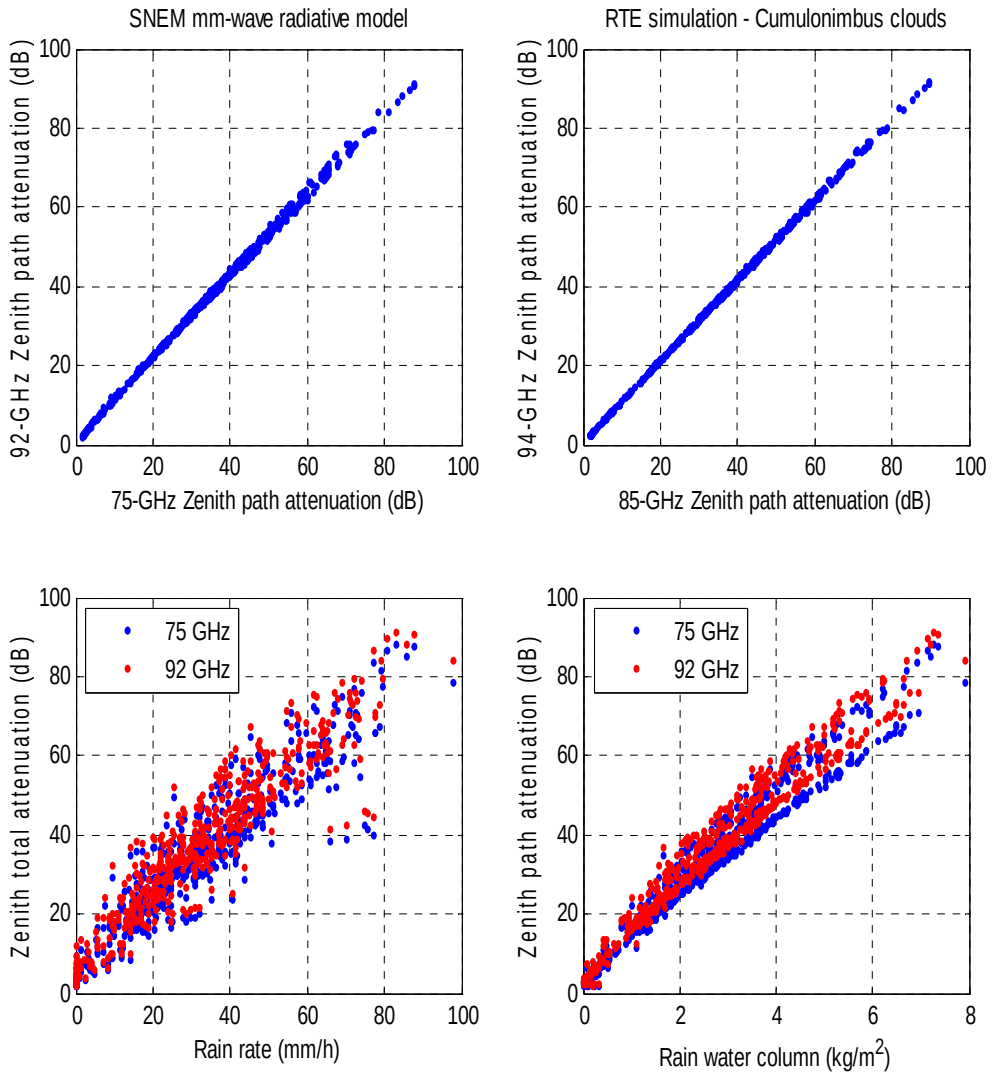

Figure 6-59: Zenithal atmospheric one-way attenuation (dB) in the microwave band at 75, 85, 92 and 94 GHz with respect to rain-rate and rain water content column for a cumulo-nimbus rain cloud

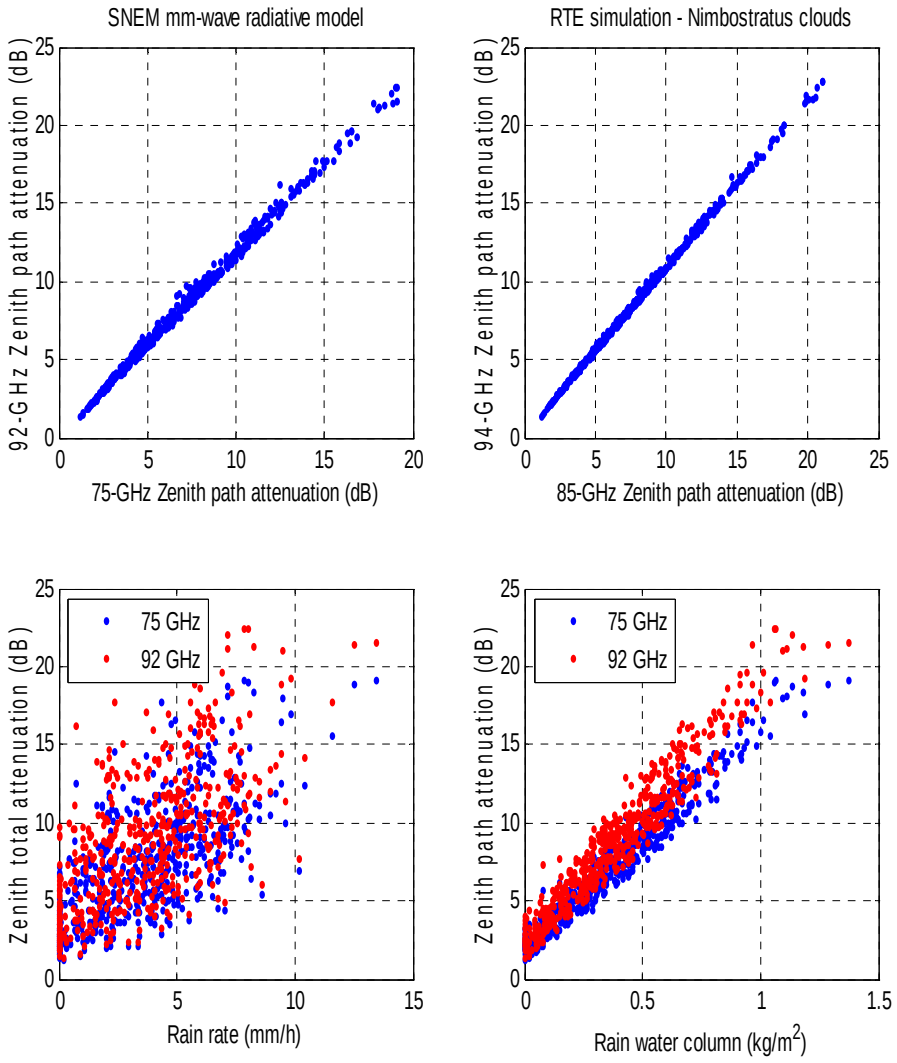

Figure 6-60: Zenithal atmospheric one-way attenuation (dB) in the microwave band at 75, 85, 92 and 94 GHz with respect to rain-rate and rain water content column for a nimbostratus rain cloud

The probability of W band slant path attenuation for the Rome site at 92 GHz is reported as an example in Figure 6-61. These results are based on the ITU-R models which may be questionable at W band, but they still represent a valuable benchmark. If a probability of 1% is chosen, the expected slant-path attenuation is about 18 dB which represents a challenge for the established link. This probability corresponds to about 87 hours / year, which is less than 4 days per year. If a campaign has to be planned, its timing should be driven by high-resolution meteorological forecast. As a matter of fact, a climatological analysis would indicate that the autumn season in Italy is characterized by heavy and diffuse rain storms. Campaign flight periods between September and November might be a good choice for Aero-WAVE mission planning.

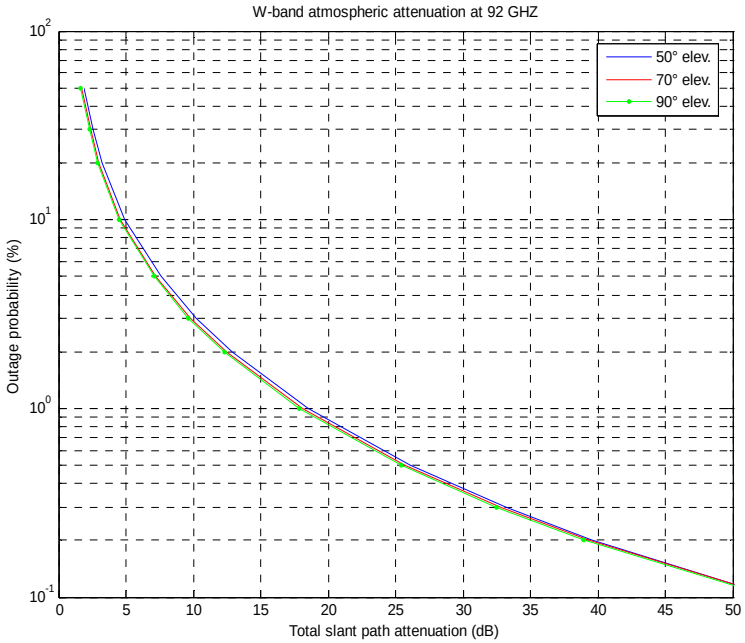

Figure 6-61: Outage probability as a function of total slant path attenuation for the site of Rome at 92 GHz

Concerning the RF receiver on-board the M-55, after the antenna subsystem, the incoming signal goes to an RF detector that compares the received power with a threshold value. This value will be pre-calculated on the basis of the link budget analysis to maximise the detection probability and at the same time minimising the false alarm probability. If the received signal power is greater than the threshold, then it is assumed that the P/L on-board M-55 is receiving the beacon from the ground station and informs the Data Acquisition Centre or store this information (together with a time stamp) in an on-board memory.

The two proposed sites for the airborne campaigns are:

1. over the area around Rome where a transportable ground station could be designed and used;
2. over the area around Spino D'Adda, near Milano, where the fixed ground-station of the Olympus and Italsat communication and propagation experiments is located.

The outage probability at W band is significantly affected by the site and its climatology. In our examples, we considered data from both Milan and Rome sites which are Alps-dominated and Coastline-dominated meteorological regions, respectively. This reflects into a different climatology which is mid-continental for Milan and typically Mediterranean for Rome with very different cloudy and precipitation regimes. With respect to this aspect, it is considered essential to acquire

data from both sites to characterize the site diversity from a radio -meteorological point of view at W band. The aircraft altitude for both campaigns will be around 17-20 km. Figure 6-62 shows a scheme of a typical flight mission. Indeed, for a given on-board antenna a higher altitude would provide a larger foot-print at ground which is preferable for tracking purposes. The flight route of all campaigns will have a diameter of about 10-20 km with an aircraft roll angle variable from 6° to 26°, due to the maneuvers that have to be performed by the pilot in order to counteract winds upheaval. The roll angle should be kept as constant as possible in order to maintain the coverage over the ground station and to acquire propagation data in a stable link for a long time. A fast and accurate antenna tracking system could be deployed, as discussed later on. Experiments at various elevation angles could also be foreseen in order to acquire a large database of propagation measurements in order to find out the variation of the attenuation at different elevation angles, and verify the validity of theoretical models (i.e. secant law). However, the baseline is to conduct some flight with the same path, because the IKNOW mission scenario is more suitable to meet this scope due to the intrinsic variation of the elevation angle during the satellite pass.

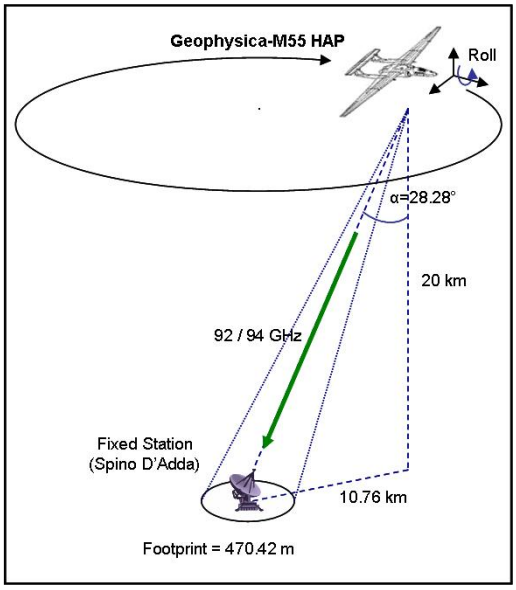

Figure 6-62: Aero-WAVE mission architecture

One of the most critical issues will be the maintenance of the correct alignment between the transmitting and receiving antennas during the flight. The on board antenna subsystem must be steerable, at least with respect to the yaw axis (eventually also with respect to other axes) of the aircraft movement, shown above in Figure 6-62, so that the roll angle changes will not cause link outages (the footprint has to cover earth station for the entire flight).

For the consequent spatial displacement of FOV, as shown in Table 6-34, it may be estimated that:

- if the pointing error angle is 0.5° at 30° off-nadir pointing, the ground FOV will be displaced by about 0.2 km;
- if the pointing error angle is 3° at 30° off-nadir pointing, the ground FOV will be displaced by about 1.2 km.

In this frame, also for the ground antenna subsystem a pointing system is foreseen. Clearly, the ground antenna pointing constraints will be set in a strict way in order to relax the on-board ones (that are more critical from a technological point of view).

On-board antenna beam width	Off-nadir pointing angle	Ground-terminal elevation angle	Slant-projected field-of-view (FOV)	Ground-projected field-of-view (FOV)
1°	0°	90°	0.35 km	0.35 km
1°	15°	75°	0.35 km	0.36 km
1°	30°	60°	0.35 km	0.40 km
3°	0°	90°	1.05 km	1.05 km
3°	15°	75°	1.05 km	1.09 km
3°	30°	60°	1.05 km	1.21 km

Table 6-34: Ground FOV as a function of antenna pointing angle and beam-width

The use of reflector antennas or conical horns with a medium directivity may allow the compliance of these requirements. Some considerations on antenna system have been provided on the ground segment section analysis. The great dynamic of roll variability will affect power and BER measurements because of the antenna gain losses. However, it is not expected that this impairment shall affect the accuracy of the acquired measurements, since, on the basis of the GPS data and recorded aircraft attitude data, it will be possible to process the collected measurements by compensating the gain losses.

6.4.2 AERO-WAVE P/L DESIGN

The functional P/L architecture should be carried out considering the use of existing proved hardware to minimise failure risks and easy integration and test procedure.

Figure 6-63 shows the functional block scheme for the Aero-WAVE P/L. In this P/L, it could be possible to use SSPA, due to the fact that the transmission distance to the HAP is relatively small

with respect to geostationary orbits. In fact, if the altitude is about 20 km and the antenna pointing could be ~30° off-nadir, the free space losses are only about ~159 dB at ~92 GHz. This may relax the constraints on the on-board and ground EIRP.

A 100 mW (i.e., -10 dBW or 20 dBm) device would be suitable both for the data transmission section and radio beacon.

A unidirectional antenna is proposed for the beacon in order to carry out the propagation experiment even in poor M-55 stability conditions. A single reflector antenna with a circular-horn feeder of about 5-mm diameter might be sufficient to ensure the fulfilment of the link requirements. The antenna pointing losses should be carefully taken into account due to the instability of the HAP. As already mentioned, one of the most critical design issue concerning Aero-WAVE P/L is the antenna and the pointing system.

During design activities, an antenna design trade off has been performed considering three different solutions:

1. Narrow beam high gain lens antenna with a mechanical pointing system;
2. Beam-shaped sectoral horn antenna;
3. Multibeam horn antenna system.

The first solution could be considered the best in terms of performance, allowing a tracking of the ground station depending on the aircraft attitude. Moreover, the approach based on such a pointing system allows both the employment of a high gain antenna, relaxing payload features like EIRP and G/T, and the achievement of a good link budget margin (about 3 dB), taking into account the characteristics of the ground station identified in Table 6-35.

In this configuration, the antenna could have narrow beam and therefore an high gain and thanks to the tracking capability the system could avoid pointing losses. The mechanical pointing system could be controlled via two different approaches:

- tracking the ground station by calculating the correct pointing direction through an algorithm based on the a-priori knowledge of the station position, of the aircraft GPS positioning data and attitude data (roll, pitch and heading angles) provided by M-55 navigation system;
- maintaining a fixed pointing on the elevation plane through a Gyro-stabilization using a two-axis gimbal compensating roll and pitch offsets through rate sensors in each axis.

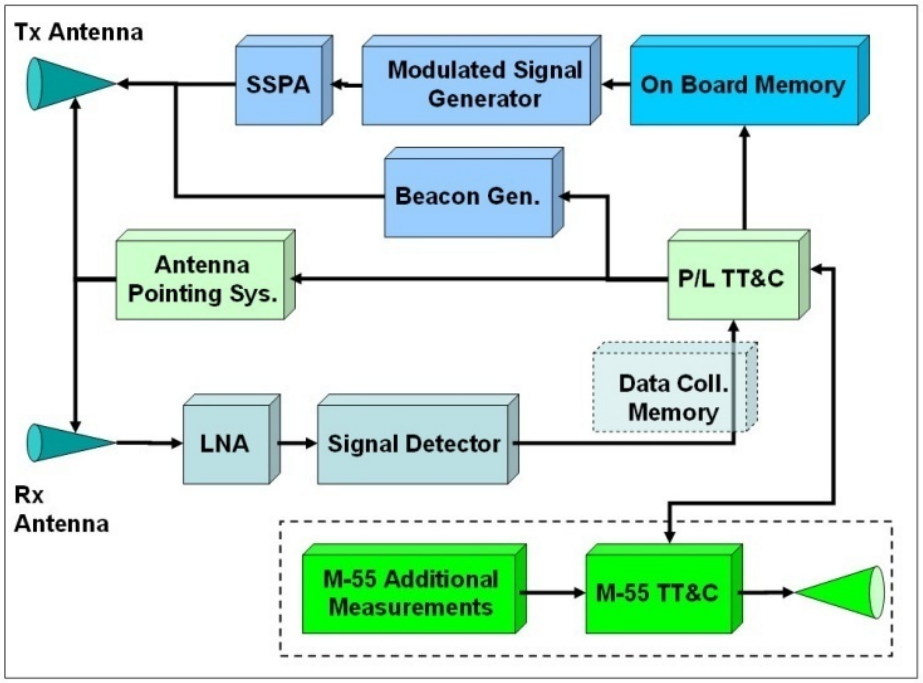

Figure 6-63: Functional block scheme of Aero-WAVE P/L

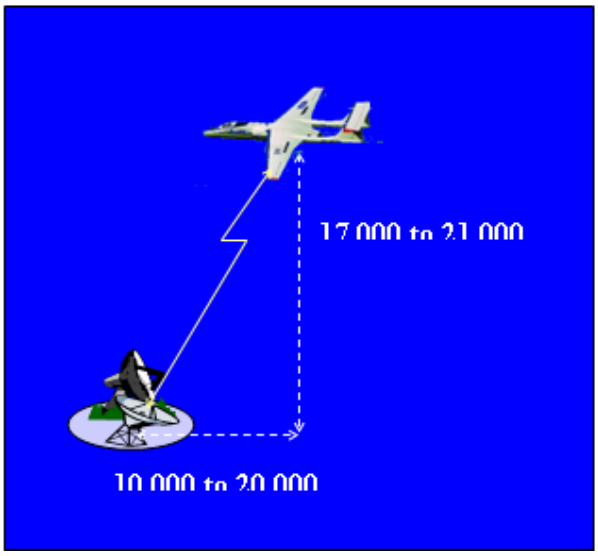

Figure 6-64: Aero-WAVE Mission Scenario

Due to the expected attitude dynamic of the M-55 during the flight, a 2-axis gimbal could be employed. The major problem of the first solution is the need for developing a real time software that is able to provide the pointing direction as the aircraft moves and changes its attitude. This problem is also present for the second solution, but it is less critical since the stabilization shall be performed on the basis of the aircraft attitude, and not considering the position. If both the propagation and data transmission experiments will be performed, the payload will be composed of two sections:

- an on-board memory containing the bit stream to be transmitted followed by the modulation section in which the signal carrier is modulated by the signal; the modulated signal is then amplified using a solid-state or a tube power amplifier, filtered and finally sent through the antenna;
- the beacon which generates a sinusoidal signal to be transmitted for power measurements. To measure the power of the sinusoidal signals, the beacon must send a sufficiently stable signal both in terms of frequency and instantaneous power. A reasonable receiver bandwidth, derived from the extension of the ITALSAT beacon experiments and Spino d'Adda station configuration, might be of the order of 1 kHz.

Ground Station Antenna Pointing Loss:	1,5	dB
Ground Station Antenna Gain:	38	dBi
Receiver NF	11	dB
Ground Station Transmission Line Temp.:	290	K
Ground Station Figure of Merit (G/T):	7	dB/K

Table 6-35: Ground station characteristics

In Table 6-36, Table 6-37 and Table 6-38 all link budgets table results are summarised.

Parameter:		*Value:*	*Units:*	*Comments:*
Spacecraft:				
Spacecraft Transmitter Power Output:		0,01	watts	
	In dBW:	-20,0	dBW	
	In dBm:	10,0	dBm	
Spacecraft Transmission Line Losses:		2,0	dB	
S/C Connector, Filter or In-Line Switch Losses:		0,0	dB	**Hypothesis**
Spacecraft Antenna Gain:		34,0	dBiC	
Spacecraft EIRP:		12,0	dBW	
Downlink Path:				
Spacecraft Antenna Pointing Loss:		0,1	dB	
Antenna Polarization Loss:		0,5	dB	**Hypothesis**
Frequency		95000,0	MHz	
Distance		26,3	Km	
Path Loss:		160,4	dB	
Atmospheric Loss:		17,9	dB	
Ionospheric Loss:		0,0	dB	**Hypothesis**
Isotropic Signal Level at Ground Station:		-166,9	dBW	
Ground Station:				
------- C/N Method -------				
Ground Station Antenna Pointing Loss:		1,9	dB	
Ground Station Antenna Gain:		52	dBiC	
Ground Station Transmission Line Losses:		2	dB	
Ground Station LNA Noise Temperature:		1163,44	K	
Ground Station Transmission Line Temp.:		290	K	
Ground Station Sky Temperature:		100	K	**Hypothesis**
G.S. Transmission Line Coefficient:		0,6310		
Ground Station Effective Noise Temperature:		1334	K	
Ground Station Figure of Merrit (G/T):		18,7	dB/K	
G.S. Carrier-to-Noise Power Density (C/No):		78,6	dBHz	
PLL Noise Bandwidth		5000	Hz	
Downlink C/N:		41,6	dB	
Downlink Required C/N:		7	dB	
System Link Margin:		**34,6**	dB	

Table 6-36: Downlink Propagation Experiment @ 95GHz (Rome)

Parameter:		*Value:*	*Units:*	*Comments:*
Ground Station:				
Ground Station Transmitter Power Output:		0,01	watts	
	In dBW:	-20,0	dBW	
	In dBm:	10,0	dBm	
Ground Station Transmission Line Losses:		2,0	dB	
S/C Connector, Filter or In-Line Switch Losses:		0,0	dB	**Hypothesis**
Ground Station Antenna Gain:		51,8	dBiC	
Ground Station EIRP:		29,8	dBW	
Uplink Path:				
Ground Station Antenna Pointing Loss:		1,9	dB	
Antenna Polarization Loss:		0,5	dB	**Hypothesis**
Frequency		92000,0	MHz	
Distance		26,3	Km	
Path Loss:		160,1	dB	
Atmospheric Loss:		19,5	dB	
Ionospheric Loss:		0,0	dB	**Hypothesis**
Isotropic Signal Level at Ground Station:		-152,2	dBW	
Spacecraft:				
------- C/N Method -------				
Spacecraft Antenna Pointing Loss:		2,3	dB	
Spacecraft Antenna Gain:		34	dBiC	
Spacecraft Transmission Line Losses:		2	dB	
Spacecraft LNA Noise Temperature:		1163,77	K	
Spacecraft Transmission Line Temp.:		290	K	
Spacecraft Sky Temperature:		273	K	**Hypothesis**
G.S. Transmission Line Coefficient:		0,6310		
Spacecraft Effective Noise Temperature:		1443	K	
Spacecraft Figure of Merrit (G/T):		0,4	dB/K	
S. Carrier-to-Noise Power Density (C/No):		74,5	dBHz	
PLL Noise Bandwidth		5000	Hz	
Uplink C/N:		37,5	dB	
Uplink Required C/N:		7	dB	
System Link Margin:		**30,5**	dB	

Table 6-37: Uplink Propagation Experiment @ 92GHz (Rome)

Parameter:		*Value:*	*Units:*	*Comments:*
Spacecraft:				
Spacecraft Transmitter Power Output:		0,01	watts	
	In dBW:	-20,0	dBW	
	In dBm:	10,0	dBm	
Spacecraft Transmission Line Losses:		2,0	dB	
S/C Connector, Filter or In-Line Switch Losses:		0,0	dB	**Hypothesis**
Spacecraft Antenna Gain:		34,0	dBiC	
Spacecraft EIRP:		12,0	dBW	
Downlink Path:				
Spacecraft Antenna Pointing Loss:		2,3	dB	
Antenna Polarization Loss:		0,5	dB	**Hypothesis**
Frequency		94000,0	MHz	
Distance		26,3	Km	
Path Loss:		160,3	dB	
Atmospheric Loss:		7,34	dB	
Ionospheric Loss:		0,0	dB	
Isotropic Signal Level at Ground Station:		-158,5	dBW	
Ground Station:				
------- Eb/No Method -------				
Ground Station Antenna Pointing Loss:		1,9	dB	
Ground Station Antenna Gain:		52,1	dBiC	
Ground Station Transmission Line Losses:		2	dB	
Ground Station LNA Noise Temperature:		1163,44	K	
Ground Station Transmission Line Temp.:		290	K	
Ground Station Sky Temperature:		100	K	**Hypothesis**
G.S. Transmission Line Coefficient:		0,6310		
Ground Station Effective Noise Temperature:		1334	K	
Ground Station Figure of Merrit (G/T):		18,8	dB/K	
G.S. Signal-to-Noise Power Density (S/No):		87,1	dBHz	
System Desired Data Rate:		20000000	bps	To be decided yet (here chosen 20 Mbps)
	In dBHz:	73,0	dBHz	
System Eb/No:		14,1	dB	Assumes Spectral Efficiency of 1.0 b.p.s./Hz of Bandwidth
System Required Bit Error Rate:		1,00E-06		
System Required Eb/No:		11,7	dB	
System Link Margin:		2,4	dB	

Table 6-38: Data Transmission Experiment @ 94GHz (Rome)

Figure 6-65 shows the P/L configuration. It addresses the propagation experiment on both uplink and downlink and the data transmission experiment on downlink as well. The antenna is shared for both the link directions (up and down). The choice to share the antenna due to the frequency diversity of UL and DL signal is compliant with commercial antenna products, that have a typical bandwidth of 10% with respect to the central frequency, corresponding to 9.4 GHz bandwidth @ 94 GHz.

The uplink signal, centered at 95.4 GHz, is filtered and then amplified by an LNA. After the RF amplification, a mixer beats the incoming signal with the one of a Local Oscillator at 94 GHz, converting the signal carrier down to 1.4 GHz. The oscillator could be a Gunn Oscillator because of

the non-coherent signal power measurement, as described later. Then the signal is filtered through an IF band pass filter.

The intermediate frequency is chosen on the basis of the M-55 instruments operating frequencies, avoiding interference. The closest frequencies to the IF are those of the M-55 GPS system, working at 1.575 and 1.227 GHz. This interval shall be considered when defining the filter specifics, taking into account the maximum interference allowed by the GPS receiver.

Finally, the signal is passed to the RF power measurement unit, including an IF logarithmic amplifier (the choice is driven by the large input dynamic), a band-pass filter, a quadratic detector, a low-pass filter and finally to the A/D converter. Data are then stored in the on-board memory. Regarding the transmitting section, it is composed by the downlink signal generator at 94.8 GHz. In addition, the data transmission section is composed by the baseband section, comprehensive of a modulator and a local oscillator converting the signal up to 12 GHz, a band-pass filter and a second oscillator upconverting the signal carrier to the final frequency of 94.3 GHz, and finally the SSPA providing the RF power level needed. The transmitter section of the propagation experiment is composed by the beacon generator, that basically amplifies and filters the continuous wave signal at 94.8 GHz of the LO. The incoming signal, after low noise amplification and down conversion is divided in two branches through a 3 dB splitter. One branch drives the signal to the power measurement unit, while the other one drives the signal to the bent pipe.

The modulated signal is down converted to an IF of 12 GHz and amplified. Then a switch operating on the basis of a pre-scheduled command selects the downlink signal between the bent pipe and the data transmission section. Then, the band-pass filter, the second local oscillator, the RF band-pass filter and the SSPA are time-shared between the two experiments.

6.4.3 OPERATIVE MODES ANALYSIS

This paragraph deals with the description of Aero-WAVE P/L operative modes, as shown in Figure 6-66.

An operative mode is considered as a set of states, functions and commands. Before the aircraft take-off, the STAND BY command is sent manually to shift the P/L in the warm up mode. During this phase, the P/L is operative, but the output signal is not forwarded to the antenna, but to a termination. The ON and OFF commands are sent manually by the M-55 pilot when the aircraft reaches the circular path and when it leaves it. Before starting power measurements in uplink, a bite signal is sent to the Rx section. This allows to record the power measurement performed on a known source, enabling offline to check if there is any anomalous behaviour of the P/L. Then, the REC command enables to pass from the bite state to the Rx state. The bite command enables to

change state back to the bite state. In fact, the bite operation is performed periodically with a certain interval (in the order of a few minutes). This is quite useful to check offline the validity of the measurements performed during the flight.

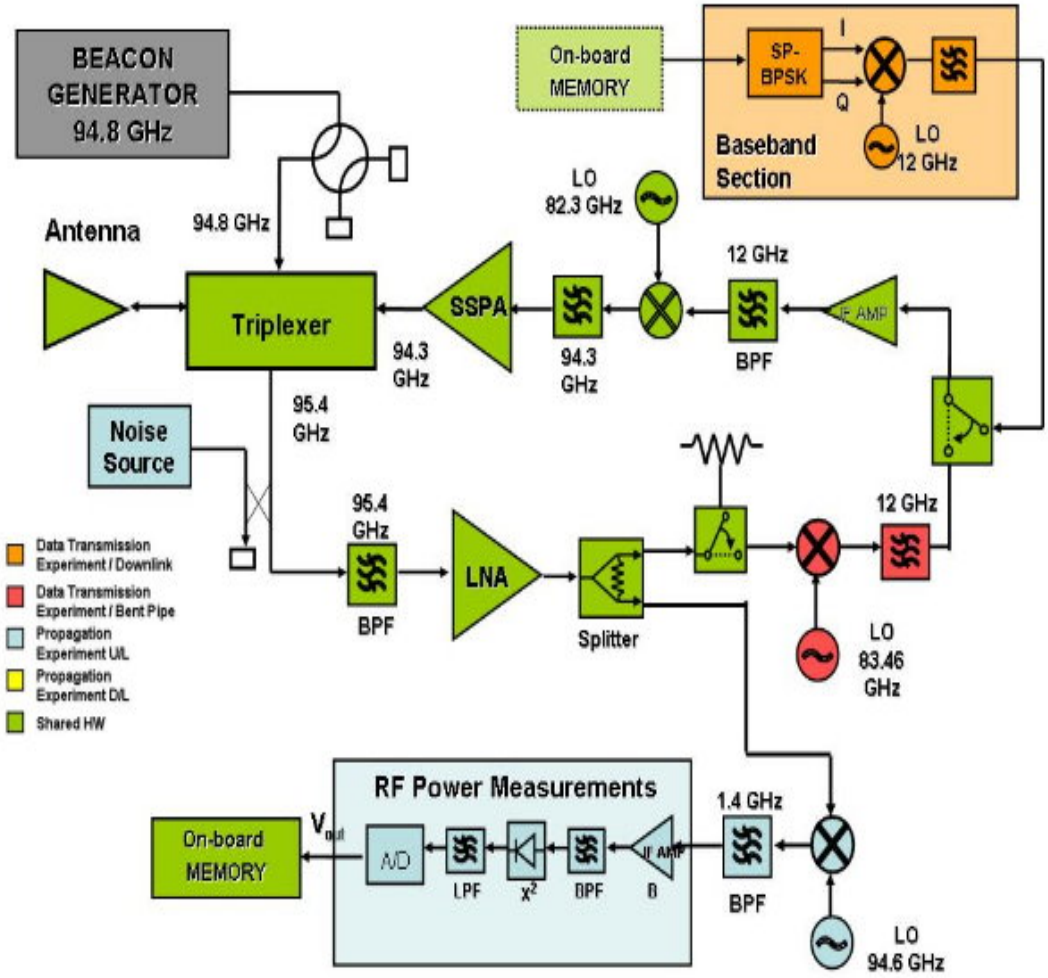

Figure 6-65: Aero-WAVE P/L Configuration

Moreover, the P/L configuration includes three different operative modes:

1. Propagation mode;
2. Data transmission mode;
3. Relay mode.

While the first two can operate at the same time, the second (Data transmission) and the third (Relay) are mutually exclusive. In fact, the SWITCH command enable the shift between the two states data Tx and relay Tx. This command is activated after a predefined time interval.

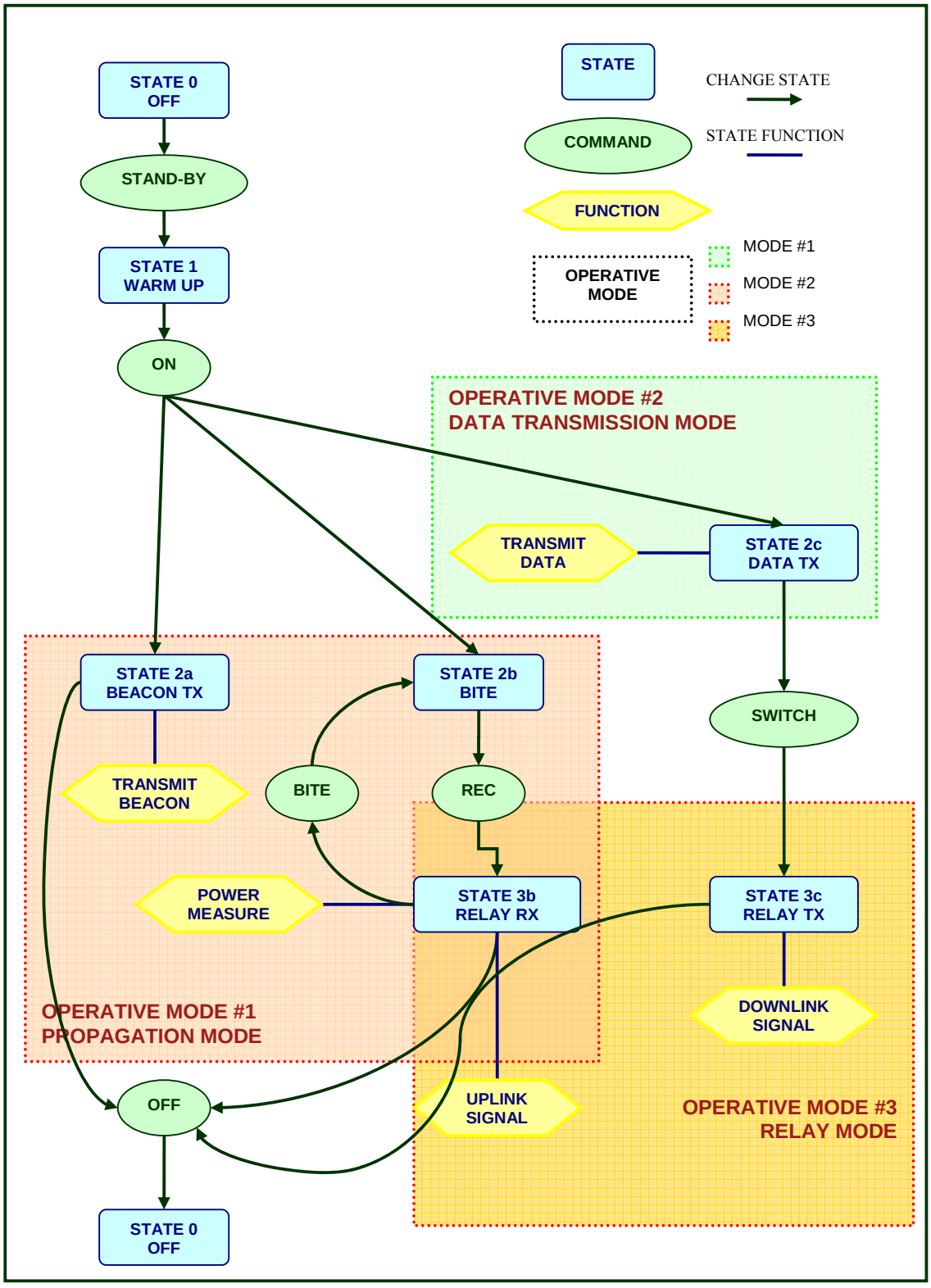

Figure 6-66: Operative modes – AeroWAVE P/L Configuration

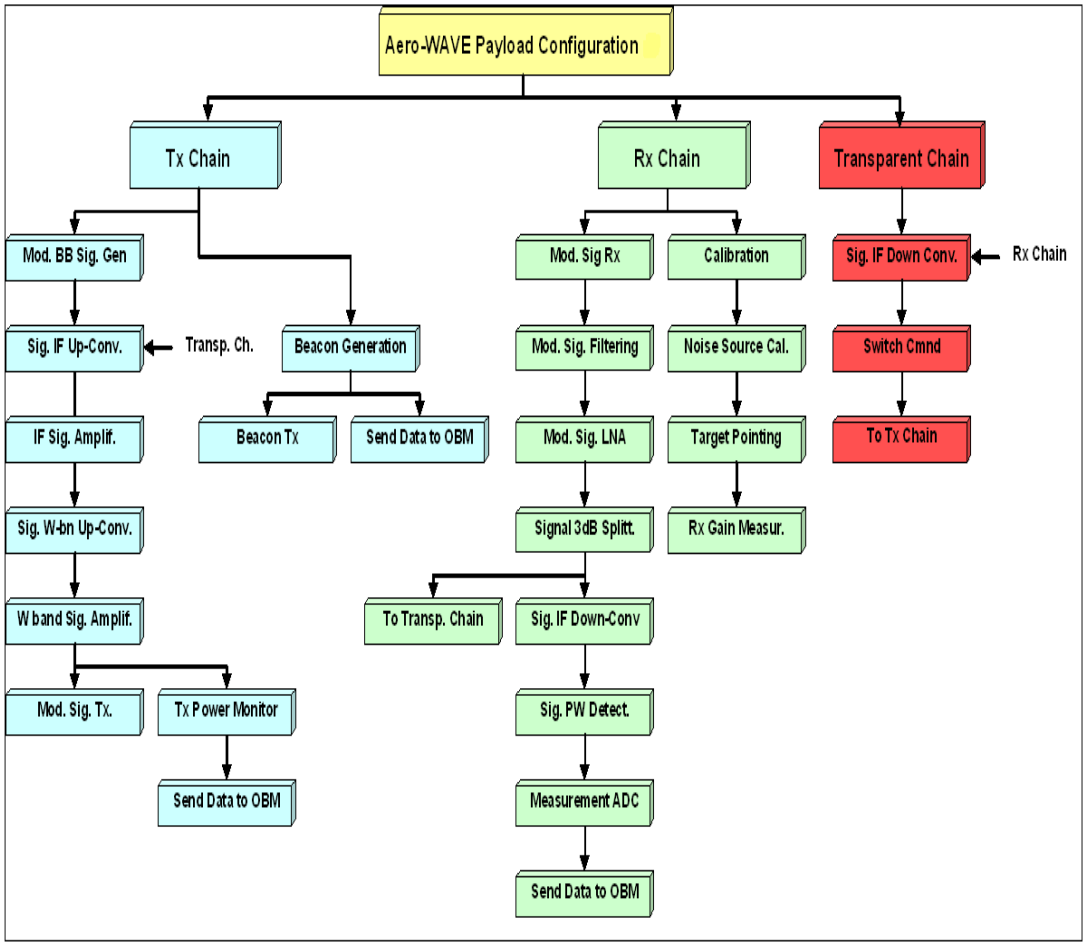

Figure 6-67: Function Tree – AeroWAVE P/L Configuration

6.4.4 PRELIMINARY SPECIFICATIONS DEFINITION AND P/L PERFORMANCE ANALYSIS

In this paragraph technical specifications have been provided.

Antenna Specifications

Type: Lens Antenna

Diameter: 7-15 cm TBD

Nominal Gain: >34-38 dBi TBD

Operating Bandwidth: ≥ 1 GHz

Centre frequency: 94.8 GHz

3dB Beamwidth: 3 – 1.5 degrees

Secondary Lobe level: <-20 dB

Front to Back Ratio: >40 dB (TBC)

Pointing System Specifications

Position Resolution: < 0.1 deg

Range of Motion: $\geq \pm$ 5° pitch and $\geq \pm$ 10° roll

Payload capacity: $\geq$ 7 kg

Travel Rate: $\geq$ 1°/sec pitch and $\geq$ 1°/sec roll

Triplexer Specifications

Ports Centre Frequencies:

PORT 1 (Uplink) : 95.4 GHz;

PORT 2 (Downlink propagation Experiment) : 94.8 GHz;

PORT 3 (Downlink data Transmission / Relay Experiment) : 94.3 GHz.

Insertion Losses: < 2 dB.

Passband width:

PORT 1 : >12 MHz;

PORT 2 : >200 KHz;

PORT 3 : >12 MHz.

Receiver Specification

Propagation Experiment (Uplink)

Considering the receiving section, the receiver components specifications are shown. Receiver specifications are listed below:

- Dynamic Range: $\geq$ 13 dB.
- Minimum IPFD : -146 dBW/m^2.
- LO Specifications: centre frequency: 94.0 GHz, output power : $\geq$ 10 dBmW.
- Mixer Specifications: RF Frequency Range 95.34 – 95.46 GHz; IF Frequency Range 1.34 – 1.46 GHz; LO output power $\geq$ 10dBm; Conversion Loss < 10 dB; LO-RF isolation > 14 dB; LO-IF isolation > 19 dB; breakdown power > 14 dBm CW. RF Connection Port : WR-10.
- LNA Specifications: NF $\leq$ 4 dB (Integrated and with transition to WR10); RF Operative Frequency Range 95.34 – 95.46 GHz. Small Signal Gain $\geq$ 18 dB; RF Connection Port : WR-10, Return loss in /out $\geq$ 20 dB.

Noise floor and signal cascade are shown in Table 6-39 and Figure 6-68.

Cascade Levels - Bent Pipe										
	Connection	Triplexer	Coupler	BPF	LNA	Splitter	Mixer	BPF	IF Amp	BPF
GAIN (dB)	-0,50	-2,00	-1,00	-1,00	18,00	-4,00	-7,00	-0,50	20,00	-0,50
NF (dB)	0,50	2,00	1,00	1,00	4,00	4,00	10,00	0,50	4,00	0,50
Cumulative Gain (dB)	-0,50	-2,50	-3,50	-4,50	13,50	9,50	2,50	2,00	22,00	21,50
Cumulative NF (dB)	0,50	2,50	3,50	4,50	8,50	8,54	9,12	9,15	9,63	9,63
Output Noise Floor (dBm)	-103,45	-103,45	-103,45	-103,45	-81,45	-85,41	-91,83	-92,29	-71,82	-72,32
Output MDS Signal (dBm)	-94,32	-96,32	-97,32	-98,32	-80,32	-84,32	-91,32	-91,82	-71,82	-72,32
Output Signal with Margin (dBm)	-87,32	-89,32	-90,32	-91,32	-73,32	-77,32	-84,32	-84,82	-64,82	-65,32
Notes	Margin = 7 dB ; Noise Bandwidth= 12 MHz									

Table 6-39: Uplink Propagation Experiment

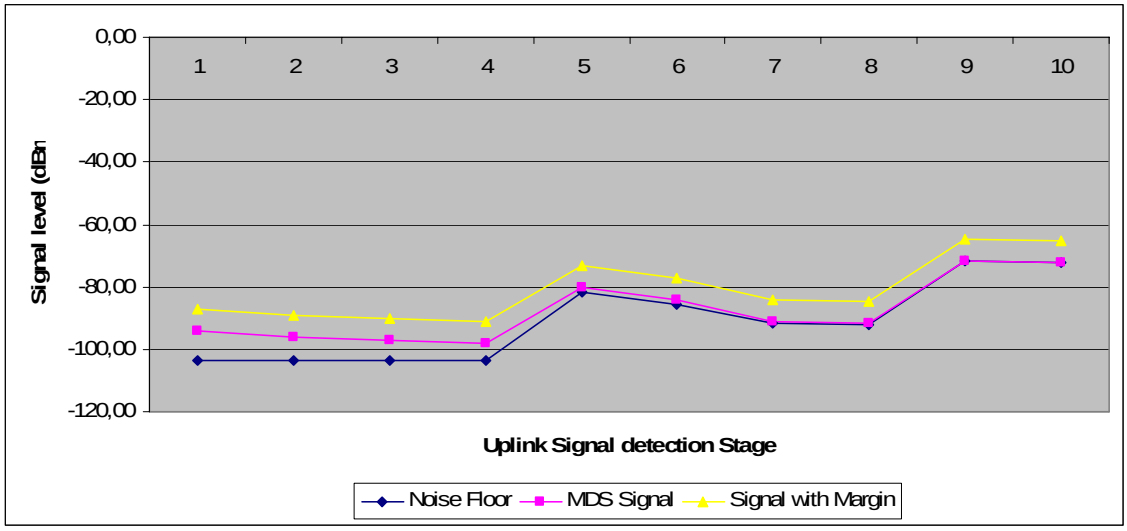

Figure 6-68: Uplink Propagation Experiment

Transmitter Specification

Propagation Experiment (Downlink)

Data Transmission

- Centre Frequency: 94.3 GHz;
- Channel Bandwidth≥ 6 MHz
- EIRP ≥ 17.5 dBW;
- Phase Noise: < -80 dBc @ 100 KHz (TBC);
- LO Frequency Stability : ± $1*10^{-10}$ over 5 hours (TBC);
- EIRP stability: ± 1.5 dB over 5 hours (TBC);
- Gain - frequency stability : ± 0,5 dB over the whole channel bandwidth (TBC).

Signal to spurious ratio must be greater than 31 dB over the whole channel bandwidth.

SSPA Specifications:

- P_{out} (1dBCP) $\geq$ 17 dBm;
- $G_{lin} \geq$ 15 dB.
- Gain - frequency stability : ± 1 dB over the whole channel bandwidth (TBC);

SSPA Specifications are summarized in Table 6-40:

SSPA Features		
Glin	15,00	dB
Pout (1dBCP)	17,00	dBmW
Pin (1dBCP)	3,00	dBmW
Centre Frequency	94.3	GHz
Operating Bandwidth	6	MHz

Table 6-40: SSPA specifications – Beacon generator

These values are calculated on the basis of the following ground stations receivers requirements:

Ground Station Antenna Pointing Loss:	1,5	dB
Ground Station Antenna Gain:	38	dBi
Receiver NF	11	dB
Ground Station Transmission Line Temp.:	290	K
Ground Station Sky Temperature:	100	K
Equivalent Noise Temperature	1248,66	
Ground Station Figure of Merrit (G/T):	7	dB/K
Noise Bandwidth	5000000	Hz
System Required Bit Error Rate:	1,00E-04	
System Required Eb/No:	10	dB
System Desired Data Rate:	5000000	bps

Table 6-41: Ground Station Receiver Requirements – Propagation Experiment

Signal cascade is shown in Table 6-42 and Figure 6-69:

	LO 12 GHz	Mixer	IF Amp	BPF	Mixer	BPF	Attenuator	SSPA	Triplexer	Connection
GAIN (dB)	-	-7,00	20,00	-1,00	-7,00	-0,50	-5,50	10,00	-2,00	-0,50
Output Signal (dBm)	8,00	1,00	21,00	20,00	13,00	12,50	7,00	17,00	15,00	14,50

Table 6-42: Transmitter Signal cascade – Data Transmission Experiment

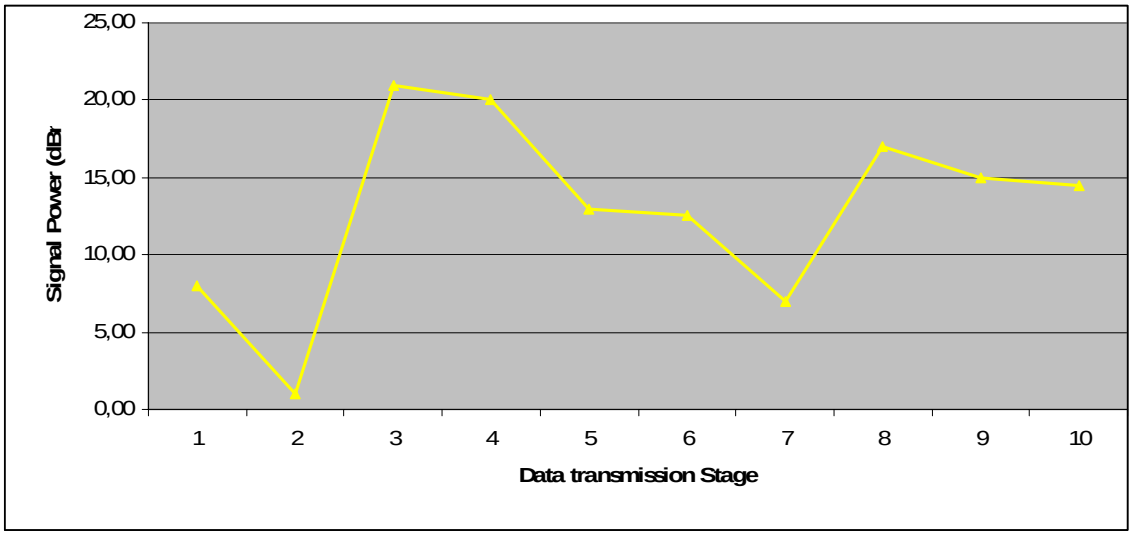

Figure 6-69: Transmitter Signal cascade diagram – Data Transmission Experiment

Power Budget

Aero-WAVE Power Budget		
Component	***# Components***	***Power (W)***
2 axis Gymbal	1	8,000
Transmission Experiment		
BB section	1	1,500
Propagation experiment		
W band Beacon Generator	1	2,000
Mixer	1	0,900
Power Measurements Unit	1	0,121
P/L Common Part		
On-board Memory	1	2,500
LNA	1	0,350
Mixer	2	0,900
X band Amplifier	1	2,000
W band SSPA	1	2,000
Thermal Control Unit	1	5,000
Frequency Generation Unit	1	20,940
Margin	**-**	**2,000**
P/L POWER CONSUMPTION		**40,211**
TOTAL POWER CONSUMPTION		**48,211**

Table 6-43: Power Budget

Mass Budget

Aero-WAVE Mass Budget		
Component	***# Components***	***Weight***
2 axis Gymbal	1	6,00
Transmission Experiment		
SP-BPSK Modulator	1	0,05
Mixer	1	0,10
X band BPF	1	0,10
Propagation experiment		
W band Beacon Generator	1	0,15
Mixer	1	0,10
IF Power Detection	1	0,05
Waveguide WR10	~4	0,15
Waveguide WR650	~2	0,05
P/L Common Part		
W band Triplexer	1	0,10
W band Antenna Assy	1	1,00
On-board Memory	1	0,20
W band input BPF	1	0,03
LNA	1	0,10
W band signal splitter	1	0,10
Mixer	2	0,10
X band BPF	2	0,10
X band Amplifier	1	0,10
W band BPF	1	0,10
W band SSPA	1	0,10
X band Switch	1	0,10
W band Switch	1	0,10
Noise Calibration Source	1	0,15
WR10 Coupler	1	0,05
Waveguide WR10	~8	0,30
Waveguide WR90	~4	0,20
Frequency Generation Unit	1	0,42
Packaging	-	0,50
P/L WEIGHT		**4,60**
TOTAL WEIGHT		**10,60**

Table 6-44: Mass Budget

6.4.4.1 FREQUENCY GENERATOR AERO-WAVE P/L CONFIGURATION

In order to achieve the required phase noise, efficiency and power output from the frequency generator of the Aero-WAVE P/L, it is suitable to use PLDRO, that are dielectric resonator oscillators locked with an external reference source.

In order to achieve the locking of PLDRO employed in the design of the Aero-WAVE P/L frequency generator, a 100 MHz crystal reference source can be used, as shown in Figure 6-70. The PLDRO is composed of fundamental frequency generator module (FGM) and frequency multiplication part (FMP). The FGCM consists of Voltage Controlled Dielectric Resonator Oscillator (VCDRO), LPFs, buffer amplifier, coupler, Sampling Phase Detector (SPD) and Oven Controlled Crystal Oscillator (OCXO). The VCDRO in the FGCM has been designed to have good phase noise characteristics using, for example, a high impedance inverter coupled with dielectric method resonator. A buffer amplifier is followed by VCDRO to amplify the VCDRO signal and to improve the pulling, as shown in Figure 6-71.

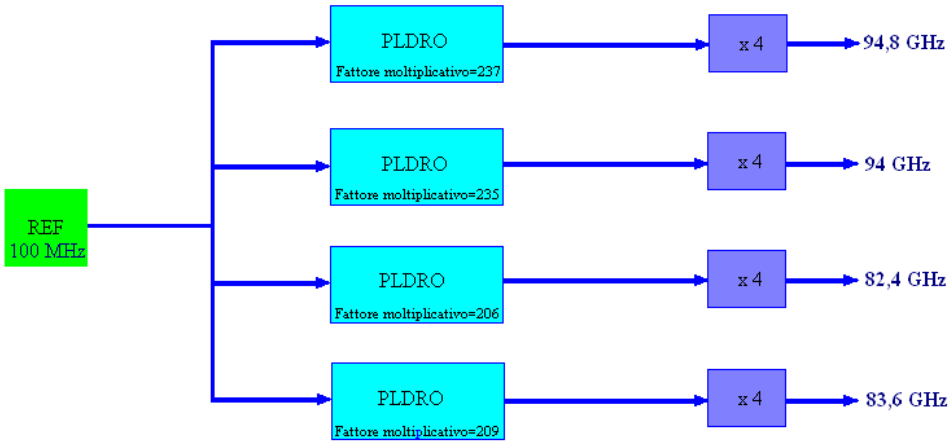

Figure 6-70: Functional Architecture of Aero-WAVE P/L Frequency Generator

The balanced type buffer amplifier is employed to increase the power compression point by 3 dB and to reduce the return loss of input and output ports. Two LPFs which are followed by VCDRO and buffer amplifier, respectively, suppress the harmonics.

The SPD consists of a step recovery diode and a pair of Schottky diodes. The step recovery diode generates the harmonic combs of the reference frequency of 100 MHz. The signal of VCDRO, for example for the 23,7 GHz PLDRO as shown in Figure 6-70, is compared to the 79th harmonic signal of the reference frequency in a pair of schottky diode to detect phase error. The FFGM can contain two chains of signal generator - one active and the other redundant – to reduce the size and mass, designing an adequate structure for space uses. The signal generated in the FFGM is tripled in the FMP.

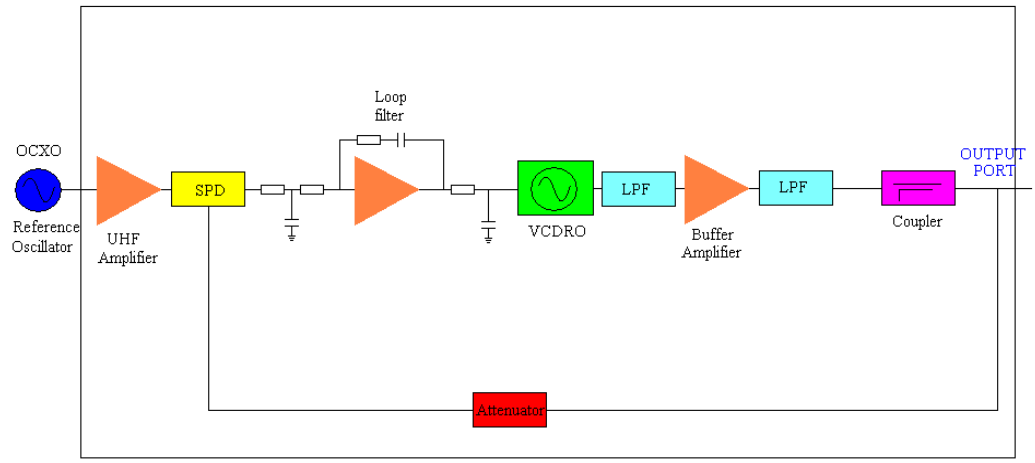

Figure 6-71: Block Diagram of fundamental Frequency Generator module

It consists of attenuator, frequency tripler, BPF, driver amplifier, and test coupler. The following Figure shows the block diagram of FMP.

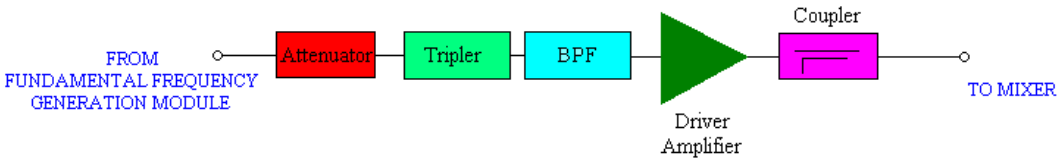

Figure 6-72: Block Diagram of fundamental frequency multiplication part

The attenuator, which is located in front of frequency tripler, is equipped for the purpose of adjusting the power level of FFGM output. A Thermopad can be used as an attenuator to deal with the attenuation level variation according to temperature variation. It is suitable to design the frequency tripler using MMIC technology to minimize the size of the FMP. PLDRO technology offers the best state of art phase noise performance for solutions not based on complete integration. Low cost, high temperature stability and efficiency, small size and light weight, excellent SSB Phase Noise are some advantages in using PLDRO oscillators.

6.4.4.2 DESIGN AND DEVELOPMENT PLAN DEFINITION

A H/W matrix is provided for AERO-WAVE P/L configuration. The H/W matrix identifies for each equipment/component the related qualification status and the required models. Taking into account the intrinsic nature of the Aero-WAVE mission (not a satellite P/L, stratosphere flight, extensive

use of COTS components and so on), the H/W matrix provided has to be necessarily modified to be suited to this context. Thus, the next H/W matrix illustrates the P/L components status (identified in previous sections) in terms of availability, development and purchase, on the basis of the following legend:

Legend	Meaning
A	Available
D	To be developed
P	To be purchased

"**A**" letter identifies units/subsystems available due to developments or purchases already carried out, "**D**" letter identifies units/subsystems to be developed and finally "**P**" letter identifies units/subsystems to be purchased. The "Considerations" column shows any critical item related to that unit/subsystem (i.e. procurement, etc.).

6.4.4.3 P/L INTEGRATION, TEST AND VERIFICATION

Procedures of integration, test and verification are strictly important and should be taken carefully into account.

A complete test and verification activity of Aero-WAVE will include both on-ground tests and in-flight tests. Specifically, activities of integration, test and verification of the Aero-WAVE P/L will be referred through the following main steps:

1. Definition of the P/L design and development specifications;
2. Definition of the subassemblies specifications;
3. Make or buy activities;
4. Procurement phase;
5. Incoming inspection of material/components purchased;
6. Subassemblies assembly;
7. Verification and test at single subassembly level;
8. Subassemblies integration;
9. Final P/L test;
10. Test report.

Concerning verification activities, they will be carried out both at subassemblies and P/L level taking into account the following scheme:

Legend	Meaning
D	Demonstration
A	Analysis
T	Test

Table 6-45: Type of envisaged verification activities

Unit/Subsystem	Status			Considerations
	A	D	P	
Antenna Block				
Antenna	●			Antenna already purchased
Triplexer	●			Not critical, developed by RHI
WG Switch			●	Not critical
Noise Calibration Source			●	Not critical
WR10 Coupler	●			Not critical
WG Plumbing			●	Not critical, integration and forming in RHI
Gimbal			●	Gimbal to be purchased by US company
Rx Block				
input BPF	●			Not critical, developed by RHI
LNA	●			Already purchased by Millitech (RHI)
Mixer			●	Critical procurement, to be purchased by Millitech US company
W band LO			●	Critical procurement
IF BPF		●		Not critical, to be developed by RHI
Tx Block				
Beacon Generator		●		Not critical, Gunn oscillator
BPF		●		Not critical, to be developed by RHI
W band Mixer			●	Critical procurement, to be purchased by Millitech US company
W band LO			●	Critical procurement
IF BPF		●		Not critical, to be developed by RHI
W band SSPA			●	Critical procurement, to be purchased by IAF, Quinstar, Northrop Grumman
Baseband Block				
I/Q Vector Modulator			●	Not critical
PLDRO			●	Not critical
PCB		●		Not critical
RF Power Measurement Block				
RF Detector Block			●	Not critical, to be purchased by Miteq
A/D Converter			●	Not critical
PCB	●			Not critical
Transparent Block				
W Band Splitter	●			Not critical
W Band Switch			●	Critical procurement
W Band Mixer			●	Critical procurement, to be purchased by Millitech US company
W Band LO				Critical procurement
IF Filter		●		Not critical
IF Switch			●	Not critical
IF Amplifier			●	Not critical
Miscellanea				
Power supplies		●		Not critical
Filters		●		Not critical
Memory/Interface/Monitoring and Control Card		●		Not critical
Harness		●		Not critical

Table 6-46: Aero-WAVE configuration: H/W matrix

"**D**" means that the verification activity will be pursued through a demonstration i.e. by comparison with other similar systems (manufactured through equivalent technological process) or through inspection, i.e. verification of a requirement by project documentation. "**A**" means that the verification activity will be based on suited simulations and analyses, and finally "**T**" means that the verification activity will be carried out through laboratory test on subassemblies/equipment/components. In Table 6-47, a verification matrix is provided for the components identified through the H/W matrix on the basis of the above illustrated legend.

Unit/Subsystem	Verification		
	D	A	T
Antenna Block	●		●
Antenna			●
Triplexer			●
WG Switch			●
Noise Calibration Source			●
WR10 Coupler			●
WG Plumbing	●		●
Gimbal			●
Rx Block	●	●	●
input BPF			●
LNA	●		●
Mixer	●		●
W band LO	●		●
IF BPF		●	●
Tx Block	●	●	●
Beacon Generator		●	●
BPF		●	●
W band Mixer	●		●
W band LO	●		●
IF BPF		●	●
W band SSPA		●	●
Baseband Block		●	●
I/Q Vector Modulator			●
PLDRO			●
PCB		●	●
RF Power Measurement Block		●	●
RF Detector Block			●
A/D Converter			●
PCB		●	●
Transparent Block	●	●	●
W Band Splitter		●	●
W Band Switch			●
W Band Mixer	●		●
W Band LO	●		●
IF Filter			●
IF Switch			●
IF Amplifier	●		●
Miscellanea	●		●
Power supplies	●		●
Filters	●		
Memory/Interface/Monitoring and Control Card	●		
Harness	●		

Table 6-47: Verification Matrix

6.4.5 AERO-WAVE CRITICAL ISSUES

At this phase of the study, the Aero-WAVE P/L does not present special technological challenges beyond the intrinsic technological feasibility of equipment and devices at W band. Actually, design, manufacturing and assembly of W band H/W constitute a critical challenge due to the high operative frequency which affects mainly high power generation, low noise amplification and losses. However, the P/L was designed with the aimed objective to employ Commercial Off The Shelf components (i.e. COTS). Therefore, most of the elements to be used do not require specific technological developments and main focus is the components and equipment assembly; just few elements need to be developed but they are not critical.

The use of COTS is based both on: 1) the use of components/equipment already existing and developed for other applications; 2) the purchase of components/equipment by microwave-specialised companies.

Rheinmetall (RHI) Italy have developed or purchased several mm-wave components/equipment suitable to be used in the Aero-WAVE P/L due to its strong involvement in the millimeter wave radars domain (95 GHz) for military and civil applications. In addition, RHI purchased or developed several components to be used in systems assemblied by companies working in the microwave domain. Specifically, with reference to the P/L configuration above mentioned, the following items are available by RHI:

- Antenna: a 15 cm diameter lens antenna produced by Millitech is currently available by RHI;
- Triplexer: a component with the required specifications has been developed by RHI and it is currently available;
- LNA: a Millitech's LNA (95 GHz) is available by RHI;
- Filter: a BPF (95 GHz) was developed by RHI and is currently available.

However, main items to be purchased are the following:

- SSPA: SSPAs produced by Quinstar, Northrop Grumman and Fraunhofer IAF are compliant with the transmitter specifications;
- Mixer: balanced mixer series MXP produced by Millitech are compliant with the required mixer specifications;
- Coupler: Millitech series CL3 3-port high directivity directional couplers are compliant with the required specifications;

- Power measurements block: specifications of such a component are compliant with those provided by Analog Devices (logarithmic detector amplifiers for both RF and IF applications) and by Miteq;
- On-board memory: currently, the most suitable product is the M-systems' (now SanDisk) Fast Flash Disk (FFD) 2.5" IDE disk.

6.4.6 ACTIVITIES TIME PLANNING

In this section, a preliminary time planning of the foreseen activities of detailed design, development, integration and test for Aero-WAVE P/L is provided. Figure 6-73 shows the Gantt diagram for Aero-WAVE P/L. The overall design, development, integration, test and verification timeline has been estimated in about 12 months. It has been divided in P/L detailed design, design subassembly, procurement, subassembly MAIT (Manufacturing, Assembly, Integration, Test), P/L MAIT.

ID	Nome attività
1	**Aero-WAVE - Overall Design and Development Timeline**
3	Payload Detailed Design
4	Design Subassembly
5	Procurement
6	Subassembly MAIT
7	Payload MAIT
8	
9	
10	
11	
12	
13	
14	
15	

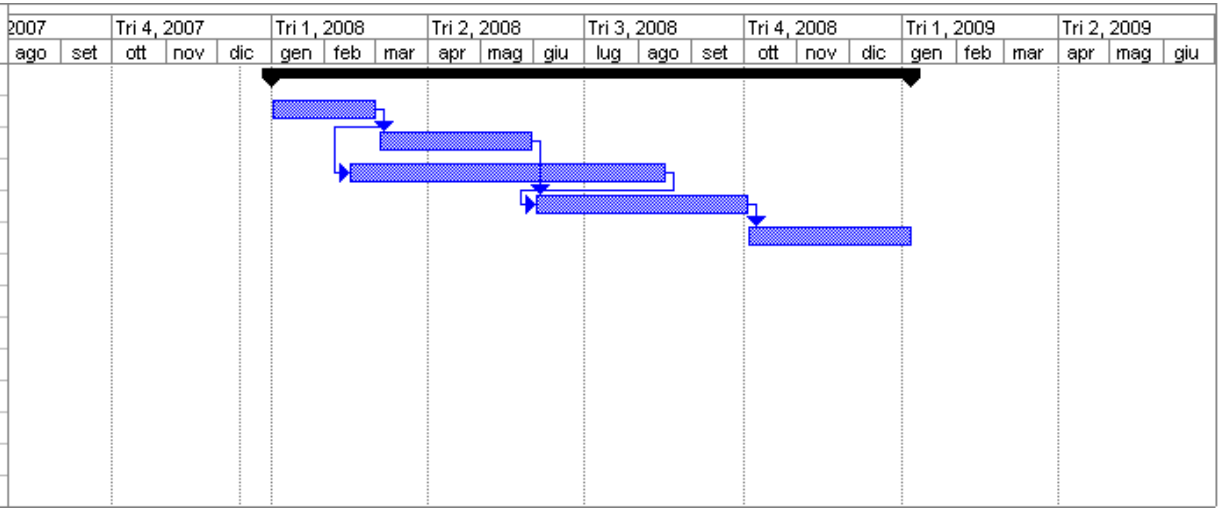

Figure 6-73: Aero-WAVE Gantt: foreseen planning of P/L design, development, integration and test

6.4.7 PAYLOAD COST EVALUATION

Scope of this paragraph is to define a preliminary evaluation of the costs related to development, manufacturing and test of Aero-WAVE P/L.

An estimate of costs has been derived in Table 6-48.

Cost Item - Aero-WAVE configuration 3	ROM Cost (kEuro)
Payload Hardware	163,20
Payload Design, Development, Integration and Test	309,60
Total	**472,80**

Table 6-48: ROM costs evaluation for Aero-WAVE P/L configuration

6.5 REFERENCES

[6-1] C. Capsoni, E. Matricciani, M. Mauri, "SIRIO-OTS 12 GHz Orbital Diversity Experiment at Fucino", IEEE Transaction on Antenna and Propagation, Vol.38, n.6, Pag.777-782, Jun. 1990.

[6-2] A. Paraboni et al., "The Main Results of the ITALSAT Propagation Experiment at 18.7, 39.6 and 49.5 GHz", 2nd Ka-band Utilization Conference, Florence, Italy, Sep. 1996.

[6-3] M. Ruggieri, et al., "The W band Data Collection Experiment of the DAVID Mission", Special Section of IEEE Transactions on AES on "The DAVID Mission of the Italian Space Agency", Vol.38, n.4, Pag.1377-1387, Oct. 2002.

[6-4] C. Bonifazi, M. Ruggieri, A. Paraboni, "The DAVID mission in the heritage of the SIRIO and ITALSAT satellites", IEEE Transaction on Aerospace and Electronic Systems, Volume 38, Issue 4, Pag.1371-1376, Oct. 2002

[6-5] A. Jebril, M. Lucente, T. Rossi, M. Ruggieri, "WAVE – A new Satellite Mission in W-band", IEEE Aerospace Conference 2005, Big Sky, Montana, March 2005.

[6-6] M. Lucente, T. Rossi, C. Stallo, M. Ruggieri, A. Iera, A. Molinaro, S. Pulitanò, 2008, "IKNOW: a Small LEO Satellite for W Band Experimentation", 26th International Communications Satellite Systems Conference (ICSSC), 10 - 12 June 2008, San Diego, CA.

[6-7] A. Jebril, M. Lucente, T. Rossi, M. Ruggieri, V. Dainelli, L. Zuliani, "New developments in the WAVE W-band mission", IEEE Aerospace Conference 2006, Big Sky, Montana, 4-11 March 2006.

[6-8] M. Lucente, E. Re, T. Rossi, E. Cianca, C. Stallo, M. Ruggieri, A. Jebril, C. Dionisio, L. Zuliani, "IKNOW Mission: Payload Design for In Orbit Test of W Band Technology", IEEE Aerospace Conference 2008, Big Sky, Montana, March 2008.

[6-9] A. De Luise, A. Paraboni, M. Ruggieri, "Satellite Communications in W-band: Experimental Set-up for Channel Characterization", IEEE Aerospace Conference, Big Sky, Montana, U.S., Mar. 2004.

[6-10] T. Rossi, M. Lucente, C. Stallo, E. Cianca, M. Ruggieri, G. Codispoti, L. Zuliani, "EHF Systems: Experimental Missions for Broadband Communications", European Conference on Antennas and Propagation (EuCAP), Berlin, Germany, March, 23-27, 2009.

[6-11] C. Sacchi, G. Gera, C. Regazzoni, "W-band physical layer design issues in the context of the DAVID-DCE experiment", International Journal of Satellite Communications and Networking, Vol.22, Pag.193-215, 2004.

[6-12] G. Galati, G. Russo, G. Dargaud, G. Pavan, Low Cost Digitalization of an X-band, non Coherent Weather Radar, IGARSS, Singapore, 1997.

[6-13] M. Lucente, E. Re, T. Rossi, M. Ruggieri, E. Cianca, A. Jebril, L. Zuliani, M. Albani, WAVE-A2: Towards New Frontiers of EHF Satellite Telecommunications, Ka and Broadband Communications Conference, Turin, Italy, Sep. 24-26, 2007.

[6-14] M. Lucente, T. Rossi, C. Stallo, M. Ruggieri, A. Iera, A. Molinaro, S. Pulitanò, 2008, "IKNOW: a Small LEO Satellite for W Band Experimentation", 26th International Communications Satellite Systems Conference (ICSSC), 10 - 12 June 2008, San Diego, CA.

[6-15] E. Re, M. Ruggieri, V. Dainelli, M. Ferri, Millimeter Wave Technology for Moon and Mars Exploration, IEEE Aerospace Conference, Big Sky, Montana, March 2008.

[6-16] Thales Alenia Space web site: http://www.thalesonline.com/space/

[6-17] Rheinmetall Italy web site: http://www.rheinmetall.it/

[6-18] United Monolithic Semiconductors, web page: http://ums.openkast.com/ums/home/home

[6-19] OMMIC web page: http://ums.openkast.com/ums/home/homepage.php

[6-20] Fraunhofer IAF web page: http://www.iaf.fraunhofer.de/

[6-21] QuinStar Technology Inc. web page: http://www.quinstar.com/

[6-22] Millitech Inc. web page: http://www.millitech.com/

[6-23] Northrop Grumman Corporation web page: http://www.northropgrumman.com/

[6-24] WiseWave Technologies Inc. (part of Ducommun Technologies) web page: http://www.wisewave-inc.com/index.html.

[6-25] R. Weber, et all. "A PLL-Stabilized W-Band MHEMT Push-Push VCO with Integrated Frequency Divider Circuit", Fraunhofer-Institute of Applied Solid-State Physics, Freiburg, Germany, 2007.

[6-26] Z. Lao, et all "31 GHz Static and 39 GHz Dynamic Frequency Divider ICs using 0.2 μm-AlGaAs/GaAs-HEMTs", Fraunhofer-Institute of Applied Solid-State Physics, Freiburg, Germany, 2000.

[6-27] M. Ferri, F. Serrano, V. Dainelli, F. Galati, "Millimeter-wave Technology for Airport Surface Movement Control", ESA Millimeter Wave Symposium, 2003.

[6-28] R. Battaglia, M. Ferri, V. Dainelli, F. Serullo, M. Demeo, "W-band Advanced Radar for Debris Early Notification from ISS", IEEE Aerospace Conference, Big Sky, Montana, Mar. 2003.

[6-29] A. Bosisio, P. Cambriani, V. Dainelli, A. Jebril, M. Lucente, S. Morosi, A. Pisano, L. Ronzitti, T. Rossi, M. Ruggieri, L. Scucchia, V. Speziale, "The WAVE Mission Payload", IEEE Aerospace Conference, Big Sky, Montana, Mar. 2005.

[6-30] A. Jebril, M. Lucente, T. Rossi, M. Ruggieri, L. Zuliani, "Aero-WAVE: A W-band preliminary test using HAP", IEEE Aerospace Conference 2006, Big Sky, Montana, 4-11 Mar. 2006.

[6-31] E. Cianca, M. Lucente, E. Re, T. Rossi, M. Ruggieri, C. Stallo, V. Dainelli, G. Codispoti, F. Marzano, V. U. Khattatov, "Aero-WAVE: a first step towards the characterization of W band", IEEE Aerospace Conference 2008, Big Sky, Montana, Mar. 2008.

[6-32] "High-altitude M-55 Geophysica aircraft Investigators" Handbook, Myasishchev Design Bureau, Third edition, Russia, 2002.

[6-33] F. S. Marzano, "Modeling antenna noise temperature due to rain clouds at microwave and millimeter-wave frequencies", IEEE Transactions on Antennas and Propagation, vol.54, Pag.1305-1317, 2006.

7 CONCLUSIONS

Advances in wireless technology such as 3G and later portable phones, IEEE 802.11/a/b/g (WiFi), and IEEE 802.11.16 (WiMAX) and exclusive subscriber growth for these applications have been triggering a big scarcity of available radio frequency resources in the microwave band.

The increasing demand for wireless connectivity and crowding of unlicensed spectra has pushed the regulatory agencies to be ever more aggressive in providing new ways to use spectra. In the past, the approach for spectrum allocation was based on specific band assignments designed for a particular service, as illustrated by the FCC's frequency allocation chart. Currently, this spectrum chart contains overlapping allocations in most frequency bands and seems to indicate a high degree of spectrum scarcity.

On the other hand, a new demand for increased capacity to handle much larger data, as uncompressed high definition video, has been rising steadily.

The unique possibility to satisfy this request is to look at EHF bands.

The millimeter wave band from 60-95 GHz offers large swathes of unlicensed and semi-unlicensed spectrum, which may well form the basis for the next revolution in wireless communication, in which wireless catches up with wires.

The recently allocated 71–76 GHz and 81–86 GHz bands provide an opportunity for LOS links with longer range and higher data rates, ideally suited for fiber replacement and backhaul applications.

The first part of my Ph. D work mainly has aimed at investigating the use of IR based communication systems, in particular the IR UWB transmission technique, to realise multigigabit/s communication beyond 60 GHz.

The purpose of my study has been to demonstrate that the IR UWB technology could provide different alternatives RF architectures more suitable for transmission beyond 60 GHz, both in terms of performance and robustness to the impairments of such high frequency bands and in terms of lower cost design.

In order to fulfil this objective, this work has showed how an IR UWB communication system is sensitive to typical hardware not idealities beyond 60 GHz and compares its performance with the ones of a more classical continuous wave communications system with FSK modulation.

One of the main problems of IR-UWB applied to beyond 60 GHz is that the over-sampling of such pulses requires extremely high-speed ADCs.

In accordance with the Nyquist theorem, the ADC sampling rate for digitizing a UWB signal at such high frequencies must be on the order of a few gigasamples/s. Even with the most modern process technologies, this constitutes a serious challenge. Most reported data converters operating at this speed employ interleaving, with each channel typically based on a FLASH converter. The latter is the architecture of choice for high-speed designs, but is not suitable for high-resolution applications. An n bit FLASH converter uses $2n$ comparators so its power and area scale exponentially with resolution. Among recently reported high-speed ADCs (>1 Gigasample) representing the state of the art none has a resolution exceeding 8 bits. The minimum number of bits needed for reliable detection of a UWB signal is, therefore, a critical parameter. If excessively large, it can render an "all-digital" receiver infeasible.

On the other hand, operations such as synchronization, equalization, demodulation and decoding are then performed in the digital domain, greatly enhancing the flexibility available to the designer. We would like to scale this "mostly digital" paradigm to multi-Gigabit speeds, in order to enable mass market multi-Gigabit WLANs and WPANs based on large amounts of unlicensed bandwidth available for communications beyond 60 GHz. The bottleneck in such scaling becomes the ADC: high-speed, high-precision ADC is either unavailable, or is too costly and power-hungry.

To counteract this problem, high speed but low precision ADCs are widely used. However, it has been seen that using low precision ADCs (1 bit in the worst case) results in severe degradations of the system performance.

Firstly, this work has analysed performance for an analog and n bit digital UWB receiver and compare them. Secondly, two solutions (i.e. channel estimation and adaptive coding and ignoring indecision bits) have been proposed based on the results described in 3.3.13.5 in order to improve the performance of the system with 1 bit ADC. Finally, four major non-idealities (gain mismatch, offset error, timing jitter and clock skew) have been modeled for M channels TI ADCs solutions in IR-UWB systems.

The design of novel radio architectures for EHF multigigabit/s communications could be considered as a preliminary useful step toward the exploitation of “beyond Q/V bands” frequencies to support forthcoming high-data-rate services demands, aiming at developing a multipurpose network-of-the-future that will integrate terrestrial and space systems.

In this scenario, the exploitation of such high frequencies represents the most suitable solution to develop a cooperative GII in order to guarantee the so-called “Gigabit Connectivity” through aerospace links making such a radio segment a potential “backbone on the air” for global wireless connectivity.

However, in this framework, one of the most important issues for the exploitation of frequency bands beyond 60 GHz (in particular of the W band) is the knowledge of the terrestrial propagation channel and satellite one.

Today, the performance behaviour of any solution for data transportation over W band frequencies across the Troposphere is still unknown, since still no scientific and/or telecommunication mission has been realized, either on an experimental basis or in an operating mode. This frequency band shows very interesting features for research purposes, being never used for telecommunication applications but being extensively used (in particular the 90-95 GHz range) in radio-astronomy and radar applications.

Therefore, future missions to the purpose of utilizing such a frequency band shall aim at performing a first empirical evaluation of the troposphere effects on the W-band radio channel and, at the same time, at determining the future methodologies to accomplish systematic measurements and gain much more information on such effects.

This attractive and challenging topic has represented the other key point of my Ph.D activities. They have been focused on design of future mission architectures for the exploitation of W band for satellite telecommunications purposes together with some preliminary P/L analysis. In particular, these activities have been carried in the frame of definition, design and performance evaluation of a Small LEO Satellite P/L mission, called IKNOW. The IKNOW mission definition has been driven by the need to develop the receiving/transmitting chain using MMIC devices, in order to fit cost, power and weight constraints, typically limited for a spacecraft.

In this study, technological critical items have been highlighted, focusing on the present state of the art and presenting some architectural choices.

In ths framework a preliminary useful step toward the W band exploitation in satellite telecommunications is represented by the analysis and the validation of a terrestrial link operating at those frequencies. Some experiments could give important feedback from the

technology point of view and also for the channel characterization: a terrestrial air link at W band can be considered representative of more challenging satellite to ground link operating at same frequencies. Specifically, a terrestrial link reproduces many of the dynamic atmospheric conditions experienced by a satellite link, allowing to evaluate how atmosphere affects signal propagation and to identify and test possible countermeasures such as PIMTs. Consequently, tests conducted on this terrestrial link would allow to quantify how to improve the performance of the communication systems operating at W band. This would constitute an expertise acquired on the field to be potentially extended to the future satellite links establishment.

On the basis of previously introduced scenario, a 96 GHz the feasibility study of a terrestrial point-to-point link with the capability to carry out transmission/reception experiments over a distance of around 7.5 Km between University of “Tor Vergata” and “Villa Mondragone” (Frascati) has been performed.

In conclusion, “beyond Ka-band” satellite systems, in particular W band ones, can be considered as a very important scientific research topic in the field of communication, being one of the key elements for the “heterogeneous network of the future”.

.

8 PUBLICATIONS BY THE AUTHOR

A. Publications on International Journals

1. E. Cianca, M. Lucente, T. Rossi, C. Stallo, M. Ruggieri, E. Morelli, "EHF Channel Sounding for Telecommunications Applications via HAPs and Balloons", Journal of the Italian Astronomical Society, 1st Workshop on Science and Technology Through Long Duration Balloons, Mem. S.A.It. Vol. 79, 932, 2008.
2. C. Stallo, E. Cianca, M. De Sanctis, T. Rossi, D. Valente, S. Mukherjee, M. Ruggieri, "UWB for Multi-gigabit Communications Beyond 60 GHz", Telecommunication Systems Journal, Springer US, ("under Review").
3. O. Stukac, C. Stallo, "The Eighth Siberian Conference on Control and Communications", IEEE Microwave Magazine, Volume 10, Issue 6, October 2009, pp. 146-148. Digital Object Identifier 10.1109/MMM.2009.933579.

B. Publications on Proceedings of International Conferences

1. S. Barbera, C. Stallo, G. Savarese, M. Ruggieri, S. Cacucci, F. Fedi, "A Geo-Referenced Swarm Agents Enabling System: Theory and Demo Application", IEEE First International Conference on Systems, Modelling and Simulation (ISMS 2010), January, 27-29, 2010, Liverpool, England, pp. 100-104, DOI: 10.1109/ISMS.2010.30.
2. C. Stallo, S. Mukherjee, E. Cianca, T. Rossi, M. De Sanctis, M. Ruggieri "On the Use of UWB Interface for EHF Satellite Communications", IEEE Aerospace Conference 2010, Big Sky, Montana, March, 6-13, 2010.
3. C. Stallo, S. Barbera, G. Savarese, M. Ruggieri, S. Cacucci, F. Fedi, "A Geo-Referenced Swarm Agents Enabling System for Hazardous Applications", UKSim 12th International Conference on Computer Modelling and Simulation, Emmanuel College, Cambridge University, (UK), March, 24-26, 2010. Product Number E4016. ISBN 978-0-7695-4016-0. BMS Number CFP1089D-CDR.

4. C. Stallo, E. Cianca, M. De Sanctis, T. Rossi, D. Valente, S. Mukherjee, M. Ruggieri, 2009, "UWB for multi-gigabit communications in EHF-band", Networking and Electronic Commerce Research Conference (NAEC), pag. 294-304, Riva del Garda, Italy, October, 8-11, 2009, ISBN 978-0-9820958-2-9.
5. C. Stallo, Lucente, T. Rossi, D. Valente, E. Cianca, M. Ruggieri, S. Barbera, 2009, "UWB concepts applied to W band Telecommunications", IEEE International Siberian Conference on Control and Communications (SIBCON) 2009, Tomsk, Russia, March, 27-28, 2009, ISBN: 978-1-4244-2007-0. Digital Object Identifier 10.1109/SIBCON.2009.5044832.
6. S. Barbera, M. Antonini, M. Ruggieri, C. Stallo, 2009, "Application of the SDR Technique to the GNSS world: improvements to realize a complete Receiver", IEEE International Siberian Conference on Control and Communications (SIBCON) 2009, Tomsk, Russia, March, 27-28, 2009, ISBN: 978-1-4244-2007-0. Digital Object Identifier 10.1109/SIBCON.2009.5044832.
7. T. Rossi, M. Lucente, C. Stallo, E. Cianca, M. Ruggieri, G. Codispoti, L. Zuliani, "EHF Systems: Experimental Missions for Broadband Communications", European Conference on Antennas and Propagation (EuCAP), Berlin, Germany, March, 23-27, 2009, ISBN: 978-1-4244-4753-4.
8. T. Rossi, E. Cianca, C. Stallo, M. Lucente, M. De Sanctis, M. Ruggieri, A. Paraboni, A. Vernucci, L. Zuliani, L. Bruca, G. Codispoti, "Experimental Italian Q/V Band Satellite Network", IEEE Aerospace Conference 2009, Big Sky, Montana, March, 7-14, 2009, ISBN: 978-1-4244-2621-8. Digital Object Identifier 10.1109/AERO.2009.4839339.
9. S. Marzano, T. Rossi, R. Giusto, M. De Sanctis, C. Stallo, E. Cianca, M. Ruggieri, D. Mortari, "Florad Mission: Millimeter Wave Atmospheric Remote Sensing through Minisatellites Flower Constellation", IEEE Aerospace Conference 2009, Big Sky, Montana, March, 7-14, 2009, ISBN: 978-1-4244-2621-8. Digital Object Identifier 10.1109/AERO.2009.4839338.
10. C. Stallo, M. Lucente, T. Rossi, E. Cianca, M. Ruggieri, A. Paraboni, C. Cornacchini, A. Vernucci, M.T. Nocerino, A. Ceccarelli, L. Bruca, G. Codispoti, M. De Sanctis, 2009, "TRANSPONDERS: Research and Analysis for the Development of Telecommunication Payloads in Q/V Bands", IEEE Aerospace Conference 2009, Big Sky, Montana, March, 7-14, 2009, ISBN: 978-1-4244-2621-8. Digital Object Identifier 10.1109/AERO.2009.4839341.

11. C. Stallo, E. Cianca, T. Rossi, M. De Sanctis, A. Vernucci, C. Cornacchini, L. Bruca, M. Lucente, "TRANSPONDERS: Effectiveness of Propagation and Impairments Mitigation Techniques at Q/V Band", Globecom 2008 – IEEE Workshop/EHF -AEROCOMM, "Exploitation of Higher Frequency Bands in Broadband Aerospace Communications", November 30 – December 4, 2008, New Orleans, LA, USA, ISBN: 978-1-4244-3061-1. Digital Object Identifier 10.1109/GLOCOMW.2008.ECP.12.
12. M. Lucente, T. Rossi, C. Stallo, D. Valente, M. Ruggieri, V. Dainelli, L. Ricci, "Preliminary Design of a Propagation Experiment for a RadioLink Analysis at W Band", Globecom 2008 – IEEE Workshop/EHF -AEROCOMM, "Exploitation of Higher Frequency Bands in Broadband Aerospace Communications", November 30 – December 4, 2008, New Orleans, LA, USA, ISBN: 978-1-4244-3061-1. Digital Object Identifier 10.1109/GLOCOMW.2008.ECP.10.
13. M. Lucente, T. Rossi, C. Stallo, M. Ruggieri, A. Iera, A. Molinaro, S. Pulitanò, 2008, "IKNOW: a Small LEO Satellite for W Band Experimentation", 26th International Communications Satellite Systems Conference (ICSSC), 10 - 12 June 2008, San Diego, CA.
14. C. Stallo, E. Cianca, F. S. Marzano, M. Ruggieri, T. Rossi, M. De Sanctis, M. Lucente, D. Cimini, M. Montopoli, A. Memmo, R. Ferretti, D. Mortari, "Florad Mission: Flower Constellation of Microsatellites for Millimeter-Wave Atmospheric Remote Sensing", IEEE Gold Remote Sensing, ESA-ESRIN, May, 22-23, 2008, Rome, Italy.
15. M. Lucente, C. Stallo, E. Re, T. Rossi, E. Cianca, M. Ruggieri, A. Jebril, C. Dionisio, G. Codispoti, L. Zuliani, "IKNOW Mission: Payload Design for In Orbit Test of W Band Technology", IEEE Aerospace Conference, Big Sky, 1-8, March, 2008, ISSN: 1095-323X, ISBN: 978-1-4244-1487-1. Digital Object Identifier 10.1109/AERO.2008.4526275.
16. E. Cianca, M. Lucente, E. Re, T. Rossi, M. Ruggieri, C. Stallo, V. Dainelli, G. Codispoti, F. Marzano, G.Belyaev, "Aero-WAVE: A First Step Towards the Characterization of W Band", IEEE Aerospace Conference, Big Sky, March, 1-8, 2008, ISSN: 1095-323X, ISBN: 978-1-4244-1487-1. Digital Object Identifier 10.1109/AERO.2008.4526274.

17. C. Stallo, S. Barbera, M. Lucente, T. Rossi, M. Antonini, M. Ruggieri, E. Cianca, 2008, "Advanced Space Systems Teaching in a Web Based Distance Learning Environment, Interactive Conference on Computer Aided Learning (ICL), Villach, Austria, 2008, ISBN: 978-3-89958-353-3.
18. M. Lucente, E. Re, T. Rossi, M. De Sanctis, C. Stallo, E. Cianca, M. Ruggieri, R. Winkler, A. Pandolfi, 2008, "Future Perspectives For The New European Data Relay System", IEEE Aerospace Conference, Big Sky, Montana, March, 1-8, 2008, ISSN: 1095-323X, ISBN: 978-1-4244-1487-1. Digital Object Identifier 10.1109/AERO.2008.4526322.
19. M. Lucente, A. Salomè, E. Limiti, M. Ferri, L. Fiorani, C. Stallo, M. Ruggieri, L. Zuliani, "PLATON: PayLoad for Advanced Telecommunication, Observation and Navigation", 2010 IEEE GOLD Remote Sensing Conference, Livorno, April, 29-30, 2010.

C. Papers accepted for publication on Proceedings of International Conferences

20. C. Stallo, S. Mukherjee, E. Cianca, M. De Sanctis, T. Rossi, M. Lucente, M. Ruggieri, "UWB for high bit rate communications beyond 60 GHz", IEEE International Conference on Personal Indoor Mobile Communications (PIRMC) 2010, Istanbul, Turkey, September, 26-29, 2010.
21. C. Stallo, S. Mukherjee, E. Cianca, M. Ruggieri, "Performance Analysis of an IR-UWB Transceiver Architecture for Multi-Gigabit/s LOS links in W Band", IEEE International Conference on Ultra-Wide Band 2010, Nanjing, China, September, 20-23, 2010.
22. C. Stallo, M. De Sanctis, M. Ruggieri, I. Bisio, M. Marchese, "ICT Applications in Green and Renewable Energy Sector", IEEE COPECH 2010 (First International Workshop on Collaboration tools for Preservation of Environment and Cultural Heritage), Larissa, Greece, June, 28-30, 2010 (Invited Paper).